Philips Research Reports

Volume 9

1954

CHRONOLOGICAL INDEX

PHILIPS RESEARCH REPORTS, VOL. 9

VOL. 9 NR 1 FEBRUARY 1954

Philips Research Reports

EDITED BY THE RESEARCH LABORATORY
OF N.V. PHILIPS' GLOEILAMPENFABRIEKEN, EINDHOVEN, NETHERLANDS

R 234 *Philips Res. Rep. 9, 1-41, 1954*

A HIGH-RESOLUTION MASS SPECTROMETER WITH VARIABLE-BANDWIDTH MEASURING CIRCUITS *)

by I. PELCHOWITCH

621.384.8

Summary

A high-resolution mass spectrometer of the magnetic-sector type is described. Following a general description of the instrument a detailed analysis and circuitry of the electronic part are given. This is planned so as to include the possibility of varying the time of observation whilst retaining a high sensitivity in the measuring circuits. Accordingly the component units are designed for static and for dynamic operation. The ion-accelerating voltage supply can give a voltage sweep variable in starting-voltage value, amplitude and time dependence. It is also constructed to have a low effective impedance to minimize the disturbing effects of induction and leakage currents. A special DC-coupled wide-band electrometer amplifier is described covering the frequency range 0-1000 c/s. The useful bandwidth can then be selected by the succeeding measuring units in order to have a high signal-to-noise ratio. The circuits of an oscillograph display of the ion currents are given. An added feature of the instrument is an improved space-charge emission regulator used in connection with a modified Nier-type ion source.

Résumé

Un spectrographe de masse à pouvoir séparateur élevé du type à secteur magnétique est décrit. Après une description générale de l'instrument, une analyse détaillée et le schéma de la partie électronique sont donnés. L'appareil est construit de sorte que l'on a la possibilité de faire varier le temps d'observation tendis que l'on garde une sensibilité élevée dans les circuits de mesure. Pour cette raison les éléments qui le composent sont conçus pour un fonctionnement statique aussi bien que dynamique. L'alimentation en tension accélératrice d'ions peut donner une tension de balayage variable dans sa tension de départ, dans son amplitude et par rapport au temps. Il est construit également pour avoir une basse impédance effective afin de réduire au minimum les effets perturbateurs de l'induction et des courants de pertes. Un électromètre amplificateur spécial à courant continu à large bande est décrit; il couvre la bande de fréquence 0-1000 c/s. La largeur de bande utile peut dès lors être choisie par le moyen des appareils de mesure qui suivent afin d'obtenir un rapport signal-souffle élevé. L'on donne les schémas des oscillogrammes des courants ioniques. Une caractéristique supplémentaire de l'instrument est un régulateur perfectionné à émission à charge d'espace utilisé en liaison avec une source ionique du type Nier modifié.

*) Part I of the author's thesis, University of Amsterdam, June 1953.

Zusammenfassung

Beschrieben wird ein hochauflösendes Massenspektrometer mit magnetischer Ablenkung. Im Anschluß an eine allgemeine Beschreibung folgen Einzelheiten über Wirkungsweise und Schaltung des elektrischen Teils. Dieser ist so gestaltet, daß es u.a. möglich ist, die Beobachtungszeit unter Beibehaltung der hohen Empfindlichkeit zu variieren. Die einzelnen Bauteile wurden daher sowohl für statischen als auch für dynamischen Betrieb eingerichtet. Die vom Speisegerät für die Ionenbeschleunigung abgegebene Spannung ist variabel in bezug auf Startspannung, Amplitude und Zeitabhängigkeit. Zur Herabsetzung der durch Induktion und Isolationsverluste verursachten Störeinflüsse wurde das Speisegerät so konstruiert, daß sich eine niedrige effektive Impedanz ergibt. Beschrieben wird ein spezieller, direktgekoppelter Breitband-Elektrometerverstärker mit einem Frequenzbereich von 0-1000 Hz. Um ein hohes Signal/Rauschspannungs-Verhältnis zu erhalten, ist die jeweils gewünschte Bandbreite durch die nachgeschalteten Messeinheiten wählbar. Dargestellt sind ferner die Schaltkreise einer Oszillographen-Anordnung zur Messung der Ionenströme. Ein weiterer Vorzug des Instrumentes ist der in Verbindung mit einer abgewandelten Nier-Ionenquelle benutzte verbesserte Raumladungs-Emissionsregler.

CONTENTS

1. INTRODUCTION

Mass spectroscopy is the field dealing with the separation and analysis of substances according to the mass of the constituent elements and molecules present. The most important principle used is that the time and space parameters of the trajectories in vacuum of charged particles in force fields depend on their m/e ratio: m being the mass of the particle, e its charge.

The numerous methods described in the literature for mass separation and analysis may be grouped into two distinct classes; one uses geometrical dispersion, the other dispersion in time. In the time system ions are collected *intermittently;* the different m/e ions have different times of flight along a path in a field of force and are thus separated. In the geometrical group ions are collected continuously while moving in a specific static or oscillating field of force; the different m/e ions are separated according to their discrete geometrical positions at the collecting boundary.

The geometrical class includes the earliest and most established as well

as some more recent systems. It includes the parabola system of Thomson[1]), who was the first to succeed in separating isotopes, and the velocity-focusing system of Aston [2]), [3]). To this class also belong the 180° direction-focusing system of Dempster [4]), the sector magnetic fields providing direction focusing based on the theory of Barber [5]), and the double focusing systems, direction and velocity, described by Bainbridge and Jordan [6]), Mattauch [7]), Jordan [8]) and others, all forming the basis for modern mass spectroscopy.

Among recent systems coming into the geometrical group we mention those with crossed electric and magnetic fields having perfect focusing properties as developed by Bleakney and Hipple [9]) and by Monk, Graves and Horton [10]) ("Trochotron"), and the "Omegatron" described by Hipple, Sommer and Thomas [11]). In the "Omegatron" an oscillating electric field perpendicular to a constant magnetic field is used, so that ions spiral out of an axis defined by the place of formation or entry of the ions, and the resonant conditions effect a geometrical dispersion in the maximum radial displacement of the different m/e ions. Separation is accomplished by placing a collector at a certain distance from the axis.

The time-dispersion group of spectroscopes is comparatively new. Stephens [12]), Cameron and Eggers [13]), and Keller [14]) made current pulses of ions all possessing the same kinetic energy travel along a tube so that the current pulses of the resolved m/e components arrive at a collector with a time dispersion. Goudsmit [15]) and Richards, Hays and Goudsmit [16]) replace the tube by a homogeneous constant magnetic field, and record the time of arrival of the resolved current pulses upon completion of an integral number of revolutions; in this way they take advantage of the perfect focusing properties in velocity and angle of this set-up. Hipple and Thomas [17]) have suggested the addition to this arrangement of a perpendicular electric field with a chosen time dependence, so that the time of flight increases while the geometrical dimensions remain unaltered, thus improving the resolution.

Heil [18]) lets a pulse of ions with constant energy travel along a cage which is being swept in voltage in the meantime, and the different m/e ions emerge with different energies as a consequence of their different times of transit. They are now ready for a simple separation.

Weisz [19]) mentions the use of particle accelerators as mass analyzers. Bennett [20]) has built a linear accelerator tube with a system of grids to which radio-frequency and DC voltages are applied. Ions are selected in a certain phase angle to the radio-frequency voltage (equivalent to pulsing) and with a definite time of flight, between the system of grids, that is mass dependent. Ions with the correct phase and mass gain energy and are collected.

Basically, the various systems should be judged according to two related criteria: their resolving power for mass, and the highest mean ion current that can be collected for that resolution. At the same time the overall dimensions should, of course, be considered.

The geometrical systems invariably use a geometrically defined ion beam. Restrictions are always imposed on the cross-section of this beam at the focal surface, or on the directional divergence of the beam; sometimes on both. Some systems also require a limited dispersion in the energy of the ions.

The resolving power in the geometrical mass spectroscopes is determined by these geometrical restrictions on the ion beam and the "effective length" of the path of the ions from entrance to collection. The mean ion current is strongly affected by the geometrical limitations on the beam and by the length of the path of the ions. Beams of high charge density are not always available and are difficult to produce, and the added space-charge forces disturb the functioning of the system. The length of the path influences the ion current by space-charge forces and by collisions of the ions with the remaining gas molecules.

The time systems on the other hand place in general less stringent limitations on the geometry of the beam. Resolution is dependent on the time definition of the arriving pulses of current. Higher resolution in m/e means a narrower time interval of the ion-current pulse with respect to the total time of flight. The mean ion current carried by the current pulse is limited by the ratio of the time interval of the current pulse to the repetition period.

Thus there is a general function correlating resolving power and mean ion current, the ion current decreasing when the resolution increases. The shape of the function is determined by the particular system and serves as the basis for comparing them.

A second point to be considered is that some set-ups for the field with its accessory instruments and geometrical arrangements are more difficult to realize and more expensive than others.

Finally the intended use of the instrument is of primary importance and the type of applications contemplated will largely influence our choice of the analyzing and separating systems.

Our purpose in designing a mass spectrometer has been to build a general-purpose instrument suited for measurements of relative abundance. It should be able to perform gas analysis in the usual way, and mass analysis up to mass 300. There should be a high degree of flexibility in source construction permitting the interchange of ion sources for study of special problems such as gas-discharge phenomena, etc. We also wished to include a device for varying the time of observation with the minimum loss of accuracy, thus permitting rapid analysis of minute amounts of gas mixtures and the study of transient changes in the sample.

The direction-focusing magnetic analyzer of the sector type is the most suitable for such a general-purpose instrument. It is economic in design and forms a unit by itself, so that it can be coupled to practically any ion source and detector arrangement. In the literature it is reported as being succesfully applied to exacting analytical work and absolute isotopic-ratio measurements (Nier [21]), Inghram [22]), etc.).

The next chapter contains a general description of the mass spectrometer we have constructed, while chapter 3 gives a detailed account of the electronic equipment. The mechanical construction was in general outline based on the spectrometer described in detail by Nier [21]).

2. GENERAL DESCRIPTION OF THE MASS SPECTROMETER DEVELOPED IN THIS LABORATORY

Fig. 1 shows the schematic lay-out of the instrument. The apparatus for handling the sample brings the substance under study into the ion source. In the ion source ionization of the material takes place under controlled conditions, and the ions formed are focused and accelerated by a system

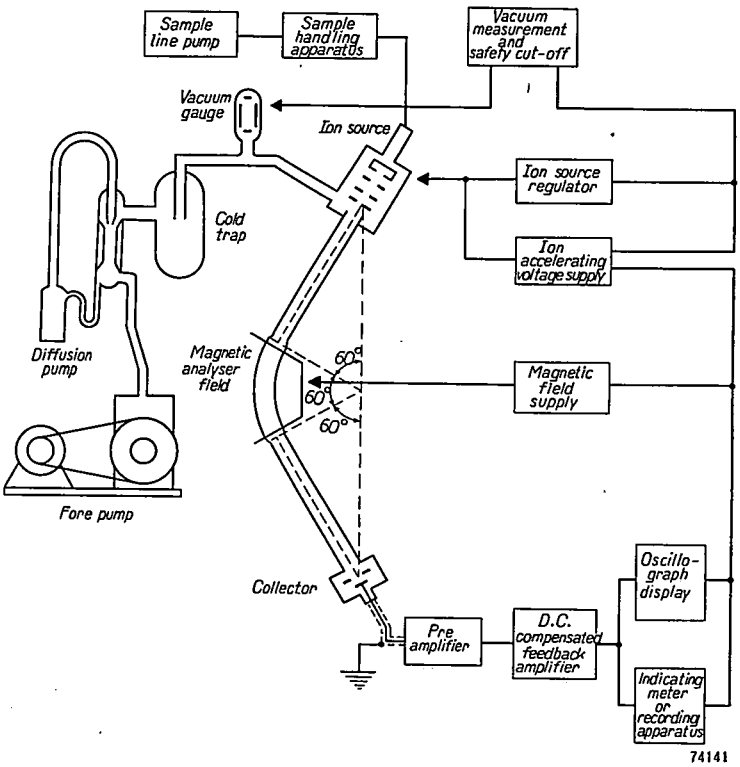

Fig. 1. Functional diagram of the mass spectrometer.

of slits fed by a stabilized high-voltage supply. The ions then enter the analyzer. The analyzer is a symmetrical 60° magnetic-sector analyzer. It consists of a highly evacuated, bent metal tube placed in a sector-shaped magnetic field, and fitted with entrance and exit slits for the ions that lie symmetrically on a straight line through the apex of the magnetic field. The magnetic field is generated between the pole shoes of an electromagnet fed by a stabilized current supply. The high vacuum in the instrument is established with the aid of a diffusion pump backed by a rotary forepump. The pressure in the tube is measured by a vacuum gauge that also operates an alarm and safety cut-off arrangement when the pressure exceeds a certain dangerous value.

After passing the analyzer, the ions are dispersed geometrically according to their momenta and those which pass the exit slit hit a collector plate

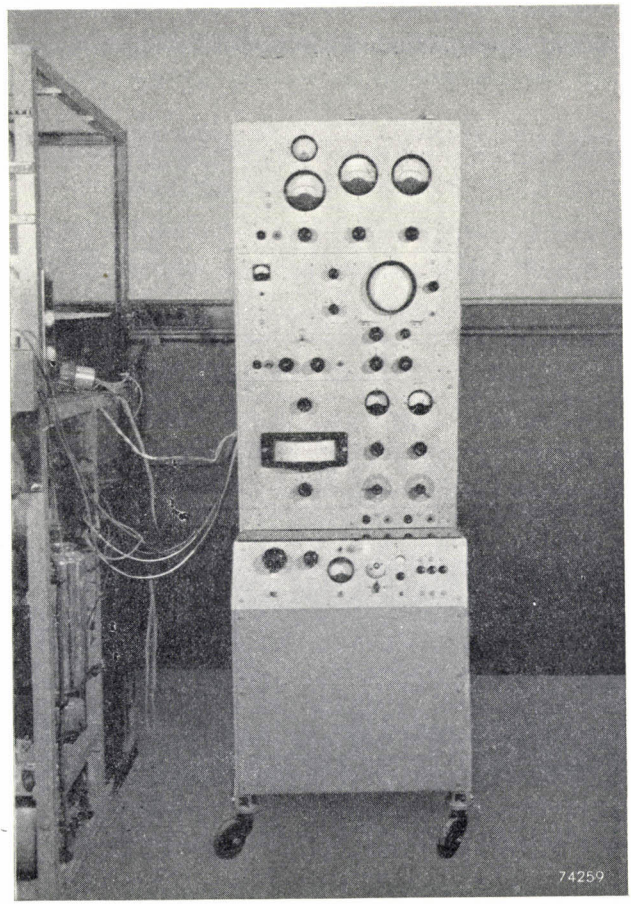

Fig. 2. Photograph of the electronic part of the mass spectrometer.

placed behind it. The ion current to the collector plate is amplified by a pre-amplifier and main amplifier constituting the electrometer circuit. The circuit has a feedback arrangement in order to obtain a flat frequency response over a wide band of frequencies. The output of the electrometer amplifier can then be indicated by instruments with a variable time constant.

Slowly changing ion currents may be indicated by a meter or a pen-and-ink recorder. Relatively rapidly changing currents, on the other hand, need quick recording instruments. A variable-bandwidth filter can be used in combination with a voltage amplifier and a cathode-ray tube, so that measurements on the screen may be made with maximum signal-to-noise ratio at the required bandwidth.

Fig. 2 shows the front panel of the complete electronic equipment of the spectometer. The upper unit is the ion-source regulator. The one below it contains the inverse feedback current amplifier, the filter, the voltage amplifier, and the oscillograph display. In the next unit are incorporated the ion-accelerating voltage divider and scanning arrangements, the magnetic-field current supply and range selector, and the meter for static measurement of ion currents. In the unit below the desk top are placed the degasing arrangements for degasing the vacuum system and ion-source filament, the vacuum meter and safety cut-off circuits, a main switch, and fuses and indicating lamps of the various circuits. The two lowest compartments contain most of the power supplies feeding the circuits of the instrument.

3. DETAILED DESCRIPTION AND ANALYSIS OF THE ELECTRONIC COMPONENTS

A. The ion-source regulator

When the mass spectrometer is used for relative abundance measurements, the recorded ion current at the representative mass numbers should bear a reproducible and known, preferably linear and independent, relation to the components of the substance under study. Next to the inlet system which must be carefully constructed (Hönig [23]), Halsted and Nier [24]), and Kistemaker [25])), the ion source, where the material is ionized and the ions accelerated into the analyzer, is the most important and complex part of the instrument.

Direction-focusing instruments, such as the magnetic sector we are using, must make use of ions with a low energy dispersion when resolving a mass spectrum. One of the most satisfactory methods used for producing constant-energy ions, is electron bombardment of the molecules of the substance in the gaseous state and subsequent acceleration of the ions produced.

We used a modified Nier [21]) source given schematically in fig. 3. Our analysis and circuit design will be confined to this type of ion source. A steady electron beam of nearly uniform energy is made to traverse the ionization chamber I. The electrons are emitted by a hot tungsten filament F and controlled by the grid-slit system G_1-G_2, S. A small magnet is used to produce a field coaxial with the beam in order to line up the electrons.

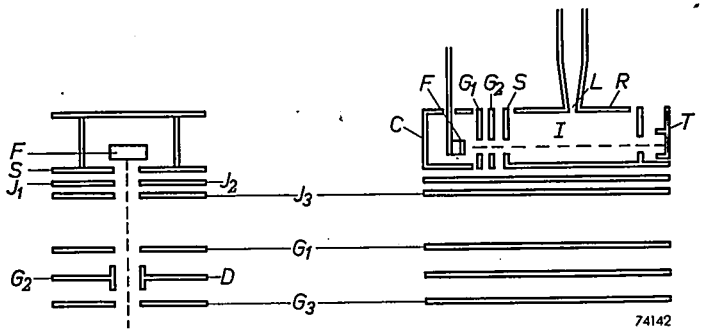

Fig. 3. Schematic drawing of the ion source.

After traversing the ionization chamber the electron beam passes a slit on the opposite side and is collected onto a small plate T referred to as the trap. The gas molecules flow into I through the leak L and become ionized upon intercepting the electron beam. The ions formed are drawn out of the ionization chamber through a slit in S. The following system J_1-G_3 serves to align and accelerate the ions into the analyzer system.

The exact mechanism taking place in the ion source is not yet completely described in the literature. A large number of effects are related to one another and depend in a complicated way on many factors, such as the ionizing electron beam, the initial velocities of the ionization products, the magnetic and electric fields, the geometrical arrangements. Many of these effects are different for the different types of ion. When trying to develop a reproducible ion source, random variations must be eliminated from the factors that affect the efficiency of formation of the ion beam from the gas molecules.

The first thing to be considered is the ionizing electron beam. The energy of the electrons must be controlled, as ionization and dissociation efficiencies of molecules depend on it. The density and position of the electron beam with respect to the geometry of the ionization chamber have a pronounced influence on the efficiency of collection of the ions. Jordan and Coggeshall [26]) have calculated the paths of electrons and ions in the ionization chamber under the simplifying assumptions of uniformity of field, zero initial velocities of the ions, homogeneous electron beam, etc. Ions formed in the

electron beam have to pass through a system of slits before being beamed into the analyzer. They move in crossed electric and magnetic fields. The position of the electron beam influences the "solid angle of collection" for the ions. Coggeshall [27]) further supplements the discussion by bringing into account the effect of the initial velocities of the ions due to thermal or dissociation energy on their chance of passing through the slit system. Similar considerations were brought forward by Washburn and Berry [28]). The geometrical and density distribution of the electron beam has a marked effect on the efficiency of formation of the ion beam, which becomes more pronounced with higher initial velocities.

This leads to the conclusion that the electron beam has to be free from random variations in energy, in density distribution, and in geometrical position with regard to the ionization-chamber boundaries.

The electron beam is emitted by a hot filament and accelerated and beamed by slit systems and a coaxial magnetic field. The emission from the filament may vary with line drifts and surface effects of gases (Caldecourt [29])). Usually the current to the trap is measured to indicate the intensity of the electron beam. Yet this total current does not fully specify the ion-forming efficiency of the electron beam. When relying on the reading of the trap current as the only indication, care must be taken that changes in the distribution of the electrons are not too great. The surface changes of the filament might be localized and beaming the electrons might introduce density and position changes while the trap current would be still constant. The situation is especially dangerous when the ion source is situated in a weak collimating magnetic field and when the emission control of the filament is effected by space charge. The method of controlling the filament emission may change the angle distribution of the electrons entering the ionization chamber and thus cause a displacement of the electron beam inside. When using a magnetic field of 200 gausses, the addition of 1 eV to the energy of the electrons in a perpendicular direction will give a spiralling radius of the order of 0·15 mm as compared with a distance of a few millimeters of the electron beam from the exit slit of the ions.

The next thing to consider is the temperature of the ion source. The effect of temperature on the absolute and relative abundances of the ions has been studied by Fox and Hipple [30]), Stevenson [31]), and Berry [32]). According to Stevenson, temperature effects occur in several operational stages of the ion source. The flow of the molecules through the ionization chamber is diffusive and the number of molecules present decreases with the temperature as $T^{-1/2}$. The second effect is the change in the relative probability of formation of the different groups of representative ions of the molecule. A rise in temperature causes a rise in the internal energy

(vibration, etc.) of the molecules favouring formation of ions by dissociation. This effect is most pronounced in complex molecules. The third effect is a change in the initial kinetic energy of all ions formed. The change in initial velocities of the ions influences the chance of collection and beaming as discussed before [27]), [28]). Some temperature coefficients of specific ion currents of organic molecules are given in the above references [30]), [31]), [32]), and they may amount to high values.

Thus it is necessary to control the temperature of the ion source within close limits. As the heat transfer in the ion-source assembly is slow, temperature equilibrium is reached slowly. When the filament emission is controlled by the filament current, special attention must be paid to this factor. From this point of view it seems desirable to employ emission-control systems which keep the filament temperature constant. It was therefore decided to employ space-charge control of the electron beam, while keeping the temperature of the ion source constant through constant current supply of the filament.

Space-charge control of filament emission has been described by Winn and Nier [33]), Reinders [34]) and Caldecourt [29]). Yet when we tried the circuits and slit arrangements advised in these publications, we met with some difficulties. In the first two references [33]), [34]) the quantity kept constant is the total emission of the filament. We found that when this is done by space-charge control, the trap current still varies with filament temperature or because of surface poisoning. The change in the electric field in the electron gun brings about a change in the distribution of the electron current to the different electrodes. Measuring the trap current for control should therefore be more direct and safe and this is done in the system used by Caldecourt [29]). When we tried this system using plates with a slit for control, the trap current could be kept constant to a high degree but the ion current itself still varied with the emitting condition of the filament.

We believe this is caused by a change in the angle distribution of the electron beam entering the ionization chamber which in turn causes a change in the ion current as discussed before. The change in direction of the electron trajectories can be explained by the highly distorted electric field in the vicinity of the slit in the control plate. The effects should be especially pronounced when the collimating magnetic field in the region of the ion source is low (of the order of 100 gausses). A marked improvement in the operation of the regulator then followed when the slits were covered with a grid network so that the electric field became more homogeneous. An extra gain followed from the fact that the transconductance of the control grid for trap current increased, thus necessitating a smaller change in the electric field for the compensation of emission deficiency.

The filament current was kept constant by feeding it from a stabilized AC power supply. The same power supply serves the filaments of all tubes where DC drifts of grid-to-cathode potential are important. The schematic diagram of the supply is given in fig. 4.

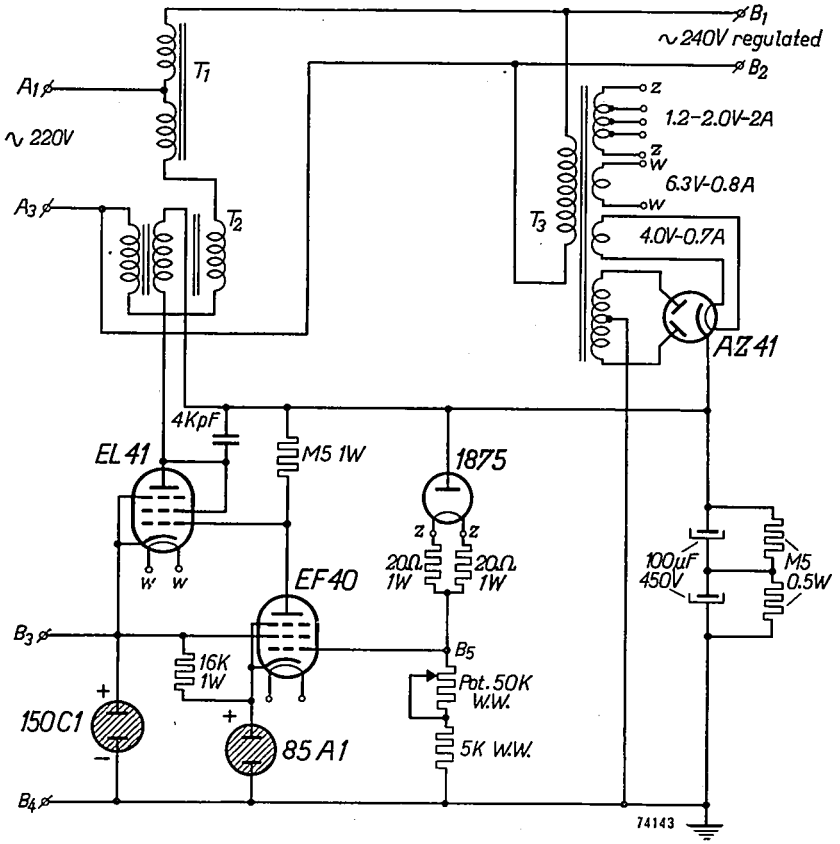

Fig. 4. Stabilized AC power supply *).

The r.m.s. value of the output voltage is measured by means of the emission current of a temperature-limited diode. Philips 1875 H.V. diode was found suitable for the purpose. The time drift of emission attains a very low value after several hours of operation. It is heated to a lower temperature than in its normal operating condition. The emission current develops a voltage over a resistance and this is compared with the voltage of a stabilizer tube 85A1. Deviations, amplified by a two-stage amplifier,

*) In some of our diagrams the values of resistors has been indicated as follows 39 k = 39 kΩ; M32 = 0·32 MΩ; 5M32 = 5·32 MΩ.

control the current through the DC coil of the transductor T_2, which in turn regulates the output of the auto-transformer T_1. A potentiometer control and taps on the feeding transformer of the measuring diode are included for bringing the circuit into the correct operating condition.

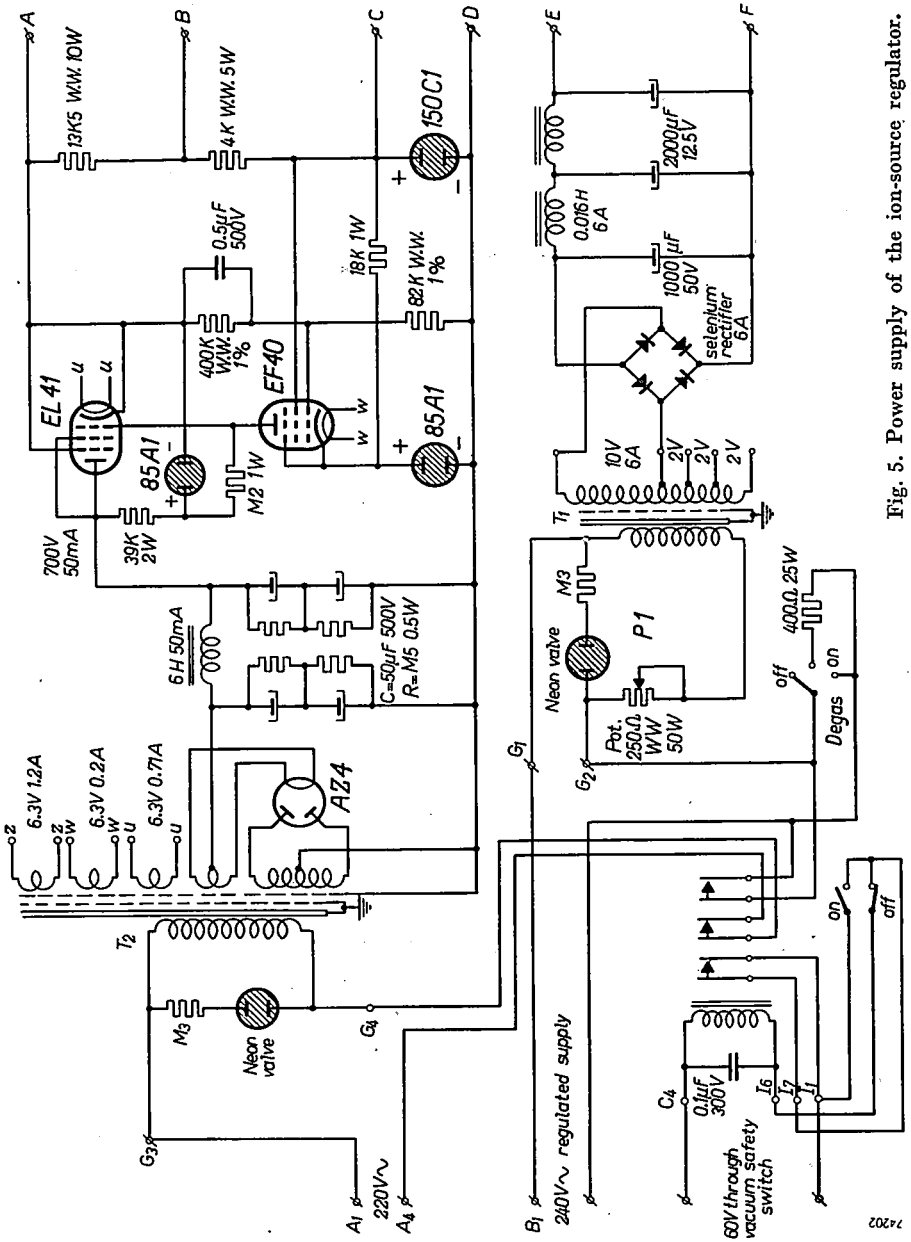

Fig. 5. Power supply of the ion-source regulator.

Stabilizer tube 150C1, apart from serving as a reference voltage in the amplifier, also indicates by its light output that the right current is flowing through the control coil of the transducer. The circuit gives a gain factor >100, sufficient for the purpose. Figs 5 and 6 give the schematic diagram of the power supply and circuit of the ion-source control system.

The filament of the ion source is fed with a rectified current. This is necessary, as the use of 50-c/s current gives a modulation of the electron-beam intensity and consequently of the ion current ($\approx 15\%$) with a 100-c/s frequency. This disturbs the measurements of ion current when the measuring bandwidth is of the same order or higher than this frequency. The alternating current to the rectifier unit is supplied from the stabilized AC power supply described above. Taps on the secondary of T_1 and the fine adjustment of the primary current by means of P_1 serve to regulate the temperature of the filament.

The operating voltages of the ion-source electrodes are taken from a stabilized power supply. By means of P_2, the energy of the electron beam in the ionization chamber is adjusted. It determines the voltage of the ionization-chamber box with respect to the middle of the filament. This voltage is supplied by a cathode follower ($\frac{1}{2}$ ECC40) and is thus coming from a source of low impedance. It can therefore still function with a certain amount of leakage current and it also serves as a low-impedance link to the ion-accelerating voltage supply for the induced 50-c/s ripple. The electron-beam energy is measured by a meter. A $\frac{1}{2}$ ECC40 serves as a series diode to protect the meter from reversed-polarity currents. The potentiometer P_3 is used to fix the voltage of the trap against the ionization box, and this setting is arranged so that it does not change with changes of P_2.

The trap current is directly measured by a μA-meter. Its setting is determined by the contactor C_1. In position "*0*" the necessary connections are so made that the operating conditions of the electron gun are fixed and not regulated. The first grid of the gun, fed via a cathode follower serving as a low-impedance source, is brought to a voltage near that of the second grid which is always kept at about 80 V positive with respect to the filament. In this position the electron beam intensity is determined by the condition of the filament. In positions "*1*" and "*2*", the trap current is regulated by the voltage on the first grid. A differential amplifier compares the voltage drop of the trap current over fixed resistors to the voltage of a stabilizer tube 85A1, while the output of the amplifier in turn controls the variations in voltage of the control grid. In this regulating position, movements of P_2 somewhat change the conditions of reference of the differential amplifier, and this is reset by adjustment of P_4. At the resistance values given, the trap current is stabilized at 100 μA in position

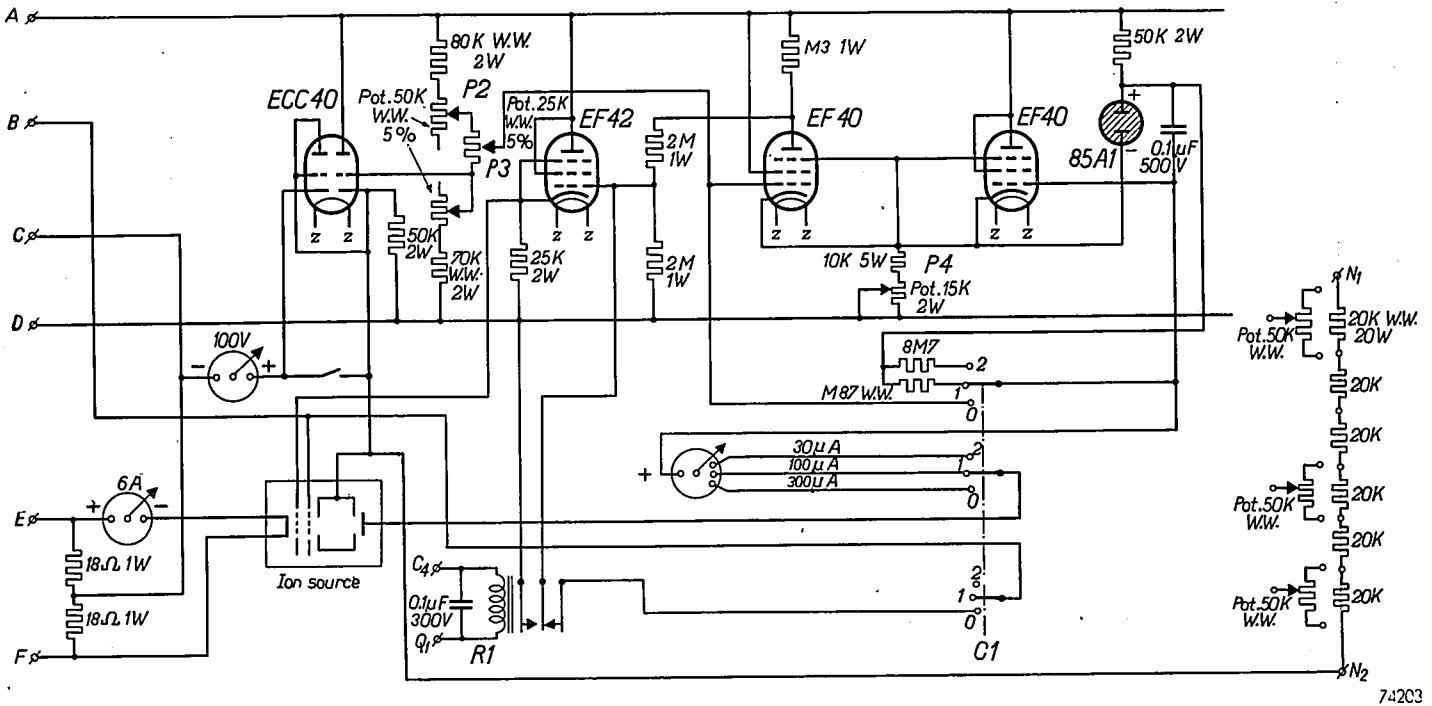

Fig. 6. Ion-source regulator-amplifier circuit.

"*1*" and 10 μA in position "*2*". A cut-off of the electron beam and, by this, of the ion current is achieved by means of R_1.

The ion-accelerating voltage supply is connected at N_1-N_2. The potential divider N_1-N_2 is used for collimating the ion gun. The unit is elevated to a high voltage, and accordingly all components should be properly insulated and protected. The unit is switched on by means of push-buttons and a relay that opens when the vacuum-safety switch operates. In this position the filament can still be heated up for degasing by the "Degas" circuit.

The ion-source control, with the above circuit and the slit-grid construction, was first tried out by varying the temperature of the filament. The mass spectrometer is tuned to collect the ion current of a chosen mass particle, and changes in this current are noted with variation of the filament current. This is a direct check on the operation of the regulator without involving gas-flow considerations, etc. This was done at several settings of the electron-beam energy, as they influence the working conditions of the electron gun. The collimating magnetic field in the ion-source region is 150 gausses.

Table I gives some results of measurements. Filament current was changed over a wide range: from 5·1 A to 6·1 A. The stabilizer was adjusted to have an electron current of 100 μA to the trap electrode. The percentage change of ion current was then measured at several settings of the electron-beam energy. The measured ion current was of Xe 132. When changing the filament current, the voltage drop over the directly heated filament changes from 2·6 V to 3·6 V for the above current values and this involves a change in the energy distribution of the electrons in the beam and influences the ion current through the dependence of the ionization efficiency of the gas molecules on the electron energy. Therefore an added column gives the percentage change of ion current with a +2V change in

TABLE I

Measurements of changes in ion current produced by changes in filament heating current.

Electron energy in volts	% change in ion current with +2V energy change	% change in ion current with filament current change; 5·1A to 6·1A
90	— 0·9	+0·1
60	— 0·4	+0·5
44	—	+0·1
30	+ 7·3	+1·8
20	+17·0	+4·3

average energy of the electron beam as measured between the ionization chamber and the middle of the filament.

Similar results are obtained when the regulator is adjusted to give 10 μA electron current to the trap. The rise in the percentage of the ion current with filament current at low values of the electron energy can be partly accounted for by the shape of the ionization-efficiency curve.

The voltage changes of the control grid that are necessary to compensate for emission from the filament were studied for the case where the filament temperature was varied through the filament current. With a trap current of 100 μA and an electron-beam energy of 90 V, the voltage of the first grid changed from + 17·0 V to + 16·0 V when the filament current was changed from 5·1A to 6·1 A.

The voltage of the first grid was then used to indicate the degree of poisoning of the filament surface by specific gases. In this way the minimum operating temperature of the filament could be chosen for any expected partial pressure of the poisoning gas in the sample analyzed. The effect of 10^{-5} mm Hg pressure of O_2 in the mass-spectrometer tube could be compensated by a rise in filament current from 5·2 A to 5·6 A. The emission of the electron current from the filament in our case is space-charge limited. The added gas molecules affect both the space charge and the filament surface.

B. The ion-accelerating voltage supply

The ions formed in the ionization chamber are accelerated and beamed into the analyzer section through the ion slits. The voltage applied to the slits is taken from a stabilized high-voltage supply. The degree of stability needed and the method of scanning the voltage are determined by the limit of the resolving power of the instrument and by the technique of measurement.

When the ions are subjected to a constant volt-energy acceleration and introduced into the analyzer, a mass spectrum issues. The mass of the "normal" particle passing the central trajectory will be given by the formula for the curvature of the path in the magnetic field:

$$R = \frac{(2mV/e)^{1/2}}{H},$$

where R is the radius of curvature of the instrument, m the elementary mass, e the elementary charge, H the magnetic field, and eV the energy.

Scanning of the accelerating voltage will move the ion mass-spectrum lines over the exit slit. The current pulses arriving at the collector behind this slit can be described by a peaked curve giving the current intensity as a

function of the accelerating voltage. The actual shape of this curve will depend on the ion optics (the radius of curvature, the dimensions of the slits and the aberrations), on the velocity scattering of the ions in the ion source, and perhaps on gas scattering and space charge.

The dispersion of a symmetrical magnetic sector is given (Walcher [35]) by

$$d = 2R\delta,$$

where d is the distance at the focus boundary between the images of two particles slightly differing in momentum (mv, m_0v_0), and δ is given by

$$mv = m_0v_0\,(1 + \delta).$$

With particles of one mass, varying the accelerating voltage gives

$$\delta = \frac{mv}{m_0v_0} - 1 = \frac{v - v_0}{v_0} \approx \frac{\Delta v}{v} = \frac{\Delta V}{2V},$$

since

$$\frac{mv^2}{2} = eV.$$

The distance between two images of particles differing ΔV in accelerating voltage will therefore be

$$d = 2R\frac{\Delta V}{2V} = R\frac{\Delta V}{V}.$$

Scanning the accelerating voltage moves the image of width a of the entrance slit over the exit slit of width b, and the ion current will be collected within a voltage range ΔV given by

$$\Delta V = V\frac{d}{R} = V\frac{a + b}{R}.$$

To this should be added the voltage scattering of the ions V_s, giving

$$\Delta V = V\frac{a + b}{R} + V_s.$$

V_s is a complicated function of the accelerating voltage, and depends on the initial conditions of the ions formed in the ionization chamber.

The degree of stability needed in the accelerating voltage can be estimated with the aid of the last equation and the constants of the instrument. In our case: $R = 15$ cm, $a = b = 0{\cdot}025$ cm, $(a + b)/R = 1/300$. In order to be able to measure the shape of the current pulse with good accuracy we need several stable measurements at stable voltage points. With a stability of 1/9000 we can have about 30 stable positions.

When scanning mass spectra electrically the accelerating voltage is varied as a certain function of time. The resolved ion currents will then appear as current-time pulses in the amplifier stages. The frequency components of the current pulse will therefore depend on the time variation of the accelerating voltage, as seen roughly from the above equation. It is difficult to find a voltage-time dependence that will give current pulses of equal bandwidth all over the voltage range. The amplifier and recording circuits should therefore be selected with a flat-response frequency curve covering the frequency band of all the current pulses.

A voltage time dependence of $V = V_0/(1 + at)$ will give a linear mass scale in time as seen from the curvature formula. An arrangement like this is not easy to realize. Instead we will take an exponential function $V = V_1 - (V_0 + V_1) \exp(-t/RC)$ which is realized by charging a capacitor C through a fixed resistor R.

There are extra technical demands to be placed upon the voltage supply. It should have a low AC impedance, to reduce the AC ripple induced by the ion-source stabilizer. It should also have a comparatively low DC impedance to be able to feed the potentiometer arrangement supplying the accelerating voltages to the ion slits. We meet both demands by having a cathode-follower circuit at the feeding point. An RC network is placed in the grid circuit of the cathode follower to give the exponential voltage scanning. The circuits of the accelerating supply and scanning arrangement are given schematically in figs 7 and 8.

Fig. 7 shows the circuit of the stabilized power supply which consists of two units. The negative supply is needed to serve as the return point for the grid and cathode resistor of the cathode follower, and as a stable reference voltage for the positive high-voltage supply.

The stability can be calculated in the following way. The gain factor of the amplifier $(V_1 - V_2)$ between the anode of V_1 and the first grid of V_2 is

$$\mu_{12} = S^2 R_a (1 + S^2 R_{\text{ef}})^{-1} \mu^1 g_2 g_1$$

where S^2 is the mutual conductance of V_2, $\mu^1 g_2 g_1$ is the gain factor in V_1 between grid 2 and grid 1, R_{ef} is the effective resistance of the reference tube 85A1 in the cathode of V_2, and R_a is the anode resistance of V_1.

From the valve data we calculate $S^2 = 0{\cdot}5$ mA/V; $\mu^1 g_1 g_2 = 16{\cdot}5$; $R_{\text{ef}} = 360\ \Omega$, and therefore $\mu_{12} = 1400$.

A voltage change ΔV_{in} at the anode of V_1 will be accompanied by a voltage change ΔV_{out} at E_3, given by the equation

$$\Delta V_{\text{in}} = \mu_{12} \left\{ \Delta V_{\text{out}} \frac{R_2}{R_1 + R_2} + \Delta V_{\text{in}} \frac{R_1 R_2}{R_1 + R_2} \cdot \frac{1}{R_5 + R_1 R_2/(R_1 + R_2)} \right\},$$

taking into account the feedback coupling through R_5. Rearranging gives

$$\left\{1-\mu_{12}\frac{R_1R_2}{R_1+R_2}\cdot\frac{1}{R_5+R_1R_2/(R_1+R_2)}\right\}\Delta V_{\text{in}}=\mu_{12}\frac{R_2}{R_1+R_2}\,\Delta V_{\text{out}}.$$

With a 5% accuracy in choosing R_5 and in calculating μ_{12}, the first factor on the left of the equation can be made smaller than 1/10, and then

$$\frac{\Delta V_{\text{out}}}{\Delta V_{\text{in}}}<\frac{R_1+R_2}{10\,\mu_{12}\,R_2}.$$

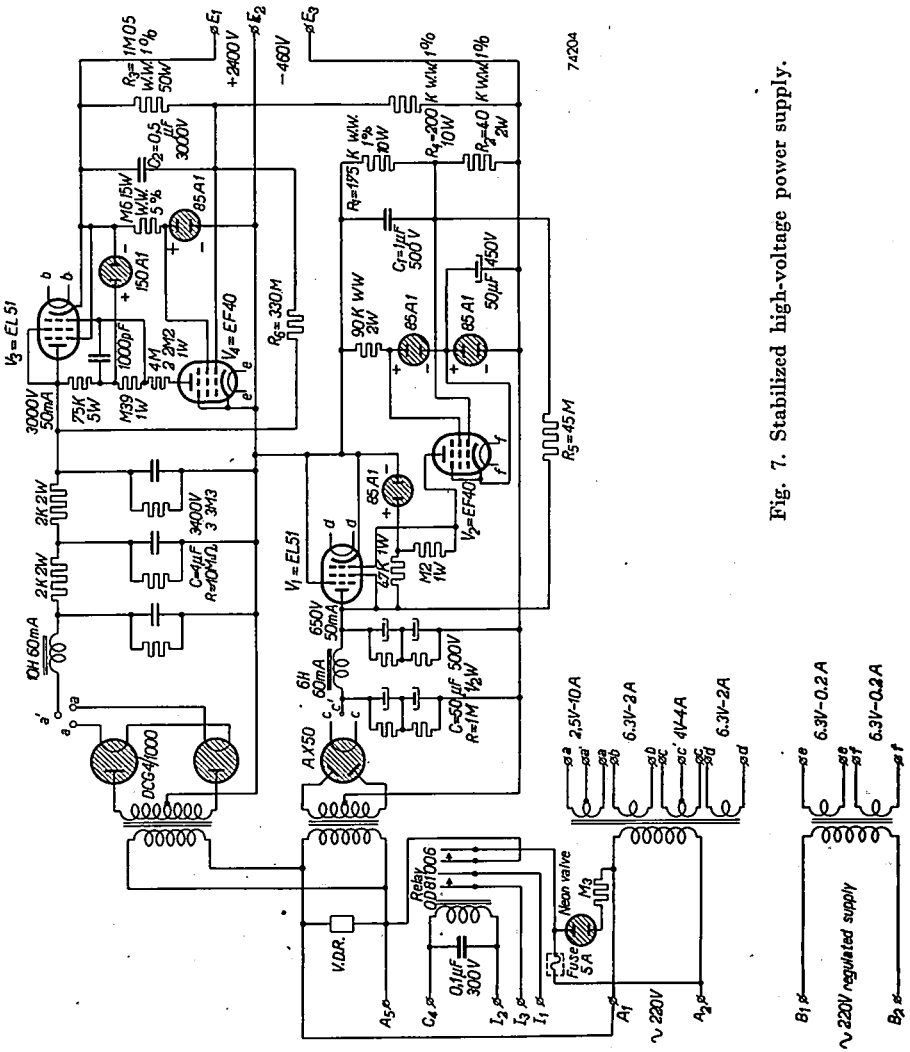

Fig. 7. Stabilized high-voltage power supply.

Insertion of the numerical values gives

$$\frac{\Delta V_{out}}{\Delta V_{in}} \approx \frac{1}{2800}.$$

V_{out} at E_3 will therefore be stable up to 1/30000 with a 10% change in V_{in}.

The filament current of V_2 is fed by a regulated supply. The reference tube 85A1 has a good time stability after the time required for warming

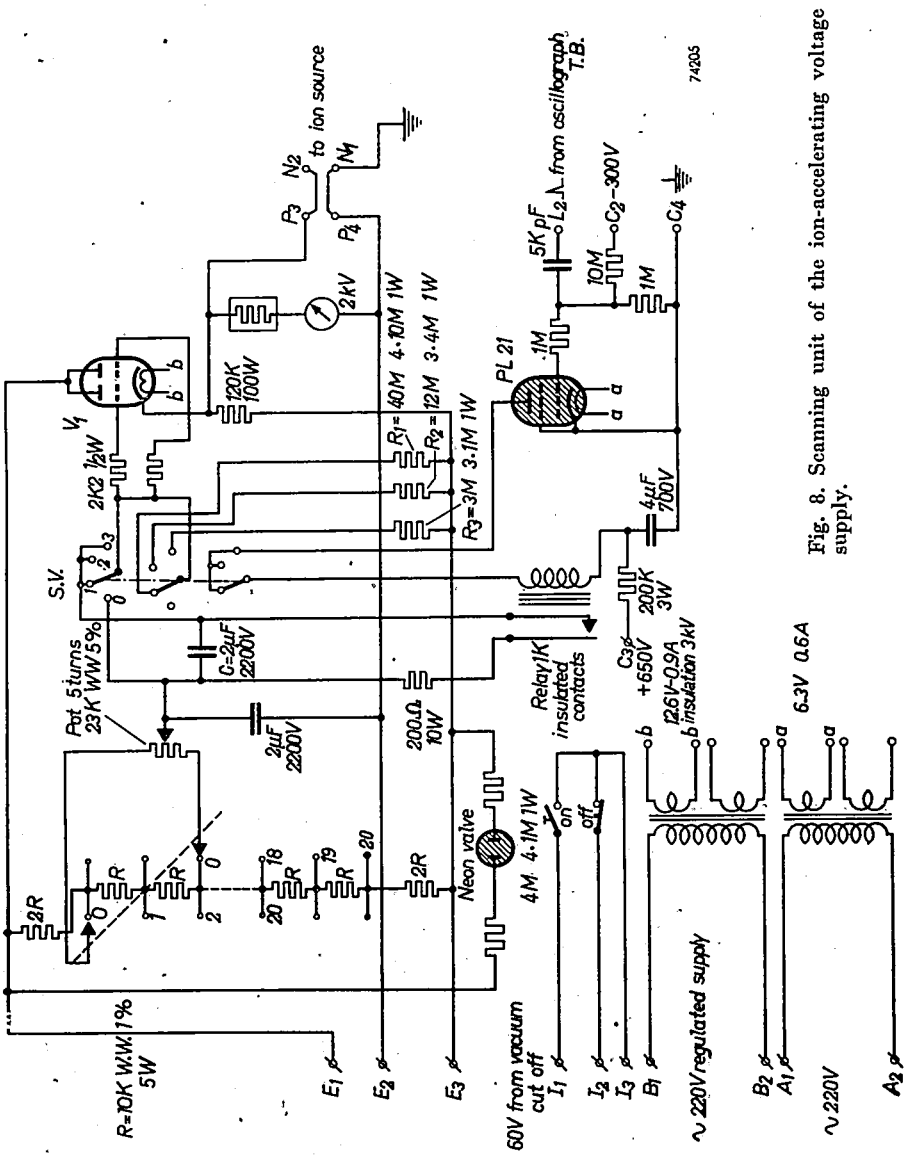

Fig. 8. Scanning unit of the ion-accelerating voltage supply.

up. The critical resistors are chosen with higher wattage rating. An analogous computation is done for the positive high-voltage supply. Using the same notation, the voltage gain of the amplifier (V_3-V_4) is given by

$$\mu_{34} = S^4 \frac{\mathrm{M39}}{1 + (4{\cdot}4\mathrm{M}/R_i^4)} \mu^3 g_2 g_1$$

when R_i^4 is the internal resistance of V_4.

From the valve data we calculate the numerical values

$$S^4 = 0{\cdot}5 \text{ mA/V}; \ \mu^3 g_2 g_1 = 16{\cdot}5; \ R_i^4 = 7{\cdot}5 \text{ M},$$

and the voltage gain μ_{34} is 2000. Applying the feedback connection through R_6 with the necessary accuracy gives a regulation factor of

$$\frac{\Delta V_{\text{out}}}{\Delta V_{\text{in}}} \approx \frac{R_3 + R_4}{R_4 \,.\, 10\mu_{34}} \approx \frac{1}{3300}.$$

The filament of V_4 is fed by a regulated supply. The 50-c/s ripple of the supply is controlled by the amplifiers, and the amplification factor is stepped up by inserting the capacitors C_1 and C_2. Extra filtering was found necessary in the voltage divider in fig. 8 to avoid excessive pick-up. The 50-c/s ripple measured at the output points P_3P_4 was then less than 10 mV. Fig. 8 gives the voltage divider and scanning arrangement. The four-position contactor *S.V.* connects the grid of V_1 either directly to the voltage divider or to the exponential voltage generated in the capacitor C and in the three charging resistors R_1, R_2, R_3. The re-cycling of the voltage waveform is effected by discharging the capacitor C through the contacts of a mechanical relay. The relay is operated by a current pulse, which is generated by discharging a loaded condenser through the coil of the relay via a thyratron. The thyratron is ignited by a synchronizing voltage pulse that comes from the time base of an oscillograph. The mechanical method of re-cycling has the advantage of making possible very small voltage swings on the capacitor C and of having the relay unit and synchronizing-pulse source insulated from the switching point.

The tube V_1 connected as a cathode follower is an experimental one. It is indirectly heated by a regulated supply and can withstand the high anode voltage required. A directly heated tube would give 50-c/s and 100-c/s components in the cathode voltage.

The complete voltage supply is a seperate unit, insulated for 3 kV to earth. This feature allows either side to be connected to earth by interchanging of P_3 and P_4. Thus it can be used to accelerate both positive and negative ions.

The power to the high-voltage transformers is applied through a self-locking relay operated by push-buttons. The relay is energized through the vacuum-safety cut-off circuit, so that the high voltage falls off when the pressure in the system exceeds the pre-set value.

C. The magnetic-field supply

The 60° magnetic-sector analyzer is described in the chapter giving the general lay-out of the instrument. The magnetic field is generated between shaped pole pieces of an electromagnet. The magnetic field intensity is controlled and kept constant by regulation of the current through the coils of the electromagnet.

The mechanical construction of the yoke and pole pieces is identical to that described by Nier [21]). The magnet coils are wound with 16 000 turns each of 0·55-mm enamelled wire. When connected in series the magnet coils have a resistance of 1000 Ω. The relation between the current through the coils and the magnetic field strength is given in fig. 9. Hysteresis troubles may be surmounted by arriving at the desired value of the magnetic field along a prescribed path of current changes.

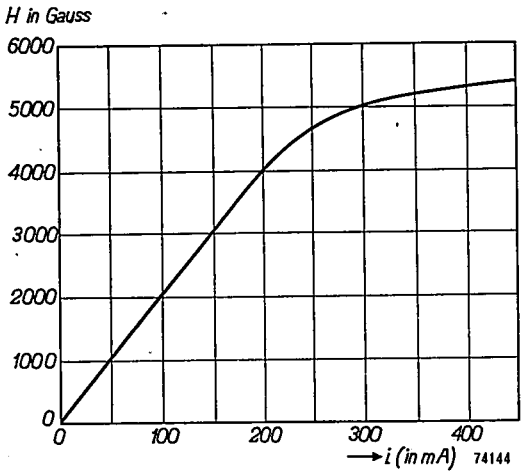

Fig. 9. *H-i* characteristic of the electromagnet.

As it has been decided to use mainly electrical scanning of the mass spectra, to facilitate the use of a wide range in sweeping velocity, the magnetic-field setting is limited to a number of discrete values of field strength. This is necessary in order to simplify the calibration of the instrument. The relation between the ion-current intensity and the partial pressure of the "mother" molecule in the ion source is dependent on the

voltage setting ("voltage effect"). The accelerating voltage and the magnetic-field controls have also to be calibrated in mass numbers. An extra control was, however, added to permit relatively slow magnetic scanning over a limited range; this might be necessary for studying mass discrimination when performing absolute ratio measurements.

The magnetic-field settings are so selected that all mass ions can be collected (except 5-9) within an effective acceleration-voltage range of 500-2000 V. This is done with the aid of fig. 9 and the formula for the trajectory curvatures of the ions in the analyzer.

The requisite stability of the magnetic field can be determined from the stability achieved in the accelerating voltage. They are connected through the trajectory formula mentioned before

$$R = \frac{(2mV/e)^{1/2}}{H},$$

giving the relation

$$\frac{\Delta H}{H} = \tfrac{1}{2}\frac{\Delta V}{V}.$$

As we asked for a stability of 1/9000 in the accelerating voltage, we shall try to achieve a stability of 1/20000 in the magnetic field. The schematic circuit of the stabilized magnet-current supply is given in fig. 10.

The calculations for the amplifier and its design for the required stability are analogous to those applied to the accelerating-voltage supply. The overall amplification factor of the amplifier (V_1—V_2) is calculated, and a compensating feedback coupling is applied, at some point at the entrance of the amplifier, from the unstabilized side of the supply (anode of V_1). In this way the stabilization factor can easily be stepped up by a factor 10 and thus reach the required value. In this case the reference tube V_3 has to be returned to the unstabilized-voltage side via a resistor and a stage of stabilization; this stabilizer, which consists of two stabilizing tubes 85A1 and a resistor, also supplies the screen-grid voltage of the amplifier tube V_2. The change of these voltages with line variation has to be included in the stability calculations. The filament of V_2 is fed by a regulated supply.

The 50-c/s ripple is reduced by stepping up the amplification; this is done by adding condensers and by extra filtering. The measured voltage ripple over the magnet coil at P_1 P_2 is less than 1 mV.

The potentiometer P is used for scanning the magnet current over a limited range at each setting of the current. The supply has four current positions for the four mass regions 1-4, 10-40, 40-160, 160-640 when collected within an accelerating voltage range of 500-2000 V.

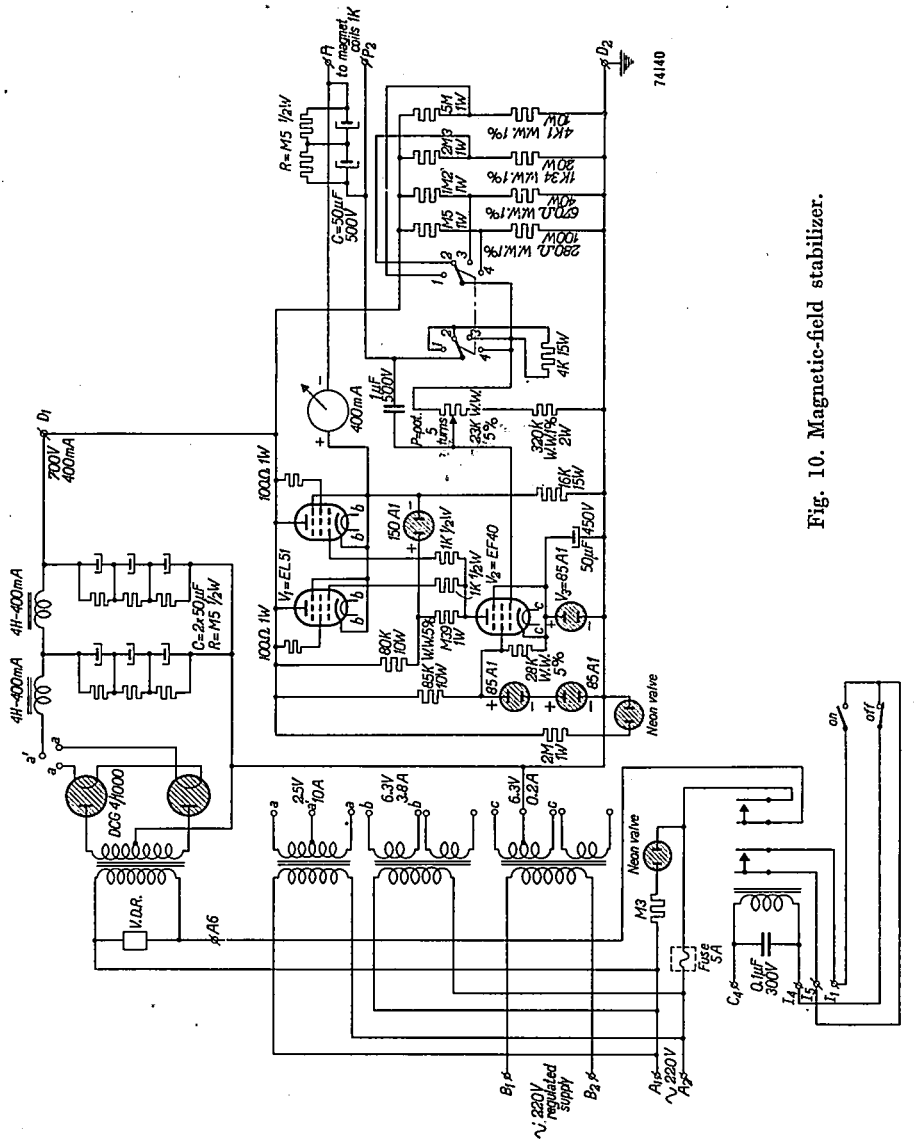

Fig. 10. Magnetic-field stabilizer.

D. The wide-band electrometer amplifier

(1) *Detection systems in mass spectometry*

After being geometrically dispersed by the analyzer, a selected part of the ion current passes through the exit slit of the system. Behind the slit is placed a device for detecting and measuring this current.

Of basic importance to the performance of a detector is its signal-to-noise ratio. Each system has an inherent noise and a certain efficiency of converting the measured quantity into a useful signal. As the noise is an energy phenomenon, a favourable ratio might be expected in systems that make efficient use of as much energy of the measured ion current as possible. In principle the ions may even be stepped up in energy before detection.

Two methods for measuring the ion current are now in use in mass spectrometry. One is the established method of measuring the charge transferred to a Faraday cup collecting the ions. The second is the comparatively new method of measuring the secondary electrons released when the ions strike a specially prepared multiplier surface [38]).

The secondary-emission detector utilizes a much larger part of the energy carried by the ions and is extremely sensitive. It has been applied to mass spectrometry by Leland [36]) and others [16]). It has, however, the disadvantage that corrections must be applied [37]) to the measured secondary current before the real ion intensity can be calculated, and that its operation is strongly dependent on the condition of the sensitive surface. The system of secondary multiplication might prove very useful in special cases such as the study of rare components in a substance, or when sensitive but only qualitative current measurements are required.

For the general application to measurements of relative abundance we prefer the use of electrometer circuits detecting the charge carried by the ion current. It is a direct and stable system, and well established in practice.

(2) *The need for a wide-band electrometer amplifier*

An important factor in the design of an amplifier is the expected frequency characteristic of the measured signal. As stated in the introduction, apart from slow measurements of the mass spectra of samples with a constant composition, we wished to include the possibility of studying transient phenomena. There are problems where the composition of the substance being analyzed changes relatively quickly with time and it is necessary to follow changes in one or more components. The mass spectrometer is then either tuned to a certain mass number and the amplifier measures the changing intensity of the collected ion current, or the amplifier records in succession the current pulses when the mass spectrum is scanned over an extended mass range in a short time. A wide-band amplifier will also permit quick measurements of mass spectra with the aid of a cathode-ray tube.

The signal-to-noise ratio of a measuring system decreases with the bandwidth. A wide-band amplifier can easily be terminated at the output side to pass only the necessary frequency components that are contained in a particular signal. This can be done with an electrical filter or by the

electrical and inertia filtering actions of a mechanical measuring unit. The stability of operation and the signal-to-noise ratio with a specified bandwidth depend on the amplifier used. A critical analysis must be made to determine the right design and to select components that will give the best results.

Most electrometer circuits described in the literature are built for measurement of slowly varying currents and feed mechanical meters and recorders. They use high-ohmic resistors in the input as needed for a high sensitivity in measuring small currents. Because of unavoidable capacity the time constant of the input impedance is then large and usually limits the useful bandwidth of the amplifier.

Uncompensated amplifier circuits have been used for displaying mass spectra on a cathode-ray tube by Forrester and Whalley[39]) and Siri[40]). In order to overcome the above-mentioned "time constant" limitation, they either reduce the velocity of sweep of the mass spectra (the frequency bandwidth of the signal) or take a smaller input resistance. In the latter case, as will be shown subsequently, the signal-to-noise ratio of the amplifier is lowered.

It is, however, possible to improve the high-frequency response of the circuit by employing a correcting network in one of the stages of a straight amplifier, but such a correction is neither easily made for a wide bandwidth nor easily made stable, because even small variations of the input capacitance will greatly affect the response.

We succeeded in designing an electrometer amplifier with a stable and flat characteristic by applying feedback through an appropriate network[41]).

(3) *The basic principle of the wide-band electrometer amplifier and noise considerations*

From the equivalence of the circuits *a* and *b* of fig. 11 where Z_1, Z_2 = impedances, i_0 = incoming current, V = voltage source of magnitude $i_0 Z_1$, and A = feedback amplifier with amplification factor A, it is seen that for the measuring circuit shown in fig. 11*c* the equation

$$V_{out} = Z_1 i_0 \tag{1}$$

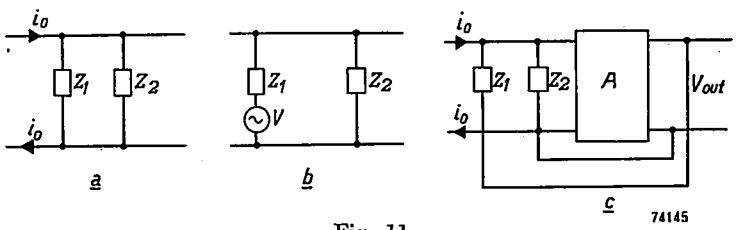

Fig. 11

will hold with the required degree of accuracy within a range of frequencies depending on the amplification factor A.

If it were possible to put a pure ohmic resistance in the place of Z_1, then we would have a flat-response amplifier. However, a flat response cannot be obtained in this way, because in practice a high-ohmic "resistor" behaves as a complex impedance, owing to shunting and distributed capacitances, the impedances of which are comparable to the ohmic resistance even at low frequencies. Now in general the response of a feedback amplifier can be influenced by introducing an attenuating network in the feedback loop. In our case, theoretically, the response can be improved by employing a correcting network, but this would not be easy to put into practice, because of the complicated nature of the impedance of the high-ohmic resistor. Therefore, we take for Z_1 a suitable network including the high-ohmic resistor and use a simple correcting network in the feedback loop as given in the accompanying calculations and figures.

In fig. 12, A = amplifier with amplification factor A, β = attenuator with attenuation factor β, i_0 = incoming current, and V_{out} = output-voltage signal. It is easy to verify that

$$A\left\{\frac{i_0 Z_1 Z_2}{Z_1+Z_2} - V_{\text{out}} \cdot \beta \frac{Z_2}{Z_1+Z_2}\right\} = V_{\text{out}},$$

or

$$i_0 Z_1 = \left\{\beta + \frac{1+(Z_1/Z_2)}{A}\right\} V_{\text{out}}.$$

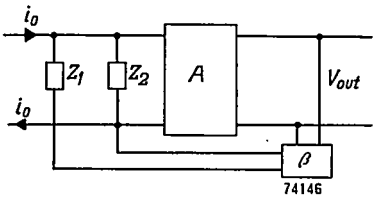

Fig. 12

We now take A high enough so that in a certain frequency range

$$|\beta| \gg \left|\frac{1+(Z_1/Z_2)}{A}\right|. \tag{3}$$

Then from (2) and (3) we have

$$V_{\text{out}} = \frac{Z_1}{\beta} i_0. \tag{4}$$

Let us choose Z_1 and β such that Z_1/β is real. We take for Z_1 the parallel combination of the high-ohmic resistor R_1 and a suitable capacitance C_1

(see fig. 13*a*). C_1 is taken sufficiently high in comparison with the distributed capacitance of the high-ohmic resistor, so that the reactive component of Z_1 is practically equal to C_1. Therefore

$$Z_1 = \frac{R_1}{1 + j\omega R_1 C_1}.$$

We apply the attenuating network given in fig. 13*b*. Then,

$$\beta = \frac{1}{1 + j\omega R_f C_f}.$$

In virtue of (4) this leads to

$$V_{out} = \frac{R_1(1 + j\omega R_f C_f)}{1 + j\omega R_1 C_1} i_0. \tag{4'}$$

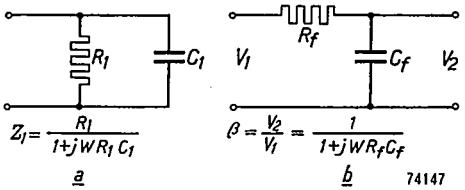

Fig. 13

By choosing equal time constants in Z_1 and β, we obtain

$$R_f C_f = R_1 C_1, \tag{5}$$

and hence

$$V_{out} \approx R_1 i_0, \tag{6}$$

where R_1 = ohmic resistance value of the high-ohmic resistor. Equation (6) holds for a frequency range $\Delta\omega$ where A satisfies (3).

In this way we accomplished our purpose of designing a wide-band electrometer amplifier. In a practical case we took the following values (for notation see fig. 14): $R_1 = 10^{11}\Omega$; $C_1 \approx 3$ $\mu\mu$F, air capacitor; $R_f \approx$ 150 kΩ, adjustable; and $C_f = 2$ μF.

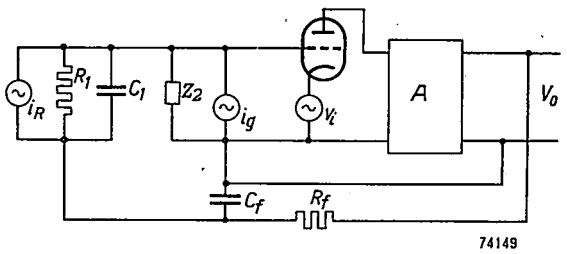

Fig. 14

Z_2 can in practice be taken as the capacitive impedance of the grid and of the ion-collector plate and associated wires, and is of the order of 15 $\mu\mu$F. For a flat response of 5 per cent at 0—1000 c/s, the amplification required is $A \approx 2.10^5$, and is given by a DC-coupled amplifier. The schematic diagrams and full description will be given subsequently.

The noise output of the amplifier has been analyzed with the aid of the diagram of fig. 14, where i_R, i_g are current sources, and v_i a voltage source. From (6) we have in the effective bandwidth

$$V_R = V_0(i_R) = R_1 i_R, \tag{7}$$

$$V_g = V_0(i_g) = R_1 i_g. \tag{8}$$

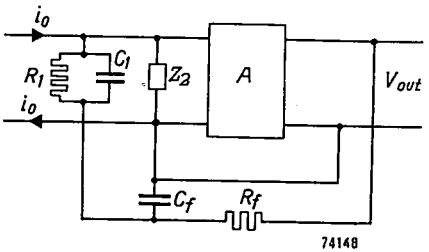

Fig. 15

For $V_i = V_0(v_i)$ we have from figs 12 and 15

$$A\, v_i - V_i\, \beta \frac{Z_2}{Z_1 + Z_2} = V_i,$$

$$V_i = \frac{1}{1/A + \beta Z_2/(Z_1 + Z_2)}\, v_i,$$

and with (3) we arrive at

$$V_i = \frac{Z_1 + Z_2}{\beta\, Z_2}\, v_i,$$

or

$$V_i = \left\{\frac{R_1}{Z_2} + 1 + j\omega R_1 C_1\right\} v_i.$$

Here, Z_2 is practically equal to the capacitance of the grid C, viz.,

$$Z_2 = 1/j\omega C \tag{9}$$

and, therefore, we have

$$V_i = \{1 + j\omega R_1 (C + C_1)\}\, v_i. \tag{10}$$

Johnson noise of the high-ohmic resistor is accounted for by taking a current source independent of frequency across the high-ohmic resistor of the value

$$\langle i_R^2(f)\rangle_{\mathrm{Av}} = 4\,kT\Delta f/R_1\,, \tag{11}$$

and from (7) we then have for the mean square of the voltage output per unit-frequency bandwidth for this noise,

$$\langle V_R^2(f)\rangle_{\mathrm{Av}} = 4\,kTR_1\,.$$

Grid-current noise can be represented by a current source i_g of a mean-square value $\langle \Delta i_g^2(f)\rangle_{\mathrm{Av}}$. In virtue of (8) the mean square of the noise output of the amplifier per unit-frequency bandwidth then becomes

$$\langle V_g^2(f)\rangle_{\mathrm{Av}} = R_1^2\langle \Delta i_g^2(f)\rangle_{\mathrm{Av}}.$$

The frequency distribution of the noise from the first valve and the following stages is not modified by the input impedance and can be represented by a voltage source between cathode and grid. Its mean-square voltage $\langle v_i^2(f)\rangle_{\mathrm{Av}}$ is the equivalent mean-square voltage, calculated at the grid, of the measured output noise with grid short-circuited.

From (10) it follows that the mean square of noise output per unit-frequency bandwidth is

$$\langle V_i^2(f)\rangle_{\mathrm{Av}} = [1 + 4\pi^2 f^2 R_1^2 (C+C_1)^2]\,\langle r_i^2(f)\rangle_{\mathrm{Av}}.$$

Thus the overall noise output per unit-frequency bandwidth is given by

$$\langle V_n^2(f)\rangle_{\mathrm{Av}} = 4\,kTR_1 + R_1^2\langle \Delta i_g^2(f)\rangle_{\mathrm{Av}} + \\ + \{1 + 4\pi^2 f^2 R_1^2 (C + C_1)^2\}\,\langle v_i^2(f)\rangle_{\mathrm{Av}}. \tag{12}$$

From (6) and (12) we obtain the signal-to-noise ratio

$$\frac{\langle V_s^2\rangle_{\mathrm{Av}}}{\langle V_n^2\rangle_{\mathrm{Av}}} = \frac{R_1^2 i_0^2}{4kTR_1 + R_1^2\langle \Delta i_g^2(f)\rangle_{\mathrm{Av}} + \{1 + 4\pi^2 f^2 R_1^2 (C + C_1)^2\}\langle v_i^2(f)\rangle_{\mathrm{Av}}} \tag{13}$$

This is a general formula for electrometer amplifiers. From (13) two conclusions can be drawn:

(a) The value of R_1 should be chosen so high that the contribution of resistance noise (first term in the denominator) becomes negligible.

(b) From a certain frequency onwards the internal noise of the electrometer tube (third term in the denominator) becomes the most important, as the energy-noise distribution always decreases more slowly than $1/f^2$; hence it is advisable to use electrometer amplifiers at a comparatively low mean frequency.

We include the low-frequency range by using DC couplings in the amplifier. R_1 is taken high ($10^{11}\ \Omega$) in order to have a good signal-to-noise ratio at low frequencies.

(4) *The practical circuit*

The practical circuits of the current amplifier are given in figs 16 and 17.

The pre-amplifier, fig. 16, is situated near the ion collector in the mass spectrometer. V_1 is the electrometer tube, $R_1 = 10^{11}\ \Omega$ the high-ohmic

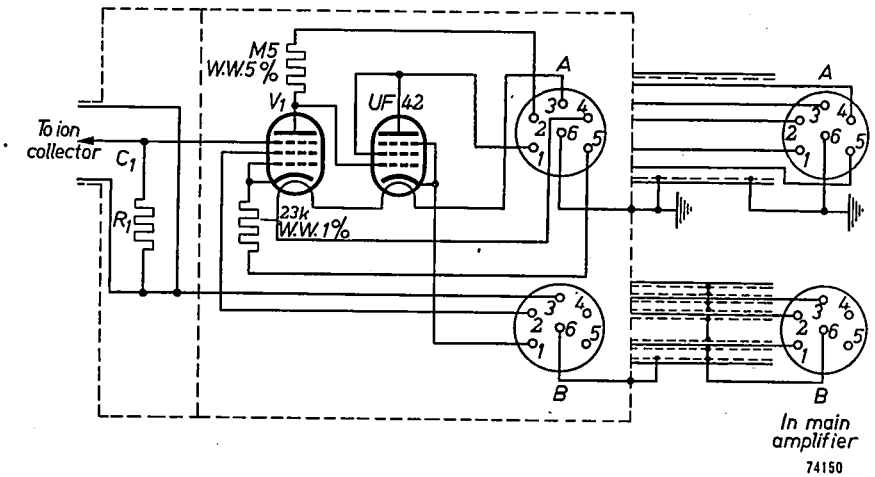

Fig. 16. Schematic circuit of the electrometer pre-amplifier.

resistor and C_1 is the shunting capacitor (see fig. 18). A cathode-follower stage feeds the signal through the connecting cable to the main amplifier.

The constructional details are seen in fig. 18. The air capacitor C_1 is made of a brass box enclosing the high-ohmic resistor and part of the connecting wires in the grid circuit of the electrometer tube. The pre-amplifier has to be thoroughly screened off from electric and magnetic interference and is placed in a double-layer box: internally copper and externally μ-metal. The box is also light-tight to minimize the grid current in the first tube. The connecting cables to the main amplifier have to be insulated electrically from near-by metal parts that are usually low-impedance low-voltage sources of 50-c/s currents.

Fig. 17 is the schematic diagram of the main amplifier. It is composed of five amplifying stages DC-coupled. There are feedback couplings between stages to limit the amplification to the required value. One of the feedback loops is frequency dependent to prevent high-frequency oscilla-

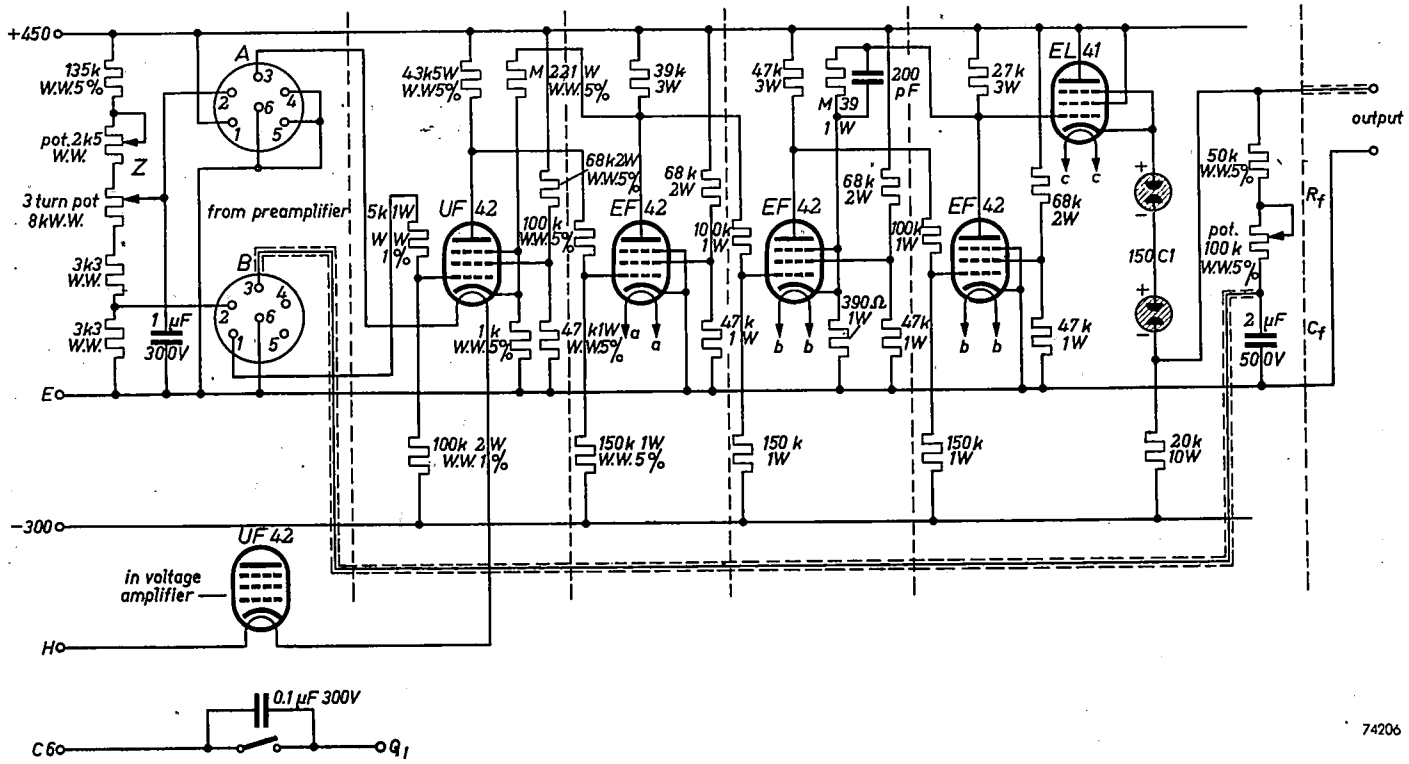

Fig. 17. Main electrometer amplifier.

tions. The stages are individually screened for the same reason. The power stage is a cathode follower able to develop high-voltage output signals over the comparatively low impedances of low-pass filters. It is designed to deliver double-polarity signals for measuring both positive and negative ions. The overall voltage-amplification factor, A, is 10^5 for the frequency band 0—500 c/s.

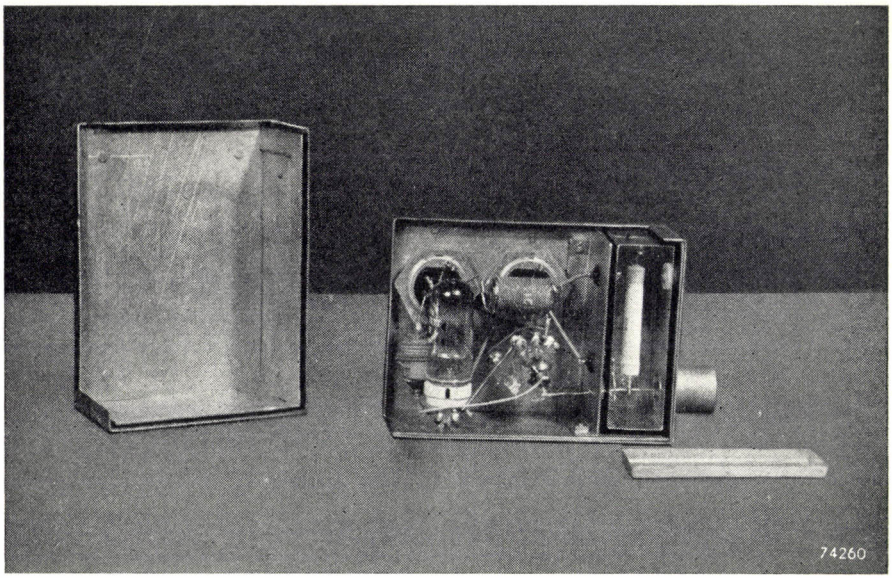

Fig. 18. Constructional details of the electrometer pre-amplifier.

The attenuator in the feedback loop, $R_f C_f$, is made variable in order to adjust the amplifier to the compensated position. Z is a control for varying the supply voltage of the anode of the electrometer tube and by this the DC-output level of the amplifier can be adjusted.

The amplifier is fed by a stabilized power supply (fig. 19) which also serves other circuits in the instrument. The first three tubes in the amplifier are heated by an electronically stabilized DC supply. The stability calculations and design are analogous to those applied to the ion-accelerating voltage supply (fig. 7). The high-voltage transformers and filter chokes are put at some distance from the amplifier. Near-by filament transformers had to be screened by μ-metal to avoid the troublesome 50-c/s induction.

(5) *Operation of the circuit; stability and noise measurements*

The first tube in the electrometer amplifier V_1 is a selected Philips 4672 or RCA 954 acorn tube in "electrometer connection" and reduced working

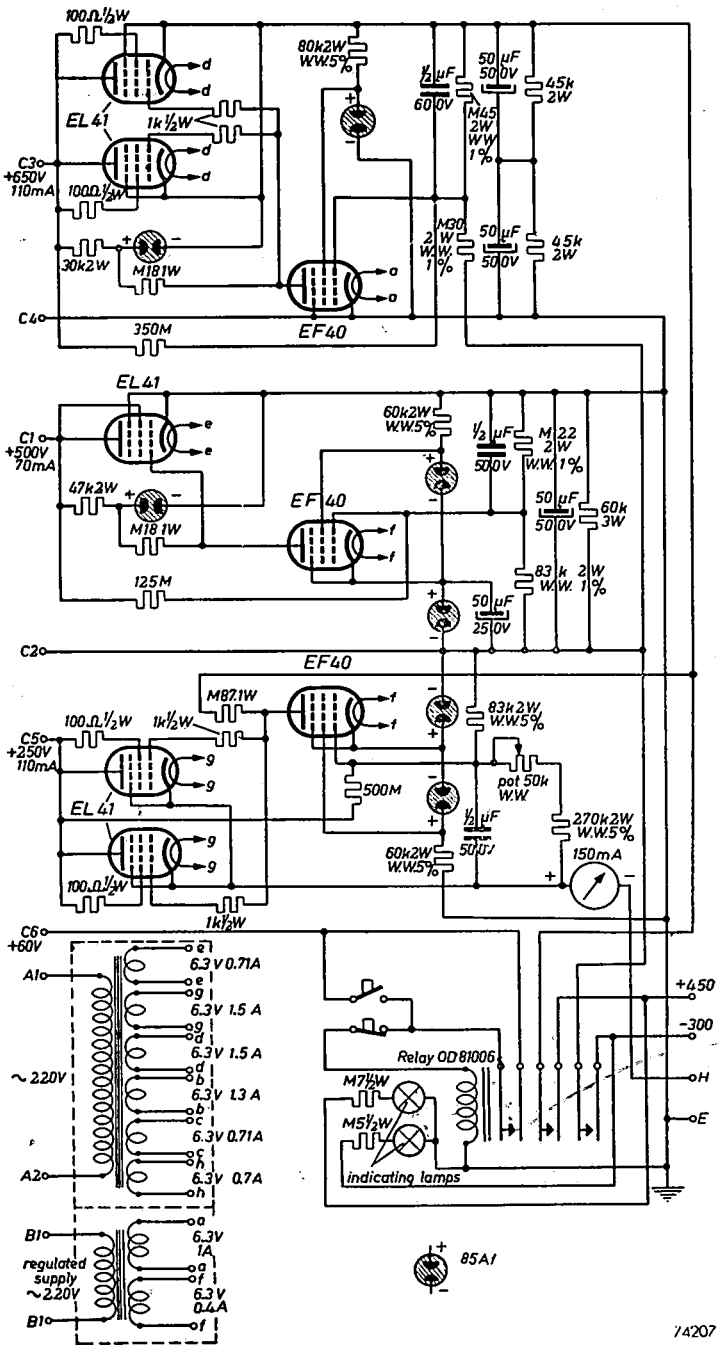

Fig. 19. Stabilized power-supply for the electrometer amplifier.

voltages as recommended by Nielsen [42]). The suppressor grid g_3 acts then as the control grid and as a typical setting the following operating conditions were used for a Philips 4672 tube:

$V_a = 6{\cdot}7$ V; $V_{g2} = 7{\cdot}2$ V; $V_{g1} = 0$ V; $V_{g3} = -2{\cdot}0$ V;
$I_a = 45$ μA; $I_{g2} = 45$ μA; $I_f = 110$ mA.

The electrometer tube was coated, after cleaning, with a silicon compound and soldered in place in the pre-amplifier. The pre-amplifier box was rigidly connected to the mass-spectrometer-collector assembly. No special vibration-free mounting was found necessary.

Long-time DC stability and noise measurements were carried out with the aid of a pen-and-ink recorder and an oscillograph preceeded by low-pass filters. Table II gives the numerical values of the r.m.s. noise current at the input of the electrometer amplifier for some bandwidths. They are estimated from the recorded fluctuations in time with the aid of Rice's theory [43]).

TABLE II

Some values of the r.m.s. noise current at the input of the electrometer amplifier

Measuring instrument	Bandwidth	R.m.s. current noise
1. Recorder	Zero DC drift per h	5.10^{-15} A
2. ,,	3 sec time constant	$1{\cdot}5.10^{-16}$ A
3. ,,	1 sec time constant	4.10^{-16} A
4. ,,	1/3 sec time constant	10^{-15} A
5. Oscillograph	0-10 c/s	5.10^{-15} A
6. ,,	0-33 c/s	15.10^{-15} A
7. ,,	0-350 c/s	22.10^{-14} A

(6) *Operation of the circuit; measurements of ion currents*

The response characteristic of the electrometer amplifier can be best seen from the oscillograms of ion-current pulses made at different sweep velocities of the mass spectra and for several sensitivities of the oscillograph amplifier.

Figs 20 *A* to *C* show the Xenon isotopes with increasing mass number from left to right. The complete oscillograph trace is made in 10 sec. Figs 20*A* and *B* are photographed with the same sensitivity at two different sweep rates of the mass spectra as seen from the picture. Fig. 20 *C* is made with the same sweep rate as fig. 20*A* but with 27-fold amplification. The accurate reproduction of the picture at different sweep rates is evident.

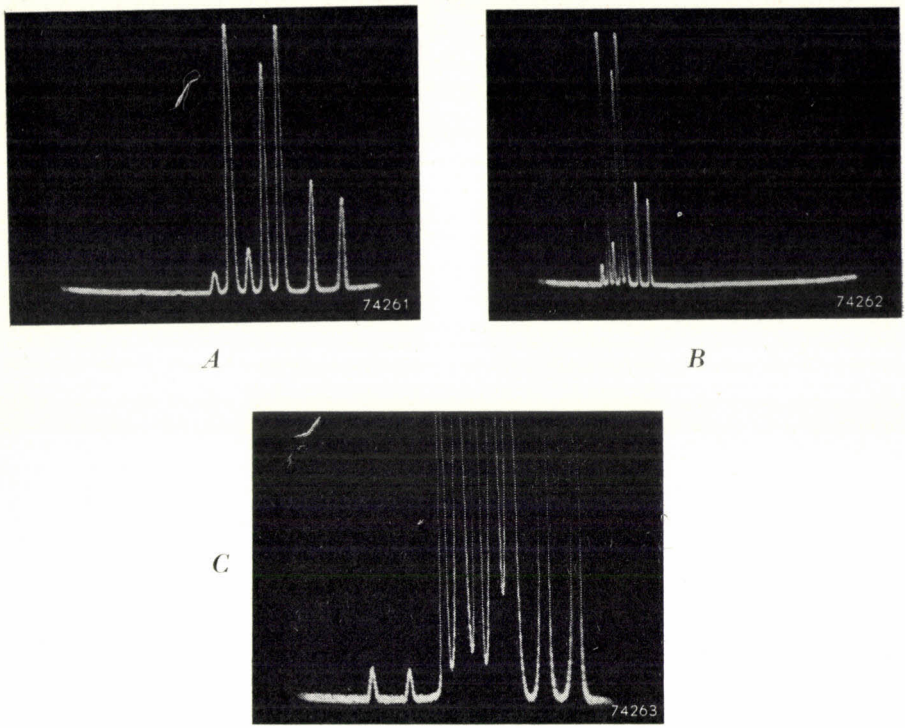

A *B*

C

Fig. 20. Oscillograph display of the Xe isotopes (see text).

Figs 21 *A* and *B* give the ion-current peak, mass 18 of H_2O. Four traces are shown in each picture with a gain-factor difference of 3 between each two successive traces. The time of a complete trace in fig. 21 *A* is 2 sec and the signal is passed through a low-pass filter of 0—10 c/s bandwidth to limit the noise. In fig. 21*B* the time is 1 sec and the bandwidth 0—33 c/s.

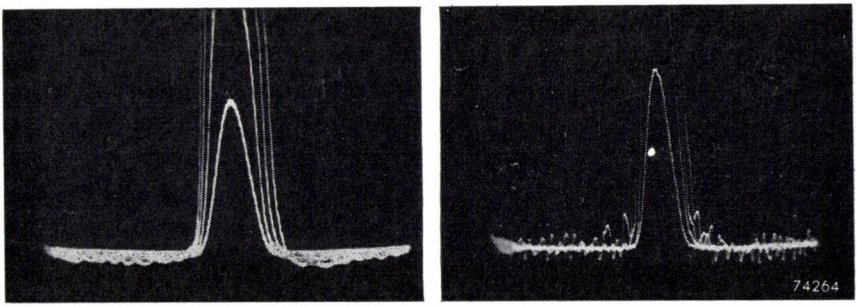

A *B*

Fig. 21. Ion peak of H_2O^+ photographed at varying sweep velocities and amplifications (see text).

The pictures show the part of the pulse at the zero line with high amplification. No distortion in the pulse shape is seen.

E. Meter and recorder measurements

Relatively slow measurements of ion currents can be made by the aid of a meter or a pen-and-ink recorder. The output of the amplifier is then connected to the input of the meter or recorder assembly. The signal-to-noise ratio obtained depends on the resultant bandwidth (see Table II). When using meter readings, the ion spectrum is scanned manually by adjusting the ion-accelerating voltage or the analyzer magnetic field. An extra control is added for cutting-off the ion beam in order to reset the zero of the electrometer amplifier and to eliminate the long-time drift.

For recorder measurements the scanning can be made automatic by having the controls of the accelerating voltage or magnetic-field regulators motor driven, or by taking a proper value of the RC combination in the sweep control of the ion-accelerating voltage supply. Scanning velocity is chosen so that the frequency bandwidth of the signal is covered by the response characteristic of the recording unit.

F. Oscillograph display and measurements

Relatively rapidly changing currents can be recorded with the aid of a cathode-ray tube. The signal from the electrometer amplifier is then passed through filters, to obtain the required bandwidth and limit the noise, and amplified by a voltage amplifier feeding the deflecting plates of the cathode-ray tube. Fig. 22 gives the schematic diagram of the filters and the voltage amplifier.

Low-pass filters are used and a switch permits the choice of three different bandwidths namely: 0-10 c/s, 0-33 c/s and 0-350 c/s. They are built from two stages of π-sections. As the electrometer amplifier has a low output impedance, proper termination of the filter is achieved by series resistors. The filter assembly must be enclosed in a μ-metal shield to avoid magnetic pick-up.

The voltage amplifier was chosen DC-coupled to cover the low-frequency range and avoid the adverse effects of the overloading of *RC*-coupled amplifiers. To reduce DC drifts, the heaters were fed by a controlled current from a stabilized supply. The heater of the first tube, UF .42, is connected in series with the critical tubes in the electrometer amplifier. The voltage amplifier supplies a balanced output signal for the horizontal deflecting plates of the cathode-ray tube. Sensitivity setting is done by a potential divider in the first stage. A push-button that short-circuits the input and a potentiometer in the first coupling serve to set

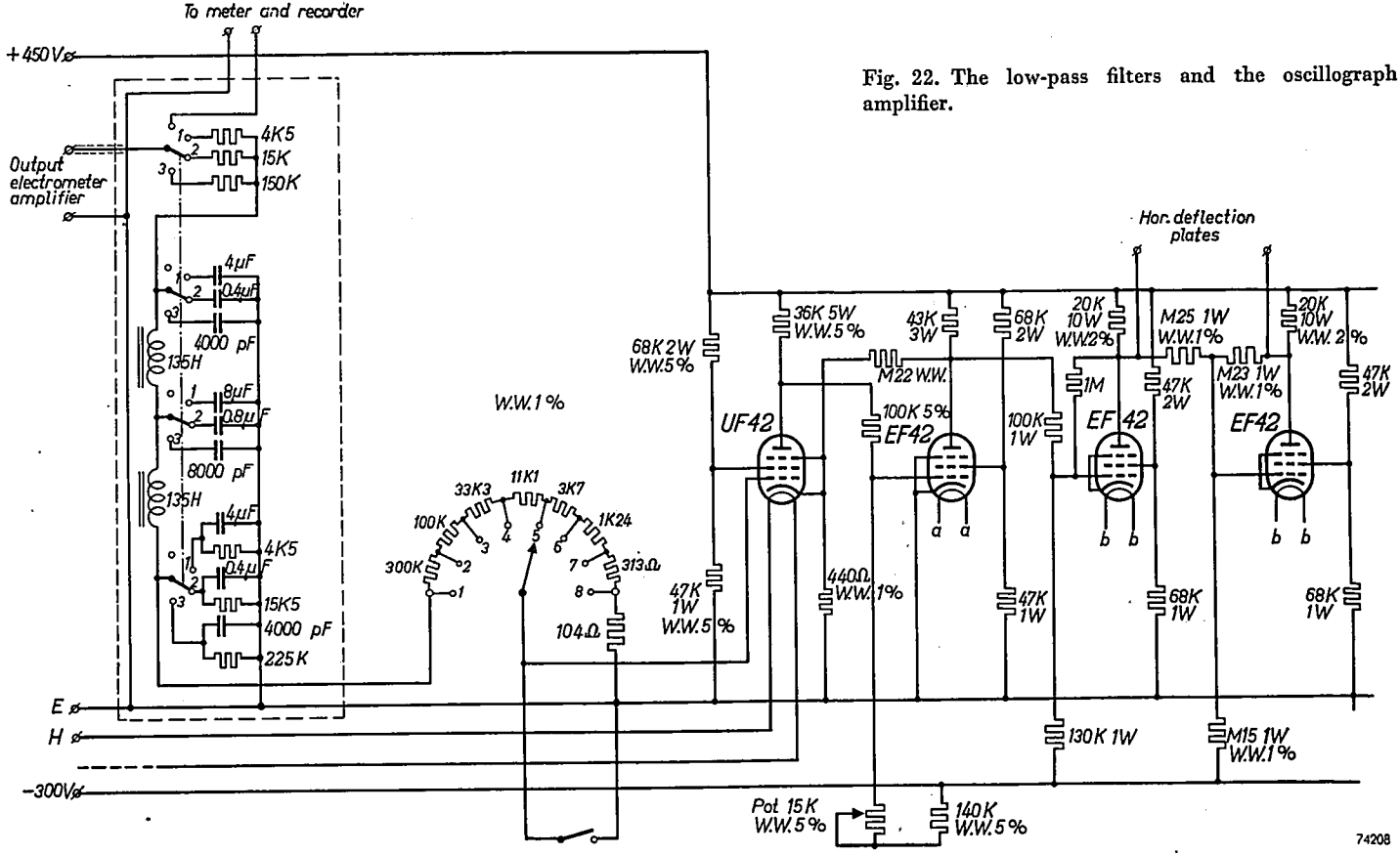

Fig. 22. The low-pass filters and the oscillograph amplifier.

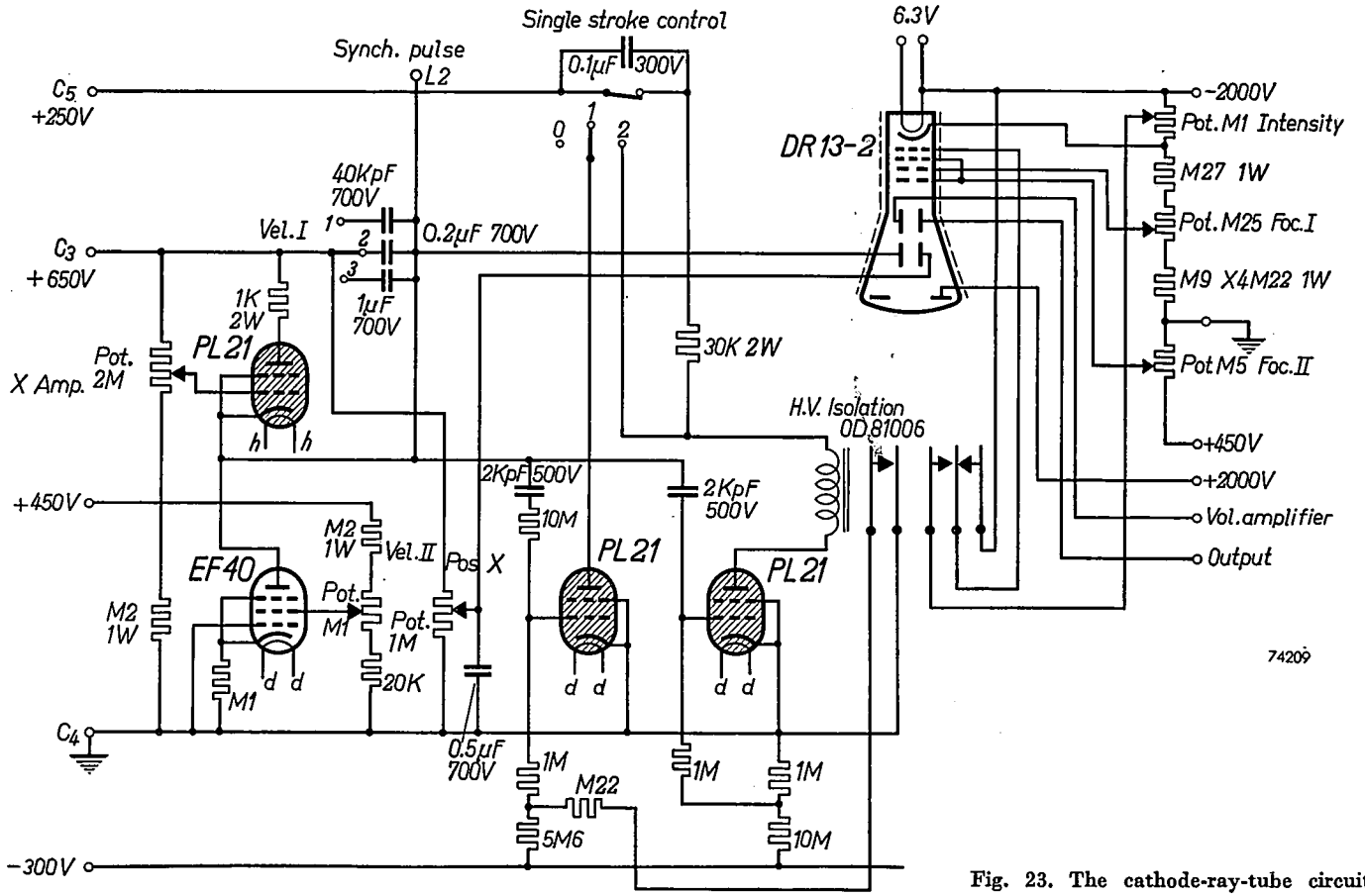

Fig. 23. The cathode-ray-tube circuit.

the height of the zero line on the screen. The total amplification factor is $\approx 15.10^3$. Fig. 23 gives the time-base circuit and other necessary controls of the cathode-ray tube.

A long-persistent screen is taken in order to be able to use long sweep times of the order of 30 sec. The time-base circuit is of the common constant-current type. Two focusing controls are necessary for achieving a sharp picture as DC couplings to the deflecting plates are used. A special circuit is added for display of a single sweep, as needed for example when taking a photograph of the oscillogram. The quenching of the light spot is done by switching the intensity-regulating grid, g_1, of the tube from operating point to a cut-off position. Switching is done mechanically by a relay controlled by two gas tubes. The gas tubes are ignited by the return pulse generated in the time-base circuit. In position *1* of the "single stroke control" only one gas tube is ignited, closing the relay and forming the light spot. In position *2*, provided both gas tubes are non-conducting, the first pulse of the time base will ignite, as in position *1*, the gas tube that closes the relay, while the following one ignites the second gas tube thus short circuiting the relay windings and reopening the contacts. When both gas tubes are ignited the relay remains without power until the circuit is reset by the push-button included in the circuit.

The time-base wave form is also used for synchronizing the automatic sweep of the ion-accelerating voltage supply as described in a preceding chapter.

When measuring ion currents with the electrometer amplifier and oscillograph display the maximum absolute sensitivity is $1{\cdot}6.10^{-14}$ A per mm horizontal deflection. The line width of the picture is 0·4 mm. Noise figures at the respective filter positions are given in table II. As all couplings in the measuring apparatus are DC, the screen surface can be directly calibrated by connecting a measured voltage source at the input of the voltage amplifier.

Eindhoven, July 1952

REFERENCES

1) J. J. Thomson, Phil. Mag. **21**, 225-249, 1911.
2) F. W. Aston, Phil. Mag. **38**, 707-714, 1919.
3) F. W. Aston, Phil. Mag. **39**, 449-455, 1920
4) A. I. Dempster, Phys. Rev. **11**, 316-325, 1918.
5) W. F. Barber, Proc. Leeds Phil. Lit. Soc. **2**, 427-434, 1933.
6) K. T. Bainbridge and E. B. Jordan, Phys. Rev. **49**, 421 (A), 1936.
7) J. Mattauch, Phys. Rev. **50**, 617-623, 1936.
8) E. B. Jordan, Phys. Rev. **57**, 1072 (A), 1940.
9) W. Bleakney and J. A. Hipple, Phys. Rev. **53**, 521-529, 1938.
10) G. W. Monk, J. B. Graves and J. L. Horton, Rev. sci. Instr. **18**, 796, 1947.

[11]) J. A. Hipple, H. Sommer and H. A. Thomas, Phys. Rev. **76**, 1877-1978 (L), 1949. Electronics **23**, June 122-124, 1950.
[12]) W. E. Stephens, Phys. Rev. **69**, 691 (A), 1946
[13]) A. E. Cameron and D. F. Eggers, Rev. sci. Instr. **19**, 605-607, 1948.
[14]) R. Keller, Helv. phys. Acta **22**, 386-388, 1949.
[15]) S. A. Goudsmit, Phys. Rev. **74**, 622-623 (L), 1948.
[16]) E. E. Hays, P. I. Richards and S. A. Goudsmit, Phys. Rev. **84**, 824-828, 1949.
[17]) J. A. Hipple and H. A. Thomas, Phys. Rev. **75**, 1616 (L), 1949.
[18]) H. Heil, Z. Phys. **128**, 36-46, 1950.
[19]) P. B. Weisz, Phys. Rev. **70**, 91 (L), 1946.
[20]) W. H. Bennet, J. appl. Phys. **21**, 143-147, 1950.
[21]) A. O. Nier, Rev. sci. Instr. **18**, 398-411, 1947.
[22]) M. G. Inghram, Phys. Rev. **70**, 653-660, 1946.
[23]) R. E. Hönig, J. appl. Phys. **16**, 646-654, 1945.
[24]) R. E. Halsted and A. O. Nier, Rev. sci. Instr. **21**, 1019-1021, 1950.
[25]) J. Kistemaker, Physica, 's-Grav., **18**, 163-176, 1952.
[26]) E. B. Jordan and N. D. Coggeshall, J. appl. Phys. **13**, 539-550, 1942.
[27]) N. D. Coggeshall, J. chem. Phys. **12**, 19-23, 1944.
[28]) H. W. Washburn and C. E. Berry, Phys. Rev. **70**, 559 (L), 1946.
[29]) V. S. Caldecourt, Rev. sci. Instr. **22**, 58-59 (L), 1951.
[30]) R. E. Fox and J. A. Hipple, J. chem. Phys. **15**, 208 (L), 1947.
[31]) D. P. Stevenson, J. chem. Phys. **17**, 101-102 (L) 1949.
[32]) C. E. Berry, J. chem. Phys. **17**, 1164-1165 (L), 1949.
[33]) E. B. Winn and A. O. Nier, Rev. sci. Instr. **20**, 773-774 1949.
[34]) M. E. Reinders, Thesis, Amsterdam, 1951.
[35]) W. Walcher, Nucleonics, October 1949, 421-451.
[36]) W. T. Leland, Phys. Rev. **77**, 634-640, 1950.
[37]) W. Bloch and W. Walcher, Rev. sci. Instr. **22**, 1028 (L). 1951.
[38]) J. S. Allen, Rev. sci. Instr. **18**, 739-749, 1947.
[39]) A. T. Forrester and B. W. Whalley, Rev. sci. Instr. **17**, 549-552, 1946.
[40]) W. Siri, Rev. sci. Instr. **18**, 540-545, 1947.
[41]) I. Pelchowitch and J. J. Zaalberg van Zelst, Rev. sci. Instr. **23**, 73-75, 195[illegible].
[42]) C. E. Nielsen, Rev. sci. Instr. **18**, 18-31, 1947.
[43]) S. O. Rice, Bell Syst. tech. J. **24**, 46-156, 1945.

A STUDY OF THE EVAPORATION PRODUCTS OF ALKALINE-EARTH OXIDES *)

by I. PELCHOWITCH 621.384.8:542.48:546.4-31

Summary

A mass spectrometer is used to study the evaporation phenomena in systems where the alkaline-earth oxides are coated on electrically heated metal ribbons. BaO evaporates mainly in the form of the oxide when it is coated on Pt and Ni or coated in admixture with SrO and CaO on Pt. When the BaO/Pt system is brought to high temperatures, an ion current of Ba_2O_2 can be measured. In the SrO/Pt and CaO/Pt systems the main evaporation product is the free element accompanied by the oxide and the singly ionized metal ions. The main evaporation product in the BaO/Ta system is free Ba accompanied by the expected amount of the oxide and by singly ionized Ba ions which can be measured at higher temperatures. When the experimental results of ion-current dependence on temperature are fitted to an equation of the form $\log I = -A/T + B$, I being the ion current at a certain M/e value measured at the sample temperature T °K, unexpected results are found. The evaporation-rate curve drawn using $\log_{10} I$ and $10^4/T$ as coordinates is not in all cases a single straight line. The evaporation curve of BaO from all BaO systems coated on Pt can be best described in the measured temperature range as two lines differing in slope joining at the temperature point $T = 1250$ °K. A critical behaviour in the evaporation-rate curve of free Ba evaporating from the system BaO/Ta seems to occur when this temperature point is reached. A different behaviour of the evaporation-rate curve of BaO is observed in the BaO/Ni system, the transition point at 1250 °K disappearing. We are then able to prove, however, that the Ni base metal evaporates through the BaO porous layer and that the evaporation-rate curve of Ni behaves critically in the neighbourhood of $T = 1250$ °K. A transition point in the evaporation-rate curve of free Sr is found in the system SrO/Pt. It is reversible with temperature and the temperature value is $T = 1600$ °K. In view of the unexpected results found in the evaporation-rate curves, resistance measurements of the systems are made using oxide layers pressed between metal electrodes. All the above-mentioned transition points appear clearly in the resistance behaviour with temperature. The difference between Pt and Ni as base metals is also indicated. Finally the experimental results are compared critically with data from the literature.

Résumé

Un spectrographe de masse est utilisé pour étudier le phénomène d'évaporation dans les systemes où des rubans métalliques chauffés électriquement sont enduits d'oxydes de terres alcalines. BaO s'évapore principalement sous la forme d'un oxyde lorsqu' il est appliqué sur Pt et Ni ou en mélange avec SrO et CaO sur Pt. Lorsque le système BaO/Pt est portée à des températures élevées, l'on peut mesurer un courant ionique de Ba_2O_2. Dans les combinaisons SrO/Pt et CaO/Pt, le principal produit de l'évaporation est l'élément libre accompagné pat l'oxyde et les ions métal à simple ionisation. Le

*) Part II of the author's thesis, University of Amsterdam, June 1953; for Part I, see Philips Res. Rep. 9, 1-41, 1954.

principal produit d'évaporation dans la combinaison BaO/Ta est du Ba libre accompagné par la quantité attendue d'oxyde et par des ions Ba à simple ionisation qui peuvent être mesurés à des températures plus élevées. Lorsque les résultats expérimentaux de la dépendance du courant ionique par rapport à la température furent traduits en équation de la forme: $\log I = -A/T + B$, I étant le courant ionique pour une certaine valeur M/e mesurée à la température de l'échantillon T °K l'on trouva des résultats inattendus. Les courbes de rapport d'évaporation dessinées utilisant $\log_{10} I$ et $10^4/T$ comme coordonnées ne sont pas dans tous les cas une simple ligne droite. La courbe d'évaporation de BaO de tous les systèmes BaO étendu sur Pt peut être mieux décrite dans la gamme de température mesurée comme deux lignes de courbe différente se joignant au point de température $T = 1250$ °K. Une allure critique dans la courbe de rapport d'évaporation du Ba libre s'évaporant du système BaO/Ta semble se produire lorsque ce point de température est atteint. Une allure différente de la courbe de rapport d'évaporation de BaO est observée dans la combinaison BaO/Ni, le point de transition à 1250 °K disparaissant. Toutefois il nous est alors possible de prouver que le métal base Ni s'évapore à travers la couche poreuse BaO et que la courbe de rapport d'évaporation de Ni se comporte de façon critique au voisinage de $T = 1250$ °K. En vue des résultats inattendus trouvés dans les courbes de rapport d'évaporation, les mesures de résistance des systèmes sont conduites en utilisant des couches d'oxydes pressées entre les électrodes métalliques. Tous les points de transition mentionnés ci-dessus apparaissent clairement dans la conduite de la résistance avec la température. La différence entre Pt et Ni en tant que métals base est également indiquée. Finalement les résultats expérimentaux sont comparés de façon critique avec les données de la documentation.

Zusammenfassung

Es wurde ein Massenspektrometer benutzt zur Untersuchung der Verdampfungserscheinungen in Systemen, in denen die erdalkalischen Oxyde auf elektrisch erhitzte Metallbänder aufgetragen worden sind. BaO verdampft hauptsächlich in Form des Oxyds, wenn es auf Pt und Ni oder als Zusatz von SrO und CaO mit diesen beiden auf Pt aufgetragen ist. Wird das BaO/Pt-Systeem auf hohe Temperaturen gebracht, so kann ein Ionenstrom oder Ba_2O_2 gemessen werden. In den SrO-Pt- und CaO/Pt-Systemen ist das Hauptverdampfungsprodukt das freie Element, das von dem Oxyd und den einzelnen ionisierten Metallionen begleitet ist. Das Hauptverdampfungsprodukt im BaO/Ta-System ist freies Ba, begleitet von der erwarteten Menge des Oxyds und von vereinzelten ionisierten Ba-Ionen, welches bei höheren Temperaturen gemessen werden kann. Paßt man die experimentellen Ergebnisse der Ionenstromabhängigkeit von der Temperatur einer Gleichung von der Form $\log I = -A/T + B$ an, wobei I der Ionenstrom bei einem bestimmten M/e-Wert, gemessen bei der Versuchstemperatur T °K ist, so ergeben sich unerwartete Resultate. Die unter Gebrauchmachung von $\log_{10} I$ und $10^4/T$ als Koordinaten gezeichneten Kurven der Verdampfungsgeschwindigkeit sind nicht in allen Fällen gerade Linien. Die Verdampfungskurve von BaO aller auf Pt aufgetragenen Ba-Systeme kann in dem gemessenen Temperaturbereich am besten beschrieben werden als zwei verschieden geneigte Linien, die sich im Temperaturpunkt $T = 1250$ °K vereinigen. Ein kritisches Verhalten in der Verdampfungsgeschwindigkeits-Kurve von freiem Ba, das aus dem System BaO/Ta verdampft, zeigt sich anscheinend, wenn dieser Temperaturpunkt erreicht ist. Ein abweichendes Verhalten der Kurve der Verdampfungsgeschwindigkeit von BaO wurde im BaO/Ni-System beobachtet, wo der Übergang bei 1250 °K verschwindet. Wie dem auch sei, wir sind dann in der Lage zu beweisen, daß das Ni Basismetall durch die poröse BaO-

Schicht hindurch verdampft und daß die Kurve der Verdampfungsgeschwindigkeit von Ni sich in der Nähe von $T = 1250$ °K kritisch verhält. Ein Übergangspunkt in der Kurve der Verdampfungsgeschwindigkeit von freiem Sr wurde im System SrO/Pt gefunden. Es besteht Umkehrbarkeit bezüglich Temperatur und der Temperaturwert ist $T = 1600$ °K. Hinsichtlich der in der Kurven der Verdampfungsgeschwindigkeit gefundenen unerwarteten Resultate wurden Widerstandsmessungen der Systeme durchgeführt, wobei zwischen Metallelektroden gepreßte Oxydschichten verwendet wurden. Die oben erwähnten Übergangspunkte erscheinen alle deutlich in dem Verhalten des Widerstandes bezüglich Temperatur. Der Unterschied zwischen Pt und Ni als Basismetalle ist somit aufgezeigt. Schließlich werden die experimentellen Ergebnisse mit der einschlägigen Literatur entnommenen Daten kritisch verglichen.

CONTENTS

1. INTRODUCTION

As a check on the operation of the mass spectrometer described in the first part of this thesis *), we studied the important problem of the evaporation products of the alkaline-earth oxides from some base metals. The potentialities of a mass-spectrometric study of the evaporation characteristics of such systems have been demonstrated by some workers in this field. Barton, Harnwell and Kunsman [44]) identified the singly ionized atoms of the alkaline-earth metals in the evaporation products of a mixture of the oxides of these metals and iron oxide coated on a platinum filament. Blewett and Jones [45]) similarly found that ions of the alkaline-earth metals are emitted when the oxide of the metal in question is heated on a tungsten

*) Cf. preceding footnote.

filament. More recently Plumlee and Smith [46]) studied the evaporation characteristics of oxide-cathode materials with the aid of a modern instrument noting many interesting phenomena. Aldrich [47]) reports the study of the evaporation products of alkaline-earth oxides using pure single carbonates and various metals as base; he was interested mainly in a possible chemical reaction between the oxide and the underlying metal. In the present work some of Aldrich's measurements are repeated in order to obtain more quantitative values for the rate of evaporation; some other systems are studied and some striking results of the measurements are correlated with resistance measurements of the oxide systems as function of temperature.

2. EXPERIMENTAL METHODS

A. The mass-spectrometer method of measuring the evaporation products

In the mass spectrometer ions formed in the ionization chamber are beamed by the ion gun, resolved in the analyzer section, and the current carried by them is measured at the collector plate. In a mass spectrum, the ion current I at any M/e value will be proportional to the density d of the "mother molecule" in the ionization chamber:

$$I = a\, d\,. \tag{1}$$

We will return to the proportionality factor a later.

When a solid system is heated to a temperature T °K, a certain product will evaporate at a rate m into the ion source. If we assume immediate condensation on the walls of the ion source, which are at a much lower temperature (justified by the sharp shadows thrown by the evaporation products in our case; see also Moore Allison and Struthers [48])), then

$$d \sim \frac{m}{\sqrt{T}}\,. \tag{2}$$

The rate of evaporation can be further connected with the equilibrium pressure of the gas phase of the product over the solid phase by kinetic-theory equations [49]). In the case of evaporation from an open surface we have

$$am = F\left(\frac{M}{2\pi RT}\right)^{1/2} p\,, \tag{3a}$$

while in the case of Knudsen evaporation from an opening in a closed system in thermal equilibrium the equation

$$m = F\left(\frac{M}{2\pi RT}\right)^{1/2} p \tag{3b}$$

applies, where M is the mass in grams of one mole of the evaporation product, R the gas constant $= 8{\cdot}314.10^7$ ergs per degree, p the vapour pressure in dynes per square centimetre, T the temperature in °K, F the area of the emitting surface in square centimetres, and a the so-called accommodation coefficient, which takes into account the mechanism of condensation of the gas molecules striking the solid-gas interface ($a = 1/(1-r)$ where r is the reflection coefficient).

Combining (1) and (2) gives

$$I \sim a \frac{m}{\sqrt{T}}, \tag{4a}$$

or

$$\ln I = \ln m - \tfrac{1}{2}\ln T + \ln a + \text{Const.} \tag{4b}$$

The factor a takes into account the ion-current dependence on the mechanism of the ion source. Ionization and dissociation probabilities depend on the energy of the electrons of the ionizing beam and on the internal energy of the bombarded molecules. Collection and beaming efficiencies of the ions formed depend on the force fields at their place of formation and their initial velocities. The factor a can be varied by changing the conditions in the ion source and in this way one can identify the real evaporation products. Bombarding a molecule by electrons will lead to different stages of ionization of the original molecule and formation of dissociation products. The proportions of the numbers of the different ions formed depend primarily on the energy of the electron beam. To form an ionized dissociation product, the energy of the electron beam must exceed the sum of the dissociation energy of the molecule and the ionization energy of the dissociated product. One way of identifying the original molecule is therefore by study of the ratios of the ion currents at the given M/e values as function of electron-beam energy, other conditions being held approximately constant. Dissociation ions will also in general have a higher initial energy and this can be studied by changing the collecting and beaming conditions of the ion source. One might change the position of the electron beam in the ion source, or the accelerating voltage, etc. Further information can be obtained from comparison of the dependence of the ion currents on the sample temperature. Difference in behaviour will mean that they are not products of electron bombardment of the same evaporation material.

Equation 4b gives the connection between ion current and evaporation rate. The complicated nature of the factor a makes it impossible to determine absolutely the rate of evaporation by measurements of ion currents. On the other hand a changes relatively slowly with the temperature of the emitting systems. The changes in a arise, firstly, by changes in the thermal initial energy of the gas molecules and, secondly, because the dissociation probability depends on the internal energy of the molecules.

Usually, this necessitates only a small correction when dependence of evaporation rate on temperature is studied through ion-current measurements. It is known from thermodynamical considerations that the rate of evaporation can be represented by an equation of the type

$$\ln m = -\frac{A}{T} + B, \tag{5}$$

where B is a constant depending only slightly on temperature.

In the experimental results we will plot the logarithm of the ion current against $1/T$, assuming a dependence of the type

$$\ln I = -\frac{A^*}{T} + C,$$

where the relation between A and A^* can be derived from eqs 4b and 5. Comparison of different systems for the same evaporation product will, of course, have the advantage of an identical value of a.

B. Instrumentation

The mass spectrometer used for the measurements is described in the first part of this report. The oscillograph display was used to advantage in studying semi-quantitatively the evaporation products, checking the resolution and residual gases, and for quick and easy identification of mass numbers. The measurements of the rate of evaporation were done statically. The ion current was measured on a mV-meter at the output of the electrometer amplifier, while the instrument was focused for collection of ions of one M/e value. Usually the most abundant isotope was chosen, and the height of the current peak measured. Fig. 24, showing the isotopic composition of mercury, illustrates the resolving power of the instrument used throughout the measurements. Equal entrance and exit slits were used, measuring 0·25 mm in width.

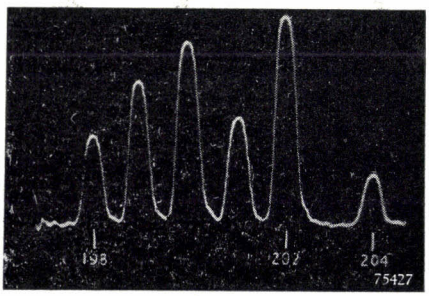

Fig. 24. Oscillograph display of Hg isotopes illustrating the resolving power of the instrument used.

The ion-source assembly is shown schematically in fig. 25; a metal ribbon coated with the necessary material is inserted through an opening in the upper side of the ionization chamber so that its emitting surface lies flush with the upper wall. The coated flat area measures $3 \times 1{\cdot}5$ mm^2; the thickness of the metal ribbon is 50 μ. The metal ribbon is directly heated by passing current through it. Its temperature is measured by a Pt-PtRh

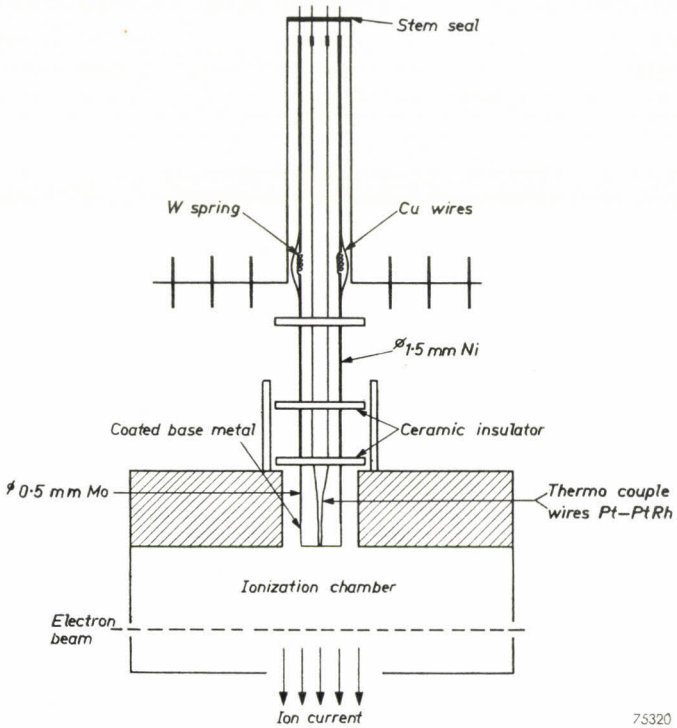

Fig. 25. Schematic drawing of the ion-source assembly used for the measurement of evaporation.

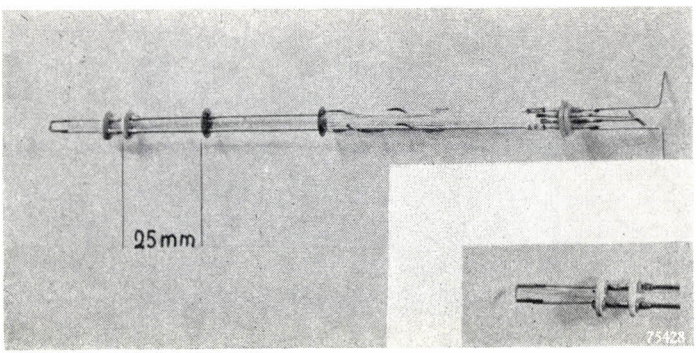

Fig. 26. The sample assembly.

couple with a wire diameter of 100 μ. The ribbon was connected electrically to the walls of the ionization chamber through the centre tap of the heating transformer. Fig. 26 shows a photograph of the sample assembly used.

C. The systems investigated

The following systems were studied:

(1) BaO, coated on Pt (4 samples);
(2) BaO, coated on Ni (1 sample);
(3) (Ba,Sr)O, coated on Pt (1 sample);
(4) (Ba,Ca)O, coated on Pt (1 sample);
(5) (Ba,Sr,Ca)O, coated on Pt (1 sample);
(6) BaO, coated on Ta (1 sample);
(7) SrO, coated on Pt (4 samples);
(8) CaO, coated on Pt (2 samples);
(9) Ni, ribbon uncoated (1 sample).

The semi-quantitative spectrochemical analysis of the single carbonates is given in Table III.

Table III

Semi-quantative spectrochemical analysis of the single carbonates in weight %

Impurity \ System	$BaCO_3$	$SrCO_3$	$CaCO_3$
BaO	—	≈·3	
SrO	·4		·05
CaO	—	·4	
MgO	·002	·1	·1
Na_2O	·3	·4	—
SiO_2	<·01	<·002	⩽·006
MnO	<·003	<·007	⩽·005
Fe_2O_3	<·0007	<·006	⩽·007
ZnO	—	—	⩽·01
PbO	<·02	<·002	⩽·004
Al_2O_3	<·01	<·01	—
TiO_2	—	<·01	—
CuO	·002	·0005	·0004
Ag_2O	·0002	·0002	
K_2O	<·3		

The underlying metals were analyzed spectrochemically as follows (semi-quantitatively in weight %):

Pt: Rh 0·5-3, Mn ·005, Fe ·05, Ni ·05, Sn <·01, Cu ·02, Ag ·005, As <·02;
Ni: Fe <·005, Cu ·0003;
Ta: Si <·005, Mg < ·001, Fe ·007.

The quantitative analysis of the mixed carbonates is given in Table IV. The mixture is made up of the components analyzed for impurities in the former table.

Table IV

Quantitave analysis of the mixed carbonates in weight %

System / Components	$(Ba,Sr)CO_3$	$(Ba,Ca)CO_3$	$(Ba,Sr,Ca)CO_3$
$BaCO_3$	56·2	59·2	45·3
$SrCO_3$	43	$\leqq$·2	33·5
$CaCO_3$	$\approx$·5	40·5	21

D. Preparation of the system

The sample assemblies were first prepared with the necessary base metal. The metal ribbon was then vacuum fired for one hour. This was done to supplement chemical cleaning (see Aldrich [47])), and to check the mechanical stability. The still uncoated sample was then glass sealed in an evacuated tube and baked out for one hour at 450 °C. After this preliminary treatment the flat top-part of the base metal was coated cataphoretically with a methyl-alcohol suspension of the carbonates, the thickness of the applied layer varying between 40 and 80 μ.

The coated sample was glass sealed into the ion-source assembly. Pumping and degasing procedures were then applied to the mass spectrometer, baking the system at 150 °C with liquid air as trap refrigerant. When the pressure dropped below 10^{-6} mm Hg degasing was stopped and with the aid of a Teflon stop the system was disconnected from the trap and mercury diffusion pump. This feature of the instrument enabled us to remove the refrigerant from the cold trap and pump away the vapours condensed on the cold surfaces. In the mean time the instrument was still being pumped by the gettering action of a Penning manometer. This completed, pumping was resumed and the conversion of the carbonate carried out while keeping the pressure below 10^{-5} mm Hg. When the pressure had dropped below 10^{-6} mm Hg at the highest temperature of the sample to be used in the measurements (the main component of the residual gas being CO_2 mostly re-evaporating from the trap), the sample was cooled down and the trap condensate pumped away as before. This procedure shortened considerably the preparatory steps prior to measurements. During measurements we succeeded thus in maintaining the pressure at 10^{-7} mm Hg.

3. EXPERIMENTAL RESULTS

A. Electron-beam dependence of ion currents in the various systems

For the purpose of determining the identity of the evaporation products from the heated systems, a study was made of the electron-beam dependence of the ion-current peaks in the various systems. With the aid of the ion-source regulator we could vary the energy of the electron beam between the values 8-100 eV, while the electron current to the catcher electrode, the trap, was kept constant at 100 μA. In this way we obtained the ionization and eventually the dissociation and ionization efficiency curves for the formation of the various ions. The efficiency curves will be *only approximately true*, as focusing effects in the electron gun will vary the density distribution of the electron beam in the ionization chamber when the electron energy is changed. Ion currents were measured also with higher ionizing currents in the ionization chamber. The following gives the results for the different systems.

(*a*) BaO/Pt

Fig. 27 shows the ion currents at *M/e* values of 154 and 138 as function of electron-beam energy. These are $IBaO_{154}$ and IBa_{138}, the currents of the single-ionized molecules of the oxide and the free element of the most abundant isotope of Ba. As already stated by Aldrich [47]), the results agree with a process of evaporation in which no chemical reaction occurs between Pt and BaO and no free Ba is formed. Since the ionization energy of Ba is 5·2 eV and the dissociation energy of BaO is 4·7 eV [50]), their sum 9·9 eV represents the energy required to produce Ba^+ from a neutral BaO molecule. Thus one would expect IBa_{138} to decrease when approaching this threshold, as is indeed the case. This is shown too in the ratio curve that gives also an upper limit for the evaporation of the material in the form of free Ba (ionization efficiencies must be considered).

Ba ions, being a dissociation product of BaO molecules by electron bombardment, should have a higher initial kinetic energy at formation than BaO ions. This is proved by observing the ratio of ion currents at the same energy of the electron beam but different density distributions. At 1 mA trap current and 70 volts electron energy, the ratio IBa/IBaO was 0·8 compared with 0·54 in fig. 27. At higher trap currents the boundaries of the electron beam approach the exit slit for the ions; this increases the solid angle of collection relatively more for ions with higher initial energy.

Further information is obtained by measuring the ion currents as function of sample temperature. $IBaO_{154}$ and IBa_{138} show the same behaviour within the experimental accuracy, supporting the assumption that both originate from the same mother molecule.

An ion current IBa_2O_2 was also measured at higher temperatures, but we could not study the dependence on electron-beam energy because of too high a rate of evaporation of the material at the temperature of observation. However, the temperature behaviour of IBa_2O_2 is different from that of IBaO, and indicates that part of the material evaporates in the form of Ba_2O_2.

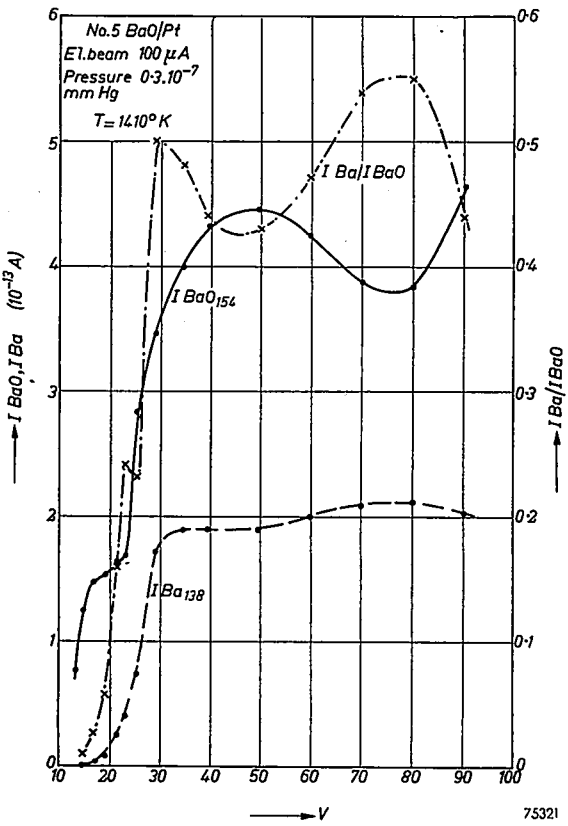

Fig. 27. $IBaO_{154}$, IBa_{138} and IBa/IBaO measured in the system BaO/Pt as function of the energy of the electron beam.

(*b*) BaO/Ni

In this system the electron-beam dependence of $IBaO_{154}$ and IBa_{138} is the same as in the BaO/Pt system. The two ion-current peaks behave in the same way with change of temperature. One should, therefore, assume in this case no chemical reaction, the evaporating product being mainly BaO.

(c) (Ba,Sr)O/Pt, (Ba,Ca)O/Pt, (Ba,Sr,Ca)O/Pt

Electron-beam dependence and behaviour with temperature indicate in this case, too, evaporation of Ba mainly in the form of the oxide.

(*d*) BaO/Ta

This system is essentially different from those preceding. Electron-energy dependence clearly indicates free-Ba evaporation. IBa_{138} is also an order of magnitude higher than $IBaO_{154}$ as compared with a ratio of about 0·5 in the system BaO/Pt (see also Aldrich[47]).

(*e*) SrO/Pt

Fig. 28 shows ISr_{88}, $ISrO_{104}$ and the ratio of the two currents as function of electron-beam energy. ISr_{88} is corrected for the evaporation of ionized Sr atoms observed when the ionizing electron beam is cut off. The situation is remarkably different from that occurring in the BaO/Pt system. It is seen that Sr atoms are a real evaporation product from the heated Pt filament, as the ratio does not decrease at low electron energies as it should do had it been an electron-bombardment dissociation product. Further ISr_{88} is about a factor 50 higher than $ISrO_{104}$ at the temperature used. As no chemical reduction of the oxide by the base metal Pt is expected, the results can be interpreted as a thermal dissociation occurring at the surface of the heated sample. We studied the oxygen peaks and found indeed an increase over background of the peaks 16 and 32 during the evaporation

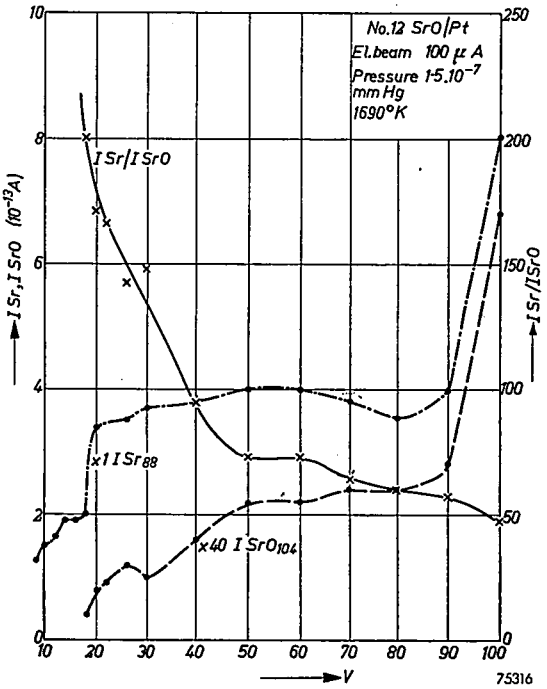

Fig. 28. ISr_{88}, $ISrO_{104}$ and ISr/ISrO measured in the system SrO/Pt as function of electron-beam energy.

process (see Aldrich [47])). We did not measure these peaks quantitatively.

The behaviour of ISr_{88} and $ISrO_{104}$ with the temperature of the system could be established as being quite different, confirming again that the free element and its oxide are real evaporation products and not a result of dissociation and ionization by the electron beam.

(f) CaO/Pt

Thermal dissociation at the surface of the heated system is seen to occur here too, as indicated by fig. 29. The ratio $ICa_{40}/ICaO_{56}$ increases at low

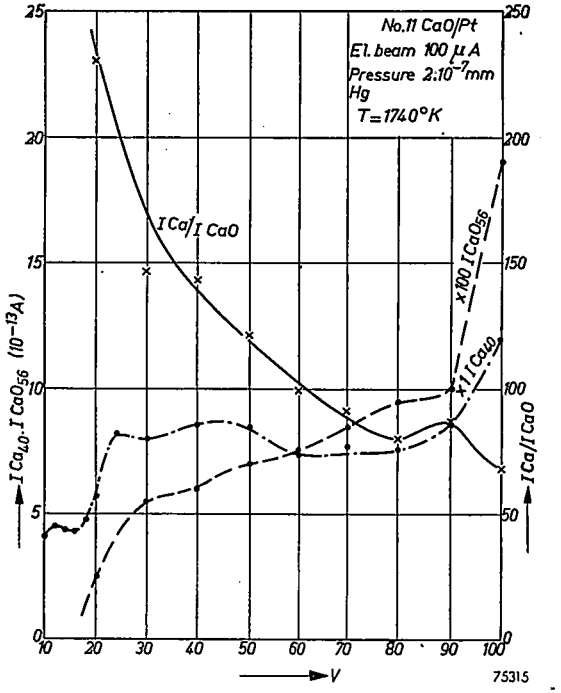

Fig. 29. ICa_{40}, $ICaO_{56}$ and ICa/ICaO measured in the system CaO/Pt as function of electron-beam energy.

energies indicating the evaporation of free Ca. ICa_{40} is corrected for the evaporation of Ca directly in the form of ions. Increase in the oxygen peaks 16 and 32 was observed during the process of evaporation. The behaviour of the ion current with temperature of the sample was difficult to observe in this system because of instrumental difficulties (see 3B) and the relatively low current of ICaO. The temperature behaviour may be the same within the present experimental accuracy.

B. Temperature dependence of ion currents

Under fixed electron-beam conditions the dependence of the ion current on the temperature of the system was studied. As discussed in the chapter dealing with the experimental method, we then measure the *rate of evaporation* as function of temperature, translated in the ion source to ion currents. In the following figures $\log_{10}$ of the ion current will be plotted against $1/T$, T being the absolute temperature of the system, as this should give essentially straight lines. The numbers indicated in the figures are the numerical values of the slope A in the equation $\log_{10} I = -A/T + B$.

The heating current of the ribbon was supplied by a stabilized power supply of the type described in the first part of this work, fig. 4. Most measurements were done with a high ionizing current in the source in order to obtain a high sensitivity, thus extending the measurements towards low temperatures of the sample. The upper temperature limit used in the measurements was dictated by the rate of loss of material by evaporation. The trap current was usually of the order of 1 mA. In this condition the ion-source emission-regulator is put out of action, stable operation being maintained through constant current supply to the electron-gun filament. In this type of work operation is carried out in a high vacuum of the order of 10^{-7} mm Hg, so that poisoning effects are small. We utilized another feature of the ion source for the purpose of stability. There proved to be a flat maximum in the ion current when the trap current was changed through control of temperature of the electron-gun filament. We then choose our working point in the middle of the flat part of the characteristics.

The ion-source assembly was removed from the instrument for cleaning and interchange of samples. This sometimes caused failure of the electron-gun filament, especially as in our measurements the filaments were run at rather high temperatures to obtain high trap currents. Replacement of filaments was not, at the time of measurement, fully reproducible. This affected the reproducibility of the absolute values of ion currents from different samples of the same material. Another factor influencing the absolute sensitivity was the condensation of the evaporated material on the walls of the ionization chamber (see also Plumlee and Smith [46])). The absolute values of ion currents for the neutral evaporating products were reproducible within a factor 2. Evaporation of ionized products varied up to a factor 6, even with the same sample. This suggests that ion evaporation takes place from special points of the sample and the effective surface for evaporation then fluctuates much more than the evaporating surface for neutral products, as a result of sintering and cracking of the material.

Our ion source was cooled mainly by radiation to the enclosing copper tube. The permissible rise in temperature of the ion-source assembly determined the sample size. The troublesome consequence of the relatively

high temperature was the appearance of residual peaks originating probably from organic compounds, which frequently necessitated long waiting times before measurements could be commenced. A very small air leak in the instrument which was difficult to locate contributed to mass 40 (argon) so that measurements of ICa_{40} were difficult to perform at low temperatures of the sample. A low electron-beam intensity, 100 μA stabilized, was then used in the measurements.

The following gives the temperature dependence of ion currents in the various systems

(*a*) Ni/Ni

As a check on the operation of our instrumental set-up for this type of work, we measured the dependence of the rate of evaporation on temperature from a clean Ni ribbon. Fig. 30 gives a plot of $\log_{10} INi_{58}$ against $1/T$

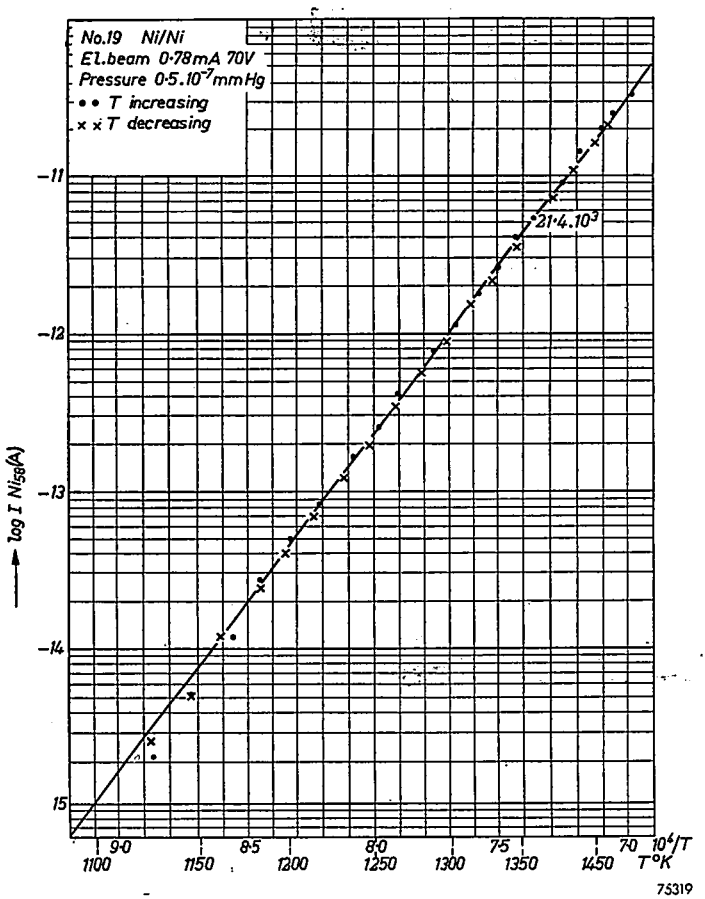

Fig. 30. Rate of evaporation of Ni metal from a Ni ribbon; INi_{58} as function of temperature.

T being the absolute temperature of the metal ribbon. The measurements were carried out with increasing and with decreasing temperature. The experimental points fit well to a straight line. The deviation of the points at low temperatures results probably from the error introduced in the measured residual peak at this mass number, which was of the order of 2.10^{-15} A. Ion-source conditions and experimental procedure were the same as those used in the study of the other systems.

(*b*) BaO/Pt

Unexpected results were obtained when $\log_{10} IBaO_{154}$ was plotted against $1/T$. The experimental points could not be fitted to one single line, the deviations then being far outside the experimental accuracy. Fig. 31 shows measurements made on one of the four samples studied for this system. The accuracy attained in the current measurements at the low temperature side was limited by the noise of the electrometer amplifier. Nevertheless the general behaviour of $IBaO_{154}$ as observed in all the samples of this system seems to indicate the existence, in the observed temperature range, of two lines with a transition region in the neighbourhood of the point $T = 1250$ °K. The existence of this transition point will be evident also in

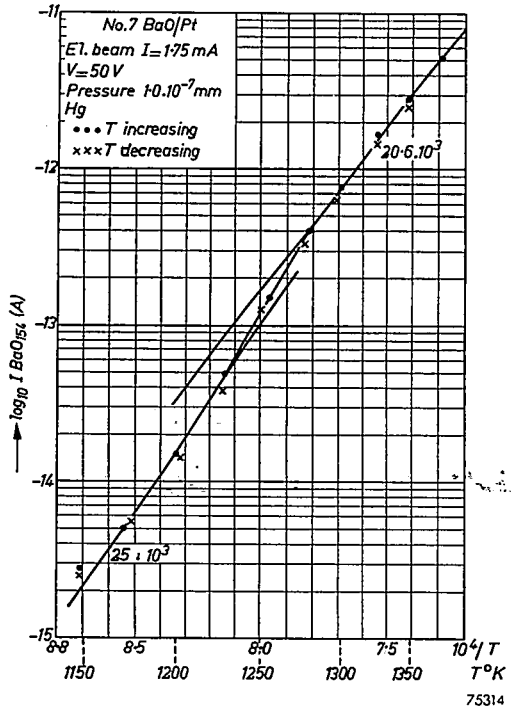

Fig. 31 Rate of evaporation of BaO in the BaO/Pt system. $IBaO_{154}$ as function of temperature.

the other systems containing BaO and it will be further confirmed by resistance measurements of a BaO layer. The effect measured is reversible with temperature, as the experimental results were taken whilst increasing and decreasing the temperature of the sample. IBa_{138} showed an identical temperature dependence, this being one of the indications that it is a dissociation product formed in the ion source by electron bombardment.

One of the samples of this system was used for the study of the temperature dependence of IBa_2O_2 which was observed at elevated temperatures of the system. Fig. 32 shows this ion peak as function of temperature, the measurements being made for increasing temperatures only. The high-temperature points indicate that the evaporation surface is diminishing during the measurements because of too high an evaporation rate at these temperatures.

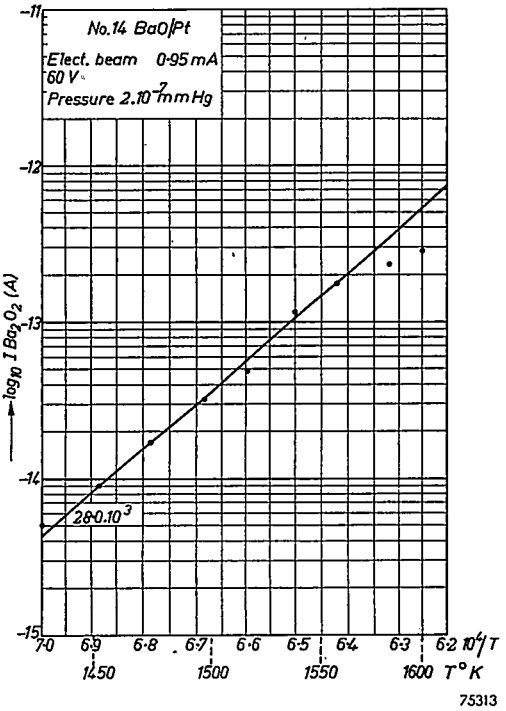

Fig. 32. Rate of evaporation of Ba_2O_2 in the BaO/Pt system. IBa_2O_2 as function of temperature.

(c) (Ba, Ca) O/Pt

Fig. 33 shows $IBaO_{154}$ as a function of the temperature in this system, measured while the sample was taken through a closed temperature cycle.

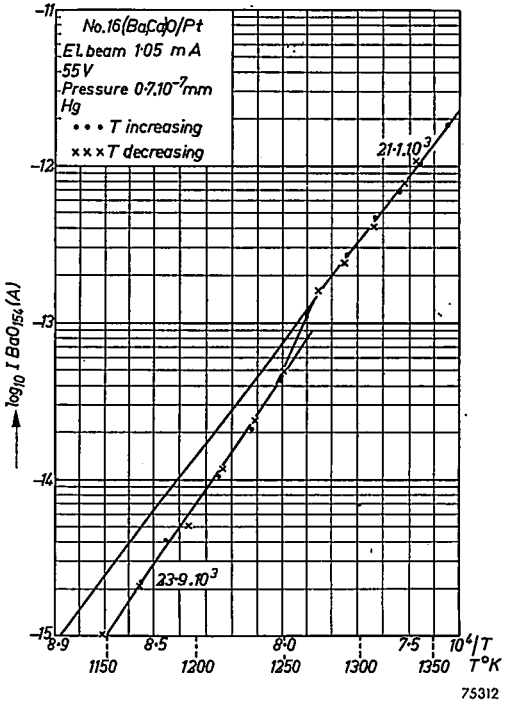

Fig. 33. Rate of evaporation of BaO in the (Ba,Ca)O/Pt system; $IBaO_{154}$ as function of temperature.

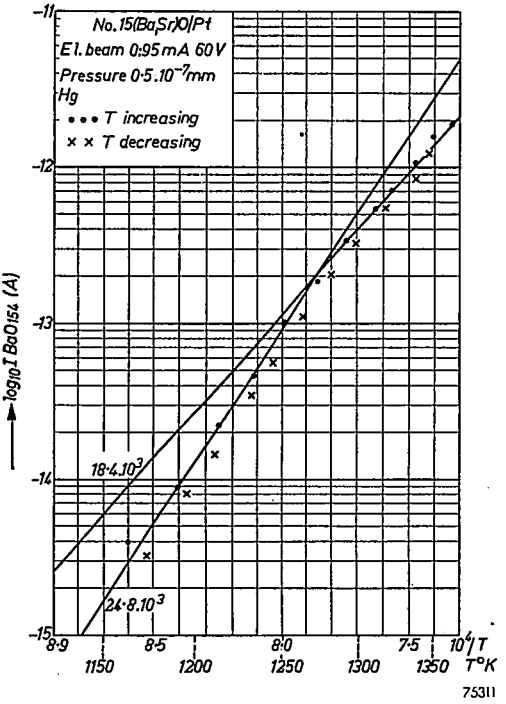

Fig. 34. Rate of evaporation of BaO in the (Ba,Sr)O/Pt system; $IBaO_{154}$ as function of temperature.

$IBaO_{154}$ shows identical temperature behaviour to that measured in the BaO/Pt system. IBa/IBaO has the same value as in that system. Here again high- and low-temperature lines are observed connected through an intermediate region at the same temperature point. It is possible that the observed absolute values of ion currents are lower in this system owing to part of the surface being occupied by CaO molecules.

(*d*) (Ba,Sr)O/Pt

$IBaO_{154}$ and IBa_{138} in this system are identical in their temperature dependence. Further, the ratio IBa/IBaO indicates that barium evaporates in the form of the oxide. The $\log_{10} IBaO_{154}$ versus $1/T$ curves seem to be composed of two straight lines cutting at about the same transition point as found in the BaO/Pt system. The intermediate region disappears. The upper temperature line has a lower slope than the one in the BaO/Pt system. Fig. 34 shows an experimental curve for this system. The points as found with decreasing temperatures show the same behaviour as those measured with increasing temperatures. The absolute values of ion currents are, however, lower, probably because of a discontinuous change in the sensitivity of the ion source caused by evaporation products condensed on the walls of the ionization chamber.

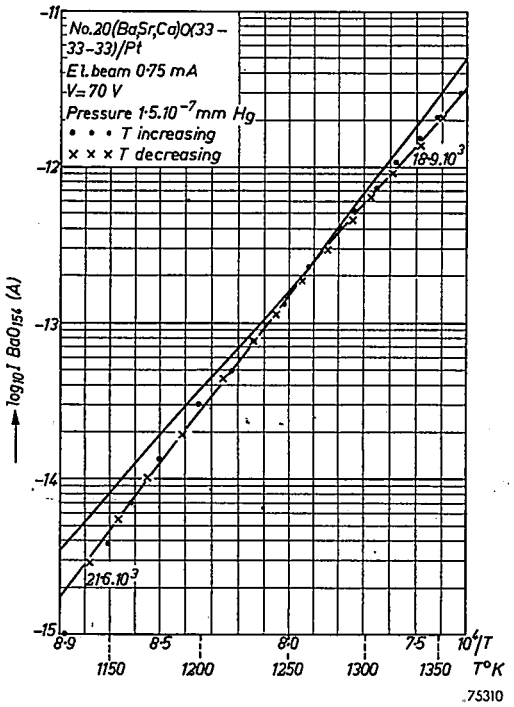

Fig. 35. Rate of evaporation of BaO in the system (Ba,Sr,Ca)O/Pt; $IBaO_{154}$ as function of temperature.

(e) (Ba, Sr, Ca)O/Pt

This system behaves similarly to the (Ba, Sr) O/Pt system. A representative curve is shown in fig. 35.

(*f*) BaO/Ni

In this system, again, the ratio IBa/IBaO and the identical behaviour with temperature of $IBaO_{154}$ and IBa_{138} indicate BaO evaporation. Fig. 36 shows a plot of $\log_{10} IBaO_{154}$ versus $1/T$. The curve is practically a straight

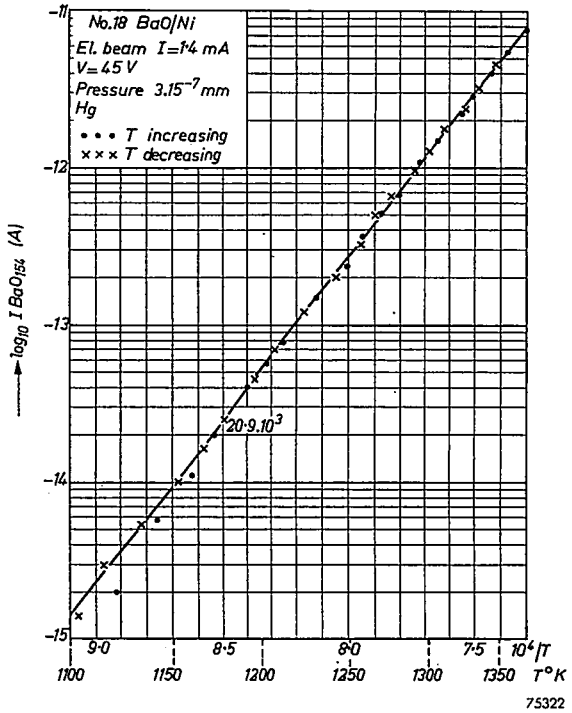

Fig. 36. Rate of evaporation of BaO in the system BaO/Ni; $IBaO_{154}$ as function of temperature.

line in the temperature range used. The difference in behaviour between this system and all the systems where the oxides were coated on Pt is immediately evident. No transition point is present at the temperature point $T = 1250$ °K. This difference cannot be explained by chemical reactions as neither of the two metals reacts with the oxide. But nickel has a notable vapour pressure at the temperatures used in the experiments as is evident from fig. 30, whilst ion currents of platinum could be observed in the mass spectrometer only at much higher temperatures. We tried

therefore to observe if Ni might evaporate through the porous layer of the BaO. Fig. 37 shows one temperature run. Comparison with fig. 31, which shows the situation for a clean Ni surface, excludes the possibility that we only measured evaporation from exposed parts of the underlying metal.

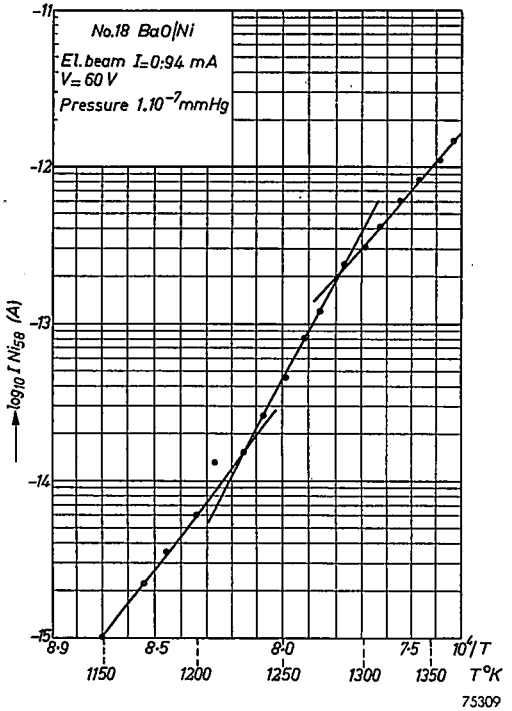

Fig. 37. INi_{58} as function of temperature, formed by electron bombardment of Ni evaporating through the porous layer of BaO coated on a Ni ribbon.

The measured points seem to fit to three lines, the middle section centering at $T = 1250$ °K the transition point of the BaO/Pt system. The explanation of the phenomena, therefore, seems to be that the reversible transition at $T = 1250$ °K is characteristic of the BaO material. In the case of Pt as an underlying metal there is no interaction between the metal and the oxide, the ribbon serving only as the heating medium. The transition point is not visible in the oxide evaporation from Ni probably because of interpenetration of Ni into the porous structure affecting the evaporation process on the surface. It is interesting to notice that the slope of the line in the BaO/Ni system is almost equal to the slope of the upper temperature line in BaO/Pt systems. The different behaviour of the two systems will be confirmed also by resistance measurements of the layer.

Fig. 38 summarizes the evaporation phenomena of BaO from the different system swith Pt and Ni as the underlying metal ribbon. The curves shown are mean values of the experimental results.

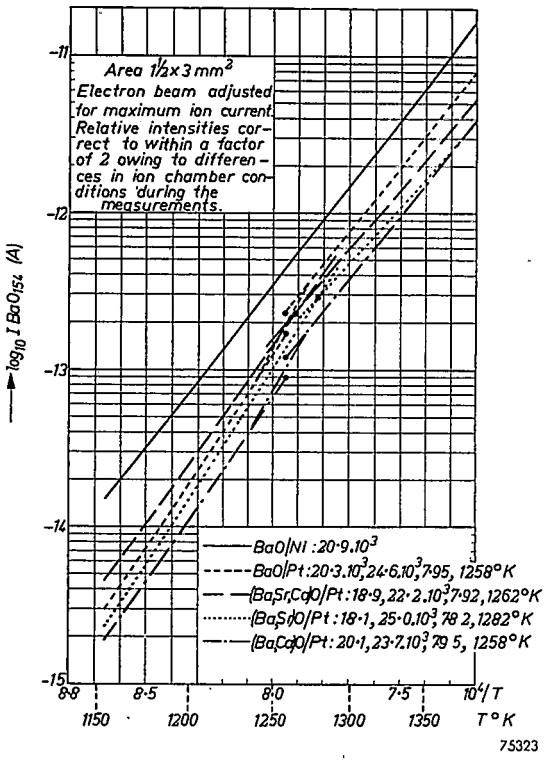

Fig. 38. Summary of mean evaporation curves of BaO in the different systems with Pt and Ni as the underlying metal base. At the bottom of the figure are given the numerical values of the slopes, $1/T$ and T values of the transition points.

(g) BaO/Ta

The main evaporation product was free atomic barium. $IBaO_{154}$ had the same absolute values as in the case of the BaO/Pt system, yet IBa_{138} was always at least an order of magnitude higher. This system proved to be very complex in its temperature behaviour and the results depended on the thermal history of the sample. We measured only one sample of this system, most measurements being carried out on IBa_{138} as this enabled us to measure at lower temperatures. Fig. 39 shows a set of curves giving the temperature dependence of IBa_{138} when the sample was taken through a temperature cycle. Each temperature cycle took about 30 min. The ion-current values are not reversible with temperature, the reason being

possibly the surplus of Ba in the coating when going from high to low temperatures. It would be interesting to study the behaviour when the temperature cycle is done in a limited region only where no transition points

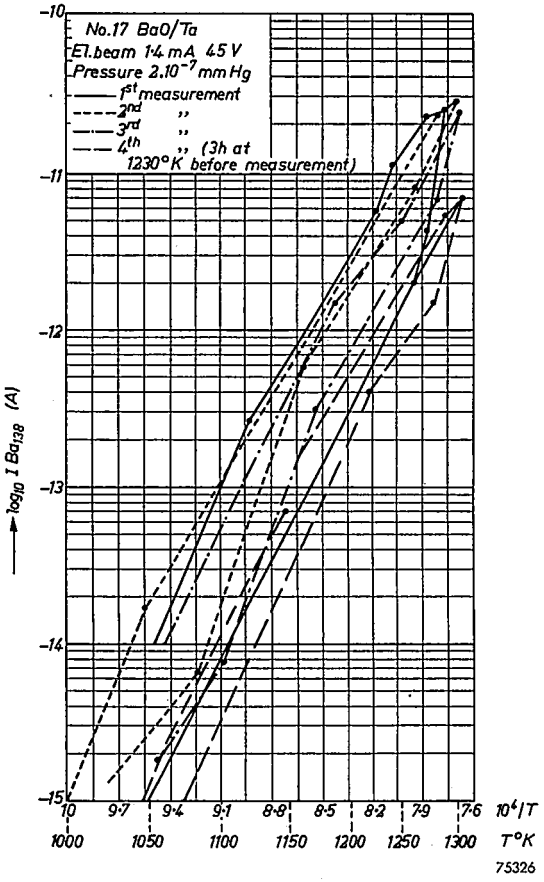

Fig. 39. Successive evaporation-rate curves of Ba_{138} in the system BaO/Ta showing temperature runs; each temperature cycle took about 30 min to measure.

occur. Of main interest to us was the behaviour of the system at the transition region of the BaO/Pt systems. One can indeed see a marked change in behaviour when this point is reached. It is especially evident in the first temperature cycle, where IBa_{138} increases by an order of magnitude over a small temperature range.

Fig. 40 shows the second temperature cycle with the experimental points. Three transition points are evident in the temperature range used, the upper point coinciding with that which we measured in the

systems of BaO on Pt. The existence of the other points in the BaO/Pt systems could not be investigated as $IBaO_{154}$ could not be measured at those temperatures. The resistance measurements of BaO layers seem to confirm the existence of at least two of the points indicated here as will be shown later.

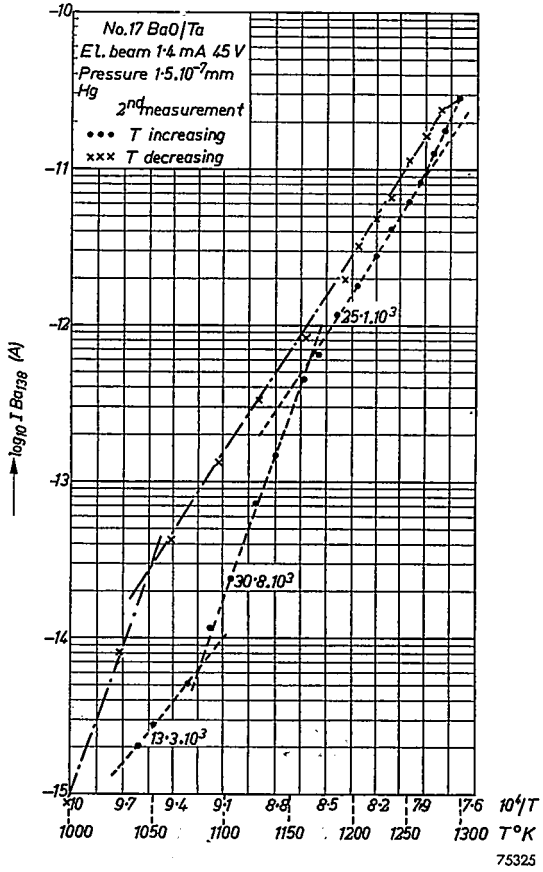

Fig. 40. Second temperature cycle measurement of the rate of evaporation, IBa_{138}, in the system BaO/Ta.

Completing the measurements on IBa_{138}, the system was heated up to higher temperatures and evaporation of barium ions was observed. The ion evaporation was also not reversible with temperature. The slope of the line in the $\log_{10} IBa^{+}_{138}$ versus $1/T$ plot turned out to have the value 50.10^3 T° (1480°-1610 °K).

(*h*) SrO/Pt

Fig. 41 summarizes with the aid of representative curves the evaporation products of the SrO/Pt system as function of temperature. The highest ion current in the temperature range used is that of the free-Sr evaporation. $ISrO_{104}$ is the ion current from the evaporated oxide; ISr_{88}^{+} is the current of Sr evaporating as ionized atoms. The lines are mean values of

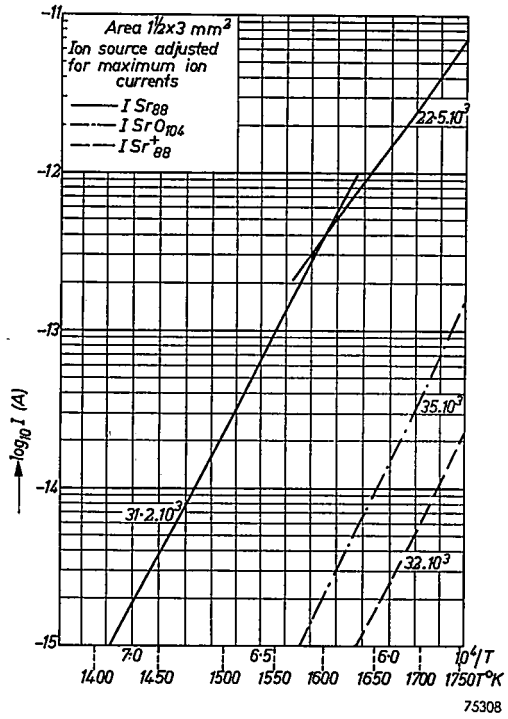

Fig. 41. Summary of evaporation rates in the SrO/Pt system.

the measurements. Fig. 42 shows the measurement of one temperature cycle of ISr_{88} with the experimental points. It is seen that a transition point exists in the ISr_{88} curve at $T = 1600$ °K. Compared with the behaviour of $IBaO_{154}$ in the BaO/Pt systems, the change in slope is proportionally larger, the transition point occurring at higher ion currents, so that the effect is more evident. The existence of this transition point has been confirmed very clearly in the resistance measurements of a SrO layer between platinum electrodes as will be shown later.

(*i*) CaO/Pt

The measurements of this system were more troublesome because of experimental difficulties. The higher temperatures used brought up the

background level of residual peaks and necessitated longer degasing times. An air leak which was difficult to locate contributed to the ion peak at mass number 40. Measurements were therefore done mostly with low electron-beam intensity and they could start only at higher temperatures of the sample than would otherwise be possible.

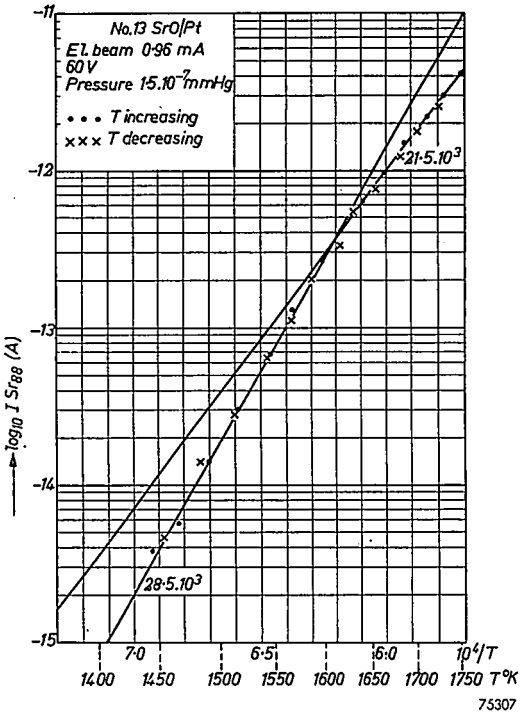

Fig. 42. Rate of evaporation of free Sr in the system SrO/Pt. ISr_{88} as function of temperature.

Fig. 43 summarizes the evaporation process in this system. The absolute value of ion currents is adjusted in the curves to the same conditions of ion-source efficiency used in the other systems. Fig. 44 is an experimental measurement of ICa_{40} when the sample was taken through a temperature cycle.

To summarize the present study of evaporation processes, fig. 45 gives representative curves of the main evaporation products of the alkaline-earth oxides as a function of temperature.

C. Resistance measurements of the systems as a function of temperature

In view of the unexpected behaviour of the evaporation rate of BaO and SrO with temperature, independent measuring methods were sought

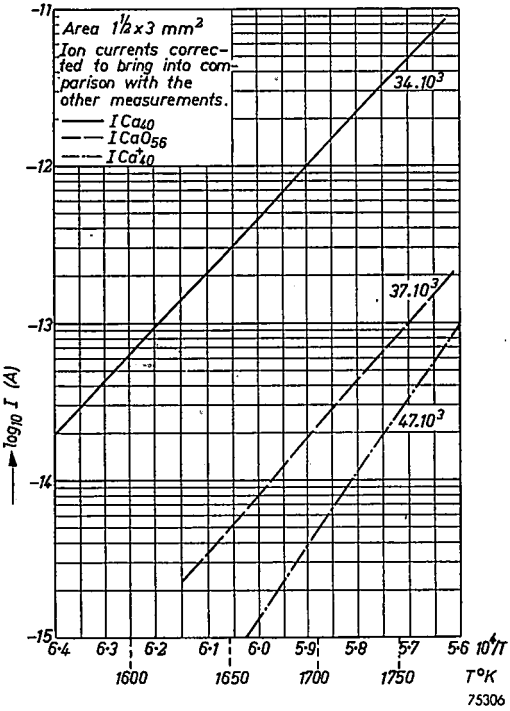

Fig. 43. Summary of evaporation rates in the CaO/Pt system.

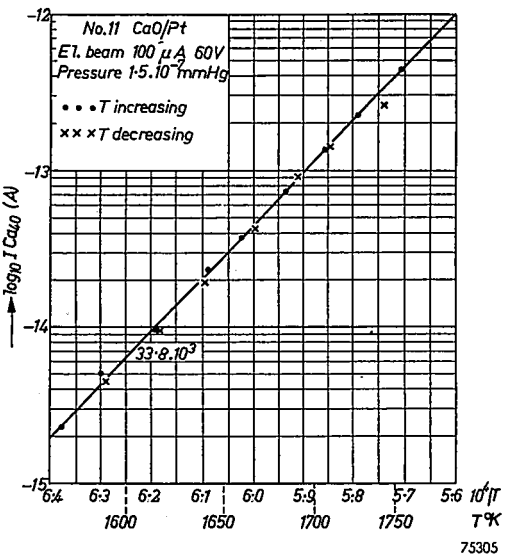

Fig. 44. Evaporation rates of free Ca in the system CaO/Pt; ICa_{40} as function of temperature.

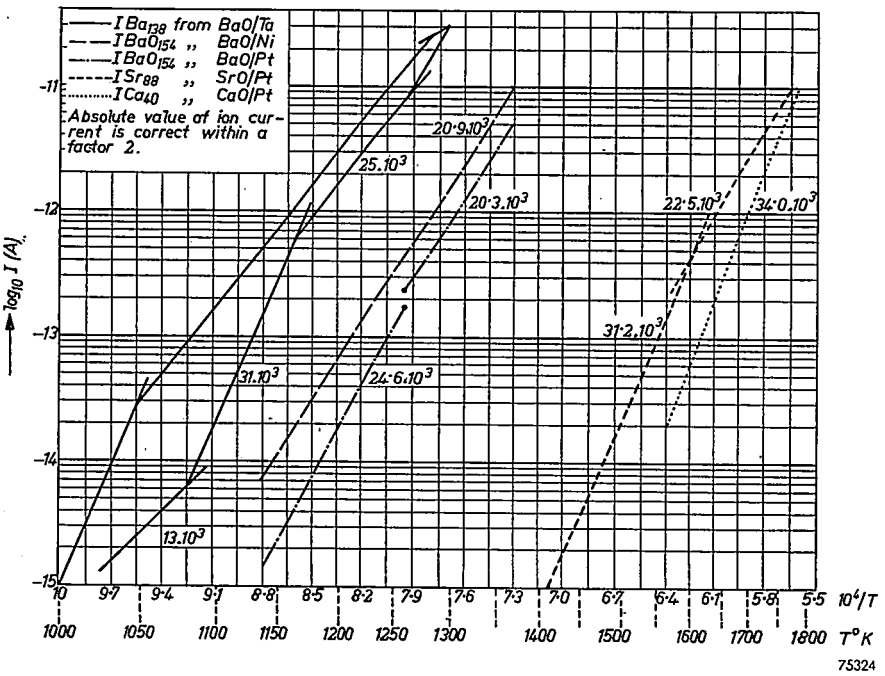

Fig. 45. Curves representing the rate of evaporation of the main evaporation products of the alkaline-earth oxides.

that might confirm and perhaps explain the phenomena. Useful results have been obtained by measuring the resistance of the oxide layer placed between the electrodes of the chosen metal, as a function of temperature. The construction of the resistance system is identical with that used by Loosjes and Vink [51]) in the study of the conduction mechanism in oxide-coated cathodes. It is shown schematically in fig. 46. A carbonate layer with a thickness of 150 μ is applied to the metal electrodes by spraying. The metal electrodes are in the form of cylinders with a flat surface of 25 mm^2 and wall thickness of 150 μ. They are pressed against each other by means of springs. The heater filament is mounted inside the cylinder. In the BaO systems it consists of a tungsten spiral insulated by Al_2O_3. In the SrO system, which is heated to higher temperatures, it is replaced by an exposed tungsten ribbon insulated from the cylinder wall by means of mounting rods. The temperature is measured by means of a Pt-PtRh thermocouple welded to the outside of the cylinder.

The resistance system is mounted in a glass envelope. The tube is then evacuated, thoroughly baked and degased. After conversion of the layer into the oxide and flashing a Ba getter, the tube is sealed off from the pumping system.

The measurements of the resistance value were carried out with an AC Wheatstone bridge, using a low fieldstrength in the layer. A complicating factor entering into the measurements was the drift with time of the resistance value, most pronounced at the high temperatures. Usually the systems had to be activated and aged for a long time before reproducible results could be obtained. As a check on the time effects all measurements were done over a closed temperature cycle, increasing and decreasing with temperature.

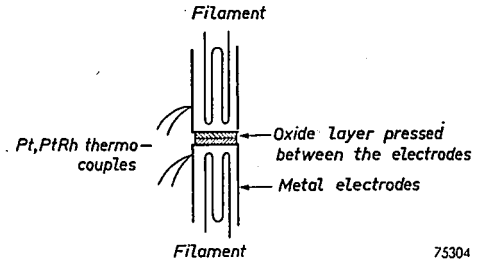

Fig. 46. Schematic construction of a resistance system where the resistance of the layer pressed between metal electrodes is measured as function of temperature.

(*a*) BaO/Pt

Two samples were measured for this system. The metal electrodes were made of Pt. It was difficult to eliminate fully the activation effects during the time of measurement, yet they could be made small enough for observation of the phenomena. One measurement made with this system is shown in fig. 47 where $\log_{10} R$ is plotted against $1/T$, R being the resistance value in ohms of the system, and T the absolute temperature. The plot is characteristic of all measurements taken with this combination.

Two transition points are seen in the plot, one in the neighbourhood of $T = 1250$ °K and the other in the neighbourhood of $T = 1150$ °K. It is possible that a third transition point, not shown in this plot, is present in this system at $T = 1050$ °K. The temperature value of the high-temperature point agrees well with the transition point observed in the evaporation rate of the BaO systems. The others may be correlated with those found in the evaporation rates of free barium in the system BaO/Ta.

(*b*) BaO/Ni

The metal cylinders in this case were made of the usual cathode nickel as we had not enough of the material used in the evaporation studies. We still expected to see a difference in resistance behaviour with temperature compared with the BaO/Pt system, as the difference should result, according to our assumptions, from interpenetration of metal into the porous structure of the layer. The experimental results are shown in fig. 48. The

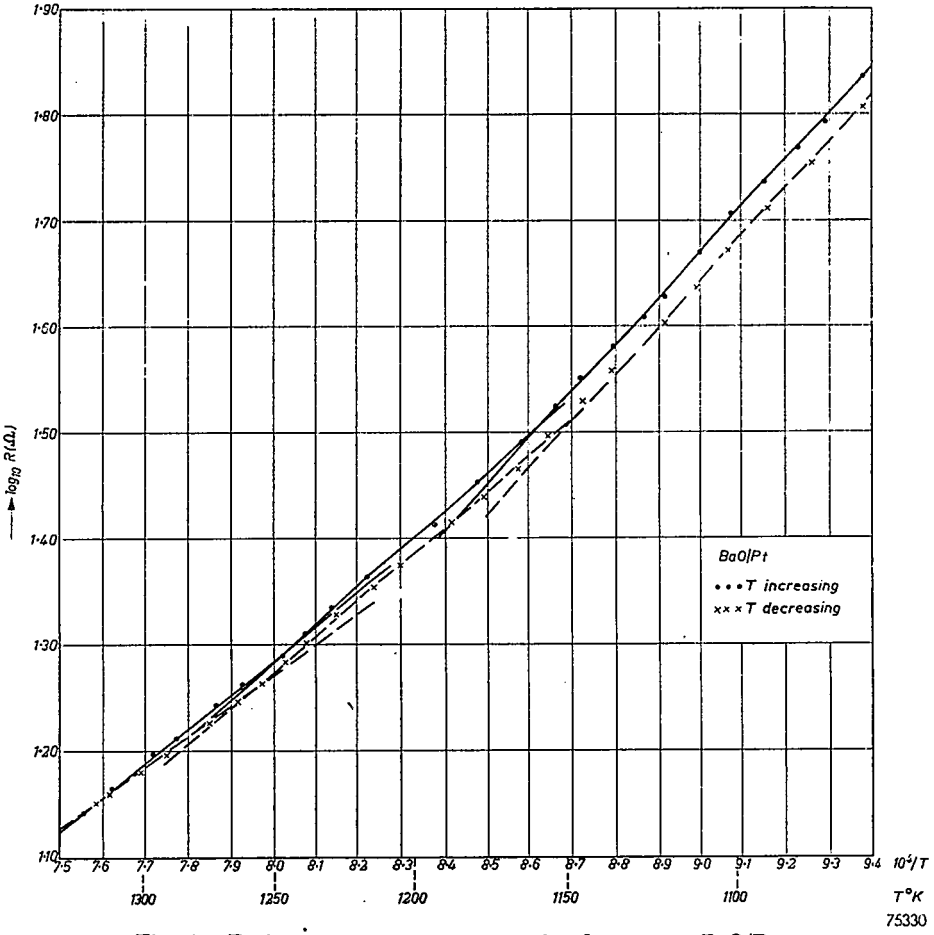

Fig. 47. Resistance-temperature curve in the system BaO/Pt.

high-temperature transition point at $T = 1250$ °K seems indeed to be missing and the slope of the line in this range is similar to the high-temperature slope in the BaO/Pt system.

(c) SrO/Pt

In this system we succeeded in obtaining reversible results immediately after the tube processing was finished. The experimental curve is given in fig. 49. The existence of a transition point at $T = 1600$ °K is evident, and agrees with the point observed in the rate of evaporation. In both cases of evaporation rate and resistance, the effect is proportionally larger and more distinct than in the BaO systems. In subsequent measurements activation effects began to show up. A second series of measurements made after the resistance system had been aged at a high temperature for a sufficiently long time, is shown in fig. 50.

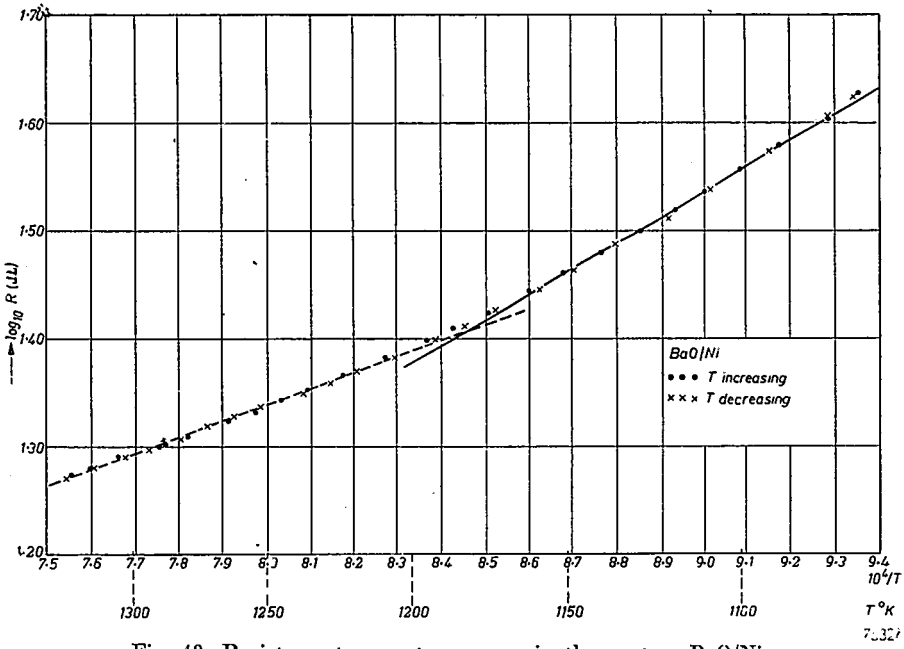

Fig. 48. Resistance-temperature curve in the system BaO/Ni.

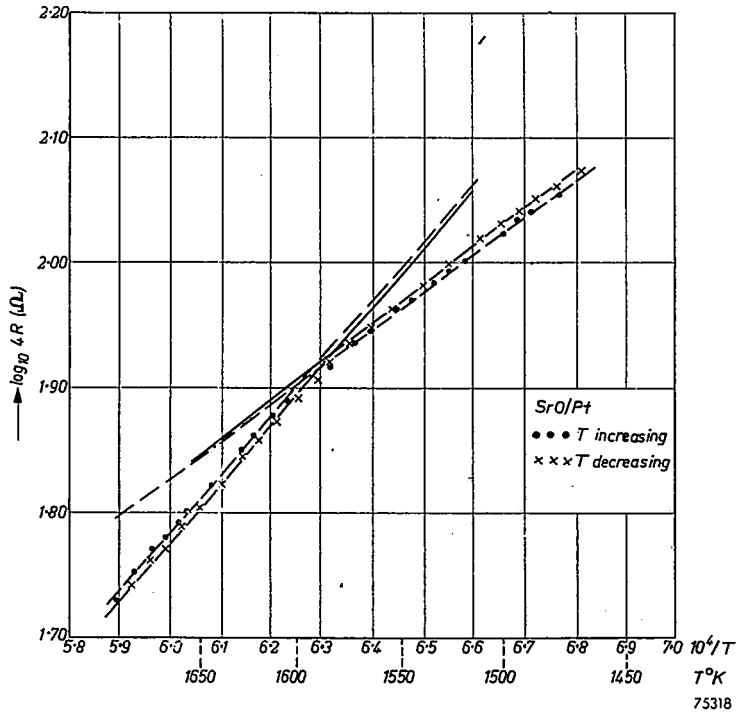

Fig. 49. Resistance-temperature curve in the system SrO/Pt, measured directly after processing the system.

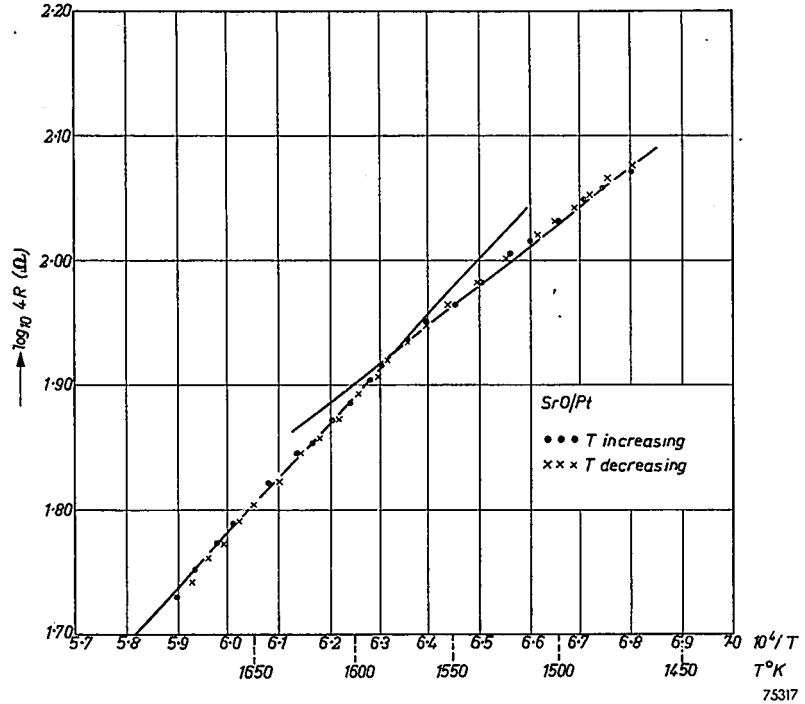

Fig. 50. Resistance-temperature curve in the system SrO/Pt measured after ageing.

4. EVALUATION OF THE MEASUREMENTS

A. Evaporation rate and temperature measurements

The drawbacks of a mass-spectrometric study of evaporation phenomena are obvious; absolute determination of the rate of evaporation is not possible because of the complicated mechanism operating in the ion source. The reproducibility in the absolute value of ion currents may be affected by the material condensing on the walls of the ionization chamber.

It is proved in this work that reproducibility in ion currents can be obtained within a factor 2 for a neutral evaporation product. It can be further improved by checking the sensitivity of the instrument by introduction of a calibration gas into the ionization chamber. Stable comparative measurements are thus possible of the same evaporation products from different systems. The correlation between ion currents and the quantitative rate of evaporation can be determined by reference to methods that measure absolute values. Even when the absolute values of the rate of evaporation are not known, estimated ionization efficiences can be used to determine the order of magnitude of quantitative evaporation rates.

The mass-spectrometer method, on the other hand, has many advantages over the weighing and radio isotope methods. It is a selective method, being able to identify and measure the primary specific evaporation products. It is sensitive so that a study of small amounts of material in the gaseous state can be made in a relatively short time. A large number of results can be obtained with one single sample. The temperature behaviour of the rate of evaporation is thus studied more quickly and more reproducibly, especially when kinetic factors are involved. This is brought out to some extent in the present work. The range of evaporation rates that can be studied is limited at the lower end of the scale by the sensitivity of the ion source, the residual peaks, and the sensitivity of the current-measuring device. It can be further extended to lower rates of evaporation by use of more efficient ion sources and more sensitive current measurements (the secondary-electron multiplier) provided that the residual peak background is suppressed (cooling the ion-source assembly).

The measuring procedure for determining the temperature of the oxide layer in our case is open to criticism. We measure by means of a thermocouple the temperature of the underlying metal ribbon which is also the heat source. With the aid of a mV-meter we can then read this temperature with a reproducibility of $\pm$ 1·5 ° as seen from the dispersion of the measured points on the evaporation curves at high current values. The problem to be solved is that of the relation between the observed temperature and the real temperature of the surface from which the evaporation takes place. We are not working under conditions of thermal equilibrium and the sample faces much colder material. There is practically no heat production in the oxide layer itself; an energy flow through the layer to the radiating surface will be accompanied by a temperature gradient over the thickness of the layer.

No reliable values of the heat conductivity of the oxides studied here are known and reference must be made to indirect information. Claassen and Veenemans [52]) and Moore, Allison and Struthers [48]) studied the vaporization of SrO from a Pt base metal. The temperature of the layer surface was assumed by the first investigators to be that of the supporting platinum cylinder, as determined by an optical pyrometer. The later investigators determined the surface temperature of the layer itself by means of a pyrometer. The values found in both cases for the evaporation rates are identical within the experimental accuracy of the temperature measurements. The evaporation of BaO from a Pt base was studied by Claassen and Veenemans [52]) who used the pyrometric temperatures of the underlying platinum cylinder and by Blewett, Liebhafsky and Hennelly [53]) who used a Knudsen method of evaporation and effectively measured "black body" radiation in the hope of reducing the temperature uncertainties. The results of the two measurements are in good agreement.

It should be realized that the rate of evaporation varies exponentially with temperature so that temperature differences can be sensitively checked by measuring the evaporation. The facts mentioned above would therefore seem to indicate a negligible temperature drop over the layer. Our own measurements of ion currents confirm this conclusion. In the course of repeated measurements on any one sample we usually reached the stage where most of the coated material evaporated and condensed on the ionization-chamber walls so that part of the metal surface became exposed. In all measurements, except in the complicated BaO/Ta system, we never observed that the ion currents became higher as the thickness of the layer diminished. Furthermore the layer thickness of the different samples in one system varied between 40 and 80 μ; but we found only a factor 2 in the reproducibility of ion currents of neutral evaporation products in the samples of the same system. This could be accounted for by differences in the ion-source setting and by the troublesome effects of condensed material on the walls of the ionization chamber. In any case this sets an upper limit of about 20 °K to the possible temperature drop over the layer. Finally one should note that the construction of the resistance system permits no net flow of energy through the layer. Yet the temperature values of the transition points found in the behaviour of the materials studied agree well in the measurements of resistance and of evaporation rate. We therefore believe that the temperature drop across the layer in the circumstances used in this work is small and that the method of temperature measurements adopted is essentially correct.

B. Comparison of the results with the literature

The reversible transition points occurring in the temperature characteristics of BaO and SrO as indicated in this work have not yet been reported in the literature. The reason for this lies probably in the difficulty of achieving a high accuracy in evaporation rate and temperature measurements in such experiments. The number of observations of the rate of evaporation is usually small and the deviations from a straight-line plot rather high. The transition points reported above also happen to be situated at the margin of, or outside of the temperature range studied in the literature [47]), [48]), [52]), [53]).

The identification of the evaporation products in BaO and SrO systems as reported in this work is in agreement with the mass-spectrometric studies of Aldrich[47]), and of Plumlee and Smith[47]). CaO systems have not yet been observed critically with a mass spectrometer.

When comparing the slopes of the evaporation curves and the order of magnitude of the absolute evaporation rate with those reported in the literature, equations (4) and (3) must be referred to. In our figures we have

given the numerical values (in T° units) of the slopes of curves showing $\log_{10}$ of the ion current versus $1/T$. These slopes should be corrected to evaporation-rate slope and equilibrium-pressure slope by incorporating the change with temperature of the extra terms given in the equations. The correction because of $\frac{1}{2}\log T$ or $\log T$ amounts in our temperature range to an increase of about 2% in the slopes given in the figures and this is still outside our experimental accuracy. The change with temperature of $\log a$ is difficult to calculate, but it is estimated to give even a smaller correction in our case [31]). The slopes can be expressed in energy units of calories by multiplying the value in T° units by the conversion factor 4·575 cal. T^{-1}.

(*a*) BaO/Pt

We established the existence of two slopes (see fig. 45) for the rate of evaporation of BaO. The numerical values are 25.10^3 (1150°-1250 °K) and $20{\cdot}3.10^3$ (1260°-1400 °K). Claassen and Veenemans [52]) report a slope of $19{\cdot}7.10^3$ (1200°-1500 °K) agreeing with the high-temperature slope found by us. Blewett, Liebhafsky and Hennely [53]) give a slope of $19{\cdot}4.10^3$ (1200°-1800°). Aldrich [47]) measured a slope of $19{\cdot}1.10^3$ (1170°-1420 °K).

(*b*) (Ba, Sr)O/Pt

Our measurements indicate a difference in the "high temperature" slopes of BaO evaporation from BaO/Pt and (Ba,Sr)O/Pt, the values being respectively $20{\cdot}3.10^3$ and $18{\cdot}1.10^3$ (1250°-1400 °K). This seems to be confirmed by the results of Claassen and Veenemans [52]).

(*c*) SrO/Pt

In our work we report a transition point in the evaporation curve of Sr metal at 1600 °K (see fig. 41). The slopes measured are $31{\cdot}2.10^3$ (1450°-1600 °K) and $22{\cdot}5.10^3$ (1600°-1750 °K). The upper temperature range borders on that measured by Aldrich [47]) who reports a slope of value of 30.10^3 (1725°-1810 °K). The low-temperature range is covered only by gravimetric and radioactive-tracer methods [52]), [48]), [54]) which are not selective and measure the total quantity of Sr evaporated irrespective of chemical bond. We found, however, that thermal dissociation occurs on the surface, the main evaporation product being Sr in the free state. We can therefore assume that the same main evaporation product is involved in all cases (at least in the temperature range from 1450°-1750 °K), and we proceed with the comparison. We find a good agreement with the results of Claassen and Veenemans [52]) who report a value of $30{\cdot}7.10^3$ (1500°-1600°K). In general the ratio of the absolute evaporation rates given in their work for the BaO, SrO and CaO systems can also be brought in agreement with our results as given in fig. 45 when allowance is made for the differences in ionization efficiencies (differences within an order of magnitude). On the other hand, there is a strong disagreement with the conclusions of Moore, Allison, and Struthers [48]). They report a slope of $23{\cdot}66.10^3$

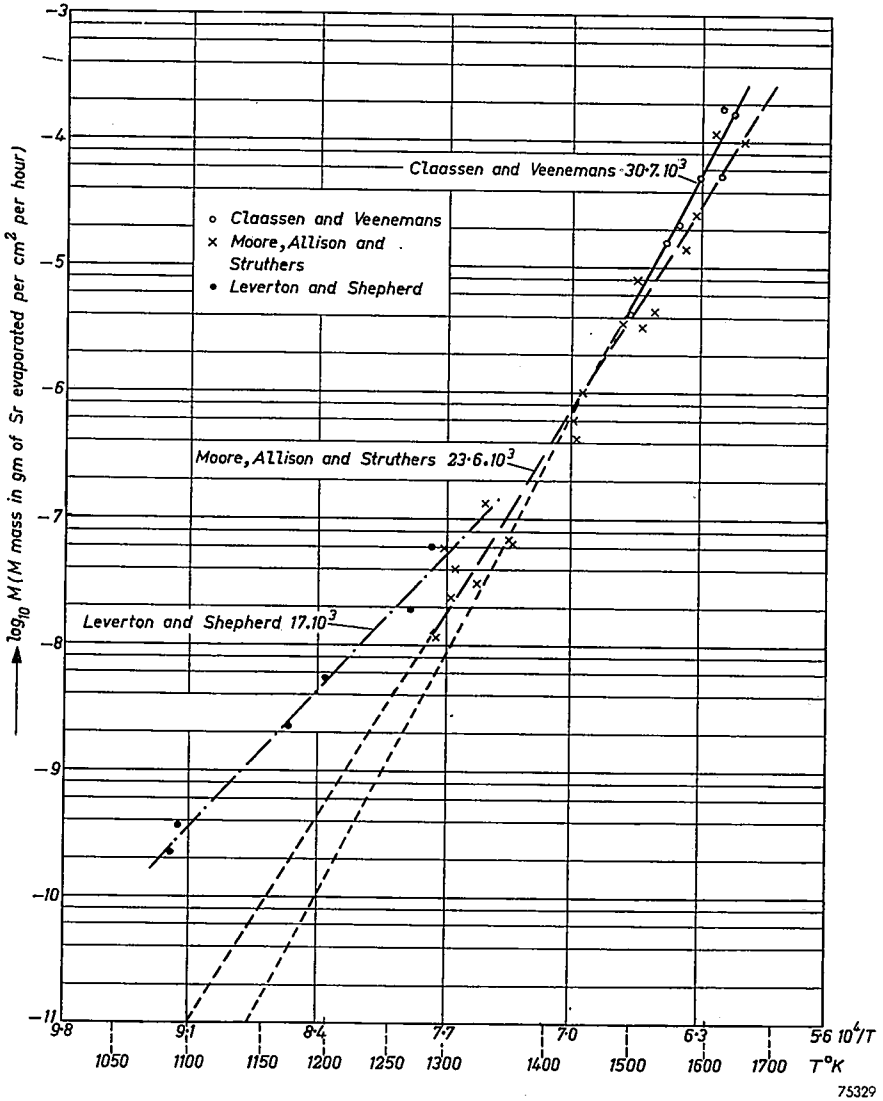

Fig. 51. Gravimetric and radioactive-tracer measurements of Sr evaporation reproduced from literature.

over an extensive temperature range 1280°-1600 °K. Their high-temperature points (1500°-1600 °K) agree well in absolute value with those of Claassen and Veenemans [52]) which are also used by them in the construction of the evaporation curve. An extension of their curve to lower temperatures can be compared with the results of Leverton and Shepherd [54]) who give the evaporation-rate curve of Sr from (Ba,Sr,Ca)O (on Ni!) measured by the radioactive-tracer method. The extrapolated values are lower than

the experimental points, which also seem to lie on a curve with a slope of 17.10^3 (1080°-1280 °K). Whilst the discrepancy in the absolute values is then about a factor 10, it rises to a factor 20 when the curve of Claassen and Veenemans, confirmed in slope by our measurements, is extrapolated to the same region, while the disagreement in the value of the slope would be still higher. The situation is shown graphically in fig. 51 where the experimental points of the three measurements are reproduced.

A probable answer to this difficulty could be that a single straight line is not the correct description of the evaporation phenomena, and that transition points exist. In order to prove this assumption we reproduce in fig. 52 the resistance curve of the SrO/Pt system as function of temperature extended to this temperature range. The good experimental accuracy and reproducibility of the experimental points clearly indicate a complex behaviour of this system with temperature. The upper transition point at $10^4/T = 6{\cdot}3$ is the identical point shown in fig. 49 and 50. Three extra points are indicated at the neighbourhood of $10^4/T$ values of 6·8, 7·3 and 8·0. We believe that the evaporation curve is made up from more than one

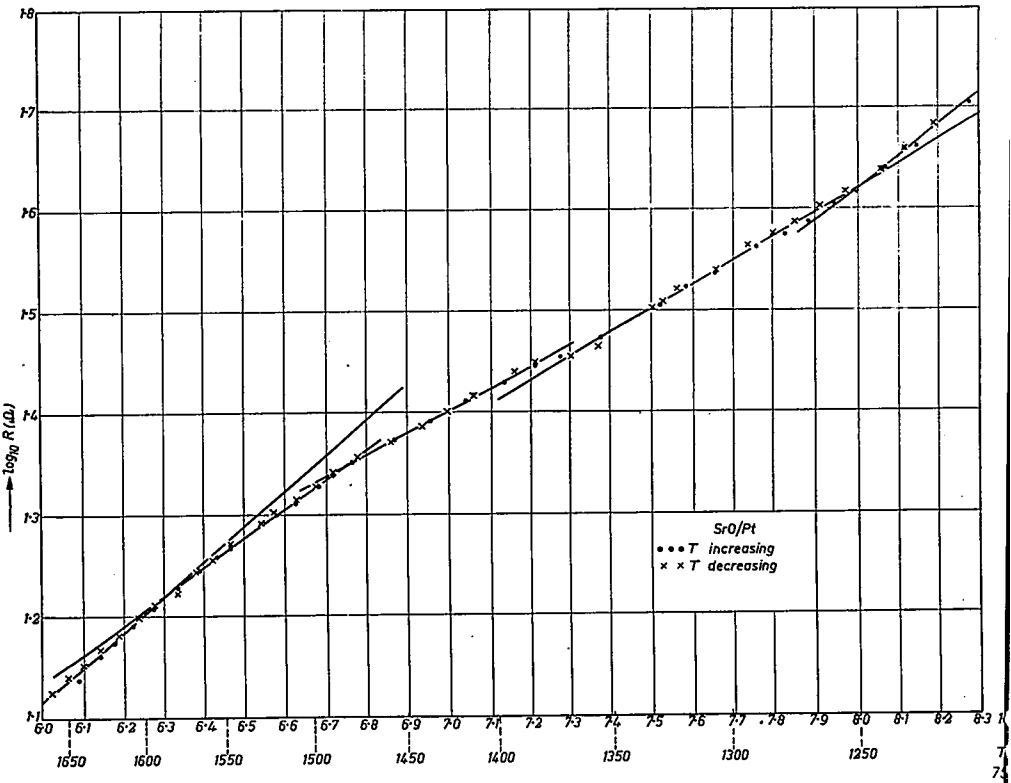

Fig. 52. Resistance-temperature curve in the system SrO/Pt.

single straight line. The slope of the group of points at the high-temperature side taken by themselves would give a value close to our numerical value of $31{\cdot}2.10^3$ (1450°-1600 °K) A statistical study of the experimental points used by Moore Allison and Struthers clearly indicate that there is a very small chance indeed that they can be represented by a single straight line.

(*d*) CaO/Pt

Our experimental value for the slope of the evaporation curve of Ca atoms is 34.10^3 (1550°-1750°K) as compared with $27{\cdot}4.10^3$ (1600°-1750°K) reported by Claassen and Veenemans [52]). The dispersion in the experimental points in the latter work is, however, very high because of experimental difficulties in temperature determination.

Evaporation of Ca from (Ba,Sr, Ca) O/Ni has been studied by Leverton and Shepherd [54]) using radioactive tracers. Their measured slope is 18.10^3 (1080°-1280°K). A discrepancy exists also in absolute evaporation rates when we try to extrapolate to low temperatures the absolute evaporation rate measurements of Claassen and Veenemans using our experimental value for the slope. Probably the evaporation mechanism is complex, similar to that assumed in the SrO/Pt system.

(*e*) Ni

Our measured slope of the Ni evaporation curve is $21{\cdot}4.10^3$ (1130°-1450 °K) as compared with $22{\cdot}1.10^3$ (1300°-1600 °K) reported by Johnston and Marshall [55]).

No clear explanation of the transition phenomena reported in this work can be suggested at present, and further investigations are being carried out towards this end.

Acknowledgement

My sincere thanks are due to many people of the Philips Research Laboratories, particularly to Dr N. Warmoltz, Dr J. J. Zaalberg van Zelst and Dr R. Loosjes, for their part in this work and valuable discussions.

Eindhoven, February 1953

REFERENCES

[44]) H. A. Barton, G. P. Harnwell and C. H. Kunsman, Phys. Rev. **27**, 739-746, 1926.
[45]) J. P. Blewett and E. J. Jones, Phys. Rev. **50**, 464-468, 1936.
[46]) R. H. Plumlee and L. P. Smith, J. appl. Phys. **21**, 811-819, 1950.
[47]) L. T. Aldrich, J. appl. Phys. **22**, 1168-1174, 1951.
[48]) G. E. Moore, H. W. Allison and J. D. Struthers J. chem. Phys. **18**, 1572-1579, 1950.
[49]) I. Langmuir, Phys. Rev. **2**, 329-342, 1913.
[50]) A. G. Gaydon, Dissociation Energies (John Wiley and Sons Inc. N.Y., 1947).
[51]) R. Loosjes and H. J. Vink, Philips Res. Rep. **4**, 449-475, 1949.
[52]) A. Claassen and G. F. Veenemans, Z. Phys. **80**, 342-351, 1933.
[53]) J. P. Blewett, H. A. Liebhafsky and E. F. Hennelly, J. chem. Phys. **7**, 478-484, 1939.
[54]) W. F. Leverton and W. G. Shepherd, J. appl. Phys. **23**, 787-793, 1952.
[55]) H. L. Johnston and A. L. Marshall, J. Am. chem. Soc. **62**, 1382-1390, 1940.

ABSTRACTS OF RECENT SCIENTIFIC PUBLICATIONS OF N.V. PHILIPS' GLOEILAMPENFABRIEKEN

Reprints of the majority of these papers can be obtained on application to the Administration of the Research Laboratory. Kastanjelaan, Eindhoven, Netherlands. Those papers of which no reprints are available are marked with an asterisk (*).

2048: K. F. Niessen: Spontaneous magnetization of nickel zinc ferrite as a function of the nickel zinc ratio (Physica **18**, 449-468, 1952).

The reduced spontaneous magnetization of nickel zinc ferrite (magnetization at temperature T, divided by that at $T = 0$) is determined as a function of the reduced temperature T^* (T divided by the Curie temperature T_C) and of the nickel/zinc ratio f. The latter is defined by the following expression for the ratio between the numbers of nickel and zinc ions: $\mathrm{Ni/Zn} = f/(1-f)$. In the case $T \ll 1$ and in the case $T = 1 - \Delta$ ($\Delta \ll 1$) formulae for the reduced magnetization are given, holding for high values of f, for instance $^1/_2 < f < 1$. For intermediate values of T^* a graphical method must be used. The results are compared with the experimental curves of Guillaud and Roux, representing the reduced magnetization as a function of T^* when several ferrites with a different nickel/zinc ratio are considered, especially at low and intermediate values of T^*. These curves diverge in a typical way. This can be explained qualitatively.

2049: H. Bremmer: On the asymptotic evaluation of diffraction integrals with a special view to the theory of defocusing and optical contrast (Physica **18**, 469-485, 1952).

An expansion is given of the function $U(x, y, z)$ that satisfies the scalar wave equation in the half-space $z < 0$ and equals a given distribution $U_0(x, y)$ in the plane $z = 0$. If U_0 is zero beyond a closed contour L in $z = 0$, $U(x, y, z)$ splits into a so-called geometrical-optical part (which vanishes outside the cylinder passing through L and having generating lines parallel to the z-axis) and a diffraction part (determined by the values of U_0 near L). Each part can be expanded into terms depending on $U_0(x, y,)$ itself and on its iterative two-dimensional Laplace operators $\Delta^n U_0 = (\partial^2/\partial x^2 + \partial^2/\partial y^2)^n\, U_0(x, y)$. The expansions are in general asymptotic for small wavelengths; however, their exact validity can be proved for functions U_0 that are polynomials inside the contour L. The terms of the diffraction part consist of contour integrals along L, the corresponding terms for the geometrical-optical part do not depend on any integration. The first few terms of the latter part are essential for defocusing effects and can be connected with the brightness-contrast existing in the plane $z = 0$.

VOL. 9 NR 2 APRIL 1954

Philips Research Reports

EDITED BY THE RESEARCH LABORATORY
OF N.V. PHILIPS' GLOEILAMPENFABRIEKEN, EINDHOVEN, NETHERLANDS

R 236 *Philips Res. Rep. 9, 81-108, 1954*

ELECTROLUMINESCENT ZnS PHOSPHORS

by P. ZALM, G. DIEMER and H. A. KLASENS

535.376:546.472.21

Summary

In Part I, an account is given of the preparation of electroluminescent zinc-sulphide powders. The preparation is based on the assumption that a copper-rich layer on the surface of the grains is necessary for electroluminescence.
In Part II, electrical and optical measurements on electroluminescent ZnS powders are described, including various oscillograms of suspended and binderless settled layers, and stroboscopic observation of the individual crystals by means of a microscope. The maximum efficiency is 1·5 (±0·2) lm/W; the brightness at 600 V, 3000 c/s is about 1000 lm/m^2. The hypothesis of a barrier action at the surface of the grains is confirmed.
In Part III, the observations of Parts I en II lead to the conclusion that electroluminescence is a kind of cathodoluminescence with "slow" electrons. The smallness of the efficiency of electroluminescent phosphors is compared with that of normal phosphors under cathode-ray excitation at low voltage and high current density. A discussion is given of an equivalent circuit for a suspended electroluminescent layer.

Résumé

La 1ère Partie renferme un exposé de la préparation des poudres de sulfure de zinc électro-luminescentes. L'on s'est basé pour cette préparation sur l'hypothèse qu'une couche riche en cuivre sur la surface des grains est nécessaire pour l'électro-luminescence.
Dans la 2ème Partie, l'on trouvera la description de mesures électriques et optiques sur les poudres de ZnS électro-luminescentes, y compris divers oscillogrammes de couches formées en suspension et sans liant, et l'observation stroboscopique des cristaux séparés au moyen d'un microscope. L'efficacité maximum est de 1,5 (±0,2) lm/W; la luminosité à 600 V, 3000 c/s est d'environ 1000 lm/m^2. L'hypothèse de l'action de barrière à la surface des grains est confirmée.
Dans la 3ème Partie, les observations des 1ère et 2ème Parties conduisent à la conclusion que l'électro-luminescence est une sorte de luminescence cathodique avec électrons "lents". On compare la faiblesse de l'efficacité des phosphores électro-luminescents avec celle des phosphores normaux, sous une excitation par rayons cathodiques à basse tension et densité élevée de courant. Un exposé est donné d'un circuit équivalent pour une couche électro-luminescente suspendue.

Zusammenfassung

In Teil I wird die Herstellung elektrolumineszierender Zinksulfid-pulver behandelt. Die Herstellung gründet sich auf die Annahme, daß eine kupferreiche Schicht auf der Oberfläche der Körner für Elektrolumineszenz notwendig ist.

In Teil II werden elektrische und optische Messungen bezüglich elektrolumineszierender ZnS-Pulver beschrieben; hierbei sind verschiedene Oszillogramme von in Suspensionsform aufgespritzten und ohne Bindemittel angelegten Schichten wiedergegeben und die stroboskopische Beobachtung der Einzelkristalle mit Hilfe eines Mikroskops behandelt. Die maximale Ausbeute beträgt 1,5 ($\pm$0,2) lm/W; die Leuchtdichte bei 600 V, 3000 Hz ist ungefähr 1000 lm/m^2. Die Hypothese einer Sperrwirkung an der Oberfläche der Körner wird bestätigt.
In Teil III führen die Beobachtungen von Teil I und Teil II zu dem Schluß, daß Elektrolumineszenz eine Erregung mit „langsamen" Elektronen ist. Der geringe Grad der Ausbeute elektrolumineszierender Phosphore wird mit dem normaler Phosphore unter Elektronenstrahlerregung bei niedriger Spannung und hoher Stromdichte verglichen. Schließlich wird ein Ersatzschaltbild für eine als Suspension aufgetragene elektrolumineszierende Schicht diskutiert.

PART I. CHEMICAL NATURE

1. Introduction

About the chemical nature of electroluminescent phosphors of the zinc-sulphide type — ZnS, (ZnCd)S, Zn(S,Se), etc. — only a few data have been reported up to now. Destriau [1a]) has given some details about the preparation of electroluminescent powders which give some indication about the chemical nature of electroluminescent ZnS. For instance: the required "fusible addition" has to be as low as possible; a rather high concentration of copper is needed (up to 3.10^{-3} atom Cu per mole ZnS) for a low threshold of the voltage at which luminescence occurs; the influence of oxygen (ZnO) on this threshold is mentioned.

Payne et al. [2]) also give some information about the preparation of electroluminescent materials in which similar conditions are mentioned (Cu contents about 10^{-3} mole per mole ZnS; addition of ZnO; low "flux" concentration: 1% $ZnCl_2$). Furthermore the influence of Pb is mentioned.

According to the theoretical interpretation given by Destriau [1a]) the phosphor is excited by electrons accelerated in the bulk of the material. Payne [2]) assumes that electroluminescence is connected with a surface effect, for instance with the presence of small particles of ZnO on the grains of ZnS, while Piper and Williams [3]) have shown that the cathode material has a great influence on the threshold voltage for at least single crystals of ZnS activated by Cu.

In the first part of this paper we have tried to correlate the observed phenomena of electroluminescence with the chemical nature of the electroluminescent powders in order to arrive at a better insight concerning the preparative conditions. Strong evidence is given that electroluminescence is caused by a copper(silver, gold)-rich layer on the grains of zinc sulphide.

For brevity attention is paid mainly to zinc sulphide with a copper-rich layer; similar results have been found with gold and silver instead of copper and with zinc-cadmium sulphide, selenide, and so on, instead of zinc sulphide.

2. Methods of preparation

We will first describe two methods of preparation whose main purpose is to confirm the assumption that a copper-rich layer on the grains is necessary for electroluminescence. Although reasonably good products may be made according to these methods, better phosphors are usually obtained by a method which we will discuss later.

(1) Luminescent but not electroluminescent ZnS is washed with a solution of $CuSO_4$. The copper it deposited as copper sulphide from the solution on the surface of the sulphide grains. The concentration is chosen such that for grains of approximately 10 μ diameter the amount of Cu on the surface is about 10^{-4} to 10^{-5} atom Cu per atom Zn of the base lattice. After drying the product shows electroluminescence.

The luminosity is increased by firing in an atmosphere of H_2S. The colour of the product is greyish, indicating that the Cu is not completely dissolved in the lattice.

(2) A photo- or cathodoluminescent (not electroluminescent) zinc sulphide is covered at room temperature with copper by evaporation in a vacuum bell-jar. This treatment makes the phosphor electroluminescent.

The emission bands during electroluminescence of phosphors prepared according to these methods depend only on the original activator in the photoluminescent phosphor. For instance: ZnS activated by Cu has a blue or green emission, ZnS-Mn an orange one.

Better results, however, are obtained if the electroluminescent phosphors are prepared in a more orthodox way. The preparation of products with a blue and green emission will be described here as an example.

(1) A blue electroluminescent product is obtained if ZnS activated by 6.10^{-4} Cu is fired in an atmosphere of 70% H_2S - 30% HCl at 1200 °C.

(2) Zinc sulphide activated by 10^{-3} Cu and 8.10^{-4} Al and fired at a temperature of 1200° C in an atmosphere of H_2S shows a green electroluminescence.

The concentrations of the activator (Cu) and promotor (coactivator) — Cl^- and Al^{3+} respectively — are chosen such that not all the copper dissolves into the lattice.

In both cases the brightness of the phosphors is affected by the rate of cooling or by an after-treatment in various atmospheres. The influence of such after-treatments can be understood from Kröger's [4]) results with ZnS-Cu phosphors of which a short summary will be given here.

The introduction of copper into zinc sulphide may give rise to green fluorescent, blue fluorescent, and quencher centres. The relative concentrations of these centres can be varied by the atmosphere and temperature of firing. At high temperatures (>1000 °C) the formation of green centres is favoured by a high HCl concentration, while low HCl contents favour

the relative concentration of blue copper centres and of quencher centres. When phosphors, made at high temperatures, are refired at a lower temperature (400° C) in a reducing atmosphere (H_2; N_2; O_2) the blue centres are enhanced and the quencher centres destroyed while refiring in atmospheres of H_2S, HCl and S has the opposite effect.

In the case where Al^{3+} is the coactivator, high Al^{3+} concentrations ($Al^{3+}/Cu^{+}>1$) increase the ratio of green to blue copper centres while low Al contents have the opposite effect.

Kröger has interpreted these effects by assuming that the green copper centres are formed by Cu^{+}, the blue copper centres by $(Cu_2)^{+}$ and the quencher centres by $(Cu_2)^{2+}$, all incorporated in the zinc-sulphide lattice*). The presence of quencher centres is indicated by the suppression of the phosphorescence and the shift of the temperature dependence to lower temperatures.

From these facts it is clear that for the preparation of electroluminescent zinc sulphides one has to find the right compromise between two counteracting effects. On the one hand Cu_2S acts as a quencher centre in ZnS while on the other hand a layer rich in copper on the surface is necessary to obtain electroluminescence. We will give an example how a reasonable compromise can be obtained in the case of a ZnS-Cu-Al phosphor.

Zinc sulphide activated by 10^{-3} Cu and 8.10^{-4} Al is fired at 1200 °C for ½ hour in H_2S; then the product is slowly cooled to room temperature in H_2S. The annealing process has a marked influence on the brightness during electroluminescence. If the product is excited by ultraviolet (3650 Å) only a weak phosphorescence is perceptible, indicating the presence of quencher centres in the lattice. Refiring the phosphor in a reducing atmosphere (e.g. air) at 550 °C during only a few minutes destroyed most of these quencher centres without seriously affecting the copper-rich layer (the time of firing is too short for an equilibrium to be reached). As a result the brightness of the electroluminescence is enhanced and also the phosphorescence.

3. Discussion of the various methods of preparation

It is interesting to compare the preparation methods of Destriau [1a]) and Payne[2]) with our methods. In all cases they use a high amount of copper in proportion to the "flux" content. Destriau even rejects the addition of fluxes completely. The addition of ZnO in their methods may perhaps be seen as a reducing agent to suppress the concentration of quencher centres.

*) This interpretation needs some revision in the light of Froelich's [5]) results with ZnS-Cu phosphors. A detailed description is always somewhat dubious. For the preparation mentioned, however, the "red" centres, as found by Froelich, are as detrimental as quencher centres are with respect to a high brightness.

The effect of lead used by Payne et al. [2]) is quite likely to regulate the chlorine contents of their products, since lead compounds are very volatile and only small fractions of the lead and chlorine are retained during the firing. An equivalent advantage is obtained when antimony is used in the preparation of electroluminescent zinc sulphide. Sb^{3+} acts as Al^{3+}, Ga^{3+}, etc., in promoting the blue and green copper bands. Since antimony is volatile the amount of Sb added before firing is not critical. Even when an excess of Sb is added, so much of it evaporates during firing that the final ratio of Sb to Cu is smaller than one, the condition for electroluminescence to occur. If aluminum is used, however, it is necessary to choose the Cu/Al ratio carefully.

When chlorine is used as the coactivator in copper-activated zinc sulphide, it is advisable to fire in a controlled atmosphere of H_2S-HCl, instead of using a flux. For the fraction of chlorine that is retained if a flux is added depends on many factors (such as the reactivity of the zinc sulphide, the size of the batch) which makes the reproduction of the electroluminescent phosphors rather difficult.

PART II. ELECTRICAL AND OPTICAL MEASUREMENTS

4. Introduction

When considering which kinds of electrical and optical properties might be studied to gain insight into the mechanism of electroluminescence one finds oneself more or less in an "embarras du choix". Properties such as light output, dissipated power, shape of current and light-output curves, (complex) electrical admittance, spectral distribution, absorption and reflexion coefficients, noise spectrum of the admittance (some of the properties being interdependent) can in a wide range of variation be measured as a function of parameters such as amplitude and frequency of the operating voltage, shape of the voltage curve (sine, square wave, pulses, d.c.), intensity and wavelength of additional radiation (continuous or intermittant), temperature, volume fraction of the phosphor, nature of the dielectric (dielectric constant, conductivity, viscosity, air or vacuum as dielectric), thickness of the layer, constitution of the phosphor (variation of chemical parameters and method of preparation, size and shape of the grains, single crystals, evaporated layers), ambient atmosphere.

Many measurements on electroluminescent cells have been described in the literature [1]), [6]), [7]). In this part of our paper we shall give similar and other experiments whose main purpose is to confirm the conclusion of Part I, that the electroluminescence of zinc-sulphide powders is restricted to the surface region of the grains.

5. Observations which show that electroluminescence is a surface effect

(a) *Stroboscopic observation.* A small electroluminescent condenser was constructed by putting a small quantity of a phosphor suspension in castor oil on a sheet of "conducting glass". The phosphor was of the green type as described in Part I. A small grid of a microwave triode was applied as a second electrode (see fig. 1). Thus the lens of a microscope could be brought very near to the luminescent crystal grains.

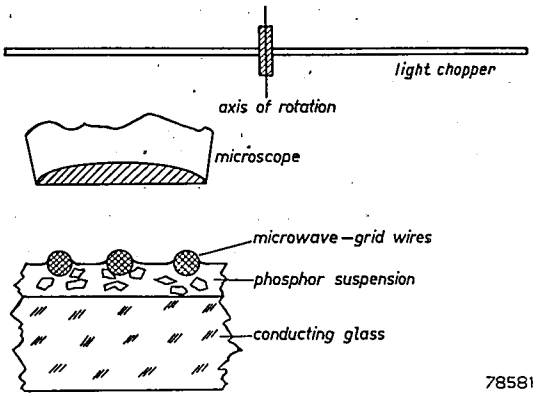

Fig. 1. Arrangement for stroboscopic view of electroluminescent grains under a microscope. The upper electrode of a small electroluminescent cell consists of a planar grid of a microwave triode.

Under the microscope, the crystals show themselves in various forms, mainly as hexagonal plates or as needles. When applying an a.c. voltage one sees the crystals move to a stable position near the wires. Some of the needles, however, keep rotating constantly. The light from the crystals is emitted for the greater part from the crystal surface and from certain imperfections in the crystals. The crystals "glitter" like salt in the sun. Some small patches on the crystals (mainly on the hexagonal plates) are very much brighter than the average (up to a factor of about 100) and with the adapted eye they can already be seen at 10 volts r.m.s.

When light is emitted from the bulk of the crystals — which happens when the same cell is excited with 3650 Å — the crystals look quite different. They do not glitter but have a dull appearance: one sees that the light is emitted throughout the bulk of the crystals. This proves that the light emission with electroluminescence is, indeed, strongly inhomogeneous.

Because of the grid structure of one of the electrodes, some of the crystals can be observed in a rather strong transverse field. The asymmetry in the emission, with respect to the sign of the electric field, is clearly

seen when interrupting the light with a rotating disc having a frequency near to that of the a.c. voltage (stroboscopic observation). In this case the main light emission shifts periodically from one side of the crystal to the opposite side.

(b) *Change in capacitance.* That the light is produced only in a relatively thin layer of each of the ZnS grains is also shown by the fact that 3650-Å irradiation, which excites the crystal throughout, changes both the apparent capacitance and parallel conductance of a normal electroluminescent cell considerably. The change in apparent capacitance and conductance of the same cell during electroluminescence at about the same level of brightness is much smaller. Since the crystals of the phosphor are already excited to some extent by daylight the cell was kept in the dark during measurements. The "dark" capacitance for a 75-μ layer in castor oil with a volume fraction of the ZnS grains of 11% is then about 50 pF per cm^2. With 3650-Å irradiation the capacitance (as measured at 50 c/s with low voltage) increased in one case by about 25%; this is of the same order of magnitude as that which can be observed with similar layers of non-electroluminescent ZnS-Cu phosphors. We must assume, therefore, that the conductivity of the suspended grains must have increased considerably by the ultraviolet excitation. When the cell was brought to electroluminescence at about the same brightness as under ultraviolet excitation the increase in capacitance was, however, not more than a few per cent.

(c) *Glow effects.* Further evidence for the fact that only a very small region of the grains is excited in the case of electroluminescence is obtained from glow experiments. It can be shown that the electron traps of an electroluminescent zinc sulphide are not filled during electroluminescence, because a rise in temperature after field excitation at —180° C does not give rise to a noticeable thermal glow. Furthermore, if the traps throughout the crystals have been filled previously by excitation with ultraviolet at liquid-air temperature, the action of an electric field at the same temperature causes no appreciable change in the glow curve. The same behaviour was observed. after previous excitation with ultraviolet (3650 Å) at —180 °C and heating up of the phosphor under a simultaneous action of an electric field.

(d) *Asymmetry of the light peaks.* Oscillograms of light output and voltage (a.c.) during electroluminescence show that the light is emitted by that surface of the zinc-sulfide grain which is turned to the cathode.

Destriau [1a]) has found that the two half cycles of the "waves of brightness" are different in height. He ascribes this to the fact that the voltage used was not perfectly sinusoidal. The same asymmetry, however, is found by Jerome and Gungle [6]), by Roberts [7]) and in our experiments although

a perfectly symmetric a.c. voltage was applied. The following experiments show conclusively that this lack of symmetry in the light peaks is due to the fact that the light is emitted only at the cathode side of the grains. If an electroluminescent phosphor is put between two transparent conducting plates (fig. 2) it is found that the two light peaks, which are observed at every half cycle, are of unequal heigth and that the position of the photomultiplier determines which peak is the higher.

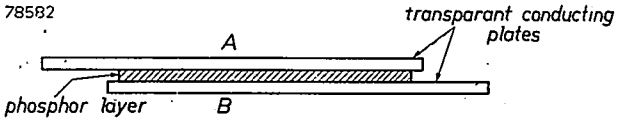

Fig. 2. Schematic drawing of an electroluminescent layer.

The oscillogram of fig. 3a was obtained when the photomultiplier was at A. With the photomultiplier at the opposite side (B) we obtained the oscillogram shown in fig. 3b. The higher peak occurs when the electrode facing the photocell is acting as the cathode.

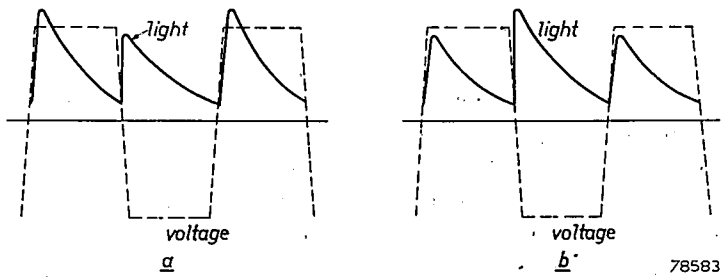

Fig. 3. Oscillogram of light output and voltage, showing the asymmetry in the light emission; *a* and *b* correspond to the photomultiplier at opposite sides of the phosphor layer.

This effect may be explained as follows: either (i) the fieldstrength is not constant throughout the layer but is stronger near the cathode, or (ii) each particle emits light only at the side facing the cathode.

The self-absorption and scattering of the emitted light by the interjacent layer or by each individual particle are responsible for the asymmetry.

In the case (i) one should expect an increase in asymmetry of the light peaks with increasing thickness of the layer. In the case (ii) the opposite should occur. With a 100-μ layer the asymmetry amounted to about 10%, with a layer of 10μ it was 25%. This shows that (ii) is the right explanation.

6. Brightness, power factor and efficiency measurements of normal cells

Various measurements of the luminous emittance H, power factor *) tan δ and efficiency η (lumen/watt) have been performed. The electroluminescent cells are of normal construction, consisting of a layer of electroluminescent powder, suspended in a dielectric between a vitrious electrode (conducting glass) and a metal electrode. To reduce the influence of the series resistance due to the conducting glass, we used rather small cell areas (about 10 cm^2) and a thick conducting layer; corrections were made for the optical absorption of this layer. The voltage of operation varied from zero to the limit of electrical breakdown (which for a 50-μ layer suspended in a good dielectric is of the order of 1000 V r.m.s.). The frequency of operation normally varied between 0 and 10 000 c/s (in one case, however, a layer was investigated up to 2 Mc/s). Araldite was used for the solid dielectric. Some results are given in figs 4 to 7 with the emittance

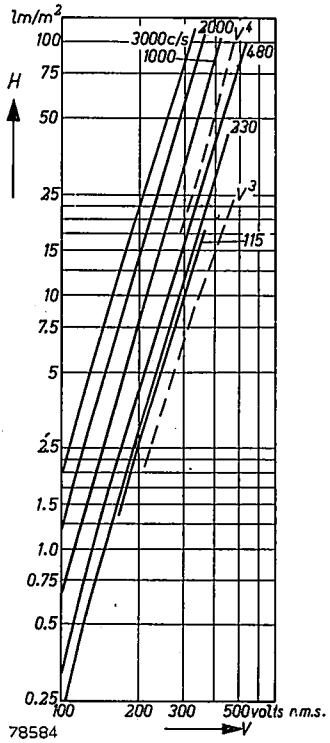

Fig. 4. The luminous emittance H of an electroluminescent cell in lumen/m^2 versus r.m.s. value of the operating a.c. voltage at various frequencies. Dashed lines: third- and fourth-power laws. At not too small voltages the dependence is given approximately by $H \sim V^{3\frac{1}{2}}$. Green ZnS powder suspended in a solid dielectric (araldite).

*) The measurement of small powers consumed in condensers with a rather low power factor (as cells are) gives rise to some experimental difficulties. For the results given we used an electro-dynamometer.

and the efficiency of a green phosphor as a function of frequency and voltage. The general aspect of our results agrees with that of others [6], [7]. Figure 4 gives the emittance H of a normal electroluminescent cell in lumen/m^2 versus the r.m.s. value of the operating a.c. voltage at various frequencies on a double-logarithmic scale. For comparison a fourth- and a third-power law are given in the same figure (dashed lines). The emittance H of the same cell is plotted versus the frequency f with constant voltage (300 V r.m.s.) in fig. 5. The experimental curve for a liquid dielectric (silicon oil) is also given (200 volts r.m.s.) For a comparison a linear relationship is given (dashed line). Figure 6 gives the luminescent efficiency (in lumen/watt) of the same cell (with araldite dielectric) versus operating voltage; frequency as a parameter.

The emittance H increases almost linearly with frequency up to about 3000 c/s (fig. 5).

As may be seen from figs 6 and 7, the efficiency η increases strongly with V at low voltages; η goes through a maximum at a voltage somewhat below the breakdown. Jerome et al. [6]) have tried to determine the inherent efficiency by subtracting from the total power consumed the amount due to the losses in the binder. We think that this analysis is somewhat arbitrary.

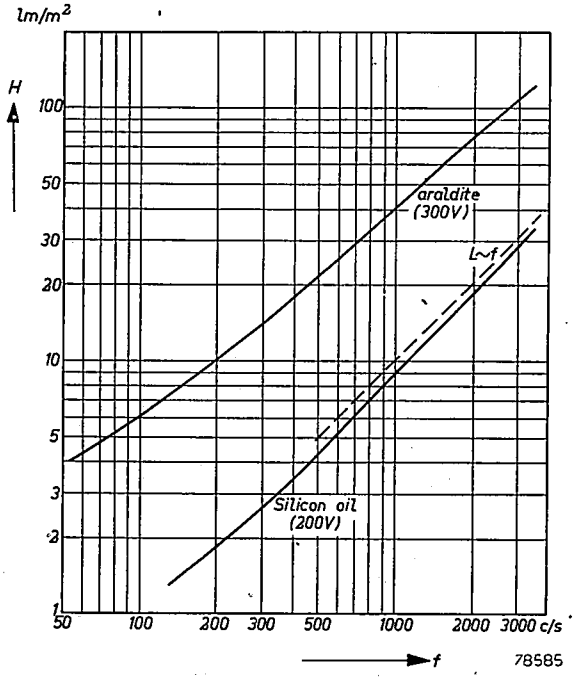

Fig. 5. The emittance H versus frequency f for a solid dielectric (araldite), and for a liquid dielectric (silicon oil). Dashed line: linear relationship.

From measurements on binderless layers we have found that non-linear conductivities may occur which are not related to the light emission. We have therefore plotted here only the overall efficiency, i.e. the light output divided by the total power consumed in the cell. The decrease of

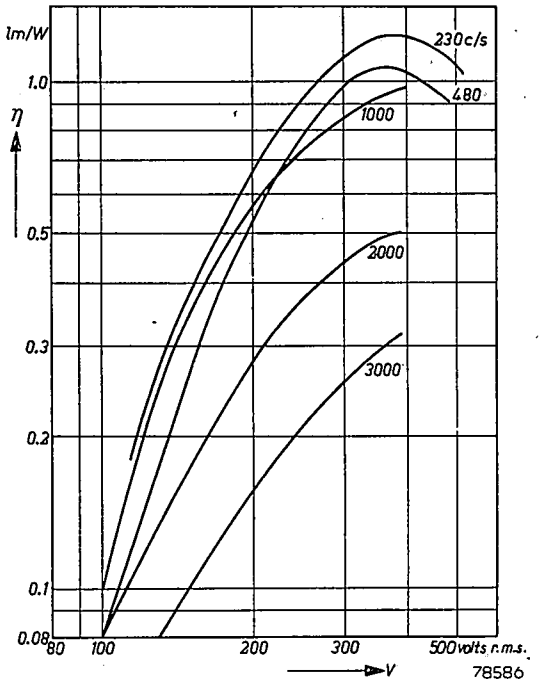

Fig. 6. Luminescent efficiency η (in lumen/watt) versus operating voltage at various frequencies. The maximum efficiency occurs somewhat below the breakdown voltage.

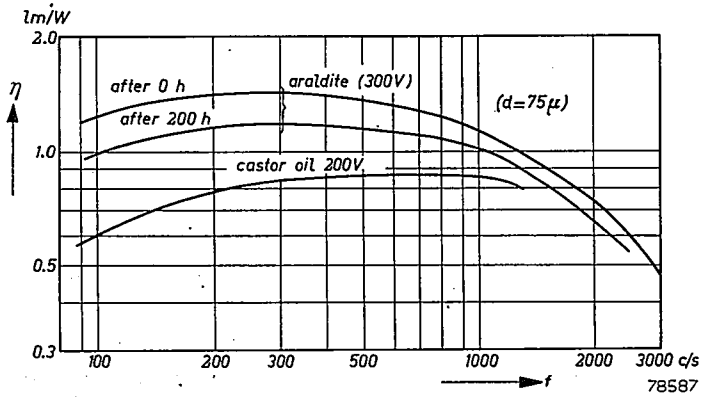

Fig. 7. Electroluminescence efficiency versus frequency at a constant operating voltage for araldite as a dielectric (after 0 hrs and after 200 hrs of operation).

η at higher f-values is for the greater part due to the series resistance of the conducting glass.

In fig. 8 the decrease of H during life is plotted as measured on an typical sample. During the first 50 hours a decrease of about 20 to 50% takes place; after this H remains nearly constant; η did not vary considerably during life (see fig. 7).

The maximum efficiency occurring in the frequency range from 250 c/s to 500 c/s with $V = 400$ volts amounts to $\eta_{max} \approx 1{\cdot}5$ lumens per watt (the accuracy of this value is about 20%). At 3000 c/s and $V = 600$ volts with a layer of about 50μ thickness an emittance of about 1000 lumens/m^2 can be obtained. The efficiency is then, however, lower. From fig. 4 we see that the voltage dependence can be roughly described by $H \sim V^n$ where n is about 3·5. At smaller voltages the dependence is stronger; near the limit of visibility it is nearly exponential.

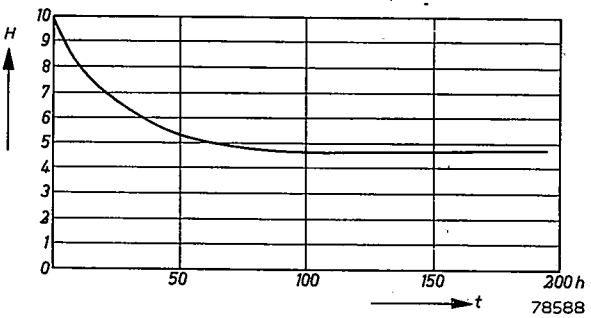

Fig. 8. Decrease of the emittance during 200 hours of operation at 500 c.p.s.

With fast decaying phosphors approximately the same amount of light is liberated during each half cycle of the a.c. voltage in the frequency range from some hundreds to some thousands of cycles per second, giving rise to the linear frequency dependence shown in fig. 5. Figure 7 shows that at low frequencies there is a slight increase of η with increasing frequency. At some hundreds of cycles per second a broad maximum occurs. As was already pointed out, the decrease of η at higher frequencies is mainly due to an increase of the losses in the series resistance of the conducting glass. The emittance H still increases almost linearly in this frequency range because the voltage drop across the glass resistance (being nearly 90° out of phase with the applied voltage) does not affect the voltage across the layer itself noticeably. At higher frequencies the luminous emittance increases more slowly, reaches a maximum and then drops with increasing frequency.

A cell of a very short broad area having a small series resistance of the

conducting glass could be brought to electroluminescence at frequencies of 100 kc/s and even at 2 Mc/s with 100 V r.m.s. The light output did decrease here with frequency but the decrease was slow. The emittance at 2 Mc/s was still about the same as it was at 1000 c/s. At 50 Mc/s the layer was heated to such an extent that breakdown occurred before light could be emitted. At 10 000 Mc/s a pellet of electroluminescent powder was studied in the waveguide output of a 3-cm magnetron. There was no light emission even at such high voltage gradients that sparking occurred. Here we have probably to do with a relaxation time of the electroluminescent mechanism itself.

The variation of the power factor tan δ of the suspended layer with voltage and with frequency is given in fig. 9. The increase of tan δ with increasing frequencies is still partly due to the influence of the series resistance of the conducting glass. The increase of tan δ with increasing voltages sets in at voltages where the electroluminescence reaches a high brightness.

The decrease of tan δ with increasing voltages, which is observed at low voltages and which is more pronounced at low frequencies, is rather peculiar. It was also measured by Roberts [7]) who derived the complex

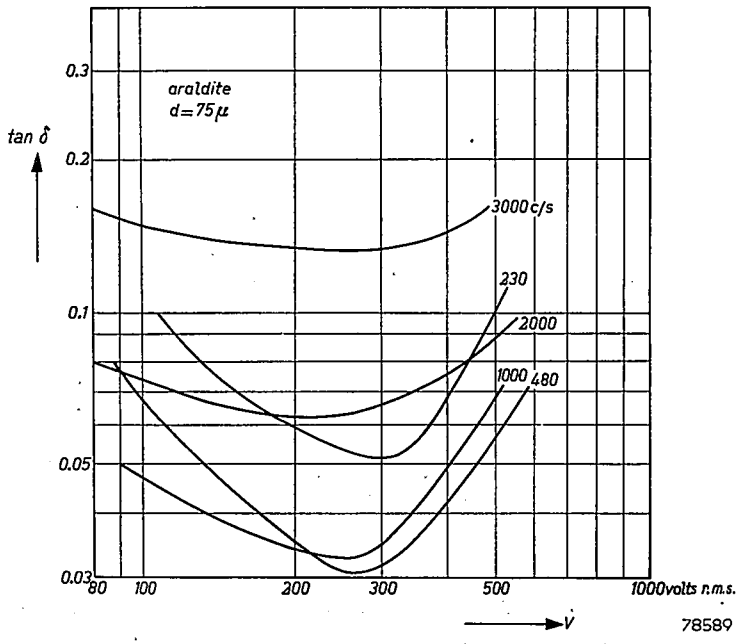

Fig. 9. Power factor tan δ of the same electroluminescent condenser as used for fig. 4 as a function of operating voltage at various frequencies; tan δ shows a minimum whose steepness is greater at lower frequencies.

admittance of the grains themselves from measurements on the suspended layer. As a rule non-linear elements have a conductivity that increases with increasing voltage. If one wants to describe the phosphor grains, therefore, in terms of (non-linear) resistances and capacitances, one has to assume that the resistance giving rise to this behaviour is a series resistance. At higher frequencies the minimum in tan δ becomes less pronounced because of the higher ohmic losses in the glass.

7. Measurements on binderless layers

In order to get somewhat more information about the behaviour of the electroluminescent phosphor grains themselves, we made some measurements on a 20-μ layer of the same phosphor made by a settling technique on conducting glass. In this way the influence of the suspending dielectric was avoided.

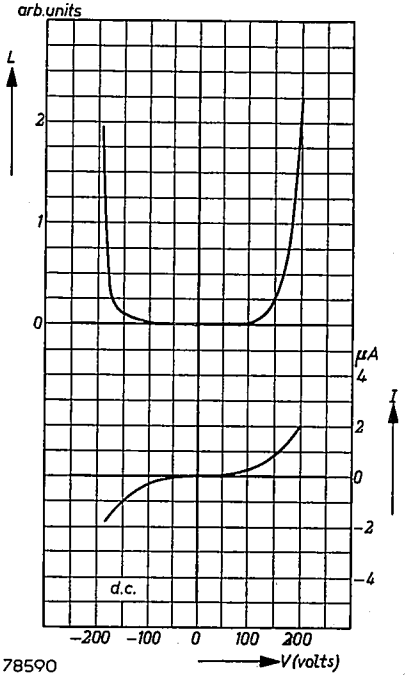

Fig. 10. The d.c. voltage-current (V-I) characteristic and voltage-light output (V-L) characteristic for a binderless electroluminescing ZnS-layer (area 3 mm^2, average thickness 20 μ). The layer shows some rectification. The characteristic is strongly non-linear.

As a second electrode a thin aluminum foil was pressed against the layer by means of a glass plate on which a layer of rubber was applied. When an a.c. voltage is applied such a layer shows an electroluminescence of about the same brightness as is obtained with suspended layers.

Figures 10, 11 and 12 give the I-V characteristic of such a layer with d.c. and a.c., $f = 50$ c/s and 2000 c/s. (figs 11 and 12 being taken from an oscilloscope). The light output L is also given. With a.c. the direction of rotation of the spot is indicated by the arrows. With d.c. there is some light output at high V-values but it is very low and it is originating from a small number of spots.

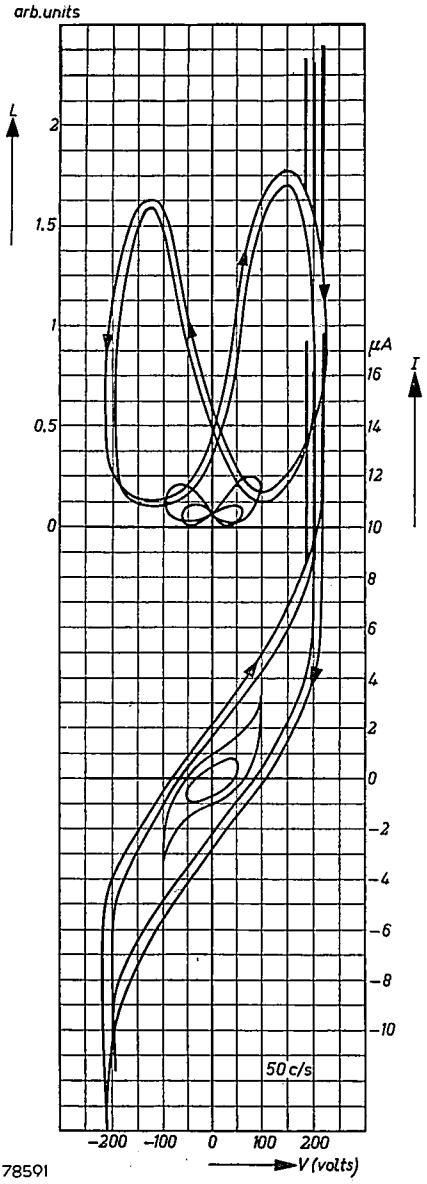

Fig. 11. Oscillograms of the a.c. voltage-current (V-I) and a.c. voltage-light output (V-L) characteristics at 50 c/s for four different voltage levels. With 250 V r.m.s. in the positive half cycle spurious in-phase peaks occur, both in the light output L and in the current I.

It is seen that at low voltages or at high frequencies the crystals have a nearly capacitive character as was to be expected. With high voltages, combined with low frequencies, however, the character is more ohmic and strongly non-linear. If we assume that the rapid increase of the current with increasing voltage is related to an in-phase charge transport through the crystals (which is also responsible for the excitation of the electro-

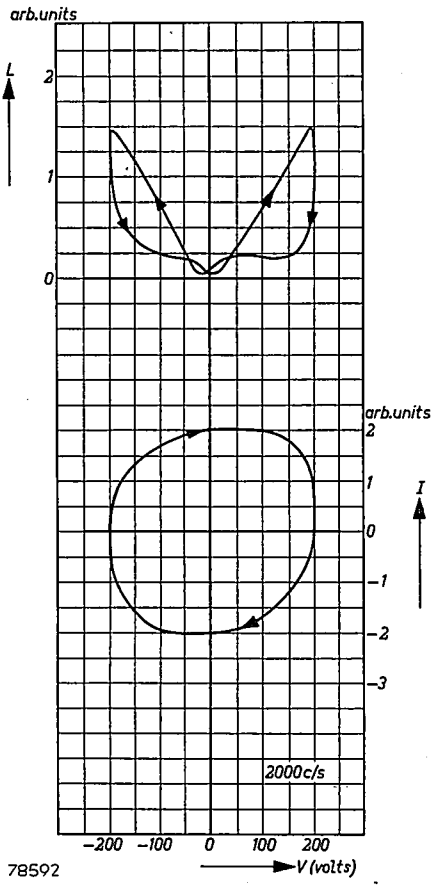

Fig. 12. The same as fig. 11 at $f = 2000$ c/s and V just below the critical value of breakdown.

luminescent centres), the decrease in tan δ mentioned above can be accounted for by this decrease of overall crystal resistance. The latter, when in a suspension, acts both as a series and a parallel resistance to the loss-free suspending dielectric.

At low frequencies (fig. 11) the light output L is about 45° out of phase with respect to V; L has the double frequency, of course, and shows the well-known small asymmetry. From the direction of the arrows it may

be seen that L is about 45° ahead of V. Perhaps this must be related to the well-known 45° phase shift occurring in the impedance of surface layers and p-n junctions [8], [9]). At high frequencies L lags behind in phase due to the afterglow.

With very high voltages spurious in-phase peaks occur both in L and in V. These non-destructive electric "breakdowns" of the crystal layer give rise to violent yellow light flashes (the normal electroluminescent light was green). Recent measurements on binderless layers in vacuum have indicated that here we probably are concerned with a breakdown of thin layers of moisture adsorbed from the atmosphere. We think that these layers also play a prominent role in the d.c. conductivity of a settled layer.

8. The effect of an electric field on the afterglow

Figure 13 gives some oscillograms of a binderless layer of an electroluminescent sulphide with various wave forms.

These oscillograms show a peculiar phenomenon: when switching off the field, a very slowly decaying light flash appears. This afterglow can be quenched by applying again a small voltage (see point A fig. 13c and also fig. 12). During this afterglow much more quanta can be emitted than during a normal electroluminescent flash with a.c. square wave or with application of d.c. pulses. This large asymmetry has nothing to do with self-absorption because reversal of the sign of the applied d.c. pulses did not change the L pattern. With high intensities, the decay becomes faster and the asymmetry less pronounced.

Perhaps the decay with a.c. or square wave is much faster than the normal afterglow without electric field because of this extinction of the phosphorescence in an electric field. This is supported by the following experiment.

When the binderless layer is irradiated with 3650 Å and the d.c. field is applied, a strong quenching of nearly all the grains occurs (as can be seen under the microscope). This shows at the same time that all these grains must have made a d.c. contact with the electrodes. When removing the d.c. field the slowly decaying light flash is again present with about the same intensity. From studies under the microscope one can conclude that this flash is coming from that side of the grains which had been charged positively. (When the field is suddenly reduced to zero this side gets a negative voltage pulse.) The d.c. quenching of the 3650-Å luminescence is strongest at the cathode side of the grains.

When an electric field is applied during the afterglow of normal non-electroluminescent phosphors, some (mostly copper activated) show a temporary increase in brightness while in others (silver activated) the application of the field has an extinguishing effect (Gudden and Pohl [10]) Schmidt [11]), Hinderer [12]), Destriau [1b])).

Destriau [1b]) pointed out that the thermal glow of an u.v. excited (non-electroluminescent) phosphor remains unchanged if after excitation a temporary increase in brightness has been effected by the application of an electric field. Our experiments confirmed these observations and the most probable explanation is that in this case also the action of the electric field is limited to the surface region of the zinc-sulphide grain, so that only the electron traps in this small region are emptied.

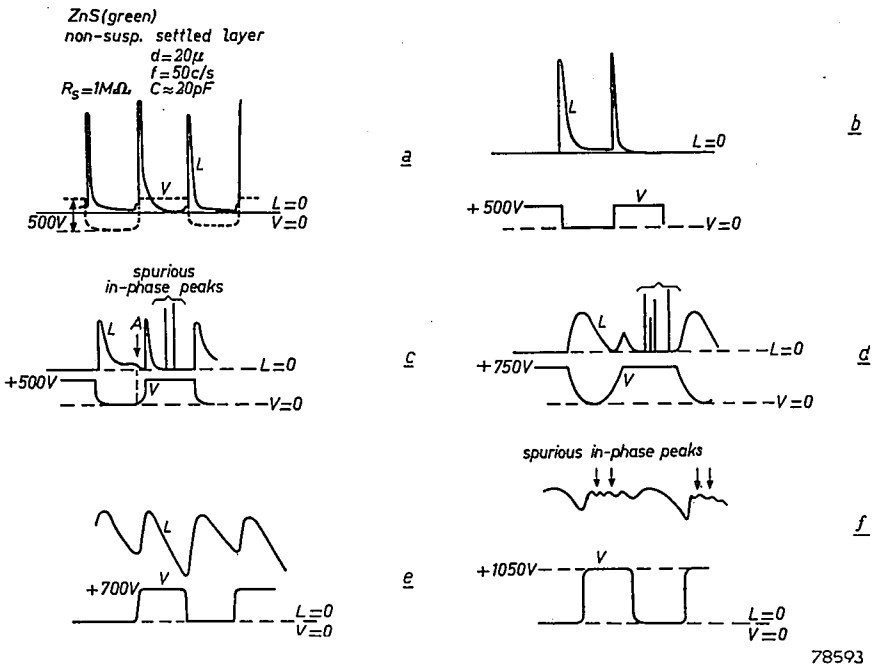

Fig. 13. The same binderless layer as was used for fig. 10 is connected via 1 MΩ to a square-wave voltage generator. Oscillograms of light output and voltage across the layer versus time with various voltage waveforms; (*a*), (*b*), (*c*) and (*d*) with $f = 50$ c/s, (*e*) and (*f*) with $f = 5000$ c/s. (*a*) Square wave a.c. There is a small asymmetry in the height of the *L*-peaks due to self-absorption. (*b*) Square wave d.c. pulses. The strong asymmetry (very slowly decaying light peak after the applied electric field is switched off) is not due to self-absorption. (*c*) The same as (*b*) but with the square-wave pulse rounded off at the lower side. Note the quenching at *A*. (*d*) Still more rounded-off pulses of a somewhat higher voltage. Note the strong asymmetry in the *L*-peaks and the spurious in-phase peaks. (*e*) With $f = 5000$ c/s, the asymmetry is less pronounced. (*f*) with a very high operating voltage; so many in-phase peaks occur that the layer is nearly continuously luminescing so long as the field is applied.

The quenching effect which is found in other phosphors by the action of an a.c. field is not caused by emptying the electron traps in a direct way but by emptying the hole traps (transition *a* in fig. 14) followed by a

radiationless recombination with electrons elsewhere, for instance with trapped electrons as indicated by transition *c*.

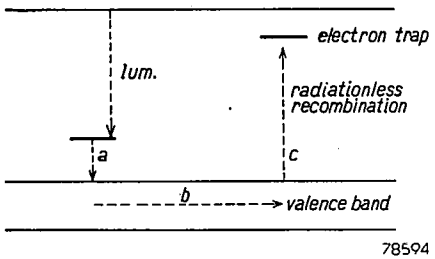

Fig. 14. Band scheme of a ZnS phosphor. The arrows *a*, *b* and *c* indicate the migration of a hole from an excited luminescent centre to a filled electron trap, resulting in a quenching of the luminescence.

9. Influence of the frequency of the applied electric field on the spectral distribution

In fig. 15 the spectral distribution of a blue electroluminescent zinc sulphide (6.10^{-4}Cu fired in 75% H_2S-25% HCl at 1200°C) and of a green phosphor (ZnS 10^{-3} Cu-10^{-3}Al, 1200 °C, H_2S) are shown. It is clear that the spectral distribution of this blue electroluminescent phosphor depends on the frequency. The higher the frequency the more the blue copper band predominates. If at a constant frequency the voltage is varied, the blue: green ratio remains the same.

The origin of the blue-green change can be found in the difference in decay of the blue and the green band. This may be seen from fig. 16*a* and *b*. Oscillogram *a* was obtained when an orange filter (Schott GG 14) was

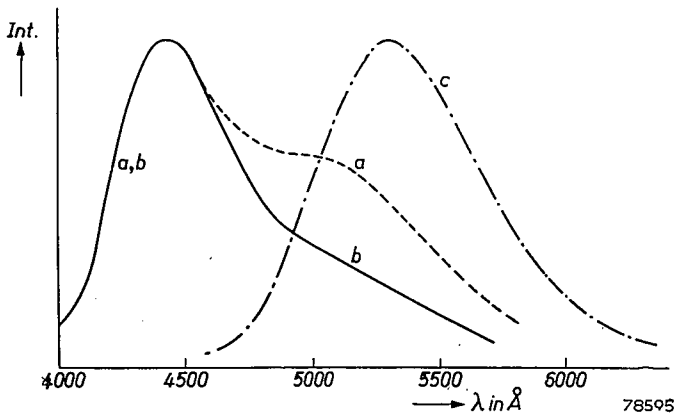

Fig. 15. Spectral distribution of a blue electroluminescent ZnS at 50 c/s (*a*) and 500 c/s (*b*) and of a green electroluminescent phosphor at 50 and 5000 c/s (*c*).

put in front of the photocell while in obtaining oscillogram *b* this filter was replaced by a blue filter (Schott BG 12). The blue band decays more rapidly than the green one, because during the afterglow holes are transferred from the blue to the green centres [13]). This process is illustrated schematically in fig. 17.

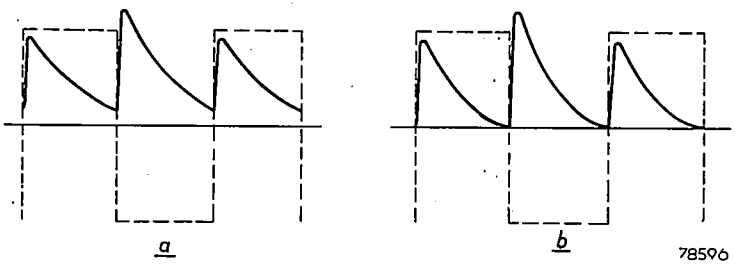

Fig. 16. Oscillograms of light output and voltage of an electroluminescent phosphor emitting a blue and a green band. (*a*) photocell equipped with an orange filter. (*b*) photocell equipped with a blue filter. (f = 250 c/s.)

Because of the afterglow one might expect the above-mentioned asymmetry of the peaks to be less pronounced at high frequencies, i.e. when the phosphorescence of the preceding excitation contributes to each light pulse. Although the difference in heights remains the same, the ratio of the heights should become smaller. The asymmetry should also be more pronounced for the blue than for the green band at high frequencies. This was, indeed, confirmed by experiment.

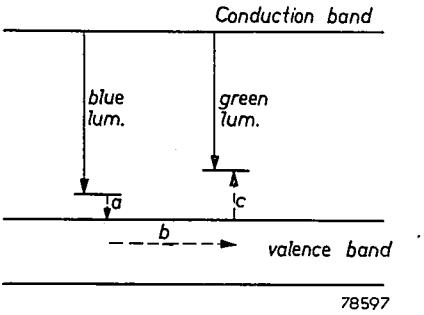

Fig. 17. Energy diagram of a ZnS phosphor, containing blue and green luminescent centres. The mechanism for the transport of energy from the blue to the green centres by a migration of holes is indicated by the arrows *a*, *b*, *c*,

10. The secondary light peaks

Within one cycle of the a.c. voltage some of the phosphors not only show two main peaks of emission, but also two — generally

much smaller — secondary peaks (see fig. 18). In fig. 19 a brightness-voltage characteristic is given for a binderless layer with a frequency of 50 c/s. Whereas the main light peak is about 45° in phase ahead of the voltage, the secondary peak lags about 45° behind the voltage,

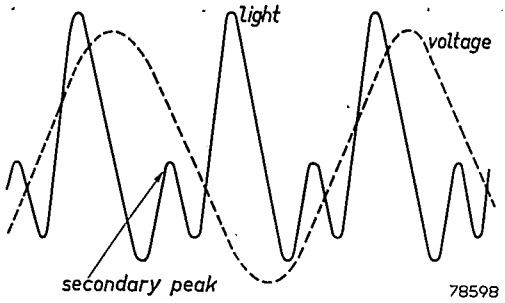

Fig. 18. Oscillogram of light output and voltage (sinusoidal) showing the secondary light peak.

thus being about 90° out of phase with the main peak. Since we must assume that the main peak attains its maximum at about the same moment that the voltage across the barrier layer has its maximum value, we may conclude that the secondary peaks occur at the moment the voltage across this layer goes through zero. These secondary peaks cannot therefore be ascribed to a new excitation similar to that which is responsible for the main peak. The emission of the secondary peak

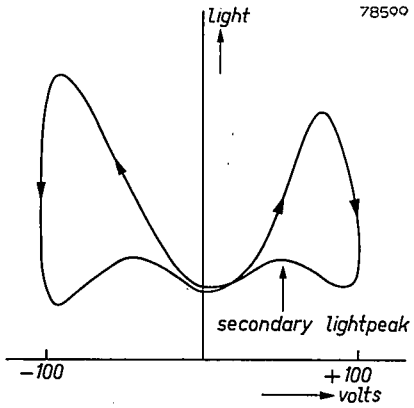

Fig. 19. Oscillogram of the voltage-light output for a binderless electroluminescing ZnS layer, showing the secondary light peak. Sinusoidal operation at 50 c/s.

proves to be of a somewhat longer wavelength than that of the main peak (see also Loebner *)).

The intensity ratio of the secondary to the main peak I_s/I_m is dependent on the following factors:

(1). The chemical nature of the traps. With some phosphors (e.g., ZnS-Cu, Al and ZnS-Cu, Cl according to Part I) the secondary peaks are not perceptible at room temperature at low frequencies. These phosphors have only traps with a small depth [22]).

(2). The temperature of operation. When heating up from liquid-nitrogen temperature to about 100 °C the ratio I_s/I_m can pass through some distinct maxima, which are related to the depths of various traps.

(3). The brightness oscillograms are, of course, dependent upon the wave form of the operating voltage. With square waves of a very steep slope the secondary peak is drowned in the main peak.

From these and other experiments we have come to the conclusion that the intensity of the secondary peaks is related to the presence of traps and to the effects of external electric fields on the liberation of electrons and holes from traps (transitions α, γ_1' and γ_2' of fig. 20). This subject is being investigated still further.

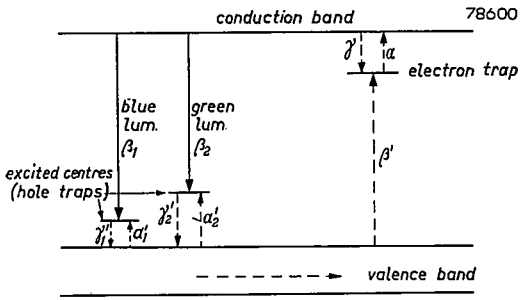

Fig. 20. Energy diagram of a ZnS phosphor.

PART III. PHYSICAL NATURE

11. Physical model

The methods of preparation of electroluminescent phosphors given in Part I, and the electrical and optical measurements described in Part II leave little doubt, in our opinion, that electroluminescence of these powders is a surface effect.

We therefore arrive at a similar explanation for the production of light in electroluminescent zinc sulphides as is given by Piper and Williams [3]).

*) E.E. Loebner, Time dependent spectra of electro-luminescent zinc sulphide. Presented at the Rochester meeting of the American Physical Society, June 18, 1953.

At the interface between the zinc-sulphide and the copper-rich phase a potential barrier exists which is of the nature of an exhaustion barrier[14]). The Fermi level of the zinc sulphide is assumed to be above that of the copper-rich phase. When both are in contact with each other, electrons escape from the zinc-sulphide to the copper-rich phase, resulting in a potential barrier as outlined in fig. 21*a*. When an electric field is applied making the copper-rich phase negative with respect to the zinc-sulphide phase the barrier broadens and the main part of the voltage drop over the grain will be found over the potential barrier (fig. 21*b*).

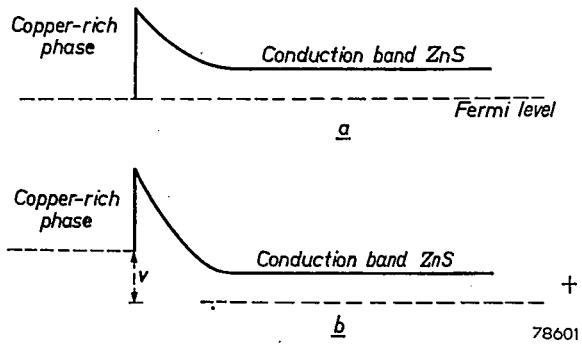

Fig. 21. Energy levels of ZnS in contact with a copper-rich phase. (*a*) Without field, (*b*) With the copper-rich phase negative; V is the potential drop across the barrier.

Now there are two possibilities for electroluminescence:
(*a*) Electrons are liberated from impurity levels in the barrier region. If the local field is strong enough, these electrons are accelerated until their energy is sufficient to excite the phosphor.
(b) electrons from the copper-rich phase may penetrate the potential barrier by a tunnel process and be accelerated by the electric field in the barrier.

We believe that we have found both types of electroluminescence (see also ref. [3])). A more extensive treatment of both cases (a) and (b) will be given later.

12. Comparison between electroluminescence and cathodoluminescence

If electroluminescence arises from an injection of low-voltage electrons into the bulk of the crystals, a correlation should exist between the efficiency of electroluminescence and that of cathode-ray excitation at low voltages. Such a correlation is shown in fig. 22, where the emittance H and the current I are plotted versus V for an electroluminescent layer at low brightness on a semi-logarithmic scale. In this voltage region

the externally measured current I through the suspension varies nearly linearly with V. In the regions below 50 volts there are only very few fluorescent spots on certain grains that produce the main light emission. For comparison the emittance of cathodoluminescent willemite is also given in fig. 22 in the same low-voltage region, as measured with a normal magic eye. In this case also only a few small spots are luminescent at low voltages.

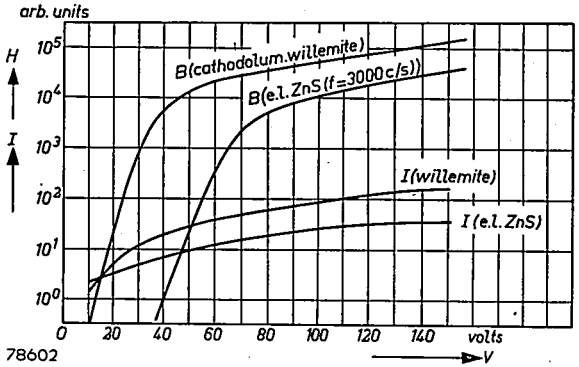

Fig. 22. Emittance H and injected electric current I as a function of voltage V for cathodoluminescent willemite (where V means the applied d.c. voltage) and for a green electroluminescent phosphor (where V means the r.m.s. value of the 3000-c/s operating voltage of the cell). At small V values the voltage dependence is nearly exponential in the two cases. (Read H for B.)

We measured the light output of an electroluminescent phosphor under cathode-ray excitation, moreover, as a function of screen-voltage. The schematic diagram of the demountable tube as well as the experimental results may be seen in fig. 23. Relating these measurements of relative efficiency values to the absolute efficiency of ZnS phosphors at higher voltages [15]), it is found that with cathode-ray excitation at voltages of the order of 100 volts the efficiency has dropped to the value of the order of 1 lumen/watt, which is the same order of magnitude as is measured for the efficiency of electroluminescence at "high" voltages.

The smallness of the light efficiency for cathodoluminescence at low voltages has been ascribed to an inactive layer at the surface [15]),[16]),[17]). The penetration depth of these slow electrons is not exactly known, but it will probably be not more than some tens of Ångströms [18]).

One must bear in mind that with electroluminescence, contrary to cathodoluminescence, one cannot vary the voltage V and the current I independently, but that the I/V ratio is always relatively high. At 5000 c/s a mean voltage gradient of 15 V/μ produces a total a.c. current of about 25 mA/cm^2. If we assume the injected current to be 10% of the total current (see tan δ measurements on suspended and binderless layers described

in sections 7 and 8) we have a current density of 2·5 mA/cm². At the small voltages used here, this is sufficiently large to bring a green phosphor of the type described in Part I (having 0·1 mole% activation centres and a decay time of the order of 10^{-3} sec) near to current saturation [16], [19].

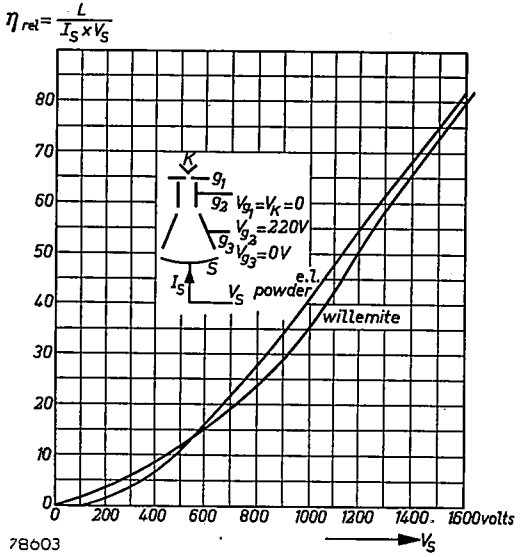

Fig. 23. Relative value of the luminescent efficiency of an electroluminescent powder under cathode-ray bombardment, plotted versus acceleration voltage V_s. Inset: schematic diagram of the cathode-ray tube. For a comparison the same is given for normal willemite (not electroluminescent).

Although the maximum efficiency which has so far been found with electroluminescent layers (≈1 lumen per watt) may seem rather low, it is really surprisingly high when the following considerations are born in mind:

(A) electroluminescence is a surface effect and from measurements of cathodoluminescence it is known that the efficiency of the surface layer is very poor;

(B) from the chemical preparation (Part I) it is known that an excess of copper is needed, which gives rise to killers and thus to a low efficiency;

(C) in electric fields normal u.v. excitation is quenched; with electroluminescence radiation-less recombination due to migrations of holes (Schön-Klasens) is concurring with light emission (the electrons are spatially separated from the excited fluorescent centres by the field);

(D) with electroluminescence the injected electron current, which gives rise to excitation, rises rapidly with the applied voltage difference; with high voltages, therefore, the high current densities set another limit to the efficiency (current saturation).

13. Equivalent circuit for a suspended electroluminescent layer

It is difficult to arrive at an equivalent circuit for a suspended electroluminescent layer, such that the electrical and optical properties may be quantitatively explained, because:

(a) non-linear elements and probably even rectifying layers are involved making the whole meaning of an equivalent circuit rather questionable (see also [20]), [21]));

(b) when using such elements as (non-linear) resistors and capacitors for the equivalent circuit, we must assume that with a suspended layer at least four different capacitances and resistances and two rectifiers are involved (when ignoring the influence of the conducting glass). The general aspect of the circuit should then be something like that of fig. 24, where C_1 = capacitance of the surface layer, C_2 = capacitance of the bulk, C_3 = series capacitance of the suspending dielectric pores, C_4 = parallel capacitance of the dielectric pores, R_1, R_2, R_3 = resistances of the barrier and the conducting layer around the crystal. R_4 accounts for the loss in the dielectric and for a possible leakage through chains of conducting layers reaching from one electrode to the other; D_1 and D_2 represent the rectifying action of the barrier; C_1, C_2, R_1, R_2 and R_3 are probably voltage dependent.

As a result of the rectifying layers the bulk will become charged positively in an a.c. field. An indication for the build-up of the voltage across the barriers when for the first time a voltage is applied can be seen from fig. 25, where oscillograms of the light output and the voltage are given as registered by means of a one-shot time base. When after 1/100 sec dead time the a.c. voltage is switched on again there is no build-up.

Whatever the proper values of the various elements may be, one may conclude that due to the series capacitance of the dielectric and to the bulk impedance the voltage across the barriers can in general only be a

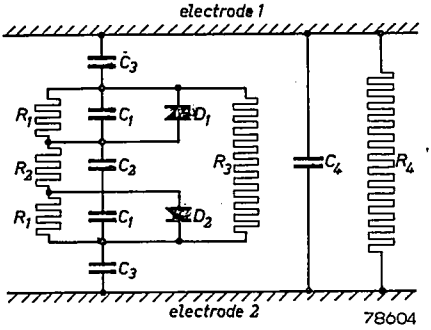

Fig. 24. Possible equivalent circuit for a normal electroluminescent layer. The series resistance of the electrodes has been neglected.

fraction of the total voltage applied. The voltage, however, must amount to at least several volts so that excitation of the centres may occur. From the microscope studies on binderless layers, we have seen that in some favourable cases this fraction must be rather large, because the limit of visibility was 5 V r.m.s. corresponding to a maximum value of about 7 volts. If one assumes that an equivalent circuit according to fig. 24

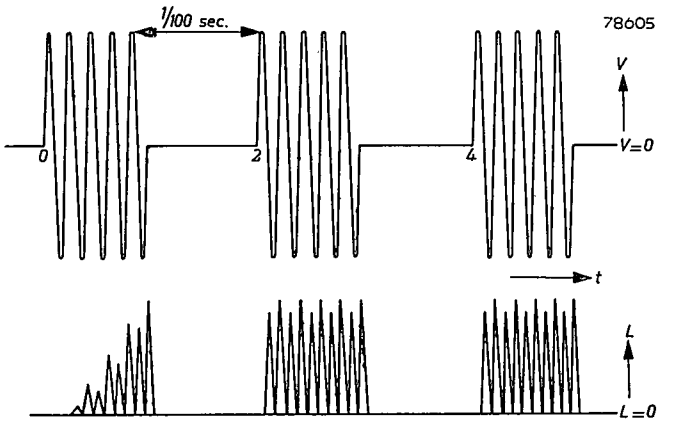

Fig. 25. Build-up of electroluminescence; $V = 200$ volts r.m.s., $f = 500$ c/s.

would make sence, then the thickness of the barriers must be very small with respect to that of the bulk (of the order of 10 Å and 10^5 Å respectively) in order that tunnelling of the electrons at moderately high voltages may occur. We then must assume that for the audio-frequency region the ohmic conductance of the bulk must be larger than its capacitive admittance (otherwise with a.c. operation the voltage across the barrier capacitance C_2 could only be of the order of 10^{-4} times the applied voltage). This, however, would make it difficult to understand why in such an extensive frequency region the light output at constant total voltage is nearly proportional to the frequency unless the bulk resistance is so small that the voltage across the barrier is nearly equal to that across the grain.

Perhaps a solution can be found in a treatment of the surface layer analogous to that for p-n barriers [8]) (see also Volger [9])). The phase shift between the light pulses and the total a.c. voltage as measured with low frequencies on a binderless layer (fig. 11) point into this direction.

Acknowledgement: We are indebted to Dr A. Bril for his measurements of the cathodoluminescence and to Mr W. Hoogenstraaten and Dr F. A. Kröger for their participation in many valuable discussions.

Eindhoven, September 1953

REFERENCES

[1]) (a) G. Destriau, Phil. Mag. **28**, 700 (1947);
(b) G. Destriau, Phil. Mag. **28**, 774 (1947).
[2]) E. C. Payne, E. L. Mager and E. F. Lowry, Patent-Anmeldung Deutschland S 18733.
[3]) W. W. Piper and F. E. Williams, Phys. Rev. **87**, 151 (1952).
[4]) F. A. Kröger, Physica, 's Grav. **15**, 990 (1949);
F. A. Kröger, Physica, 's Grav. **16**, 297 (1950).
[5]) H. C. Froelich, J. electrochem. Soc. **100**, 280 (1953).
[6]) W. Jerome and W. C. Gungle, J. electrochem. Soc. **100**, 34 (1953);
J. F. Waymouth, W. Jerome and W. C. Gungle, Sylv. Technologist **3**, 53 (1952).
[7]) S. Roberts, J. opt. Soc. Amer. **42**, 850 (1952).
[8]) W. Shockley, Electrons and Holes in Semiconductors, Van Nostrand Comp., New York, 1951, pp. 316-318.
[9]) J. Volger, J. M. Stevels and C. W. van Amerongen, Philips Res. Rep. **8**, 452 (1953).
[10]) B. Gudden and R. Pohl, Z. Phys. **2**, 192 (1920).
[11]) F. Schmidt, Ann. Phys., Lpz., **70**, 161 (1923).
[12]) H. Hinderer, Ann. Phys., Lpz., **10**, 265 (1931).
[13]) H. A. Klasens, Nature **158**, 483 (1946).
[14]) N. F. Mott and R. W. Gurney, Electronic Processes in Ionic Crystals, Oxford, 1940, Chapter V.
[15]) A. Bril and H. A. Klasens, Philips Res. Rep. **7**, 401 (1952).
[16]) U. Fano, Phys. Rev. **58**, 544 (1940).
[17]) P. H. Dowling and J. R. Sewell, J. electrochem. Soc. **100**, 34 (1953).
[18]) G. Diemer and J. L. H. Jonker, Philips Res. Rep. **5**, 161 (1950).
[19]) A. Bril and F. A. Kröger, Philips tech. Rev. **12**, 122 (1950).
[20]) W. Shockley, Electrons and Holes in Semiconductors, Van Nostrand Comp., New York 1951, p. 100.
[21]) J. Bardeen, Bell. Syst. tech. J. **28**, 428 (1949).
[22]) W. Hoogenstraten, J. electrochem. Soc. **100**, 356 (1953).

ELECTRIC BREAKDOWN AND LIGHT EMISSION IN CdS SINGLE CRYSTALS

by G. DIEMER

537.529

Summary

With measurements on D.C. breakdown in photo-conducting CdS single crystals, activated with Cl, *I-V* characteristics are obtained very similar to those of arc discharges in gases. There is a Townsend region, giving rise to anode light, a region of negative slope where light phenomena occur pointing to a positive streamer discharge, and an arc region of thermal character.

Résumé

Lors des mesures sur la disruption en courant continu dans les monocristaux photo-conducteurs CdS, activés par Cl, l'on a obtenu des caractéristiques *I-V* se rapprochant beaucoup de celles des décharges des arcs dans les gaz. Il y a une région de Townsend qui donne naissance à de la lumière anodique, une région de pente négative où se produisent des phénomènes lumineux indiquant des décharges du type „streamer" et une région d'arc de caractère thermique.

Zusammenfassung

Bei Gleichstrom-Messungen an Durchschlägen in photoleitenden, mit Cl aktivierten CdS-Einkristallen werden *I-V* Kennlinien erhalten, die denjenigen von Lichtbogenentladungen in Gasen sehr ähnlich sind. Hierbei sind der Reihe nach zu unterscheiden: ein Townsend-Gebiet, wo Anodenlicht entsteht, ein Gebiet mit negativen Neigung der Kennlinie, in dem Lichterscheinungen auftreten, die auf eine positive „streamer"-Entladung deuten, und ein Lichtbogen-Gebiet thermischen Charakters.

Boër, Kümmel and Rompe [1]) have reported measurements on photo-conducting CdS single crystals. They found that in a small voltage region just below the "dark" breakdown voltage in which the current through the crystal increased exponentially with voltage, light was produced throughout the bulk if the current was raised above a certain level. They varied the conductivity by additional illumination and came to the conclusion that any breakdown in the crystal was of a thermal character.

In trying to repeat their measurements we chose a somewhat different electrode arrangement, such that all of the bulk was visible through a microscope (fig. 1a). In this way we were able to study the light emission in detail. Moreover special care was taken in dimensioning the electric circuit in such a way that a very good stabilization of the crystal current was obtained throughout the whole breakdown region. The electrodes consisted of carbon (aquadag), silver (applied as a paste and baked hereafter) or copper (applied by evaporation). Since no essential difference in

the breakdown phenomena was observed with different electrode materials we finally used carbon only because of its easy way of application and its stability with respect to heating.

The CdS single crystals, which were kindly provided to us by Dr F. A. Kröger of this laboratory, had been activated by small amounts of Cl. They showed a good photoconductivity (i.e., the ratio of photocurrent to dark current was high). The electric field with such an electrode arrangement (two half-planes lying in the same plane) is not homogeneous: in fig. 2 the lines of force in the neighbourhood of one of the electrodes are given [2]). Because the surface of the crystal is not quite flat, additional irregularities in the field will occur near the carbon electrodes.

In fig. 3 the circuit for measuring I-V characteristics is shown. Because it is important to know the voltage across the crystal accurately and at the same time to protect the crystal by means of a large series resistance from being destroyed, we used as a voltmeter a sensitive galvanometer 2 connected directly across the crystal by means of a large series resistance R_2. In series with all this is a resistance R_1, to limit the current. R_2 should be much larger than R_1, lest this limiting action should lessen. We chose $R_2 = 3.10^9\ \Omega$ and R_1 between $10^8\ \Omega$ and $10^6\ \Omega$. The crystal voltage and

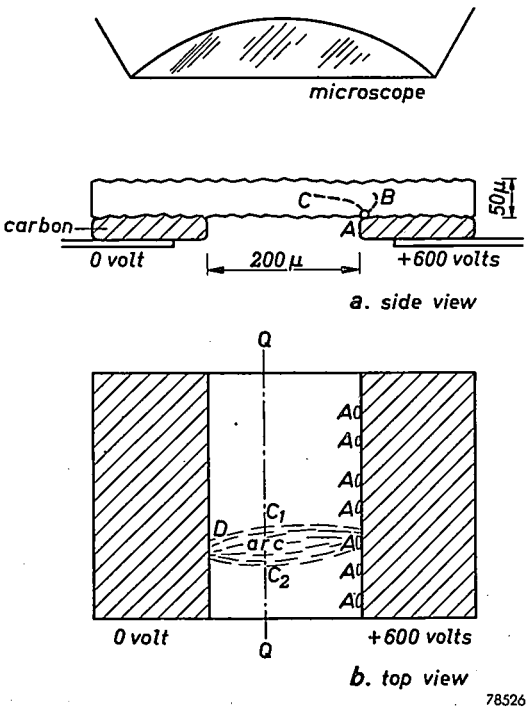

Fig. 1. Electrode arrangement used for D.C. measurements on CdS single crystals.

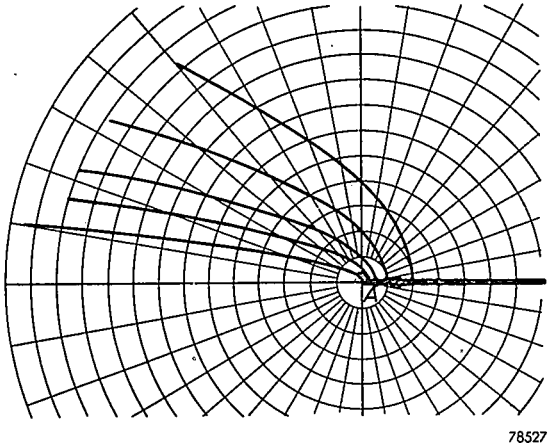

Fig. 2. Field lines near one of the electrodes. The field is strongest near A, the edge of the electrode.

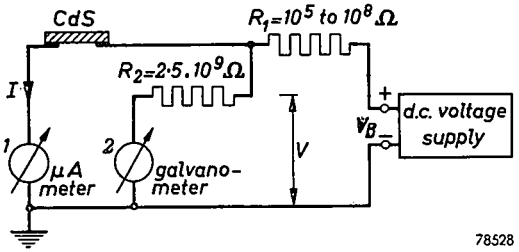

Fig. 3. Circuit used for measuring the I-V characteristics.

current can be adjusted by varying either the series resistance R_1 or the supply voltage V_B.

In accordance with Boër et al., we found that beyond a certain voltage threshold the current through the crystal increases very strongly. In fig. 4 such a characteristic is given. In our preliminary experiments the value of R_1 was decreased by such large steps that breakdown occurred before the most interesting phenomena had been observed. In the right-hand side of fig. 4 the crystal, after such a partial breakdown, is schematically drawn: a crack in the crystal has started from the anode. (Looking through the crystal this crack had a dark appearance; when illuminated from aside it looked brighter than the rest of the bulk.) Such disruptions always started from the anode (see also von Hippel [3]). When the current is raised to a few μA's orange-red lightspots with a diameter of about 10 μ begin to appear at the anode border near A of fig. 2 (see fig. 5), that is, in the region where the field is strongest. This, combined with the fact that breakdown starts from the anode, makes it very probable that in the region of steep

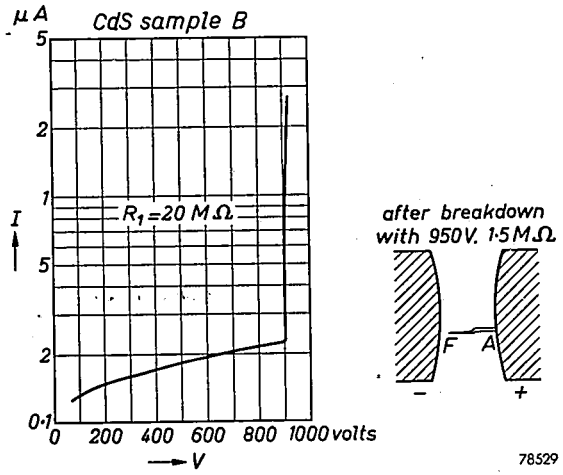

Fig. 4. *I-V* characteristic of a CdS single crystal. After a partial breakdown, due to too small a value of the stabilizing resistance, a crack *AF* has proceeded from the anode into the inter-electrode space.

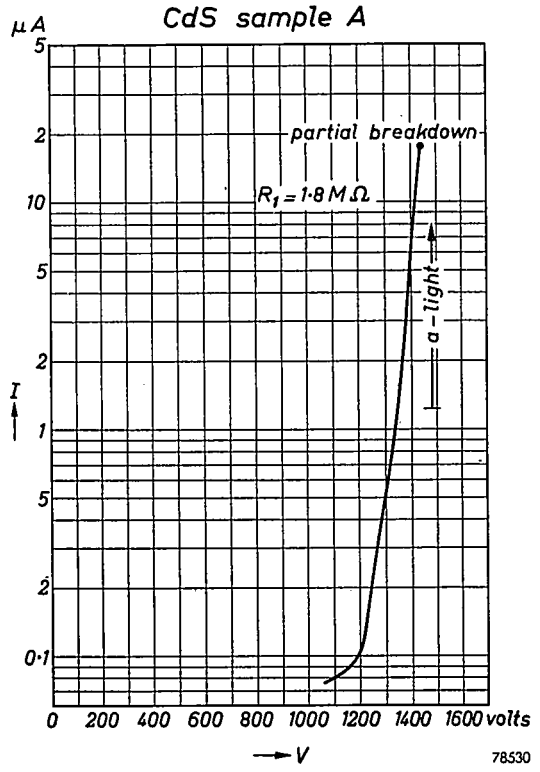

Fig. 5. Similar as fig. 4. For currents somewhat larger than 1 μA near the anode orange-red light spots *A* can be seen (see fig. 1*a* and 1*b*).

rise of I an electron avalanche is beginning to occur, analogous to that of the Townsend region of gas discharges. Most probably at lower voltages the field within the crystal is more or less distorted by space charge due to electrons that are injected from the cathode (Rose [4])). The I-V dependence in our "Townsend region" is very much stronger than that with a space-charge limited characteristic as given by Rose, showing that we have here to do with a different mechanism.

When the field is strong enough, electrons in the conduction band can be accellerated to such an extent that they can liberate secondary electrons. These secondaries can originate from (a) traps near the conduction band, (b) centres near the valence bond energy band or from this band itself.

Since at the luminescence the anode can be sustained for several hours we must assume that it cannot be caused by the "glow" following the liberation of trapped electrons, but that here the excitation of the kind (b) is taking place. Therefore most probably with such large field strengths all the traps in the bulk of the crystal will have been emptied already.

Just as is the case with a gas discharge so the D.C. current can only be sustained if: (1) electrons from the cathode can enter into the inter-electrode space of the crystal, (2) the positive charges created after the liberation of secondary electrons have a certain mobility, albeit much smaller than the electron mobility. We know that (1) is fulfilled because of the presence of dark current. Since CdS shows the Klasens-Schön [5]) effect (2) will also become true in strong fields.

To avoid the breakdowns mentioned above, the limiting resistance R_1 was decreased by much smaller steps or sometimes it was not varied at all, adjusting the current by an increase of the supply voltage V_B (see below). In this way curve 1 of fig. 6 was obtained. Contrary to Boër's experimental results (where only an exponential rise of I was found with a very steep positive slope), this characteristic after the initial region of high slope turns back towards a region of lower voltages and higher currents. In this region the slope is negative.

It is clear that with such a negative slope the resistance R_1 should have an appropriate value to stabilize the current. The minimum value needed for R_1 proved to be in accordance with the value of this negative slope. When chosing e.g. three different values for R_1 (R_1', R_1'' and R_1''' respectively) with a constant supply voltage V_B three different load lines are obtained, such that the region of negative slope near the Townsend region is just missed: with R_1''' the operating point jumps from P to Q where breakdown occurs (see fig. 7). If, however, R_1 is not decreased thus far, but on the other hand V_B is increased to a sufficiently high value V_B' with appropriate values of R_1 this part of the characteristic can be measured. When the crystal does not remain too long in this region of negative slope the charac-

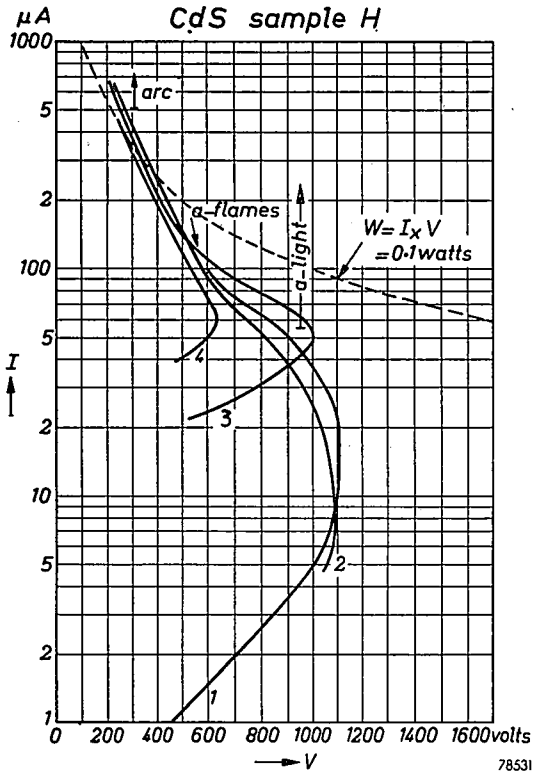

Fig. 6. Set of I-V characteristics measured successively. For currents, larger than some tens of μA the characteristic bends to the left and gets a negative slope. For $I = 50$ μA small "tongues" are wandering from A to B (see fig. 1a). For $I > 500$ μA an arc can be seen, reaching from one electrode to the other. Dashed line: curve of constant dissipation of 0·1 watt.

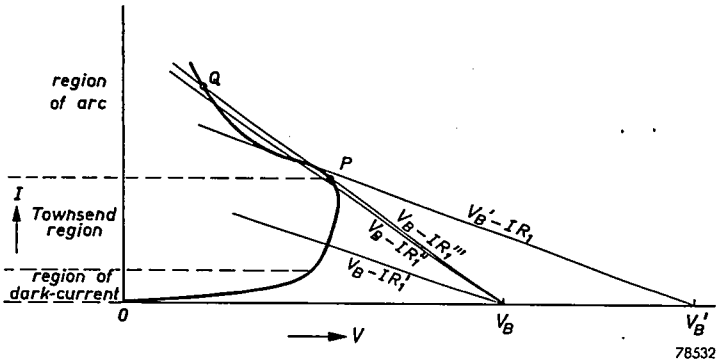

Fig. 7. I-V characteristic and load lines showing on a linear scale the adjusting of the crystal current I and crystal voltage V by variation of either the series resistance R_1 or the supply voltage V_B (see also fig. 3).

teristic is rather well reproducible after the field has been switched off and the experiments are repeated, though the region of high slope tends to shift to smaller V values.

After having repeated the measurements along the characteristic 1 up to a rather high current ($I \approx 100$ μA) the voltage was switched off. Directly after this the region of negative slope was investigated up to still higher I values, resulting in curve 2. With increasing I the light emission remains at first concentrated in the orange-red spots A mentioned above (see fig. 1). With larger I the number as well as the intensity of these spots increases.

Above a certain I value ($I > 120$ μA) suddenly a peculiar light phenomenon occurs: small orange-red tongues, about 20 μ long, loosen themselves from the bright spots A and wander into the direction AB of fig. 1*a* (i.e., sideways with respect to the applied electric field). The velocity of propagation of these tongues is about 100 μ/sec. They die out at a distance of about 50 μ to 100 μ from A. When the current I is raised to about 200 μA the flames become more frequent and finally form a continuous "curtain" of light extending from A. The direction of the plane of this curtain turns meanwhile from the direction AB towards AC (fig. 1*a*). The light emission and the current are not quite stable in this region; if V_B (fig. 3) is kept constant the operating point tends to shift along the characteristic towards higher currents and lower voltages. The absorption colour of these regions in the crystal when illuminated from underneath shifts from orange-yellow towards the red. Since such a variation is known to occur upon increase of temperature (Seiwert [6])) it may be concluded that in these regions (where light emission takes place) the crystal is locally heated. This heating explains the negative characteristic because the number of electrons in the conduction band will increase with temperature (see also Boër [1])). In the experiments described below further evidence for such an explanation will be given.

We now return to the peculiar fact that in a certain region of the characteristic the "curtain" of light emission is turned away from the region of the crystal situated between the electrons. For the explanation of this and other experimental facts the following mechanism is proposed. As was already pointed out, electron multiplication occurs near the anode edge in the steep region of the characteristic (the "Townsend region"). This causes a strong positive space charge to be built up in the neighbourhood of this edge, due to the fact that the positive charges left behind have a much smaller mobility than the electrons. If now near this region of positive space charge new electrons are liberated, either through thermal agitation or through self-absorption of light quanta, originating from recombination in the space-charge cloud, these new electrons and the avalanches they give rise to will tend to move along the lines of force

of the applied field of fig. 2. The positive space-charge cloud, however, gives rise to an additional field that tends to draw the electrons sideways into its own direction. Meek [7]) has shown that, if this is the case, a cumulative effect will result, which brings about a so-called positive streamer discharge, well known for electric sparks in gases under high pressure. When the numerous electrons, originating from the avalanches near the space-charge cloud, are drawn into it, they form together with the positive charges a region of highly conducting plasma which is growing in extension as the streamer develops. See also fig. 8 where the development of a streamer is schemetically drawn (after Meek but changed in accordance with our circumstances).

Meek gave the following criterion for such a streamer to develop, which enabled him to describe the high-pressure spark discharge in gases; *the radial field due to the positive space-charge cloud must be of the same order of magnitude as that of the applied* (space-charge free) *field.* If the field due to the space charge is much smaller, the new electrons will tend to follow the lines of force of the applied field and most of the new avalanches will then miss the space-charge cloud. A rough estimation for the applied fields we used shows that Meek's criteron will be fulfilled if the number of positive charges in a spherical cloud of 10 μ diameter is about 10^{-8} times the number of atoms in that cloud. This is not an improbable value, even if only excitation in centres near the valence band would occur and not in the band itself.

Now from fig. 2 it is clear that the applied field strength is largest near the anode edge; it decreases along the anode surface in a direction away from the inter-electrode surface. Therefore Meek's criterion is easier

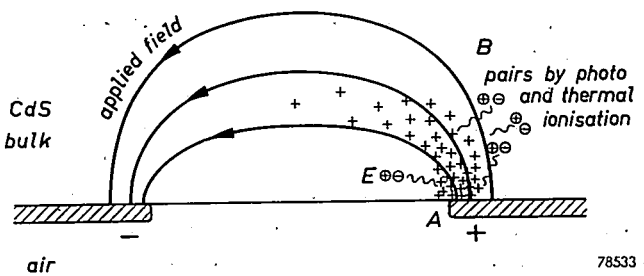

Fig. 8. History of an avalanche after the electrons have disappeared into the anode (according to Meek, with some modifications). A positive space-charge boss appears on the anode near A (point of maximum applied field strength). Ion pairs out from the trail of the primary avalanche indicate the appearance of photo-electric and thermal ion pairs in the bulb, produced from photons due to recombination near A and from heat conduction from the region near A. (These pairs are denser in the avalanche channel from which they have been omitted for the sake of clarity.) The electrons of the pairs near B and the secondary avalanches they give rise to are more likely to be drawn into the space-charge boss than those near E. Therefore the streamer is developing into the direction of B.

fulfilled in these regions, so that the streamer is at first developing in a direction which is somewhat turned away from the inter-electrode space. The same effect can take place in gas sparks from a positive point to a plane[8]). One might suppose that similarly to the apparently easy injection of electrons at the cathode, with sufficiently strong field strengths at the anode, hole injection into the CdS bulk might start, giving also rise to a positive space charge near the anode even in the absence of electron multiplication. There are, however, two experimental facts that can be explained by electron multiplication as mentioned above, whilst a hole injection mechanism fails here. They are: the very steep, exponential rise of the characterstic (Townsend region) and the development of a curtain of light in the direction AB of fig. 1*a*. We think, therefore, that in our experiments hole injection was negligible. For a further explanation of the streamer mechanism we refer to the legend to fig. 8 and to the book by Loeb and Meek [7]).

With higher crystal currents the light emission as a whole extends into the inter-electrode region of the crystal, the border of the light remaining parallel to the anode edge. With still higher currents this extension proceeds more locally, a "spear head" is formed, so that with $I>500$ μA the cathode is reached at D (fig. 1*b*). A diffuse arc discharge can then be seen between A and D. Near this discharge the bulk has a rather high temperature (about 600 °C as estimated from vision through a pocket spectrometer when the crystal was illuminated from underneath; see Seiwert[6]). In fig. 9 the temperature distribution along the cross-section QQ if fig. 1*b* is roughly sketched. The measurement of the characteristic 2 of fig. 6 lasted about 15 minutes in total. After this, characteristic no 3 was measured: apparently the crystal has got a much larger dark conductivity and a somewhat lower breakdown voltage. The characteristic in the arc region is nearly unaltered. When the crystal is operated in the arc region during some

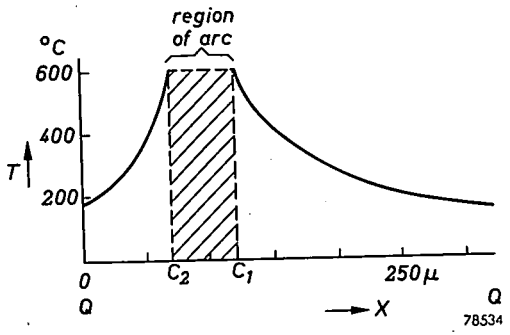

Fig. 9. Roughly sketched temperature distribution along the section QQ of fig. 1*a* through the crystal bulk when an arc is present (visually estimated from the position of the absorption edge of the crystal by means of a pocket spectroscope).

minutes with $I \approx 0{\cdot}6$ mA the arc tends to deplace itself sideways till it has crossed the whole inter-electrons region of the bulk. The characteristic is meanwhile shifted to larger dark currents and a lower breakdown voltage (curve 4). During this shifting of the arc a spot of green light can sometimes be seen at the electrodes near the border of the arc (excitation and recombination in the valence band ?).

The orange-red emission of the arc lies in the wavelength region of 5000-6500 Å. We think this light emission to be of thermal origin; it is due to local heating, produced by the rather high conductivity of the crystal bulk in the arc region of the characteristic (see also below where additional arguments will be given for the thermal nature of the arc).

Sometimes the arc jumps very suddenly from one region to another. (time of a jump $\ll 1$ sec), just as gas discharges sometimes do. We may point to the fact that a curve of constant dissipation ($W = I \times V = 0{\cdot}1$ watt) as given in fig. 6, is crossed by the characteristic in a direction opposite to that found by Boër when he used strong additional illumination.

The arc can also be operated with an A.C. voltage or a square wave. Fig. 10 gives some oscillograms of the voltage and light output. It may be seen that the build-up of the arc is rather slow, due to its thermal nature.

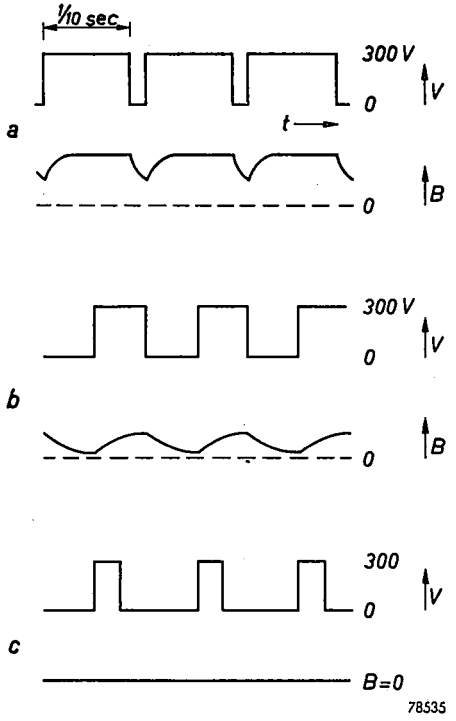

Fig. 10 Various oscillograms of the arc showing the slowness of the build-up and the decay.

When the dead time between two voltage pulses is too large, no arc is observed. The current shows a similar behaviour as the brightness B. Fig. 11 shows the I-V characteristic of a small A.C. ripple superimposed on the D.C. voltage; the slow character is also shown here, firstly by the direction of rotation in the I-V loops (as indicated by an arrow) and secondly by the fact that the main axis of the elliptic loops do not coincide with the tangent of the I-V characteristic.

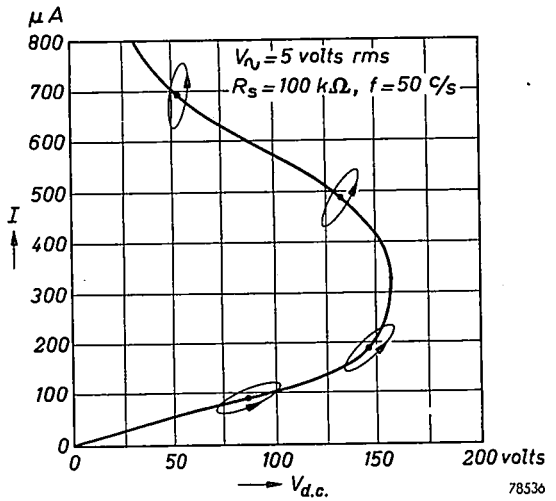

Fig. 11. Oscillograms of the arc obtained by superimposing a 50 c/s A.C. ripple upon the operating D.C. voltage.

Similar characteristics and light phenomena were observed on several crystal samples. Fig. 12 gives another series of characteristics measured in succession. Numbers 2 and 2a were obtained with additional illumination. Curve 2a shows a maximum analogous to the curves of Boër. Because the series resistance R_1 was rather low during measurement of 2 and 2a, the crystal was able to jump along its negative characteristic towards the point P. After this the dark conduction had increased and the breakdown voltage had decreased (curve 3). The crystal was operated during some minutes at 800 V, 50 μA. This caused a decrease of the breakdown voltage by more than a factor 2 (curve 4), but after 24 hrs of rest it came back towards its original value (curve 5): clearly the large space charge formed during the measurements of 2a, 3 and 4 had cleared away in the meantime. The other characteristics are quite analogous to those obtained with the sample H of fig. 6.

In some of the investigated crystals, not discussed here in detail, the

luminescence at low currents starts at spots somewhere midway in the inter-electrode region, evidently due to inhomogeneities that are present there. When a crystal has been operated for some time in the Townsend region and the sign of the applied voltage difference is suddenly reversed, the Townsend region is often shifted to higher voltages, pointing also to the build-up of a space charge that distorts the applied field (see also Keller[9]).

When an arc is sustained in a crystal and the latter is cooled down by means of forced air blowing, the light emission disappears and the operating point shifts along the characteristic towards smaller currents and higher voltages. This proves once more the thermal nature of the arc.

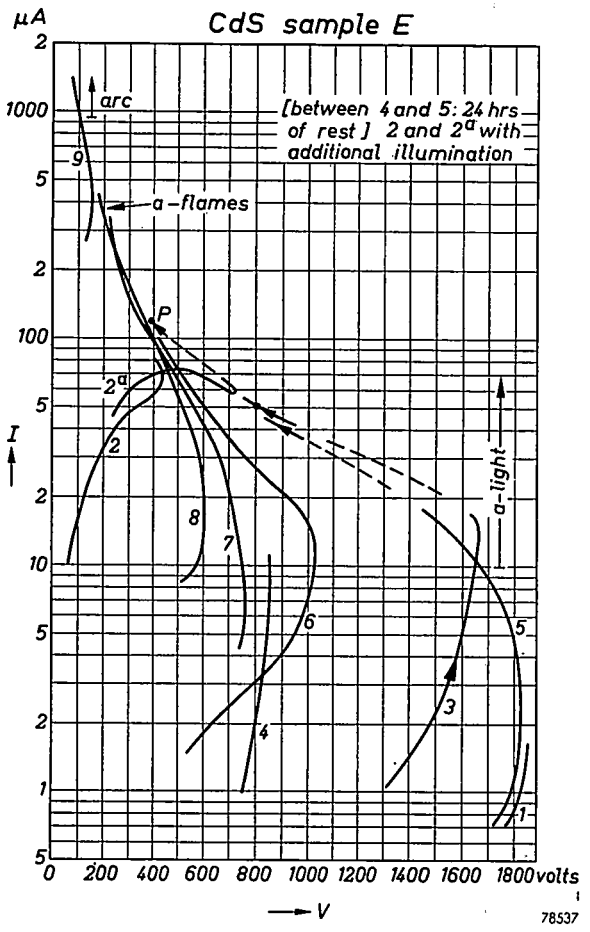

Fig. 12. As fig. 6 for a different sample. The curves 2 and 2a are obtained with additional illumination; 2a shows a maximum, analogously to Boër's curves. Between the curves 4 and 5, a 24 hrs rest had been given to the crystal.

A magnetic field of 6000 oersteds in a direction perpendicular to the plane of the electrodes (i.e. perpendicular to the plane of drawing in fig. 1*b*) did not change the shape of the arc nor its intensity. From this we may conclude that the mean free path of the electrons in the arc is much smaller than 10μ, because otherwise the paths of the slowly moving electrons in the conduction band would have become so strongly curved by the magnetic field that a large variation in the number of collisions would have occurred. So with field strengths as low as 25 volts/250 μ (being sufficient to sustain the arc) between two successive collissions the electrons cannot gain sufficient energy for excitation. This is another proof for the thermal origin of the light emission from the arc.

A crystal in which an arc has been sustained during a long time gets an increasingly higher dark current, which does not disappear even after long times of rest (see e.g. curve 9 of fig. 12). Permanent chemical and physical changes have then clearly taken place; the surface structure is then roughened somewhat. Although no big damage as cracks etc. is visible, one might say that in such a crystal a "breakdown" has taken place, and because the arc discharge causing this "breakdown" is of a thermal nature, one might conclude that the electric breakdown in CdS is in any case a thermal breakdown (as Boër et al.[1]) did). The present experiments have shown, however, that the proceeding of the breakdown can be controlled continuously by means of an appropriate measuring equipment and that the various phases of the breakdown may be stabilized up to a high degree. Accurate observation of local light emission by means of a microscope with large amplification gives very useful additional information concerning the breakdown mechanism. It was only in this way that the positive space charge near the anode, and the streamer discharge it gives rise to, could be discovered.

Eindhoven, October 1953

REFERENCES

1) K. W. Boër, U. Kümmel and R. Rompe, Z. phys. Chem. **200**, 180-192, 1952; K. W. Boër und U. Kümmel, Z. phys. Chem. **200**, 193-198, 1952.
2) W. K. Westmijze, Philips Res. Rep. **8**, 161-183, 1953; see pp. 161-171.
3) A. von Hippel, J. appl. Phys. **8**, 815-824, 1937; R. W. Smith and A. Rose, Bull. Amer. phys. Soc. **28**, 21, 1953 (S_1).
4) A. Rose and R. W. Smith, Bull. Amer. phys. Soc. **28**, 21, 1953 (S_2).
5) H. A. Klasens, Nature **158**, 483, 1946.
6) R. Seiwert, Ann. Phys., Lpz. **6**, 241-252, 1949.
7) L. B. Loeb and J. M. Meek, The mechanism of the electric spark, Stanford University Press, 19 (see chapter II, especially sections 1-4).
8) J. M. Meek, private cummunication.
9) K. J. Keller, Phys. Rev. **86**, 804-805, 1952.

 Philips Res. Rep. 9, 122-130, 1954

DIE NEGATIVE IONENKOMPONENTE DES ELEKTRONENSTRAHLES IN KATHODENSTRAHLRÖHREN, INSBESONDERE FERNSEHBILDRÖHREN

by W. F. NIKLAS *)

537.56:537.533.3:621.385.832

Summary

The electron beam of a cathode-ray tube contains apart from the electrons also negative ions which inactivate the fluorescent screen. When in a cathode-ray tube with an electrostatic lens system a transverse magnetic field is superposed on the electrostatic field, it is possible to focus the ions on the screen in sharp points which are arranged according to the mass of the ions. A sharp focus is only obtained if the ions are generated at the same spot as the electrons because the lens system is arranged for sharp focusing of these electrons. An unsharp focus of the ions therefore indicates that the ions must have been generated elsewhere than the electrons. The mass of the ions is obtained by suitable calibration. By means of the degree of sharpness of the focus two ion components can be distinguished: ions coming from a cathode (cathode ions) and ions generated in the remaining gasses contained in the cathode-ray tube (gass ions). By means of the cathode of the fine network placed at different spots in the cathode-ray tube it is shown that the gass ions are generated between the grid and the first anode. By the mass and nature the cathode ions are identified as Cl^{37}, Cl^{35} and CN or C_2H_2, and the gass ions as O, CH, C. The reduction in the residual pressure results in the elimination of the gass ions; the intensity of CN (or C_2H_2) cathode ions reduces with increasing life of the tube.

Résumé

Le faisceau électronique d'un tube à rayons cathodiques comprend, outre les électrons, également des ions négatifs qui désactivent l'écran fluorescent. Lorsque l'on utilise dans un tube de télévision une lentille électrostatique et que l'on ajoute un champ magnétique transversal, il est possible de projeter les ions négatifs sur l'écran fluorescent sous forme de points nets, groupés suivant la masse d'ions. L'image est nette dans le cas où les ions sont engendrés au même endroit que les électrons, la lentille étant réglée pour assurer une représentation nette des électrons. Si l'image des ions est floue, c'est que les ions et les électrons sont engendrés à des endroits différents. La détermination de la masse des ions s'effectue par étalonnage et par calcul relatif. La netteté de l'image permet de distinguer deux composantes d'ions: ceux émanant de la cathode (ions cathodiques) et ceux émanant de l'espace occupé par le gaz (ions de gaz). A l'aide d'une méthode de masquage (utilisation d'un réseau à mailles fines), on constate que la formation des ions de gaz s'opère dans l'espace compris entre le cylindre de Wehnelt et la première anode. On trouve pour la masse et la nature des ions cathodiques: Cl^{37}, Cl^{35}, CN ou C_2H_2, et pour les ions de gaz O, CH, C. Une réduction de la pression de gaz résiduelle a pour effet d'éliminer les ions de gaz, et de même,

*) At present with "The Ranland Corporation Engineers", 4245 N. Knox Ave, Chicago, Ill., U.S.A.

l'intensité des CN/C_2H_2 (ions cathodiques) faiblit en fonction de la durée de vie du tube.

Zusammenfassung

Der Elektronenstrahl in einer Kathodenstrahlröhre umfaßt neben den Elektronen auch negative Ionen, die den Leuchtschirm inaktivieren. Verwendet man in einer Fernsehröhre ein elektrostatisches Strahlensammelsystem und überlagert ein transversales Magnetfeld, so ist es möglich, die negativen Ionen am Leuchtschirm als scharfe Punkte, nach der Ionenmasse gegliedert, abzubilden. Die Abbildung ist dann scharf, wenn die Ionen am gleichen Ort entstehen wie die Elektronen, da das Strahlensammelsystem für eine scharfe Elektronenabbildung eingestellt ist. Eine Unscharfe Ionenabbildung deutet auf einen verschiedenen Entstehungsort für Ionen und Elektronen hin. Die Bestimmung der Masse der Ionen erfolgt durch Eichung und relative Berechnung. Man kann an Hand der Schärfe der Abbildung zwei Ionenkomponenten unterscheiden: Ionen aus der Kathode (Kathodenionen) und Ionen aus dem Gasraum (Gasionen). Mittels einer Schattenmethode (Verwendung eines feinmaschigen Netzes) wird als Enstehungsort der Gasionen der Raum zwischen Wehneltzylinder und Sauganode bestimmt. Für die Masse und Natur der Kathodenionen ergibt sich Cl^{37}, Cl^{35}, CN oder C_2H_2 und für die Gasionen O, CH, C. Herabsetzen des Restgasdruckes eliminiert die Gasionen, gleichfalls wird die Intensität von CN/C_2H_2 (Kathodenionen) mit der Brenndauer der Röhre schwächer.

1. Einleitung

Der Elektronenstrahl, der in Kathodenstrahlröhren mittels der Elektronenkanone erzeugt wird, besteht nicht nur aus Elektronen, sondern auch aus negativen Ionen [1]). Negative Ionen und Elektronen werden durch das elektrostatische Linsensystem der Elektronenkanone gleichartig beeinflußt und treffen mit beträchtlicher Geschwindigkeit auf dem Leuchtschirm der Kathodenstrahlröhre auf.

Eine Kathodenstrahlröhre für Fernsehempfang besitzt im allgemeinen ein elektromagnetisches Ablenksystem, während die Strahlensammeleinrichtung magnetisch oder elektrostatisch ausgeführt sein kann. Das magnetische Ablenksystem beeinflußt die negativen Ionen wegen ihrer großen Masse praktisch nicht [2]), sodaß sie in der Schirmmitte auftreffen, und zwar angenähert konzentriert im Falle einer elektrostatischen Strahlensammeleinrichting und nicht konzentriert im Falle einer magnetischen Strahlensammeleinrichtung. (Analog der Nichtbeeinflußung der Ionen durch das magnetische Ablenksystem werden die Ionen auch durch ein magnetisches Strahlensammelsystem nicht beeinflußt.)

Der Leuchtschirm einer Fernsehbildröhre besteht in den meisten Fällen aus Sulfidephosphoren, die durch die negativen Ionen inaktiviert werden. Es zeigt sich dann bei gleichmäßiger Anregung des Schirmes ein dunkler Fleck in der Mitte, der bekannte „Ionenfleck", der das Fernsehbild stark stören kann.

Da es bisher noch nicht gelungen ist, Leuchtstoffe herzustellen, die gegen negative Ionen unempfindlich sind, muß verhindert werden, daß die Ionen

den Leuchtschirm erreichen. Zu diesem Zweck werden im allgemeinen sogenannte „Ionenfallen" in die Elektronenkanone eingebaut [3]). Ionenfallen komplizieren jedoch den Aufbau der Elektronenkanone und es wäre daher erwünscht, das Entstehen der negativen Ionen zu unterbinden. Stellt man sich diese Aufgabe, so ist die Untersuchung der Natur und des Entstehungsortes der negativen Ionen in der Kathodenstrahlröhre der erste Schritt.

2. Methode

Kathodenstrahlröhren, die eine elektrostatische Strahlensammeleinrichtung besitzen, eignen sich zur magnetischen Aufspaltung des negativen Ionenbündels und zur Erzeugung eines nach der Ionenmasse gegliederten Spektrums, da wie bereits im 1. Abschnitt ausgeführt, Ionen durch elektrostatische Linsen konzentriert werden. Es entstehen dann am Leuchtschirm der Versuchsröhre Reihen von schwarzen Punkten, von denen jeder Ionen einer bestimmten Masse darstellt.

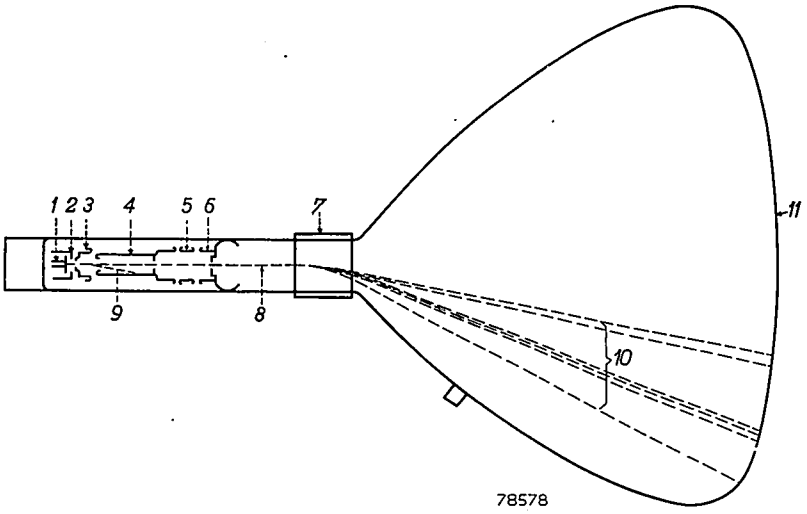

Abb. 1

Abbildung 1 zeigt schematisch die Versuchsanordnung, bestehend aus einer Fernsehbildröhre ohne Ionenfalle und einem Permanentmagnet; *1-6* ist die Elektronenkanone, bestehend aus der Ba-Sr-Oxyd-Kathode *1*, dem Wehneltzylinder *2*, der Sauganode *3*, der Beschleunigungsanode *4*, die zugleich als erste Elektrode der elektrostatischen Strahlensammeleinrichtung dient (Einzellinse mit den Elektroden *4*, *5* und *6*, wobei *4* und *6* an der gleichen Spannung liegen); *7* deutet das transversale Magnetfeld an, das in der Mitte des Luftspaltes die Stärke von etwa 2 Wb/cm² besitzt;

8 ist das negative Ionenbündel, *9* der Elektronenstrahl, der bereits früh durch das Streugebiet des Magnetfeldes *7* gegen die Innenwand des Anodenzylinders *4* abgebogen wird; *10* ist das nun nach Masse aufgefächerte Ionenbündel und *11* der Leuchtschirm aus Sulfidephosphoren (Zn-Sulfid plus Zn-Cd-Sulfid). Zwischen dem Leuchtstoff und dem Glas des Ballons befindet sich eine leitende, durchsichtige Metallschicht (aufgedampft). Diese Schicht bewirkt, daß keine örtlichen Potentialunterschiede am Leuchtschirm auftreten können, die zu einer Verzeichnung der Spektrumspunkte führen könnten.

Die Röhre wird mit den folgenden Spannungen betrieben: $V_3 = 300$ V, $V_4 = 15\,000$ V. Die „Belichtungszeit" für die Aufnahme eines Spektrums beträgt etwa 20 min.

Die Abbildung der Ionen, wobei zwischen „scharf" und „unscharf" unterschieden werden soll, läßt Rückschlüsse auf ihren Entstehungsort zu. Werden nämlich Ionen und Elektronen am gleichen Ort gebildet und durch das gleiche elektrostatische System beschleunigt bzw. gebündelt, so müssen die Ionenabbildungen dann scharf sein, wenn auch die Elektronenabbildung scharf ist. Wählt man daher die Spannung V_5 (Mittelelektrode der Einzellinse) so, daß bei einem bestimmten, schwachen Elektronenstrom (ca. 50 μA) der Elektronenstrahl am Schirm fokusiert ist, dann muß nach Anlegen des transversalen Magnetfeldes *7* (Abb. 1) auch das Ionenbündel am Schirm fokusiert sein. Weiter unten wird darauf noch einmal zurückgekommen.

Um Masse und Natur der Ionen der Spektren zu bestimmen, wurde eine der Versuchsröhren geeicht. Zu diesem Zweck wurde etwas HCl auf die Ba-Sr-Karbonatschicht der Kathode getropft und dann auf übliche Weise die Karbonate in der geschlossenen Röhre in Oxyde verwandelt. Wegen des aufgetropften HCl wurde die Anwesenheit von starken Punkten der beiden Chlorisotope Cl^{35} und Cl^{37} erwartet. In den mit dieser Röhre erhaltenen Spektren traten jedoch keine zusätzlichen Spektrenpunkte auf. Es wurde deshalb geschlossen, daß die beiden Punkte *1* und *2* (Abb. 2) mit Cl^{37} und Cl^{35} anzusprechen sind. Außerdem stimmt die Isotopenverteilung (Cl^{35}...70-80%, Cl^{37}...30-20%) mit der Intensität dieser beiden Punkte überein.

Kennt man einmal die Masse eines Punktes des Spektrogramms, dann kann man die restlichen Punkte leicht berechnen, da gilt:

$$m_x/m = d^2/d_x^2$$

worin m = Masse des bekannten Punktes, d = Abstand des bekannten Punktes von der Schirmmitte, m_x = Masse des fraglichen Punktes, d_x = Abstand des fraglichen Punktes von der Schirmmitte.

3. Resultate

3.1 *Entstehungsort der negativen Ionen*

Abbildung 2 zeigt einige typische Ionenspektren, die mittels der oben beschriebenen Methode erhalten wurden. *A* und *B* sind Spektren, die bei einen Restgasdruck von etwa 5.10^{-7} cm aufgenommen wurden. Für die Messung des Gasdruckes wird die Röhre selbst als Ionisationsmanometer verwendet [2]). Die Spektren I und II sind unter anderen Verhältnissen aufgenommen und werden später erklärt. Betrachtet man die Spektren *A* und *B*, so erkennt man, daß die Abbildungen *1*, *2* und *3* „scharf" und die Abbildungen *4*, *5* und *6* „unscharf" erscheinen.

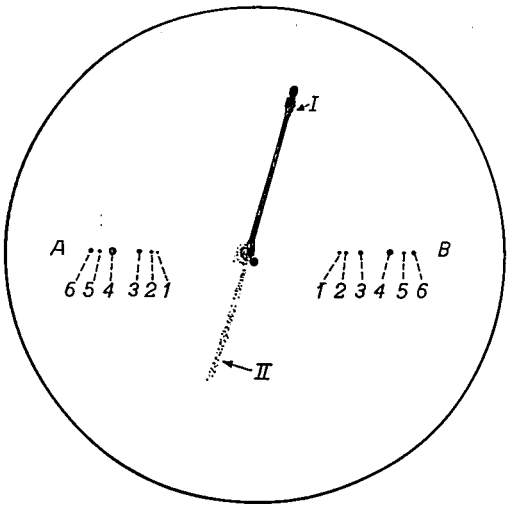

Abb. 2

Nach dem im Abschnitt 2 gesagten ist zu schließen, daß die Ionen der Punkte *1*, *2* und *3* am gleichen Ort entstehen wie die Elektronen, d.h. an der Kathodenoberfläche. Ueber den Entstehungsort der Ionen der Punkte *4*, *5* und *6* läßt sich bei der angewendeten Methode nur aussagen, daß sie irgendwo im Tetrodenteil der Elektronenkanone, d.h. zwischen Kathode und Beschleunigungsanode, entstehen. (An sich könnten negative Ionen auch noch zwischen den Linsenelektroden *5* und *6* entstehen. Es wären dann jedoch bei weitem größere und diffusere Flecke zu erwarten.)

Im Weiteren werden die Ionen der Punkte *1*, *2* und *3* mit „Kathodenionen" und die Ionen der Punkte *4*, *5* und *6* mit „Gasionen" bezeichnet.

3.2 *Entstehungsort der Gasionen*

Die oben getroffene Aussage, daß die sogenannten Gasionen nicht an der Kathodenoberfläche entstehen, soll nun gestützt werden.

Man kann den Raum, in dem mit einiger Wahrscheinlichkeit Gasionen entstehen können, nämlich zwischen Kathode und Beschleunigungsanode, in zwei Teile unterteilen:

(a) den Raum Kathode — Sauganode (zwischen *1* und *3*, Abb. 1), Raum *a*;
(b) den Raum Sauganode — Beschleunigungsanode (zwischen *3* und *4*, Abb. 1), Raum *b*.

Die Wahrscheinlichkeit für die Bildung von negativen Ionen ist im Raum *a* größer als im Raum *b*, da die Geschwindigkeit der Elektronen im Raum *a* viel kleiner ist, nämlich 300 V, als im Raum *b*, wo sie bis angenähert 15 000 V beträgt. Deshalb wurde eine Versuchsröhre mit einer modifizierten Elektronenkanone ausgestattet, die in Abb. 3 dargestellt ist. Der Teil *A* zeigt in Uebersicht die gesammte Kanone, während der Teil *B* den Triodenteil der Kanone vergrößert wiedergibt; *1* ist die Kathode, *2* der Wehneltzylinder, *3* ein feinmaschiges Gitter, das an einem Ring *4* befestigt ist, *5* die Sauganode und *6* die Beschleunigungsanode. Es werden die gleichen Spannungen wie oben verwendet und $V_3 = \frac{2}{3} V_5$.

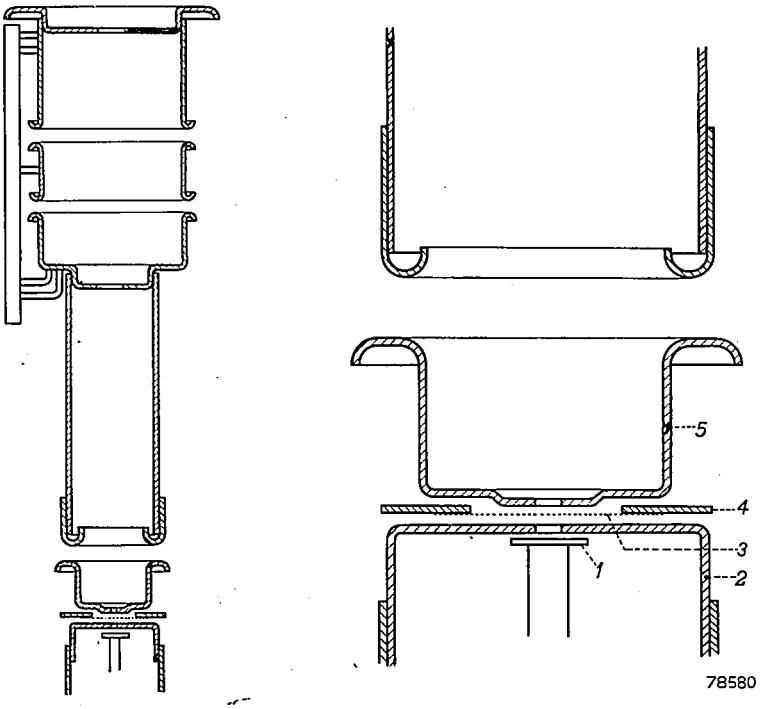

A Abb. 3 *B*

Ein Spektrum, erhalten mit dieser Röhre, ist in Abb. 4 (vergrößert) dargestellt; *1*, *2* und *3* sind wieder die Punkte der Kathodenionen und *4*, *5* und *6* die Punkte der Gasionen.

Bei letzteren kann man deutlich innerhalb der geschwärzten Fläche die Struktur des feinmaschigen Netzes erkennen, was darauf hindeutet, daß die korrelierten Ionen in unmittelbarer Umgebung des Netzes, d.h. in der Bewegungsrichtung der Elektronen gesehen, *unmittelbar vor* oder *unmittelbar hinter* diesem gebildet werden. Man kann also schließen, daß die Gasionen zwischen Wehneltzylinder und Sauganode entstehen. Die diffusen bzw. ringförmigen Flecke um die Abbildungen der Kathodenionen stammen wahrscheinlich von sekundären Ionen, wie auch Bachmann [4]) erwähnt.

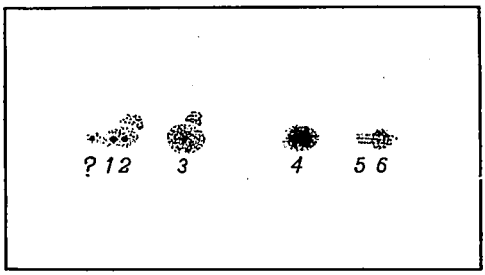

Abb. 4

3.3 *Masse und Natur der Gas- und Kathodenionen*

Der Geschwindigkeitsunterschied zwischen Gas- und Kathodenionen beträgt 300 V, oder die Gasionen sind um etwa 2% langsamer als die Kathodenionen. Hinsichtlich der Ganauigkeit der verwendeten Versuchsanordnung spielt dieser Unterschied keine Rolle und kann bei der Bestimmung der den Spektrumspunkten korrelierten Masse vernachlässigt werden.

Berechnet man unter der Voraussetzung der gleichen Geschwindigkeit für alle Ionen die zugeordnete Masse, wie in Abschnitt 2 angegeben, so erhält man die folgenden Resultate:

Gekennzeichnet in Abb. 2	Masse	Natur	Entstehungsort
1	37	Cl^{37}	Kathode
2	35	Cl^{35}	Kathode
3	26	CN, C_2H_2	Kathode
4	16	O	Gas
5	13	CH	Gas
6	12	C	Gas

3.4 *Einfluß des Restgasdruckes in der Röhre*

Wird die eine Komponente des negativen Ionenbündels als Gasionen angesprochen, dann muß eine Veränderung des Restgasdruckes die Intensität der Spektren beeinflussen.

Versuche in dieser Richtung haben dies bestätigt. Erniedrigt man den Restgasdruck in einer Versuchsröhre (z.B. durch Nachverstäuben eines Getters), dann findet man, daß die Punkte *4*, *5* und *6*, zumindest bei der angewendeten „Belichtungszeit", nicht mehr auftreten, wenn der Gasdruck unter 10^{-7} cm sinkt. Erhöht man jedoch den Gasdruck bis etwa 10^{-5} cm (z.B. durch hochfrequentes Erhitzen der Metallbestandteile der Elektronenkanone, wobei Gase freikommen), so erhält man die Spektren I und II der Abb. 2, die bei der *gleichen* Aufnahme entstanden sind. Spektrum I liegt in der Ablenkrichtung für negative Ionen und Spektrum II in der Ablenkrichtung für postive Ionen. Die Kontinuität der Spektren ist durch eine kontinuierliche Ionisation bzw. das Entstehen von tertiären negativen Ionen entlang des gesammten Weges der primären negativen Ionen zu erklären. Als Erklärung für die positiven Ionen des Spektrums II können sekundäre positive Ionen dienen, die zwischen den Elektroden *4* und *5* (Abb. 1) gebildet werden und durch das Gegenfeld dieser ersten Linsenhälfte beschleunigt werden.

3.5 *Einfluß der Brenndauer der Röhre*

Die Spektren zeigen auch einen Einfluß der Brenndauer der Röhre. Wird ein Spektrum unmittelbar nach dem Abschluß des Herstellungsprozesses der Röhren aufgenommen, so treten alle 6 Punkte des Spektrums auf. Hat die Röhre jedoch einige Stunden gearbeitet, so werden

(a) die Punkte der Gasionen intensitätsschwächer und

(b) der Punkt *3* (Kathodenionen CN oder C_2H_2) ebenfalls schwächer.

Das Schwächerwerden der Gasionen ist darauf zurückzuführen, daß im allgemeinen die Getter (in den Versuchsröhren wurden Ba-Al-Getter verwendet, „geflashed" mittels Hochfrequenzerwärmung) metastabile Moleküle leichter aufnehmen als neutrale Moleküle und daher der Restgasdruck der Röhre sinkt, was durch direkte Gasmessungen bestätigt wird.

4. Möglichkeiten, das Entstehen von negativen Ionen zu verhindern

Wie gezeigt, ist es möglich, *eine* Komponente des negativen Ionenbündels, nämlich die Gasionen, durch sehr gutes Evakuieren der Röhre, bzw. durch einen guten Getter oder entsprechendes Vorbrennen der Röhre zu beseitigen. Ebenfalls kann der Einfluß der Kathodenionen durch Vorbrennen geschwächt werden.

Es ist jedoch nicht möglich gewesen, durch einfache Mittel die Cl-Kom-

ponenten der Spektren zu unterbinden. Cl kann vom Glas des Ballons herrühren. Hamaker, Bruining und Aten haben ebenfalls auf die Rolle des Chlors in Röhren mit Oxydkathoden hingewiesen [5]).

Eindhoven, November 1953

REFERENCES

[1]) M. von Ardenne, Arch. Elektrotech. **29**, 731 (1935). Siehe auch die *Literaturangaben*. Die positiven Ionen, die durch Bombardement von neutralen Restgasmolekülen oder durch Bombardement einer Blende entstehen können und sich entgegengesetzt den Elektronen zur Kathode bewegen, werden hier nicht behandelt.

[2]) J. de Gier, De Ingenieur **65**, O36 (1953), insbesondere Seite O42 oben.

[3]) Im Artikel W. F. Niklas, „Een verbeterde ionenvalmagneet", Philips techn. Tijdschr. **15**, 278 (1953), ist die Wirkungsweise von Ionenfallenkonstruktionen behandelt.

[4]) C. H. Bachmann, G. L. Hall und P. A. Silberg, J. appl. Phys. **24**, 427 (1953).

[5]) H. C. Hamaker, H. Bruining und A. H. W. Aten Jr., Philips Res. Rep. **2**, 171 (1947).

Literaturangaben

C. H. Bachmann und C. W. Carnahan, Proc. Inst. Radio Engrs **26**, 529 (1938).
L. F. Broadway und A. F. Pearce, Proc. Phys. Soc. (London) **51**, 335 (1939).
C. H. Bachmann, J. appl. Phys. **11**, 83 (1940).
H. Schäfer und W. Walcher, Z. Phys. **121**, 679 (1943).
R. H. Sloane und C. S. Watt, Proc. phys. Soc. (London) **61**, 217 (1948).
F. E. Dart, Phys. Rev. **78**, 761 (1950).
C. H. Bachmann, A. C. Eubank und G. L. Hall, J. appl. Phys. **22**, 1208 (1951).

Diese Aufzählung erhebt keinen Anspruch auf Vollständigkeit.

FARADAY EFFECT IN MAGNETIC MATERIALS WITH TRAVELLING AND STANDING WAVES

by H. G. BELJERS 621.392.26:538.6

Summary

The ferromagnetic Faraday effect in a circular wave guide is described and the approximate theory for the angle of rotation of the plane of polarization is recapitulated. A few experiments are described for Ferroxcube and Ferroxdure samples and the experimental results are compared with the theoretical ones. Finally an experiment with a ferrite specimen in a resonance cavity is reported, demonstrating the positively and negatively rotating components of the mode of oscillation.

Résumé

L'on donne la description de l'effet ferromagnétique de Faraday dans un guide d'ondes circulaire et l'on récapitule dans ses grandes lignes la théorie sur l'angle de rotation du plan de polarisation. L'on décrit quelques expériences portant sur des échantillons de Ferroxcube et de Ferroxdure, et l'on compare les résultats expérimentaux à ceux tirés de la théorie. Enfin, l'on relate une expérience effectuée avec un specimen de ferrite dans une cavité résonante, en démonstrant les composantes à rotation positive et négative du mode d'oscillation.

Zusammenfassung

Der Artikel gibt eine Beschreibung des ferromagnetischen Faraday-Effektes in einem runden Hohlleiter und eine zusammenfassende Darstellung der Näherungstheorie für den Rotationswinkel der Polarisationsebene. Es werden einige Experimente mit Ferroxcube- und Ferroxdure-Proben beschrieben und die experimentellen Ergebnisse mit den theoretischen verglichen. Schließlich wird über ein Experiment mit einem Ferritmuster in einem Hollraumresonator berichtet, wobei die positiven und negativen Rotationskomponenten der Schwingungsweise aufgezeigt werden.

1. Introduction

The ferromagnetic Faraday effect is the phenomenon of rotation of the plane of polarization of a linearly polarized electromagnetic guided wave in a ferromagnetic insulating material, caused by a magnetic field in the direction of propagation.

Various experiments have been described by Hogan [1]) and others, especially in circular wave guides propagating a TE_{11}-mode in the 3-cm region. A cylindrical specimen of ferrite material inserted coaxially in the wave guide gives rise to a rotation of the plane of polarization. For relatively small magnetostatic fields, the rotation is in the positive sense, with regard to the direction of propagation (that is, the direction of the applied magnetic field).

We shall briefly recapitulate the approximate calculation of the angle of rotation as was given by Hogan. Owing to the internal magnetic field H_z, electron-spin precessions are possible producing components of the magnetization m_x and m_y. It has been shown by Polder [3]) that the permeability can be written as a certain tensor. If h is the microwave magnetic field (time dependence exp $(j\omega t)$) and b is the flux density, one can write, when terms of higher order are neglected,

$$\left.\begin{aligned} b_x &= \mu h_x - jKh_y, \\ b_y &= jKh_x + \mu h_y, \\ b_z &= \mu_z h_z. \end{aligned}\right\} \tag{1}$$

If precession damping and anisotropy effects in the material are neglected, we further have

$$\mu/\mu_0 = 1 + \chi = 1 + \frac{M_z\gamma^2 H_z}{\gamma^2 H_z^2 - \omega^2} \text{ and } K/\mu_0 = \frac{M_z\gamma\omega}{\gamma^2 H_z^2 - \omega^2}, \tag{2}$$

where χ is the susceptibility and γ the gyromagnetic ratio *).

It should be borne in mind that the value of γ is negative, since the magnetic and the impuls moments of the electron are oppositely directed.

The non-reciprocal character of the permeability, i.e. $\mu_{xy} \neq \mu_{yx}$, is conspicuous and is apparently caused by the angular momentum of the spins giving rise to a preferred sense of rotation.

Propagation of a plane wave in the z-direction can be successfully described by decomposing the wave into positive and negative circularly polarized components:

positive component: $h_x = he^{j\omega t}$, $h_y = -jhe^{j\omega t}$,
negative component: $h_x = he^{j\omega t}$, $h_y = jhe^{j\omega t}$.

Substitution in (1) results in the permeabilities:

$$\mu_\pm = \frac{\mu h \pm jK \,.\, jh}{h} = \mu \mp K, \tag{3}$$

and after substitution of (2) one obtains

$$\mu_\pm = \mu_0 \left(1 + \frac{\gamma M_z}{\gamma H_z \pm \omega}\right). \tag{4}$$

From this equation it is obvious that resonance is possible for the positive component only. This resonance occurs if the internal field reaches the value

$$H_z = -\omega/\gamma = \omega/|\gamma|.$$

*) In this paper rationalized Giorgi units are used except for the units gauss and oersted.

This relation can also be deduced immediately from the equation of motion: $\dot{\mathbf{M}} = \gamma(\mathbf{M} \times \mathbf{H})$.

If $he^{\pm j\omega t}$ are the two rotating magnetic fields and a is the small angle between the vector $\mathbf{H}$ and the rotating $\mathbf{M}$ one gets:

$$\pm (\omega/\gamma)\ M \sin a = -MH \sin a + Mh,$$

and thus $\chi_{\pm} = (M/h) \sin a = M/(H \pm \omega/\gamma)$.

In this case the propagation in the wave guide can be approximated to a plane wave, because the rather large value of the permittivity ε (12 to 16) results in a considerably decreased cut-off frequency. The rotation per unit length of the positive and negative rotating waves is $2\pi/\lambda_{\pm} = \omega/v_{\pm}$, where v is the velocity of propagation in the medium.

There is a resulting rotation of the plane of polarization which, per unit length, equals $\Theta = \frac{1}{2}\omega(1/v_- - 1/v_+) = (\omega/2c)\ \sqrt{\varepsilon}\ (\sqrt{\mu_-} - \sqrt{\mu_+})$. After substitution of (2) one finds that

$$\Theta = \frac{\omega\sqrt{\varepsilon}}{2c}\left\{\sqrt{1 + \frac{\gamma M}{\gamma H_z - \omega}} - \sqrt{1 + \frac{\gamma M}{\gamma H_z + \omega}}\right\}. \qquad (5)$$

If $|\gamma|H_z \ll \omega$ and $\gamma M \ll \omega$ eq. (5) reduces to the simple relation

$$\Theta = \frac{\sqrt{\varepsilon}}{2c}\,|\gamma| M_z,$$

predicting a rotation proportional to the magnetization of the material and independent of the frequency.

2. Faraday effect in ferrites

The Faraday effect of a few ferrites has been measured using a measuring equipment described in general lines by Hogan [2]).

According to Gamo [4]) the Faraday rotation in a circular wave guide is smaller than the free-space rotation, and new modes of propagation are moreover excited in the medium, e.g., a quasi-TM-mode. The latter can give rise to beats with the original mode causing periodic disturbances in the angle of rotation and in the ratio of the maximum and minimum amplitudes (ellipticity). This is illustrated in fig. 1 where the Faraday rotation in a sample of Ferroxcube IVB of 1 cm length is plotted versus the applied magnetic field.

Only in slices of ferrite thin compared to a half wavelength does one succeed in measuring a regularly progressing rotation and ellipticity, as may be seen in fig. 2, giving the Faraday rotation in 5 mm Ferroxcube IV B at 9400 Mc/s.

The result of an approximate calculation of Θ is given by the dashed curve. To get a mean value for the internal field we have assumed that the sample can be approximated by a spheroid having demagnetization factors $N_x = N_y = 0{\cdot}14$ and $N_z = 0{\cdot}72$. If we apply the relations

$$H_z = H_e + (N_x - N_z)\, M/\mu_0, \tag{6}$$

and

$$M = \mu_{\text{eff}}\, H_e = (\mu_0/N_z) H_e, \tag{7}$$

where H_z and H_e are the internal and external magnetic fields respectively, Θ can be calculated by substitution of H_z and M in (5). The result is given

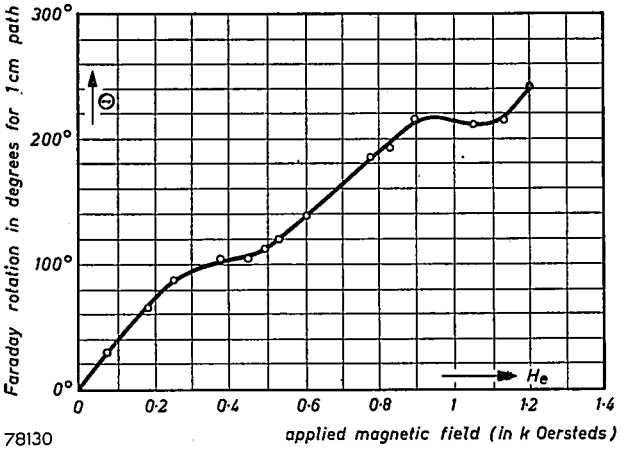

Fig. 1. Faraday rotation versus external magnetic field in a column of 1 cm Ferroxcube IV B, in a circular wave guide, measured at 24000 Mc/s.

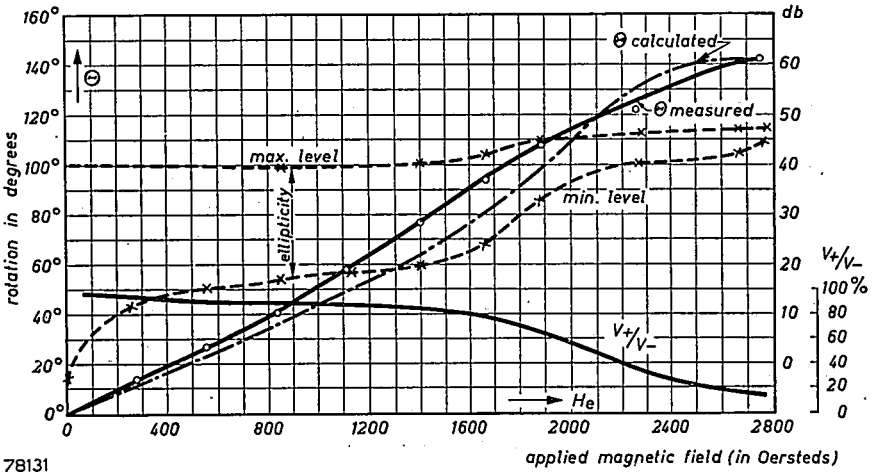

Fig. 2. Faraday rotation versus external magnetic field in 5 mm Ferroxcube IV D, in a circular wave guide, measured at 9400 Mc/s.

in fig. 2 by the dashed curve. Above 2000 Oe the value of μ_+ turns out to be negative. Formally this means that propagation is impossible and the contribution to rotation due to the μ_+ term has been omitted. Actually this situation is reached much more gradually an account of the losses in the material. This is also evident from the course of V_+/V_- (ratio of the amplitudes of positive and negative components) having a value of 0·27 at 2400 Oe, concluded from the measurements on the ellipticity of the wave.

Notwithstanding many approximations there is in general agreement between the calculated and experimental values of Θ.

3. Faraday rotation in Ferroxdure

Faraday rotation has been measured in a ceramic permanent magnetic material with high remanence caused by oriented crystals having essentially the composition $BaO \cdot 6\ Fe_2O_3$, called Ferroxdure [5]). Rotations are slightly influenced by external magnetic fields, as is shown in figs 3 and 4.

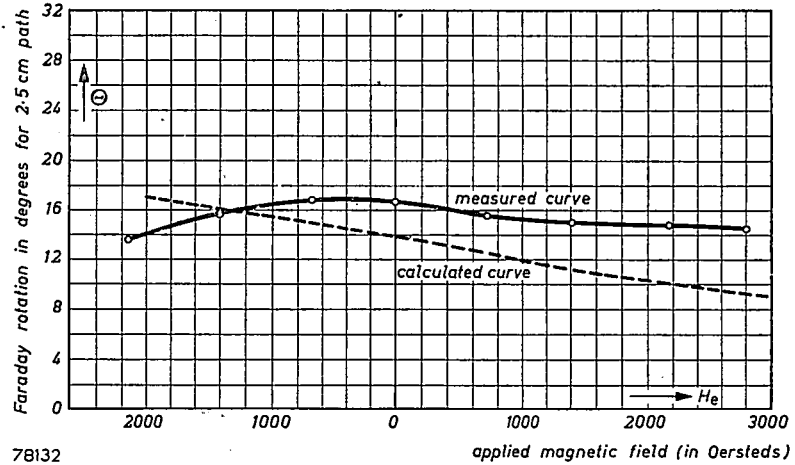

Fig. 3. Faraday rotation versus applied magnetic field at 9400 Mc/s in 2·5 cm Ferroxdure in a circular wave guide (dashed line: calculated by eq. 5).

In fig. 3 the measured rotations in a column of 2·5 cm Ferroxdure at 9400 Mc/s are plotted versus an external field directed equally and one oppositely to the magnetization. In fig. 4 we have a similar rotation at 24000 Mc/s in 5·5 mm of a pseudo-unicrystalline Ferroxdure.

The same eq. (5) is able to describe generally the measured effect, if for H_z the anisotropy field is substituted, this being about 16000 Oe at room temperature [5]). The value of the remanent magnetization was about 2000 gausses and for the pseudo-unicrystalline material about 3800 gausses.

From unpublished measurements is obtained a value of $\varepsilon = 16$ and a g-factor of 2·19 ± 3%, giving rise to a gyromagnetic ratio

$$|\gamma| = g \cdot \frac{e}{2mc} \cdot 10^4 = 2\pi \times 3{\cdot}07 \text{ Mc/s Oe}.$$

Addition (or subtraction) of the external magnetic field to the anisotropy field and applying eq. (5) yields calculated values of the Faraday rotation which are plotted in figs 3 and 4. The computed decrease of the angle in an external field is always greater than the experimentally found decrease, which may be caused by the increasing value of the magnetization, being held constant in the calculation. With an oppositely directed field there is a sudden breakdown of the magnetization, especially for the pseudo-unicrystalline sample which has a low coercive force.

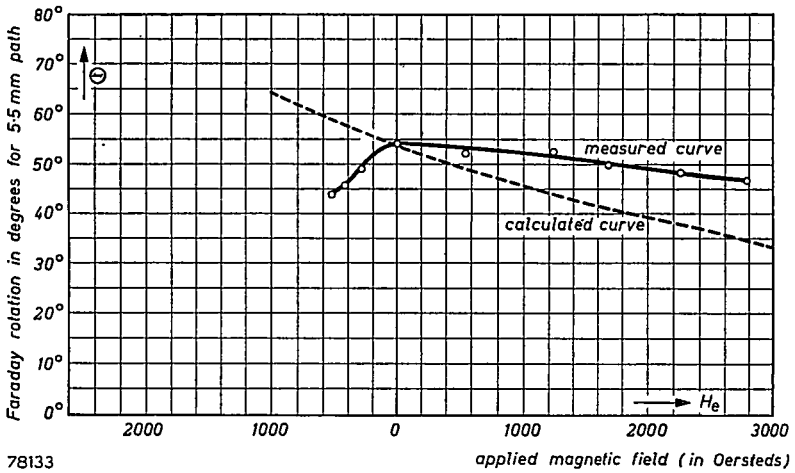

Fig. 4. Faraday rotation versus applied magnetic field at 24000 Mc/s for 5·5 mm of a pseudo-unicrystalline Ferroxdure (preferred axis coinciding with the axis of propagation).

Application of eq. (5) for these materials gives negative values of the angle of rotation, that is, the Faraday rotation in the Ferroxdure is opposite to that in ferrites.

The reason is that in a ferrite the applied frequency is usually higher than the resonance frequency corresponding to a moderate magnetic field, whereas in Ferroxdure the resonance frequency is higher, viz. 45000 Mc/s according to the anisotropy field.

Transmission losses in Ferroxdure are rather low at the applied frequencies. Reflection losses are substantially eliminated if we apply slices

of glass with permittivity 4, acting as $\lambda/4$ transformers. The total insertion loss in the Ferroxdure sample from fig. 4 amounted to about 0·5 dB. As the linear polarization of the wave is fairly well preversed at the end of the Faraday rotator (ellipticity $\approx$ 20 dB) this material seems to be suitable for the composition of a uni-directional transmission system [6]).

4. Faraday effect in a resonance cavity

In the case of a standing wave, e.g. in a resonance cavity, the Faraday effect results in a splitting up of the resonance frequency, as will be shown in this section.

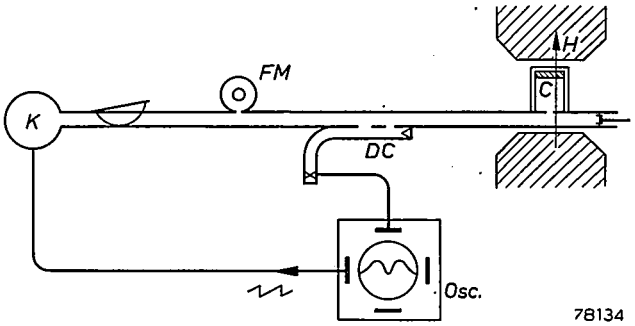

Fig. 5. Experimental set-up for a resonating cavity loaded with a ferrite slice at 24000 Mc/s. The Faraday effect is demonstrated by a splitting up of the resonance curve in a magnetic field.

We used a cylindrical cavity C (mode TE_{111}) coupled to a wave guide by a hole (see fig. 5). A reflecting piston near the hole can be adjusted so as to match the cavity to the guide at the resonance frequency, about 24000 Mc/s. At the bottom of the cavity a circular slice of Ferroxcube IV B was placed. To limit the change in resonance frequency the thickness was reduced to 0·195 mm. A similar experiment with rods of Ferroxcube has been described by Van Trier [7]).

The measuring technique for exploring the resonances is outlined in fig. 5. A frequency-modulated klystron (K) provided the microwave energy. The reflected signal from the cacity is fed to a crystal detector by means of a directional coupler (DC). The rectified voltage is displaying the mode of oscillation of the klystron on a cathode-ray oscilloscope, the time base being the same as the modulation voltage. Resonances are observed as dips in the mode and small dips of a frequency meter can be brought to coincidence in order to measure the resonance frequency.

If a magnetic field H is applied in the axial direction of the cylinder one observes initially a broadening of the resonance curve, then a splitting

up, and finally a separation into two resonance curves. Figure 6 shows the graph of the resonance frequencies at various values of the magnetic field. Apparently the positive and negative components of the oscillation are split up, in view of the different permeabilities given by eq. (4). The positive component evidently shows resonance at a definite value of the magnetic field accompanied by high losses and large detuning, making measurements near resonance impossible. Surprisingly the losses in the negative component were also high in this region. Probably this fact may be attributed to mode conversion, giving rise to heavily damped modes.

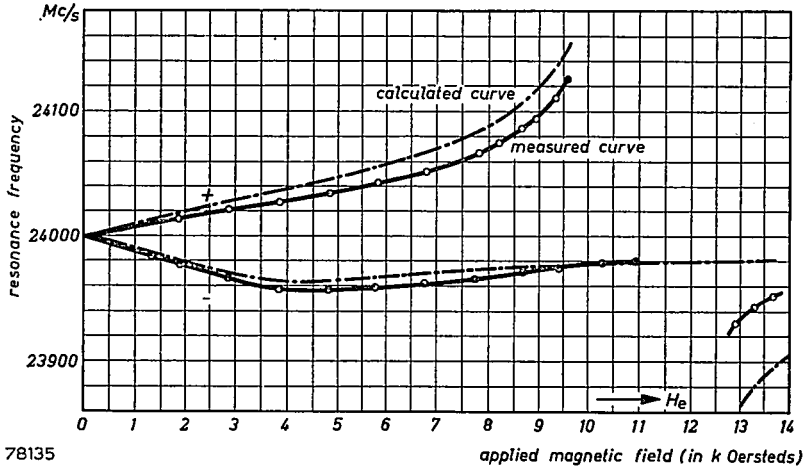

Fig. 6. Resonance frequencies of a ferrite-loaded TE_{111} cavity exposed to an axial magnetic field.

The measured curves can be described generally by the theory developed if two regions are distinguished: the unsaturated region ($H<4000$ Oe) and the saturated region ($H>4000$ Oe).

Whereas in the latter region eq. (6) is valid, the internal field within the specimen in the former can be neglected and the susceptibility is given by

$$\chi_{\pm} = \mp |\gamma| M/\omega . \tag{8}$$

A relation is needed between the detuning Δf and χ which can be derived from the boundary conditions imposed on the field equations in the cavity.

From the two equations of continuity of the tangential E and normal B components we get

$$(\beta_\varepsilon/\beta_1) \tan \{\beta_1 (L-d)\} = \mu_1 \tan (\beta_\varepsilon d) , \tag{9}$$

β_1 and β_ε being the wavelength constants in the circular guide in air and

in the ferrite respectively, while L is the height of the empty cavity and d is the thickness of the specimen.

From wave-guide theory [2]) it follows that $\beta_\varepsilon = \beta_0 \sqrt{\varepsilon\mu_1 - (\lambda/\lambda_c)^2}$ where $\beta_0 = \pi/L$ and λ_c is the cut-off wavelength. If we denote $\beta_1 - \beta_0 = \delta\beta = -\beta\,(2L/\lambda)^2\,\delta\lambda/\lambda$ and when the tangents are approximated according to $\tan x = x + (1/3)x^3$ one finds

$$\frac{\delta\lambda}{\lambda} = \chi\,\frac{d}{L}\left(\frac{\lambda}{2L}\right)^2 + \frac{\pi^2}{24}\,\frac{d^3\lambda^2}{L^5}\,(\mu_1{}^2\varepsilon - 1)\,. \tag{10}$$

For small changes in frequency caused by the magnetic field there is to the first approximation a proportionality between δf and χ viz.

$$\frac{\delta f}{f} = \chi_\pm\left(\frac{d\lambda^2}{4L^2} + \frac{\pi^2}{12}\,\frac{d^3\lambda^2\varepsilon}{L^5}\right). \tag{11}$$

After substitution of the following data: $L = 12{\cdot}5$ mm; $f = 24000$ Mc/s; $\varepsilon = 15$; $N_z = 0{\cdot}96$ and $N_x = N_y = 0{\cdot}02$ one finds $\delta f = 98{\cdot}5\,\chi$ Mc/s.

Applying equations (6), (8), and (11) one gets a good qualitative picture of the measured curves. There are two linear diverging curves in the unsaturated range, joining the curves in the saturated region, one of which shows a resonance.

Quantitatively there is a descrepancy between the measured value of M/μ_0, viz. 3900 Oe, and the value joining as well as possible the resonance curve which appears to be about 2560 Oe. Calculated curves using this value of M/μ_0 have been plotted in the figure, giving in general a satisfactory picture.

I wish to thank Mr L. van der Kint for his assistance during the measurements. I am also indebted to Ir A. A. T. M. van Trier for his remarks on the paper.

Eindhoven, September 1953

REFERENCES

1) C. L. Hogan, Rev. mod. Phys. **25**, 253-263, 1953.
2) H. R. L. Lamont, Wave Guides, Methuen & Co Ltd., London, 1946.
3) D. Polder, Phil. Mag. **40**, 99-115, 1949.
4) H. Gamo, J. phys. Soc. Japan **8**, 176-182, 1953.
5) G. W. Rathenau, J. Smit and A. L. Stuyts, Z. Phys. **133**, 250-260, 1952.
6) A. A. T. M. van Trier, T. ned. Radiogenootsch. **18**, 211-229, 1953.
7) A. A. T. M. van Trier, Appl. sci. Res. **B3**, 142, 1953.

INVESTIGATIONS ON PHOTOSYNTHESIS; THE HILL REACTION *)

by J. S. C. WESSELS

541.144.7

Summary

The photochemical reduction of various quinones and dyes by isolated chloroplasts is studied by measuring the redox potential during illumination. The experimental details are described in chapter I. In chapter II the possibility of the formation of free radicals in the Hill reaction is discussed. Neither polymerization of acrylonitrile nor formation of phenol in the presence of benzene could be demonstrated. From this it is concluded that free radicals are either not present or only present in very low concentrations in the solution during this reaction. The results of an investigation into the factors which are essential for the ability of a redox compound to undergo photochemical reduction by illuminated chloroplast suspensions are described in chapter III. Whether a redox substance is able to serve as a Hill oxidant appears to be determined mainly by its E_0' **). The maximal reducing power of chloroplasts in vitro is, to a high degree, dependent on the oxygen concentration. In an oxygen atmosphere, final potentials lower than about 230 mV were never attained whereas the lowest final potential observed upon exclusion of oxygen amounted to about 0 mV. Redox systems with a negative E_0' value, the reduction of which requires more energy than corresponds to one light quantum, are hardly reduced at all by chloroplasts. The theoretical and biochemical aspects of these results are discussed, particularly in connection with the fact that recent investigations give the impression that D.P.N. also is able to act as a substrate in the Hill reaction. The primary formation of an intermediate hydrogen donor (XH_2) is considered as probable, on the basis of which the following simplified scheme is proposed for the Hill reaction

$$X + H_2O \overset{h\nu}{\rightleftarrows} XH_2 + \tfrac{1}{2}O_2,$$
$$XH_2 + \text{quinone} \rightleftarrows X + \text{hydroquinone},$$
$$\text{hydroquinone} + \tfrac{1}{2}O_2 \rightarrow \text{quinone} + H_2O.$$

In chapter IV it is pointed out that some characteristic features of the reaction can be interpreted satisfactorily by this scheme. The discrepancies in literature in the field of inhibitors induced an investigation on the influence of these substances upon the Hill reaction by means of the redox potentiometric method. The results of this investigation are described in chapter V. The concentration of various inhibitors which has an inhibitory effect is i.a. dependent on the nature of the redox compound used as a hydrogen acceptor. This is caused by a difference in reoxidation rate of the reduced components and sometimes by the occurrence of a reaction between inhibitor and substrate. o-Phenanthroline, 2,4-dinitrophenol, thymol, phenylurethane and hydroxylamine completely inhibit the Hill reaction at relatively low concentrations ($< 0{\cdot}01$ molar). Sodium fluoride, sodium azide, iodoacetamide and potassium cyanide, on the other hand, inhibit only at higher concentrations. The fact that

*) "Investigations into some aspects of the Hill reaction", Thesis, University of Leyden, January, 1954.

**) For definition of E_0' see first page of chapter I.

the reaction rate is not affected by p-chloromercuribenzoate and p-aminophenyldichlorarsine indicates that free sulphydryl groups are not essential for the activity of the chloroplasts. Some antibiotics and other biochemically important compounds like oxidized glutathione, dehydroascorbic acid, riboflavin, D.P.N., A.T.P., and dihydroxyphenylalanine, have likewise no influence upon the Hill reaction.

Résumé

La réduction photo-chimique de diverses quinones et matières colorantes par des chloroplastes isolés est étudiée par la mesure du potentiel rédox pendant l'illumination. Les détails expérimentaux sont exposés dans le chapitre I. Le chapitre II traite la possibilité de formation de radicaux libres lors de la réaction de Hill. L'addition d'acrylonitrile ou de benzène au mélange de réaction ne permet pas de déceler une polymérisation, respectivement une formation de phénol. On en conclut que dans cette réaction il n'existe pas de radicaux libres, ou s'il en existe, ce n'est que dans une concentration extrèmement faible. Les résultats d'une recherche des facteurs qui déterminent si une substance de rédox peut être réduite ou non par des chloroplastes sont mentionnés au chapitre III. Il s'avère que c'est principalement le E_0' qui détermine si une telle substance convient comme oxydant de Hill. Le pouvoir réducteur maximum de chloroplastes in vitro dépend, en une mesure importante, de la concentration en oxygène. Dans une atmosphère d'oxygène, on n'obtient jamais des potentiels finaux inférieurs à $\approx$ 230 mV, tandis que le plus bas potentiel final relevé lors de l'exclusion d'oxygène est de $\approx$ 0 mV. Les systèmes rédox à valeur E_0' négative, dont la réduction requiert notablement plus d'énergie que celle correspondant à un quantum de lumière, ne sont pratiquement pas réduits par les chloroplastes. Les aspects théoriques et biochimiques de ces résultats sont discutés, spécialement en rapport avec le fait que des recherches récentes laissent l'impression que le D.P.N. peut également agir comme substrat dans la réaction de Hill. La formation primaire d'un donneur d'hydrogène intermédiaire (XH_2) est estimée probable, et sur cette base, pour la réaction de Hill, le schéma simplifié suivant est proposé:

$$X + H_2O \overset{h\nu}{\rightleftarrows} XH_2 + \tfrac{1}{2}O_2\,,$$
$$XH_2 + \text{quinone} \rightleftarrows X + \text{hydroquinone}\,,$$
$$\text{hydroquinone} + \tfrac{1}{2}O_2 \rightarrow \text{quinone} + H_2O\,.$$

Le chapitre IV mentionne que les traits charactéristiques de la réaction peuvent être interprétés d'une façon satisfaisante à l'aide de ce schéma. L'absence de concordance dans les publications relatives aux inhibiteurs a incité à étudier ces substances, par voie de détermination de potentiel rédox, en ce qui concerne leur influence sur la réaction de Hill. Les résultats de cette étude sont mentionnés au chapitre V. La concentration active de divers inhibiteurs est déterminée entre autres par la nature de la substance rédox utilisée comme accepteur d'hydrogène. La cause de ce fait doit être cherchée dans une différence en vitesse de réoxydation des composants réduits et parfois dans l'existence d'une réaction entre l'inhibiteur et le substrat. l'O-phénanthroline, le 2,4-dinitrophénol, le thymol, le phényluréthane et l'hydroxylamine freinent complètement la réaction de Hill en concentration relativement faible ($<$ 0,01 molaire). Le fluorure de sodium, l'azide de sodium, l'iodoacétamide et le cyanure de potassium, par contre, ne freinent qu'aux fortes concentrations. Le fait que la vitesse de réaction n'est pas influencée par le benzoate p-chloromercurique et par le p-aminophényldichloroarsine prouve que les groupes SH libres ne sont pas essentiels pour l'activité des chloroplastes. Quelques antibiotiques et autres substances biochimiques importantes telles que le glutathion oxydé, l'acide déhydroascorbique,

la riboflavine, le D.P.N., l'A.T.P. et le dihydroxyphénylalanine n'exercent pas non plus d'influence sur la réaction de Hill.

Zusammenfassung

Die photochemische Reduktion verschiedener Chinone und Farbstoffe durch isolierte Chloroplaste wird durch Messung des Redoxpotentials während der Belichtung untersucht. Die experimentellen Einzelheiten der Meßmethode werden in Kapitel I beschrieben. In Kapitel II wird die Möglichkeit einer Bildung von freien Radikalen bei der Hill-Reaktion diskutiert. Wurde dem Reaktionsgemisch Acrylonitril oder Benzol zugesetzt, so war keine Polymerisation bzw. Phenolbildung nachweisbar. Hieraus wird der Schluß gezogen, daß bei dieser Reaktion freie Radikale nicht oder nur in äußerst geringer Konzentration in der Lösung vorhanden sind. Die Ergebnisse einer Untersuchung nach den Faktoren, welche bestimmend dafür sind, ob ein Redoxstoff durch Chloroplaste reduziert werden kann oder nicht, werden in Kapitel III mitgeteilt. Es zeigt sich, daß vor allem das E_0' bestimmt, ob der betreffende Stoff sich dazu eignet, als Hill-Oxydant zu fungieren. Die maximale reduzierende Kraft von Chloroplasten in vitro ist in beträchtlichem Maße von der Sauerstoffkonzentration abhängig. In Sauerstoffatmosphäre werden niemals niedrigere Endpotentiale als ca. 230 mV erreicht, wogegen bei Ausschließung von Sauerstoff das niedrigste beobachtete Endpotential ca. 0 mV beträgt. Redoxsysteme mit einem negativen E_0'-Wert, deren Reduktion erheblich mehr Energie erfordert, als einem Lichtquant entspricht, werden praktisch nicht durch Chloroplaste reduziert. Die theoretische und biochemische Bedeutung dieser Resultate wird eingehend besprochen, speziell im Zusammenhang mit der Tatsache, daß in jüngster Zeit durchgeführte Untersuchungen den Eindruck hinterlassen, daß auch D.P.N. als Substrat bei der Hill-Reaktion dienen kann. Die primäre Bildung eines intermediären Wasserstoffdonors (XH_2) wird als wahrscheinlich erachtet und auf Grund davon folgendes vereinfachtes Schema für die Hill-Reaktion vorgeschlagen:

$$X + H_2O \overset{h\nu}{\rightleftarrows} XH_2 + \tfrac{1}{2}O_2\,,$$
$$XH_2 + \text{Chinon} \rightleftarrows X + \text{Hydrochinon}\,,$$
$$\text{Hydrochinon} + \tfrac{1}{2}O_2 \longrightarrow \text{Chinon} + H_2O\,.$$

In Kapitel IV wird auseinandergesetzt, daß die Kinetik der Reaktion mit Hilfe dieses Schemas in befriedigender Weise interpretiert werden kann. Die mangelnde Einheitlichkeit der Auffassungen in der Literatur auf dem Gebiet der Inhibitoren bildete den Anlaß, diese Stoffe auf redoxpotentiometrischem Weg hinsichtlich ihres Einflusses auf die Hill-Reaktion zu untersuchen. Die Ergebnisse dieser Untersuchung werden in Kapitel V beschrieben. Die Konzentration verschiedener Inhibitoren, welche eine hemmende Wirkung ausübt, ist u.a. abhängig von der Art der Redoxverbindung, die als Wasserstoffempfänger verwendet wird. Dies ist auf Unterschiede in der Reoxydationsgeschwindigkeit der reduzierten Komponenten zurückzuführen, und manchmal auf das Auftreten einer Reaktion zwischen Inhibitor und Substrat. o-Phenanthrolin, 2,4-Dinitrophenol, Thymol, Phenyluretan und Hydroxylamin hemmen die Hill-Reaktion vollständig bei relativ niedrigen Konzentrationen ($< 0{,}01$ molar). Natriumfluorid, Natriumazid, Jodacetamid und Kaliumcyanid hemmen dagegen erst bei höheren Konzentrationen. Die Tatsache, daß die Reaktionsgeschwindigkeit nicht durch p-Chlormercuribenzoat und p-Aminophenyldichlorarsin beeinflußt wird, weist darauf hin, daß freie Sulfhydrylgruppen nicht wesentlich für die Aktivität der Chloroplaste sind. Einige Antibiotika und andere biochemisch wichtige Verbindungen, wie oxydiertes Glutathion, Dehydroascorbinsäure, Riboflavin, D.P.N., A.T.P. und Dihydroxyphenylalanin haben gleichfalls keinen Einfluß auf die Hill-Reaktion.

INTRODUCTION

The term "photosynthesis" is usually applied to the process by which green plants are, under the influence of light, able to synthesize organic compounds from CO_2 and water. This could be said to be the most fundamental reaction of life on earth. Although all living organisms have the capacity of synthesizing complicated organic molecules, they are almost entirely dependent upon starting material which originated from photosynthesis.

The overall result of the process of photosynthesis may be represented by the equation

$$6\ CO_2 + 6\ H_2O \rightarrow C_6H_{12}O_6 + 6\ O_2.$$

It involves an increase in free energy by about 120 kcal per mole of reduced CO_2. The annual accumulation of energy by photosynthesis amounts to 3.10^{18} kcal, which corresponds to the fixation of 3.10^{11} tons of carbon in organic compounds. To illustrate more clearly what a yield of 3.10^{11} tons per year means, we may compare it with the yearly world production of the chemical, metallurgical and mining industries, which is of the order of 10^9 tons [1]).

It is now generally agreed that the specific photochemical process of photosynthesis may be described as a decomposition of water under the influence of light absorbed by chlorophyll. This photolysis of water involves the production of reducing compounds, which accomplish — directly or indirectly — the reductive transformation of carbon dioxide to carbohydrates in a series of dark reactions. This idea is supported by many experimental data; we mention, for instance, the character of the CO_2 uptake in the dark after illumination of algae [2]), the fact that chemoautotrophic bacteria are able to convert CO_2 into organic material without light energy [3]) (in this process the required energy is furnished by oxidation of inorganic substrates), fluorescence and redox potential measurements [4]),[5]),[6]), and the experiments with isolated chloroplasts [7]).

The photochemical process of photosynthesis takes place in the chloroplasts, the green granules in the cells containing chlorophyll. Chlorophyll is not evenly distributed in the chloroplasts; it is located in very small granular particles, called grana. Upon exposure to light chloroplasts are, in the presence of ferric oxalate, able to produce O_2 under simultaneous reduction of ferric oxalate to ferrous oxalate ("Hill reaction"). This phenomenon may be interpreted as a photolysis of water, ferric oxalate taking the place of CO_2 as hydrogen acceptor. The increase in free energy (ΔF) of the reaction

$$2\ Fe^{3+} + H_2O \rightarrow 2\ Fe^{2+} + 2\ H^+ + \tfrac{1}{2}\ O_2$$

amounts to 32 kcal so that actually light energy is converted into chemical energy.

Also in connection with the fact that several known carboxylases are located in the cytoplasm [8]), it is now generally accepted that the reductive incorporation of CO_2 takes place in the cytoplasm (see also [9])). As the photolytical splitting of water, however, takes place in the chloroplast, one may conclude that a photochemically formed reducing agent diffuses into the cytoplasm. The question of whether the primary photochemical process produces a relatively stable and highly reducing intermediate is, however, one of the most disputed problems in the field of photosynthesis.

Although the process of CO_2 reduction (the path of carbon) is not yet elucidated, we have, largely through the work of Calvin and his coworkers [10]),[11]),[12]),[13]),[14]), obtained a much better insight into this matter. In these experiments green algae are allowed to fix $C^{14}O_2$ in the light for short periods, after which the cells are killed and extracted with alcohol. The extract is analysed by paper chromatography for C^{14}-labelled compounds.

After a short exposure to $C^{14}O_2$ in the light radioactivity is found in alanine, serine, phosphoglyceric acid, hexose phosphate, etc., i.e. in intermediates of hexose and amino acid synthesis in general. After a long exposure lipoids, carbohydrates and proteins also appear to contain C^{14}. A very short exposure to C^{14}-labelled carbon dioxide (a few seconds) results in only phosphoglyceric acid, phosphopyruvic acid, and malic acid becoming active.

Phosphoglyceric acid, the first active product, has to be considered as the primary stable photochemical intermediate. This conclusion was arrived at only after a thorough experimental research and a highly critical discussion of the results. So, of course, the fact has to be taken into account that the occurrence of a C^{14}-containing compound in the light and not in the dark indicates this compound to be a product, though not necessarily an intermediate of photosynthesis.

The identity of a number of phosphate esters with those involved in glycolysis suggests that the synthesis of the hexoses is accomplished through a reversal of glycolysis. A support of this hypothesis is found in the identity of the distribution of C^{14} in the C_3, C_4, the C_2, C_5 and the C_1, C_6 of hexose with that in the carboxyl, α and β carbon atoms, respectively of phosphoglyceric acid.

In the dark only a very small $C^{14}O_2$ uptake takes place while in this case the active products are malic acid, fumaric acid, succinic acid, alanine, aspartic acid and glutamic acid. This is probably due to reversibility of the well-known decarboxylation reactions of the respiration. On the other hand, when $C^{14}O_2$ is supplied to algae in the dark immediately after a period of illumination in the absence of carbon dioxide, the same products are found

as in short exposures in the light. Calvin, therefore, concludes that in the dark after pre-illumination a photochemically produced, nonspecific reducing agent survives, which in the dark also is able to reduce CO_2.

The fact that phosphoglyceric acid and alanine appear to contain the largest percentage of C^{14} in the carboxyl groups, suggests that phosphoglyceric acid is formed by carboxylation of a C_2 compound. A similar reasoning holds for malic acid and aspartic acid, so that — also in connection with the observation that phosphopyruvic acid and malic acid successively become active after phosphoglyceric acid in an early stage of the process — one may tentatively conclude that phosphoglyceric acid is converted into phosphopyruvic acid, which then is carboxylated as in the Wood-Werkman reaction to give oxalacetic acid, from which malic acid may be formed by reduction.

According to Calvin the CO_2 reduction process thus includes two carboxylations. First, an addition of CO_2 to an unknown C_2 compound, by which phosphoglyceric acid is formed; secondly, the carboxylation of a C_3 compound, probably phosphopyruvic acid, to oxalacetic acid. The question remains which one is the C_2 compound and how this compound is formed in the plant. In connection with the fact that oxalic acid, formaldehyde and formic acid have not been found labelled, and that C^{14} appears only later on in glycolic acid and glycin, Calvin originally thought the splitting of a C_4 dicarboxylic acid into two C_2 molecules the most probable.

The hypothesis that during exposure to light a stable reducing intermediate is formed, is disputed by Gaffron who, in contradiction to Calvin, observed that after preliminary illumination only phosphoglyceric acid is formed [15]). Besides, according to the former, an after-effect, i.e. reduction of quinone, should be detectable also for the Hill reaction after pre-illumination, which was not observed however. Gaffron suggests, inter alia, the following scheme for the CO_2 reduction

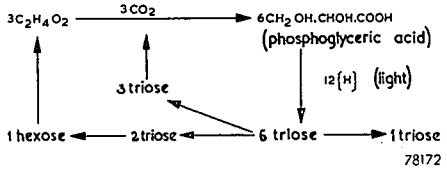

The photochemical step is the reduction of phosphoglyceric acid to triose. Of the six triose molecules formed one is used for the synthesis of cell constituents, three are needed as hydrogen donors for the reductive carboxylation of three acceptor molecules, and two are used to reproduce the three acceptor molecules. This relatively simple scheme thus implies a strict specificity of the photochemical part which here, in contrast with

Calvin's scheme, is coupled only with one reduction step. The hydrogen transferring agent for the dark reduction by triose, however, may be a coenzyme of the diphosphopyridine nucleotide (D.P.N.) type, playing a part also in many other redox reactions.

The C_4 dicarboxylic acids do not, according to Gaffron, participate in the photosynthetic cycle but originate from secondary reactions. That malic acid, at any rate, is no intermediate in photosynthesis has been confirmed by Calvin, because he was able to show that inhibition of the formation of malic acid by malonate does not change the activity of other intermediates [16]). The recent identification of sedoheptulose and ribulose as products of short period photosynthesis [17]) has now brought Calvin to the following scheme

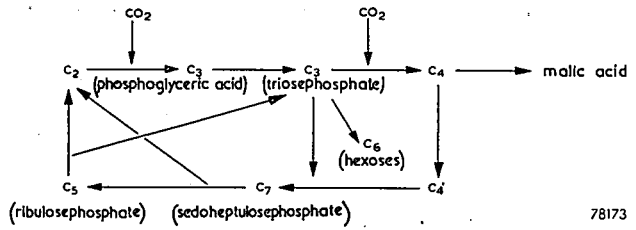

Investigators of the Berkeley and Chicago groups, however, agree that the first stable product of the CO_2 fixation in photosynthesis is phosphoglyceric acid, which is formed by carboxylation of a C_2 compound. The origin and identity of this C_2 compound and the mechanism of its carboxylation form some of the most important problems which are being submitted to investigation at the present time. In this connection it is important to note that Fager [18]) has obtained a cell-free spinach macerate which appeared to be able to fix CO_2 under phosphoglyceric acid formation.

Extremely interesting are the observations by Vishniac and Ochoa [19]), Arnon [20]) and Tolmach [21]), proving that, exposed to the influence of light, chloroplasts + triphosphopyridine nucleotide + Mn^{2+} ions + "malic enzyme" are able to carboxylate reductively pyruvic acid to malic acid according to the equation

$$H_2O + \text{T.P.N.} \xrightarrow[h\nu]{\text{chloroplasts}} \text{T.P.N. } 2H + \tfrac{1}{2}\,O_2,$$

$$\text{T.P.N. } 2H + \text{pyruvic acid} + CO_2 \xrightarrow[Mn^{2+}]{\text{"malic enzyme"}} \text{malic acid} + \text{T.P.N.},$$

$$H_2O + CO_2 + \text{pyruvic acid} \longrightarrow \text{malic acid} + \tfrac{1}{2}\,O_2.$$

Thus for the first time this is a realization of the photochemical reductive CO_2 fixation outside the living cell, so long looked for. The importance of these investigations can hardly be overestimated although they do not imply that photosynthesis in vivo would proceed in quite the same way.

Vishniac and Ochoa [22]) found that also other enzyme systems like isocitric acid, lactic acid and glutamic acid dehydrogenase, are able to function in a manner analogous to that of the "malic enzyme" system. The carboxylation of the C_2 carbon dioxide acceptor in photosynthesis might take place in a similar way.

Vishniac and Ochoa thus come to the conclusion that, upon exposure to light, chloroplasts are able to reduce T.P.N. (the E_0' of both T.P.N. and D.P.N. is about — 0·30 V at pH 7·0), and that reduced T.P.N. is present in a quantity sufficient to effect the reductive carboxylation of pyruvic acid, which proceeds with an increase in free energy. They have also succeeded in detecting the reduction of D.P.N. by the formation of lactate when pyruvate, D.P.N. and lactic dehydrogenase were incubated with chloroplasts in the light.

As mentioned before, Hill was the first who observed the photochemical reduction of ferric to ferrous salts by a chloroplast suspension [7]). Warburg and Lüttgens [23]) found that p-benzoquinone, too, can be reduced by illuminated chloroplasts, whereas Aronoff [24]) observed that at a high light intensity the rate of O_2 evolution in the Hill reaction decreases in the series benzoquinone, K-naphthoquinone-sulfonate, K-anthraquinone-sulfonate. Holt and French [25]) obtained good results also with some indophenols such as phenol-indophenol ($E_0' = 0{\cdot}254$ V at $pH = 6{\cdot}6$), 2,6-dichlorophenol-indophenol ($E_0' = 0{\cdot}247$ V), and o-cresol-indophenol ($E_0' = 0{\cdot}217$ V). With thionine ($E_0' = 0{\cdot}074$ V) the results were doubtful, whereas 1-naphthol-2-sulfonate-indophenol ($E_0' = 0{\cdot}147$ V), methylene blue ($E_0' = 0{\cdot}024$ V) and indigodisulfonate ($E_0' = -0{\cdot}104$ V) showed no reduction. From these experiments the impression is obtained that a simple relation between the redox potential of a compound and its photochemical reduction by chloroplasts does not exist.

Besides manometry the following methods were used for the study of the Hill reaction: photometry (especially with dyes; Holt, Smith and French [26])), measurement of the pH (Holt and French [27]), Clendenning and Gorham [28])), and redox potentiometry (Spikes, Lumry, Eyring and Wayrynen [29]), Van der Veen [30])).

Mehler [31]) showed that O_2 also can act as hydrogen acceptor in the Hill reaction, being itself reduced to H_2O_2. This may indicate that photoautoxidations in vivo take place under the influence of O_2, which then takes the place of CO_2 as hydrogen acceptor in photosynthesis. Of the biological redox compounds cytochrome *c* appeared to be reduced by

chloroplasts, but this was not the case with D.P.N. [31]). As mentioned before, Vishniac and Ochoa, Arnon and Tolmach, on the other hand, observed reduction of D.P.N. and T.P.N. by coupling with appropriate enzyme systems. Quick reoxidation of the formed D.P.N.2H might be the reason why no reduction could be demonstrated in systems containing only chloroplast material and D.P.N.

In connection with the foregoing it seemed very important to investigate which factors are essential for the ability to undergo photochemical reduction by chloroplasts. For this reason a number of quinones and dyes was examined by the redox potentiometric method, and special attention was paid to the redox potential as a possible decisive factor [32a]). Also, the influence of some biochemically important compounds like D.P.N., A.T.P., dehydroascorbic acid, riboflavin, etc., upon the Hill reaction was investigated. Mixtures of two quinones or dyes, too, were submitted to an investigation; besides, the kinetics of the Hill reaction were studied more closely [32b]).

That the Hill reaction has, indeed, to be considered as the part of photosynthesis containing the photochemical reaction in which the natural H-acceptor is replaced by e.g. quinone, becomes clear from the fact that the evolved oxygen actually originates from the water. Holt and French [33]) were able to demonstrate this by means of O^{18}. Clendenning and Ehrmantraut [34]) found that the kinetic characteristics of the Hill reaction closely resemble those of photosynthesis. Hill reaction and photosynthesis contain, therefore, the same primary photochemical process.

A further confirmation of this view is found in the fact that several inhibitors of photosynthesis inhibit the Hill reaction as well, although the literature enumerates some contradictory results. Hill and Scarisbrick [35]) and Macdowall [38]) observed that the Hill reaction is not inhibited by cyanide, which indicates that in photosynthesis cyanide is a specific poison to the carboxylation process and does not affect the primary photochemical process. Inhibition of the Hill reaction by azide and hydroxylamine is reported by Arnon and Whatley [37]) and Macdowall [38]), but not by Hill [35]) and Aronoff [24]). Clendenning and Gorham [28]) found that sodium azide and hydroxylamine inhibit the photochemical reduction of ferricyanide-ferric oxalate and quinone to various degrees. The Hill reaction is inhibited very strongly by o-phenanthroline [23]),[24]),[37]),[38]), Cu^{2+} and Hg^{2+} ions [38]), and 2,4-dinitrophenol [38]), less by narcotica like phenylurethane [24]),[36]),[38]).

The difference of opinion on the active concentrations of various inhibitors and in some cases even on the question of whether a compound is an inhibitor or not, induced us to investigate these problems again by means of redox potential measurements. The effect of some other known enzyme poisons was also submitted to investigation.

Efforts to separate reversibly some essential organic compound from the chloroplast system, i.e. to restore the activity by mixing two individually inactive fractions, were fruitless. However, a very fine disintegration of chloroplast material could be effected whilst retaining activity [39),40),41),42)], although 90% of the material still had a particle weight of 6-7 millions and the activity was less than that of intact chloroplasts.

Concentration of the active material by salt precipitation, lowering of the *pH*, etc., was quite unsuccessful. This suggests that the activity is due to the co-operating of several components in such a way that purification of any one of these components automatically brings about a decrease of activity owing to the loss of other factors needed for the reaction.

Isolated chloroplasts may be considered, in a sense, as intermediate between the living cell and chlorophyll preparations. This material resembles the cell in its capacity to sensitize oxidation-reduction reactions in which light energy is converted into chemical energy, and to use H_2O as hydrogen donor in these reactions. Chlorophyll has lost the latter property but is still able to sensitize oxidation-reduction reactions. This can be a "physical" sensitization, in which the photocatalyst has the function of transferring energy only, or a "chemical" sensitization, in which the catalyst undergoes a reversible oxidation-reduction.

A reversible photoreduction of chlorophyll was observed by Krasnovsky [43),44),45),46)]. When exposed to light in pyridine solution, ascorbic acid, cystein, phenylhydrazine and H_2S all give reduced chlorophyll with an absorption maximum at 525 mμ. In the dark reoxidation of the chlorophyll takes place. He also found that chlorophyll, upon illumination, is able to transfer hydrogen from ascorbic acid to D.P.N. or riboflavin, which involves a considerable increase in free energy of the system. Here also reduced chlorophyll with an absorption maximum at 525 mμ acts as an active intermediate. It is reported [47),48)], that chlorophyll can also be oxidized reversibly and that this reaction is affected by light.

The great difference with the Hill reaction, however, is the fact that chlorophyll in contrast to chloroplasts is no longer able to use H_2O as H-donor for photochemical reductions. The way in which H_2O is split in photosynthesis still constitutes an unsolved problem. It seemed possible, in connection also with the investigations of Evans and Uri [49),50)] and Weiss [51)] on the photolysis of water by metal ions, that free radicals might function as intermediates in the Hill reaction. We have therefore investigated whether (OH) radicals could be demonstrated in systems in which the Hill reaction was actively proceeding.

In the following chapters we will deal successively with:

Chapter I : Methods and materials used for redox potential measurements.

„ II : Investigation into the occurrence of radicals as intermediates in the Hill reaction.

„ III: Relation between redox potential and photochemical reduction by chloroplasts.

„ IV : Kinetics of the Hill reaction.

„ V : Inhibitors and activators.

REFERENCES

1) E. I. Rabinowitch, Photosynthesis and related processes, vol. I; Interscience Publishers, New York, 1945.
2) M. Calvin and A. A. Benson, Science **107**, 476, 1948.
3) C. B. van Niel, Photosynthesis in plants, ed. by J. Franck and W. E. Loomis; Iowa State College press, 1949.
4) E. C. Wassink, Advanc. Enzymol. **XI**, 91, 1951.
5) E. C. Wassink, Leeuwenhoek Ned. Tijdschr. **12**, 281, 1947.
6) E. C. Wassink, Symp. Soc. exp. Biol. **V**, 251, 1952.
7) R. Hill, Nature, Lond. **139**, 881, 1937.
8) E. R. Waygood and K. A. Clendenning, Canad. J. Res. **C 28**, 673, 1950.
9) A. W. Frenkel, Plant Physiol. **16**, 654, 1941.
10) M. Calvin, J. chem. Educ. **26**, 639, 1949.
11) M. Calvin, J. A. Bassham and A. A. Benson, Fed. Proc. **9**, 524, 1950.
12) M. Calvin, J. A. Bassham, A. A. Benson, V. H. Lynch, C. Ouellet, L. Schou, W. Stepka and N. E. Tolbert, Symp. Soc. exp. Biol. **V**, 284, 1951.
13) S. Kawaguchi, A. A. Benson, M. Calvin and P. M. Hayes, J. Amer. chem. Soc. **74**, 4477, 1952.
14) M. Calvin and P. Massini, Experientia **8**, 445, 1952.
15) H. Gaffron, E. W. Fager and J. L. Rosenberg, Symp. Soc. exp. Biol. **V**, 262, 1951.
16) J. A. Bassham, A. A. Benson and M. Calvin, J. biol. Chem. **185**, 781, 1950.
17) A. A. Benson, J. A. Bassham and M. Calvin, J. Amer. chem. Soc. **73**, 2970, 1951.
18) E. W. Fager, Arch. Biochem. Biophys. **37**, 5, 1952.
19) W. Vishniac and S. Ochoa, Nature, Lond. **167**, 768, 1951.
20) D. I. Arnon, Nature, Lond. **167**, 1008, 1951.
21) L. J. Tolmach, Nature, Lond. **167**, 946, 1951.
22) W. Vishniac and S. Ochoa, J. biol. Chem. **195**, 75, 1952.
23) O. Warburg and W. Lüttgens, Naturwissenschaften **32**, 161, 301, 1944.
24) S. Aronoff, Plant Physiol. **21**, 393, 1946.
25) A. S. Holt and C. S. French, Arch. Biochem. **19**, 368, 1948.
26) A. S. Holt, R. F. Smith and C. S. French, Plant Physiol. **26**, 164, 1951.
27) A. S. Holt and C. S. French, Arch. Biochem. **9**, 25, 1946.
28) K. A. Clendenning and P. R. Gorham, Canad. J. Res. **C 28**, 78, 102, 114, 1950.
29) J. D. Spikes, R. Lumry, H. Eyring and R. E. Wayrynen, Arch. Biochem. **28**, 48, 1950.
30) R. van der Veen, unpublished.
31) A. H. Mehler, Arch. Biochem. Biophys. **33**, 65, 1951.
32a) J. S. C. Wessels and E. Havinga, Rec. Trav. chim. Pays-Bas **71**, 809, 1952.
32b) J. S. C. Wessels and E. Havinga, Rec. Trav. chim. Pays-Bas **72**, 1076, 1953.
33) A. S. Holt and C. S. French, Arch. Biochem. **19**, 429, 1948.
34) K. A. Clendenning and H. C. Ehrmantraut, Arch. Biochem. **29**, 387, 1950.
35) R. Hill, Proc. roy. Soc. **B 127**, 192, 1939.
36) R. Hill and R. Scarisbrick, Proc. roy. Soc. **B 129**, 238, 1940.
37) D. I. Arnon and F. R. Whatley, Arch. Biochem. **23**, 141, 1949.
38) F. D. H. Macdowall, Plant Physiol. **24**, 462, 1949.

[39]) H. W. Milner, N. S. Lawrence and C. S. French, Science **111**, 633, 1950.
[40]) H. W. Milner, M. L. G. Koenig and N. S. Lawrence, Arch. Biochem. **28**, 185, 1950.
[41]) H. W. Milner, C. S. French, M. L. G. Koenig and N. S. Lawrence, Arch. Biochem. **28**, 193, 1950.
[42]) C. S. French and H. W. Milner, Symp. Soc. exp. Biol. **V**, 232, 1951.
[43]) A. A. Krasnovsky, C. R. Acad. Sci. U.R.S.S. **60**, 42, 1948.
[44]) A. A. Krasnovsky, C. R. Acad. Sci. U.R.S.S. **61**, 91, 1948.
[45]) A. A. Krasnovsky and G. P. Brin, C. R. Acad. Sci. U.R.S.S. **67**, 325, 1949.
[46]) A. A. Krasnovsky and G. P. Brin, C. R. Acad. Sci. U.R.S.S. **73**, 1239, 1950.
[47]) D. Porret and E. Rabinowitch, Nature, Lond. **140**, 321, 1937.
[48]) E. Rabinowitch, Annu. Rev. Pl. Physiol. **3**, 229, 1952.
[49]) M. G. Evans and N. Uri, Nature, Lond. **164**, 404, 1949.
[50]) M. G. Evans and N. Uri, Symp. Soc. exp. Biol. **V**, 130, 1951.
[51]) J. Weiss, Symp. Soc. exp. Biol. **V**, 141, 1951.

CHAPTER I

METHODS AND MATERIALS USED FOR REDOX POTENTIAL MEASUREMENTS

1. Introduction

If a chemically inert metallic electrode, such as platinum, is immersed in a solution of a reversible oxidation-reduction system, a potential difference will be set up between the electrode and the solution. This potential difference appears to be dependent on the ratio of the concentrations (activities) of the oxidized and reduced forms of the system. The more highly oxidized the redox substance is the higher will be the electrode potential. At constant *pH* the redox potential of the system

$$\mathrm{R} \rightleftarrows \mathrm{Ox} + ne$$

is represented by the equation

$$E = E_0' + \frac{RT}{nF} \ln \frac{(\mathrm{Ox})}{(\mathrm{R})},$$

in which (Ox) and (R) are the concentrations (activities) of the oxidized and reduced forms respectively. The quantity E_0' is a constant specific to a given oxidation-reduction system, and is defined as the potential of the half-reduced system at the *pH* under consideration.

If two redox systems are present in the same solution, the system of higher E_0' will generally be in the reduced form for a greater percentage than the system of lower E_0'. For the sake of brevity, systems of lower E_0'

are said to be oxidized by systems of higher E'_0. This reaction will proceed until equilibrium has been reached, that is to say, until both systems have arrived at the same potential. The equilibrium potential can be described by the equation

$$E = E'_{01} + \frac{RT}{nF} \ln \frac{(\mathrm{Ox}_1)}{(R_1)} = E'_{02} + \frac{RT}{nF} \ln \frac{(\mathrm{Ox}_2)}{(R_2)}.$$

As the reduced form defined above is often a base which takes up protons to a certain extent in the system under consideration, the pH of the solution should usually be taken into account. The reduction of quinones and of many dyes may be represented in a convenient way by an equation of the following type

$$\mathrm{H_2R} \rightleftarrows \mathrm{Ox} + 2\,\mathrm{H^+} + 2\,\mathrm{e},$$

in which the reduced form $\mathrm{H_2R}$ is a (mostly weak) dibasic acid, characterized by two ionisation constants. The redox potential of such a reversible oxidation-reduction system is given by the equation

$$E = E_0 + \frac{RT}{2F} \ln \frac{(\mathrm{Ox})}{(\mathrm{R})} + \frac{RT}{2F} \ln \left[(\mathrm{H^+})^2 + K_1(\mathrm{H^+}) + K_1K_2\right].$$

Here (R) is the total concentration of the reduced form; K_1 and K_2 are the ionisation constants. It is easy to see that if K_1 and K_2 are very small when compared to the hydrogen ion concentration, the equation reduces to

$$E = E_0 + \frac{RT}{2F} \ln \frac{(\mathrm{Ox})}{(\mathrm{R})} + \frac{RT}{F} \ln (\mathrm{H^+}).$$

In this E_0 is the normal (standard) potential of the redox system under consideration. Only in this simple case may the relationship between E'_0 and E_0 be represented by

$$E'_0 = E_0 + \frac{RT}{F} \ln (\mathrm{H^+}).$$

The photochemical splitting of water, in the presence of chloroplasts and a suitable redox substance as hydrogen acceptor, was achieved for the first time by Hill [1]). This "Hill reaction" which has been the most important subject of study in our investigation, can be represented by the equation (benzoquinone has been chosen as an example of a hydrogen acceptor)

$$\mathrm{H_2O} + \text{benzoquinone} \xrightarrow{\text{chloroplasts, } h\nu} \text{hydroquinone} + \tfrac{1}{2}\mathrm{O_2}.$$

According to this equation it should be possible to follow the reaction by means of redox potential measurements. The advantage of this with

respect to other methods, such as manometric or photometric measurements, is that the reduction of slightly soluble and uncoloured substances can also be observed. The redox potential can still be measured when the redox substances are present in low concentrations (6.10^{-5} molar).

2. Isolation of the chloroplasts *)

300 g of fresh lettuce or spinach leaves are disintegrated in a waring blendor for one minute in 250 ml of 0·025 molar phosphate buffer (KH_2PO_4-NaOH) of *pH* 6·5, the latter containing 0·25 g of KCl per litre. The obtained suspension is filtered through cloth and centrifuged for a very short period of time in order to remove fragments of cells. The chloroplasts are then separated by centrifuging the supernatant for at least 45 to 60 minutes at 2000 *g*. The green sediment is washed twice by suspending in phosphate buffer followed by centrifugation. The washed chloroplasts are suspended in 100 ml of phosphate buffer and then stored in the dark at about 2 °C. To obtain a highly active suspension all operations have to be performed at a low temperature (0-3 °C).

3. Measurement of the redox potential

The redox potential was measured by means of a Philips potentiometer (GM 4491). Figs 1 and 2 give an impression of the arrangement used by us.

The front and the back of the cuvette holder consist partially of glass (drawn as a shaded area in fig. 1) and are provided with a metallic shutter which is removed to start illumination. The temperature during measurement is maintained at 16 to 17 °C by cooling with tap water.

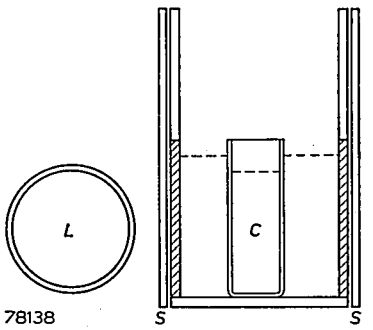

Fig. 1. Cuvette holder (cross-section).
L = sodium-vapour lamp,
S = shutter,
C = cuvette.

*) Here the indication chloroplasts does not only refer to intact chloroplasts but also to fragments of chloroplasts and grana.

In the cuvette, containing for instance 50 ml of a 6.10^{-5} molar 2,6-dichlorophenol-indophenol solution in phosphate buffer (*pH* 6·5), a platinum and a saturated-calomel electrode are immersed. Pure, practically oxygen-free nitrogen is passed through the solution in order to stir as well as to counteract the reoxidation of the reduced component. The influence of oxygen upon the Hill reaction will be described in detail in the chapters III and IV, but it is worth mentioning already here that photoreduction of many oxidants (for instance benzoquinone and 2,6-dichlorophenol-indophenol) occurs to a considerable percentage even when oxygen is passed through.

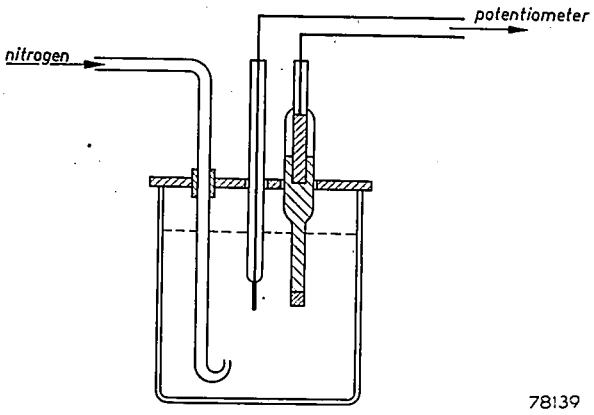

Fig. 2. Cuvette with electrodes.
Dimensions of the cuvette: 6·5 × 5·5 × 2 cm.

As soon as the redox potential of the solution has become constant 2 ml of chloroplast suspension is added; this normally causes little or no change in potential. The solution is then exposed to the light of a Philips sodium-vapour lamp (SO 140 W) by removing the shutter and the redox potential drop is observed until a constant level has been reached. In our experiments the distance between sodium-vapour lamp and cuvette amounted to 4 cm; this corresponds to a light intensity of 15000 lux.

A characteristic example of the change of the redox potential as a function of time is the curve of 2,6-dichlorophenol-indophenol represented in fig. 3.

The slope of the redox potential curve is determined by the activity of the chloroplasts, the latter being strongly dependent on the season and on the age of the chloroplasts used. The rate of the photochemical reduction of 2,6-dichlorophenol-indophenol by a 1, 2, 6, 8 and 11 days old chloroplast suspension is shown in fig. 4.

Gorham and Clendenning [2]) reported that chloroplasts can be stored at −40 °C for a whole year without distinct decrease of the photochemical activity. If chloroplasts are heated, however, at a temperature of 50 °C for a few minutes the activity is lost completely. In this connection it seems probable that the decrease of activity during storage, represented in fig. 4, is caused by inactivation of one or more thermo-labile components essential for the Hill reaction.

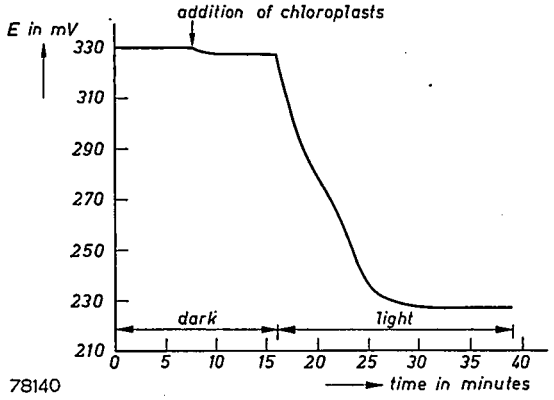

Fig. 3. Change of the redox potential as a function of time for 2,6-dichlorophenol-indophenol.

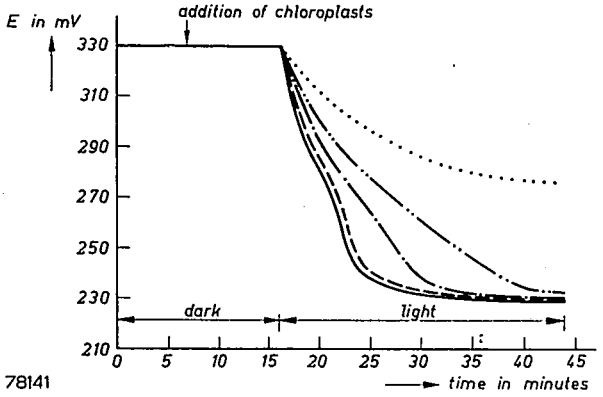

Fig. 4. Change of the redox potential of 2,6-dichlorophenol-indophenol by the same chloroplast suspension after 1 (——), 2 (----), 6 (-------), 8 (·-·-·-·), and 11 (·····) days.

The redox potential drop of 2,6-dichlorophenol-indophenol usually amounts to about 100 mV, which in this case corresponds to nearly complete reduction. A redox potential drop of 100 mV may be caused, for instance, by an increase of the percentage of the reduced form from 2% to 98%, as appears from the equation

$$\Delta E = E_0' + 0{\cdot}03 \log \tfrac{98}{2} - E_0' - 0{\cdot}03 \log \tfrac{2}{98} = 0{\cdot}06 \log 49 = 0{\cdot}1 \text{ V}.$$

The E_0' then is half-way between the initial and final potentials. As is shown in fig. 3 this is actually the case for 2,6-dichlorophenol-indophenol. The E_0' of this compound under the experimental conditions is given by the inflexion point of the redox potential curve. Unfortunately, an inflexion point is not found for every substrate so that in many cases a quantitative interpretation of the potential curve presents difficulties. As an example of a curve lacking an inflection point the redox potential curve for benzoquinone is represented in fig. 5.

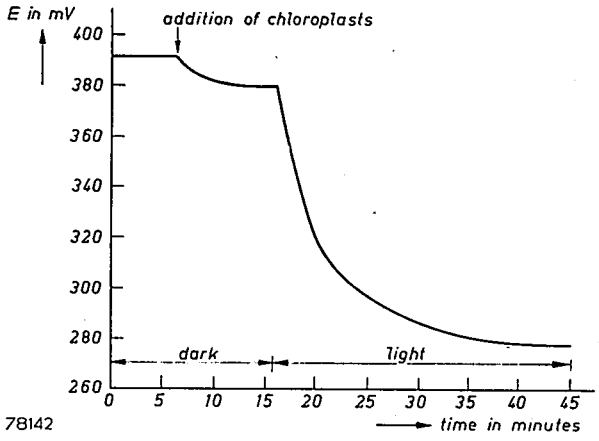

Fig. 5. Change of the redox potential as a function of time for benzoquinone.

Besides, the E_0' values under the conditions of our experiments need not be exactly equal to the literature data referring to more concentrated solutions. Thus in the case of benzoquinone, for instance, ($E_0' = 332$ mV at pH 6·5 and at 16 °C) a potential drop from about 380 to about 280 mV would be expected. Our experience was, however, that at low concentrations a too high redox potential is found with this compound. The deviation usually amounts to about 10 mV. Moreover, various platinum electrodes give somewhat different values. For 2,6-dichlorophenol-indophenol, on the other hand, the deviation is at most a few mV whereas the mutual differences between various platinum electrodes are much smaller than for benzoquinone.

In table I the redox potential of a quinhydrone solution in 0·025 M phosphate buffer is given as a function of the concentration. From this table it appears that the redox potential rises on decreasing the concentration of the quinhydrone while the deviations between the various platinum

TABLE I

Redox potential (mV) of quinhydrone solution as a function of the concentration (*pH* 6·5; nitrogen atmosphere) *)

Concentration of quinhydrone	Platinum electrode 1	Platinum electrode 2
6.10^{-4} M	78	77
3.10^{-4} M	81	78
$1{\cdot}2.10^{-4}$ M	85	81
6.10^{-5} M	90	86
3.10^{-5} M	99	97
$1{\cdot}2.10^{-5}$ M	117	111
6.10^{-6} M	124	123

*) The redox potentials are given with reference to the saturated-calomel electrode in these tables.

electrodes become larger upon dilution. Enlargement or reduction of the platinum area and purification of the nitrogen by leading the gas over heated copper gauze do not effect improvements (see table II). When any contact with atmospheric oxygen in these experiments was prevented by the use of a cuvette as represented in fig. 6 the results were not better.

The increase of the redox potential upon dilution of a quinhydrone solution is apparently not caused by oxidation of the system by traces of oxygen, possibly still present in the nitrogen used.

No increase of the redox potential was observed polarographically at

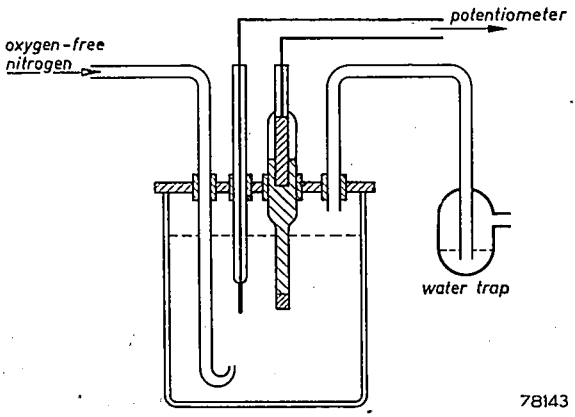

Fig. 6. Cuvette with electrodes.

TABLE II

Redox potential (mV) of quinhydrone solution (*pH* 6·6).

	Platinum electrode 1	Platinum electrode 2
6.10^{-5} M quinhydrone; purified nitrogen passed through	86	82
6.10^{-5} M quinhydrone; unpurified nitrogen passed through	86	81
6.10^{-6} M quinhydrone; purified nitrogen passed through	116	108
6.10^{-6} M quinhydrone; unpurified nitrogen passed through	116	106
6.10^{-6} M quinhydrone; no nitrogen passed through	154	128
saturated quinhydrone solution (with or without passing through of nitrogen)	72	72

the lower concentrations of quinhydrone (see table III); this phenomenon is undoubtedly due, therefore, to the platinum electrodes. The deviation of the redox potential from the literature data may well be attributed to a long time of adjustment of the electrodes, since it had decreased after several hours. (The readings, given in the tables, were taken when the potential has become practically, although not completely constant, which was usually the case after about 30 minutes.) Biilmann and Jensen [3]) have stated already that the quinhydrone electrode gives rise to an erroneous *pH* measurement if too small concentrations of quinhydrone are used.

In spite of these difficulties the application of the redox potentiometric method to the Hill reaction appears to lead to quite reproducible results.

TABLE III

Polarographically determined normal potential of benzoquinone ($pH = 0$; 24 °C)

Concentration of benzoquinone	E_0(mV)
5.10^{-4} M	475
	474
$2{\cdot}5.10^{-4}$ M	476
10^{-4} M	472
	477
8.10^{-5} M	469
6.10^{-5} M	462

The polarographical measurements were performed in phosphate buffer of pH 6·5, containing 0·05 molar KCl.

In order to compare reduction rates, however, it is recommendable to use always the same platinum electrodes. For a quantitative interpretation of the potential curve 2,6-dichlorophenol-indophenol is preferred to benzoquinone, as only for the first-mentioned substance the E_0' can readily be determined from the curve itself, owing to the occurrence of an inflexion point. A further advantage of the use of this compound is the fact that not only the redox potential drop but also the decolorization of the dye indicates photochemical reduction.

(To be continued)

REFERENCES

1) R. Hill, Nature, Lond. **139**, 881, 1937.
2) P. R. Gorham and K. A. Clendenning, Canad. J. Res. **C 28**, 513, 1950.
3) E. Biilmann and A. L. Jensen, Bull. Soc. chim. Fr. **41**, 151, 1927.

ABSTRACTS OF RECENT SCIENTIFIC PUBLICATIONS OF N.V. PHILIPS' GLOEILAMPENFABRIEKEN

Reprints of the majority of these papers can be obtained on application to the Administration of the Research Laboratory, Kastanjelaan, Eindhoven, Netherlands. Those papers of which no reprints are available are marked with an asterisk (*).

2050: G. Diemer, Z. van Gelder and J. J. P. Valeton: An interference in television pictures (Wireless Engnr **29**, 164-168, 1952).

Interference manifesting itself in the form of vertical lines on the left-hand side of a television picture is studied. It can be ascribed to intrinsic properties of the I_a-V_a characteristics of the power valve used for generating the line-deflection current. These properties cause irregularities in the anode current and give rise to signals of very high frequency, which may penetrate into the r.f. or i.f. amplifier of the receiver.

2051*: J. J. Went, G. W. Rathenau, E. W. Gorter and G. W. van Oosterhout: Hexagonal iron-oxide compounds as permanent-magnet materials (Phys. Rev. **86**, 424-425, 1952).

Oxides of hexagonal structure of the composition $BaO.6Fe_2O_3$ and $BaO.2Fe_3O_4.6Fe_2O_3$ are investigated in detail. The saturation magnetic moment per gram as measured for small single crystals along the direction of preferred magnetization is plotted as a function of temperature. The value at absolute zero temperature can be accounted for on the basis of Néel's and Anderson's theories. The paramagnetic behaviour of $BaO.6Fe_2O_3$ above the Curie point (450 °C) is shown. Approximate values of the anisotropy constant K (in erg/cm^3) for $BaO.6Fe_2O_3$ are plotted against temperature. The curve showing the intrinsic force ${}_JH_c$ for a fine-grained sample of $BaO.6Fe_2O_3$ as a function of temperature cannot be explained by pure rotational processes. The $(BH)_{max}$ value of fine-grained $BaO.6Fe_2O_3$ at 20 °C amounts to about $0{\cdot}85.\ 10^6$ gauss oersted at $B = 1100$ gauss.

2052*: J. S. C. Wessels and E. Havinga: The redox potential as a critical factor in the Hill reaction (Rec. Trav. chim. Pays-Bas **71**, 809-812, 1952).

The photomechanical reduction of various quinones and dyes by water in the presence of chloroplasts is studied by measurement of the redox potential during illumination. Whether this so-called Hill reaction will proceed to a measurable degree appears to be determined by the standard potential of the redox substance. With systems having a standard potential of about 40 millivolts or lower, no reduction is observed.

VOL. 9 NR 3 JUNE 1954

Philips Research Reports

EDITED BY THE RESEARCH LABORATORY
OF N.V. PHILIPS' GLOEILAMPENFABRIEKEN, EINDHOVEN, NETHERLANDS

R 241 *Philips Res. Rep. 9, 161-196, 1954*

INVESTIGATIONS ON PHOTOSYNTHESIS; THE HILL REACTION *)

by J. S. C. WESSELS 541.144.7

CHAPTER II

INVESTIGATION INTO THE OCCURRENCE OF RADICALS AS INTERMEDIATES IN THE HILL REACTION

1. Introduction

Weiss and Porret [1]) were the first to report the photolysis of water by ceric ions. They interpreted it as a process involving the intermediate formation of OH radicals, in accordance with the scheme

$$\begin{aligned} Ce^{4+} &\xrightarrow{h\nu} Ce^{4+*}, \\ Ce^{4+*} + H_2O &\rightarrow Ce^{3+} + H^+ + OH, \\ 2\ OH &\rightarrow H_2O + \tfrac{1}{2}\ O_2. \end{aligned}$$

Evans and Uri [2]) assume that in this reaction light is absorbed by an ion-pair complex, in which an electron transfer from anion to cation then takes place. This results in reduction of the metal ion to a lower valency and in oxidation of the anion to an atom or free radical:

$$M^{n+}X^- \xrightarrow{h\nu} M^{(n-1)+}X.$$

The atom or free radical so formed can lead in a subsequent reaction to polymerization of vinyl compounds (e.g. methacrylic acid, acrylonitrile), to oxidation of organic substrates (e.g. benzene, benzoic acid) and to photolysis of water. The latter reaction is assumed by Evans and Uri to proceed in accordance with the scheme

$$\begin{aligned} Ce^{4+}OH^- &\underset{\leftarrow}{\overset{h\nu}{\rightarrow}} Ce^{3+}OH, \\ Ce^{3+}OH &\rightarrow Ce^{3+} + OH, \\ Ce^{3+} + OH &\rightarrow Ce^{4+} + OH^-, \end{aligned}$$

*) Continued from Philips Res. Rep. 9, 140-159, 1954.

$$Ce^{4+}OH^- + OH \rightarrow Ce^{3+} + H_2O_2,$$
$$2\ Ce^{4+}OH^- + H_2O_2 \rightarrow 2\ H_2O + 2\ Ce^{3+} + O_2.$$

Baxendale, Evans and Park [3]) have shown that OH radicals, produced in the reaction between ferrous ions and hydrogen peroxide, can be detected by their ability to initiate the polymerization of vinyl compounds according to

$$Fe^{2+} + H_2O_2 \rightarrow Fe^{3+} + OH^- + OH,$$
$$Fe^{2+} + OH \rightarrow Fe^{3+} + OH^-,$$
$$OH + CH_2 = CHR \rightarrow HO - CH_2 - \underset{R}{\overset{H}{C}}\text{.} \text{ etc.}$$

Similarly, polymerization occurs when ion-pair complexes as $Fe^{3+}OH^-$, $Fe^{3+}Cl^-$ or $Fe^{3+}C_2O_4^{2-}$, are irradiated in aqueous solution in the presence of a vinyl monomer with light of wavelength in the range 300-380 mμ, where no direct photopolymerization of the monomer would occur. The experimental results can be accounted for on the basis of the following scheme

$$Fe^{3+}X^- \underset{\leftarrow}{\overset{h\nu}{\rightarrow}} Fe^{2+}X,$$
$$Fe^{2+}X \rightarrow Fe^{2+} + X,$$
$$Fe^{2+} + X \rightarrow Fe^{3+} + X^-,$$
$$X + CH_2 = CHR \rightarrow X - CH_2 - \underset{R}{\overset{H}{C}}\text{.}\ .$$

Another way to detect OH radicals was discovered by Stein and Weiss [4]). This method is based on oxidation of the benzene nucleus by the OH radicals. The reaction scheme for the ion-pair complex $Fe^{3+}\ OH^-$ consists of the following stages

$$Fe^{3+}OH^- \underset{\leftarrow}{\overset{h\nu}{\rightarrow}} Fe^{2+}OH,$$
$$Fe^{2+}OH \rightarrow Fe^{2+} + OH,$$
$$Fe^{2+} + OH \rightarrow Fe^{3+} + OH^-,$$
$$OH + C_6H_6 \rightarrow C_6H_5^{\bullet} + H_2O,$$
$$C_6H_5^{\bullet} + OH \rightarrow C_6H_5OH,$$
$$2\ C_6H_5^{\bullet} \rightarrow C_6H_5 - C_6H_5.$$

Phenol and diphenyl are thus formed as the principal products.

The photolysis of water by ceric ions, leading to the production of molecular oxygen, bears a certain resemblance to the Hill reaction. Therefore the Hill reaction may be considered to be, in a sense, a photosensitized version of this photolysis. Thus the following hypothetical scheme is suggested for the Hill reaction by Weiss [5]). Weiss assumes here that the light is absorbed by a chlorophyll-metal complex (Me^{2+} Chlor), where Me denotes some metal and Chlor stands for chlorophyll.

$$(Me^{2+}\ Chlor)\ .\ H_2O \xrightarrow{h\nu} (Me^{2+}\ Chlor)^*\ .\ H_2O \qquad \text{Light absorption.}$$

$$(Me^{2+}\ Chlor)^*\ .\ H_2O \rightarrow (Me^{+}\ Chlor)\ .\ H_2O^+ \qquad \text{Electron transfer.}$$

$$(Me^{+}\ Chlor) + H_2O^+$$

$$\left.\begin{aligned} H_2O^+ &\rightarrow H^+ + OH \\ 2\ OH &\rightarrow H_2O + \tfrac{1}{2}\ O_2 \end{aligned}\right\} \text{Formation of molecular oxygen.}$$

$$(Me^{+}\ Chlor) + Ox \rightarrow (Me^{2+}\ Chlor) + Ox^- \qquad \text{Action of added oxidizing agent (Ox).}$$

$$(Me^{+}\ Chlor) + OH \rightarrow (Me^{2+}\ Chlor) + OH^- \qquad \text{Reverse process.}$$

In connection with the above and with the fact that the occurrence of radicals as intermediates has indeed been established for some enzyme reactions [6]), it seemed important to investigate whether the formation of OH radicals might be demonstrated also in the Hill reaction. For this purpose the methods of Evans and Uri (polymerization of acrylonitrile) and Weiss (reaction with benzene) were used, which can be applied generally for the detection of free OH radicals.

2. Detection of free radicals in the reaction between $FeSO_4$ and H_2O_2

(a) *Reaction with benzene*

To a mechanically stirred emulsion of 1·5 ml of benzene in 200 ml of 0·35 M $FeSO_4$, acidified with 1·3 ml of concentrated sulfuric acid, 26·7 ml of 1·4 M H_2O_2 are added dropwise from a burette. The brownish solution is extracted with ether and the extract is shaken twice with 20 ml of 5% NaOH solution and afterwards with distilled water. NaOH and water extract are combined and filtered. To the acidified, reddish-brown-coloured solution an excess of bromine water is added, upon which a yellowish-white precipitate of tribromophenol is formed.

The original ethereal extract, after treatment with the alkaline solution and washing with water, is dried over Na_2SO_4 and evaporated in vacuo. As a residue, red-coloured oil drops are obtained which yield a crystalline product after crystallization from aqueous acetic acid (1 : 1). The product is dissolved in warm methyl alcohol and precipitated by the addition of a little water. Then the product is filtered, washed and dried. The melting point appeared to be 68-69 °C; it was not depressed by admixture with pure diphenyl (m.p. 70 °C). Yield 8·5 mg.

The yellowish-white precipitate of tribromophenol is identified as follows. After filtration the precipitate is transferred to a small beaker and covered with water. $NaHSO_3$ solution is now gradually added (to convert the compound $C_6H_2Br_4O$ formed by the excess of bromine water into tribromophenol) until a strong odour of SO_2 remains after stirring and warming to 40 °C. Then the precipitate is filtered, washed well with

water, and recrystallized twice from 40% alcohol. The dry product had a melting point of 93 °C which was not depressed by admixture with authentic 2,4,6-tribromophenol (m.p. tribromophenol 93 °C). The yield was 150 mg, corresponding to 43 mg of phenol.

The sensitivity of the reaction on phenol with bromine water was determined. In 50 ml of solution 2 mg of phenol appeared to be just detectable.

(b) *Polymerization of acrylonitrile*

4·3 ml of 1·4 M H_2O_2 is added to a mixture of 17·1 ml of 0·35 M $FeSO_4$, 1 ml of concentrated H_2SO_4, 173 ml of distilled water and 5 ml of distilled acrylonitrile. Within a few minutes a turbidity develops, after which a white flocculent precipitate separates. The precipitated polymer is centrifuged, washed with methanol and dried in vacuo. The yield of polyacrylonitrile was 60 mg.

At concentrations of $FeSO_4$ and H_2O_2 of 0·003 M also polymerization occurred. However, with concentrations of $FeSO_4$ and H_2O_2 of 0·0003 M polymerization was only observed when the reaction was carried out in an atmosphere of nitrogen. The most favourable result always was obtained when an excess of acrylonitrile and equivalent amounts of $FeSO_4$ and H_2O_2 were used.

3. Hill reaction with benzene and acrylonitrile

From figs 1 and 2 it appears that the Hill reaction is not at all inhibited by benzene and only at high concentrations by acrylonitrile.

The inhibition by high concentrations of acrylonitrile increases upon dilution of the chloroplast suspension.

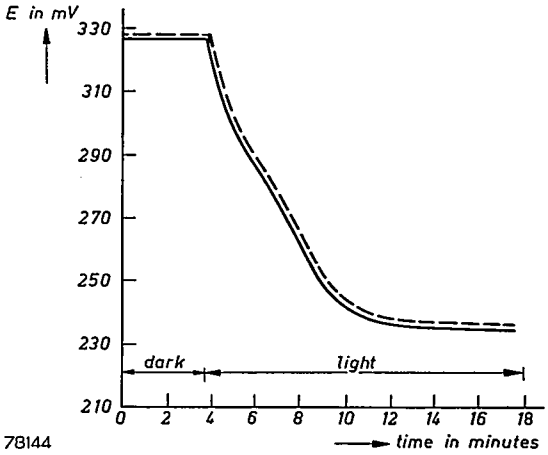

Fig. 1. Change of the redox potential as a function of time for 2,6-dichlorophenol-indophenol with (------) and without (———) addition of benzene.

Polymerization was neither observed in these experiments, nor in the case where chloroplasts treated with acrylonitrile were exposed to light without 2,6-dichlorophenol-indophenol or benzoquinone.

A demonstration of the formation of phenol proved also to be impossible. For this purpose a 6.10^{-5} M solution of 2,6-dichlorophenol-indophenol or benzoquinone in 50 ml of 0·025 M phosphate buffer (*pH* 6·5), to which 1 ml of benzene and 2 ml of chloroplast suspension were added, was illuminated for one and a half hour in an atmosphere of nitrogen. The contents of four cuvettes were then extracted with ether and the extract shaken twice with 10 ml of 5% NaOH solution. The acidified aqueous layer was treated with an excess of bromine water. However, no precipitate of tribromophenol separated, and no diphenyl could be obtained from the ethereal layer after evaporation.

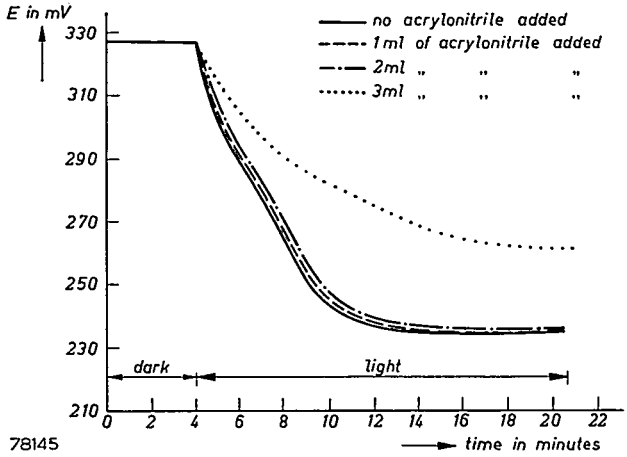

Fig. 2. Influence of acrylonitrile upon the change of the redox potential of 2,6-dichlorophenol-indophenol.

As far as it is allowed to make a comparison with the formation of radicals in the reaction between $FeSO_4$ and H_2O_2, we may calculate from the sensitivity of the acrylonitrile and benzene reagents determined for this reaction that polymerization of acrylonitrile and formation of phenol would only be detectable when at least 0·25 mg of OH radicals are formed per cuvette. This is just the maximal concentration of OH radicals which may be formed in a cuvette as intermediates in the photochemical reduction of 2,6-dichlorophenol-indophenol or quinone so that probably a more concentrated chloroplast suspension is needed for the detection of radicals. As the cuvettes in normal use appeared to be incapable of transmitting light any longer when filled with a concentrated chloroplast suspension

we employed a very thin cuvette (area 40 × 10 cm^2; thickness 4 mm). This cuvette was filled with 70 ml of chloroplast suspension, 70 ml of benzoquinone solution (containing 11·4 mg of benzoquinone) and 1 ml of benzene. The mixture was exposed to light for five hours in a pure nitrogen atmosphere. The solution was then extracted with ether in the usual manner, the extract shaken with 5% NaOH solution, and the NaOH extract after acidification treated with bromine water. From the fact that no precipitate of tribromophenol separated it was clear that also in this case no reaction with benzene had occurred.

Likewise, polymerization of acrylonitrile did not occur under these conditions, as separation of the polymer could be observed neither after a longer time of illumination, nor with chloroplasts which previously were disintegrated as much as possible by prolonged grinding with sand. Omission of the hydrogen acceptor and substitution of benzoquinone by 2,6-dichlorophenol-indophenol, potassium ferricyanide or potassium chromate had also no effect.

In order to investigate whether the polymerization of acrylonitrile might be inhibited by chloroplasts or the hydrogen acceptor, the influence of these substances upon the polymerization by $FeSO_4$ and H_2O_2 was studied. From this the concentrations of 2,6-dichlorophenol-indophenol, benzoquinone, hydroquinone and chloroplast suspension applied by us did not appear to inhibit the polymerization of acrylonitrile in a 0·0003 M solution of $FeSO_4$ and H_2O_2 (nitrogen atmosphere).

Although a demonstration of the presence of radicals proved to be impossible in this way *), it would be quite premature to conclude from this that radicals do not play a part in the Hill reaction. This investigation only establishes that the concentration of radicals in the solution is either very small or nil in this process, but the possibility remains of course that the OH radicals have reacted further, possibly at an enzyme surface, before they could make contact with benzene or acrylonitrile.

*) After this investigation was brought to an end Uri (J. Amer. chem. Soc. **74**, 5805, 1952) reported in a short communication that he has not obtained evidence suggesting free radical intermediates in photochemical experiments with isolated chloroplasts.

REFERENCES

1) J. Weiss and D. Porret, Nature, Lond. **139**, 1019, 1937.
2) M. G. Evans and N. Uri, Symp. Soc. exp. Biol. **V**, 130, 1951.
3) J. H. Baxendale, M. G. Evans and G. S. Park, Trans. Faraday Soc. **42**, 155, 1946.
4) G. Stein and J. Weiss, Nature, Lond. **161**, 650, 1948.
G. Stein and J. Weiss, Nature, Lond. **166**, 1104, 1950.
5) J. Weiss, Symp. Soc. exp. Biol. **V**, 141, 1951.
6) See for instance G. Parravano, J. Amer. chem. Soc. **73**, 183, 1951.

CHAPTER III

RELATION BETWEEN REDOX POTENTIAL AND PHOTOCHEMICAL REDUCTION BY CHLOROPLASTS

1. Photochemical reduction of various quinones and dyes by chloroplasts

It has already been mentioned in the introduction that the maximal reducing power of chloroplasts in vitro still needs more detailed study, whereas some investigations give the impression that a simple relationship between capacity for being reduced and the redox potential of a compound does not exist. We therefore investigated, for a number of quinones and dyes, which factors determine whether or not the redox substance undergoes photochemical reduction by isolated chloroplasts. Drop of the redox potential of the system and decolorisation of the dye point to reduction in this case. Oxidation of the reduced component by oxygen was counteracted by passing pure nitrogen through the solution. The results of this investigation are summarized in tables I and II. As characteristic examples of the change of the redox potential as a function of time, the curves for tetrachloro-ortho-benzoquinone ($E_0' = 0{\cdot}444$ V), benzoquinone ($E_0' = 0{\cdot}332$ V), toluylene blue ($E_0' = 0{\cdot}137$ V), and indigotetrasulfonate ($E_0' = -0{\cdot}022$ V) are reproduced in fig. 1.

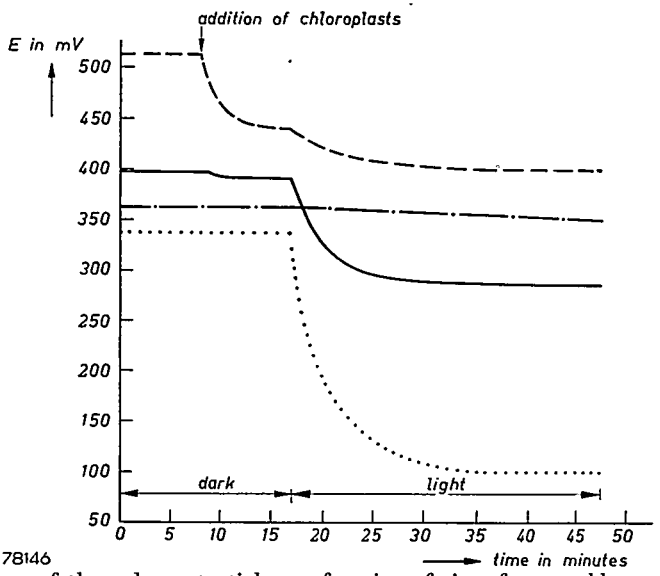

Fig. 1. Change of the redox potential as a function of time for tetrachloro-ortho-benzoquinone (- - - - -), benzoquinone (———), indigotetrasulfonate (·· ·· ··) and toluylene blue (. . . . .). 6.10^{-5} M solution of the quinone or dye in 50 ml of 0·025 M phosphate buffer ($pH = 6{\cdot}5$) + 2 ml of chloroplast suspension; nitrogen passed through the solution; temperature = 16 °C.

TABLE I

Photochemical reduction by chloroplasts of some quinones

quinone	E_0' at $pH = 6{\cdot}5$ (volts)		redox potential drop
tetrachloro-ortho-benzoquinone	0·444	(25 °C)	+
tetrabromo-ortho-benzoquinone	0·437	(25 °C)	+
potassium-benzoquinone-sulfonate			+
2,6-dibromobenzoquinone	0·355	(16 °C)	+
p-benzoquinone	0·332	(16 °C)	+
3-nitro-1,2-naphthoquinone			+
toluquinone	0·277	(16 °C)	+
potassium-1,2-naphthoquinone-4-sulfonate	0·245	(25 °C)	+
p-xyloquinone	0·223	(16 °C)	+
p-thymoquinone	0·221	(16 °C)	+
1,2-naphthoquinone	0·181	(16 °C)	+
potassium-1,4-naphthoquinone-2-sulfonate	0·167	(16 °C)	+
potassium-2,3-dichloronaphthoquinone-2-sulfonate	0·119	(16 °C)*	+
1,4-naphthoquinone	0·086	(25 °C)	+
potassium-phenanthrenequinone-2-sulfonate	0·083	(25 °C)	+
2,5-dimethoxybenzoquinone	0·079	(25 °C)	+
phenanthrenequinone	0·058	(25 °C)	±
2-methyl-1,4-naphthoquinone	0·020	(25 °C)	−
2,5-dihydroxybenzoquinone	−0·078	(25 °C)	−
2-hydroxy-1,4-naphthoquinone	−0·090	(25 °C)	−
tetrahydroxybenzoquinone	−0·090	(30 °C)	−
potassium-6-nitro-anthraquinone-1-sulfonate phthiocol	−0·135	(30 °C)	−
sodium-anthraquinone-2,7-disulfonate	−0·137	(16 °C)	−
potassium-3-nitro-2-hydroxy-naphthoquinone-6-sulfonate	−0·167	(16 °C)*	−
sodium-anthraquinone-2-sulfonate	−0·180	(16 °C)	−
3-nitro-2-hydroxynaphthoquinone	−0·200	(16 °C)*	−
chloranilic acid	−0·21	(25 °C)	−
potassium-euthiochronate			−

+ redox potential drop,
− no redox potential drop,
± fall in potential only with highly active chloroplast suspensions.
With tetrachloro- and tetrabromo-ortho-benzoquinone the addition of the chloroplasts already causes a drop of around 70 mV in the dark.
The E_0' values are literature data, with the exception of the potentials marked with an asterisk which have been measured by us polarographically. The polarographical measurements were performed in a 10^{-3} molar solution of the compound in 0·025 molar phosphate buffer of pH 6·5, containing 0·05 mol of KCl per litre. The E_0' is given with reference to the normal hydrogen electrode at $pH = 6{\cdot}5$.

The quinones and dyes were purified by crystallization or by sublimation, as far as they were not prepared by us.

TABLE II

Photochemical reduction by chloroplasts of some dyes

dye	E_0' at $pH = 6{\cdot}5$ and 30 °C (volts)	redox potential drop	decolorisation of dye
2,6-dichlorophenol-indophenol	0·255	+	complete decolorisation
Binschedler's green	0·25	+	,, ,,
m-cresol-indophenol	0·240	+	,, ,,
o-cresol-indophenol	0·224	+	,, ,,
guaiacol-indo-2,6-dibromophenol	0·19	+	,, ,,
1-naphthol-2-sodium-sulfonate-indo-2,6-dichlorophenol	0·158	+	,, ,,
toluylene blue	0·137	+	nearly complete decolorisation
thionine	0·077	+	no decolorisation
methylene blue	0·028	±	,, ,,
indigotetrasulfonate	−0·022	−	,, ,,
indigotrisulfonate	−0·056	−	,, ,,
indigodisulfonate	−0·098	−	,, ,,
indigomonosulfonate	−0·130	−	,, ,,
phenosafranine	−0·234	−	,, ,,
safranine-T	−0·269	−	,, ,,

From the tables I and II it appears that among the redox systems investigated by us only those with an E_0' of 40-50 mV ($pH = 6{\cdot}5$; 16 °C) or higher can be reduced to a considerable extent. Practically complete reduction takes place with substances having an E_0' of at least 150 mV. The degree of reduction of a quinone or dye with an E_0' between 150 and 50 mV is, in addition to its E_0', somewhat dependent on the activity of the chloroplasts used. Substances are evidently formed during illumination of chloroplasts that make the potential drop to about 90 mV. Neither immediately after isolation of the chloroplasts, nor after a longer time of illumination was a lower potential observed under these conditions.

The fact that with tetrachloro- and tetrabromo-ortho-benzoquinone, as well as with potassium ferricyanide (see fig. 2), addition of the chloroplasts causes a considerable potential drop already in the dark, leads to the conclusion that reducing compounds are present in the chloroplast suspension, and that the redox potential of this suspension is at the very most 430 mV.

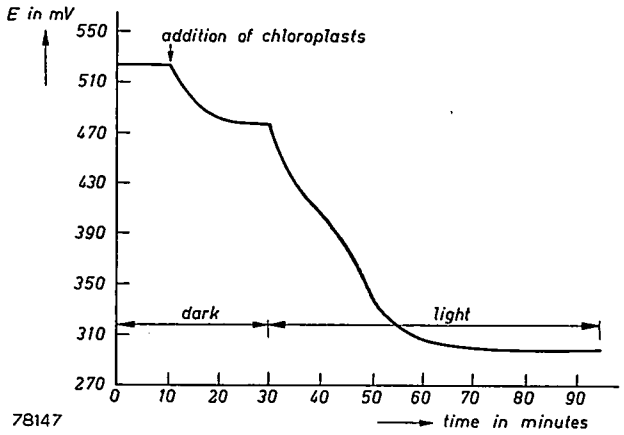

Fig. 2. Change of the redox potential as a function of time for potassium ferricyanide (6.10^{-5} M).

The high initial potential, observed also in the presence of substances having a low E_0', may be due to the fact that the redox potential of the chloroplast suspension in the dark, being normally of small effective oxidation-reduction capacity, becomes important if the added redox substance is present in the oxidized form for a high percentage. Actually a redox potential of about 330 mV is measured for the chloroplast suspension if no hydrogen acceptor is added. It must be emphasized, however, that this does not imply that the redox state within the chloroplasts is actually represented by this potential value. We can, in fact, hardly speak of one general redox potential

of such systems, as it is not known which of the reversible and irreversible redox substances present are responsible for the observed potential.

As only the E_0' of the oxidation-reduction system appears to determine whether photochemical reduction will proceed or not, it seems probable that adsorption of the quinone or dye is not essential in the Hill reaction. An intermediate hydrogen donor XH_2 is probably formed first; this is capable of reducing the added hydrogen acceptor according to the equation

$$X + H_2O \xrightarrow[\text{chloroplasts, } h\nu]{} XH_2 + \tfrac{1}{2}\,O_2,$$

$$XH_2 + \text{quinone} \rightleftarrows \text{hydroquinone} + X.$$

The increase of the free energy in the standard state (ΔF) of the reaction

$$\text{quinone} + H_2O \rightarrow \text{hydroquinone} + \tfrac{1}{2}\,O_2,$$

can be calculated by addition of the changes in standard free energy of the reactions

$$H_2O \rightarrow H_2 + \tfrac{1}{2}\,O_2 \qquad \Delta F_1 = 56600 \text{ cal}$$

and $H_2 + \text{quinone} \rightarrow \text{hydroquinone}$ $\qquad \Delta F_2 = -2FE_0 =$
$= -2 \,.\, 23070 \,.\, 0{\cdot}704 = -32500$ cal.

$$\Delta F = \Delta F_1 + \Delta F_2 = 24100 \text{ cal.}$$

For 1,4-naphthoquinone, a substance which can just be reduced by chloroplasts under the experimental conditions, this change in standard free energy amounts to

$$56600 - 2 \,.\, 23070 \,.\, 0{\cdot}476 = 34600 \text{ cal.}$$

As the oxygen tension is maintained at a rather low level by passing nitrogen through the solution, the increase of the free energy is actually several thousands of calories smaller.

From the fact that the energy of the triplet state of chlorophyll *a* amounts to 32000 to 37000 cal, it is obvious that all observed photochemical reductions may be effected by one light quantum only. In chapter IV we shall see that the lowest final potential observed when passing oxygen through the solution, amounts to about 0·230 volt. We can calculate that in order to arrive at this potential an energy of 28000 cal is needed. This value is of the same order of magnitude as the 29000 cal recently given by Franck [1]) as the maximal amount of energy available for chemical use from one light quantum.

For the reduction of a quinone or dye with a highly negative E_0', on the other hand, at least two light quanta would be needed, unless the supplemental energy is put at the disposal of the system from another source. Thus from the point of view of available energy also, a direct reduction

of diphosphopyridine nucleotide (= D.P.N.; $E'_0 = -0{\cdot}282$ V at pH 7·0) by one light quantum has to be considered as improbable. From the E'_0 of D.P.N. we can calculate that at a redox potential of 0·090 volt only one out of more than 10^{11} D.P.N. molecules is present in reduced state.

Mehler [2]) showed spectrophotometrically that chloroplasts are incapable of reducing D.P.N. We could support this by means of potentiometric measurements. D.P.N. does not affect the photochemical reduction of benzoquinone or 2,6-dichlorophenol-indophenol; furthermore, it is also unable to stimulate the reduction of sodium-anthraquinone-2-sulfonate or methylene blue.

Reduction of D.P.N. by one light quantum is, of course, quite possible energetically, if the supplementary free energy required is supplied by a coupled reaction involving a decrease in free energy. In this connection, the coupling between the photochemical reduction of D.P.N. by chloroplasts and the oxidative phosphorylation by a mitochondrial preparation, as observed by Vishniac and Ochoa [3]), is important. These authors suggest the formation of high-energy phosphate bonds in photosynthesis by oxidation of photochemically reduced D.P.N., in accordance with the scheme

$$H_2O + \text{D.P.N.} \xrightarrow{h\nu} \text{D.P.N.2H} + \tfrac{1}{2}\,O_2, \qquad (1)$$

$$\text{D.P.N. 2 H} + \tfrac{1}{2}\,O_2 + 3\ \text{A.D.P.} + 3\ PO_4^{3-} \rightarrow \text{D.P.N.} + H_2O + 3\ \text{A.T.P.}, \qquad (2)$$

$$3\ \text{A.D.P.} + 3\ PO_4^{3-} \xrightarrow{h\nu} 3\ \text{A.T.P.}$$

The reoxidation of D.P.N.2H keeps its concentration very low, allowing reaction (1) to proceed to the right. In order to allow for a sufficient rate of reaction, however, one must assume that reaction (1) when coupled to the reduction or reductive carboxylation of pyruvic acid, is achieved by: (a) either the primary formation of a reducing agent of intermediate redox potential (XH_2), the partial reoxidation of which generates energy-rich phosphate bonds which co-operate in the reduction of D.P.N. by XH_2; (b) or with the aid of high-energy phosphate bonds formed in reaction (2). Experiments of Wassink, Tjia and Wintermans [4]) with Chromatium showed already that energy-rich phosphate bonds are built up in the light. Recent experiments on the influence of light on the A.T.P. content of Chlorella pyrenoidosa induced Strehler [5]) to the suggestion that the photochemical process produces a primary reductant of intermediate oxidation-reduction potential, a part of which is consumed in a coupled oxidative phosphorylation. The high-energy phosphate bonds thus formed are used to achieve, in a stepwise manner, hydrogen transfer from this reductant to a redox system with an oxidation-reduction potential low enough to bring about reductions at the level of D.P.N. and carbohydrate metabolism.

As no negative redox potentials are attained in the light even in the

absence of oxygen (see further), the reduction of D.P.N. or T.P.N., as reported by Vishniac and Ochoa [6]), Arnon [7]) and Tolmach [8]), has undoubtedly to be considered as a reaction which is accomplished by the specific coupling of this reduction with energy-supplying processes. If we compare our results with the suggestion of Strehler, mentioned before, we might assume that the primary reductant of intermediate redox potential is represented by XH_2 in our scheme, and that the mechanism leading to the attainment of highly negative oxidation-reduction potentials does not function in the Hill reaction.

2. Substrate mixtures

An investigation on the photochemical reduction of a number of substrate mixtures showed that generally both hydrogen acceptors are reduced by chloroplasts. As an example the redox potential curve for a mixture of benzoquinone and 2,6-dichlorophenol-indophenol is given in fig. 3.

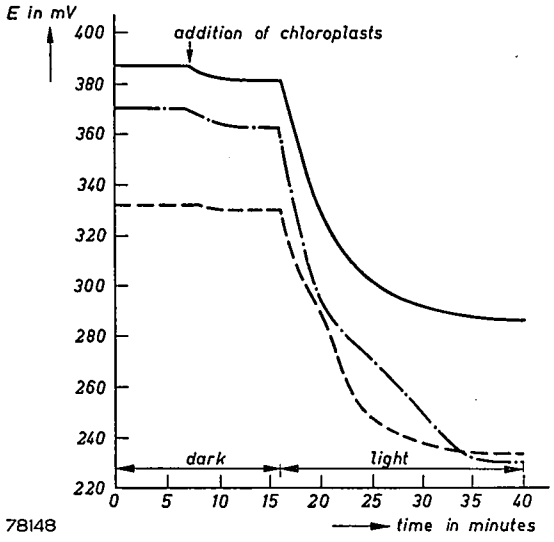

Fig. 3. Change of the redox potential as a function of time for benzoquinone (———), 2,6-dichlorophenol-indophenol (------), and a mixture of both substances (1:1) (·····). Substrate concentration 6.10^{-5} M.

However, if one of the components is a substance which can just be reduced by chloroplasts, as for instance thionine, the system with the higher redox potential is almost exclusively reduced. This may be caused by the fact that the reoxidation of reduced thionine in this case is also effected by the oxidized form of the other redox compound still present. As an example the mixture of 2,6-dichlorophenol-indophenol and thionine can be mentioned.

The redox potential curve for this mixture is represented in fig. 4. At the same time it appears from this figure that the final level shifts to a lower potential value when the ratio between the concentrations of thionine and 2,6-dichlorophenol-indophenol is raised.

A mixture of a reducible hydrogen acceptor and a quinone or dye incapable of being reduced by chloroplasts follows the redox potential curve of the former system. Only phthiocol constitutes an exception because this substance inhibits the Hill reaction (see chapter V).

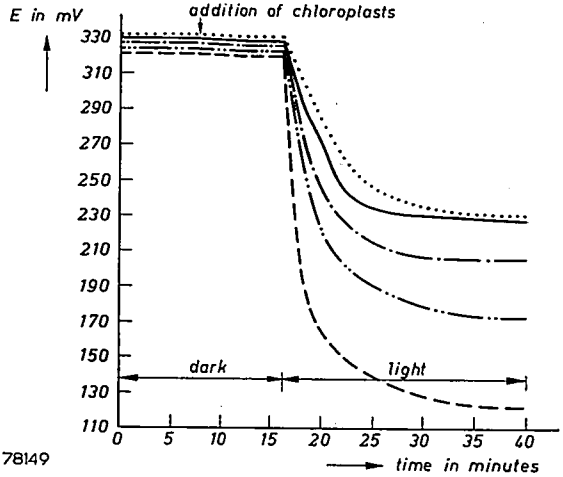

Fig. 4. Redox potential curves of thionine (-----), 2,6-dichlorophenol-indophenol (———), and mixtures of both substances.
Ratio of the concentrations of thionine and 2,6-dichlorophenol-indophenol 1 : 1 (.....), 3 : 1 (- - - - - -), and 9 : 1 (- · - · - · -).
Total concentration of the dyes 6.10^{-5} M.

3. Experiments under exclusion and removal of oxygen *)

In connection with the fact that reoxidations by oxygen will undoubtedly proceed, it seemed important to us to investigate if it would be possible to reduce also redox systems with an E_0' lower than 40 mV if oxygen is excluded as completely as possible. For that purpose oxygen-free nitrogen was passed through the solution during the measurement and contact with atmospheric oxygen prevented by the use of the cuvette represented in chapter I, fig. 6. To remove the last traces of oxygen from the practically oxygen-free nitrogen, normally used by us, the gas was

*) Of course, reoxidations by the oxygen evolved during the Hill reaction cannot be completely excluded.

passed through two washing bottles filled with Fieser's solution (an alkaline solution of $Na_2S_2O_4$, containing sodium-anthraquinone-β-sulfonate as a catalyst).

We found that actually lower final potentials are attained under these conditions than in presence of some oxygen, and that quinones and dyes with an E_0' lower than 40 mV can also be partially reduced. Some of the obtained results are summarized in table III.

TABLE III

Photochemical reduction by chloroplasts of some quinones and dyes in the absence of oxygen

quinone or dye	E_0' at $pH = 6{\cdot}5$ (volts)	redox potential drop	final potential (mV)	decolorisation of dye
tetrachloro-ortho-benzoquinone	0·444 (25 °C)	+	80	
p-benzoquinone	0·332 (16 °C)	+	80	
2,6-dichlorophenol-indophenol	0·255 (30 °C)	+	70	complete decolorisation
potassium-1,4-naphthoquinone-2-sulfonate	0·167 (16 °C)	+	80	
toluylene blue	0·137 (30 °C)	+	0	complete decolorisation
thionine	0·077 (30 °C)	+	70	no decolorisation
methylene blue	0·028 (30 °C)	+	10	" "
2-methyl-1,4-naphthoquinone	0·020 (25 °C)	+	30	
indigotetrasulfonate	−0·022 (30 °C)	+	10	" "
indigotrisulfonate	−0·056 (30 °C)	+	10	" "
2,5-dihydroxybenzoquinone	−0·078 (25 °C)	+	30	" "
2-hydroxy-1,4-naphthoquinone	−0·090 (25 °C)	+	<100	
indigodisulfonate	−0·098 (30 °C)	+	0	" "
indigomonosulfonate	−0·130 (30 °C)	−		" "
sodium-anthraquinone-2,7-disulfonate	−0·137 (16 °C)	−		
sodium-anthraquinone-2-sulfonate	−0·180 (16 °C)	−		

For an explanation of the marks reference is made to the caption of table I.

From this table it appears that, if oxygen is excluded as much as possible, a potential drop can be observed with redox substances having an E_0' of at least — 100 mV, whereas the lowest redox potential observed amounts to about 0 mV. In our experiments with toluylene blue sometimes a much lower potential was reached (—150 mV or still lower after three hours), but a closer investigation showed that the attainment of this low redox potential occurs only when the used toluylene blue solution was not prepared shortly before use (see fig. 5). It is a well-known fact that toluylene blue (I) is easily transformed into neutral red (II), which has a very strongly negative E_0' (— 0·325 V at pH 7·0) [9]).

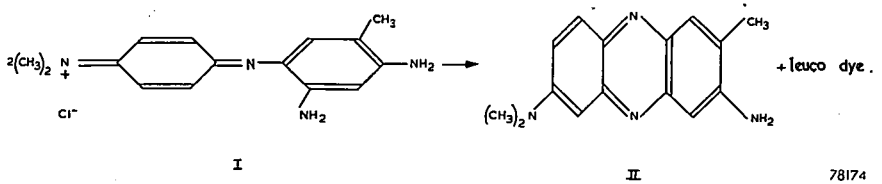

Hence it is conceivable that after the photochemical reduction of toluylene blue the redox potential of the system will drop if some leuco neutral red is present in the solution. That transformation of toluylene blue into neutral red actually takes place appears from the fact that the original blue colour of a solution of the dye in distilled water turns to red on being stored.

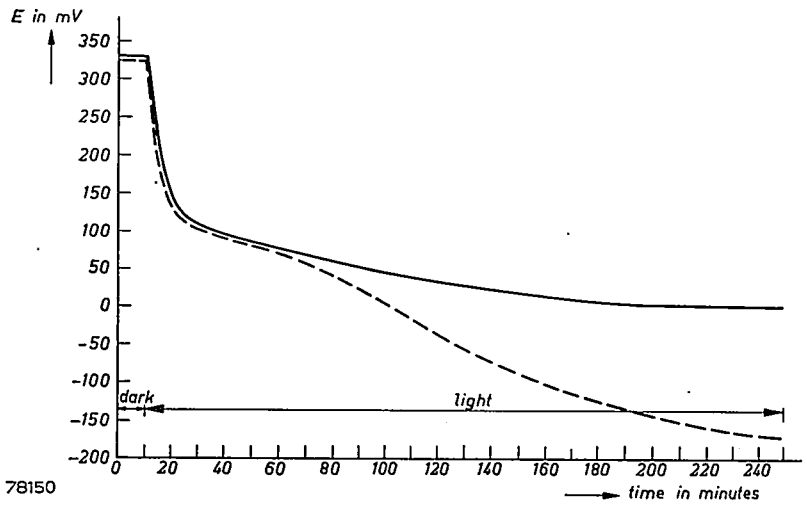

Fig. 5. Change of the redox potential as a function of time in the absence of oxygen for toluylene blue.
—— Toluylene blue solution prepared shortly before use.
------ Use of a toluylene blue solution which had been stored for a few days.

From a recent publication it appears that Macdowall [10]) also obtained a very low redox potential (— 239 mV) with toluylene blue. On account of the foregoing we think that the abnormally low potentials measured in long lasting experiments with this dye cannot simply be considered to indicate that redox substances with negative E_0' values also may be strongly reduced by chloroplasts.

As is obvious from table III all active quinones and dyes reach a final potential between 0 and 80 mV in an oxygen-free medium. The final potential, however, is usually attained after a longer lapse of time (one to three hours) than in the experiments where small amounts of oxygen are still present, particularly with redox systems having a high E_0'. This may be caused by the fact that the oxygen evolved in the Hill reaction is removed from the solution at a slow rate only. An alternative explanation may be that the highly reduced quinones and dyes are of such a small oxidation-reduction capacity that the redox potential of the system is determined more and more by natural components of the chloroplast suspension.

A very slow potential drop takes place with 2-hydroxy-1,4-naphthoquinone; only after three and a half hours appeared the potential of the system to be decreased to 100 mV. As the redox potential, however, still showed a very slow yet noticeable decrease, the final potential for this substance in any case is below 100 mV.

The fact that with indigotrisulfonate, 2,5-dihydroxybenzoquinone, 2-hydroxy-1,4-naphthoquinone and indigodisulfonate no negative final potentials are found indicates that these redox substances are reduced only to a very small degree by chloroplasts.

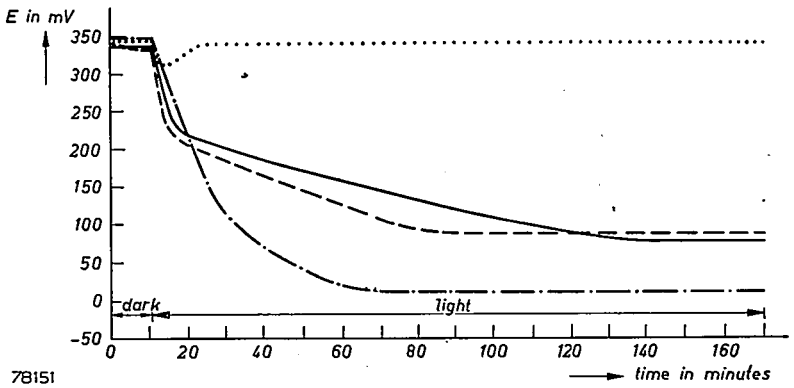

Fig. 6. Change of the redox potential as a function of time in the absence of oxygen for 2,6-dichlorophenol-indophenol (——), potassium- 1,4-naphthoquinone-2-sulfonate (------), indigotetrasulfonate (-·-·-·-·), and sodium-anthraquinone-2-sulfonate (.....). 6.10^{-5} M solution of the substance in 50 ml of 0·025 M phosphate buffer (pH = 6·5) + 2 ml of chloroplast suspension; temperature = 16 °C.

As characteristic examples of the change of the potential as a function of time in the absence of oxygen the curves for 2,6-dichlorophenol-indophenol, potassium-1,4-naphthoquinone-2-sulfonate, indigotetrasulfonate and sodium-anthraquinone-2-sulfonate are represented in fig. 6.

A relationship between the E_0' of a redox substance and its ability to undergo photochemical reduction by chloroplasts is thus also found "in the absence of oxygen". Although the final potential is lower under these conditions than in the presence of oxygen, we nevertheless observed no negative potentials so that an indication that redox substances with a very low E_0', e.g. D.P.N., are able to serve as true Hill reagents could not be found.

The experimental results mentioned will be discussed further in the following chapter.

Preparation of the investigated quinones and dyes

The following quinones and dyes have been synthesized by us. If the described procedure could be followed without alteration only a literature reference is given.

Tetrachloro-ortho-benzoquinone

C. Loring Jackson and R. D. Mac Laurin, Amer. chem. J. **37**, 11, 1907.
C. Loring Jackson and P. W. Carleton, Amer. chem. J. **39**, 496, 1908.

Tetrabromo-ortho-benzoquinone

C. Loring Jackson and W. Koch, Amer. chem. J. **26**, 35, 1901.
C. Loring Jackson and P. A. Shaffer, Amer. chem. J. **34**, 461, 1905.
C. Loring Jackson and H. A. Flint, Amer. chem. J. **39**, 83, 1908.

Potassium-benzoquinone-sulfonate

A description of the preparation of hydroquinone-sulfonate has been given by J. Pinnow, Z. Elektrochem. **21**, 387, 1915.

Potassium-benzoquinone-sulfonate was prepared from hydroquinone-sulfonate analogous to the synthesis of potassium-1,4-naphthoquinone-2-sulfonate according to Fieser.

1·4 g of potassium-hydroquinone-sulfonate is dissolved by heating in 5 ml of water and 0·1 ml of concentrated sulfuric acid. To the cooled mixture a solution of 750 mg of potassium dichromate in 0·56 ml of concentrated sulfuric acid and 2·2 ml of water is added at once. The quinone separates as yellow crystals. After the addition of 4 ml of a saturated KCl solution the product is filtered, washed, and suspended in saturated KCl solution. The suspension is stirred for some time and the benzoquinone-sulfonate collected and washed successively with saturated KCl solution, cold water, alcohol and ether.

3-Nitro-1,2-naphthoquinone

L. Fieser and M. A. Ames, J. Amer. chem. Soc. **49**, 2614, 1927.

Potassium-1,2-naphthoquinone-4-sulfonate

L. Fieser and M. Fieser, J. Amer. chem. Soc. **57**, 494, 1935.

1,2-Naphthoquinone

L. Fieser and M. Fieser, J. Amer. chem. Soc. **57**, 493, 1935.

Potassium-1,4-naphthoquinone-2-sulfonate

L. Fieser and M. Fieser, J. Amer. chem. Soc. **57**, 494, 1935.

Potassium-2,3-dichloronaphthoquinone-6-sulfonate

Claus, J. prakt. Chem. **37**, 181, 1888.

Potassium-phenanthrenequinone-2-sulfonate

Potassium-phenanthrene-2-sulfonate was prepared according to L. Fieser, J. Amer. chem. Soc. **51**, 2464, 1929.

3 g of this substance is suspended in 25 ml of acetic acid. While stirring a solution of 3 g of chromic acid in a minimum amount of water and 10 ml of acetic acid is added. The

mixture is heated slowly and boiled for some time. After cooling 35 ml of alcohol is added and the separated orange crystals are collected, washed with alcohol and dissolved in a little hot water. The hot solution is filtered and treated with a fifth of its volume of alcohol. On cooling, the potassium-phenanthrenequinone-2-sulfonate crystallizes as yellowish-orange, brilliant leaflets.

2,5-Dihydroxy-benzoquinone

R. G. Jones and H. A. Shonle, J. Amer. chem. Soc. **67**, 1034, 1945.

Potassium-6-nitro-anthraquinone-1-sulfonate

R. Schmidt, Ber. dtsch. chem. Ges. **37**, 67, 1904.

H. E. Fierz-David, Helv. chim. acta **10**, 206, 1927.

Potassium-3-nitro-2-hydroxy-naphthoquinone-6-sulfonate

Kehrmann, Ber. dtsch. chem. Ges. **21**, 1777, 1888.

500 mg of potassium-2,3-dichloronaphthoquinone-6-sulfonate is heated on the water-bath with a solution of 400 mg of KNO_2 in a water-alcohol mixture (1 : 1) untill all the quinone has dissolved (about one hour). On cooling, the solution solidifies as a result of the formation of yellowish-orange crystals. The product is collected, washed, and crystallized from aqueous alcohol several times. An analysis of the quinone showed the substance to contain 3·68% of nitrogen (computed 3·73%), whereas the percentage of chlorine appeared to be nil. *)

3-Nitro-2-hydroxynaphthoquinone

Diehl and Merz, Ber. dtsch. chem. Ges. **11**, 1317, 1878.

Chloranilic acid

Graebe, Liebigs Ann. **263**, 25, 1891.

Potassium-euthiochronate

Hesse, Liebigs Ann. **114**, 318, 1860.

C. Loring Jackson and S. A. Beggs, J. Amer. chem. Soc. **36**, 1214, 1914.

Indigomonosulfonate, indigodisulfonate, indigotrisulfonate and indigotetrasulfonate

W. P. Bloxam, J. Indian chem. Soc. **25**, 736, 1906.

Diphosphopyridine-nucleotide (D.P.N.)

G. A. Le Page, J. biol. Chem. **168**, 623, 1947.

The purity of the prepared D.P.N. was determined by measurement of the absorption of reduced D.P.N. at 340 mμ (Le Page).

In a 50 ml tube were brought successively 0·50 ml of distilled water, 1·25 ml of fresh 1% $NaHCO_3$ solution, 0·25 ml of a 1% solution of the D.P.N. preparation, and 0·50 ml of 3% $Na_2S_2O_4$ solution in 1% $NaHCO_3$. The solution was allowed to stand twenty minutes at room temperature, after which 22·5 ml of a 1% $NaHCO_3$-1% Na_2CO_3 solution was added to the mixture. The solution was aerated for ten minutes to remove excess of hydrosulfite. The extinction of the solution at 340 mμ was determined in a Beckmann spectrophotometer. A value of 0·597 was found, corresponding to 70% pure D.P.N.

REFERENCES

1) J. Franck, Arch. Biochem. Biophys. **45**, 190, 1953.
2) A. H. Mehler, Arch. Biochem. Biophys. **33**, 65, 1951.
3) W. Vishniac and S. Ochoa, J. biol. Chem. **198**, 501, 1952.
4) E. C. Wassink, J. E. Tjia and J. F. G. M. Wintermans, Proc. Kon. Acad. Wetensch. **52**, 412, 1949.
5) B. L. Strehler, Arch. Biochem. Biophys. **43**, 67, 1953.
6) W. Vishniac and S. Ochoa, Nature, Lond. **167**, 768, 1951.
7) D. I. Arnon, Nature, Lond. **167**, 1008, 1951.
8) L. J. Tolmach, Nature, Lond. **167**, 946, 1951.
9) M. Phillips, W. M. Clark and Barnett Cohen, Publ. Hlth Rep., Wash. 1927, Suppl. 61.
10) F. D. H. Macdowall, Science **116**, 398, 1952.

*) This analysis was performed by Mr P. J. Hubers at Amsterdam.

CHAPTER IV

KINETICS OF THE HILL REACTION

In chapter III we concluded that the primary formation of an intermediate hydrogen donor has to be considered as probable in the Hill reaction. The reaction scheme may be represented by the equations

$$X + H_2O \xrightarrow{h\nu} XH_2 + \tfrac{1}{2}O_2, \quad (1)$$

$$XH_2 + \tfrac{1}{2}O_2 \rightarrow X + H_2O, \quad (2)$$

$$XH_2 + \text{quinone} \rightarrow X + \text{hydroquinone}, \quad (3)$$

$$X + \text{hydroquinone} \rightarrow XH_2 + \text{quinone}. \quad (4)$$

Of course, reactions as indicated by (1) and (2) may actually be much more complicated and consist of a chain of several reaction stages.

The fact that for any substrate a constant final level of the redox potential is found indicates that a steady state *) is reached. As a simple explanation we may assume that one or several oxidation reactions take place in addition to the photochemical reduction of the added substrate. In the steady state the rates of oxidation and reduction are equal. Fig. 1 shows that reoxidation of the reduced component can clearly be observed when the photochemical reaction is stopped, for instance, by switching off the light or by adding the inhibitor o-phenanthroline.

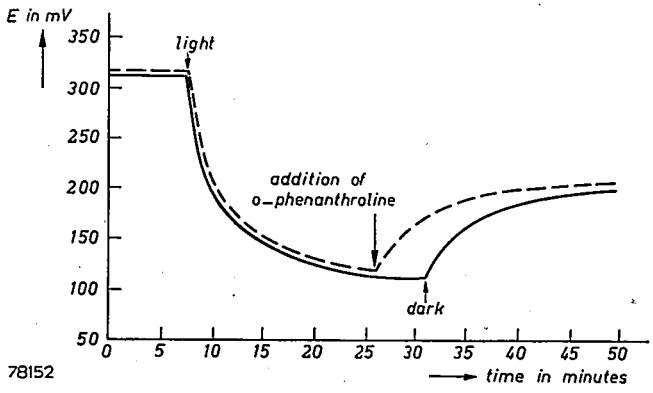

Fig. 1. Change of the redox potential upon switching off the light (——) or upon adding o-phenanthroline (------) after the photochemical reduction of toluylene blue by chloroplasts.

*) Under the simplifying assumptions indicated one might be tempted to use the term equilibrium with regard to the transformation of matter. The transformation of energy, however, certainly suggests the use of the expression "steady state".

The rise in potential in the dark after pre-illumination is greater and proceeds more rapidly as the concentration and the E'_0 of the redox compound are lower. That this increase in potential has to be attributed to reoxidation of the system by oxygen still present appears from the fact that the redox potential does not — or only slightly — increase upon exclusion of oxygen. In this connection the rate of the oxidation by oxygen was determined for a number of redox substances, by passing this gas through a 6.10^{-5} M solution of the hydroquinone or the leuco dye in 0·025 M phosphate buffer (pH 6·5), while at the same time measuring the redox potential. The preliminary reduction of the dye was performed with hydrogen, using palladium asbestos as a catalyst.

In accordance with the observation of Barron [1]), that the rate of the oxidation by oxygen usually is higher the lower the E'_0, redox substances with a low E'_0, like naphthohydroquinone and reduced toluylene blue, appeared to be quickly oxidized by oxygen. Redox systems with a high E'_0, such as hydroquinone, on the other hand, are slowly oxidized.

In an oxygen atmosphere, only substances with a very high E'_0, like benzoquinone and 2,6-dichlorophenol-indophenol, are photochemically reduced by chloroplasts to a measurable percentage. With 1,4-naphthoquinone, thionine, and toluylene blue no redox-potential drop can be observed; even potassium-1,4-naphthoquinone-2-sulfonate is reduced only to a very slight degree under these conditions. The lowest final potential observed in oxygen atmosphere amounts to about 230 mV. From this the great influence of oxygen upon the potential attainable by chloroplasts in vitro, to which attention was already drawn in the preceding chapter, is thus also obvious. In principle, therefore, we should take into account the direct oxidation of the reduced component by oxygen, according to the equation

$$\text{hydroquinone} + \tfrac{1}{2}\,O_2 \rightarrow \text{quinone} + H_2O\,. \qquad (5)$$

Because of the low concentration of oxygen in our experiments, however, the rate of this reaction will be considerably slower than if oxygen is passed through. This is particularly the case when the experiment is performed in an as much as possible oxygen-free medium. Reaction (5) proceeds then in fact only under the influence of the oxygen produced by the photochemical reaction. It can hardly be decided, beforehand, how far reaction (5) plays a part in the establishment of the steady state, as we know nothing about the relative rates of the reactions (2), (4) and (5).

We shall investigate now whether an interpretation of the kinetics of the Hill reaction is possible on the basis of the reaction scheme consisting of equations (1) to (5) inclusive.

The first reaction in this scheme, which results in the formation of

XH_2 and O_2, is undoubtedly oversimplified by equation (1). This equation has to be considered as the total result of a light reaction and of one or more dark reactions. The rate of reaction (1) is, in simple cases, determined by the slowest reaction stage. This is the light reaction at low light intensities, and it may be an enzymatic process at light saturation. Experimentally it appears that the rate of the Hill reaction is a linear function of the light intensity at low light intensities, whereas it reaches a constant ceiling value at high light intensities [2],[3]). In the former case the rate of reaction (1) may thus be represented by the equation

$$v_1 = k_1 I_{abs} \qquad (I_{abs} = \text{absorbed light intensity}).$$

In the latter case v_1 equals $k_1(E)$, in which (E) represents the concentration of the enzyme in the rate-determining reaction stage. The latter formulation is only exact, of course, if the rate is exclusively limited by the concentration of the enzyme. When the reaction rate is also determined by the concentration of the hydrogen acceptor acting as the substrate of the enzyme under consideration, it will be generally a function of the concentrations of enzyme and hydrogen acceptor, as is obvious from the Michaelis-Menten formula

$$v = \frac{k_3' k_1' (E)(S)}{k'(S) + k' + k_3'} = \frac{k_3' (E)(S)}{(S) + K}. \tag{6}$$

In this formula v represents the reaction rate of the enzymatic process

$$E(\text{enzyme}) + S(\text{substrate}) \underset{k_2'}{\overset{k_1'}{\rightleftarrows}} ES(\text{enzyme-substrate complex}) \xrightarrow{k_3'} E + \text{reaction products}.$$

Equation (6) reduces to $v = k_3' (E)$ only when $(S) \gg K$. When $(S) \ll K$, however, the reaction rate is represented by $v = k''(E)(S)$.

As the enzyme concentration (E) is proportional to the concentration of the chloroplasts in the Hill reaction, the formula $v_1 = k_1 (E)$ implies that the initial rate of the photochemical reduction of redox compounds with a high E_0' is a linear function of the chloroplast concentration at light saturation. Spikes et al. [4]) have actually shown that the reaction is first order in chloroplast concentration, which could be confirmed by us (see fig. 2).

As according to the formula $v_1 = k_1 (E)$ (X) (assuming X to act as the substrate of the enzyme), on the other hand, the initial rate should be a linear function of the square of the chloroplast concentration, it seems probable that the rate at light saturation is only determined by the concentration of the enzyme. The rate of reaction (1) may therefore be represented by the formula

$$v_1 = k_1 (E).$$

The steady state at light saturation will be determined by the equations

$$\frac{d(XH_2)}{dt} = k_1(E) - k_2(XH_2)\,(O_2)^{1/3} - k_3(XH_2)\,(q) + k_4(hq)\,(X) = 0 \qquad (7)$$

and $$\frac{d(hq)}{dt} = k_3(XH_2)\,(q) - k_4(X)\,(hq) - k_5(hq)(O_2)^{1/3} = 0. \qquad (8)$$

From equation (7) the following value for (XH_2) can be calculated

$$(XH_2) = \frac{k_1(E) + k_4(hq)\,(X)}{k_2(O_2)^{1/3} + k_3(q)}.$$

Substituting this value in equation (8) we find

$$\frac{k_1k_3\,(E)\,(q) + k_3k_4(q)\,(hq)\,(X)}{k_2(O_2)^{1/3} + k_3(q)} - k_4(X)\,(hq) - k_5(hq)\,(O_2)^{1/3} = 0,$$

$$k_1k_3(E)(q) - k_2k_4(X)\,(hq)\,(O_2)^{1/3} - k_2k_5(hq)\,(O_2) - k_3k_5(q)\,(hq)\,(O_2)^{1/3} = 0,$$

$$\frac{(q)}{(hq)} = \frac{k_2k_4\,(X)\,(O_2)^{1/3} + k_2k_5\,(O_2) + k_3k_5\,(q)\,(O_2)^{1/3}}{k_1k_3\,(E)}. \qquad (9)$$

The rate of reaction (1) at low light intensities may be represented by the equation

$$v_1 = k_1\,I_{abs}.$$

As our experiments were performed with highly diluted chloroplast suspensions the absorbed light intensity I_{abs} may be approximated by the term

$$I_{abs} = k\,I\,(Chlor).$$

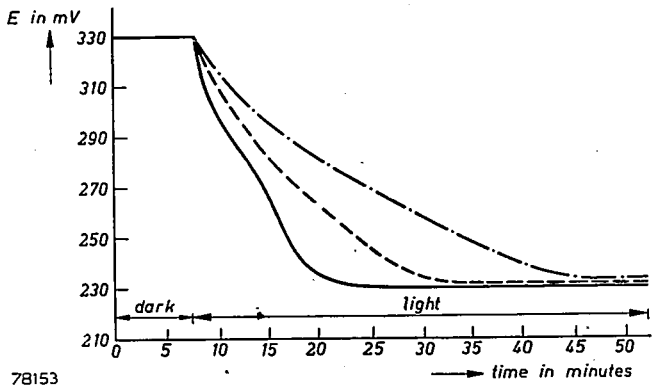

Fig. 2. Influence of the concentration of the chloroplasts upon the redox potential curve of 2,6-dichlorophenol-indophenol.
Ratio of the chloroplast concentrations 4 (——) : 2 (------) : 1 (·· ·· ··).

In this formula (Chlor) is the chlorophyll concentration.

If we substitute $v_1 = k_1 I\,(\text{Chlor})$ for $v_1 = k_1 (E)$ in the above calculation, the following formula is obtained for the steady state at low light intensities

$$\frac{(q)}{(hq)} = \frac{k_2k_4(\text{X})\ (\text{O}_2)^{1/2} + k_2k_5(\text{O}_2) + k_3k_5(q)\ (\text{O}_2)^{1/2}}{k_1k_3 I\ (\text{Chlor})}. \tag{10}$$

We can distinguish the following two limiting cases:

(a) The direct oxidation of hydroquinone by oxygen proceeds so slowly that it is negligible in comparison with the other oxidation reactions in the scheme.

The formulae (9) and (10) are reduced in this case to

$$\frac{(q)}{(hq)} = \frac{k_2k_4(\text{X})\ (\text{O}_2)^{1/2}}{k_1k_3\ (E)}, \tag{11}$$

and

$$\frac{(q)}{(hq)} = \frac{k_2k_4(\text{X})\ (\text{O}_2)^{1/2}}{k_1k_3 I\ (\text{Chlor})}. \tag{12}$$

(b) The direct oxidation of hydroquinone by oxygen proceeds much more rapidly than the oxidation via X. When the latter is neglected the steady state is determined by the equations

$$\frac{(q)}{(hq)} = \frac{k_2k_5(\text{O}_2) + k_3k_5(q)\ (\text{O}_2)^{1/2}}{k_1k_3(E)}, \tag{13}$$

and

$$\frac{(q)}{(hq)} = \frac{k_2k_5(\text{O}_2) + k_3k_5(q)\ (\text{O}_2)^{1/2}}{k_1k_3\ I\ (\text{Chlor})}. \tag{14}$$

As (X), (E), and (Chlor) are proportional to the chloroplast concentration, the degree of reduction of the substrate is, according to equations (13) and (14), strongly dependent on, and conversely, according to equations (11) and (12), independent of the concentration of the chloroplasts. Experimentally the final level of the redox potential does not appear to be influenced noticeably by the chloroplast concentration (see, for instance, figs 2 and 3). This may indicate that the direct oxidation of the hydroquinone (leuco dye) by oxygen proceeds slowly in comparison with the reactions (2) and (4).

From the formulae (9) to (14) inclusive it is obvious that the final level is dependent on the oxygen concentration and, at low light intensities, on the light intensity. The influence of the light intensity upon the rate and the final level of the photochemical reduction of 2,6-dichlorophenol-indophenol is represented in fig. 4.

With benzoquinone and thionine a similar influence of the light intensity upon the reduction rate and the final level of the redox potential was observed. In these experiments the light intensity was varied by means of filters.

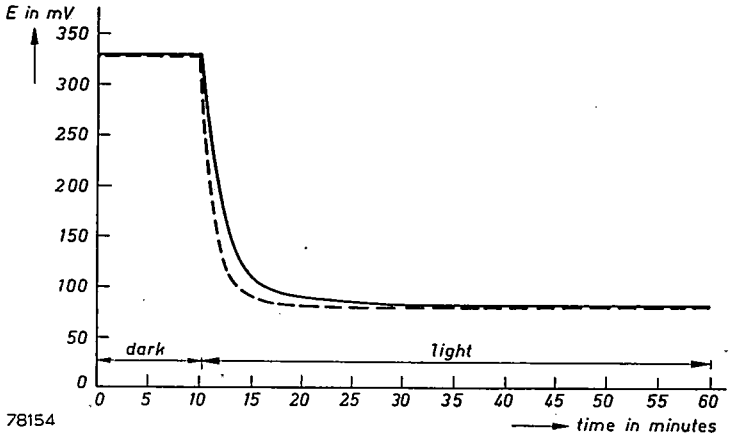

Fig. 3. Influence of the concentration of the chloroplasts upon the redox potential curve of thionine.
Ratio of the chloroplast concentrations 3 (------) : 1 (——).
This experiment was performed in the absence of oxygen.

The increase of the final potential under the influence of oxygen has already been mentioned in the preceding pages.

The relationship observed between the E_0' of the substrate and the

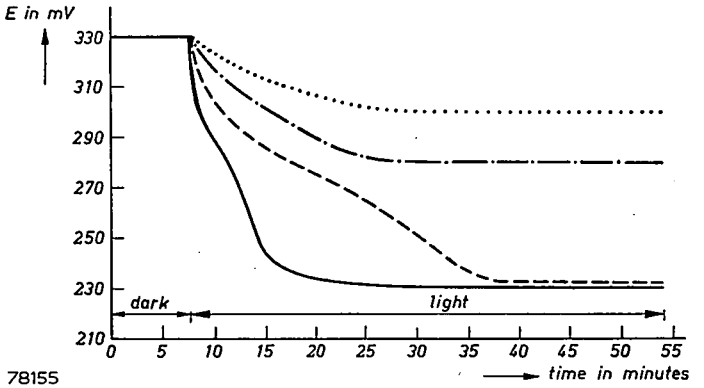

Fig. 4. Change of the redox potential as a function of time at various light intensities for 2,6-dichlorophenol-indophenol.
—— 15000 and 12000 lux, -·-·-·- 2300 lux,
------ 6000 lux, ... 900 lux.

photochemical reduction by chloroplasts can also be accounted for by the above formulae. Decrease of the E_0' of the substrate will usually result in a rise of the ratio k_4/k_3, consequently in a lower percentage of reduction.

Finally the reaction scheme under consideration implies that the initial rate of the photochemical reduction of redox substances with a not too low E_0' is independent of the substrate concentration, on account of the fact that back reactions then only become important towards the end of the reaction. Spikes, Lumry, Eyring and Wayrynen [4]) have shown that the rate of the Hill reaction with benzoquinone or ferricyanide as hydrogen acceptor is of zero order in substrate concentration. Our experiments showed that the rate of the reduction of 2,6-dichlorophenol-indophenol is also independent of the substrate concentration (see fig. 5). The E_0' of most other redox compounds could not be determined with sufficient precision to make a positive conclusion in this respect.

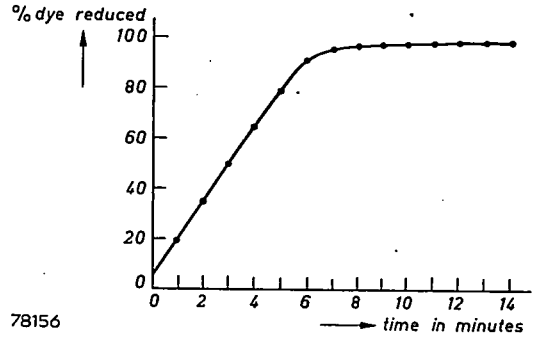

Fig. 5. % Reduction as a function of time for 2,6-dichlorophenol-indophenol.

The percentage of the oxidized component was determined from the formula

$$\% \text{ 2,6-dichlorophenol-indophenol} = \frac{100}{e^{\frac{2(E_0' - E)F}{RT}} + 1} = \frac{100}{e^{(E_0' - E).80 \cdot 316} + 1}.$$

In this formula E is the measured redox potential in volts.

The reasons why no drop of the potential is registered in the presence of a redox substance of E_0' very much lower than the potential attainable by the Hill reaction, may be:

(1) very rapid reoxidation of the substrate by O_2 (reaction (5));

(2) too low a concentration of the reduced compound in the redox system for imposing its potential on the electrode or for reducing other systems at a sufficient rate.

Fig. 6 shows that the influence of the temperature upon the initial rate of the Hill reaction is very small at light saturation, which points to a low activation energy.

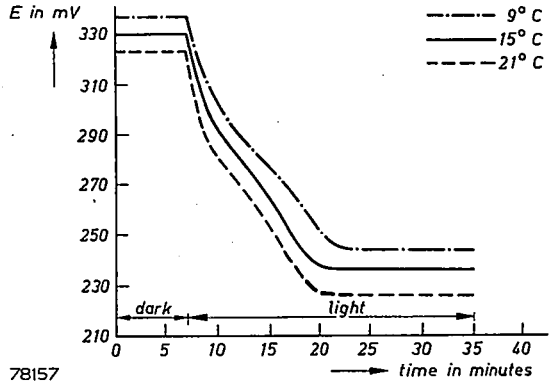

Fig. 6. Influence of the temperature upon the redox potential curve of 2,6-dichlorophenol-indophenol.
The rise of the initial and final level of the potential curve upon decreasing the temperature is probably caused chiefly by the dependence on temperature of the E_0.

From the formula

$$\ln \frac{k_A}{k_B} = \frac{E_a}{R}\left(\frac{1}{T_B} - \frac{1}{T_A}\right),$$

in which k_A/k_B represents the ratio of the reaction rates at the temperatures T_A and T_B, we calculate a value of 8-9·5 kcal for the activation energy E_a. A more precise determination of the activation energy is not possible in this way, since the difference in reduction rate at various temperatures is rather low. As is well known it is very risky to try to draw detailed conclusions from the value of the apparent energy of activation in the case of complicated biochemical reactions. Besides, one should take into account the fact that a decrease in activity of the chloroplasts occurs when raising the temperature, which results in an apparent lowering of the activation energy.

Concluding this chapter we can thus say that an interpretation of the kinetics of the Hill reaction is really possible on the basis of the proposed reaction scheme. This does not imply, of course, that this undoubtedly simplified scheme has actually to be considered the correct one, as more reaction schemes may certainly be set up which are in accordance with the kinetics of this reaction. The assumption that an intermediate hydrogen donor is first formed in the Hill reaction is considerably supported, however, by the fact that this view leads also kinetically to satisfactory results.

REFERENCES

1) E. S. G. Barron, J. biol. Chem. **97**, 287, 1932.
2) A. S. Holt and C. S. French, in Photosynthesis in plants, ed. by J. Franck and W. E. Loomis; Iowa State College Press, 1949.
3) K. A. Clendenning and H. C. Ehrmantraut, Arch. Biochem. **29**, 387, 1950.
4) J. D. Spikes, R. Lumry, H. Eyring and R. E. Wayrynen, Arch. Biochem. **28**, 48, 1950.

CHAPTER V

INHIBITORS AND ACTIVATORS

In this chapter a survey is given of the results of an investigation, by means of redox potential measurements, into the influence upon the Hill reaction of

(1) inhibitors and other enzyme poisons,
(2) metal ions and biochemically important compounds such as riboflavin, adenosine triphosphate (A.T.P.), dehydroascorbic acid, etc.,
(3) washing of the chloroplasts,
(4) nature and *pH* of the buffer.

1. Inhibitors and other enzyme poisons

It has already been mentioned in the introduction that unanimity about the active concentrations of various inhibitors does not exist, whereas in some cases a different opinion is found even on the question of whether or not a certain compound is an inhibitor. The redox potentiometric method is also of great value for the investigation of inhibition, as with complete inhibition no, and with partial inhibition only a slow and small potential drop is observed. As a characteristic example the influence of o-phenanthroline upon the redox potential curve of 2,6-dichlorophenol-indophenol is represented in fig. 1.

The following inhibitors, most of which belong to the so-called metal poisons and some to the narcotics (phenylurethane and thymol), have been investigated:

o-Phenanthroline

The photochemical reduction of benzoquinone and 2,6-dichlorophenol-indophenol is inhibited to a different degree by the same concentration of o-phenanthroline. Whereas a concentration of 6.10^{-5} M o-phenanthroline is able to inhibit the reduction of 2,6-dichlorophenol-indophenol almost completely, generally a six to tenfold concentration of this compound is required for the inhibition of the photochemical reduction of benzoquinone.

This is presumably connected with the fact that reduced 2,6-dichlorophenol-indophenol, on account of its lower redox potential, is oxidized at greater speed than hydroquinone. The activity of the chloroplasts can be restored completely by the addition of 10^{-3} M $ZnSO_4$, $CoSO_4$ or $NiSO_4$, also during the exposure to light, but not by $MnSO_4$, $CaCl_2$ or $MgCl_2$.

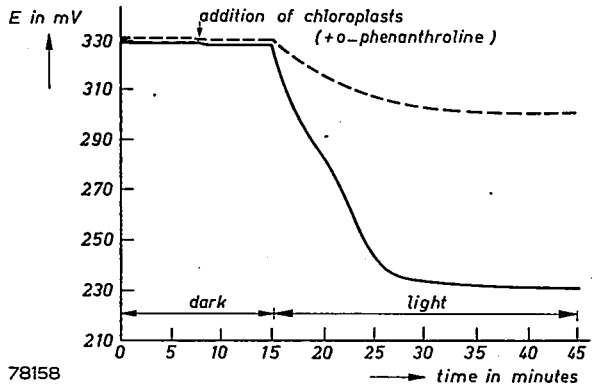

Fig. 1. Change of the redox potential as a function of time for 2,6-dichlorophenol-indophenol with (------) and without (——) addition of 6.10^{-5} M o-phenanthroline.

To investigate whether the inhibition by o-phenanthroline is really due to a chelate formation with zinc ions, as is postulated by Warburg and Lüttgens [1]), isolated chloroplasts were well shaken with an excess of saturated o-phenanthroline solution, centrifuged, and washed a few times with phosphate buffer. After that the photochemical activity was compared with the activity of chloroplasts which had been washed the same number of times, but had not been treated with o-phenanthroline. The activity of both chloroplast suspensions (measured with benzoquinone and 2,6-dichlorophenol-indophenol) now appeared to be practically the same, so that lowering of the concentration of free zinc ions by o-phenanthroline can hardly be the cause of the inhibitory effect. Presumably specific adsorption of o-phenanthroline on an active spot of an enzyme surface (e.g. by combination with a metal bound to the enzyme) occurs. This view is supported by the fact that other compounds related to o-phenanthroline, like α, α'- dipyridyl and 3,3'-dimethyl-2,2'-dipyridyl, which also form chelates with metal ions, do not inhibit the Hill reaction even in saturated solution. The stimulating action of 10^{-3} M complexon (ethylenediamine-tetra-acetic acid), a very strong chelating agent, is also remarkable in this connection. That the metal which may combine with o-phenanthroline need not be zinc, appears from the above-mentioned fact that in addition to $ZnSO_4$, $CoSO_4$ and $NiSO_4$ are also able to restore the activity

of the chloroplasts. p-Phenanthroline, which contrary to o-phenanthroline does not form chelates with metals, is unable to inhibit the photochemical reduction of benzoquinone or 2,6-dichlorophenol-indophenol.

2,4-Dinitrophenol

The photoreduction of benzoquinone and 2,6-dichlorophenol-indophenol is inhibited completely by 6.10^{-3} M 2,4-dinitrophenol whereas a concentration of 6.10^{-4} M, in full accordance with the results obtained by Macdowall [2]), causes only a partial inhibition. Once again the inhibition is found to be stronger for 2,6-dichlorophenol-indophenol than for benzoquinone. 2,4-Dinitrophenol is supposed to uncouple phosphate metabolism in general.

Phenylurethane

According to Arnon and Whatley [3]) and Macdowall [2]) the Hill reaction is inhibited to 50% by 2.10^{-4} M and 2.10^{-3} M phenylurethane respectively. Aronoff [4]), on the contrary, has not observed complete inhibition of the photoreduction even in a saturated solution. From redox potential measurements it appears that 3.10^{-3} M phenylurethane does not inhibit the reduction of benzoquinone completely. The photoreduction of 2,6-dichlorophenol-indophenol is inhibited completely by 3.10^{-3} M phenylurethane and to about 50% by 3.10^{-4} M phenylurethane.

8-Oxyquinoline

The slight inhibition of the Hill reaction by a saturated solution of 8-oxyquinoline ($2{\cdot}2.10^{-3}$M), observed by Macdowall [2]), has been confirmed by us. This inhibition cannot be reversed by the addition of $ZnSO_4$.

Sodium fluoride

The inhibition by fluoride, reported by French et al. [5]), is contradicted by Aronoff [4]) and Clendenning and Gorham [6]). The reduction of benzoquinone and 2,6-dichlorophenol-indophenol does not really appear to be inhibited by NaF. A slight slowing down of the reduction of 2,6-dichlorophenol-indophenol occurs only at a concentration of 0·1 M NaF.

Thymol

The photoreduction of benzoquinone is inhibited almost completely by 3.10^{-3} M thymol. That of 2,6-dichlorophenol-indophenol is inhibited completely by 3.10^{-3} M and partially by 10^{-3}M thymol, which is in accordance with the results of Macdowall [2]).

Iodoacetamide

Iodoacetamide does not appear to inhibit the Hill reaction even at a concentration of 0·03 M.

Potassium cyanide

In accordance with the results of other investigators we did not observe inhibition of the Hill reaction by 0·01 M KCN.

Sodium azide

The results of various investigators and their methods of measuring activity are briefly summarized in table I.

TABLE I

Inhibition of the Hill reaction by sodium azide

	inhibition	method of measuring activity
Aronoff [4])	no inhibition	manometric oxygen determination with benzoquinone
Hill [7])	no inhibition	ferric oxalate-hemoglobin method
Macdowall [2])	50% inhibition by 0·08 M NaN_3	photometric measurement of dye reduction
Clendenning and Gorham [6])	10^{-3} M NaN_3 inhibits the photochemical reduction of ferric oxalate-ferricyanide and benzoquinone to a different degree	manometric oxygen determination with (a) benzoquinone (b) ferric oxalate-ferricyanide
Arnon and Whatley [3])	50% inhibition by 8.10^{-4}M NaN_3. Gradual increase of the inhibition with increasing concentration of the azide; the initial rate is only slightly influenced	manometric oxygen determination with benzoquinone

Addition of sodium azide to a (chloroplast-free) benzoquinone solution causes a strong redox potential drop and browning of the solution, from which we can conclude the occurrence of a reaction between both compounds. The redox potential of a 6.10^{-5} M benzoquinone solution in phosphate buffer after the addition of various amounts of sodium azide is given in table II.

TABLE II

Redox potential of a 6.10^{-5} M benzoquinone solution in 0·025 M phosphate buffer (*pH* 6·5) after the addition of sodium azide.

concentration of sodium azide	redox potential
0	395 mV
6.10^{-4} M	390 mV
6.10^{-3} M	350 mV
6.10^{-2} M	250 mV

The *pH* of the benzoquinone solution was not altered by sodium azide. At the lower concentrations of sodium azide (6.10^{-4} and 6.10^{-3} M) a complete inhibition of the photoreduction of benzoquinone does not occur, as in this case a distinct potential drop is still observed upon illumination in the presence of chloroplasts. The photochemical reduction of 2,6-dichlorophenol-indophenol, on the contrary, can also be observed in the presence of higher concentrations of NaN_3 as with this compound no reaction takes place, as appears from the fact that addition of sodium azide to a chloroplast-free solution of the dye does not cause a potential drop. The photoreduction of 2,6-dichlorophenol-indophenol is not inhibited by 6.10^{-4} M, only partially inhibited by 6.10^{-3} M, and completely inhibited by 6.10^{-2} M NaN_3.

The inhibition of the photochemical reduction of benzoquinone by rather low concentrations of sodium azide and the gradual increase of this inhibition with the concentration of the azide, reported by Arnon and Whatley [3]), have probably to be attributed to reaction of the azide with the quinone, causing a lower oxygen evolution in the manometric determinations.

Hydroxylamine

The opinions about the influence upon the Hill reaction of hydroxylamine, which is supposed to inhibit enzymes containing essential carbonyl groups, are also controversial. Whereas Hill [7]) and Aronoff [4]) have not found any effect, Macdowall [2]) and Arnon and Whatley [3]) observed 50%

inhibition at a concentration of 3.10^{-4} M and 2.10^{-4} M NH_2OH respectively. Clendenning and Gorham [6]) report inhibition of the photochemical reduction of benzoquinone, but not of ferric oxalate-ferricyanide, by 10^{-3} M NH_2OH.

Just like sodium azide however, hydroxylamine also reacts with benzoquinone. Moreover, this compound is able to reduce 2,6-dichlorophenol-indophenol and potassium ferricyanide. The redox potential of a 6.10^{-5} M solution of either of these substrates in phosphate buffer (pH 6·5) drops considerably after the addition of $NH_2OH.HCl$ (6.10^{-4} M), whereas the pH remains practically constant. 2,6-Dichlorophenol-indophenol is quickly decolorized upon addition of hydroxylamine. The reduction involves probably the formation of N_2O, according to the equation

2,6-dichlorophenol-indophenol + $NH_2OH \rightarrow$ leuco - 2,6 - dichlorophenol-indophenol + $^1/_2$ N_2O + $\frac{1}{2}$ H_2O.

For that reason a redox substance with a low E_0', which cannot be reduced by NH_2OH, is needed for the detection of inhibition by hydroxylamine. Neither reduction of toluylene blue nor oxidation of the reduced dye was observed upon addition of NH_2OH, so that this compound enables the influence upon the Hill reaction of hydroxylamine to be investigated. The photochemical reduction of toluylene blue by chloroplasts is inhibited strongly, although not completely, by 6.10^{-4} M NH_2OH. Hydroxylamine has thus to be considered as an inhibitor for this reaction. That Hill and Aronoff did not find an influence upon the Hill reaction of hydroxylamine and sodium azide may be due to the fact that they have used too low concentrations of these substances.

Summarizing we come to the conclusion that the discrepancies in the literature have their origin mainly in the use of different substrates and in the lack of attention given to the concentrations at which the various substances were tested on their inhibitory effect.

Besides the inhibitors for which data already were reported in the literature, the following substances have been investigated concerning their influence upon the Hill reaction: sulfanilamide, nicotinic acid, p-chloromercuribenzoate, p-aminophenyldichlorarsine, chloromycetin, penicillin, streptomycin, sodium nitrite and phthiocol.

The photochemical reduction of benzoquinone and 2,6-dichlorophenol-indophenol is not inhibited by 6.10^{-4} M p-chloromercuribenzoate or 6.10^{-4} M p-aminophenyldichlorarsine. This, added to the observation that iodoacetamide is not an inhibitor either, indicates that the activity of the enzymes functioning in the Hill reaction does not depend upon free sulphydryl groups.

The photochemical reduction of 2,6-dichlorophenol-indophenol is

inhibited partially, that of benzoquinone only to a slight degree, by 3.10^{-2} M sodium nitrite. Phthiocol (6.10^{-5} M) inhibits only the photoreduction of 2,6-dichlorophenol-indophenol. Chloromycetin and penicillin have no inhibitory influence upon the Hill reaction at a concentration of 10^{-3} M, while the other compounds investigated have no influence even at a concentration of 10^{-2} M.

2. Influence of metal ions and biochemically important compounds

The photochemical reduction of benzoquinone is accelerated by $ZnSO_4$(10^{-3} M), but this compound does not affect the reduction of 2,6-dichlorophenol-indophenol. $MnSO_4$(10^{-3} M), on the contrary, accelerates both the reduction of benzoquinone and that of 2,6-dichlorophenol-indophenol. $MgCl_2$(10^{-3}M) has practically no influence upon the reduction rate of both these substances, whereas $CaCl_2$ (10^{-3} M) accelerates the photoreduction of benzoquinone but has no influence in the case of 2,6-dichlorophenol-indophenol. $CuSO_4$ already inhibits the Hill reaction at a concentration of 10^{-4} M, $HgCl_2$ even at a still lower concentration (10^{-5} to 10^{-6} M). The influence of the metal ions upon the Hill reaction appears to be independent of the origin and the activity of the chloroplasts.

Biochemically important compounds like oxidized glutathione, dehydroascorbic acid, riboflavin, D.P.N., dihydroxyphenylalanine (all at a concentration of 6.10^{-5} M) and adenosine triphosphate (6.10^{-4} and 6.10^{-5} M) do not affect the photochemical reduction of benzoquinone and 2,6-dichlorophenol-indophenol. We were thus unable to demonstrate a function of one of these compounds in the Hill reaction in this way.

After illumination of chloroplasts with oxidized glutathione, dehydroascorbic acid or D.P.N., no reduction of benzoquinone or 2,6-dichlorophenol-indophenol was observed in the dark. These compounds are apparently not present in the reduced state immediately after illumination. Disregarding the possibility of extremely rapid reoxidation we can conclude that they are not reduced by illuminated chloroplasts to an appreciable degree.

3. Washing of the chloroplasts

Chloroplasts frequently washed with phosphate buffer show a low activity, especially with respect to the photochemical reduction of 2,6-dichlorophenol-indophenol. The activity can be restored by the addition of the washing liquid when using benzoquinone as hydrogen acceptor, but not when 2,6-dichlorophenol-indophenol is used. Noteworthy is the fact that the slightly green-coloured washing liquid itself is also able to reduce benzoquinone in the light; 2,6-dichlorophenol-indophenol is reduced to a less extent. $ZnSO_4$(10^{-3} M) accelerates the photochemical reduction of benzoquinone by the second and third washing liquid, but does not affect

the rate of the reduction by the first one. The reduction of 2,6-dichlorophenol-indophenol by the various washing liquids is not affected by $ZnSO_4$.

That, inter alia, a reducing compound is removed by washing, appears from the fact that benzoquinone and 2,6-dichlorophenol-indophenol are partially reduced by once-washed chloroplasts, the first washing liquid, and especially by the supernatant of the centrifugation of the chloroplasts, already in the dark. It is a question whether this reducing agent has to be considered as an essential factor in the Hill reaction or as an impurity belonging to the cytoplasm.

Frequently washed chloroplasts are not activated by the addition of dehydroascorbic acid, oxidized glutathione or D.P.N., so that the inactivation occurring on washing cannot be exclusively attributed to a removal of one of these compounds.

4. Influence of the buffer

A comparison of the rate of reduction of benzoquinone and 2,6-dichlorophenol-indophenol by chloroplasts treated with and suspended in phosphate, borax, and citrate buffer (*pH* 6·5), showed chloroplasts to be most active when they are washed with and stored in 0·2 M borax buffer (boric acid + borax + 1/20 M NaCl), while the activity is also maintained for a longer time in this buffer. Chloroplasts stored in phosphate buffer (as usual containing 0·25 g of KCl per litre) show the same activity whether the measurement is carried out in borax or in phosphate buffer. The difference in activity between both buffers is obviously not due to an accelerating action of borax or boric acid, but to the fact that the activity of the chloroplasts is maintained better in borax buffer. KH_2PO_4(0·025 M) has rather a retarding than an accelerating influence upon the reduction of benzoquinone and 2,6-dichlorophenol-indophenol by chloroplasts stored in borax buffer, even when the chloroplasts are frequently washed with borax buffer. Phosphate is apparently either not required in the Hill reaction, or is still available in sufficient amounts in the washed chloroplasts.

Chloroplasts are very slightly active if they are washed with and stored in 0·1 M citrate buffer (secondary sodium citrate + NaOH; *pH* 6·5), and the activity cannot be enhanced by the addition of 0·025 M KH_2PO_4 or KCl. However, the chloroplasts appear to be fairly active if some KCl or NaCl (0·025 M) has previously been added to the citrate buffer. Also in that case, however, rather a retarding than an accelerating influence of KH_2PO_4 (0·025 M) upon the photoreduction is found.

The important part played by chloride ions, reported by Warburg and Lüttgens [1]), could thus be confirmed, but we cannot support their assumption that the chloride ion is a coenzyme of photosynthesis. Our results indicate that chloride ions do not enhance the activity of a chloroplast

suspension but retard the inactivation of the chloroplasts. That chloride ions may exert some protective action on the chloroplasts has already been suggested by Arnon and Whatley [8]).

Regarding the influence of the *pH* we found that the reduction rate of 2,6-dichlorophenol-indophenol and thionine is lower at *pH* 6·0 and considerably lower at *pH* 7·5 than at *pH* 6·5; with benzoquinone a smaller difference is found. Further the total redox potential drop of thionine at *pH* 7·5 appears to be also considerably smaller than at *pH* 6·5.

The following compounds used in this investigation have been synthesized by us:
p-Chloromercuribenzoate
via sodium-p-toluenesulfinate and p-tolylmercurichloride,
Org. Synth., Coll. Vol. I, 159.
p-Aminophenyldichlorarsine
via arsanilic acid,
Org. Synth., Coll. Vol. I, 70,
A. J. Quick and R. Adams, J. Amer. chem. Soc. **44**, 815, 1922.
Iodoacetamide
via chloroacetamide,
Org. Synth., Coll. Vol. I, 153,
O. M. Friedman and A. M. Rutenburg, J. Amer. chem. Soc. **72**, 3285, 1950.
p-Phenanthroline
C. R. Smith, J. Amer. chem. Soc. **52**, 397, 1930.
3,3'-Dimethyl-2,2'-dipyridyl
via α-amino-β-picoline and α-bromo-β-picoline,
O. Seide, Ber. dtsch. chem. Ges. **57B**, 1802, 1924,
F. H. Case, J. Amer. chem. Soc. **68**, 2574, 1946.
Oxidized glutathione
L. W. Mapson and D. R. Goddard, Biochem. J. **49**, 592, 1951.
Dehydroascorbic acid
L. W. Mapson and M. Ingram, Biochem. J. **48**, 552, 1951.

ACKNOWLEDGEMENT

The author is much indebted to Professor Dr E. Havinga for his guidance and advice at all times, and to Dr R. van der Veen, Dr J. de Jonge, Dr P. Massini and Dr L. A. Æ. Sluyterman for stimulating discussions and suggestions. Thanks are also due to Mr P. van Dijk and Mr M. Schenk who prepared some of the investigated compounds, and to Mr J. Lupinski, who performed the polarographical measurements.

Eindhoven, January 1954

REFERENCES

1) O. Warburg and W. Lüttgens, Biochemistry, Leningr. **11**, 303, 1946.
2) F. D. H. Macdowall, Plant Physiol. **24**, 462, 1949.
3) D. I. Arnon and F. R. Whatley, Arch. Biochem. **23**, 141, 1949.
4) S. Aronoff, Plant Physiol. **21**, 393, 1946.
5) C. S. French, A. S. Holt, R. D. Powell and M. L. Anson, Science **103**, 505, 1946.
6) K. A. Clendenning and P. R. Gorham, Canad. J. Res. **C 28**, 78, 1950.
7) R. Hill, Proc. roy. Soc. **B 127**, 192, 1939.
8) D. I. Arnon and F. R. Whatley, Science **110**, 554, 1949.

SPONTANEOUS MAGNETIZATION AS A FUNCTION OF TEMPERATURE FOR MIXED CRYSTALS OF FERRITES WITH SEVERAL CURIE TEMPERATURES

by K. F. NIESSEN 538.24:549.731.11:538.662.13

Summary

For mixed crystals of ferrites with more than one Curie temperature it is shown by an example how the spontaneous magnetization can be calculated as a function of temperature.

Résumé

Un exemple montre comment il est possible de calculer l'aimantation spontanée en fonction de la température pour des cristaux mixtes de ferrites avec plusieurs températures de Curie.

Zusammenfassung

Mit einem Beispiel wird gezeigt, wie der Verlauf der spontanen Magnetisierung für Ferrit-Mischkristalle mit mehreren Curie-Temperaturen, berechnet werden kann.

1. Introduction

Yafet and Kittel [1]) have predicted the existence of more than one Curie temperature for a spinel structure containing only one kind of magnetic ions. They expressed these Curie temperatures in some basic coefficients which play a role in Néel's [2]) theory of antiferromagnetism. The possibility of more than one Curie temperature was a consequence of the lattice of (tetrahedral) A sites and that of (octahedral) B sites each being composed of two sublattices (A_{I}, A_{II} and B_{I}, B_{II} respectively). Between these sublattices A_{I} and A_{II} and also between B_{I} and B_{II} the same kind of antiferromagnetic interaction exists as between an A and a B sublattice. When calculating the molecular magnetic fields the AB interaction is taken into account by means of a term containing the interaction coefficient n whereas the $A_{\mathrm{I}}A_{\mathrm{II}}$ and the $B_{\mathrm{I}}B_{\mathrm{II}}$ antiferromagnetic interactions are accounted for by a term containing $|\alpha_2|n$ and $|\gamma_2|n$ respectively. The coefficient n is taken positive (owing to a later choice for positive directions for partial magnetizations) and $|\alpha_2|$ and $|\gamma_2|$ are the absolute values of negative coefficients α_2 and γ_2 which in some respects may be called demagnetization coefficients.

The coefficient $|\alpha_2|$ is to be distinguished from an analogous coefficient $|\alpha_1|$ which is used in the expression for the $A_{\mathrm{I}}A_{\mathrm{I}}$ interaction and also for the $A_{\mathrm{II}}A_{\mathrm{II}}$ interaction. In the same manner $|\gamma_2|$ is different from the coefficient $|\gamma_1|$ which must be introduced for the $B_{\mathrm{I}}B_{\mathrm{II}}$ and the $B_{\mathrm{II}}B_{\mathrm{II}}$

interactions. Therefore α_1 and γ_1 resemble demagnetization coefficients still better than α_2 and γ_2.

To show the use of all these coefficients we will calculate the molecular field h_{aI} for an ion of the sublattice A_I. Besides n, α_1, α_2, γ_1 and γ_2 we still need the number (λN) of magnetic ions on A sites and the number (μN) of the same kind of magnetic ions on B sites in one "grammole", N being Avogadro's number. These ions are assumed to be distributed equally over the sublattices ($\frac{1}{2}\lambda N$ on both A_I and A_{II} and $\frac{1}{2}\mu N$ on both B_I and B_{II}).

The spontaneous magnetization brought about by N magnetic ions of the $A_I(A_{II})$ sublattice is called $I_{asI}(I_{asII})$ and that originating from N ions in $B_I(B_{II})$ will be called $I_{bsI}(I_{bsII})$.

If I_{asI} and I_{asII} are parallel we assume them to be directed toward the left and I_{bsI} and I_{bsII} (if parallel) directed toward the right. Analogous assumptions will be made for the molecular fields h_{aI}, h_{aII}, h_{bI}, h_{bII} at an ion of A_I, A_{II}, B_I, B_{II} respectively.

In the case $I_{asI}//I_{asII}$ and $I_{bsI}//I_{bsII}$ the role of the coefficients is shown in

$$\begin{aligned} h_{aI} &= n\tfrac{1}{2}\mu I_{bsI} + n\tfrac{1}{2}\mu I_{bsII} - |\alpha_2| n\tfrac{1}{2}\lambda I_{asII} - |\alpha_1| n\tfrac{1}{2}\lambda I_{asI}, \\ h_{bI} &= n\tfrac{1}{2}\lambda I_{asI} + n\tfrac{1}{2}\lambda I_{asII} - |\gamma_2| n\tfrac{1}{2}\mu I_{bsII} - |\gamma_1| n\tfrac{1}{2}\mu I_{bsI}. \end{aligned} \tag{1}$$

We did not use different symbols to distinguish the vectors I_{asI}, I_{bsI}, h_{aI}, etc., from their absolute values, the latter being meant in the above equations. In equations these symbols will always mean absolute values. The first two terms in the right-hand members originate from the antiferromagnetic AB interaction, the last two from the "demagnetizing" action in the A lattice or B lattice.

According to Yafet and Kittel the spin directions in A_I and A_{II} may be the same but they may also differ from one another (the angle between I_{asI} and I_{asII} then being called 2φ). The spin directions in B_I and B_{II} need not always be the same either: there may also be an angle 2ψ between I_{bsI} and I_{bsII} *). Since I_{asI}, of course, always points into the direction of h_{aI} and I_{asII} into that of h_{aII} (the same holding for I_{bsI} and h_{bI} and for I_{bsII} and h_{bII}), the same angles 2φ and 2ψ will exist between the directions of h_{aI} and h_{aII} and between h_{bI} and h_{bII} respectively, as has been indicated separately in fig. 1. The relations between the molecular fields and the partial magnetizations in the case $\varphi>0$, $\psi>0$ will be more complicated than the equations (1) holding for the case $\varphi = \psi = 0$. Since the magnetic contribution (if antiferromagnetic) of a partial magnetization to some molecular field is always antiparallel to this partial magnetization we have in fig. 1 where $\varphi > 0$, $\psi > 0$:

*) The angles here called φ and ψ are not the same as those indicated by φ and ψ by Yafet and Kittel [1]).

$$h_{aI} = n\tfrac{1}{2}\mu I_{bsI}\cos(\psi+\varphi) + n\tfrac{1}{2}\mu I_{bsII}\cos(\psi-\varphi) - \\ - |\alpha_2|\, n\tfrac{1}{2}\lambda I_{asII}\cos 2\varphi - |\alpha_1|\, n\tfrac{1}{2}\lambda I_{asI},$$

$$h_{bI} = n\tfrac{1}{2}\lambda I_{asI}\cos(\psi+\varphi) + n\tfrac{1}{2}\lambda I_{asII}\cos(\psi-\varphi) - \\ - |\gamma_2|\, n\tfrac{1}{2}\mu I_{bsII}\cos 2\psi - |\gamma_1|\, n\tfrac{1}{2}\mu I_{bsI}.$$

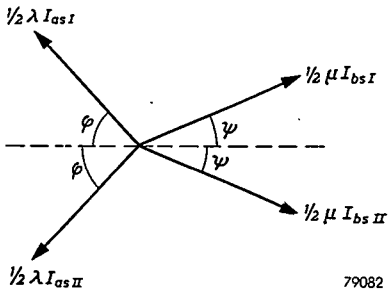

Fig. 1. Partial magnetizations in the sublattices A_{I}, A_{II}, B_{I} and B_{II}.

It may also occur that for instance the sublattices A_{I} and A_{II} are spontaneously magnetized but the sublattices B_{I} and B_{II} not yet ($I_{bsI} = I_{bsII} = 0$) or vice versa. In this way, according to Yafet and Kittel, several Curie points may be found where some ordering effect or some change in the ordering of spins occurs. These authors for instance considered a very interesting but complicated case where the highest Curie temperature (T_1) was given by the first occurrence of the spontaneous magnetization of the ions on A_{I} and A_{II} (with $\varphi = \pi/2$), the spins of the ions on B_{I} and B_{II} remaining still unordered. For this temperature they found

$$T_1 = Cn\tfrac{1}{2}\lambda(|\alpha_2| - |\alpha_1|), \tag{2}$$

where C is a constant defined by

$$C = Ng^2\mu_{\mathrm{B}}^2\, j(j+1)/3k, \tag{3}$$

μ_{B} being the Bohr magneton, k the Boltzmann constant and g and j the gyromagnetic ratio and the inner quantum number of the magnetic ion.

In this example the spontaneous magnetization of the ions on B_{I} and B_{II} took place at a lower temperature

$$T_2 = Cn\mu(1/|\alpha_2| - |\beta|) < T_1$$

with the abbreviation

$$|\beta| = \tfrac{1}{2}(|\gamma_1| + |\gamma_2|),$$

and the partial magnetizations I_{bsI} and I_{bsII} (born at $T = T_2$ and increasing with decreasing temperature) were parallel ($\psi = 0$). Their antiferromagnetic action on the A lattice caused the vectors I_{asI} and I_{asII} to

turn more and more to the left (φ became $<\pi/2$) and at a temperature T_3 which could be found only in a graphical way the value $\varphi = 0$ was attained. In the whole interval $T_2 > T > T_3$ ψ remained zero. These values, $\varphi = \psi = 0$, for the first time occurring together at T_3, remained undisturbed for somewhat lower temperatures but not for very low temperatures since Yafet and Kittel assumed the basic coefficients (including λ and μ) to make $\varphi = 0$ but $\psi > 0$ at $T = 0$. The lowest temperature (T_4) at which both φ and ψ were still zero could be found from the basic coefficients only by means of a graphical solution. In the last interval $T_4 > T > 0$ the angle φ remained zero whereas ψ increased from 0 to arccos $(\lambda/\mu|\gamma_2|)$ at $T = 0$.

This example of Yafet and Kittel considered mathematically for the case of one kind of magnetic ions only will be extended in the present paper to the case of two kinds of magnetic ions (M and M′) of which one kind (M) can occupy A sites as well as B sites whereas the other kind (M′) occupies B sites only. This kind of mixed ferrites occurs often and may be important enough for a study in detail. Not only T_2, T_3 and T_4 but also the course of the spontaneous magnetization between these temperatures can be determined (graphically). Only the change in T_2 caused by the presence of the M′ ions can be given by a simple formula.

2. Mixed ferrites, determination of T_1

We extend the case considered by Yafet and Kittel by assuming that one "grammole" contains λN magnetic ions M on A sites and μN ions M together with $\mu' N$ magnetic ions M′ on B sites. Thus this extension disappears for $\mu' = 0$.

The introduction of a second kind of magnetic ions in the B lattice implies the necessity to distinguish between the molecular magnetic field h'_{bI} at an M′ ion in B_I and that (h_{bI}) at an M ion in B_I and also between h'_{bII} and h_{bII} (at M′ and M ions in B_{II}).

The molecular magnetic field at each M ion is brought about now not only by M ions (contribution proportional to n) but also by M' ions (contribution proportional to n'). On the other hand the molecular field at each M′ ion now consists of contributions (proportional to n') from M ions but also of contributions (proportional to n'') from M' ions. Just as in earlier papers [3]) the assumption

$$nn'' = n'^2 \tag{4}$$

will be made. Properly we should have to introduce more than one factor γ_1, and more than one factor γ_2 for the antiferromagnetic action in the B lattice since several combinations in the B lattice would be possible owing to the presence of two kinds of magnetic ions. This, however, will not be done. The spontaneous magnetization (I'_{bsI}) of N M′ ions on B_I

is to be distinguished from the spontaneous magnetization (I_{bsI}) of N M ions on B_I and analogously I'_{bsII} from I_{bsII} in the sublattice B_{II}.

The highest Curie temperature may be similar to that in the paper by Yafet and Kittel with only M ions:

$$T_1 = Cn\tfrac{1}{2}\lambda(|\alpha_2| - |\alpha_1|), \tag{5}$$

at which the spontaneous magnetizations of A_I and A_{II} are born (being directed antiparallel to one another, $\varphi = \pi/2$) whereas all spins in the B lattice remain still unordered.

3. Determination of T_2

The presence of M′ ions can influence only the calculation of the lower Curie temperature T_2 at which also the ions on B_I and B_{II} will be magnetized spontaneously. Here, however, one should know whether one kind of magnetic ions occupying B will be magnetized earlier, i.e. at a higher temperature than the other kind of occupants of B. To answer this question we choose the temperature low enough to have to consider the situation given in fig. 2. The M an M′ ions are assumed to be distributed equally over B_I and B_{II}. Therefore we have in fig. 2

$$\begin{aligned} h_{bI} = {} & n\tfrac{1}{2}\lambda I_{asI}\cos\varphi + n\tfrac{1}{2}\lambda I_{asII}\cos\varphi - |\gamma_2| n\tfrac{1}{2}\mu I_{bsII} - \\ & - |\gamma_2| n'\tfrac{1}{2}\mu' I'_{bsII} - |\gamma_1| n\tfrac{1}{2}\mu I_{bsI} - |\gamma_1| n'\tfrac{1}{2}\mu' I'_{bsI}, \end{aligned} \tag{6}$$

$$\begin{aligned} h'_{bI} = {} & n'\tfrac{1}{2}\lambda I_{asI}\cos\varphi + n'\tfrac{1}{2}\lambda I_{asII}\cos\varphi - |\gamma_2| n'\tfrac{1}{2}\mu I_{bsII} - \\ & - |\gamma_2| n''\tfrac{1}{2}\mu' I'_{bsII} - |\gamma_1| n'\tfrac{1}{2}\mu I_{bsI} - |\gamma_1| n''\tfrac{1}{2}\mu' I'_{bsI}. \end{aligned} \tag{7}$$

Application of (4) here gives

$$h'_{bI} = (n'/n)\, h_{bI}$$

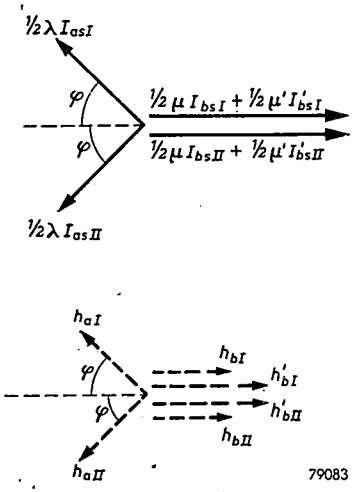

Fig. 2. Partial magnetizations and molecular fields for $T_2 > T > T_3$.

and analogously one can derive

$$h'_{bII} = (n'/n)\, h_{bII}.$$

The assumption (4) therefore implies the simultaneous appearance or disappearance of the molecular fields at both kinds of ions (M, M') in B. The simultaneous appearance may take place at some temperature T_2 which now will be calculated. The values

$$\eta = I_{bsI}/Ng\mu_B \text{ and } \eta' = I'_{bsI}/Ng'\mu_B$$

are still small for T just below T_2. The general formulae

$$\eta = (j+\tfrac{1}{2}) \coth (j+\tfrac{1}{2})\, Q - \tfrac{1}{2} \coth \tfrac{1}{2}Q, \tag{8}$$

$$\begin{aligned}\eta' &= (j'+\tfrac{1}{2}) \coth (j'+\tfrac{1}{2})\, Q' - \tfrac{1}{2} \coth \tfrac{1}{2}Q' = \\ &= (j'+\tfrac{1}{2}) \coth (j'+\tfrac{1}{2})\, (n'g'/ng)\, Q - \tfrac{1}{2} \coth \tfrac{1}{2}(n'g'/ng)Q,\end{aligned} \tag{9}$$

with

$$Q = g\mu_B\, h_{bI}/kT \text{ and } Q' = g'\mu_B h'_{bI}/kT \tag{10}$$

may be approximated giving

$$h_{bI} = (T/C)I_{bsI} \quad \text{and} \quad h'_{bI} = (T/C')I'_{bsI}. \tag{11}$$

Here C is defined by (3) and C' by

$$C' = Ng'^2\mu_B^2 j'(j'+1)/3k,$$

where g' and j' are the gyromagnetic ratio and the inner quantum number for the M' ion. If the equations (6) and (7) are taken for T just below T_2, h_{bI} may be replaced by (11) and if further all symbols with index II are replaced by the corresponding ones with index I (on account of the symmetry in fig. 2) we obtain

$$\begin{aligned}(T/C)I_{bsI} &= n\lambda I_{asI} \cos\varphi - |\beta| n\mu I_{bsI} - |\beta| n'\mu' I'_{bsI}, \\ (T/C')I'_{bsI} &= n'\lambda I_{asI} \cos\varphi - |\beta| n'\mu I_{bsI} - |\beta| n''\mu' I'_{bsI},\end{aligned} \tag{12}$$

valid for $T_2 - T \ll T_2$.

Application of (4) gives with the same restriction

$$I'_{bsI} = (n'C'/nC)I_{bsI} \quad (T_2 - T \ll T_2). \tag{13}$$

An equation for h_{aI} analogous to (11) could not be given for T below T_2, the temperature then being too far from T_1 where h_{aI} was small. Instead of the value of h_{aI} we have, however, to consider the *direction* of h_{aI}. Since I_{asI} as a matter of fact will point in the same direction as h_{aI}, the contributions to h_{aI} originating from the several partial magnetizations must have components perpendicular to I_{asI} which compensate one another. This gives in fig. 2 the equation

$$n\tfrac{1}{2}\mu(I_{bsI}+I_{bsII})+n'\tfrac{1}{2}\mu'(I'_{bsI}+I'_{bsII})\sin\varphi=|\alpha_2|\,n\tfrac{1}{2}\lambda I_{asII}\sin 2\varphi.$$

Replacing II by I and dividing by $\sin\varphi$ we have

$$n\mu I_{bsI}+n'\mu' I'_{bsI}=|\alpha_2|n\lambda I_{asI}\cos\varphi. \tag{14}$$

Using this equation together with (13) in order to express all partial magnetizations occurring in (12) in I_{bsI}, we then obtain after dividing by I_{bsI}

$$T_2=[Cn\mu+C'n''\mu']\,(1/|\alpha_2|-|\beta|). \tag{15}$$

If for a spinel containing M′ and M ions in the ratio μ_1': $(\lambda+\mu)$ the temperature T_2 is determined experimentally and if this is done also for a spinel containing these ions in the ratio μ_2': $(\lambda+\mu)$ the quotient of these temperatures will lead to the value of n''/n, i.e. of $(n'/n)^2$. The value of T_2 can be found from the experimental course of the spontaneous magnetization. For $T_1>T>T_2$ we have $\varphi=\pi/2$ and $I_{bsI}=I_{bsII}=I'_{bsI}=I'_{bsII}=0$. Since $I_{asI}=I_{asII}$ and $\varphi=\pi/2$ the total spontaneous magnetization is zero in this interval of temperature. At T_2 it begins to appear and its course for lower temperatures will be studied below.

4. Molecular spontaneous magnetization for $T_2>T>T_3$

In a following interval $T_2>T>T_3$ the angle φ will decrease from $\pi/2$ to zero under the influence of increasing partial magnetizations in the B lattice which remain parallel ($\psi=0$). A method for the determination of T_3 will be given afterwards.

The spontaneous magnetization m_s, calculated per "molecule" and expressed in μ_B is

$$m_s=|\tfrac{1}{2}\lambda(I_{asI}+I_{asII})\cos\varphi-\tfrac{1}{2}\mu(I_{bsI}+I_{bsII})-\tfrac{1}{2}\mu'(I'_{bsI}+I'_{bsII})|/N\mu_B.$$

Introducing as an analogue of (8) and (9)

$$\xi=I_{asI}/Ng\mu_B=(j+\tfrac{1}{2})\coth(j+\tfrac{1}{2})P-\tfrac{1}{2}\coth\tfrac{1}{2}P \text{ with } P=g\mu_B h_{aI}/kT, \tag{16}$$

and replacing the index II by I (on account of symmetry) we have

$$m_s=g|\lambda\xi\cos\varphi-\mu\eta-\mu'\eta'g'/g|$$

in which according to (14)

$$\lambda\xi\cos\varphi=(1/|\alpha_2|)\,[\mu\eta+(n'g'/ng)\,\mu'\eta']. \tag{17}$$

So in order to know m_s as a function of T it is sufficient to determine η and η' as functions of T and to substitute in

$$m_s=g|\mu(1/|\alpha_2|-1)\eta+(g'/g)\,(n'/n|\alpha_2|-1)\mu'\eta'|.$$

An expression for η follows here from (8) and (10), where h_{bI} is given by the right-hand member of (6). Expressing here the first term by means of (14) in I_{bsI} and I'_{bsI} one obtains

$$Q = (g\mu_B/kT)\,[n\mu I_{bsI} + n'\mu' I'_{bsI}]\;(1/|\alpha_2| - |\beta|).$$

By using the expression (15) for T_2, this equation can be written in the form

$$a(T/T_2)Q = \mu\eta + (n'g'/ng)\,\mu'\eta' \tag{18}$$

with the abbreviation

$$a = [j(j+1)\,(2-f) + j'(j'+1)\,(n'g'/ng)^2 f]/\beta.$$

With (8) and (9) the right-hand member of (18) can be drawn as a function of Q and the left-hand member is represented as a function of Q by means of a straight line through the origin, the inclination depending on T/T_2. Thus the abscissa Q of the common point is found as a function of T/T_2 and consequently also η and η' by (8) and (9), and with these the spontaneous magnetization m_s as a function of T/T_2 (at least in the interval $T_2 < T < T_3$).

5. Determination of T_3

For the graphical determination of T_3 (the highest temperature where $\varphi = 0$) we should first determine $\cos\varphi$ as a function of T/T_2 in the region $T_2 > T > T_3$ since T_3 is found by the condition $\varphi = 0$. The expression for $\cos\varphi$ following from (14) contains η, η' and ξ. In the preceding section we learned to find η and η' as functions of T/T_2, so that now also ξ is to be determined as a function of T/T_2. For ξ we need in (16)

$$\begin{aligned} h_{aI} &= [n\tfrac{1}{2}\mu(I_{bsI} + I_{bsII}) + n'\tfrac{1}{2}\mu'(I'_{bsI} + I'_{bsII})]\cos\varphi - \\ &\quad - |\lambda_2| n\tfrac{1}{2}\lambda I_{asII}\cos 2\varphi - |\alpha_1| n\tfrac{1}{2}\lambda I_{asI} = \\ &= \cos\varphi\,[n\mu I_{bsI} + n'\mu' I'_{bsI} - |\alpha_2|\, n\lambda I_{asI}\cos\varphi] + (|\alpha_2| - |\alpha_1|) n\tfrac{1}{2}\lambda I_{asI}. \end{aligned}$$

The first term disappears according to (14) and $|\alpha_2| - |\alpha_1|$ can be expressed in T_1 by means of (5). Thus we have

$$P = g\mu_B h_{aI}/kT = [3/j(j+1)]\,(T_1/T)\,\xi.$$

Cutting the curve

$$y = (j+\tfrac{1}{2})\coth(j+\tfrac{1}{2})x - \tfrac{1}{2}\coth\tfrac{1}{2}x \tag{19}$$

by the straight line

$$y = (1/3)j\,(j+1)\,(T/T_1)x$$

ξ is found as the ordinate of the common point, obviously as a function of T/T_1 and then easily as a function of T/T_2. The T/T_2-dependence of $\cos\varphi$ is now known, and where $\cos\varphi$ becomes unity we find the value T_3/T_2.

6. Course of m_s in the region $T_3 > T > T_4$

From T_3 to the temperature $T_4 < T_3$ which afterwards will be derived from the basic coefficients, the angles φ and ψ remain zero. In this rectilinear case the partial magnetizations $\frac{1}{2}\lambda I_{asI}$ and $\frac{1}{2}\lambda I_{asII}$ point to the left and $\frac{1}{2}\mu I_{bsI}$, $\frac{1}{2}\mu I_{bsII}$, $\frac{1}{2}\mu' I'_{bsI}$ and $\frac{1}{2}\mu' I'_{bsII}$ to the right and these vectors are equal in pairs (fig. 3). Per "molecule" the spontaneous magnetization, expressed in μ_B, amounts to

$$m = g|\lambda\xi - \mu\eta - (g'/g)\,\mu'\eta'|\,.$$

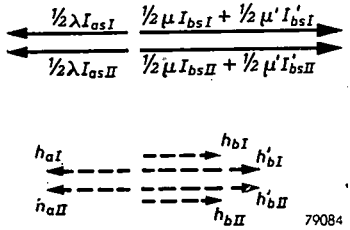

Fig. 3. Partial magnetizations and molecular fields for $T_3 > T > T_4$.

In the present region of T none of the three Brillouin functions for ξ, η and η' can be replaced by a simple approximation since T generally is far from both Curie temperatures T_1 and T_2. The three arguments of these functions are

$$P = (g\mu_B/kT)\,[n\mu I_{bsI} + n'\mu' I'_{bsI} - |\alpha| n\lambda I_{asI}], \tag{20}$$

where symbols with II have been replaced by those with I and $|\alpha|$ has been introduced, defined by $|\alpha| = \frac{1}{2}(|\alpha_1| + |\alpha_2|)$,

$$Q = (g\mu_B/kT)\,[n\lambda I_{asI} - |\beta|\, n\mu I_{bsI} - |\beta|\, n'\mu' I'_{bsI}], \tag{21}$$
$$Q' = (n'g'/ng)Q\,.$$

Fortunately Q can be expressed in P since from (20) and (21)

$$|\beta|P + Q = (g\mu_B/kT)\;(1 - |\alpha|\;|\beta|)\;n\lambda I_{asI}$$

and therefore

$$Q = (1 - |\alpha|\;|\beta|)\;[(j + \tfrac{1}{2})\coth(j + \tfrac{1}{2})P - \tfrac{1}{2}\coth\tfrac{1}{2}P]\;(\tau/T) - |\beta|P$$

with $$\tau = 3Cn\lambda/j(j+1)\,.$$

Thus all three values ξ, η and η' are expressible in P and in order to find m_s as a function of T we first should find P as a function of T. This can be done by writing (20) in the form

$$(T/\tau)P + |\alpha|\xi = (\mu/\lambda)\eta + (n'g'/ng)\;(\mu'/\lambda)\eta'$$

and replacing ξ, η and η' by the functions of P mentioned above. P thus being found graphically as a function of T/τ we finally know ξ, η, and η'; thus m_s in the linear case, i.e. for $T_3 > T > T_4$, is found as a function of T/τ.

7. Determination of T_4

In order to find T_4, the lowest temperature for the rectilinear case, we have to consider the situation illustrated in fig. 4 and holding for the next region $T_4 > T > 0$. Here ψ and ψ' are angles varying with T and indicating the directions of I_{bsI} and I'_{bsI} separately. However, it will be shown that $\psi = \psi'$ on account of the introduction of only one factor $|\gamma_1|$ and only one factor $|\gamma_2|$ notwithstanding B_I and B_{II} are occupied by two different kinds of magnetic ions.

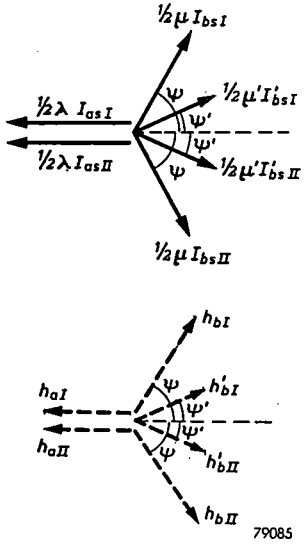

Fig. 4. Partial magnetizations and molecular fields for $T_4 > T > 0$.

Since I_{bsI} must have the direction of h_{bI}, the contributions to h_{bI}, made by the several partial magnetizations must have components perpendicular to I_{bsI}, the sum of which is zero, those on one side compensating those on the other side:

$$n\tfrac{1}{2}\lambda(I_{asI}+I_{asII}) \sin\psi = |\gamma_2| n\tfrac{1}{2}\mu I_{bsII} \sin 2\psi + \\ + |\gamma_2| n'\tfrac{1}{2}\mu' I'_{bsII} \sin(\psi+\psi') + |\gamma_1| n'\tfrac{1}{2}\mu' I'_{bsI} \sin(\psi-\psi').$$

The same holds for the directions of I'_{bsI} and h'_{bI}, so that

$$n'\tfrac{1}{2}\lambda\,(I_{asI}+I_{asII}) \sin\psi' + |\gamma_1| n'\tfrac{1}{2}\mu I_{bsI} \sin(\psi-\psi') = \\ = |\gamma_2| n'\tfrac{1}{2}\mu I_{bsII} \sin(\psi+\psi') + |\gamma_2| n''\tfrac{1}{2}\mu' I'_{bsII} \sin 2\psi'.$$

These equations can be written in the form

$$n\lambda I_{asI} \sin\psi = |\gamma_2| n\tfrac{1}{2}\mu I_{bsI} \sin 2\psi + |\beta| n'\mu' I'_{bsI} \sin\psi \cos\psi' + \\ + \tfrac{1}{2}(|\gamma_2| - |\gamma_1|) n'\mu' I'_{bsI} \sin\psi' \cos\psi,$$

$$n'\lambda I_{asI} \sin\psi' = \tfrac{1}{2}(|\gamma_2| - |\gamma_1|) n'\mu I_{bsI} \sin\psi \cos\psi' + \\ + |\beta| n'\mu I_{bsI} \sin\psi' \cos\psi + |\gamma_2| n''\tfrac{1}{2}\, \mu' I'_{bsI} \sin 2\psi'.$$

Dividing the first equation by $n \sin\psi$ and the second by $n' \sin\psi'$ (replacing n''/n' by n'/n) and then subtracting, one obtains

$$\tfrac{1}{2}(|\gamma_2| - |\gamma_1|) \sin(\psi' - \psi) \left[\mu I_{bsI}/\sin\psi' + (n'/n)\mu' I'_{bsI}/\sin\psi\right] = 0,$$

from which follows: $\psi = \psi'$. Therefore further on we will use fig. 5 instead of fig. 4. The two conditions, now being identical, give

$$n\lambda I_{asI} = |\gamma_2| \left[n\mu I_{bsI} + n'\mu' I'_{bsI}\right] \cos\psi. \tag{22}$$

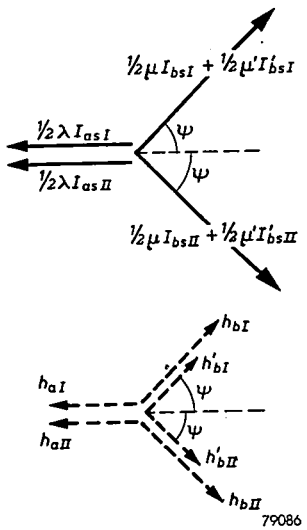

Fig. 5. Approximate partial magnetizations and molecular fields for $T_4 > T > 0$.

That temperature for which (22) gives $\cos\psi = 1$ is identical with the required temperature T_4. For the temperature dependence of I_{asI}, needed in (22), we calculate the quantity $P = g\mu_B h_{aI}/kT$ for the situation illustrated in fig. 5:

$$P = (g\mu_B/kT) \left[n\mu I_{bsI} \cos\psi + n'\mu' I'_{bsI} \cos\psi - |\alpha| n\lambda I_{asI}\right]$$

which by means of (22) can be expressed in I_{asI}, so that

$$P = [3/j(j+1)] \; (\tau'/T)\xi$$

with $\tau' = Cn\lambda(1/|\gamma_2| - |\alpha|)$.

Cutting the curve (19) by the straight line

$$y = (1/3)\, j(j+1)\, (T/\tau')\, x,$$

we obtain in the ordinate of the common point the value of ξ obviously as a function of T/τ. The temperature dependence of I_{bsI} and I'_{bsI} also needed in (22), cannot be found in a similar manner since in the case of fig. 5 we have

$$h_{bI} = n\lambda I_{asI} \cos\psi - \tfrac{1}{2}[n\mu I_{bsI} + n'\mu' I'_{bsI}]\, (|\gamma_2| \cos 2\psi + |\gamma_1|),$$

so that expressing $\cos 2\psi$ in $\cos\psi$ and then applying (22) we obtain for $Q = g\mu_B h_{bI}/kT$

$$Q = [3Cn/2j(j+1)T]\, (|\gamma_2| - |\gamma_1|)[\mu\eta + (n'g'/ng)\mu'\eta'], \qquad (23)$$

which contains not only η but also η'. This requires quite another method for the determination of η than we could use for ξ. We will use (23) as an equation to determine Q as a function of T, namely by substituting (8) and (9) for η and η':

$$(T/\tau')Q = A(\mu/\lambda)\, ((8)) + (\mu'/\lambda)\, (n'g'/ng)\, ((9)),$$

in which ((8)) and ((9)) represent the right-hand members of (8) and (9), whereas

$$A = (3/2)\, (|\gamma_2| - |\gamma_1|)\, /\, (1/|\gamma_2| - |\alpha|)\, j\, (j+1).$$

Q being found as a function of T/τ', the quantities η and η' follow and these together with ξ give in

$$\cos\psi = \lambda\xi/|\gamma_2|\, [\mu\eta + (n'g'/ng)\mu'\eta'] \qquad (24)$$

$\cos\psi$ as a function of T/τ'. The abscissa where $\cos\psi$ becomes unity is identical with T_4/τ'.

8. Course of m_s for $T_4 > T > 0$

In the region $T_4 > T > 0$ the spontaneous magnetization per "molecule" amounts (in μ_B) to

$$m_s = g|\lambda\xi - [\mu\eta + (g'/g)\mu\eta']\, \cos\psi|$$

and its dependence on T/τ' follows immediately from the preceding section, where $\cos\psi$ is given by (24) and where ξ, η and η' were found as functions of T/τ'. For $T = 0$ we have $\xi = \eta = j$, $\eta' = j'$ and $\cos\psi = |\gamma_2|^{-1}[\mu/\lambda + (\mu'/\lambda)\, n'g'j'/ngj]^{-1}$.

Eindhoven, January 1954

REFERENCES

1) Y. Yafet and C. Kittel, Phys. Rev. **87**, 290-294, 1952.
2) L. Néel, Ann. Phys., Paris **3**, 137-180, 1948.
3) K. F. Niessen, Physica, **17**, 1033-1049, 1951; **18**, 449-468, 1952; **19**, 445-450, 1953.

Philips Res. Rep. **9**, 209-224, 1954

REFLECTION PROPERTIES OF DRY AND WET ROAD SURFACES AND A SIMPLE METHOD FOR THEIR MEASUREMENT

by J. B. de BOER and A. OOSTRIJCK

628.971.6:628.936

Summary

During the last 20 years or so, much work has been devoted to the study of the reflection properties of road surfaces. However, for the purpose of road lighting, the results published up to now are either incomplete or insufficiently accurate. Methods and equipment which have been applied up to now for the measurement of the reflection properties of road surfaces have been rather complicated. The very simple means used by the authors for making measurements in the laboratory and in the field are briefly described. In this paper quantitative data are given on the reflection properties of a number of road surfaces common in the Netherlands. These data have been given for those directions of light incidence and observation which are of importance in lighting practice. They have been presented in a special diagram in order to enable the public lighting engineer to make calculations on the luminance of road surfaces in a quick and simple manner.

Résumé

Au cours des 20 dernières années des études approfondies ont été consacrées aux propriétés de réflexion des surfaces routières. Pour l'éclairage routier, cependant, les résultats publiés jusqu'à présent sont incomplets ou manquent d'exactitude. Jusqu'à présent les méthodes et l'appareillage, utilisés pour la mesure des propriétés de réflexion des surfaces routières ont été assez compliqués. Les moyens très simples, utilisés par les auteurs pour effectuer des mesures, tant au laboratoire qu'à l'extérieur, ont été brièvement décrits. Dans cet article, des données quantitatives ont été données sur les propriétés de réflexion d'un certain nombre de surfaces routières prédominantes aux Pays-Bas. Ces données s'appliquent aux directives de l'incidence de la lumière et de l'observation qui sont importantes pour la pratique de l'éclairage. Elles ont été présentées dans un tableau spécial afin de permettre à l'expert en éclairage routier de calculer, d'une façon rapide et simple, la luminance des surfaces routières.

Zusammenfassung

In den letzten 20 Jahren wurde der Untersuchung der Reflexionseigenschaften von Straßendecken sehr viel Arbeit gewidmet. Trotzdem sind die bisher veröffentlichten Resultate für den Zweck der Straßenbeleuchtung entweder unvollständig oder nicht hinreichend genau. Bis jetzt wurden zur Messung der Reflexionseigenschaften von Straßendecken Methoden und Instrumente angewandt, die ziemlich kompliziert sind. Der vorliegende Artikel gibt eine kurze Beschreibung der sehr einfachen Mittel, welche die Verfasser zur Durchführung von Messungen im Laboratorium und im Freien benutzten. Es werden hier quantitative Daten über die Reflexionseigenschaften einer Anzahl in den Niederlanden vorherrschender Straßendecken mitgeteilt. Diese Daten wurden für diejenigen Rich-

tungen des Lichteinfalls und der Beobachtung gegeben, die für die Beleuchtungspraxis von Bedeutung sind. Sie werden hier in einem speziellen Diagram dargeboten, um es dem Ingenieur für öffentliche Beleuchtung zu ermöglichen, in schneller und einfacher Weise Berechnungen über die Leuchtdichte von Straßendecken vorzunehmen.

1. Introduction

In an earlier publication [1]) a description has been given of a procedure for predetermining the distribution of the luminance of the road surface in a lighted street. This procedure is well suited for every-day practice in street lighting. It will be summarized in section 2 in order to make this paper intelligible in itself. The procedure is a graphical one in which a diagram is used to represent the reflection properties of the road surface.

Apart from a diagram for dry concrete and one for dry asphalt derived from measurements by Reid and Chanon [7]), the reflecting properties for one road surface only (dry asphalt) have been given in the earlier study [1]). The former diagrams, however, are not entirely satisfactory owing to the rather sparse coverage of the graphs representing the original results of these investigators. So in fact, up to now, a quick predetermination of road luminance could only be made for one single road surface in dry condition. In the first place this paper provides further material in this respect by showing the reflection properties of four road surfaces, all of them in dry as well as in wet condition.

When carrying out the investigations we found it possible to simplify considerably the arrangements required for the measurements. A detailed description of the measuring devices used for the final measurements is given in sections 4 and 5 of this paper. These paragraphs indicate methods for a quick determination of the reflection properties of any given road surface by simple means. It is this simplicity which offers wide possibilities of obtaining more fundamental knowledge concerning the reflection properties of road surfaces, knowledge which is of basic importance for the whole problem of street lighting.

2. Short description of a practical procedure for predetermining the luminance of a road surface

If, in fig. 1, I is the luminous intensity of the light source L towards the point P on the road surface, the illumination at P is $(I/h^2)\cos^3\gamma$. An observer O looking towards P sees this point at a luminance proportional to the illumination at P. If the ratio between the luminance and the illumination is expressed by a factor q, the luminance at P seen by the observer O is $q(I/h^2)\cos^3\gamma$. The direction of observation and the direction of light incidence are determined by the angles α, β and γ. These three angles determine the value of $q\cos^3\gamma$.

A simple graphical representation of $q \cos^3\gamma$ is obtained in a manner as illustrated in fig. 2. The plane of drawing in this figure represents the road surface. The observer is above O', and is looking towards point P.

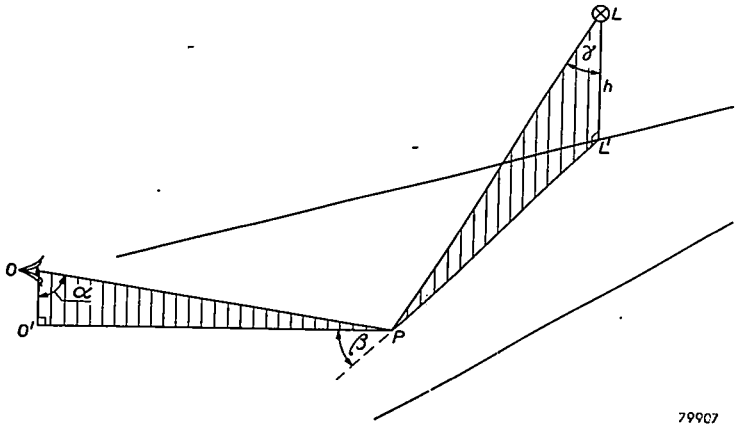

Fig. 1. Geometrical figure with angles α, β and γ determining the luminance coefficient q. L = light source, O = observer's eye, P = point under obervation, h = height of lightsource above road surface,

Let us suppose we move a lamp with a luminous intensity of one candela in all directions at a fixed height h over the road surface in such a way that the luminance at point P, and therefore $q \cos^3\gamma$, does not change. For every value of the luminance we will find a definite trace of the lamp. Now the curves in fig. 2 represent the projection of a few of these traces on the

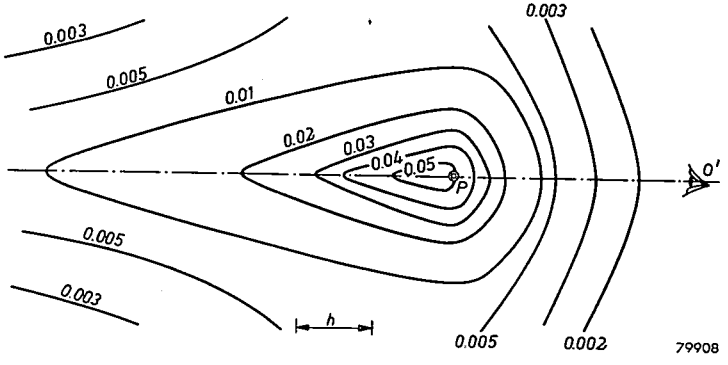

Fig. 2. Representation of the reflection properties of a road surface by means of an E.P. diagram. The observer is over point O' and looking at point P on the road surface. The curves represent projections of lamp positions for which the product $q \cos^3 \gamma$ for point P as seen by the observer has the value indicated at each curve. The diagram can be used for distances O'P greater than 40 × the height of the observer's eye above the road surface.

road surface. In order to make the diagram valid for different values of the height h of the lamp, it has been drawn on a scale with h as the unit of length. The numbers placed beside the curves, representing the value of $q \cos^3\gamma$, should be divided by h^2 in order to find the luminance. The diagram given in fig. 2 will be referred to as the "E.P. diagram", "E.P." standing for "equivalent positions", i.e. lamp positions equivalent in producing a certain value of $q \cos^3\gamma$ at P.

Strictly speaking, for every distance O'P another E.P. diagram should be provided. However, errors of only a few per cent are introduced if one and the same diagram is applied for all distances O'P greater than 40 times the height of the observer's eye above the road surface.

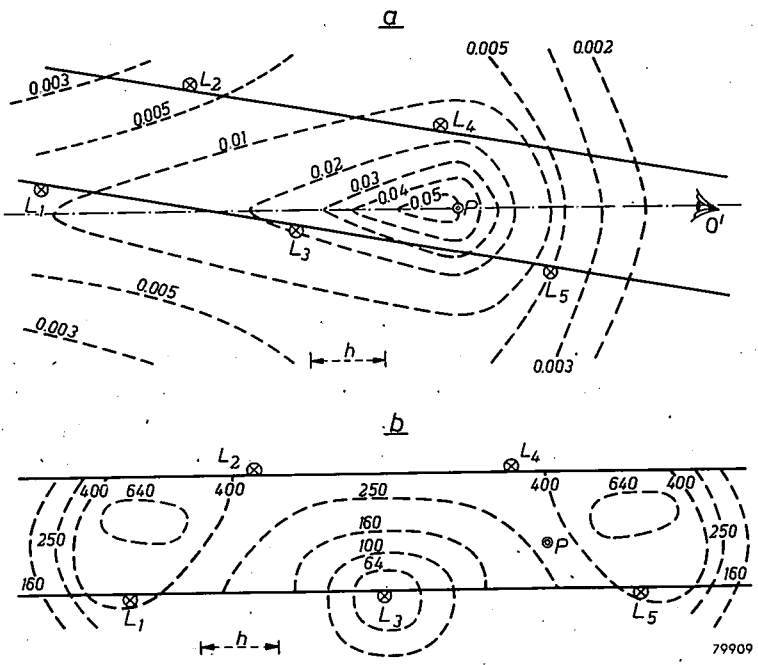

Fig. 3. Explaining the use of the E.P. diagrams.

Fig. 3 illustrates how luminance values are calculated for selected points of a road surface more than 60 m away from the observer with the aid of an E.P. diagram. A plan of the road with a lighting installation (lanterns L_1 to L_5) is drawn on a sheet of transparent paper, expressing the dimensions of the road in the same unit of length h as indicated in the E.P. diagram. Let P_1 in the plan be one of the points on the road to be observed by the observer O. The E.P. diagram is now covered with

the transparent road plan in such a way that P_1 coincides with P in the E.P. diagram and the direction P_1O' with the axis of symmetry of the E.P. diagram. Fig. 3*a* shows the situation. For the lantern positions L_1 to L_5 the values of $q \cos^3\gamma$ are then read off and entered in table I (second column). Then the luminous intensity in the direction of P_1 has to be determined for each lamp.

TABLE I

Lamp	$q \cos^3\gamma$ at P_1	$I_{\rightarrow P_1}$	$h^2 \Delta B$
L_1	0·008	40 cd	0·3 cd
L_2	0·0045	640 cd	2·9 cd
L_3	0·020	325 cd	5·6 cd
L_4	0·015	205 cd	3·1 cd
L_5	0·005	190 cd	1·0 cd
			$\Sigma(h^2 \Delta B) = 13{\cdot}8$ cd
$h = 8$ m			$B = 0{\cdot}216$ cd/m²

The simplest way to do this is to apply an iso-candela diagram plotted in a plan of the road (unit of length h) and showing for one lamp, by means of isocandela lines, all points on the road surface towards which the lamp radiates certain luminous intensities. This iso-candela diagram is covered with the transparent road plan in such a way that L_1 to L_5 of the plan coincide successively with L (the position of the lantern) of the iso-candela diagram, making sure that in the case of a non-axially-symmetrical light distribution the iso-candela diagram is in the correct position with respect to the road. In this way the values of the luminous intensity in the direction of P_1 can be obtained for each lamp.

For lantern L_3 this is as shown in fig. 3*b*. The third column of table I gives the various I values found in this way. It remains now to multiply the numbers in column two by those in column three for each row. The results entered in column four contain the contributions ΔB of each lantern to the luminance of the observed point P_1 multiplied by h^2. Adding the values in column four and dividing the sum by h^2 gives the total luminance of the road surface at P_1 as seen by the observer O.

The same operation has to be applied to each point P_2, P_3, etc. Once that has been done for a sufficiently large number of points, iso-luminance lines can be drawn for one particular observer O on a road with a number of fixtures L_1, ..., L_n.

For further details of the procedure and a discussion of its accuracy reference is made to an earlier publication in these Reports [1]).

3. The determination of the reflection properties of road surfaces

The reflection properties of road surfaces have already been measured by several investigators. In general a method of measurement has been followed in which a photo-electric receiver was applied. Notwithstanding the very high sensitivity of modern types of photo-electric receiver, the very small quantities of light to be measured compel one to adopt either a large area for the light-sensitive surface of the photo-electric cell or a powerful and therefore large light source, or even both. In this way inadmissible errors can arise in view of the influence of the angle between the horizontal projections of direction of observation and light incidence. It is understandable that in Cohu's [2]) investigations errors of this nature were not avoided as Cohu was the first to make an extensive study of the reflection properties of road surfaces. The same error, however, has been repeated by Weigel [3]) and again in a recent study by Kraehenbuehl [4]).

Furthermore, in all the investigations carried out up to now (see also a study of Finch and Marxheimer [5])) equipment is used which is far more complicated than that necessary if only reflection data are to be determined for street-lighting problems. The description of the measuring device by the authors will make this clear. Many investigators carried out their measurements for a large angular range of directions of light incidence and directions of observations, whereas in street lighting only a very limited region for both directions is of interest.

Finally it must be kept in mind that the main purpose of collecting data on the reflection porperties of road surfaces is to provide the possibility of predetermining the luminance of a lighted road surface. To this end many tedious calculations are required if the results of measurements on the reflection properties of road surfaces are recorded as has been done by the majority of investigators. In fact only Bergmans [6]) and Reid and Chanon [7]) have tried to present their results in a form suitable for practical calculations. In an earlier publication [1]) we have indicated the reasons why we prefer another method of representing the reflection properties (the E.P. diagram described in section 2 of this paper). In sections 4 and 5 we will describe how to compose these E.P. diagrams. It will be shown that this is possible in a manner which for the following reasons is to be preferred to the above mentioned investigations:

(a) errors due to badly defined directions of light incidence and observation are avoided;
(b) the equipment is extremely simple;
(c) the measurements give results for all directions of incidence of light

and of observation which are of interest from the point of view of street lighting, and do not give superfluous data for other directions;

(d) the method of representation of the results is directly suited for practical calculations on the luminance of the road surface.

In fact, two methods have been developed for measuring the reflection properties of road surfaces, one for the laboratory where only samples of traffic-worn road surfaces were available and the other for the road itself.

4. A laboratory method for measuring the reflection properties of road surfaces.

The investigations in the laboratory made on small samples of the road surfaces are based on the following considerations. The direct determination of the traces shown in the E.P. diagram representing distinct values of $q \cos^3\gamma$ would be rather difficult from an experimental point of view. In order to avoid these difficulties the value of $q \cos^3\gamma$ can be measured for a number of points regularly distributed over the E.P. diagram. Lines for constant values of $q \cos^3\gamma$ can be found from these results by interpolation.

The value of $q \cos^3\gamma$, being equal to Bh^2/I (see section 2) can easily be measured if both I and h are kept at a constant value for all measuring conditions. If the values of I and h are first determined, the value of $q \cos^3\gamma$ follows directly from the measurement of B for each condition. Provided that the measurements are carried out on a small scale, which means that the light source is then easily movable with respect to the sample of the road surface, a practical way to perform these investigations in the laboratory is to put a small sample of the road surface at a fixed place and to move the adjustable light source around this sample. It will be shown below that for various reasons the choice of a small scale for the measurements is really advantageous. The measuring arrangement has been given schematically in fig. 4*a*. The observer O looks towards the sample of the road surface P. Both the observer and the sample have fixed positions. The sample has a rectangular form, 0·25 m long and 0·05 m wide. The direction of observation of the observer makes an angle of 1° with the surface of the sample and lies in the vertical plane through the longitudinal axis of the sample. The observer therefore sees the sample apparently as a small rectangle of which the long sides are horizontal and approximately 10× the magnitude of the "vertical" sides. A small screen S has been placed between observer and sample in such a way that this screen and the sample seem to be adjacent when viewed from the observer's position. The size and dimensions of both screen S and road sample are apparently the same. What the observer actually sees

is shown in fig. 4*b* of which the right-hand half is the screen S and the left-hand half is the sample of the road surface, seen foreshortened. The luminance of the screen S is obtained by means of a narrow beam from the projector Pr within the observer's reach. The observer can adjust the luminous intensity of the projector and therefore the luminance of the screen S in a manner permitting measurement.

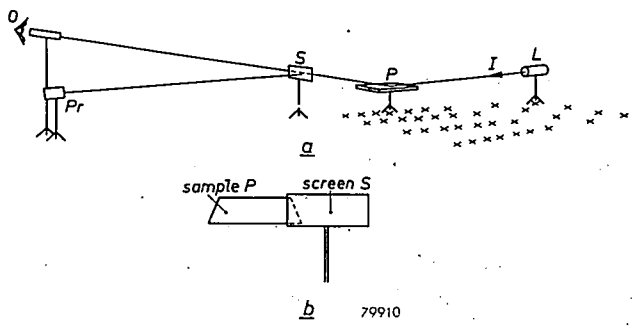

Fig. 4. Schematical representation of the measuring arrangement used in the laboratory for measuring the reflection properties of road surfaces.

The observer makes a balance between the brightness of the sample P and that of screen S for every position of the lantern L relative to the sample P. The light source L is placed at a great many points distributed in such a way relative to the point P that an E.P. diagram of adequate dimensions can be derived from the results found in these points. Fig. 5 shows the distribution of the lantern positions used in our measurements with h as the unit of scale.

The observations were made with the aid of a telescope in order to increase the observer's contrast sensitivity. The angular magnification of this telescope should be at least 5 times but preferably 10 times. The screen had to be placed at such a distance from the sample P that the lantern L could be brought on the points between observer and sample according to fig. 5 without light from L falling on the side of the screen facing the observer. In order to see both screen and sample sharply

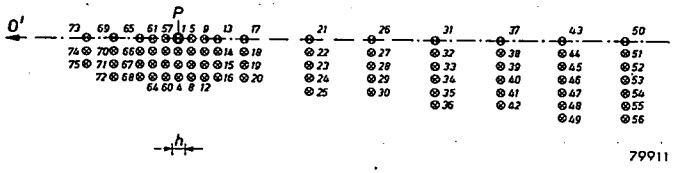

Fig. 5. Plan, showing the distribution of the lantern positions used for determining an E.P. diagram, with the lantern height h as the unit of scale.

through the telescope the observer should be positioned at a fair distance.

As light source a lantern should be used which throws a beam just wide enough to cover the sample of the road surface from the nearest position. In all directions within this beam the luminous intensity of the light source should be the same. As, in general, the value of $q \cos^3\gamma$ decreases with increasing distance between light source and sample P, it will facilitate the measurements if rather high values of luminous intensity of the light source are available for the larger distances between light source and sample. At these distances a narrow beam will already cover the entire sample. At the shorter distances wider beams are needed in order to cover the sample entirely; however, much smaller luminous intensities will suffice. It is therefore advisable when making these measurements in practice to use a few types of beams varying from narrow ones of rather high luminous intensity to wide beams of much smaller candlepower. We found it practical to use only one light source provided with an optical system which threw a narrow intense beam, whilst either a frosted glass or an opal glass could be placed in front of this light source whenever wider and "weaker" beams were necessary. From a practical point of view it is important, although not fundamental, to decide on what scale the measurements will be made. A small scale has the following advantages:

(a) the whole investigations can be made in a rather small space;
(b) high luminance of the sample for the same luminous intensity of the lantern, which means easy luminance measurements;
(c) small height of the lantern above the sample which makes it easily movable, while the distances over which the lantern should be moved are shorter.

Of course, the scale cannot be taken too small, as then the irregularities of the surface, which retain their real size, affect the results of the measurements to an inadmissible degree.

In general it can be stated that no errors need be feared so long as each single element of the texture in the surface of the road is small compared with the section of road concerned in the measurements. In our investigation we applied a height of the light source over the sample of 0·5 m, which means approximately a scale of 1:15. At this scale the measurements can be made in a space 3 m wide and 50 m long. The size of the sample to be used should be at least 0·25 m by 0·05 m.

5. A field method for measuring the reflection properties of road surfaces

In the field an extremely simple method, which is at the same time sufficiently accurate, can be obtained by applying a standard reflection surface (s.r.s.).

The reflection properties of this s.r.s. have been measured for all relevant directions of observation and of light incidence e.g. by means of the method described in the foregoing section. The principle of the field method is to light and to observe the road surface and the s.r.s. in the same way (simply by placing them adjacent to each other in the same arrangement of light source and observer). Both will be seen with a different luminance. The luminance of one of the two is decreased in a manner permitting measurement until both luminances are balanced. The reflection of the pavement can be calculated from the known reflection of the s.r.s. and the ratio in which one of the two luminances has to be decreased.

If the s.r.s. is laid on the road surface adjacent to the place to be measured (see fig. 6) all that is needed is a small screen S provided with a horizontal slit, half of which can be covered by filters F of different transmission, a telescope T and a light source L on a tripod. The s.r.s., the screen S and the telescope T are placed in such a way that the observer sees the horizontal slit in the screen covered for one half by the s.r.s. and for the other half by the part of the road surface to be investigated. A rather large distance between observer and s.r.s. is desirable in order to:

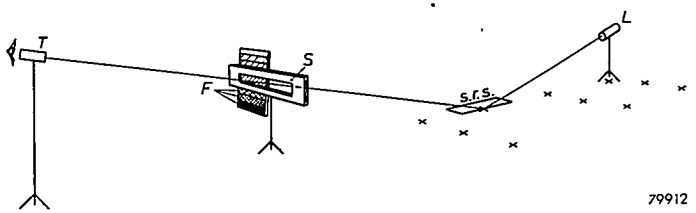

Fig. 6. Schematical representation of the measuring arrangement used in the field for measuring the reflection properties of road surfaces.

(a) arrive at a convenient measuring height (at an angle of observation of 1°, a distance of 57 m from the s.r.s. is required for a height of the eye of 1 m);
(b) see both the s.r.s. and the part of the road surface to be measured at approximately the same angle β (see fig. 1);
(c) accomodate the eye simultaneously to the screen S and the s.r.s.

The latter reason is clear when one considers that the screen S should be placed at a certain height above the ground in order to be able to cover one half of the slit with filters. A practical distance between S and s.r.s. is approximately 10 m.

The large distance between observer and screen S necessitates the use of the telescope T in order to maintain a sufficiently high contrast sensitivity.

For each position of the light source relative to the s.r.s. a balance

is made between the luminance of the left-hand and right-hand halves of the slit in the screen S by means of a set of neutral filters. If an s.r.s. is chosen with rather high reflection factors these filters should be placed in front of the half covering the s.r.s. The accuracy of the method depends on the extent of the range of filters available. If an accuracy of 10 per cent is aimed at, a set of filters in which the transmission factor of a filter is $1{\cdot}2\times$ the transmission factor of the next one in density will be satisfactory, as an estimation of the right balance can be made from the two not quite correct balances obtained with the best-fitting filters.

The number of filters required depends largely on the choice of the s.r.s. It has been found possible to use an s.r.s. which behaves, as far as its reflection properties are concerned, very similarly to normal road surfaces. More or less to our surprise, we found that normal white drawing paper is very suited to the purpose as even the matt varieties of this paper prove to be very glossy when viewed and lighted at oblique angles. It was found that such a strip of white drawing paper has a luminance factor q that lies between 2 and 20 times that of normal dry road surfaces for corresponding directions of observation and light incidence. In order to cover this range of differences in luminance factor, a set of 12 filters is required if the successive filters comprising the set show the above-mentioned ratio in the transmission factor. For wet road surfaces, however, the luminance factor q of the road surface is very frequently higher than that of the drawing paper. In these cases the filters should be placed in front of that part of the slit which covers the road surface. Four filters should be added to the above-mentioned set in order to make possible a balance between brightnesses differing in a ratio smaller than 2.

For the points presented in fig. 5 the paper which we used as an s.r.s. showed the values of $q \cos^3\gamma$ given in table II.

As the whole method can be reduced to a comparison of the luminance factor between two samples, variations in the luminance intensity of the light source, e.g. due to voltage fluctuations, do not influence the results. All measurements required for a complete E.P. diagram can be carried out in approximately three hours.

It can be seen from this description that with the exception of a dozen neutral filters (dimensions 1×6 cm) no special instruments are required for this measuring method.

6. Results

In figures 7, 8, 9 and 10 the results of our measurements on bricks, cobblestones, asphalt and concrete, all of them in both dry and wet conditions, are given in the form of E.P. diagrams. All these measurements were carried out on samples in the laboratory (method described in section 4).

TABLE II

Reflection properties of a strip of white drawing paper
Measured points numbered accordig to fig. 5

Point Nr	$q \cos^3\gamma$	Point Nr	$q \cos^3\gamma$	Point Nr	$q \cos^3\gamma$
1	0·19	26	0·051	51	0·0057
2	0·065	27	0·004	52	0·0012
3	0·018	28	0·0015	53	0·00053
4	0·0075	29	0·00095	54	0·00031
5	0·13	30	0·0006	55	0·0002
6	0·035	31	0·049	56	0·00015
7	0·013	32	0·0033	57	0·08
8	0·0072	33	0·0012	58	0·038
9	0·08	34	0·00063	59	0·015
10	0·026	35	0·00049	60	0·007
11	0·013	36	0·00041	61	0·024
12	0·006	37	0 047	62	0·020
13	0·071	38	0·003	63	0·0086
14	0·02	39	0·001	64	0·0049
15	0·011	40	0·00055	65	0·0062
16	0·006	41	0·0004	66	0·0055
17	0·063	42	0·00028	67	0·0042
18	0·014	43	0·046	68	0·0023
19	0·0068	44	0·0036	69	0·0021
20	0·004	45	0·0014	70	0·0018
21	0·055	46	0·00085	71	0·0014
22	0·04	47	0·00045	72	0·00037
23	0·0024	48	0·00023	73	0·0012
24	0·0017	49	0·00015	74	0·00096
25	0·0011	50	0·044	75	0·00055

The road surfaces investigated have been in use for several years in rather heavy traffic, with the exception of the concrete surface which was new.

7. Discussion of the results

In order to be able to compare the reflecting properties of the road surfaces under consideration, the course of the value of $q \cos^3\gamma$ in a lengthwise section and in some cross-sections of the E.P. diagrams has been given

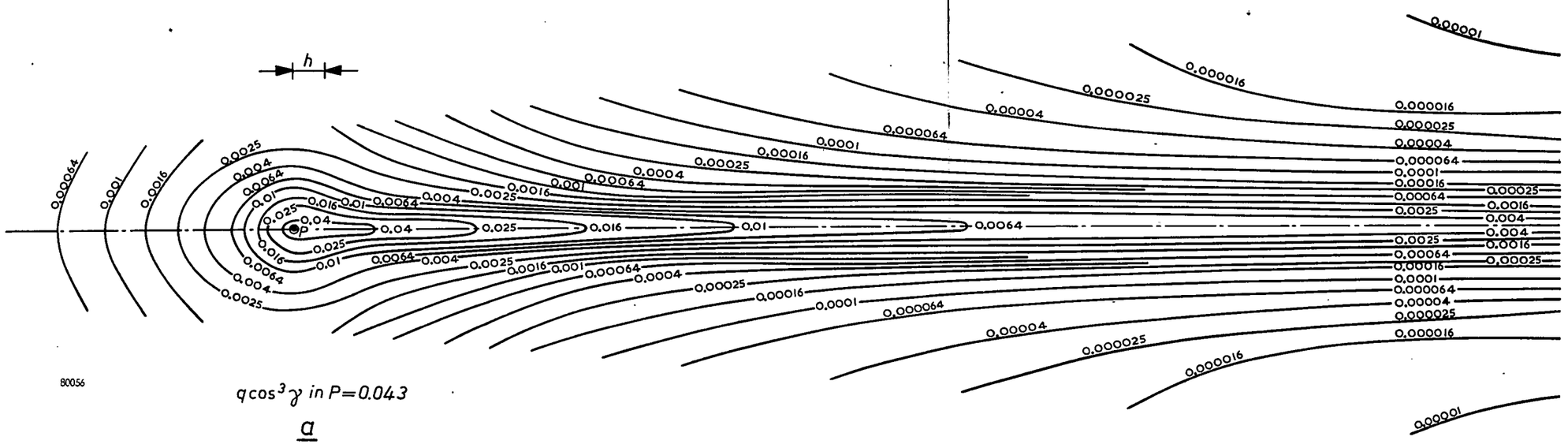

Fig. 7a. E.P. Diagram for dry bricks.
The plane of the drawing represents the road surface. The observer is over the line of symmetry of the diagram to the left of the point P considered at a distance from P which is at least 40× the height of his eye. The curves connect projections on the road surface of lamp positions having one value of $q \cos^3\gamma$ (indicated by the figures at the curves). q is the luminance coefficient in cd/m²/lux and γ is the angle of incidence of the light. The unit of length in the diagram is equal to the height h of the lamp above the road surface (indicated by a short line in the diagram).
Directions for use.
Plot a plan of the road on a scale such that the distance h of the E.P. diagram equals the fixture height. Indicate in this plan the positions of the lamps and of the observer as well as the points on the road under consideration for which the luminance has to be calculated. Lay the plan over the E.P. diagram in such a way that one of these points coincides with the point P of the E.P. diagram, while the observer is over the line of symmetry of the E.P. diagram. Read the value of $q \cos^3\gamma$ for each lamp. Determine the luminous intensity radiated by each lamp in the direction of the point considered (e.g. by means of an iso-candela diagram). Multiply this value by the corresponding value of $q \cos^3\gamma$ and divide by h^2. The result gives the contribution of each lamp to the luminance at the point considered.

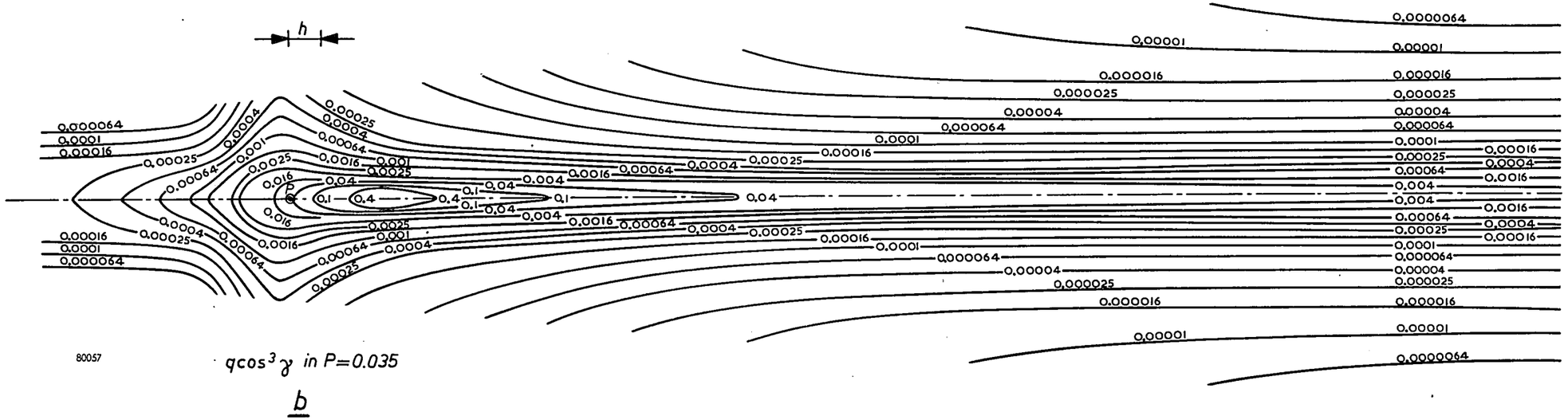

Fig. 7b. E.P. diagram for wet bricks. See further fig. 7a.

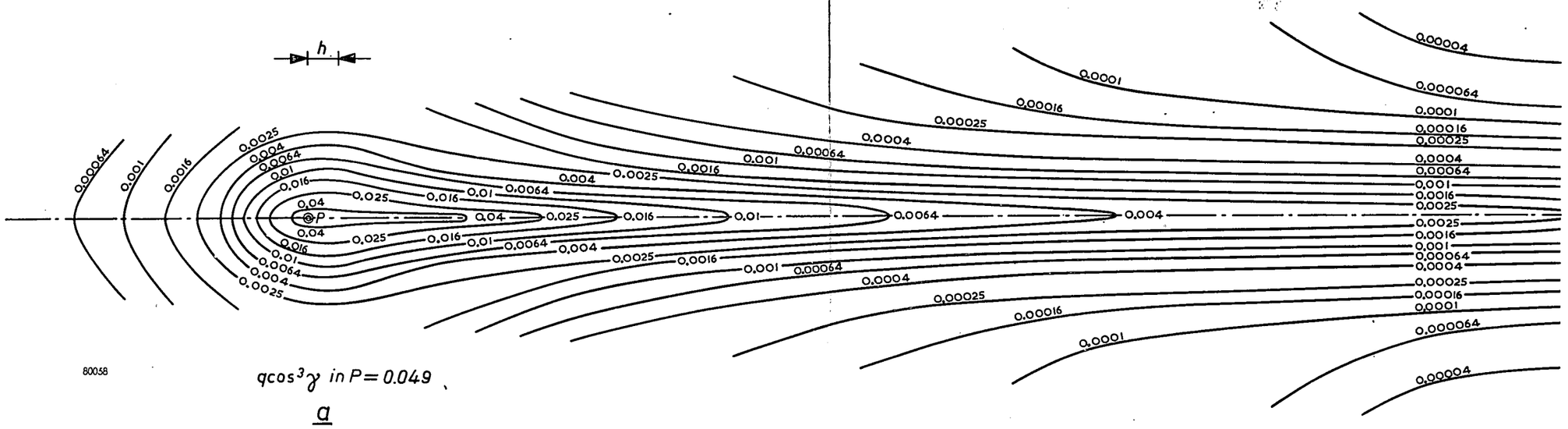

Fig. 8*a*. E.P. diagram for dry cobblestones. See further fig. 7*a*.

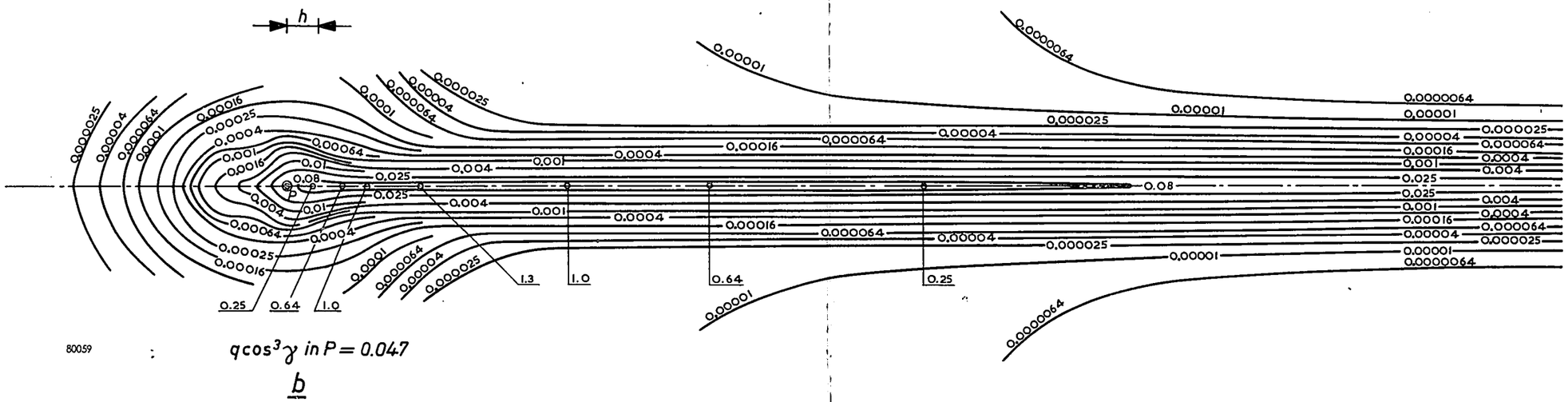

Fig. 8*b*. E.P. diagram for wet cobblestones. See further fig. 7*a*.

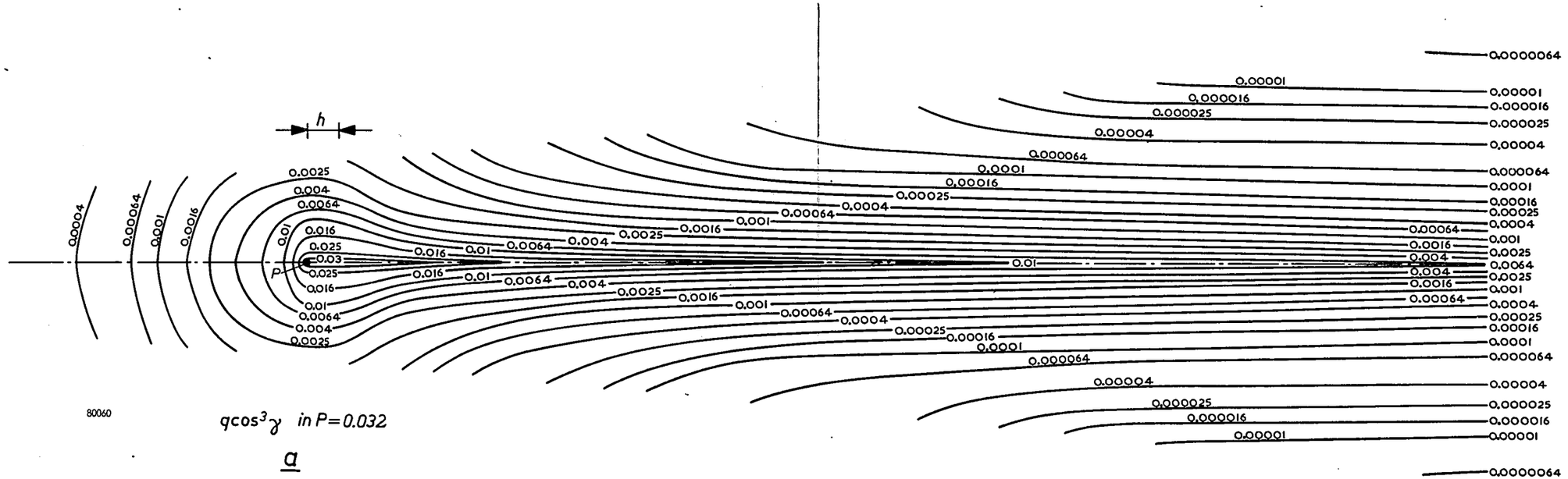

Fig. 9*a*. E.P. diagram for dry asphalt. See further fig. 7*a*.

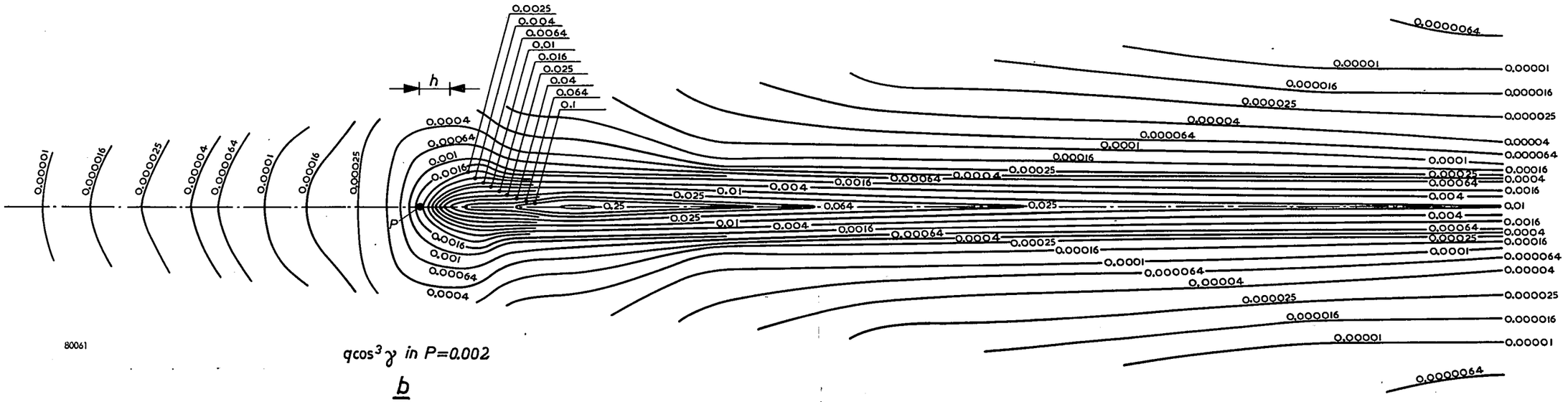

Fig. 9*b*. E.P. diagram for wet asphalt. See further fig. 7*a*.

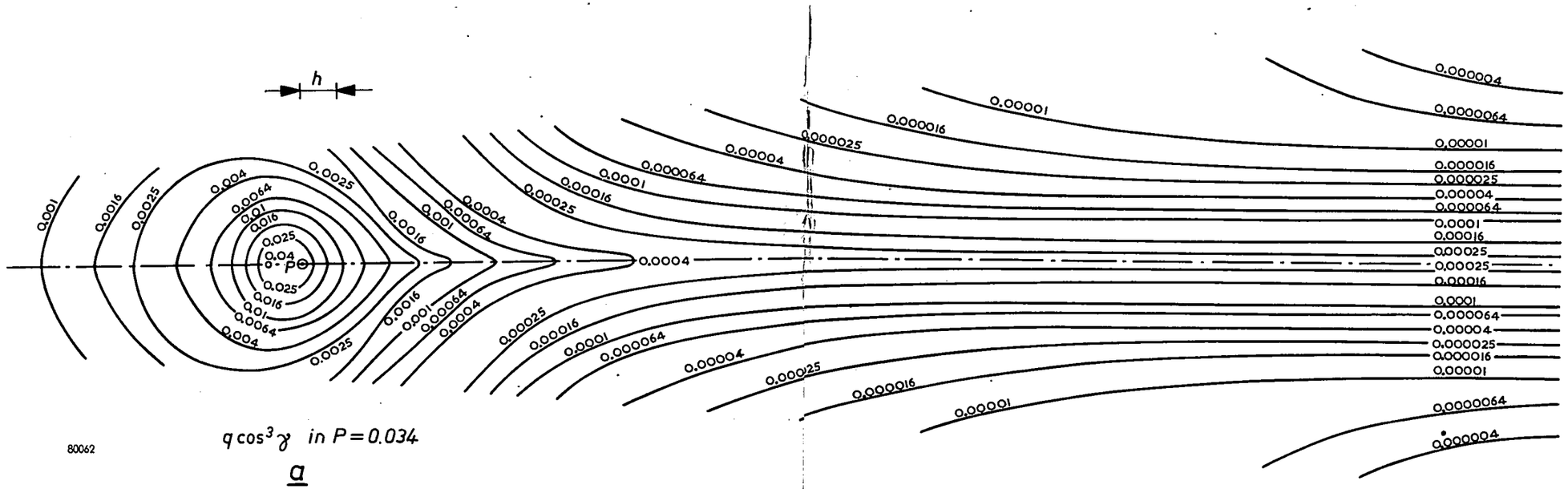

Fig. 10*a*. E.P. diagram for dry concrete. See further fig. 7*a*.

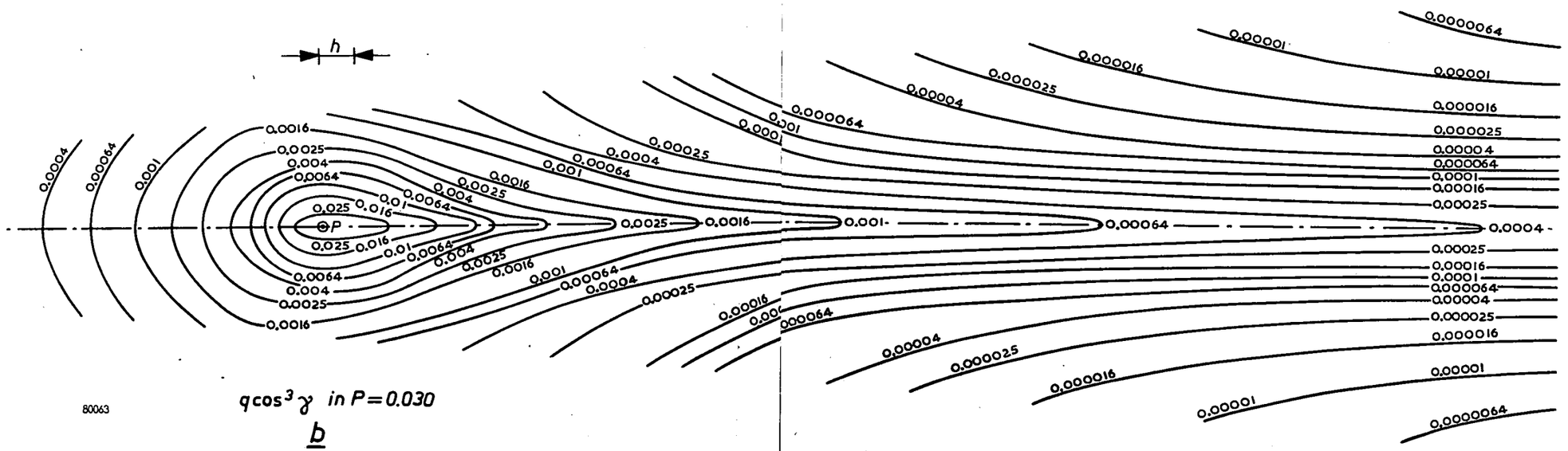

Fig. 10*b*. E.P. diagram for wet concrete. See further fig. 7*a*.

in figs 11 to 14 (the lengthwise section over the points 73, P and 50, the cross-sections over the points 1 to 4, 26 to 30 and 43 to 49 respectively; see fig. 5). Figs 11 and 12 are related to the dry condition, figs 13 and 14 to the wet condition of the considered road surfaces.

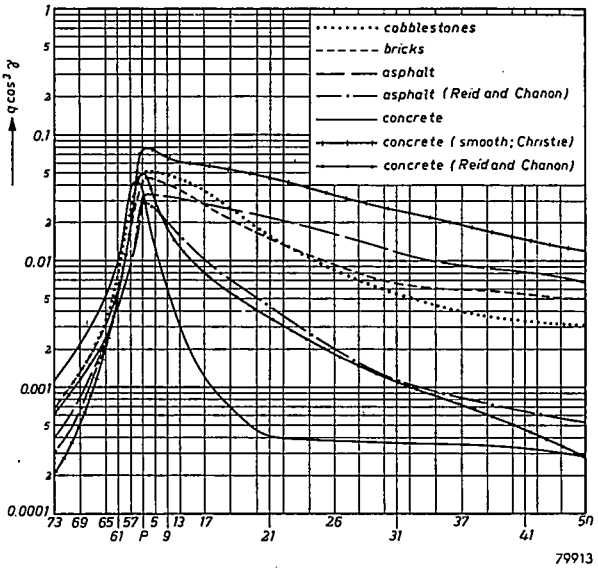

Fig. 11. Lengthwise section of the E.P. diagram for several dry road surfaces.

From figs 11 to 14 inclusive it can be seen that it is not justifiable to speak of the reflection properties of the average road surface. Concrete, especially, shows a picture quite different from that of the other road surfaces, which also differ considerably in several points amongst themselves (see the cross-sections of figs 12 and 14). The concrete studied, which was as already mentioned entirely new, showed rather pronounced grooves. This explains the diffuse character of the surface which persists quite markedly even in the wet condition.

For the sake of comparison results of measurements by Reid and Chanon [7]) carried out on dry asphalt and dry concrete as well as those of Christie [8]) carried out on dry smooth concrete have been inserted in fig. 11. It can be seen from this figure that considerable differences prevail between the results of different investigators. This is to a large extent due to differences in surface texture in so far as road surfaces of the same type have been investigated.

In this respect the classification of road surfaces used by Christie is of interest. Christie classifies the surface texture of road surfaces according to "form" and "scale", distinguishing between "peaky" and "even"

surface texture (form) and "fine" or "coarse" surface texture (scale). Moreover Christie gives a quantitative indication, depending as much on form as on scale, which he calls "texture depth". Christie measures this

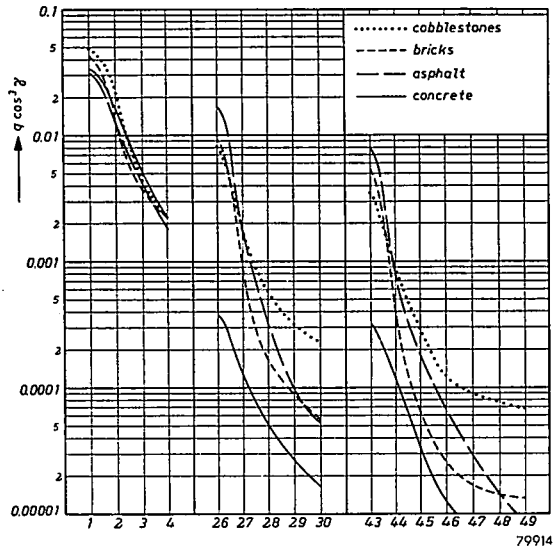

Fig. 12. Cross-sections of the E.P. diagram for several dry road surfaces.

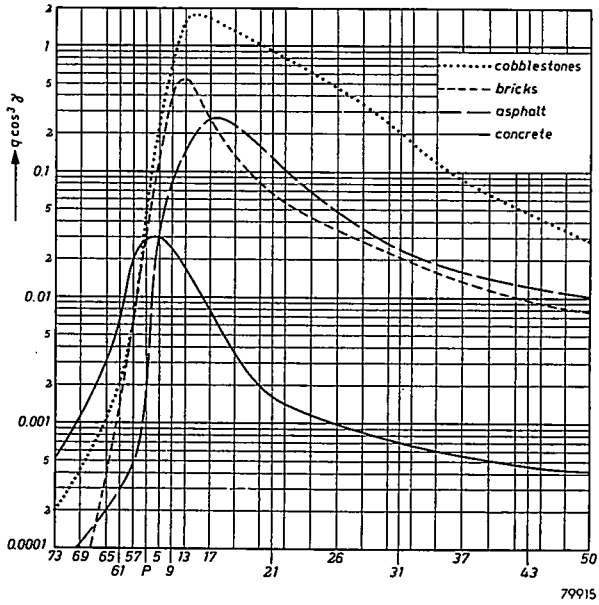

Fig. 13. Lengthwise section of the E.P. diagram for several wet road surfaces.

depth by spreading a known volume of fine sand on the road surface in such a way that all valleys are just filled up. The "texture depth" is equal to the average thickness of the layer of sand, this being the ratio of the volume of sand to the surface area covered.

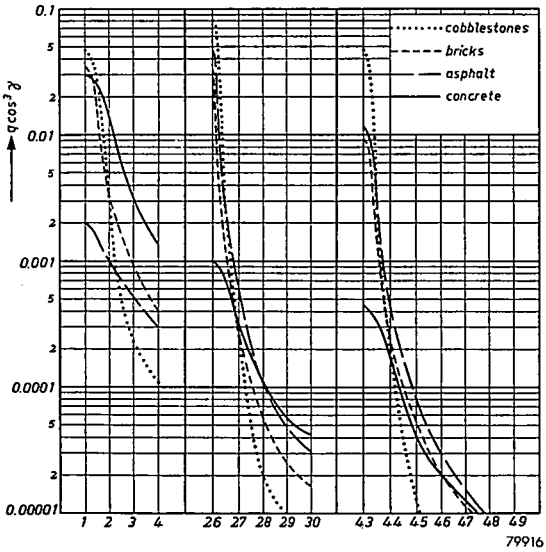

Fig. 14. Cross-sections of the E.P. diagram for several wet road surfaces.

In the table given below an attempt has been made to characterize the road surfaces investigated, according to Christie's method. As far as the classification according to form and scale is concerned it should be borne in mind that this classification remains rather subjective so long as no detailed definition is available of the concepts "peaky" or "even" and "fine" or "coarse". In table III, also, the texture depth, form and scale have been indicated for the concrete investigated by Christie.

When considering the classification of road surfaces in table III it should be borne in mind that the brick and cobblestone surfaces differ considerably from the other ones due to the joints between the stones. When classifying the latter road surfaces these joints have not been taken into consideration.

The very great differences in reflecting properties found by Christie and by the authors for concrete become comprehensible when considering the entirely different surface texture as indicated in table III.

When considering furthermore the three jointless surfaces separately (the two concrete surfaces and the asphalt one), the information of table III seems to indicate greater similarity in surface texture between Christie's

TABLE III

Road surface		Texture depth in mm	Form	Scale
investigated by	type			
Christie	concrete	0·025	even	fine
Authors	bricks	0·13	peaky	fine
	cobblestones	0·01	even	fine
	asphalt	0·09	even	fine
	concrete	0·34	peaky	coarse

concrete and the asphalt investigated than between the authors' concrete and either of the other two. Further, the curves of fig. 11 show greater similarity in reflecting properties between the two first-mentioned surfaces than between the authors' concrete and either of the two others.

It seems to be worthwile, therefore, to make further investigations into the relationship between surface texture and reflecting properties. If such a relationship could be found and surface-texture classified simply along the lines suggested by Christie, sufficiently complete information concerning reflecting properties of road surfaces for the purposes of street lighting could be obtained from the characteristics of only a few surfaces which are typical from the point of view of surface texture.

Eindhoven, April 1954

REFERENCES

1) J. B. de Boer, V. Oñate and A. Oostrijck, Practical methods for measuring and calculating the luminance of road surfaces, Philips Res. Rep. **7**, 54-76, 1952.

2) M. Cohu, Premiers résultats des essais effectués par la Société pour le Perfectionnement de l'Eclairage pour la détermination des characteristiques réfléchissantes des divers revêtements utilisées dans les voies publiques, Rev. gén. Elect. **37**, 755-767, 1935.

3) R. G. Weigel and P. Schlüsser, Ueber die lichttechnischen Eigenschaften von Strassendecken, Das Licht **5**, 161-166; 237-240, 1935.

4) J. O. Kraehenbuehl, Measurement of pavement surface characteristics, Ill. Eng. **47**, 278-287, 1952.

5) D. M. Finch and R. B. Marxheimer, Pavement brightness measurements, I.E.S. 1952 Conference Paper No. 17.

6) J. Bergmans, Lichtreflectie door wegdekken (in Dutch with an English summary at each chapter), Thesis, Delft 1938.
J. Bergmans and W. L. Vervest, A new fitting for road lighting, Philips tech. Rev. **5**, 222-230, 1940.

7) K. M. Reid and H. J. Chanon, Evaluation of street lighting, Trans. Ill. Eng. Soc. **34**, 1209-1232, 1939.

8) A. W. Christie, Road surfaces as reflectors of light, from the point of view of street lighting, Chem. and Ind. 468-475, 1953.
A method of presenting the reflection characteristics of a road surface for use in streetlighting investigations. Road Research Laboratory, Dept. Sci. Ind. Res. Note RN/1651 AWC Oct. '51 unpublished.

Philips Res. Rep. **9**, 225-230, 1954

THE SOLID SOLUBILITY AND THE DIFFUSION OF NICKEL IN GERMANIUM

by F. van der MAESEN and J. A. BRENKMAN

546.289:546.74:532.72/3

Summary

Nickel produces rapidly diffusing acceptors in germanium, just as copper. Hall and resistivity measurements show the existence of a Ni acceptor level lying 0·23 eV above the valence band. On the basis of this picture the solid solubility between 700 and 900 °C is derived from resistivity measurements. From these values and the liquidus curve of the phase diagram Ge-Ni, the distribution coefficients (k) at various temperatures are calculated. The distribution coefficient (k^*) of Ni at the melting point of Ge is calculated at $1{\cdot}8.10^{-6}$ according to a method of Thurmond and Struthers. The diffusion coefficient of Ni in Ge is measured between 700 and 850 °C; the activation energy of diffusion is found to be 21 kcal/mole. Annealing of a Ni-saturated Ge sample restores the original resistivity.

Résumé

Le nickel, exactement comme le cuivre, produit des accepteurs à diffusion rapide dans le germanium. L'effet Hall et les mesures de la résistivité démontrent l'existence d'un niveau accepteur Ni qui se tient 0,23 eV au-dessus de la bande de valence. Sur la base de cette description, la solubilité solide entre 700 et 900 °C fut tirée des mesures de résistivité. Les coefficients de distribution (k) à différentes températures ont été calculés d'après ces valeurs et de la courbe de liquide du système Ge-Ni. Le coefficient de distribution (k^*) de Ni au point de fusion de Ge a été calculé à $1{,}8 \times 10^{-6}$ suivant la méthode de Thurmond et Struthers. Le coefficient de diffusion de Ni dans Ge entre 700 et 850 °C a été mesuré, et l'on a trouvé comme valeur de l'énergie d'activation de la diffusion: 21 kcal/mol. Le recuit d'un échantillon de Ge saturé de Ni fait revenir la résistivité originale.

Zusammenfassung

Ebenso wie Kupfer erzeugt auch Nickel schnell diffundierende Akzeptoren in Germanium. Messungen des Hall-Effektes und des Widerstandes zeigen das Vorhandensein eines 0,23 eV über dem Valenzband liegenden Ni-Akzeptorniveaus an. Auf Grund dieser Vorstellung wird die feste Löslichkeit zwischen 700 und 900 °C aus Widerstandsmessungen abgeleitet. Aus diesen Werten und der Flüssigkeitskurve des Phasendiagramms Ge-Ni werden die Verteilungskoeffizienten (k) bei verschiedenen Temperaturen berechnet. Der Verteilungskoeffizient (k^*) von Ni beim Schmelzpunkt von Ge wird errechnet zu $1{,}8 \times 10^{-6}$ nach der Methode von Thurmond und Struthers. Es wird der Diffusionskoeffizient von Ni in Ge gemessen zwischen 700 und 850 °C; die Aktivierungsenergie für die Diffusion beträgt 21 kcal/Mol. Durch Ausglühen einer Ni-gesättigten Ge-Probe wird der ursprungliche Widerstand wieder zurückerhalten.

1. Solid solubility

It is known that nickel in germanium shows an acceptor activity [1],[2]) causing conversion of an *n*-type germanium sample of appropriate resistivity into *p*-type on heating at 800 °C.

In order to avoid the presence of copper impurities the Ge samples were cleaned with double-distilled concentrated HNO_3 [2]). After this the pieces were covered electrolytically with pure Ni and then heated for some time at the desired temperature. After quenching, the resistivity was measured.

To be sure of saturation the samples were cleaned, plated again and reheated at the same temperature. After quenching no change in resistivity was found, showing saturation and the absence of copper impurities in the nickel at the same time.

From measurements of the Hall constant at various temperatures of a sample saturated with Ni at 800 °C we calculated the position of the Ni acceptor level in the forbidden band. We found over the range of 170 to 250 °K a consistent value of 0·23 eV for the distance between the level and the valence band. This result is in good agreement with the value of 0·25 to 0·30 eV given by Burton [1]).

Assuming each Ni atom to give one acceptor level, we can evaluate the concentration of Ni atoms from resistivity measurements. Results of the saturation concentration c_s at various temperatures are given in table I.

TABLE I

Temperature (°C)	Heating time (hours)	c_s (at./cm^3)
700	22	$2{\cdot}4.10^{14}$
750	18	7·6
800	7	16·0
850	3	36·8
875	2·5	43·9
900	2	47·5
920	2	46·4

Fig. 1 shows a plot of log c_s versus $1/T$. From 700 up to 850 °C the graph is linear corresponding to

$$(c_s)_{\mathrm{Ni}} = 1{\cdot}9.10^{23} \exp\left(-\frac{39500}{RT}\right) \text{ at./cm}^3 \qquad (RT \text{ in cal}). \qquad (1)$$

Above 850 °C the curve bends; at about 900 °C the solubility decreases rapidly showing a retrograde character.

On the basis of quantitative thermodynamical considerations Meijering [8]) has pointed out that when the solid solubility is very low compared with that in the liquid a retrograde solidus curve is normally expected.

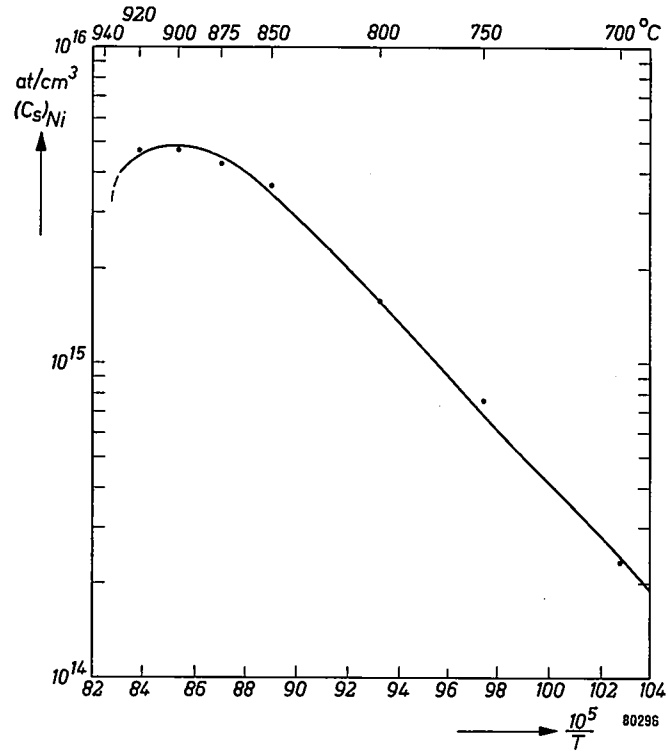

Fig. 1. Plot of log $(c_s)_{Ni}$ versus $1/T$. The rectilinear part of the curve can be represented by equation (1).

2. Distribution coefficient (k)

Recently Thurmond and Struthers [3]) reported on alloys of Ge and of Si. They found the logarithm of the experimentally measured distribution coefficient k of Sb in Ge, Cu in Ge, and Cu in Si to be a linear function of the reciprocal of the absolute temperature:

$$\log k = B - \frac{A}{T}. \qquad (2)$$

Values of k at the melting points (T_1^f) of Si and of Ge are obtained

by extrapolation. The solidus curves of these binary alloys show also a retrograde character.

Considering the properties of a liquid solution in equilibrium with a dilute solid solution Thurmond and Struthers obtained the following thermodynamical expression:

$$\ln k = \frac{\Delta H_2^f - \overline{\Delta H_2^s}}{RT} + \frac{\sigma - \Delta S_2^f}{R} + \ln \gamma_2^l, \tag{3}$$

where ΔH_2^f is the heat of fusion and ΔS_2^f the entropy of fusion of the pure solute (both at the melting point of the pure solute), σ an extra positive entropy term occurring in the differential entropy of the solid solution, and γ_2^l the activity coefficient of the solute in the liquid phase, equal to 1 for an ideal liquid solution.

Comparing (2) with (3) A and B can be related to thermodynamical properties.

The differential heat of solution of the solute ($\overline{\Delta H_2^s}$) can be written as

$$\overline{\Delta H_2^s} = \Delta H_2^f + 2{\cdot}303\, RA\,. \tag{4}$$

We will apply the above considerations also to the Ge-Ni system. The atomic fraction of Ni in the liquid solution (x_l) at a certain temperature can be determined from the phase diagram, and the atomic fraction of Ni in the solid solution (x_s) from c_s at the same temperature.

The phase diagram Ge-Ni has a eutecticum at 775 °C; so the distribution coefficient can be calculated only above this temperature. The results are given in table II and fig. 2.

TABLE II

Temp. (°C)	x_s (at. fr.)	x_l (at. fr.)	k ($= x_s/x_l$)
800	$3{\cdot}5.10^{-8}$	$3{\cdot}4.10^{-1}$	$0{\cdot}10.10^{-6}$
850	8·1	2·4	0·33
875	9·6	1·9	0·52
900	10·4	1·3	0·84
920	10·2	0·75	1·36

The plot of $\log k$ versus $1/T$ gives a straight line which can be represented by

$$\log k = 3{\cdot}52 - \frac{11250}{T}. \tag{5}$$

Extrapolation to $T_1^f = 1209$ °K [5]) gives the distribution coefficient $k^* = 1{\cdot}8.10^{-6}$. Measurements by Burton a.o. [6]) with radioactive nickel (Ni^{63}) give a distribution coefficient $k^* = 5.10^{-6}$ in reasonable agreement with our experiments.

With $\Delta H_2^f = 4{\cdot}2$ kcal/mole for Ni [7]) and $A = 11250$ we find, using equation (4) for the differential heat of solution of Ni, that $\overline{\Delta H}_2^s = 55{\cdot}6$ kcal/mole.

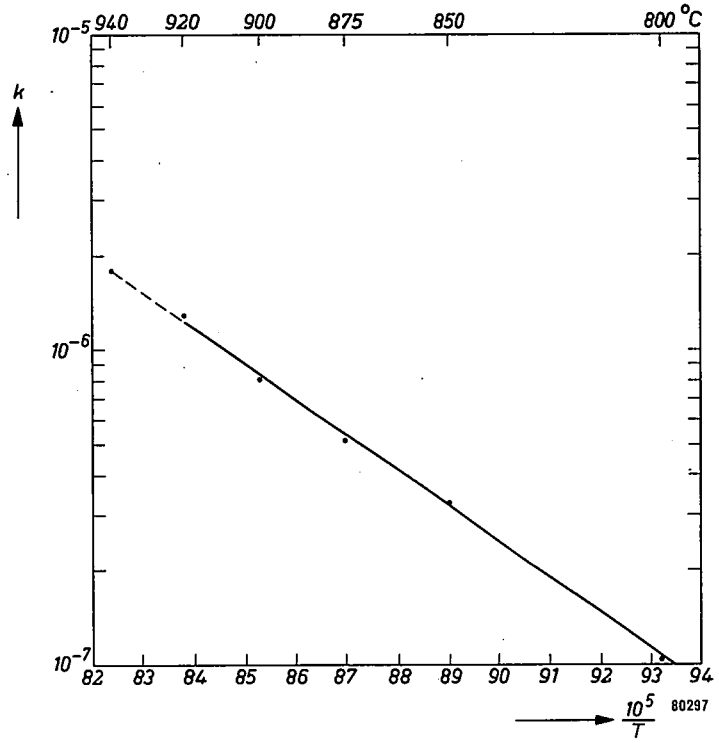

Fig. 2. Plot of log k versus $1/T$ represented by equation (5).

3. Diffusion coefficient (D)

The diffusivity of Ni in Ge at several temperatures was determined from measurements of the penetration depth x of the p-n barrier, the original n-type resistivity and the diffusion time t. From the resistivity one can calculate the acceptor concentration c at the p-n barrier. The results are collected in table III.

The diffusion coefficient D as a function of the absolute temperature can be expressed as

$$D = 0{\cdot}8 \exp\left(-\frac{21000}{RT}\right) \text{cm}^2/\text{sec} \qquad (RT \text{ in cal}). \tag{6}$$

TABLE III

temp. (°C)	t (sec)	x (cm)	c_s (at./cm^3)	c (at./cm^3)	D (cm^2/sec)
700	900	0·15	$0{\cdot}85.10^{14}$	$2{\cdot}4.10^{14}$	$1{\cdot}5.10^{-5}$
750	900	0·30	1·01	7·6	2·2
800	900	0·51	1·11	16·0	4·4
850	900	0·57	1·24	23·8	4·8
875	900	0·75	0·65	36·8	5·5

There is evidence that the diffusion coefficient at a given temperature is not constant over the diffusion range [2]). This phenomenon is also found with the diffusion of Cu in Ge. More experiments with respect to this effect are in progress.

4. Annealing

An n-type Ge sample of 37 Ωcm covered with Ni becomes p-type on heating at 800 °C. After annealing at 500 °C during 80 hours the sample reaches its original n-type resistivity.

The lifetime of electrons in the Ni-saturated Ge sample is very small (< 1 μsec) whereas after annealing the lifetime of holes reaches only 70 μsec, as compared with a value of 1100 μsec in the original n-type sample.

Acknowledgements

The authors are indebted to Dr B. H. Schultz for valuable discussions and to Mr A. Plugge for carrying out the Hall and resistivity measurements.

Eindhoven, April 1954

REFERENCES

1) J. A. Burton, G. W. Hull, F. J. Morin and J. C. Severiens, J. phys. Chem. **57**, 853-859, 1953.
2) F. van der Maesen, P. Penning and A. van Wieringen, Philips Res. Rep. **8**, 241-244, 1953.
3) C. D. Thurmond and J. D. Struthers, J. phys. Chem. **57**, 831-835, 1953.
4) K. Ruttewit and G. Masing, Z. Metallk. **32**, 52-61, 1940.
5) E. S. Greiner, J. Metals **4**, 1044, 1952.
6) J. A. Burton, E. D. Kolb, W. P. Slichter and J. D. Struthers, J. chem. Phys. **21**, 1991-1996, 1953.
7) L. L. Quill, The chemistry and metallurgy of miscellaneous materials, McGraw-Hill Book Company, Inc., New York, 1950, p. 29.
8) J. L. Meijering, Philips Res. Rep. **3**, 281-302, 1948.

Philips Res. Rep. **9**, 231-237, 1954

CONVERTING A NUMBER DISTRIBUTION OF PARTICLE SIZE INTO ONE FOR VOLUME OR SURFACE AREA

by M. E. WISE

519.242.35:539.215.2

Summary

A number distribution of equivalent radii of particles in a powder can be accurately converted into a distribution by volume or surface area, even if the data are highly and/or non-uniformly grouped. A formula is derived to do this and is applied to a microscopic analysis into a frequency distribution of radii between 1, $\sqrt{2}$, 2, $2\sqrt{2}$, 4,... units.

Résumé

Une distribution de nombres de rayons équivalents de particules dans une poudre peut être convertie avec précision en une distribution par volume ou par surface, même si les éléments sont fortement et/ou non uniformément groupés. Pour cela une formule est calculée et appliquée à une analyse microscopique dans une distribution de fréquences de rayons entre 1, $\sqrt{2}$, 2, $2\sqrt{2}$, 4, ... unités.

Zusammenfassung

Eine statistische Verteilung äquivalenter Radien von Teilchen in einem Pulver läßt sich sehr genau umwandeln in eine Verteilung nach Volumen oder Oberfläche, selbst wenn die Daten in großen Größenunterschieden und/oder nicht einheitlich gruppiert sind. Zur Durchführung dieser Umwandlung wird ein Formel abgeleitet und zu einer mikroskopischen Analyse in einer Frequenzverteilung von Radien zwischen 1, $\sqrt{2}$, 2, $2\sqrt{2}$, 4, ... Einheiten verwendet.

1. Introduction

The distribution of grain sizes in a powder is often wanted. An obvious way to find it is to examine the particles under a microscope; with the help of a suitable graticule of concentric circles, for example, it is quite easy to count the number of particles having "effective radii" (that is to say, radii of spheres of equal volume) between two given radii.

However chemists and physicists are more often interested in the proportion by volume (or weight) of particles with effective radii between two given values; the corresponding proportion of the total surface area, or the surface area itself, is sometimes important also. It seems generally believed impracticable to estimate these weighted proportions accurately, given only the data from a microscopic count, on the grounds that (i) the weighted proportions are too sensitive to sample fluctuations, (ii) apart from these the unavoidable grouping of the observed radii into frequency intervals — and in practice rather broad and sometimes non-uniform ones— makes an accurate calculation impossible; for example it would be wrong

to assume that every particle in one group has the volume of a sphere with radius equal to the mid-value of the frequency interval.

These arguments have caused the microscopic count method to be condemned as unreliable for estimating volume distributions. But this is unjustified, and this note has been written to show why. Three simple mathematical principles can be combined to produce a fairly simple yet accurate method of calculating the weighted distributions; a method of this kind has in fact been in regular use for some time*). Such a simple device has surely been found and used elsewhere, but I could not find any mention of it in Herdan's recent very full treatment of "small-particle statistics" [1]).

2. Mathematical derivation

What is obtained from the observations is the proportion by number of particles having effective radii between various pairs of values, and hence the accumulated proportions. If $P(r)$ is the probability function, so that $P(r)\mathrm{d}r$ is the proportion between r and $r + \mathrm{d}r$, the observations can give

$$\int_{r_1}^{R} P(r)\mathrm{d}r = \text{(definition) } P^{-1}(r_1), \tag{1}$$

where R is a radius larger than that of the largest particle observed, so that $P^{-1}(r_1)$ is the proportion by number of particles larger than r_1 in radius. The observed values of $P^{-1}(r_1)$ can be plotted against r_1 (on ordinary graph paper or perhaps better on logarithmic-probability paper), and if the points lie about a smooth curve this curve can be used to reduce the more obvious sample fluctuations, if need be.

The next point is that the proportions (or the percentages) are accumulated from the *upper* end; why this is done will become clear later.

Now we want to find proportions by volume (say); the weighted proportion for particles larger than r_1 is

$$W_p(r_1) = \frac{\int_{r_1}^{R} r^p P(r)\mathrm{d}r}{\int_{r_0}^{R} r^p P(r)\mathrm{d}r}, \tag{2}$$

where r_0 is less than the smallest radius observed. For $p = 3$ eq. (2) gives the proportion by volume whilst $p = 2$ gives the proportion of surface area, in or on particles larger than r_1, assuming of course that the surface area of a particle is equal to kr^2 where k is the same for every particle.

*) e.g. in the Material Research Laboratory of Philips Electrical Ltd, Mitcham Surrey, England. Acknowledgements are due to Dr M. L. Smith and Dr J. A. M. van Moll, its head, who suggested the problem originally in this laboratory.

What is often done is to take $P(r_1)$ to be the relative frequency of particles with radii between $r_1 \pm \varepsilon$, hence $P(r_1) = F(r_1)/N$ (say) where N is the number counted, and to sum the values of $F(r_1)r_1^p$. But many distributions are very skew, with a long tail of large r values (see fig. 1), and in this tail the proportion by volume will be continually underestimated if the middle value of the grouping interval is cubed (or squared). From experience it seems better to cube or square the lowest value of r_1 in the interval, i.e. $r_1 - \frac{1}{2}\varepsilon$, but obviously this cannot be quite right either.

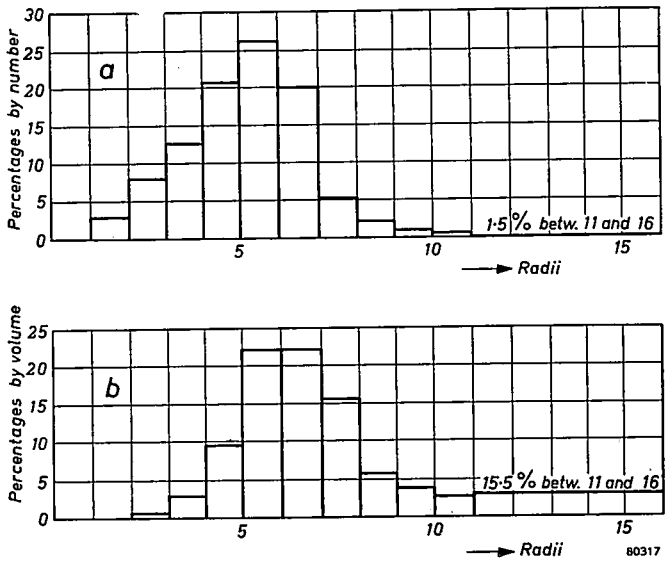

Fig. 1. Histograms of the radius distribution (a) by number and (b) by volume.

All that has to be done to avoid this difficulty is to convert the integrals into ones involving accumulated probabilities. Integrating by parts

$$\int_{r_1}^{R} r^p P(r)\mathrm{d}r = -\int_{r_1}^{R} r^p \frac{\mathrm{d}}{\mathrm{d}r}\{P^{-1}(r)\}\mathrm{d}r = [r^p P^{-1}(r)]_{R}^{r_1} + p\int_{r_1}^{R} r^{p-1}P^{-1}(r)\mathrm{d}r, \quad (3)$$

whence

$$W_p(r_1) = \frac{r_1^p P^{-1}(r) + p\int_{r_1}^{R} r^{p-1}P^{-1}(r)\mathrm{d}r}{r_0^p + p\int_{r_0}^{R} r^{p-1}P^{-1}(r)\mathrm{d}r}. \quad (4)$$

Since $P^{-1}(r)$ decreases while r^{p-1} increases with r, their product is usually easy to integrate to good numerical accuracy using the trapezoidal rule.

In a microscopic count the values of r_1 are often taken in geometrical progression, that is, the particles are examined against a graticule of concentric circles of radii 1, $\sqrt{2}$, 2, $2\sqrt{2}$,... units (microns, say). Then it is better to transform the integral by putting $r = 2^{1/2}u$, $R = 2^{1/2}U$ and so on, whence

$$W_p(r_1) = \frac{\frac{1}{2}p \log 2 \int_{u_1}^{U} r^p \, P^{-1}(r) \, du + r_1^3 \, P^{-1}(r_1)}{\frac{1}{2}p \log 2 \int_{u_0}^{U} r^p \, P^{-1}(r) \, du + r_0^3 \, P^{-1}(r_0)} \qquad (5)$$

for the observed accumulated percentages or propertions now correspond to values of u equally spaced, which simplifies the numerical integration.

3. Numerical example

A complete calculation is set out, using (5), for finding a volume distribution. Only slide-rule accuracy is needed, so that the time spent in carrying out a similar one will generally be much less than the time needed for counting the particles. The microscopic count, it is supposed, yielded the accumulated percentages given in row (d) of the table. These are multiplied by the corresponding r_1^3 values of row (e), yielding (f), then continued addition gives (g), values of double the integral; if any one of them is wrong the summation check (see under the table) on (f) will show it. The values have to be multiplied by $\frac{1}{4}p \log 2$, with $p = 3$, which comes to 0·5199. Row (i) gives accumulated volumes in arbitrary units; their differences (j) are then divided by the total volume to give percentages by volume (k) and accumulated ones (l).

The continued addition should be checked, e.g. the sum of row (f) minus $\frac{1}{2} \times 2{\cdot}8 = 192{\cdot}7 = \frac{1}{2} \times 385{\cdot}4$.

The only error not inherent in the data is in the numerical integration, and in many practical cases this is either negligible or unimportant. But a correction term can easily be brought into the calculation; to do so there has to be added to (g) the expression (6)

$$\frac{1}{6}\left\{\frac{\mathrm{d(f)}}{\mathrm{d}u(u=u_1)} - \frac{\mathrm{d(f)}}{\mathrm{d}u(u=U)}\right\}. \qquad (6)$$

The slopes of most particle-size distributions are zero at both ends, unless the distributions have been cut off (e.g. by sieving). Assuming this is not so, the correction term reduces to

$$\frac{1}{6}\frac{\mathrm{d(f)}}{\mathrm{d}u_1} \doteq \frac{1}{12}\{\mathrm{f}(u_1+1) - \mathrm{f}(u_1-1)\},$$

(the derivative is about equal to half the difference between the neigh-

TABLE I

The calculation of the volume distribution

(a) u	$(u_0 =)1$	2	3	4	5	6	7	$8(=U)$
(b) r	$(r_0) = \sqrt{2}$	2	$2\sqrt{2}$	4	$4\sqrt{2}$	8	$8\sqrt{2}$	$16(=R)$
(c) Percentages by number	2·7	6·6	14·2	38·3	33·4	3·4	1·4	
(d) Accumulated percentages	100	97·3	90·7	76·5	38·2	4·8	1·4	0
(e) r_1^3	2·83	8	22·62	64	181·0	512	1448	4096
(f) $r_1^3 \; P^{-1}(r_1)$	2·8	7·8	20·5	49·0	69·1	24·6	20·3	0
*) (g) $2 \int_{U_1}^{U} r^3 P^{-1}(r_1)\, du$	385·4	374·8	346·5	277·0	158·9	65·2	20·3	0
(h) 0·5199 (g)	200·3	194·9	180·0	144·0	82·6	33·9	10·6	0
(i) = (f) + (h)	203·1	202·7	200·5	193·0	151·7	58·5	30·9	0
(j) Relative proportions by volume	0·4	2·2	7·5	41·3	93·2	27·6	30·9	
(k) Percentages by volume; here (k) = 100 (j)/203·1.	0·2	1·1	3·7	20·3	45·9	13·6	15·2	
(l) Accumulated percentages	100·0	99·8	98·7	95·0	74·7	28·8	15·2	0

*) Values of the integral obtained by continued addition, e.g. 158·9 = 65·2 + 24·6 + 69·1.

bouring values on either side, divided by the interval, here 1). In table II, row (δ) shows the estimated numerical values of the derivatives, δ(g) is what has to be added to (g), and the remaining rows show the changes thereby brought about. Evidently the change at the lower end of the table is not negligible, but this indicates rather that the lower end of the volume distribution cannot be obtained too accurately. The results in fact are now as accurate as the data permit, which would certainly not be so if they had been obtained by a direct summation and integration from the original counts.

TABLE II

Effect of correction term in the numerical integration

u	1	2	3	4	5	6	7	8
(δ)	4	9	21	24	—12	—12	—12	0
$\delta(g) = \frac{1}{12}(\delta)$	0·3	0·7	1·8	2·0	—1·0	—1·0	—1·0	0
(i)′	203·4	203·4	202·3	195·0	150·7	57·5	29·9	0
(j)′	0	1·1	7·3	44·3	93·2	27·6	29·9	
(k)′	0	0·5	3·6	21·8	45·8	13·6	14·7	
(l)′	100·0	99·5	95·9	74·1	28·3	14·7	0	

(δ) estimated values of d(f)/du, (i)′ accumulated volumes in arbitrary units, (j)′ volumes between given radii in arbitrary units, (k)′ percentages by volume, (l)′ accumulated percentages.

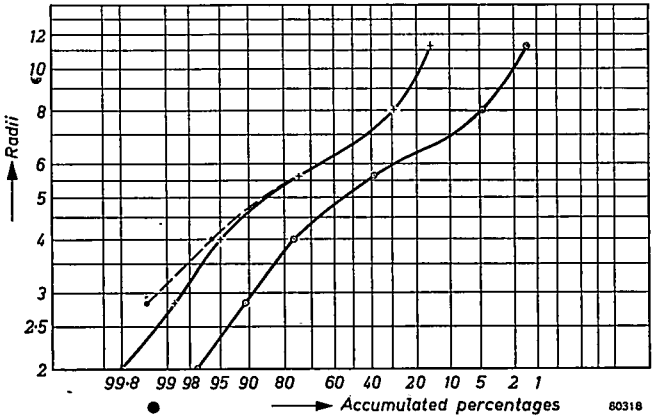

Fig. 2. Percentages greater than a given radius, plotted on logarithmic-probability paper.
—⊙— percentages by number of particles;
—+— percentages by volume of particles, calculated from integral by trapezoidal rule;
—●— the same, integration by trapezoidal rule with correction term.

Finally, it is worth reminding the reader that all this work is unnecessary if the number distribution is log-normal. This is known as Kapteyn's law when applied to grain sizes; the accumulated percentages then lie on (or about) a straight line when plotted on log-probability paper. The weighted distribution is a parallel line and is simply displaced a distance $p\sigma$ vertically, where σ is the standard deviation of log r. This can be found from the slope of the straight line, for $\overline{\log r}$, the mean of log r, is the 50-percent point, and $(\log r_1 - \overline{\log r})/\sigma$ is equal to 1·645, 2·326 and 3·09 at 95%, 99% and 99·9% respectively. This short cut is well known; for full details and references see Herdan's book [1]). However, the 'integration-by-parts' method is valid for any distribution function.

Eindhoven, February 1954

REFERENCE

[1]) G. Herdan, Small Particle Statistics, Elsevier, 1953.

Erratum

W. de Groot, Philips Res. Rep. 8, 401-410, 1953.
The factor $(p+4)$ in eq. (25), page 407, should be deleted.

ABSTRACTS OF RECENT SCIENTIFIC PUBLICATIONS OF N.V. PHILIPS' GLOEILAMPENFABRIEKEN

Reprints of the majority of these papers can be obtained on application to the Administration of the Research Laboratory, Kastanjelaan, Eindhoven, Netherlands. Those papers of which no reprints are available are marked with an asterisk (*).

2053: J. de Jonge, R. Dijkstra and G. L. Wiggerink: The quantum yield of the photo-decomposition of some aromatic diazonium salts (Rec. Trav. chim. Pays-Bas **71**, 846-852, 1952).

The quantum yield of the photo-decomposition of some aromatic diazonium salts in solution is estimated, using light with a wavelength of 3650 Å. The photo-decomposition of phenyl-amine benzene diazonium sulphate is proposed as a suitable actinometer. The quantum yield of the photochemical isomerization of the stable form of p-methoxy-benzene diazo-cyanide is found to be about 0·35.

2054: J. I. de Jong and J. de Jonge: The reaction between urea and formaldehyde in concentrated solutions (Rec. Trav. chim. Pays-Bas **71**, 890-898, 1952).

The nature and the velocities of the reactions occurring in concentrated solutions of urea and formaldehyde are very similar to those found in dilute systems. A rapid initial reaction between urea and formaldehyde, as reported in literature, is not observed and is shown to be due to the analytical methods used.

2055: K. H. Klaassens and C. J. Schoot: The preparation of 1-methyl-2-hydroxy-3-diazobenzene-5-sulphonic acid (Rec. Trav. chim. Pays-Bas **71**, 920-924, 1952).

The preparation of 1-methyl-2-hydroxy-3-diazobenzene-5-sulphonic acid, starting from o-cresol, is described. With a small quantity of a strong acid a suspension of 1-methyl-2-hydroxy-3-aminobenzene-5-sulphonic acid in a solution of sodium nitrite gives the sodium salt of the diazonium compound.

2056: J. G. Bos, R. J. H. Alink and C. J. Dippel: Photodecomposition of aqueous solutions of diazonium salts in the presence of mercurous ions (Rec. Trav. chim. Pays-Bas **71**, 945-953, 1952).

Photo-decomposition of aqueous solutions of o-hydroxydiazonium salts leads to formation of mercury by disproportion of mercurous ions, in contrast to p-aminobenzenediazonium salts where mercury results from reduction of mercurous ions by the photo-decomposition products.

2057: H. Bremmer: The derivation of paraxial constants of electron lenses from an integral equation (Appl. sci. Res. **B2**, 416-428, 1952).

The paraxial trajectories in electron lenses are derived from an integral equation. The Liouville-Neumann expansions of the solutions of this equation lead to expressions for the magnification, the focal distances and the positions of the focal and cardinal points. The numbers of integrations to be performed in the individual terms of the expansions are reduced to one half, as compared with the normal treatment. The focal and cardinal points are defined as osculating elements similar to those introduced by Glaser.

2058: A. H. Boerdijk: A new aspect in the calculation of toothed gearing (De Ingenieur **64**, W63-W65, 1952).

This paper deals with the calculation of the numbers of teeth of the wheels in a gearing with a prescribed gear ratio, equal to the ratio of two integers k/l. The known methods of decomposing k and l into prime factors, and of developing k/l in continued fractions often fail to give a practical and exact solution. A new method is described, based on the introduction of planet gearings (or simple differentials) in the conventional gearing. Practical and exact solutions can be obtained for arbitrary values of k and l, even for very large primes.

2059: G. W. Rathenau, J. Smit and A. L. Stuyts: Ferromagnetic properties of hexagonal iron-oxide compounds with and without a preferred orientation (Z. Phys. **133**, 250-260, 1952).

Observation of grain growth in cold-rolled homogeneous Ni-Fe alloys on annealing. The grain growth which accompanies the α-γ phase transformation of a Si-Fe alloy has also been studied by electron-optical means. Since in equilibrium the Si content of the α phase surpasses that of the γ phase the velocity of phase-boundary movement depends essentially on the concentration gradient which determines the diffusion at the moving boundary. In agreement with expectation the advancing boundary of a γ grain curves often heavily convex towards the disappearing α grains. γ grains repel each other because of the high Si content of the α phase in between. The grains of the growing phase are thus enveloped by material having the structure and orientation of the disappearing phase. On lowering the temperature these α inclusions lead to about the initial α structure while on quickly heating they give rise to nuclei of δ phase.

2060: J. Smit: The influence of elastic shear strains on the conductivity and thermo-electric force of cubic metals (Physica **18**, 587-596, 1952).

Elastic shear strains cause a change in the shape of the Fermi surface of metals. The influence that such a change has upon the electrical conductivity and the thermo e.m.f. has been calculated for monovalent face-centred cubic metals, and the results have been compared with the experimental values for Cu, Ag and Au. The theory also accounts qualitatively for the experimental values of trivalent Al.

2061: P. M. van Alphen, C. G. E. Burger, W. J. Oosterkamp, M. C. Teves and T. Tol: Detailerkennbarkeit bei Durchleuchtung und Photographie mit der Bildverstärkerröhre (Fortschr. Röntgenstrahlen-Röntgenpraxis **77**, 469-470, 1952). (Performance of an X-ray image intensifier with visual and photographic observation; in German).

A "bakelite" thorax phantom was used to test the performance of an X-ray image intensifier. The visual acuity during fluoroscopy in a room with fair illumination after 1 min of adaptation and with only 1/5 of the dose rate is almost twice as good as during ordinary fluoroscopy. Photographs of the intensified image can be made with 1/10 of the energy used for ordinary contact photographs and 1/50 of the energy used for ordinary camera photographs. These photographs show a resolution of detail which lies midway between contact photography and ordinary fluoroscopy. The results are in good agreement with calculated data based upon the photon-fluctuation theory of Morgan and Sturm.

2062*: G. W. Rathenau: Grain growth observed by electronoptical means (L'état solide, Rapp. 9 Cons. Phys., Inst. int. Phys. Solvay, 25-29 Sept. 1951, Stoops, Brussels 1952, p. 55-72).

Observations on grain growth of homogeneous alloys (NiFe) and at a phase transition (SiFe). (See these abstracts, Nos **1926** and **1986**.)

2063: K. H. Klaassens and C. J. Schoot: Preparation of 2-ethoxy-4-diethylaminobenzene-1-diazonium borofluoride (Rec. Trav. chim. Pays-Bas **71**, 1086-1088, 1952).

Description of the preparation of the compound named in the title. A stable diacetyl derivative is formed by treating 2-ethoxy-4-diethylamino-1-aminobenzene with acetic anhydride.

VOL. 9 NR 4 AUGUST 1954

Philips Research Reports

EDITED BY THE RESEARCH LABORATORY
OF N.V. PHILIPS' GLOEILAMPENFABRIEKEN, EINDHOVEN, NETHERLANDS

R 246 *Philips Res. Rep. 9, 241-258, 1954*

THE VELOCITY DISTRIBUTION OF ELECTRONS OF THERMIONIC EMITTERS UNDER PULSED OPERATION

PART II. EXPERIMENTAL RESULTS AND A TENTATIVE THEORETICAL EXPLANATION

by C. G. J. JANSEN, R. LOOSJES and K. COMPAAN

537.533:537.583

Summary

The velocity distribution among electrons emitted by metallic and oxide-coated cathodes is investigated by means of the apparatus described in a previous paper. Both under square-pulsed and DC loads metallic cathodes emit electrons with a single well-defined velocity, the dispersion in velocity lying below the resolving power of the observational technique. (BaSr)O and SrO coatings, on the other hand, show under square-pulsed conditions a large dispersion in electron velocities up to several hundreds of volts with spectra consisting of a set of more or less discrete lines. Under a DC load the same oxide coatings emit electrons with nearly uniform velocities, the spectrum consisting of one rather sharp line. When DC is added to a square-pulsed load the line spectrum gradually contracts into a single line when the proportion DC is increased. Coatings of BaO, ThO_2, and of a mixture of (BaSr)O and nickel powder give a one-line spectrum, although this line is less sharp than with metallic cathodes. The velocity spectra of (BaSr)O and SrO are explained by a high resistance in the surface layer of the coating which arises owing to the combined effect of the conduction through the solid material and through the pores. The occurrence of discrete lines is tentatively attributed to the combined effect of the potential distribution in the surface layer, of secondary emission, and of the geometry of the pores. The effect of a DC load is ascribed to polarization in the oxide layer.

Résumé

Au moyen d'un appareil décrit dans un article précédent on procède à des recherches sur la distribution des vitesses des électrons émis par les cathodes métalliques et à couches d'oxydes. Les cathodes métalliques émettent des électrons possédant une vitesse unique bien déterminée, à la fois sous des charges par impulsions rectangulaires et par courant continu, la dispersion des vitesses restant inférieure au pouvoir séparateur de la technique d'observation. Les couches de (BaSr)O et SrO, au contraire, accusent, sous impulsions rectangulaires, une grande dispersion des vitesses des électrons, dispersion pouvant se monter jusqu'à plusieurs centaines de volts,

et avec des spectres consistant en une série de lignes isolées. Sous une charge continue, les mêmes couches d'oxydes émettent des électrons à vitesses presque uniformes, le spectre se composant d'une ligne assez fine. Lorsqu'un courant continu est superposé à une charge par impulsions rectangulaires, le spectre se contracte graduellement en une seule ligne, lorsque l'on augmente la proportion de courant continu. Des couches de BaO, ThO_2, et d'un mélange de (BaSr)O et de poudre de nickel donnent un spectre d'une seule ligne, quoique cette ligne ne soit pas aussi bien définie qu'avec des cathodes métalliques. Les spectres de (BaSr)O et SrO s'expliquent par une résistance élevée dans la couche de surface, qui se produit par suite d'un effet combiné de la conduction à travers les grains des oxydes et à travers les pores. La formation de lignes isolées est attribuée à l'effet combiné de la distribution du potentiel dans la couche de surface, de l'émission secondaire, et de la disposition géométrique des pores. L'effet d'une charge continue est imputé à une polarisation de la couche d'oxydes.

Zusammenfassung

Die Geschwindigkeitsverteilung unter den von metallischen und oxydbedeckten Kathoden emittierten Elektronen wird mittels des in einem früheren Artikel beschriebenen Gerätes untersucht. Sowohl bei Anlegen einer rechteckförmigen als auch einer Gleichspannung emittieren metallische Kathoden Elektronen mit einer einzigen genau definierten Geschwindigkeit, wobei die Streuung hinsichtlich der Geschwindigkeit unterhalb des Auflösungsvermögens der angewandten Versuchsanordnung liegt. Andererseits zeigen (BaSr)O- und SrO-Schichten unter Bedingungen einer Rechtecksspannung eine große Streuung hinsichtlich der Elektronengeschwindigkeiten, die sich über mehrere Hundert Volt erstreckt, mit Spektren, die aus einer Schar mehr oder weniger diskreter Linien bestehen. Bei einer angelegten Gleichspannung emittieren dieselben Oxydschichten Elektronen mit nahezu einheitlichen Geschwindigkeiten, wobei das Spektrum aus einer ziemlich scharfen Linie besteht. Wird der Rechtecksspannung eine Gleichspannung hinzugefügt, so nimmt das Linienspektrum nach und nach die Form einer einzigen Linie an, wenn das Gleichspannungsverhältnis anwächst. Schichten von BaO, ThO_2, sowie eines Gemisches von (BaSr)O und Nickelpulver ergeben ein einziges Linienspektrum, wenngleich diese Linie weniger scharf ist als bei Metallkathoden. Die Geschwindigkeitsspektren von (BaSr)O und SrO werden durch einen hohen Widerstand in der Oberflächenlage der Schicht erklärt, welcher Widerstand auf die gemeinsame Wirkung der Leitung durch das feste Material und durch die Poren hindurch zurückzuführen ist. Das Auftreten diskreter Linien wird versuchsweise der kombinierten Wirkung der Potentialverteilung in der Oberflächenlage, der Sekundäremission, und der Geometrie der Poren zugeschrieben. Die Wirkung einer Gleichspannung wird auf die Polarisation der Oxydschicht zurückgeführt.

1. Introduction

In part I of this paper [1]) we described an apparatus for measuring the velocity distribution of electrons emitted by cathodes under pulsed conditions. In this part II we shall describe and try to explain the velocity spectra observed with the aid of that apparatus with metallic and oxide-coated cathodes under varying experimental conditions. We begin with a brief review of some previous investigations.

2. Review of investigations on oxide-coated cathodes under pulsed operation

Several post-war investigations [2]) resulted in a number of findings of

great practical and theoretical importance. It was established that under pulsed operation the thermionic emission of a normal oxide-cathode coated with (BaSr)O can attain current densities some factors of ten higher than under DC operation, the current density being limited by sparking. With fresh cathodes this sparking occurs in the space-charge region of the current-voltage characteristic. With aged cathodes, which have a lower i-V characteristic, sparking occurs in the saturation area. An important heat generation in combination with a great fieldstrength in the coating is supposed to be a predominant cause of sparking. The heat generation is explained as follows.

Because the resistance R of an oxide coating is not negligible the additional heating of the coating by $i_{\text{pulse}}^2 R$ may be important when i_{pulse} reaches high values at average current densities which would produce only a slight heating under DC operation. Besides, the high resistance of an interface layer between nickel core and oxide can lead to an extra heat generation. Increases of 100 °C in the temperature of the nickel base as a result of the passage of a pulse current are not exceptional.

An interface layer may be caused by the reaction products of the oxide coating with the reducing components of the nickel core (for example Si) which are necessary to obtain a satisfactory emission. If these reaction products have a high resistance this results, besides in an extra heat generation, also in a large potential drop (e.g. 100 volts) in the interface layer. Since this layer is only a few microns thick, fieldstrengths of 10^5-10^6 volts/cm can occur.

From investigations in these laboratories [3] [4]) it was concluded that the potential drop across a normal (BaSr)O coating (55 mole % BaO, 45 mole % SrO) at high current densities can attain a value of about 200 volts. Moreover, it was shown by probe measurements that this potential drop is mainly concentrated near the surface of the oxide coating. Biguenet [5]) and Nergaard [22]) also found that the major voltage drop occurs in the coating and not in the interface area. The absence of a high resistance in the interface layer between metal and oxide is probably due to the composition of the cathode nickel used; the reducing components consisted principally of 0·1 % to 0·2 % magnesium and some silicion *).

A normal (BaSr)O coating has a very porous structure (up to 85 % pores). This leads to the assumption that electrons arriving in the space between the oxide surface and the anode are not only emitted from the surface grains but also from places deeper in the coating, and may have to pass through a fairly large potential difference before arriving at the surface [4]). It can then be expected that the emitted electrons will have

*) An analysis of the average composition in weight % is: Ni 99, Co 0·6, Mg 0·14, Si 0·05, Al 0·03, Fe 0·02, Cu 0·008, Mn $<$ 0·006.

velocities differing by tens of electron volts. If so, the velocity distribution of the electrons must show marked deviations from the Maxwell distribution the dispersion of which amounts to about 2 kT ($\approx$0·1 eV) at a working temperature of 1000 °K. These considerations led us to investigate the velocity distribution of the emitted electrons.

3. The velocity distribution of emitted electrons

(a) *Metallic cathodes*

In the electron-velocity spectra of a nickel, a tantalum, or an L-cathode [6]), all three metallic cathodes without an oxide coating, we observed one sharp line (see figs 1*a* and 1*b*) under all circumstances with DC or

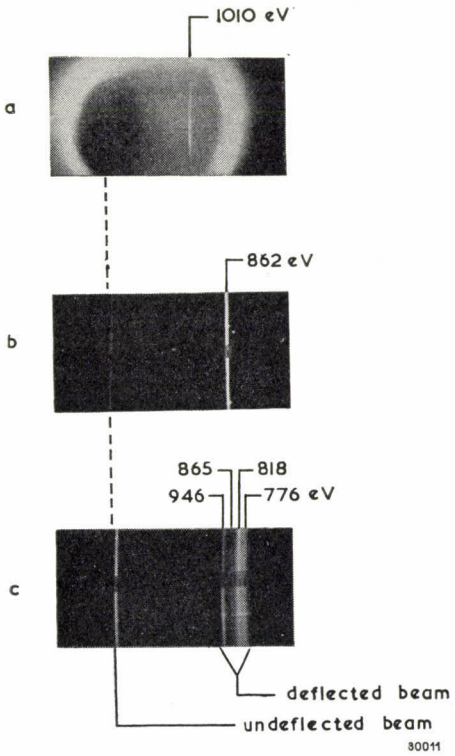

Fig. 1. (*a*) Nickel activated with Ba,
T_k = 1483 °K, V_a = 1010 V, J_a = 0·26 A/cm²;
(*b*) L-cathode,
T_k = 1404 °K, V_a = 862 V, J_a = 26·5 A/cm²;
(*c*) (BaSr)O (55/45 mole %) on Ni, thickness 60 microns,
T_k = 1168 °K, V_a = 951 V, J_a = 21 A/cm².
Electron-velocity spectra of a nickel cathode, an L-cathode and a (BaSr)O cathode under pulsed operation. Square micro-second pulses with a pulse width of $1{\cdot}9.10^{-6}$ sec, and a pulse-repetition frequency of 1000 c/sec.

square-pulsed load. Taking the resolving power of the tube into account, this means that the velocity spread is, at most, 0·01 V_e electron volts (V_e is the mean velocity of the emitted electrons). Moreover the velocity of the emitted electrons corresponds to within ± 1 electron volt to the numerical value of the anode voltage. All electrons are evidently emitted from places having practically the same potential, and the metallic cathodes have no observable resistance. This is as expected.

(b) *The (BaSr)O coating*

We investigated normal (BaSr)O coatings with a composition of 55 mole % BaO, 45 mole % SrO and a thickness of about 60 microns, sprayed in the form of carbonates with a density of about 1 g/cm^3 on a 0·08-cm^2 nickel base of composition mentioned in the preceding footnote. Immediately after activation the velocity spectrum of the emitted electrons under square-pulsed load shows one line or at least a narrow spectrum. When the oxide coating is aged under pulsed emission at a working temperature of about 1150 °K, the spectrum gradually broadens and finally splits up, usually into 3 rather sharp lines on a continuous background, two lines of slow electrons close together and one fairly sharp line of rapid electrons. Generally the lines of slow electrons are the most intensive (fig. 1c). With DC up to 1 A/cm^2, however, one sharp line of electrons is observed.

The velocity of even the fastest electrons is usually less than the maximum velocity attainable (V_a), while the difference in velocity between the fastest and slowest electrons can rise to about 200 eV. The hole in the movable anode having a diameter of 0·2 mm, the area from which electrons are drawn is only about 0·004 times the total cathode surface. By moving the anode over the cathode surface it was observed that the velocity spectra for different spots on one and the same cathode are not identical (see Part I, fig. 5). Especially in the neighbourhood of a spot where sparking has occurred the number of lines varies considerably. The 3-line spectrum is, however, representative of the majority of the (BaSr)O cathodes investigated.

Further, we studied the influence of the temperature at constant anode voltage, and the relation between the velocity spectrum and current density at constant cathode temperature. Fig. 2 illustrates the spectra of a (BaSr)O cathode at different temperatures and nearly constant anode voltages. Below 925 °K no velocity spread could be observed. The largest dispersion occurred at about 1125 °K. It is noteworthy that the variation in velocity spread as a function of temperature goes through a maximum and that the temperature below which no velocity spread is observed coincides with the temperature below which the pore conduction is believed to be negligible [7]).

The results of measurements of the relation between the velocity spectrum and current density at constant cathode temperature have been

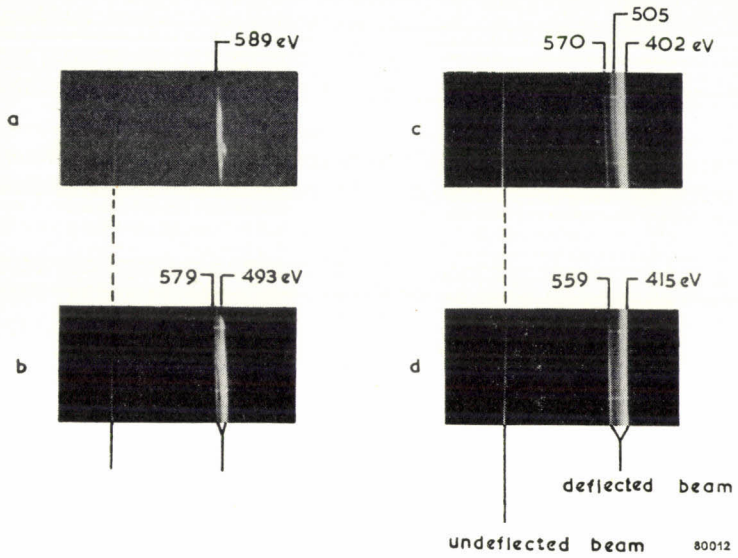

Fig. 2. (*a*) $T_k =$ 949 °K, $V_a =$ 591 V, $J_a =$ 0·69 A/cm²;
(*b*) $T_k =$ 1039 °K, $V_a =$ 584 V, $J_a =$ 3·5 A/cm²;
(*c*) $T_k =$ 1162 °K, $V_a =$ 574 V, $J_a =$ 23·0 A/cm²;
(*d*) $T_k =$ 1259 °K, $V_a =$ 562 V, $J_a =$ 39·4 A/cm².
Electron-velocity spectra from the same spot (3.10^{-4} cm²) on a (BaSr)O cathode (55/45 mole %; thickness 60 microns), at different temperatures. Square-pulsed operation with a pulse width $1{\cdot}9.10^{-6}$ sec, and a pulse-repetition frequency 1000 c/sec.

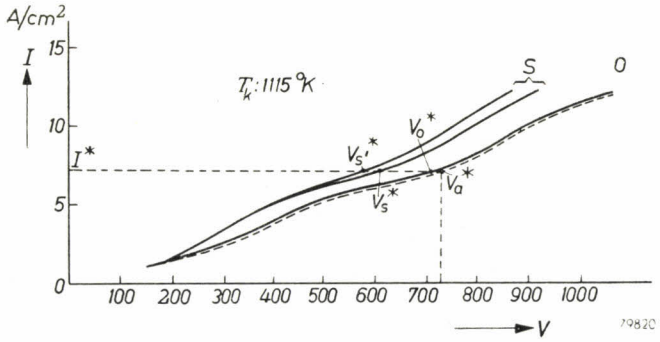

Fig. 3. Current density versus voltage for the different electron groups emitted from the same spot (3.10^{-4} cm²) on a (BaSr)O cathode at a temperature of 1115 °K. The voltage difference traversed by each group of electrons is plotted as a function of the total current density. *S* "slow lines", *O* "rapid line". The broken line represents the anode voltage as a function of the total current density. The line is, therefore, the normal diode characteristic. The graph must be read as follows (note the points indicated in the figure): at a current density J^* and an anode voltage V_a^* the spectrum shows groups of electrons with velocities (in eV): $V_{s'}^*$, V_s^*, V_0^*. (For I and I^* read J and J^*.)

summarized in fig. 3 for one cathode temperature (1115 °K). The potential difference which accelerated each group of electrons has been plotted as a function of the total current density. The dashed line gives the total current density as a function of the anode voltage. These curves show that in general the velocity spread increases with increasing current density. It is striking that the dashed diode characteristic, once past the saturation area, again bends upwards. This has been observed by others [2]), with oxide-coated cathodes under pulsed operation, and is known as the abnormal Schottky effect. In this part of the characteristic the heating of the cathode is greatest.

Another remarkable phenomenon is the behaviour of the velocity spectra of pulsed (BaSr)O coatings if a DC is superimposed. With increasing DC the spectrum of the square pulse contracts gradually to one rather sharp

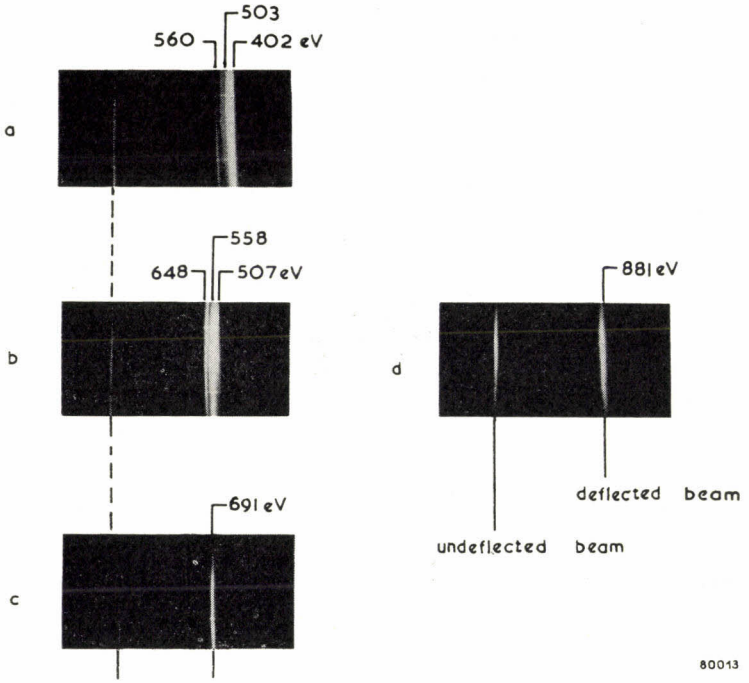

Fig. 4. (*a*) (BaSr)O on Ni, $T_k = 1162$ °K, $V_a = 564$ V, $J_{pulse} = 22{\cdot}6$ A/cm²;
(*b*) id., $T_k = 1142$ °K, $V_a = 648$ V, $J_{pulse} = 10{\cdot}5$ A/cm² + $J_{DC} = 0{\cdot}16$ A/cm²;
(*c*) id., $T_k = 1140$ °K, $V_a = 694$ V, $J_{pulse} = 5{\cdot}5$ A/cm² + $J_{DC} = 0{\cdot}18$ A/cm²;
(*d*) (BaSr)O + 60 % (weight) Ni-powder on Ni,
$T_k = 1135$ °K, $V_a = 888$ V, $J_a = 6{\cdot}0$ A/cm².
(*a*), (*b*) and (*c*): electron-velocity spectra from the same spot (3.10^{-4} cm²) on a (BaSr)O cathode (55/45 mole %; thickness 60 microns) with the same heater input under square-pulse plus varying DC operation; pulse width $1{\cdot}9.10^{-6}$ sec, pulse-repetition frequency 1000 c/sec.

line, while the ratio of the intensities of the slowest and fastest electron group generally decreases. The spectrum of the DC between the pulses remains one sharp line. At the same time the cathode temperature and the pulse emission decrease (see figs 4*a*-4*c*). This phenomenon is reversible.

Finally we investigated a sprayed (BaSr)O coating of 60 microns thickness mixed with 60 % nickel powder on a nickel base. The spectrum of this coating shows one rather sharp line (fig. 4*d*) under all circumstances. The difference of the velocity of the emitted electrons and the maximum velocity attainable is a function of current density. At a square-pulse current density of 14·5 A/cm² a velocity loss of the electrons of 18 eV was measured.

(c) *Other oxide coatings*

Compared with the spectrum of a (BaSr)O cathode, that of a BaO cathode is very simple. There is only one somewhat diffuse line (see fig. 5*a*). The velocities of the electrons differ a few electron volts from the maximum that can be attained.

In contrast to this an SrO cathode shows with square pulses a very broad and multiple-line spectrum (fig. 6), the velocity spread reaching values of 500 eV. Below 1050 °K no velocity spread is observable. With

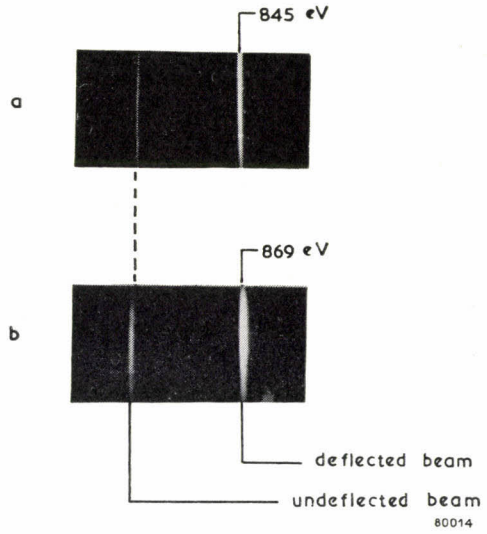

Fig. 5. (*a*) BaO on Ni, thickness 60 microns,
$T_k = 1145$ °K, $V_a = 850$ V, $J_a = 7{\cdot}0$ A/cm²;
(*b*) ThO_2 on Ta,
$T_k = 2130$ °K, $V_a = 869$ V, $J_a = 7{\cdot}4$ A/cm².
Electron-velocity spectra of a BaO and ThO_2 cathode under pulsed operation. Square micro-second pulses, pulse width $1{\cdot}9.10^{-6}$ sec, pulse-repetition frequency 1000 c/sec.

DC the spectrum shows one sharp line at low current densities, but at higher current densities more lines are observed; e.g. at a DC current density of 0·04 A/cm² two sharp lines with a velocity difference of 40 eV (fig. 6*f*). With square pulses plus DC load the behaviour is the same as with a (BaSr)O cathode: increasing DC leads to a contraction of the pulse spectrum to one line, to a decrease of the ratio of the intensities of the slowest and fastest electron groups, and to a decrease of pulse emission at constant temperature and pulse voltage. Fig. 6 illustrates the behaviour of the SrO coatings.

The spectrum of a ThO_2 cathode also consists of one line. See fig. 5*b*.

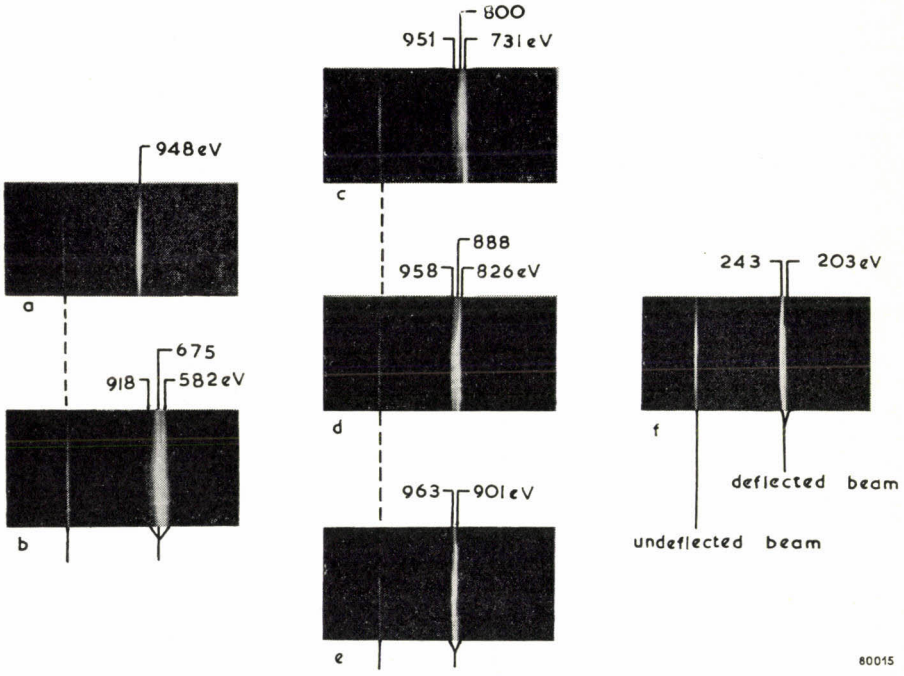

Fig. 6. (*a*) T_k = 1071 °K, V_a = 953 V, J_{pulse} = 0·15 A/cm²;
(*b*) T_k = 1319 °K, V_a = 920 V, J_{pulse} = 5·8 A/cm²;
(*c*) T_k = 1314 °K, V_a = 951 V, J_{pulse} = 1·35 A/cm² + J_{DC} = 0·13 A/cm²;
(*d*) T_k = 1314 °K, V_a = 958 V, J_{pulse} = 0·95 A/cm² + J_{DC} = 0·19 A/cm²;
(*e*) T_k = 1314 °K, V_a = 963 V, J_{pulse} = 0·72 A/cm² + J_{DC} = 0·25 A/cm²;
(*f*) T_k = 1195 °K, J_{DC} = 0·04 A/cm².
Electron-velocity spectra of SrO on Ni, thickness 60 microns.
(*a*), (*b*): Spectra from the same spot (3.10^{-4} cm²) at different temperatures; square-pulsed operation.
(*b*), (*c*), (*d*), (*e*): Spectra from the same spot at the same heater input under square-pulsed plus varying DC operation. Pulse width $1{\cdot}9.10^{-6}$ sec, pulse-repetition frequency 1000 c/sec.
(*f*): Spectrum under DC operation.

4. Proposed explanation of the electron-velocity spectra and accompanying phenomena

From the results of section 3 we may conclude that the oxide coatings we observed may be divided into two groups: one group, to which belong (BaSr)O and SrO, showing under pulsed operation a spectrum with several more or less discrete electron velocities, and another group, (BaSr)O with nickel powder, BaO, and ThO_2, with only one more or less sharp electron group.

As stated in the introduction the dispersion in electron velocities is thought to be intimately connected with the potential drop close to the cathode surface. To understand the different behaviour of the various oxides we first have to trace how this potential drop comes into existence and how it will be influenced by the nature and conditions of the emitting oxide.

The two processes which most probably determine the electron conduction have been extensively discussed [7]); they are:

(a) the conduction through the grains or along the surface of the oxide material,

(b) the conduction through the pores between the grains.

The potential drop near the surface layer of the oxide coating depends upon the relative contribution of the two mechanisms to the conductivity. This should be understood as follows. First of all we assume that there is no conduction through the surface grains and that the pores adjacent to the surface layer are filled with electrons emitted by the surrounding grains. By applying a strong field between the cathode and the anode most of the electrons will be drawn out of these pores. Thereby the pore conduction in the surface layer is disturbed. Electrons will continue to be drawn away from the surface grains until these grains are charged up to anode potential. Consequently there will exist a large potential drop in the surface layer. Owing to conduction through the grains, however, the actual potential of the surface grains will lie between that of the anode and that of the cathode and depends upon the ratio of grain emission, which is closely connected to pore conduction, and grain conduction.

On the other hand, under conditions where the pore conduction is unimportant the potential gradient in the oxide coating will be equal to that in a normal resistance, and no large potential drop at the surface of the oxide coating will occur. If this argument is correct, the relative importance of the pore conduction with respect to grain conduction determines the magnitude of the potential drop in the surface layer and hence also the extent of the velocity spread.

It is known [7]) that at low temperatures where no abnormal velocity spread is observed, pore conduction is negligible. When the temperature

is raised the pore conduction will first become increasingly important because the emission, which is the source of pore conduction, increases more rapidly with temperature than the conductivity of the grains. But if we increase the temperature yet further, at constant anode potential V_a, the current will be limited by space charge and therefore become constant; and the pore conduction will likewise be limited. As the grain conductivity continues to increase, however, the potential drop at the surface, and with it the velocity spread of the electrons, will gradually disappear.

Although this has given us a broad idea of the mechanism which causes the large velocity spreads, it is more difficult to understand why the velocity spectrum is more or less discrete instead of continuous. One possible explanation is as follows: The electrons with the highest velocities, which are visible in the spectrum as a rather sharp line, might be emitted from grains which are situated so deeply inside the coating that the conduction is no longer disturbed by the emission, as it is in the surface layer (see fig. 7). In relation to the metal base the potential of the grains in the interior of the oxide coating is determined by the total conductivity of the oxide and by the current density. Because the variation in potential between the different layers in the interior of the coating cannot be more than a few volts [4]) the line of rapid electrons in the velocity spectrum must be rather sharp.

The slowest electrons, which are observed in the velocity spectrum as a diffuse line, are emitted by the surface grains. That they are grouped in a diffuse "line" could be explained by the fact that the diameter of the anode hole (200 microns) is about a factor 10-20 larger than the

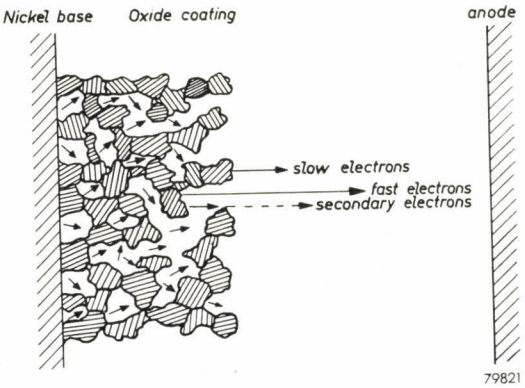

Fig. 7. Cross-section through an oxide coating. Because of the porous structure of the oxide coating the emitted electrons may be divided into slow thermal electrons, fast thermal electrons, and secondary electrons.

diameter of the grains so that the electrons of the spectrum are emitted by a great number of grains, and that apparently the ratio between residual conduction and emission, and therefore the potential, is approximately equal for all grains situated in such a way that they can be charged. The occurrence of two "lines" of slow electrons indicates that two kinds of electrons are emitted from the charged grains.

A somewhat more exact picture may be gained from the following consideration. With an anode voltage of 950 volts and the usual distance of 300 microns between the oxide coating and the anode the maximum potential difference across the surface pores of a (BaSr)O coating amounts to about 170 volts, while the two "lines" of slow electrons are as a rule clearly separated (see fig. 1*c*). In this case the electric fieldstrength in the vacuum space amounts to $2{\cdot}6.10^4$ volts/cm, while the fieldstrength in the pores may have a value of about 10^5 volts/cm if we assume that they have an average depth of about 15 microns. Generally we can say that with (BaSr)O the three-line spectrum is observed with an electric fieldstrength in the pores which is higher than that in the vacuum space between the coating and the anode. As a consequence of this the potential distribution in a pore must be as shown in fig. 8*a*. This can be understood in the following way. In a cross-section through the surface grain the potential distribution must be as shown by the curve $a_1b_1c_1$. If the surface of the bottom of the pore is very large compared to the height of the pore the potential distribution along its axis is according to the line $a_2b_2c_2$. Therefore in an actual pore with about equal height and diameter the potential distribution in the axis of it must be situated between $a_1b_1c_1$ and $a_2b_2c_2$ and may be as shown in fig. 8*a*.

Now an important part of the electrons originating from the bottom of the pores must impinge on the walls of the pores where they will liberate secondary electrons. From investigations of Pomerantz [8]) and Johnson [9]) it may be concluded that the yield of secondary electrons of (BaSr)O coatings at high temperatures (> 900 °K) corresponds to $\delta \gg 1$ if the impinging electrons have velocities > 100 eV, and, moreover, that the velocities of the released secondaries are of the order of 2 eV.

From the potential distribution in a pore as shown in fig. 8*a* it follows that the electrons emitted by the walls must pass the line of force K before they can reach the anode. Calculations showed that with a potential difference of 200 V across a cylindrical pore, electrons departing from the walls with velocities of about 2 eV may pass this line K except those emitted in a region AB which are pushed back to the walls by the electric field. As a consequence there will be no electrons in the spectrum from the region AB, which fact causes a dark space between the two low-velocity lines.

The electrons emitted by the walls with thermal velocities (about 0·1 eV at 1000 °K) have in general no chance to escape from the pore. A part of them, however, may be elastically reflected [10]) when they return to the walls and in this way gain so much energy in the electric field that they also can pass the line of force K. These reflected electrons may reach energies of all values lying between the fastest and slowest electron groups and therefore cause the continuous background which is always visible in the spectrum.

We may conclude that if the electric field in the pores is higher than that between the oxide coating and the anode, the thermal electrons emitted

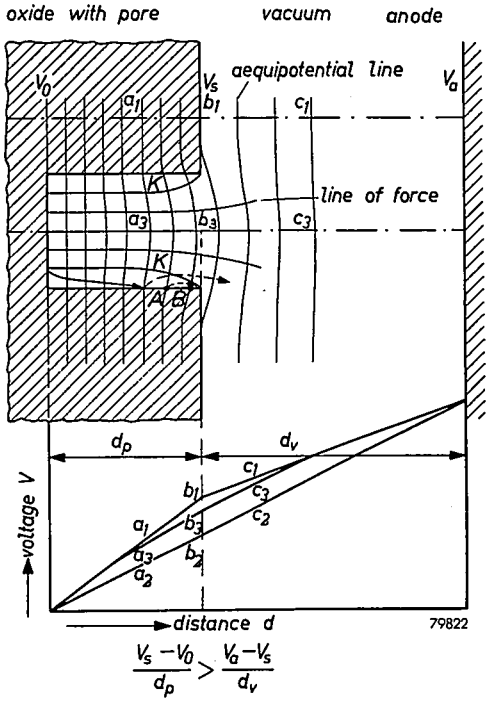

Fig. 8*a*. Potential distribution in a surface pore of an oxide coating.
V_0 = potential at the bottom of the pore; V_s = potential on the surface of the pore; V_a = anode potential;
d_p = depth of the pore; d_v = distance oxide coating to anode.
$a_1b_1c_1$ potential distribution in a cross-section through the grains;
$a_2b_2c_2$ potential distribution in the vacuum between a flat oxide coating and the anode at a distance $d_p + d_v$;
$a_3b_3c_3$ potential distribution in cross-section through the axis of the pore.
Electric fieldstrength in the pore $(V_s - V_0)/d_p >$ electric fieldstrength between the oxide coating and the anode $(V_a - V_s)/d_v$. A part of the electrons emitted by the bottom of the pore impinges on the pore walls. Secondary electrons can reach the anode by passing the line of force K, except those released in the region AB of the pore walls.

from the top of the surface grains and a part emitted from the bottom of the surface pores may directly reach the anode. Thermal electrons emitted by the walls of the pores have only a chance if they are elastically reflected. The total number of electrons which causes the fastest and slowest lines will therefore be higher than those with interjacent velocities. The usually weaker intensity of the fastest electron group may be caused by the fact that a part of the electrons emitted from the bottom of the pores impinges on the walls. The secondary electrons released in the pore walls again may directly escape from the pores. In this way it can be understood that the secondary electrons are visible as a rather diffuse line on a continuous background situated between the fastest and the slowest line and in the neighbourhood of the latter. In reality the pores have no flat cylindrical walls. Electrons emitted on the upper side of protruding points can also directly leave the pores; they may be visible as extra lines of variable sharpness situated at any place in the spectrum between the fastest and slowest lines.

The potential distribution in a surface pore as shown in fig. 8*a* occurs with oxide coatings such as (BaSr)O and SrO if there exists a large potential

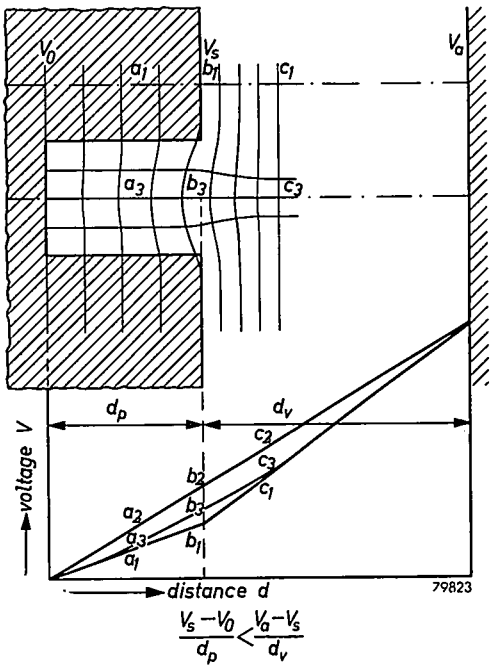

Fig. 8*b*. Electric fieldstrength in the pore $(V_s-V_0)/d_p <$ electric fieldstrength between the oxide coating and the anode $(V_a-V_s)/d_v$. All the electrons emitted by the bottom and the walls of the pore can reach the anode. For the explanation of symbols, see legend to fig. 8*a*.

drop in the surface layer. If there is no large potential drop (e.g.$<$ 20 volts) across the oxide coating and the electric fieldstrength in the vacuum space between the coating and the anode is high compared with that across the coating, the potential distribution in the surface pores becomes as shown in fig. 8*b*. All the electrons emitted from the bottom and the walls of a pore are directly drawn to the anode; secondary emission is absent. This may be the case with (BaSr)O plus nickel powder, BaO and ThO_2 coatings.

If the explanation of the electron-velocity spectra is correct, we might draw some conclusions regarding the conducting properties of the oxide coatings investigated. Because of the high velocity spread at temperatures above 1050 °K the pore conduction of an SrO coating must be relatively high with respect to grain conduction. A homogeneous (BaSr)O coating has at temperatures above 800 °K also an important pore conduction as shown by Loosjes and Vink [7]), Hughes and Coppola [11]), Shepherd [12]) and Young [13]). Moreover Young found no significant difference in the conduction properties of BaO as compared with (BaSr)O. This is not in contradiction with the phenomenon that the electron-velocity spectra of BaO and aged (BaSr)O coatings are not the same, because, as shown by Burgers [14]), Gärtner [15]), Darbyshire [16]) and Eisenstein [17]), the surface layer of an aged (BaSr)O coating is mainly composed of SrO. This SrO surface layer has probably a ratio of pore to grain conduction which is higher than that of the bulk of the coating, which is composed of (BaSr)O and may therefore be an extra cause of the large potential drop at high current densities ($>$2 A/cm^2). In agreement with Young's measurements of the conduction of the bulk of (BaSr)O and BaO coatings it is found that with square-pulsed load the electron-velocity spectrum of (BaSr)O (55/45 mole %) immediately after activation, when the surface layer has the same composition as the bulk of the coating, mostly shows one line of the same sharpness as observed with BaO coatings.

In the case of (BaSr)O mixed with nickel powder it is probable that the nickel powder short-circuits the surface grains of the oxide coating; with ThO_2 it is experimentally confirmed that grain conduction must be important with respect to pore conduction [18]).

The difference between the electron-velocity spectra of aged (BaSr)O and SrO coatings with pulsed and/or DC load is in reality a difference caused by the duty cycle. For with pulsed emission the cathode is measured practically during idling. Currents are drawn during time intervals (about 10^{-6} sec) which are short compared with the time (about 10^{-3} sec) after which the pulses are repeated; the duty cycle is about 10^{-3}. With DC, however, the cathode is measured in a loaded condition. Currents are continuously drawn; the duty cycle is 1. To explain the difference in

behaviour in both conditions we must look for an argument which takes these into account.

We wish to emphasize that the so-called decay effects are also a function of the duty cycle [19]) and run parallel with the disappearance of the spread in the electron-velocity spectra. The usual explanation of the decay effects is a polarization of the oxide due to electrolysis [20]), [21]), or donor depletion [22]).

From these theories we may conclude that an increasing duty cycle leads to a decrease of the excess Ba (and Sr) in the surface layer of a (BaSr)O coating. This means that the emission of the outer surface of the surface grains is decreased to a greater extent than the conductivity of the solid in the surface layer. Therefore the potential difference in the outer layer decreases with an increasing duty cycle which leads to a gradual disappearance of the electron-velocity spread.

On the other hand we wish to draw attention to another effect which has the same consequences as polarization. This is the temperature gradient which is present in an oxide coating due to heat flow through the oxide. The heat effect of the emission current is twofold, (*i*) the Joule heat generation by the electrical resistance i^2R, (*ii*) the cooling effect by the emission itself $i(\varphi + 2kT/e)$, where φ is the work function. With low duty cycles i^2R predominates. With the same average current density and high duty cycles, however, the cooling by $i(\varphi + 2kT/e)$ is relatively more important. This means that in the case of low duty cycles the temperature gradient will be less steep than with high duty cycles, as i^2R is generated throughout the coating and $-i(\varphi + 2kT/e)$ only at the surface.

According to our views the potential difference in the surface layer is

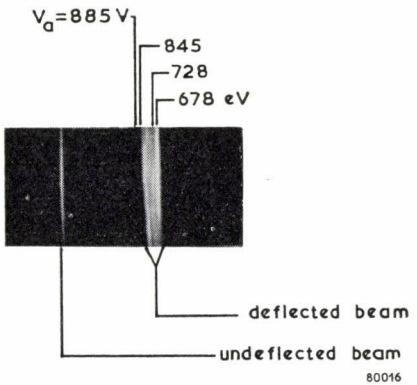

Fig. 9. $T_k = 1179$ °K; $V_a = 885$ V; $J_a = 6{\cdot}1$ A/cm².
Electron-velocity spectrum of (BaSr)O (55/45 mole %; thickness 120 microns), sprayed on a nickel base electrolytically coated with a layer of chromium of about 1 micron thickness. Square micro-second pulse operation, pulse width $1{\cdot}9.10^{-6}$ sec, pulse-repetition frequency 2000 c/sec.

determined by the ratio of emission and conductivity. A higher duty cycle gives rise to a steeper temperature gradient, which causes a decrease of the ratio of emission and conductivity and leads to a disappearance of the electron-velocity spread.

The results we have obtained do not exclude the occurrence of a high resistance in the interface area between nickel base and oxide coating. It is expected that if an interface resistance is present the same phenomena will exist, the only difference being a greater difference in velocity between the fastest electron group and the anode voltage. This is confirmed with (BaSr)O sprayed on a nickel base electrolytically coated with a layer of chromium of about 1 micron thickness. Fineman and Eisenstein [23]) showed already that (BaSr)O on chromium-plated nickel gives an interface with a high resistance. At a cathode temperature of 1179 °K and at a current density of 6·1 A/cm^2 the velocity difference between the fastest and the slowest group was 167 eV, while the difference between the fastest electron group and the maximum velocity attainable (V_a) had a value of 40 eV; see fig. 9.

5. Consequences of the use of (BaSr)O cathodes for pulsed operation

The heat dissipation due to the passage of a pulse current through a (BaSr)O coating with a large electron-velocity spread ($\approx$200 eV) occurs for the greater part in the outer layer. This outer layer has a comparatively bad thermal contact with the neighbouring region. Therefore the temperature increase in this region must be considerable and makes temperature measurements on the nickel base of dubious value.

The large potential gradient in the outer layer of the (BaSr)O coating may also directly influence the behaviour of the cathode. If we assume that the potential changes by 200 volts within a trajectory of 20 microns (i.e. within a layer having a thickness of only a few grains) a field of 10^5 V/cm will be present in this area. It is conceivable that a slightly larger field-strength might cause a dielectric breakdown in the outer layer (which moreover also has a higher temperature). Such a breakdown might induce sparking between cathode and anode. Adding a DC to the pulsed emission can eliminate the large potential gradient in the outer layer and may, therefore, reduce sparking, in accordance with the investigations of Pomerantz [2]). Mixing of the oxide with a metallic powder may have the same effect.

6. Acknowledgement

The authors are greatly indebted to Dr E. J. W. Verwey, Prof. Dr Ir J. L. H. Jonker, Dr H. J. Vink and Dr A. Venema of these laboratories for their helpful criticism and advices with the theoretical interpretation of the results.

Eindhoven, February 1954

REFERENCES

1) C. G. J. Jansen and R. Loosjes, Philips Res. Rep. **8**, 21-34, 1953.
2) See for example: E. A. Coomes, J. appl. Phys. **17**, 647-654, 1946; M. A. Pomerantz, Proc. Inst. Radio Engrs, **34**, 903-910, 1946; A. S. Eisenstein, Advances in Electronics **I**, 1-64, 1948.
3) R. Loosjes and H. J. Vink, Philips Res. Rep. **2**, 190-204, 1947.
4) R. Loosjes and H. J. Vink, Le Vide **5**, 731-738, 1950.
5) Ch. Biguenet, Le Vide **7**, 1123-1130, 1952.
6) H. J. Lemmens, M. J. Jansen and R. Loosjes, Philips tech. Rev. **11**, 341-350, 1950.
7) R. Loosjes and H. J. Vink, Philips Res. Rep. **4**, 449-475, 1949.
8) M. A. Pomerantz, J. Franklin Inst. **241**, 415-433, 1946.
9) J. B. Johnson, Phys. Rev. **73**, 1058-1073, 1948.
10) H. Bruining, Diss. Leyden, 1938.
11) R. C. Hughes and P. P. Coppola, Phys. Rev. **88**, 364-368, 1952.
12) A. A. Shepherd, Brit. J. appl. Phys. **4**, 70-75, 1953.
13) J. R. Young, J. appl. Phys. **23**, 1129-1138, 1952.
14) W. G. Burgers, Z. Phys. **80**, 253-360, 1935.
15) H. Gärtner, Phil. Mag. **19**, 82-103, 1935.
16) J. A. Darbyshire, Proc. phys. Soc. **50**, 635-641, 1938.
17) A. Eisenstein, J. appl. Phys. **17**, 654-663, 1946.
18) R. Loosjes, unpublished.
19) E. Sugata, J. Nakai and S. Nakamura, Tech. Rep. Osaka University **3**, 79-86, 1953.
20) R. L. Sproull, Phys. Rev. **67**, 166-178, 1945.
21) S. Wagener, Proc. phys. Soc. **61**, 521-525, 1948.
22) L. S. Nergaard, R.C.A. Rev. **13**, 464-545, 1952.
23) A. Fineman and A. Eisenstein, J. appl. Phys. **17**, 663-668, 1946.

R 247 Philips Res. Rep. 9, 259-294, 1954

SOME INVESTIGATIONS ON THE ELECTRICAL PROPERTIES OF HEXAGONAL SELENIUM *)

by L. M. NIJLAND 546.23:548.1.023:537

Summary

A short survey of the recent literature on selenium is given in the first chapter. The resistivity of polycrystalline, hexagonal selenium can be lowered by halogens and can be raised by thallium. No reliable data on fundamental quantities like hole densities and mobilities are found in the literature. Investigations on these subjects are described in the next chapters. A method to purify selenium by evaporation near its melting point is developed (chapter II). High-frequency measurements of the conductivity of pure and of thallium-doped selenium samples comply with the assumption that polycrystalline selenium consists of rather well-conducting crystals embedded in badly conducting layers of more or less amorphous selenium. Thallium increases the resistance of the layers and does not or only slightly affect the resistance of the crystals (chapter III). Measurements of the Hall effect and of the shunt resistivity vs frequency of pure and of bromine-containing selenium samples point to the same layer structure. Bromine does not affect the resistivity of crystals but lowers that of the layers. Single crystals prepared in a bromine-containing atmosphere have the same resistivities as pure crystals have (chapter III). The last chapter contains a discussion of the experimental results and points to a model with both amorphous and crystallized parts in the same selenium chain.

Résumé

Le premier chapitre contient un résumé de la littérature récemment parue sur le sélénium. La résistivité du sélénium hexagonal polycristallin peut être abaissée par les halogènes et élevée par le thallium. L'on n'y pourra trouver aucune donnée sûre quant aux quantités fondamentales comme les densités et la mobilité des trous. Des recherches sur ces sujets sont décrites dans les chapitres suivants. Une méthode de purification du sélénium par l'évaporation près de son point de fusion a été développée (chapitre II). Les mesures à haute fréquence de la conductivité d'échantillons de sélénium pur et de sélénium additionnés de thallium ont confirmé l'affirmation que le sélénium polycristallin consiste en cristaux d'assez bonne conductivité enrobés dans des couches mal conductrices de sélénium plus ou moins amorphe. Le thallium augmente la résistance des couches et influence tout au plus légèrement la résistance des cristaux (chapitre III). Les mesures de l'effet de Hall et de la résistivité de shunt en fonction de la fréquence d'échantillons de sélénium pur ou additionnés de brome, indiquent la même structure de couche. Le brome n'affecte pas la résistivité des cristaux, mais abaisse celle des couches. Les monocristaux préparés en atmosphère contenant du brome ont les mêmes résistivités que les cristaux purs (chapitre III). Le dernier chapitre contient une discussion des résultats expérimentaux et prescrit un modèle comprenant ensemble des parties amorphes et cristallisées dans la même chaine du sélénium.

*) Thesis, University of Amsterdam, April 1954.

Zusammenfassung

Im ersten Kapitel wird eine kurze Übersicht des jüngsten Schrifttums über Selen gegeben. Der Widerstand von polykristallinischem, hexagonalem Selen kann durch Halogene vermindert und durch Thallium erhöht werden. Über grundlegende Eigenschaften wie Löcherkonzentration und -beweglichkeit sind keine zuverlässigen Daten in der Literatur zu finden. Untersuchungen über diese Fragen werden in den folgenden Kapiteln beschrieben. Ein Verfahren zur Reinigung von Selen durch Verdampfung nahe seinem Schmelzpunkt wird in Kapitel II entwickelt. HF-Messungen der Leitfähigkeit reiner und thalliumhaltiger Selenproben bestätigen die Annahme, daß polykristallinisches Selen hauptsächlich aus ziemlich gut leitenden Kristallen besteht, die in schlecht leitenden Schichten von mehr oder weniger amorphem Selen eingebettet sind. Thallium erhöht den Widerstand der Schichten und beeinflußt nicht oder nur schwach den Widerstand der Kristalle (Kapitel III). Messungen des Hall-Effektes und des Nebenschluß-Widerstandes als Funktion der Frequenz von reinen und von bromhaltigen Selenproben weisen auf dieselbe Schichtstruktur. Brom beeinflußt nicht den Widerstand von Kristallen, vermindert aber den der Schichten. In einer bromhaltigen Atmosphäre bereitete Einkristalle weisen dieselben Widerstände auf wie reine Kristalle (Kapitel III). Das letzte Kapitel enthält eine Erörterung der experimentellen Ergebnisse und deutet darauf hin, daß in einer Selenkette sowohl amorphe als auch kristallinische Teile enthalten sind.

INTRODUCTION

There are many problems found in the research on selenium rectifiers. The forward resistance of these rectifiers can be decreased by adding, for instance, halogens such as chlorine or bromine, or halides (such as have been described in patent literature by Dr W. Ch. van Geel of this laboratory already in 1936) to the selenium to be used; it is possible, according to patent literature, to stabilize a once gained high conductivity of the selenium by various other compounds. Almost all these additions have one thing in common: it is not easy to find a suitable position for these impurities in the selenium lattice. Thus it might be of interest to measure the density of electrical charge carriers both in pure and in impurified selenium to trace its possible correlation with the density of the impurities. Such measurements might also give information on the length of selenium chains in crystallized selenium, and on the whole, on the mechanism of electrical conduction in selenium.

Many other problems arise when investigating the possibilities of increasing the quality of the current-voltage characteristic of a selenium rectifier in the inverse direction: patent literature describes a multitude of elements and chemical compounds which, when applied under favourable conditions, should change the properties of the rectifier in the way desired.

Thallium and its compounds are often used for this purpose: because not only the electrical properties of the selenium surface, but also the bulk resistivity of selenium are strongly influenced by thallium, the electrical properties of the system thallium-selenium seem to be extremely suitable for research.

The reader will find a résumé of the recent literature on the electrical properties of selenium in chapter I. A purifying method for selenium is described in chapter II. Measurements of the conductivity, and of the Hall effect of both pure selenium and selenium to which thallium or bromine has been added, are discussed in chapter III. Chapter IV contains a discussion of the results obtained.

CHAPTER I

SURVEY OF THE RECENT LITERATURE ON THE CRYSTALLOGRAPHICAL PROPERTIES AND THE ELECTRICAL CONDUCTIVITY OF SELENIUM

Because the literature on the electrical properties of selenium is not easily accessible, a résumé of these properties seems to be appropriate. It will contain:

(1) A description of the modifications of selenium.
(2) A survey of their electrical properties, most of which will be devoted to the mechanism of electrical conduction in hexagonal selenium.
(3) A programme of investigations.

The atomic weight of selenium is 78·96. The element boils at 685 °C[1]); the melting point is not exactly known but is, according to various authors, 219·5 °C ± 1·5 °C. A vapour-pressure diagram of the various forms of selenium is sketched in fig. 1 [2]).

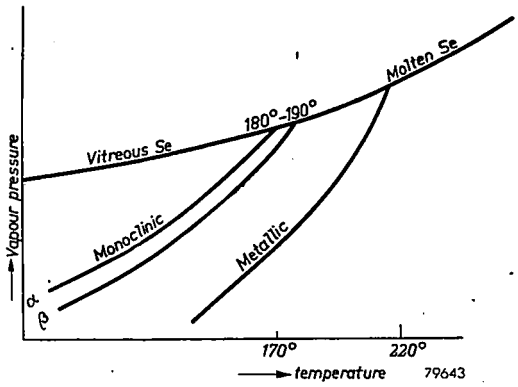

Fig. 1. Vapour-pressure curves of the various forms of selenium. Temperatures in °C.

1. The modifications of selenium

Solid selenium appears in the following modifications:
(1) Amorphous selenium (known in a red and in a black, "vitreous" form).
(2) α-Monoclinic selenium.
(3) β-Monoclinic selenium.
(4) Hexagonal selenium.

Ad (1). Vitreous selenium (spec. weight 4·2 - 4·4) can be obtained by rapid cooling of the melt. According to many investigations, among which the very recent one of Richter, Kulcke and Specht [3]), vitreous selenium is identical with supercooled selenium.

Ad (2) and (3). A mixture of the two monoclinic forms can be prepared by evaporation of the solvent from a solution of selenium in carbon disulphide. Burbank [4]) and Marsh [5]) found the selenium atoms in these modifications ordered to eight-membered rings.

Ad (4). Hexagonal (metallic or grey) selenium (spec. weight 4·81 - 4·82) is made up of parallel, spiralized chains of selenium atoms (fig. 2). This stable modification can be obtained from any of the other forms by heating. The mechanism of these transitions has been described by De Boer [6]). Molten selenium too is supposed to consist of long chains which may be entangled to coils, and perhaps also of poly-membered rings [6]), [7]), [8]). The viscosity of this molten selenium increases rapidly with decreasing temperature. Morsch [7]) explains this by supposing an increase of the mean chain length at decreasing temperatures. When cooled below 220 °C (the melting point of hexagonal selenium), the entanglement of long chains persists; this supercooled fluid is called "vitreous selenium", and

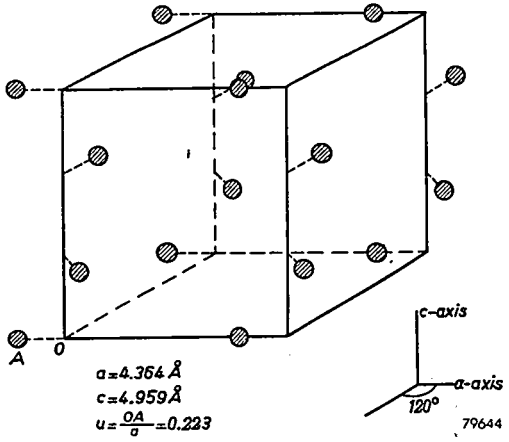

Fig. 2. The crystal structure of hexagonal selenium. The shortest distance between two atoms in one chain is equal to 2·36 Å; the shortest distance between two atoms in neighbouring chains is equal to 3·45 Å.

shows a great deal of resemblance in structural and physical properties with plastic sulphur. By annealing this vitreous selenium some of the chains arrange themselves to a structure as occurring in hexagonal selenium. The crystallization proceeds in this way and gives at last polycrystalline hexagonal selenium. It will be clear that the properties of the ultimate product will be connected with its thermal history.

It is well known that small amounts of some impurities (halogens, phosphorus, arsenic) strongly affect the rate of crystallization. This may be caused by a shortening or a branching of the chains in the melt and in the vitreous form.

Single crystals of hexagonal selenium can be prepared either by sublimation out of the vapour [9]) or by very slow crystallization of the melt [10]). The first method almost always supplies hollow needles: the directions of greatest lengths coincide with those of the hexagonal c-axis. The faces of these crystals are very seldom well-formed: twisting and twinning of the needles often occurs. Crystals out of the melt are often better formed, but very small.

2. The electrical properties of selenium

(1) *Molten and vitreous selenium*

The resistivity of molten selenium is dependent on the temperature and on the nature and quantity of the impurities [11]),[12]),[13]). The behaviour of liquid selenium of rectifier quality or better is described by

$$\log \varrho = -A + \frac{B}{T},$$

where ϱ is the value of the resistivity in Ω cm. A and B are constants dependent on the type of selenium used:

$$3{\cdot}5 < A < 4{\cdot}0,\ 5600\,^{\circ}\mathrm{K} < B < 6000\,^{\circ}\mathrm{K} \text{ for } 520\,^{\circ}\mathrm{K} < T < 770\,^{\circ}\mathrm{K},$$

so that the resistivity at 260 °C will be about 10^7 Ω cm.

Many impurities, for instance the halogens and some halides such as cerous iodide and selenium chloride, cause a large decrease of this resistivity: this property can be as low as some thousands Ω cm. We found that the relation between the values of the resistivity ϱ and of the bromine content c is given by

$$\log \varrho = a - b \log c$$

(a and b are parameters, dependent on the temperature) within a wide range of c-values.

Not much is known about the resistivity of vitreous selenium. At 20 °C

the resistivity is very high (10^{10} to 10^{14} Ω cm) and strongly dependent on the illumination.

(2) *Both kinds of monoclinic selenium* have got very high and light-dependent resistivities. Due perhaps to the small technical importance of these modifications, little more than their crystal structures are described in literature.

(3) *Hexagonal selenium*

Large differences must be emphasized between the properties of the polycrystalline material and those of single crystals.

The description of the process of crystallization will explain the large range of resistivities which will be found after crystallizing vitreous selenium under different conditions: the number of crystallization centres in vitreous selenium and their rate of growth will be dependent on the temperature.

Resistivities at 20 °C ranging from some thousands to about 10^5 Ω cm are found: the lower values appear after crystallizing at temperatures not far from the melting point, the higher resistivities occur after thermal treatment between 70 and 100 °C.

Thoroughly crystallizing of vitreous selenium with impurities like the halogens supplies samples with a resistivity of a few hundreds Ω cm at 20 °C [14]); impurifying with thallium, however, can raise the resistivity of polycrystalline selenium to 10^9 Ω cm [15]), [16]), [17]).

The conductivity of selenium single crystals in the direction of the hexagonal *c*-axis is three to ten times as large as when perpendicular to this axis [18]),[19]),[20]). According to investigations of Lehovec [21]) and of the writer (pp. 282, 287, 291) neither of these resistivities can be altered by preparing or keeping single crystals in a bromine-containing atmosphere. It is known [19]) that the resistivity of selenium single crystals is dependent on the applied field strength, this pointing to internal barriers.

The conductivity of single crystals is also light-dependent. Henceforth only the dark-resistance will be discussed.

The mechanism of the electrical conduction in hexagonal selenium

The electrical properties of semiconductors like silicon and germanium can be discussed by means of an energy diagram (fig. 3). Pure germanium, for instance, is an intrinsic semiconductor; an increase of the temperature is followed by an increase of the density of the electrons in the conduction band and of the holes in the valence band. Isomorphous substitution of some germanium atoms by atoms of suitable fifth-column elements (As, Sb) gives rise to donor levels just below the conduction band and therefore increases the density of conduction electrons. Introduction of

third-column elements (such as In or Al) causes acceptor levels near above the valence band and so increases the density of holes.

A discussion on the mobility of these charge carriers (conduction electrons and holes) in the lattice will be given in section (3d).

Because such energy diagrams can be constructed only after studying the density of charge carriers, many investigations are devoted to this subject in connection with selenium. In most cases the carrier density has been calculated from the thermo-electric power [23],[24],[25]. Plessner [26] estimated its value in a selenium single crystal from the Hall effect. Other measurements of the Hall effect of rather pure polycrystalline selenium have been published by Iglitsen [27], while Eckart and Kittel [28] succeeded in measuring the Hall effect of rather well-conducting selenium like that used in the manufacturing of selenium rectifiers (these authors did not disclose any details on the composition or preparation of the samples used).

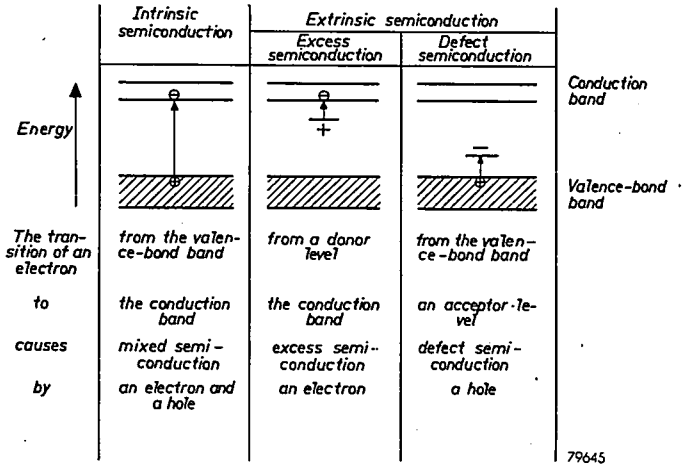

Fig. 3. Energy diagrams for semiconductors.

According to Schottky [29] the density of carriers near the counter-electrode of a selenium rectifier can be calculated from the change of the rectifier capacity caused by the applied potential difference.

Summarizing the result of these authors:

(1) The density of holes in selenium single crystals is about 10^{14} cm^{-3} (i.e. one carrier in $3 \cdot 7.10^8$ selenium atoms) and does not much depend on the temperature. The mobility of these carriers is equal to or less than 1 cm^2/V sec (which would be an extremely small value) according to d.c. measurements; h.f. measurements point to higher values.

(2) The electrical current is carried through polycrystalline selenium by holes with a density between 10^{14} and 10^{17} cm^{-3}. This number would depend rather strongly on the temperature according to measurements of the thermo-electric power, in contradiction to the estimates based upon the Hall effect. The mobility of the holes is dependent on the impurity content and on the thermal treatment of the samples and may amount from 0·003 to 3 cm^2/V sec.

3. Research programme

It is obvious that systematical investigations on the changes of the number of carriers in selenium by varying the activator content are still necessary. It seems reasonable to perform these experiments with bromine-containing selenium, so that the conductivity of the samples can reach a relatively high value. Direct information about the number of carriers can be supplied by measurements of the Hall effect. Measurements of the thermo-electric power seem easier to perform. This physical quantity, however, varies rather slowly with the density of carriers; a relatively small change of the thermo-electric power should therefore be explained by a considerable change in the carrier density, which fact might introduce important errors. The formulae for the relation between thermo-electric power and carrier density, moreover, apply only for the idealized case of free carriers in an isotropic medium, which is not always strictly necessary for the application of the formulae for the Hall effect. See ref. [30]) and section (3e).

A second key to the problem could be offered by investigations on selenium impurified with thallium. This metal can multiply the resistivity of hexagonal pure selenium by as much as a hundred thousand without a reasonable explanation being known [15]), [16]), [17]). Samples with resistivities higher than a hundred thousand Ω cm and mobilities as low as one cm^2/V sec or less are not suitable for measurements in conventional direct-current Hall circuits, so that other methods must be applied. Hoffman [31]) estimated the carrier density near the thallium-containing counter-electrode by the method of Schottky [29]). In this way a hole density (the word used was "Störstellendichte") in the order of 10^{16} cm^{-3} was found. Assuming a resistivity of more than 10^6 Ω cm for the layer of selenium near the electrode, a hole mobility of less than 10^{-3} cm^2/V sec will be calculated. Such values are very improbable. The thermo-electric power of selenium which contains traces of thallium cannot be measured by a simple method; such thermo-elements have a very large internal resistance. Therefore we have chosen the easier but less informative method of measuring the high-frequency conductivity.

CHAPTER II

THE PURIFICATION OF SELENIUM

1. The purpose of the purifying process and disadvantages of chemical methods

Considerable information on the relation between the resistivity of hexagonal selenium and its impurity content is found in literature. It is known, for instance, that an appreciable lowering of the resistance occurs after adding 1 bromine atom to every 10^5 selenium atoms; adding of 1 thallium atom to every 10^6 selenium atoms may multiply the resistivity of hexagonal selenium by two or more. Small amounts of many other impurities (sulphur, phosphorus, arsenic, sodium chloride and many others of the most differing kinds) may have an effect after a well-selected thermal treatment. Investigations on the mechanism of electrical conductivity in selenium must be preceded, therefore, by a purification of the selenium to be used, which should lead preferably to less than traceable amounts of *all* impurities.

"Selenium for rectifiers" (this containing on the average more than 99·9 % of selenium) may contain the following contaminations: P, O, S, Te, Cl, Na, Mg, Ca, Al, Si, Mn, Fe, Ni, Sn, Zn, Cu, Ag, Pb, Hg. Some of these (Te, Cl) occur "freely" in selenium, most of these impurities are bound; metals for instance are often found as sulphides or selenides. The traceable quantity (by means of spectrochemical or "wet" analytical methods) of each of these impurities may vary between about 1 atom to 10^4 and 1 atom to 10^7 selenium atoms.

When using a "wet" method of purification, apparatus (glassware) and chemicals should be carefully checked; small amounts of impurities being present in the chemicals to be used are likely to be adsorbed on the surface of precipitated selenium. Moreover applying solutions of selenium or compounds of this element means bringing comparatively large quantities of chemicals into close contact with the substance to be purified, thus increasing its chance of becoming contaminated.

Chromatographical methods (used for instance with aluminium oxide as an adsorbent for the impurities in an aqueous solution of selenium dioxide) increased the aluminium contents of the samples and decreased insignificantly the amounts of other impurities *).

Exactly the same objections can be raised against the purification of

*) The large number of chemical and spectrochemical analyses were performed by Dr A. Claassen, Mr J. Visser, Dr N. W. H. Addink and Mr J. A. M. Dikhoff of this laboratory.

selenium dioxide by physical methods followed by reducing this selenium dioxide to selenium. This reduction was carried out by means of sulphur dioxide or hydrazine in an aqueous solution, or "dry" with ammonia gas. In all these cases much heat was developed; in the last case especially, this resulted in a transition of impurities from the wall of the vessel via the water (present or formed) to the selenium.

After having experienced the disadvantages of these wet purifying methods, it was clear that ultimate purity can only be reached after applying physical methods, at least at the last stage of purification. A complete description of the rather simple process found for this is given below.

2. Description of the purification process

Selenium of 99·9 % purity or more (such as supplied by manufacturers of selenium for rectifiers) is heated to about 450 °C in a quartz-glazed vessel of Rotosil (made by Heraeus, Munich, Germany), if necessary in a stream of nitrogen or argon. Volatile impurities (i.e. water, sulphuric acid, halogens, mercury, selenium dioxide, a.o.) evaporate during this treatment. After about half an hour the vessel is cooled to 260 °C and placed into a high-vacuum jar. The recipient, consisting of a cylindrical vessel, at one end closed, of Rotosil which has been quartz-glazed internally, is placed over the evaporator. After closing the vacuum jar and evacuating it to 10^{-3} mm mercury pressure or less, the selenium evaporates and sublimates on the inner side of the recipient (temperature 20 - 60 °C). After some time (15 - 60 minutes) the vacuum jar is opened and the selenium removed from the recipient with a nickel-plated spatula. After repeating this process three or four times (the previous heating to 450 °C can be omitted after the first evaporation) spectroscopically pure selenium is obtained.

The following technical details may be important:

(1) The high-vacuum furnace used for heating the vessel with selenium carries as little electrical insulation material as possible: it contains a nickel-chromium heating wire which is insulated by a very thin layer of magnesium oxide or aluminium oxide. This layer is surrounded by a V_2A-tube for mechanical protection. The almost completely enclosed and very scantily applied electrical insulation material is not noticeably detrimental to the high-vacuum; the vulnerable heating wire is effectively protected against the selenium vapour.

(2) Very small amounts of mercury may affect appreciably the electrical behaviour of selenium; it is therefore better to avoid the use of mercury diffusion pumps.

3. Checking the purification method

Selenium purified by means of the method described is spectroscopically pure: this means that there is less than one atom of every possible metal impurity, free or bound, to every 10^4 or 10^6 selenium atoms. In a few samples, however, spectroscopical analysis showed the presence of about 1 atom of silicon in every 10^5 selenium atoms.

The presence of sulphur, phosphorus, halogens, both free or chemically bound, or selenium dioxide cannot be shown.

(1) *The sublimation method*

A purification method found by Mr J. J. A. Ploos van Amstel of this laboratory gives additional information on the purity of selenium; this investigator heated selenium in a high vacuum to a temperature just below its melting point. The very slowly sublimating selenium leaves a residue, which may be considered as a measure for the total amount of impurities in so far as the latter are less volatile than selenium.

It has been found that selenium, when purified in the way described in section (2), leaves a residue about 3.10^{-6} by weight of the selenium. This, difficultly to sublimate material consisted for about 95 % of quartz fragments and contained less than 5 % (and thus about 10^{-5} % by weight of the selenium) of a copper compound likely to be copper selenide.

It may be of interest that traces of quartz can easily be separated from molten selenium by removing the upper layer from this melt.

(2) *Checking by means of a radioactive tracer*

Radioactive tracers can be applied to measure the decrease of impurity content by one distillation-sublimation *). In this case radioactive copper Cu^{64} (β-radiation 0·57 MeV, $t_h = 12{\cdot}8$ h) was used, supplied by the Institute for Nuclear Research in Amsterdam as a solution of cupric chloride in water with a total activity of about 1500 μc. After adding inactive copper chloride and some powdered selenium to the solution, copper sulphide was precipitated, this compound thus being thoroughly mixed with the added selenium. After this mixture had been dried, it was ground for several hours together with 400 g of inactive selenium; the total copper content of this mixture was 0·008 %. Its homogeneity could easily be checked by means of a Geiger-Müller counter (Philips GM 4810 with a Philips pulse shaper PW 4020 and a Philips Geiger-Müller tube 18514). Under the circumstances 100 mg of the mixture caused 2100 counts per minute, $19{\cdot}8 \pm 0{\cdot}6$ of these (the "background") being caused by the

*) Mr M. van Tol of this laboratory and Mr B. Verkerk of the Institute for Nuclear Research kindly advised the writer during his experiments with radioactive materials.

neighbourhood. About 200 g of the impurified selenium was distilled-sublimated as previously described. The sublimated selenium was powdered; the intensity of its radiation, together with that of the background, was estimated to be (after correction for decay) $18{\cdot}3 \pm 3{\cdot}3$ counts per minute and per 100 mg under the same conditions as prevailed before. An inactive selenium sample weighing 100 mg "absorbed" $3{\cdot}9 \pm 0{\cdot}3$ counts per minute. The intensity of radiation (corrected for this absorption) of samples and background together in counts per minute and per 100 mg was thus $22{\cdot}2 \pm 3{\cdot}6$; the intensity caused by the sample alone is therefore very small and does not exceed 7 counts per minute and per 100 mg of sublimated selenium under the circumstances. Each distillation-sublimation thus decreases the copper content by at least a factor 300.

Samples of sublimated selenium collected from different parts of the recipient (and measured in the same way) did not show significant differences.

It may be supposed that other impurities with low vapour tensions will behave in about the same way as copper sulphide.

CHAPTER III

THE ELECTRICAL CONDUCTIVITY AND THE HALL EFFECT OF POLYCRYSTALLINE HEXAGONAL SELENIUM

1. General remarks on the electrical conductivity of selenium

As has been stated before, the conductivity of polycrystalline, hexagonal selenium is dependent on

(1) The impurities (halogens increase, metals in general decrease the conductivity).

(2) The thermal treatment (high crystallization temperatures cause large conductivities).

(3) The density (the increase of the specific weight from about 4·3 to 4·8 during the transition from amorphous to hexagonal selenium causes gaps in polycrystalline samples, which can be prevented by applying pressure during the crystallization).

(4) The temperature (the conductivity almost always increases with increasing temperature).

(5) The pressure on the contacts (the effect may be negligible if the distance between the contacts is large).

(6) The frequency (if not stated otherwise, d.c. conductivities have been measured).

(7) The illumination (in all cases only dark-conductivities have been measured).

On the following pages the word "selenium" will mean: pure, polycrystalline, hexagonal selenium, pressed during its transition from the amorphous form.

2. The influence of thallium on the electrical properties of selenium

It has been mentioned before that thallium considerably reduces the conductivity of selenium. Moreover, Lehovec [16]) found a rather large mobility of thallium in selenium. According to this author the diffusion of the Tl particles (most probably Tl^{3+} ions) is dependent on the temperature and can be influenced by applying an electric field.

While repeating the experiments of Lehovec with radioactive thallium (Tl^{204}, β-radiation, $t_h = 2{\cdot}7$ y) and cylindrical selenium samples (which were prepared under a pressure of maximally 4000 kg/cm^2 at a temperature of 110 - 200 °C over about an hour), a velocity of the moving thallium front was measured equal to be 0·01 - 0·1 cm in an hour at 216 °C with an applied field of some hundreds V/cm.

These velocities were measured in two ways:

(1) According to Lehovec, the distribution of the electrical potential along the selenium sample was measured by means of a simple potentiometer circuit; the distribution of the electric field strength along the sample was derived from these measurements and was understood as a measure for the distribution of thallium.

(2) These measurements were checked by, and in general were found to be in accordance with, measurements of the radioactivity of cylindrical slices, prepared by sawing the cylindrical selenium samples.

The distribution of thallium in the sample cannot be predicted very easily. When using a cylindrical selenium sample with positive thallium electrode and negative "neutral" electrode (e.g. carbon), both diffusion by concentration gradient and by electric field increase the thallium content of the selenium on the side of the thallium electrode, thus raising the resistivity of this part of the cylinder and changing the distribution of electric field strength. This causes a change in drift velocity of the thallium ions. The calculations are complicated by the decrease of resistance which may occur after adding thallium to selenium containing already more than 10^{-2} % thallium.

It is remarkable, however, that the velocity of thallium ions in selenium is strongly dependent on the density of the selenium samples. The electrodiffusion of thallium ions in selenium with specific weight 4·78 is about ten times as fast as that measured in selenium with density 4·80, thus suggesting diffusion of thallium along the edges of the crystals in polycrystalline

selenium. It is a pity Lehovec did not mention the density of his samples; this phenomenon might explain the large difference between the rate of electro-diffusion measured by Lehovec (about 10^{-6} cm displacement of the thallium front is caused by 1 V/cm in 1 second at 216 °C) and by the present author (10^{-7} - 10^{-8} cm displacement under the same circumstances). Only by using samples with densities as low as 4·60 - 4·70 could Lehovec's velocity values be reproduced.

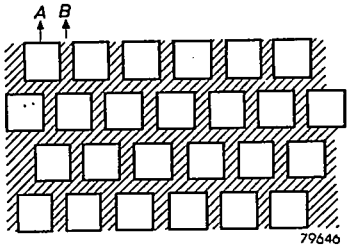

Fig. 4. Sketch of the structure of polycrystalline hexagonal selenium.

The diffusion of thallium along the crystal faces, however, presupposes that there are at least two different materials in the selenium sample. Therefore it was important to measure the resistances of selenium samples as a function of thallium content and frequency. A two-phase system like that sketched in fig. 4 can be represented to a sufficient approximation by the circuit of fig. 5*a*, the sections of material $A(B)$ together having a d.c. resistance r_A (r_B) and a capacity C_A (C_B). The a.c. parallel resistance r_p and capacity C_p of the equivalent circuit sketched in fig. 5*b* are given by

$$r_p = \frac{(r_A + r_B)^2 + r_A^2 r_B^2 \omega^2 (C_A + C_B)^2}{r_A(r_B^2 \omega^2 C_B^2 + 1) + r_B(r_A^2 \omega^2 C_A^2 + 1)},$$

$$C_p = \frac{r_A^2 C_A(r_B^2 \omega^2 C_B^2 + 1) + r_B^2 C_B (r_A^2 \omega^2 C_A^2 + 1)}{(r_A + r_B)^2 + r_A^2 r_B^2 \omega^2 (C_A + C_B)^2},$$

where ω is the angular frequency.

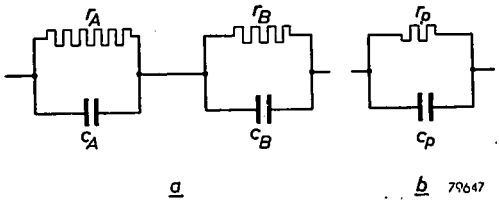

Fig. 5. Approximate equivalent circuits of the structure sketched in fig. 4.

At zero frequency $r_p = r_A + r_B$; with increasing frequency r_p decreases to (fig. 6)

$$\lim_{\omega \to \infty} r_p = \frac{r_A r_B (C_A + C_B)^2}{r_B C_B^2 + r_A C_A^2}.$$

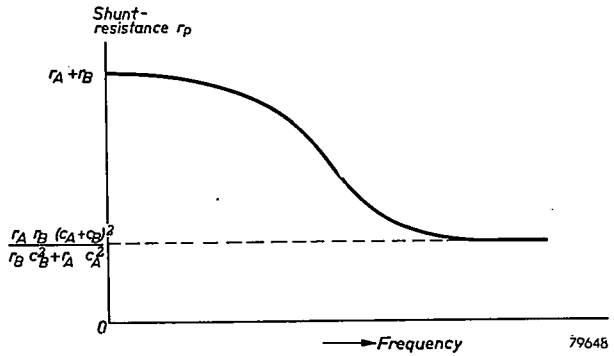

Fig. 6. Resistance vs frequency diagram of the circuit sketched in fig. 5*a*.

C_p in this range then decreases to

$$\lim_{\omega \to \infty} C_p = \frac{C_A C_B}{C_A + C_B}.$$

If the crystals A are very large compared with their mutual distance, then

$$C_A \ll C_B,$$

and the value of r_p at very high frequencies is about equal to the resistance of the crystals A, the capacity C_p is about the same as the capacity of the crystals A.

The r_p and C_p of cylindrical selenium samples with graphite electrodes and different thallium contents have been measured up to 30 Mc/s. The course of the resistivity with frequency is shown in fig. 7; C_p is of the order of 1 pF at high frequencies and is therefore too small to be discussed *).

It is probable that the high d.c. resistivity of selenium, to which thallium has been added, is localized in layers between the selenium crystals. These insulating layers will be short-circuited capacitively at high frequencies, thus leaving only the comparatively small shunt resistivity of the crystals. The r_p of pure polycrystalline selenium is also a function of the frequency,

*) The high-frequency measurements mentioned here and on other pages were performed by Dr J. Volger, Dr M. Gevers and Mr H. G. Beljers of this laboratory.

thus suggesting that there are badly conducting layers between the crystals in about the same way as in selenium with thallium. Investigations on this subject will be discussed afterwards.

No fundamental differences seem to exist between samples with thallium diffused into the selenium and samples prepared by mixing thallium with the melt, these samples being subsequently crystallized. In the latter preparations thallium can be moved by electric fields in the same way as in the first ones, the dependence of the resistivity on the thallium content is about the same in both kinds of sample.

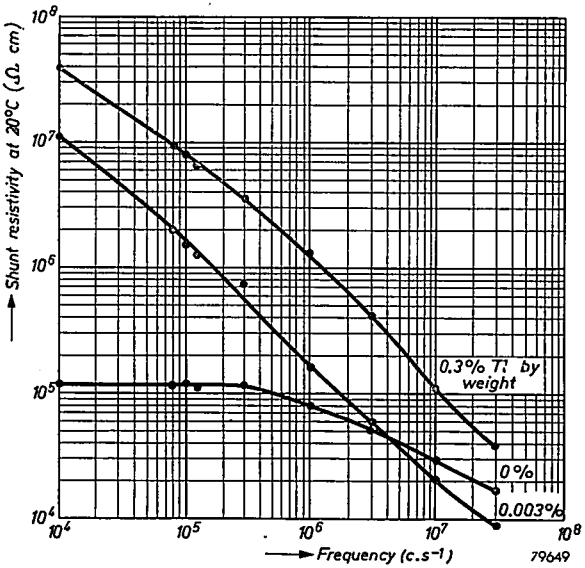

Fig. 7. Resistivity vs frequency diagrams of pure selenium and of selenium which contains thallium. The cylindrical samples were prepared by mixing thallium with the molten selenium, cooling down to 20 °C, and pressing at 110 °C for two hours.

It may therefore be concluded that thallium diffuses between the crystals of polycrystalline selenium and builds up insulating layers between the latter.

The question as to which type of charge carrier occurs in selenium with thallium has not been answered till now. It may be interesting to know that samples with less than about 10^{-2} atomic per cent of thallium show p-type semiconduction, more than about 10^{-2} atomic per cent of thallium causes n-type semiconduction, both according to the direction of rectification with pressed-on metal electrodes and according to the direction of the thermo-electric power. Some samples of selenium with diffused thallium

also showed a reversal of the sign of point-contact rectification; at large distances from the thallium electrode the selenium behaved as a p-type semiconductor, at small distances, however, n-type rectification was measured. The transition region contained about 10^{-2} % thallium by weight, and showed internal d.c. rectification in the same way as a p-n diffusion rectifier does.

Due to their high resistivities, the Hall effect of thallium-containing selenium samples could not be measured, and thus prevented us from obtaining direct information on the density of charge carriers and other fundamental quantities.

3. The Hall effect and the conductivity of pure and of bromine-containing selenium

(3a) *General remarks*

The most direct method of obtaining the density of charge carriers in a conductor is that of measuring the Hall effect.

Using a rectangular sample of length l, width b and thickness d, the current I (parallel to l) being carried by electrons *or* by holes with charges e and with density n (m^{-3}), a magnetic field strength B (B parallel to the thickness of the sample d) causes a potential difference V_H across the sample, given by

$$\left|V_H\right| = \left|R_H \frac{IB}{d}\right|. \tag{1}$$

Both this formula and the next ones, which express the relation between the Hall constant R_H, the carrier density n, the mobility μ and the conductivity σ, use Giorgi practical units:

$$\left|R_H\right| = \left|\frac{1}{ne}\right|, \tag{2}$$

$$\sigma = \left|ne\mu\right|, \tag{3}$$

$$\mu = \left|R_H\sigma\right|. \tag{4}$$

As is customary in the literature on semiconductors, however, the carrier density will henceforth be expressed in cm^{-3}, the mobility will be expressed in cm^2/V sec.

The formulae (2) and (4) are valid in the case of "degenerate" semiconductors which possess a comparatively large number of carriers in the conduction band; the Hall constant for non-degenerate semiconductors is given by

$$\left|R_H\right| = \left|\frac{3\pi}{8}\,\frac{1}{ne}\right| \quad \text{(Giorgi units)}. \tag{5}$$

This formula will not be used when discussing the following experiments; a systematical error of about 20 % may, therefore, be introduced by neglecting the factor $3\pi/8$.

If the d.c. circuit sketched in fig. 9 is used, small sensitivity of measurements may be expected for samples with high resistivities and small mobilities: supposing the bridge is not in equilibrium, the Hall potential difference V_H causes a current in a circuit with a resistance which is not much greater than the resistance of the sample between the Hall electrodes; this current is proportional to $V_H\sigma$. Because of formula (3) the current through the galvanometer will be proportional to the mobility of the charge carriers. If we consider the maximum current allowed by heat development, we shall then find that the sensitivity of the measurements is proportional to

$$\mu\sigma^{1/2} = n^{1/2}\mu^{3/2}. \tag{6}$$

The sensitivity of measurements on selenium samples was indeed rather small, and thus pointed to small mobilities of the charge carriers.

(3b) *Preparing the samples*

Pure or bromine-containing, flat samples of high-density polycrystalline hexagonal selenium could easily be obtained by pouring the molten selenium (if required with a small amount of bromine) at a temperature of about 250 °C on a sheet of electrolitically oxidized aluminium. After cooling to room temperature the amorphous selenium is covered with another oxidized aluminium sheet and is pressed at the desired temperature for at least five minutes. After cutting out samples of 8 × 25 mm² with a thickness of about 0·5 mm (fig. 8), the latter were thermally treated and provided with electrodes of evaporated gold. These electrodes have many advantages over others:

(1) They can be fixed without an additional heat-treatment (compare with soldered contacts).

(2) Their fixing does not increase the risk of impurifying the selenium samples (compare with electrodes of aquadag).

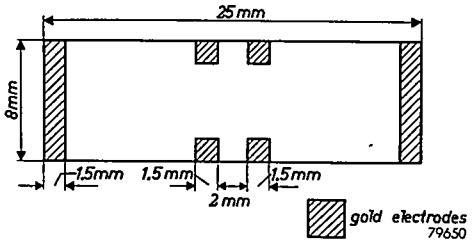

Fig. 8. Sample of selenium with gold electrodes.

(3) Electrodes of evaporated gold are almost non-forming, i.e. their current-voltage characteristics will not be influenced by electrical currents of reasonable magnitude. Strong forming will be observed when using alloys of cadmium and tin or of cadmium and bismuth as electrodes.
(4) These gold-selenium contacts are very bad rectifiers: they are almost ohmic and thus transmit electrical current even at low voltages. Moreover, this bad rectifying performance decreases the disturbing effects of electrical transmitters in the neighbourhood of the measuring circuits.

(3c) *Measurements*

Using the d.c. Hall-effect measuring circuit sketched in fig. 9, the accuracy of the measurements was badly influenced by instability (noise) of the principal current through the sample. It was therefore necessary to repeat measurements some twenty to fifty times. Each measurement, moreover, was checked by commuting the principal current and the magnetic field (thus allowing the elimination of the Ettingshausen-Nernst effect, the Righi-Leduc effect, and the change of resistance caused by the magnetic field) and by changing the absolute value of one or both of them.

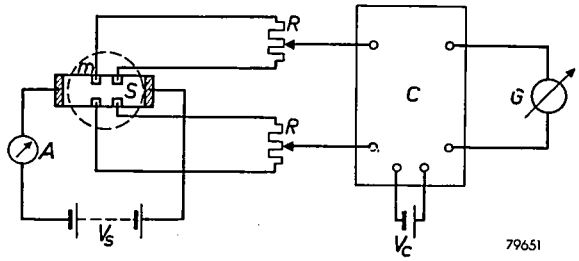

Fig. 9. Conventional d.c. circuit for measurements of Hall effects. V_s = battery, A = amperemeter, S = sample, m = magnetic field, R = potentiometer 50 000 Ω or more, C = Diesselhorst compensator, V_c = battery, G = galvanometer.

Although the stabilization of the principal current and the conduction of an extra current through the transversal electrodes increased the reproducibility of the measurements, about two thirds of the samples had to be discarded.

All conductivities were estimated by measuring the drop of potential along a current-carrying sample by means of a potentiometer circuit.

The temperature of the samples could be changed by a stream of air (heated if necessary) and was measured by means of a chromel-alumel thermocouple and a millivoltmeter.

Figs 10 and 11 show the densities of charge carriers and the carrier mobilities of selenium samples (calculated by means of formulae (1), (2)

and (4) of section (3a)) as a function of the bromine content and of the temperature, all samples being crystallized by heating for ten minutes at 165 °C under the press and after that for six hours at 165 °C in air.

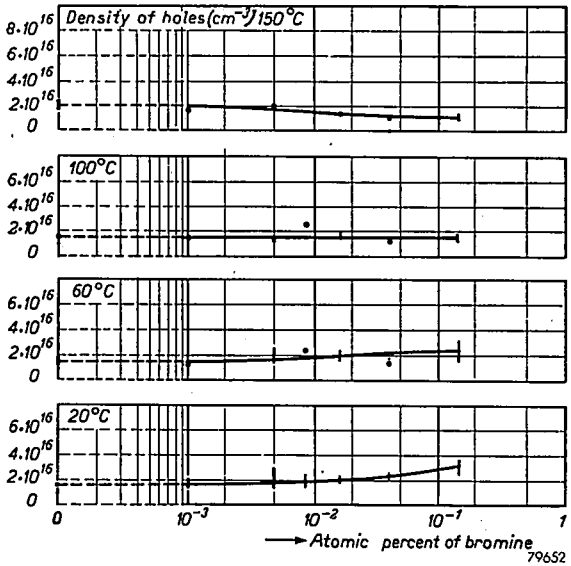

Fig. 10. The density of holes in selenium as a function of the bromine content at various temperatures.

In all cases the sign of the Hall coefficient is positive and thus shows the current to be fully or mainly carried by holes. If the selenium is both homogeneous and isotropic, then the formulae (1) and (2) of section (3a)

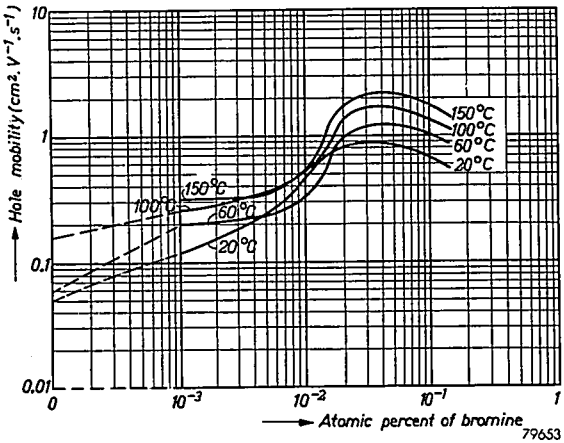

Fig. 11. Hole mobilities in selenium. These mobilities have been calculated from the average values of the hole density (fig. 10) and the resistivities.

can be applied. The thus calculated density of holes is only slightly dependent on the temperature and the bromine content, this number on the average being about 2.10^{16} cm^{-3} (thus there is one hole present in every 2.10^6 selenium atoms). This is clearly shown in fig. 12, demonstrating the average density and the maximum and minimum values of this density at given temperatures regardless of the bromine content.

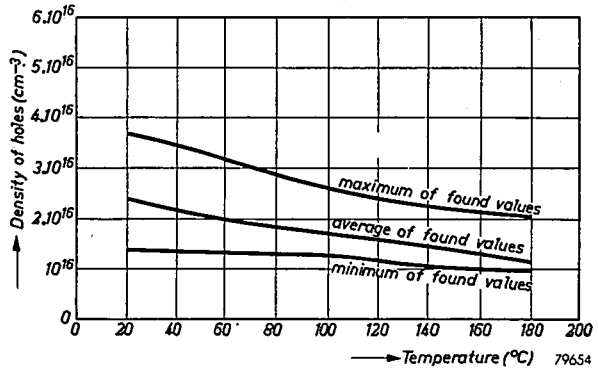

Fig. 12. Diagram demonstrating the rather small differences between the hole densities of samples of pure selenium and samples of bromine-containing selenium.

One series of measurements on pure selenium was carried out from —78 °C to + 210 °C, the density of holes being almost constant within this temperature range and equal to 2.10^{16} cm^{-3}.

To neglect the influence of the Ettingshausen effect is no major mistake: some rough measurements showed that this effect produces a maximum error of 10 % and in most cases 1 % or less in the density of the holes.

Some samples were heat-treated at other temperatures, using the same or a different length of time. The same Hall coefficient as mentioned before, indicating about 2.10^{16} holes cm^{-3}, was found, combined, however, with other mobilities.

(3d) *The mobility of the holes*

Calculation of the carrier mobility shows that

(1) Generally speaking the mobility increases with the temperature.

(2) Starting from low concentrations the mobility increases with the bromine content and decreases again at about 0·04 atomic per cent.

(3) The mobility varies between 0·06 and 2·2 cm^2/V sec.

Now the motion of a charge carrier in a lattice will be influenced by several quantities.

(1) Without thermal vibrations of the lattice being present, the moving

charge carriers will be deflected by any deviations from ideal structure ("impurity scattering").
(2) These charge carriers will be deflected by the thermally vibrating lattice atoms ("lattice scattering").
(3) The temperature governs the mean velocity of the charge carriers between deflections.

Calculations based on these principles predict that
(1) An increase of the concentration of ionized impurities will cause a decrease of the mean free path of a charge carrier and thus will cause a decrease of its mobility.
(2) Starting from low temperatures, the mobility will increase with the temperature to a certain value; at still higher temperatures the mobility will decrease again.
(3) The mean free path of a charge carrier will be proportional to its mobility; at room temperature the mean free path of an electron or of a hole with a mobility 1 cm^2/V sec will be about 0·6 Å.

This theory has been adequately confirmed by measurements on samples of germanium and silicon; the behaviour of selenium, however, is contradictory to that predicted.

The discrepancy between theory and experiments is exceptionally clear while calculating the mean free paths of the carriers. These would be much shorter than the distance of the selenium atoms (2·36 Å), thus giving a very unsatisfactory mechanism of electrical conduction.

Due to the very slight dependence of the Hall effect on the temperature, no justification will be found for a conducting mechanism using electrons and holes simultaneously as charge carriers, such as has been useful in Fritzsche's theory [32]) of the double reversal of the Hall constant in tellurium.

(3e) *Explanation of the results by means of a layer model*

Measurements of the shunt-resistivity versus the frequency of pure selenium, mentioned previously (section 2), showed the heterogeneity of the samples used. It is possible to explain this frequency dependence by one of the three models described below.
(1) Because of the anisotropy of selenium single crystals, polycrystalline selenium will be a heterogeneous material from an electrical point of view.
(2) The layers of distorted chains between the crystals in polycrystalline selenium act as a second material.
(3) The crystals in polycrystalline selenium may be separated by air or vacuum.

Ad (1). Undoubtedly, much too simplified substitution schemes of polycrystalline selenium are sketched in figs 13*a* and 13*b* (the rectangles in

these figures represent selenium single crystals). Now the ratio l_A/l_B in these figures is about 10 or 100 by microscopical examination (fig. 16), the resistivity perpendicular to the c-axis is about three to ten times as much as that parallel to the c-axis [18]), [19]), [20]).

Ad fig. 13a. The resistance of crystals A thus is at least equal to and maximal thirty times as great as that of crystals B, the capacity of crystals B being ten to a hundred times as great as that of crystals A.

Introducing p and q by $\varrho_B = p\varrho_A$ (ϱ = resistivity), $l_A = ql_B$, assuming $\varepsilon_A \approx \varepsilon_B$ (ε = dielectric constant), and using the formulae of section 2, the relation between the shunt resistance r_p and the angular frequency ω is approximated by

$$r_p = r_A \frac{(p+q)^2 + p^2(q+1)^2\omega^2 r_A^2 C_A^2}{q(p+q) + pq(pq+1)\omega^2 r_A^2 C_A^2}.$$

The d.c. resistance of the sample thus is equal to

$$r_{p,\omega=0} = r_A \frac{p+q}{q}$$

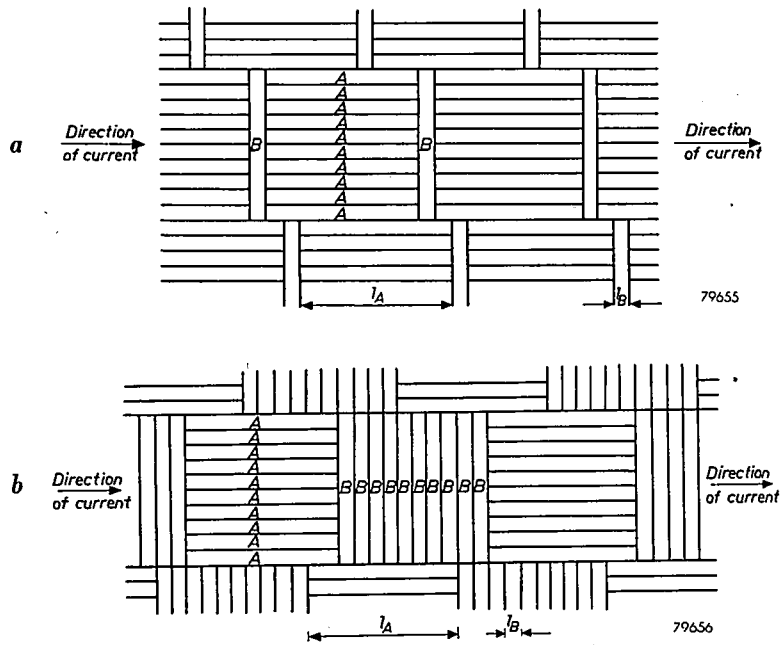

Fig. 13a, b. Simplified structures of polycrystalline selenium, which include the anisotropic behaviour of single crystals.

and the shunt resistance at very high frequencies will be

$$r_{p,\omega=\infty} = r_A \frac{p(q+1)^2}{q(pq+1)}.$$

Table I shows the values of

$$D \equiv \frac{r_{p,\omega=\infty}}{r_{p,\omega=0}} = \frac{p(q+1)^2}{(pq+1)(p+q)}$$

for some values of p and q.

TABLE I

$p \equiv \frac{\varrho_B}{\varrho_A}$	$q \equiv l_A/l_B$						
	1	3	10	30	100	300	1000
1	1·00	1·00	1·00	1·00	1·00	1·00	1·00
3	0·75	0·80	0·90	0·96	0·99	1·00	1·00
10	0·33	0·40	0·60	0·80	0·93	0·97	0·99
30	0·12	0·16	0·30	0·53	0·78	0·92	0·97

Bearing in mind that $3 < p < 10$ and $10 < q < 100$, it will be seen that the d.c. resistivity of this model is maximal twice as large as the resistivity at very high frequencies.

Ad fig. 13*b*. Using the structure sketched in fig. 13*b* ($3 < p < 10$, $q \approx 1$), a factor equal to a maximum of three will be calculated.

Figs 7, 14 and 15 show this proportion to be more than two. Measurements at about 10^{10} c/s showed, moreover, a shunt resistivity of about 100 Ω cm for pure selenium, the proportion mentioned thus being equal to about a hundred; therefore the models of figs 13*a* and *b* seem to be unsatisfactory. Another reason for not accepting this structure is given by the electrical conductivities of selenium single crystals which have been grown in a bromine-containing atmosphere. These conductivities, measured parallel and perpendicular to the *c*-axis of the crystals, are the same as those obtained from single crystals prepared in a high vacuum or in argon. The relation between the bromine content and the resistivity of polycrystalline selenium thus cannot be explained by these models.

Ad (2). The model in which the layers of distorted chains between the crystals are held responsible for the electrical behaviour of selenium gives better agreement between theory and experiment. In this case the

crystals A will be much larger than the layers B, the resistivity of the layers B will be very large compared with the resistivity of the crystals A.

Denoting again

$$\varrho_B = p\varrho_A,$$

$$l_A = ql_B,$$

and assuming $\varepsilon_A \approx \varepsilon_B$

and $p \gg q$,

p and q being more than a hundred, calculation gives

$$D \equiv \frac{r_{p,\omega=\infty}}{r_{p,\omega=0}} \approx \frac{q}{p}.$$

The condition $p \gg q$ is fulfilled according to d.c. and h.f. measurements: $D \leqslant 10^{-2}$.

In pure polycrystalline selenium, crystals have a length between 10^{-4}

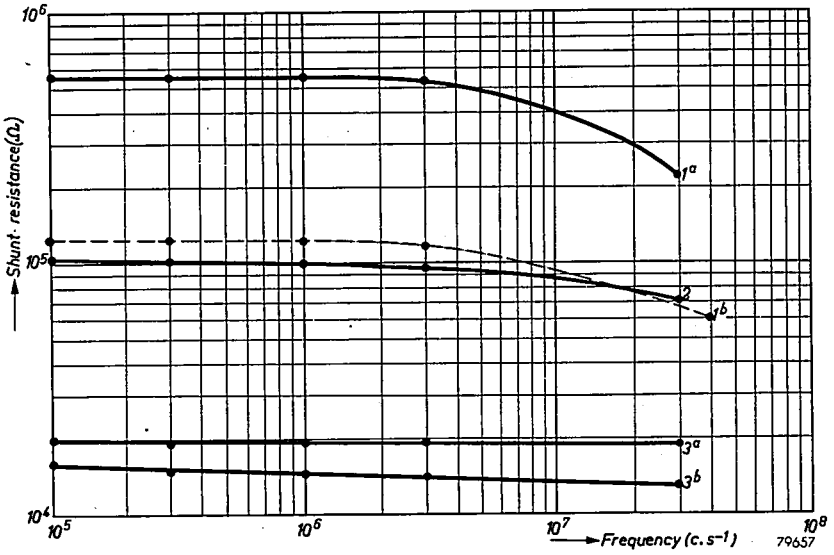

Fig. 14. Resistance vs frequency diagrams of some samples of pure and brominated selenium. The d.c. resistance of all samples is some per cent larger than the shunt resistance at 10^5 c/s.
Samples 1*a* and 1*b* do not contain bromine, but have different dimensions, thus allowing a better comparison of samples 1*b* and 2.
Sample 2 contains 0·002 atomic per cent of bromine.
Samples 3*a* and 3*b* contain 0·05 atomic per cent of bromine.
The samples 1*a*, 2, 3*a* and 3*b*, having dimensions like those shown in fig. 9, have also been used for measurements of the Hall effect.
Thermal treatment: pressed 10 min at 165 °C, 6 h heated at 165 °C without pressing.

and 10^{-2} cm (see electron-optical photo, fig. 16). The layers between the crystals are supposed to have thicknesses between 10^{-7} and 10^{-6} cm, thus $10^2 \leqslant q \leqslant 10^5$, so that $p \geqslant 10^4$.

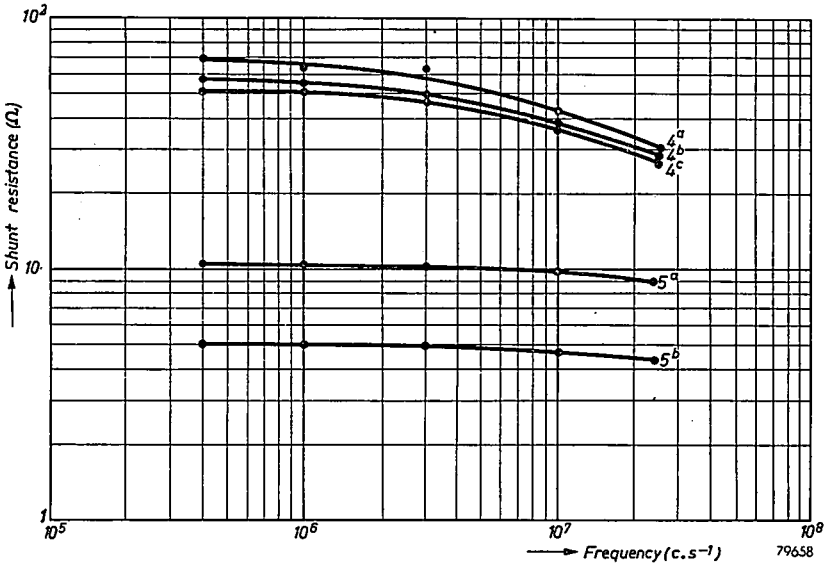

Fig. 15. Resistance vs frequency diagrams for some samples of pure and brominated selenium. These samples have gold electrodes with an area of 9 cm^2, the distance between these electrodes being about 0·5 mm.
Samples 4*a*, 4*b* and 4*c* do not contain bromine.
Samples 5*a* and 5*b* contain 0·01 atomic per cent of bromine.
All samples were pressed 10 min at 165 °C; 4*c* and 5*b* received an additional treatment at 165 °C for 6 hours.

Now it has been shown in section 2 that the shunt resistivity at infinitely high frequencies in cases like this will be equal to the d.c. resistivity of the well-conducting phase, thus ϱ_A will be a hundred Ω cm or less, ϱ_B will be more than 10^6 Ω cm. These very reasonable values lend support to the picture claiming that the intermediate layers are responsible for the electrical behaviour of selenium.

Assuming $D = 10^{-2}$ and $q = 10^5$, ϱ_B will be calculated to be 10^9 Ω cm. This is much less than the value of the resistivity in samples of pure amorphous selenium, which was measured to be about 10^{12} Ω cm. The distortion of the chains in the intermediate layers, therefore, seems to be much less grave than the distortion of the chains in pure amorphous selenium.

The small mobilities found in pure and also in bromine-containing selenium, can be explained by this picture. Volger [30]) showed that for

structures consisting of well-conducting crystals surrounded by layers of comparatively low conductivity the density of carriers in the well-conducting phase is connected with the *overall* Hall voltages in the usual way. In such structures the badly conducting layers may thus contribute a great deal to the total resistance; the carrier density found by measuring the Hall voltage is equal, however, to that in the well-conducting phase.

Fig. 16. Electron-optical image of polycrystalline, hexagonal selenium. This photograph was made by Mr H. B. Haanstra of this laboratory with the Philips electron microscope EM 100. Magnification by microscope: 2500 ×. Photographical magnification: 5 ×. Thus 1μ in selenium is equal to 1·25 cm on the photograph.

Mobilities found by using the formula $\mu = \bar{\sigma}/ne$ thus will have no important physical meaning and will give completely wrong values of the real mobilities. According to this structure the carrier density (2.10^{16} cm^{-3}) in the rather well-conducting crystals in polycrystalline selenium is not or only slightly dependent on the temperature and on the overall bromine content. Because the resistivity of these crystals is about one hundred Ω cm or less, the mobility within the crystals is calculated to be about 3 cm^2/V sec or more, a value which seems to be more probable than the very small ones (less than 0·1 cm^2/V sec) found by more conventional calculations.

The hole density in brominated selenium is about equal to that in pure selenium. Thus it may be supposed that the mechanism of electrical conduction within the crystals will either not or only slightly be affected by the bromine atoms present; this impurity only decreases the resistance of the layers and increases the effective mobility of the holes. In confirmation of this assumption, the shunt resistivity of brominated selenium is less dependent on frequency than the resistivity of pure selenium is. Brominated selenium with a d.c. resistivity equal to about 2000 Ω cm showed a shunt resistivity equal to a hundred Ω cm at 10^{10} c/s. Due to their strong tendency to crystallization, bromine-containing samples with d.c. resistivities of 300 Ω cm and suitable for measuring the shunt resistivity at 10^{10} c/s could not be prepared; the previous supposition therefore could not definitely be proved.

The electrical behaviour of selenium-tellurium alloys complies with the layer model. Alloys of this composition have been made by melting mixtures of selenium and tellurium (tellurium content ranging from zero over 10^{-2}, 4.10^{-2}, 10^{-1}, etc., to 100 atomic per cent) and crystallizing these mixtures in the way described in section (3b). This annealing process, however, can be applied only from 0 to 16 atomic per cent of tellurium. Alloys with more than this amount of tellurium crystallize immediately when cooling down below their melting points, just as does pure tellurium. Thus there seems to exist a selenium-like slow crystallization in the range from 0 to 16 atomic per cent of tellurium, the alloys with more tellurium behaving more or less like pure tellurium. In the range first mentioned the d.c. resistivity slowly increases from about 10^4 Ω cm (pure Se) to about 3.10^4 Ω cm (16 at. % Te); the density of holes is almost independent of the tellurium content and is equal to $(2 \pm 0{\cdot}5).10^{16}$ cm^{-3}. The small (pseudo) mobilities are readily explained by the layer model. The relatively small decrease can be explained by the interruption of the periodicity in a "copolymerized" chain of selenium atoms and tellurium atoms [33]).

The alloys which contain more than 16 atomic per cent of tellurium crystallize very rapidly to rather coarse-grained materials. The resistivity of these alloys decreases when their tellurium content increases.

Ad (3). It is not possible to explain the electrical behaviour of selenium by means of air-filled or vacuum gaps between the crystals in polycrystalline material. In this case bromine atoms could be placed in two ways: either they could enter the lattice and thus change its electrical properties, or the bromine atoms could be adsorbed on the surface of the crystals. The first supposition would cause, according to Volger [30]), a strong dependence of the Hall constant upon the bromine content, which is not in agreement with the experiments. The second supposition, however, shows a close resemblance to the picture of the badly conducting layers.

CHAPTER IV

DISCUSSION AND CONCLUSION

1. Introduction

A satisfactory description of the conduction mechanism in polycrystalline, hexagonal selenium must account for the following facts:
(1) Thallium increases the resistivity of selenium very strongly. The diffusion of thallium into selenium is strongly increased by electric fields. The shunt resistivities of thallium-containing samples decrease with increasing frequency to a value about equal to that of pure selenium.
(2) Bromine decreases the d.c. resistivity of selenium strongly. The Hall coefficient of pure and of bromine-containing, hexagonal selenium at temperatures above 20 °C is, however, almost independent of the bromine content. When applying a conventional interpretation of the Hall effect, electrical current in such samples is carried by 2.10^{16} holes per cm^3.
(3) This hole density is only slightly dependent on the temperature within the range mentioned.
(4) When using the conventional calculation, based only on the values of the Hall coefficients and of the d.c. conductivities, unusually small hole mobilities are found.
(5) Generally speaking, these mobilities increase with increasing content of bromine and with increasing temperature of the samples, which facts are not in agreement with conventional semiconductor theory.
(6) The resistivities of samples of pure and of brominated selenium decrease with increasing frequency. Both kinds of samples have resistivities of about 100 Ω cm at 10^{10} c/s.
(7) Bromine is only very loosely bound to the selenium lattice [14], [34]. Already at room temperature bromine escapes from samples, thus raising their resistances. At elevated temperatures this process may end in a few hours, the final resistivity being that of pure selenium. No traceable amount of residual bromine is found in these samples.
(8) The hole densities in polycrystalline selenium, when calculated from measurements of the thermo-electric power, are in contradiction with the values obtained from measurements of the Hall effect.

The behaviour of hexagonal selenium single crystals can be briefly described by:
(9) When preparing selenium single crystals by sublimation methods, the resistivity in both crystallographical directions is independent of the bromine content of the surrounding atmosphere (the resistivity of sublimated polycrystalline selenium, however, depends very strongly on the bromine pressure).

(10) Measurements of the Hall effect and of the thermo-electric power of selenium single crystals with a length in the order of one cm point to a slightly temperature-dependent hole density of about 10^{14} cm^{-3}.
(11) Measurements of selenium single crystals in both crystallographical directions point to voltage-dependent d.c. conductivities.

2. The layer model for polycrystalline hexagonal selenium

With the intention of avoiding calculations in the discussion, these have been performed in chapter III. These calculations point to a structure containing small crystalls of selenium which are separated from each other by layers of low conductivity.

There is a close resemblance between this model and the structures of many oxidic semiconductors, which have been disclosed by investigations of Koops [35]).

The addition of impurities such as thallium or bromine changes the overall resistivity of hexagonal polycrystalline selenium by way of changing the resistance of the layers, but does not or only slightly affect the resistivities of the crystals.

The structure of these layers is not known: they cannot be separated from the crystals, so that a determination of their composition escapes chemical analysis (this might perhaps show an accumulation of added or residual impurities). Also X-ray analysis cannot elucidate their structure, the fraction of layer material being too small. A reasonable assumption, however, identifies the layers with the "amorphous" material remaining after crystallizing a sample of vitreous selenium. This material may consist of loose, short and perhaps distorted selenium chains or of the more or less disordered junctions between "crystallized" parts of selenium chains (fig. 17).

The next part of this discussion will contain remarks on the eleven points of discussion, which will account for the observed facts.

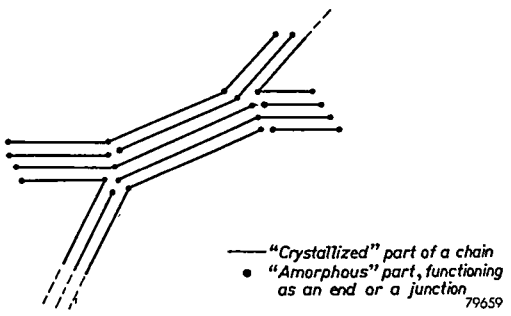

Fig. 17. Probable structure of hexagonally crystallized selenium.

Ad (1) (*chapter III, section* 2)

Since thallium ions increase the resistivities of the layers, on applying a potential difference between the electrodes of the sample the electric field strengths will be very much larger in the layers than within the crystals. In these strong fields the thallium ions can migrate at considerable velocities. The reason why thallium increases the resistance of the layers is not very clear; this fact might be explained by supposing that some residual hole-conductivity in loose, amorphous chains is compensated by electrons supplied by the thallium atoms. The exceptionally high resistivities caused by thallium and not by other metals (except mercury, see [36]) cannot, however, be understood in this way.

We found some thallium chemically bound during the diffusing process. After electro-diffusing radioactive thallium into selenium and reversing the voltage, the resistance decreases and after some time reaches the value for pure selenium; the selenium, however, still contains an amount of radioactive thallium which would cause a raised resistivity when added in the usual way. The forming of thallous selenide and particularly that of thallous thallic selenide with its chain-like structure [37]) and its property to contain simultaneously monovalent and trivalent thallium ions may be responsible for the exceptional behaviour of thallium towards selenium.

Some additional proof of the assumption that layers of amorphous selenium are responsible for the behaviour of polycrystalline selenium towards thallium is offered by our observation that the resistivity of thallium-containing amorphous selenium ($\approx 10^{14}$ Ω cm) is more than a hundred times as large as that of pure amorphous selenium ($\approx 10^{12}$ Ω cm), both kinds of samples being prepared by the same method.

Ad (2) - (7) (*chapter* III, *sections* (3c) - (3e))

According to the theory on layer structures of Volger [30]), the hole density 2.10^{16} cm^{-3} in samples of selenium is equal to the hole density in the rather well-conducting crystals; the overall resistivity, however, depends mainly on the resistance of the layers between the crystals. This theory accounts for the small effective mobility of holes in selenium and for the unconventional dependency of these mobilities on the impurity content and on the temperature.

Bromine may be present in hexagonal polycrystalline selenium:

(a) In the crystals, as interstitially admitted atoms or ions;

(b) In the crystals, as chemically bound atoms or ions within the selenium chains;

(c) As atoms or ions in the layers between the crystals.

Ad (a). The only possible way to explain the increase of the conductivity

caused by bromine would be given by assuming an increase of the hole density. This supposition is not sustained by the facts.

Ad (b). Assuming that bromine causes no change of the mean length of a selenium chain, this supposition is in contradiction with discussion point (9). Bromine, however, might shorten the length of a selenium chain by reactions such as

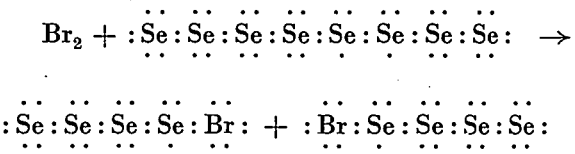

In such chains a rearrangement such as

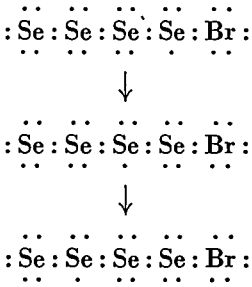

would be equivalent to the motion of a hole along the chain. Bromine would then increase the hole density of selenium, which is in contradiction to the measurements of the Hall effect.

Ad (c). This assumption is sustained by measurements of the Hall effect, by those of the shunt resistivities versus frequency, and by the considerable lowering of the resistivity of amorphous selenium which occurs after adding bromine (i.e. from $\approx 10^{12}$ Ω cm to $\approx 10^{10}$ Ω cm).

No stable bond seems to exist between selenium chains and bromine (discussion point (7)).

It is not possible to give an explanation of the conduction mechanism within these very thin layers without making speculative assumptions. When comparing with the mobility of thallium in selenium and the assumption of Lizell [13]), that electrical conduction in molten selenium has both electronic and ionic character, it is obvious to suppose the electrical conduction in these layers to be at least partly ionic by bromine ions. In this case an electric field should displace the bromine ions and thus perhaps change the overall resistance of the sample. No such effect could be traced either by d.c. or with high-tension "d.c." pulses.

Ad (8) (*chapter* I, *section* 3)

The contradiction between the carrier densities calculated from the Hall effect and those estimated by means of the thermo-electric power can easily be explained by the layer model; thermo-electric power is measured across a sample which contains not only (anisotropic) crystals, but also somewhat vitreous layers with small thermal conductivities. It may be of interest to point out the fact that the thermo-electric forces of hexagonal selenium and molten selenium both are very large compared with the thermo-electric power of other semiconductors and in the order of 1 mV/°C.

3. Discussion on selenium single crystals

Ad (9) (*chapter* III, *section* (3e))

It is probable that the hexagonal selenium lattice does not admit bromine atoms.

Ad (10) (*chapter* I, *section* 3)

Realizing that a hexagonal selenium crystal shows a considerable difference between the resistivities parallel and perpendicular to the *c*-axis, it is reasonable to suppose that the charge carriers (holes) move easily between selenium atoms in one chain, but meet considerable difficulties when moving to atoms in a neighbouring chain. Because each chain is short of two electrons for the saturated condition, it is reasonable to suppose that each chain produces maximally two holes, as will be shown by the Lewis schemes of some possible electron distributions. These may be such as

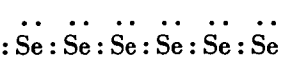

(*a*)

or

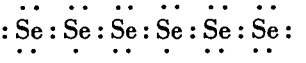

(*b*) .

When accepting the second structure as being actually present, we can calculate the chain length from Plessner's data [25]), [26]) for the hole density.

Taking into account the dependence of the mobility upon the crystallographical orientation of the current, this number (10^{14} cm^{-3}) should be increased to 3.10^{14} cm^{-3} or to 10^{15} cm^{-3}. Because one chain gives two holes in case (*b*), the density of chains would approximately be given by 4.10^{14} cm^{-3}. Selenium contains $3{\cdot}7.10^{22}$ atoms per cm^3, thus one chain would contain about 10^8 atoms and would have a length in the order of one cm, which is the actual length of selenium single crystals prepared by way of sublimation.

Ad (11) (*ref.* [19]))

The voltage-dependent d.c. resistivities point to internal barriers in single crystals of selenium. This assumption is adequately confirmed by the small mobility of holes in such crystals, which has been calculated to be in the order of 1 cm^2/V sec from the values of the hole density and of the d.c. conductivity. The presence of these barriers could be explained by the supposition that one chain of selenium atoms contains both crystallized and "amorphous" parts, such as is known to exist in fibres of e.g. cellulose.

The conclusions from measurements on selenium "single crystals" need much more justification than has been given here; the effects of electrical cross-coupling of chains, perhaps strongly influenced by the tendency of these crystals to grow in somewhat twisted shapes, may be more important than has hitherto been supposed.

4. Comparison of the conclusions obtained from measurements on selenium single crystals and those on polycrystalline selenium

Supposing that also in polycrystalline selenium one chain contributes two holes, the density of chains in polycrystalline selenium must be equal to about 10^{16} cm^{-3}. One chain thus contains about 4.10^6 atoms and therefore must have a length of at least some tenths of a millimeter.

In polycrystalline selenium, however, the dimensions of crystals have never been observed to exceed about 50 μ. It is obvious to suppose here, as has been done so previously in the discussion on point (11), both amorphous and crystallized parts in the same chain (fig. 17).

In this model amorphous layers of three kinds exist:

(a) Layers of the first kind join crystallized parts of continuous chains.

(b) Layers of the second kind separate different chains.

(c) The third and most frequently occurring kind contains both junctions between crystallized parts of the same chain and ends of chains.

5. Postcript

The fact that impurities like thallium and bromine do not influence the properties of the crystals in polycrystalline selenium, but only change the properties of the transition regions between these crystals, will be beneficial to a better understanding of the rectifying contacts on selenium: the influence of thallium on such rectifiers, for instance, can at least partly be explained by the fact that this thallium causes inhomogeneous and internally rectifying barrier layers of selenium near the counter-electrode.

Patent literature describes additions of the most different kinds (for instance selenium chloride, sodium chloride, powder of glass) with the purpose of lowering the resistance of hexagonal selenium or of stabilizing

a high conductivity already present. It is obvious that only a few of these impurities will fit into the selenium lattice: it is thus very probable that these contaminations only influence the electrical properties of the regions between the crystals and do not change the properties of the crystallized regions.

Acknowledgements

The author wishes to express his special thanks to Dr E. J. W. Verwey for his stimulating suggestions.

He is indebted to Dr W. Ch. van Geel, Dr P. W. Haaijman and Dr J. Volger for their interest in this work and for valuable advice, and to Mr H. M. Rietveld and Mr W. A. M. Cammel for their laboratory assistance.

Eindhoven, April 1954

REFERENCES

1) L. S. Brooks, J. Amer. chem. Soc. **74**, 227-229, 1952.
2) J. W. Mellor, Inorganic and theoretical chemistry, Longmans, Green and Company, New York, 1940, Vol. X, p. 705.
3) H. Richter, W. Kulcke and H. Specht, Z. Naturf. **7a**, 511-532, 1952.
4) R. D. Burbank, Tech. Repts **37** (June 1950) and **43** (April 1951) of the Massachusetts Institute of Technology;
Acta cryst. **4**, 140-148, 1951;
Acta cryst. **5**, 236-246, 1952.
5) R. E. Marsh, L. Pauling and J. D. Mc Cullough, Acta cryst. **6**, 71-75, 1953.
6) F. de Boer, Rec. Trav. chim. Pays-Bas **62**, 151-157, 1943.
7) W. Morsch, Thesis 1950 (Bonn, Germany).
8) H. Krebs, Z. anorg. Chem. **265**, 156-168, 1951.
9) F. de Boer, Philips Res. Rep. **2**, 349-351, 1947.
10) H. W. Henkels, Phys. Rev. **76**, 1737-1738, 1949.
11) H. W. Henkels, J. appl. Phys. **21**, 725-731, 1950.
12) G. Borelius, F. Pihlstrand, J. Andersson and K. Gullberg, Ark. Mat. Astr. Fys. **30A**, Nr 14, 1-30, 1944.
13) B. Lizell, Tech. Rep. **47** (Sept. 1951) of the Massachusetts Institute of Technology; J. chem. Phys. **20**, 672-676, 1952.
14) H. Schweickert, Z. Phys. **128**, 47-55, 1950. (This fact has been used a long time before this publication by manufacturers of selenium rectifiers.)
15) B. Gudden and K. Lehovec, Z. Naturf. **1**, 508-511, 1946.
16) K. Lehovec, Z. Phys. **124**, 278-285, 1948.
17) K. Lehovec, Z. Phys. **125**, 451-454, 1949.
18) F. de Boer, Philips Res. Rep. **2**, 352-356, 1947.
19) H. W. Henkels, J. appl. Phys. **22**, 916-925, 1951.
20) H. W. Henkels, Phys. Rev. **91**, 1562-1563, 1953.
21) K. Lehovec, Private communication to H. W. Henkels mentioned in J. appl. Phys. **22**, 918, 1951.
22) W. Shockley, Electrons and holes in semiconductors, Van Nostrand Company, Inc., New York, 1951.
23) H. W. Henkels, Phys. Rev. **77**, 734-736, 1950.

[24]) H. W. Henkels, J. appl. Phys. **22**, 1265-1278, 1951.
[25]) K. W. Plessner, Nature **165**, 970-971, 1950.
[26]) K. W. Plessner, Nature **166**, 1073, 1950.
[27]) I. M. Iglitsen, J. tech. Phys., Moscow, **22**, 885-887, 1952.
[28]) F. Eckart and A. Kittel, Naturwissenschaften **24/25**, 371, 1941.
[29]) W. Schottky, A simple summary of Schottky's theories has been given by J. Joffé, Elect. Commun. **22**, 217-225, 1945.
[30]) J. Volger, Phys. Rev. **79**, 1023-1024, 1950.
[31]) A. Hoffmann, Z. Phys. **128**, 414-431, 1950.
[32]) H. Fritzsche, Science **115**, 571-572, 1952.
[33]) E. Grison, Tech. Rep. **38** (March 1951) of the Massachusetts Institute of Technology.
[34]) W. Ch. van Geel, Private communication.
[35]) E. J. W. Verwey, Semiconducting materials (Proceedings of a conference held as the University of Reading, edited by H. K. Henisch), Butterworths Scientific Publications Ltd, London, 1951, pp. 158-160.
[36]) H. K. Henisch and E. W. Saker, Proc. phys. Soc. **65B**, 149-154, 1952.
[37]) J. A. A. Ketelaar, W. H. 't Hart, M. Moerel and D. Polder, Z. Kristallogr. **101**, 396-405, 1935.

Philips Res. Rep. 9, 295-320, 1954

SATURATION MAGNETIZATION AND CRYSTAL CHEMISTRY OF FERRIMAGNETIC OXIDES *)

by E. W. GORTER

621.317.421:548.3:548.736.453.2

Summary

Measurements of the saturation magnetization (σ) against temperature are carried out for a number of mixed crystal oxides with spinel structure. The results are in agreement with Néel's theory of ferrimagnetism: the resultant magnetic moment m is the difference of the moments of the tetrahedral (A) and octahedral (B) sublattices, either (a) with complete parallelism of the ionic moments inside each sublattice, or (b) with angles between the ionic moments inside one of the sublattices. The spinel structure is described in section 1.1, experimental and theoretical data from literature on cation distribution are summarized in section 1.2. Néel's theory is reviewed in section 2.2.1, with Yafet and Kittel's modification (section 2.2.2). When the moments of the two sublattices are approximately equal, Néel predicts a number of anomalous σ-T curves. All of these should occur in a series of mixed crystals of type (a) in which the resultant moment m changes sign. Our experimental methods are given in section 3. The measurements on the single ferrites $Me^{II}Fe_2^{III}O_4$, with $Me^{II} = Mn^{2+}$, Fe^{2+}, Co^{2+}, Ni^{2+}, Cu^{2+}, Mg^{2+} or $(0{\cdot}5\,Li^{+} + 0{\cdot}5\,Fe^{3+})$ show that these belong to group (a); the mixed crystals $Me_{1-a}Zn_aFe_2O_4$ with $a >$ appr. 0·4 belong to group (b) (section 4). The moment of $Ca_{0{\cdot}35}Zn_{0{\cdot}65}Fe_2O_4$ is higher than that of any MgZn ferrite, perhaps because the angle A-O-B is increased by the presence of the greater part of the large Ca ions in the B sites, thus increasing the AB interaction; this behaviour would be in agreement with Anderson's theory (section 5.1; Anderson's theory is reviewed in section 2.3.2). The moments of ferrimagnetic oxides with other crystal structures may be predicted from the angles (metal ion)-(O^{2-} ion)-(metal ion); cf. $BaFe^{III}_{12}O_{19}$ and $KFe^{III}_{11}O_{17}$ (section 5.2). In a number of mixed-crystal series anomalous σ-T curves have been looked for: these are not found in the systems $Ni_{1+a}Fe^{III}_{2-2a}Ti_aO_4$ and $Ni_{1{\cdot}5-a}Zn_aFe^{III}Ti_{0{\cdot}5}O_4$ because of the unexpected presence of Ti^{4+} ions in tetrahedral sites, proved for $Ni_{1{\cdot}5}Fe^{III}Ti_{0{\cdot}5}O_4$ by measurements of the effective g-factor (section 6.1-2). In the system $Li_{0{\cdot}5}Fe^{III}_{2{\cdot}5-a}Cr_aO_4$ $(0<a<2{\cdot}0)$ the distribution of the Li^{+} and Fe^{3+} ions is anomalous as a result of short-range order. The resultant moment remains positive, and only one type of anomalous σ-T curve, viz. that for which the spontaneous magnetization changes sign with temperature, occurs in a wide range of compositions. For $a \leqslant 1{\cdot}25$ the materials belong to group (a) (section 7). A change of sign of the resultant moment does occur in the system $NiFe^{III}_{2-a}Al_aO_4$. Anomalous σ-T curves are here found in a narrow range of compositions, but not all types predicted by Néel: the reasons are discussed (section 8). The presence of Mn^{2+} ions apparently promotes the formation of angles between the ionic moments in B sites: the complete system $MnFe^{III}_{2-a}Cr_aO_4$ belongs to group (b) (section 9), as well as $MnFe_2O_4$ prepared by other authors (section 4) and part of the system $Ni_{1{\cdot}5-a}Mn_aFe^{III}Ti_{0{\cdot}5}O_4$ (section 6.3). In the first-named system m probably changes sign only as a result of these angles.

*) Thesis, University of Leyden, June 1954.

Résumé

Les mesures de l'aimantation de saturation (σ) en fonction de la température ont été faites pour un certain nombre de cristaux mixtes d'oxydes à structure spinelle. Les résultats concordent avec la théorie de Néel sur le ferrimagnétisme: le moment magnétique résultant m est la différence des moments des sous-réseaux tétraèdrique (A) et octaèdrique (B), soit: (a) avec parallélisme complet des moments ioniques à l'intérieur de chaque sous-réseau, ou (b) avec des angles entre les moments ioniques à l'intérieur d'un des sous-réseaux. La structure spinelle est décrite dans la section 1.1, données expérimentales et théoriques, tirées de la litérature, sur la distribution des cations sont résumées dans la section 1.2. La théorie de Néel est revue dans la section 2.2.1, avec la modification par Yafet et Kittel (section 2.2.2). Quand les moments des deux sous-réseaux sont à peu près égaux, Néel prévoit un certain nombre de courbes σ-T anormales. Il faut trouver toutes ces courbes dans une série de cristaux mixtes du type (a) dans laquelle le moment résultant m change de signe. Nos méthodes expérimentales sont données dans la section 3. Les mesures sur les ferrites simples $Me^{II}Fe^{III}_2O_4$, avec $Me^{II} = Mn^{2+}$, Fe^{2+}, Co^{2+}, Ni^{2+}, Cu^{2+}, Mg^{2+} ou ($0{,}5\,Li^+ + 0{,}5\,Fe^{3+}$) montrent que celles-ci appartiennent au groupe (a); les cristaux mixtes $Me_{1-a}Zn_aFe_2O_4$ à partir de $a >$ appr. 0,4 appartiennent au groupe (b) (section 4). Le moment de $Ca_{0,35}Zn_{0,65}Fe_2O_4$ est plus élevé que celui d'une ferrite quelconque Mg-Zn, probablement parce que l'angle A-O-B est agrandi par la présence de la plupart des grands ions-Ca dans les sites B, accroissant ainsi l'interaction A-B. Ce comportement est conforme à la théorie d'Anderson (section 5.1). La théorie d'Anderson est revue à la section 2.3.2. L'on peut prévoir le moment d'oxydes ferrimagnétiques à structures crystallographiques différentes d'après les angles (ion-métal)-(ion-oxygène)-(ion-métal), cf. $BaFe^{III}_{12}O_{19}$ et $KFe^{III}_{11}O_{17}$ (section 5.2.) Dans un certain nombre de séries de cristaux mixtes on a cherché des courbes σ-T anormales; on ne les trouve pas dans les systèmes $Ni_{1+a}Fe^{III}_{2-2a}Ti_aO_4$ et $Ni_{1,5-a}Zn_aFe^{III}Ti_{0,5}O_4$ à cause de la présence inattendue d'ions Ti^{4+} dans les sites tetraèdriques, démontrée pour $Ni_{1,5}Fe^{III}Ti_{0,5}O_4$ par des mesures du facteur g efficace (section 6.1-2). Dans le système $Li_{0,5}Fe^{III}_{2,5-a}Cr_aO_4$ ($0 < a < 2{,}0$) la distribution des ions Li^+ et Fe^{3+} est anormale à cause d'une ordre à courte distance. Le moment résultant reste positif, et il apparaît dans une large gamme de compositions un seul type de courbe anormale σ-T, notamment celui où l'aimantation spontanée change de signe avec la température. Pour $a < 1{,}25$ les produits appartiennent au groupe (a) (section 7). Il se produit bien un changement de signe dans le système $NiFe^{III}_{2-a}Al_aO_4$. L'on trouve ici des courbes anormales σ-T dans une étroite gamme de compositions, mais non tous les types prévus par Néel: les raisons sont discutées (section 8). La présence d'ions Mn^{2+} apparemment favorise la formation d'angles entre les moments ioniques dans les sites B: le système complet $MnFe^{III}_{2-a}Cr_aO_4$ appartient au groupe (b), comme $MnFe_2O_4$ préparé par d'autres auteurs (section 4) et une partie du système $Ni_{1,5-a}Mn_aFe^{III}Ti_{0,5}O_4$ (section 6.3). Dans le premier système cité, le changement de signe de m n'est que le résultat de ces angles.

Zusammenfassung

Es wird die Sättigungsmagnetisierung (σ) einer Anzahl Mischkristalle von Oxyden mit Spinellstruktur in Abhängigkeit von der Temperatur gemessen. Die Ergebnisse entsprechen der Néelschen Theorie des Ferrimagnetismus: das resultierende magnetische Moment ist der Unterschied der Momente der Tetraeder- (A) und Oktaeder- (B) Teilgitter, und zwar entweder (a) mit vollständig parallelen Ionenmomenten innerhalb jedes Teilgitters, oder (b) mit Winkeln

zwischen den Ionenmomenten in einem der Teilgitter. Die Spinellstruktur ist in (1.1) beschrieben, experimentelle und theoretische Daten aus der Literatur über die Ionenverteilung sind in (1.2) zusammengefaßt. Eine Besprechung der Néelschen Theorie ist in (2.2.1) gegeben, dazu die durch Yafet und Kittel gelieferte Abänderung (2.2.2). Wenn die Momente der zwei Teilgitter einander nahezu gleich sind, sagt Néel eine Anzahl anomaler σ-T Kurven vorher. Alle diese Kurven müssen in einer Reihe von Mischkristallen vom Typus (a), in welcher das resultierende Moment m das Vorzeichen ändert, vorkommen. Die von uns benutzten experimentellen Methoden werden in (3) beschrieben. Aus den Messungen an einfachen Ferriten $Me^{II}Fe_2^{III}O_4$ mit $Me^{II} = Mn^{2+}$, Fe^{2+}, Co^{2+}, Ni^{2+}, Cu^{2+}, Mg^{2+} oder ($0{,}5\ Li^{+} + 0{,}5\ Fe^{3+}$) geht hervor, daß diese zur Gruppe (a) gehören; die Mischkristalle $Me^{II}_{1-a}Zn_aFe_2O_4$ von $a >$ ungefähr 0,4 an gehören zur Gruppe (b) (4). Das Moment von $Ca_{0,35}Zn_{0,65}Fe_2O_4$ ist höher als das aller MgZn-Ferrite, vielleicht weil der Winkel A-O-B infolge der Anwesenheit der Mehrzahl der großen Ca^{2+}-Ionen am B-Platz größer wird: dadurch wird die AB-Wechselwirkung im Einklang mit der Theorie von Anderson vergrößert. ((5.1), eine Besprechung der Theorie von Anderson gibt (2.3.2)). Das Moment von ferrimagnetischen Oxyden mit anderen Kristallstrukturen kann aus den Winkeln Metallion-Sauerstoffion-Metallion vorhergesagt werden, wie z.B. für $Ba\,Fe_{12}^{III}O_{19}$ und $K\,Fe_{11}^{III}O_{17}$ (5.2). In einer Anzahl von Mischkristallreihen ist nach eventuellem Auftreten von anomalen σ-T Kurven gesucht worden: man findet diese nicht in den Systemen $Ni_{1+a}Fe^{III}_{2-2a}Ti_aO_4$, weil entgegen den Erwartungen Ti^{4+}-Ionen an Tetraederplätzen auftreten, was für $Ni_{1,5}Fe^{III}Ti_{0,5}O_4$ durch Messung des effektiven g-Faktors bewiesen worden ist (6.1-2). Im System $Li_{0,5}Fe^{III}_{2,5-a}Cr_aO_4$ ($0 < a < 2{,}0$) tritt eine unerwartete Verteilung der Li^{+}- und Fe^{3+}-Ionen über die beiden Gitterplätze auf als Folge einer Ordnung kurzer Reichweite. Das resultierende Moment bleibt positiv, und es tritt nur eine anomale σ/T-Kurve auf, nämlich diejenige, bei der die spontane Magnetisierung mit der Temperatur das Vorzeichen ändert, und zwar in einem breiten Gebiet von Zusammensetzungen. Für $a \leqslant 1{,}25$ gehören diese Stoffe zur Gruppe (a). (7). Eine Änderung des Vorzeichens von m tritt dagegen in dem System $NiFe^{III}_{2-2a}Al_aO_4$ auf. Anomale σ/T-Kurven treten hier in einem schmalen Gebiet von Zusammensetzungen auf, aber nicht alle Typen die von Néel vorhergesagt worden sind; hiervon werden die Ursachen besprochen (8). Die Anwesenheit von Mn^{2+}-Ionen begünstigt anscheinend das Auftreten von Winkeln zwischen den Ionenmomenten an den B-Plätzen: das ganze System $MnFe^{III}_{2-a}Cr_aO_4$, gehört zur Gruppe (b), ebenso wie das von anderen hergestellte $MnFe_2O_4$ (4) und ein Teil des Systemes $Ni_{1,5-a}Mn_aFe^{III}Ti_{0,5}O_4$ (6.3). Im erstgenannten System ändert das Vorzeichen nur infolge dieser Winkel.

CONTENTS

INTRODUCTION

Largely as a consequence of Snoek's work, the "ferrites", i.e. oxides with a formula $MeO.Fe_2O_3$ or $Me^{II}Fe_2{}^{III}O_4$, are becoming increasingly important as high-frequency core materials because they combine useful ferromagnetic properties with a high electrical resistivity. In the above formula Me^{II} represents divalent Mn, Fe, Co, Ni, Cu, Zn, Cd, Mg, ($0{\cdot}5Li + 0{\cdot}5\ Fe^{III}$), or two or more of these in mixed crystals. In recent years the fundamental ferromagnetic properties have been investigated extensively. In the following we shall deal with the saturation magnetization of these ferrites and similar materials.

Practically all these materials have the same crystal structure as the mineral spinel, which structure (Bragg, 1915) may be regarded as a cubic, approximately close-packed arrangement of oxygen ions ($r = 1{\cdot}32$ Å), with metal ions having radii of 0·4-1·0 Å distributed amongst two kinds of interstices A and B, surrounded by 4 and 6 oxygen ions respectively. The structure is described in some detail in section 1.1.

X-ray and theoretical investigations, mainly by Verwey et al., have shown that the distribution of the different metallic ions amongst A and B sites is determined mainly by the Coulomb energy, including ordering energy inside each sublattice A or B, and by an individual preference of a number of ions for four- or six-fold coordination. One type of ion often occurs in both lattice sites. These investigations are summarized in section 1.2.

The ferromagnetic moment per formula unit, obtained from saturation-magnetization (σ) measurements at low temperatures, is not simply the sum of the moments of the magnetic moments present, but much lower; $ZnFe_2O_4$ and $CdFe_2O_4$ are not even ferromagnetic. Néel in 1948 gave a theory for these materials using the basic assumption that a preponderant negative (AB) interaction between the magnetic moments of the A and B sublattices causes these to have antiparallel orientation, so that the resultant moment m equals the difference between the moments of sublattices A and B. This non-compensated antiferromagnetism Néel calls *ferrimagnetism*. With the aid of this theory he could explain such susceptibility and saturation data as were at the time available, and predicted the occurrence of several types of anomalous magnetization vs temperature curves, which are expected to occur when the moments of the A and B sublattices are not very different. This anomalous behaviour can only occur in ferrimagnetism.

The equally negative AA and BB interactions may be either negligible against the AB interaction, so that the moment of each sublattice is the sum of the ionic moments in that sublattice, or they may be comparable with the AB interaction, for which case the moment of one of the sublattices is smaller than the sum of the ionic moments it contains. Yafet and Kittel (1952) have shown theoretically that in this case this sublattice splits up into 2 or 4 different parts: in each of these parts the ionic moments are parallel, but the moments of different parts form angles with each other.

The nature of the exchange coupling is an indirect exchange interaction involving the diamagnetic oxygen ions, the theory of which was outlined by Kramers in 1934. A treatment by Anderson (1950) shows that the strength of this superexchange interaction is dependent on the angle (metal ion)-(oxygen ion)-(metal ion). These theories are reviewed in section 2.

The object of the present investigation was primarily to obtain experimental evidence supporting Néel's theory. The results of our measurements of the saturation magnetization of a number of series of mixed crystals with spinel structure can almost all be accounted for by Néel's theory. For a group of materials, which mostly have relatively high Curie temperatures, the resultant moments are in agreement with the theory for the case of a preponderant AB interaction.

In several cases the ionic distribution, as obtained from these measurements, appears to be different from what knowledge on binary spinels would lead one to expect. The cation distribution can in most cases be understood from statistical considerations, assuming a certain order of preference of the cations for the A position inside one series of compositions. In some cases the influence of short-range order is noticeable.

In one series this could be confirmed by X-ray diffraction, in another case the effective g-factor was used in addition to the saturation data to find the ionic distribution. Some of the anomalous σ-T curves predicted by Néel have been found, a.o. in one series in which m changes sign with composition. It is shown that the absence in this series of those σ-T curves for which σ is zero at some temperature between 0 °K and the Curie temperature is due to the inhomogeneity of the cation distribution. In another system we have found materials for which such σ-T curves do occur.

For another group of materials, which have relatively low Curie temperatures, the results are in agreement with the theory for the case of comparable AB and BB interactions. In one system the resultant moment m changes sign, which when assuming parallel ionic moments in each sublattice would not occur for any ionic distribution.

Experimental indications for the dependence of the strength of the interaction on the angle (metal ion)-(oxygen ion)-(metal ion) are discussed and it is shown that this relationship enables one to account for the resultant moment in other crystal structures.

1. THE SPINEL STRUCTURE

1.1. The geometry of the spinel lattice

As we shall deal extensively with the magnetic properties of oxidic spinels in relation to the crystal structure, we shall give a fuller description of the structure than is found in literature, drawing attention to those features that are of interest in connection with these magnetic properties.

As only oxides will be discussed, the words oxygen ion will be substituted for anion throughout the description.

The crystal structure was determined for the minerals magnetite (Fe_3O_4) and spinel ($MgAl_2O_4$) by W.H. Bragg [1]) in 1915 and at the same time by Nishikawa [2]).

The space group is O_h^7-F3dm [3]) (cubic). The atomic positions in the spinel structure are [4])

8-fold position: 8 metal ions in (a) *) 0 0 0; $\frac{1}{4}\ \frac{1}{4}\ \frac{1}{4}$;
16-fold position: 16 metal ions in (d) *) $\frac{5}{8}\ \frac{5}{8}\ \frac{5}{8}$; $\frac{5}{8}\ \frac{7}{8}\ \frac{7}{8}$; $\frac{7}{8}\ \frac{5}{8}\ \frac{7}{8}$; $\frac{7}{8}\ \frac{7}{8}\ \frac{5}{8}$;
32-fold position: 32 oxygen ions in (e)
$u\ u\ u$; $u\ \bar{u}\ \bar{u}$; $\frac{1}{4}-u,\ \frac{1}{4}-u,\ \frac{1}{4}-u$; $\frac{1}{4}-u,\ \frac{1}{4}+u,\ \frac{1}{4}+u$;
$\bar{u}\ u\ \bar{u}$; $\bar{u}\ \bar{u}\ u$; $\frac{1}{4}+u,\ \frac{1}{4}-u,\ \frac{1}{4}+u$; $\frac{1}{4}+u,\ \frac{1}{4}+u,\ \frac{1}{4}-u$;
with the translations + (0 0 0; 0 $\frac{1}{2}\ \frac{1}{2}$; $\frac{1}{2}$ 0 $\frac{1}{2}$; $\frac{1}{2}\ \frac{1}{2}$ 0).

A centre of symmetry exists at each point of the 16-fold position.

The unit cell is seen to contain eight formula units or "molecules" $MgAl_2O_4$, or generally Me_3O_4, if Me represents any number of metal ions in any proportions.

From the translations + (0 0 0; 0 $\frac{1}{2}\ \frac{1}{2}$; $\frac{1}{2}$ 0 $\frac{1}{2}$; $\frac{1}{2}\ \frac{1}{2}$ 0) it is seen that the unit cell (cube edge = a) consists of two different groups of four cubes with edges $\frac{1}{2}a$ (octants) with identical ionic positions.

The ionic positions are different in two octants sharing a face and identical in two octants sharing only an edge. Thus a simple picture is obtained if the positions of the ions are drawn in two adjacent octants only (fig. 1).

Fig. 1 is drawn for the "idealized" structure with the oxygen parameter $u = \frac{3}{8}$. In reality u usually is slightly larger: for $u > \frac{3}{8}$ the oxygen ions move from their ideal position in a [111] direction away from the nearest tetrahedral ion. The radii of the ions in figs 1-5 are completely arbitrary and rather too small.

It is seen from fig. 1 that each octant contains four oxygen ions (large spheres) on the body diagonals of the octants and lying on the corners of a tetrahedron, thus forming a face-centred cubic lattice for $u = \frac{3}{8}$, and four interpenetrating face-centred cubic lattices for $u \neq \frac{3}{8}$. The left-hand octant contains in the centre a metal ion in the ($8a$) position (small sphere, unhatched), lying in the centre of a tetrahedron of oxygen ions. We shall call this an ion in a tetrahedral site, or tetrahedral ion. The right-hand octant shows four metal ions in the ($16d$) position (small spheres, hatched), each surrounded by an octahedron formed by six oxygen ions. We shall call each of these an ion in an octahedral site, or octahedral ion.

Each octant moreover contains metal ions in the ($8a$) position (i.e. tetrahedral ions) in every other corner, in such a way that nearest-neighbour tetrahedral ions (e.g. those in corners and centre of the left-hand octant) are not separated by an oxygen ion.

*) In several publications another position of the unit cell has been used for which there are 8 metal ions in ($8f$) and 16 metal ions in ($16c$).

Figs 2 and 3 show the positions of the metal ions on tetrahedral sites only, and of the metal ions on octahedral sites only, respectively. Figs 4 and 5 show one octahedral ion surrounded by tetrahedral ions, and one tetrahedral ion surrounded by octahedral ions, respectively; in fig. 5 the origin is at $\frac{1}{2}\ \frac{1}{2}\ \frac{1}{2}$.

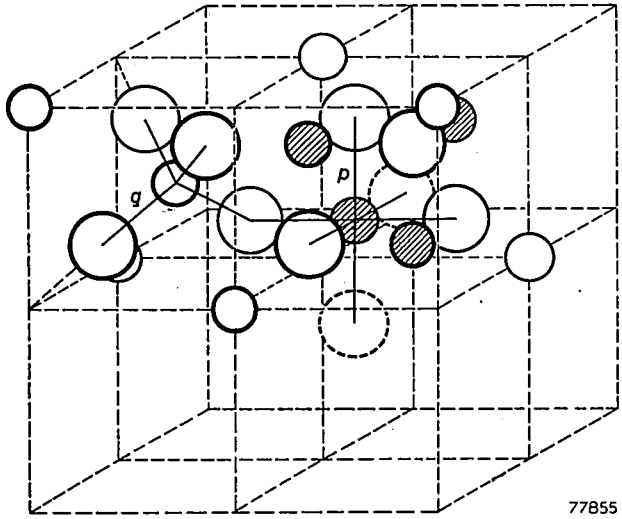

Fig. 1. Unit cell of spinel structure. The position of the ions in only two octants is shown. The dashed circles belong to other octants. The drawn lines indicate the fourfold and sixfold coordination of the respective metal-ion positions.
) $x = 0 - \frac{1}{4}$) $x = \frac{3}{8} - \frac{5}{8}$) $x = \frac{3}{4} - 1$
Large circles: oxygen ions; small hatched circles: metal ions at octahedral sites; small unhatched circles: metal ions at tetrahedral sites. The figure is drawn for $u = \frac{3}{8}$.

We shall see that in superexchange interaction, to be discussed in section 2.3.2, the distances Me-Me do not play a role. The distances Me-O and the angles Me-O-Me are important here. Therefore a number of triangular configurations Me-O-Me have been drawn in fig. 6 (thick drawn lines), for u slightly above $\frac{3}{8}$, which for all ferrimagnetic spinels is very probably the case. The shortest distances Me-O fall in distinct groups: those of nearest neighbours, indicated by p and q, and a group of larger distances indicated by r, s and t; all other distances are again appreciably larger. We have restricted ourselves in fig. 6 to all those triangles for which one distance Me-O is equal to p or q and the second distance Me-O equal to p, q, r, s or t.

The ten triangles shown have five different Me-Me distances: b, c, d, e and f.

These ten distances are given in table I as a function of a and u, or rather for convenience's sake expressed in a and $\delta = u - \frac{3}{8}$.

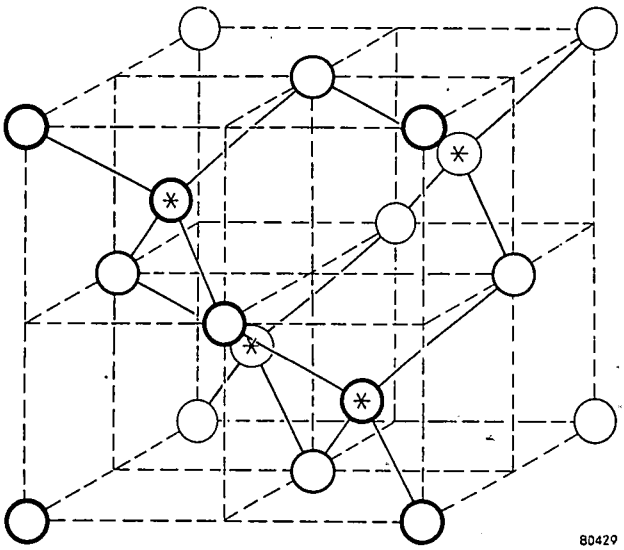

Fig. 2. The position of the metal ions on tetrahedral sites only. Each ion is surrounded by a regular tetrahedron of tetrahedral ions. The asterisks refer to a superstructure to be discussed in section 1.2.3.
) $x = 0 - \frac{1}{2}$) $x = \frac{3}{8} - \frac{5}{8}$) $x = \frac{3}{4} - 1$
Large circles: oxygen ions; small hatched circles: metal ions at octahedral sites; small unhatched circles: metal ions at tetrahedral sites.

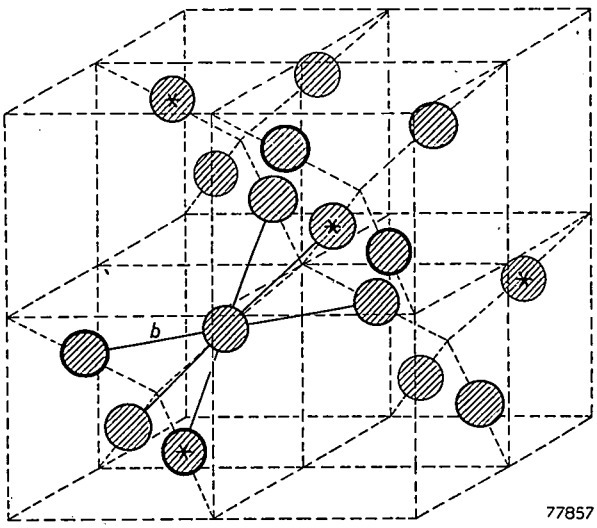

Fig. 3. The position of the metal ions on octahedral sites only. Each ion forms part of two regular tetrahedra of octahedral ions having only this one ion in common. The asterisks refer to another superstructure to be discussed in section 1.2.3.
) $x = 0 - \frac{1}{2}$) $x = \frac{3}{8} - \frac{5}{8}$) $x = \frac{3}{4} - 1$
Large circles: oxygen ions; small hatched circles: metal ions at octahedral sites; small unhatched circles: metal ions at tetrahedral sites.

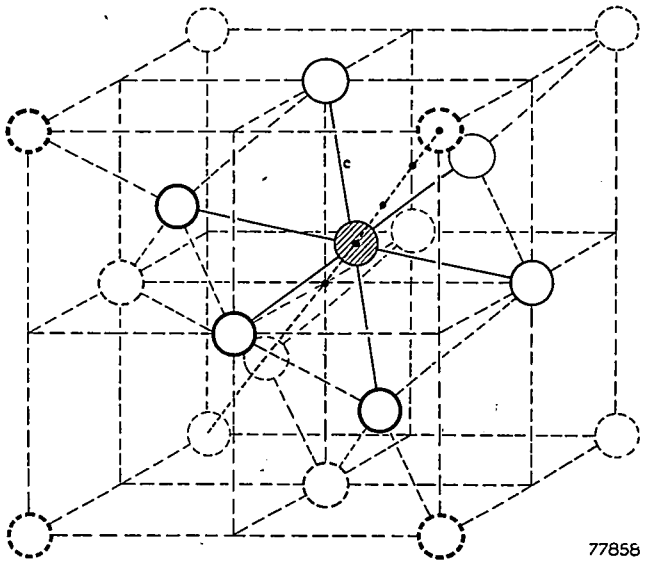

Fig. 4. The position of the metal ions on tetrahedral sites only and one octahedral ion: its six nearest-neighbour tetrahedral ions are indicated by drawn circles. The six neighbours form two equilateral triangles each lying in a plane cut by the body diagonal perpendicular to them (indicated by - - - -) at short distances ($\pm \frac{1}{24} a\sqrt{3}$) from the octahedral ion.
) $x = 0 - \frac{1}{2}$) $x = \frac{3}{8} - \frac{5}{8}$) $x = \frac{3}{4} - 1$
Large circles: oxygen ions; small hatched circles: metal ions at octahedral sites; small unhatched circles: metal ions at tetrahedral sites.

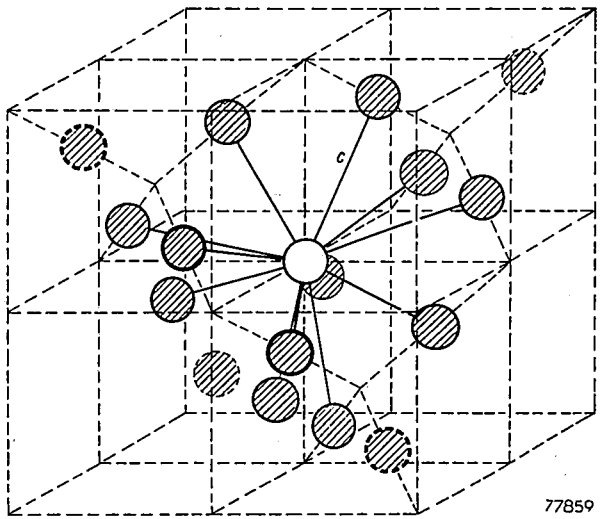

Fig. 5. The octahedral sublattice and one tetrahedral ion; the origin has been moved to $\frac{1}{2}\frac{1}{2}\frac{1}{2}$ in order to show the tetrahedral ion with its twelve nearest-neighbour octahedral ions; these ions are indicated by drawn circles.
) $x = 0 - \frac{1}{2}$) $x = \frac{3}{8} - \frac{5}{8}$) $x = \frac{3}{4} - 1$
Large circles: oxygen ions; small hatched circles: metal ions at octahedral sites; small unhatched circles: metal ions at tetrahedral sites.

TABLE I

distances Me-O	distances Me-Me
$p = a\sqrt{\frac{1}{16} - \frac{1}{2}\delta + 3\delta^2}$	$b = \frac{1}{4}a\sqrt{2}$
$q = a\,(\frac{1}{8} + \delta)\sqrt{3}$	$c = \frac{1}{8}a\sqrt{11}$
$r = a\sqrt{\frac{11}{64} + \frac{1}{4}\delta + 3\delta^2}$	$d = \frac{1}{4}a\sqrt{3}$
$s = a\sqrt{\frac{3}{16} + \frac{1}{2}\delta + 3\delta^2}$	$e = \frac{3}{8}a\sqrt{3}$
$t = a\,(\frac{1}{4} - \delta)\sqrt{3}$	$f = \frac{1}{4}a\sqrt{6}$

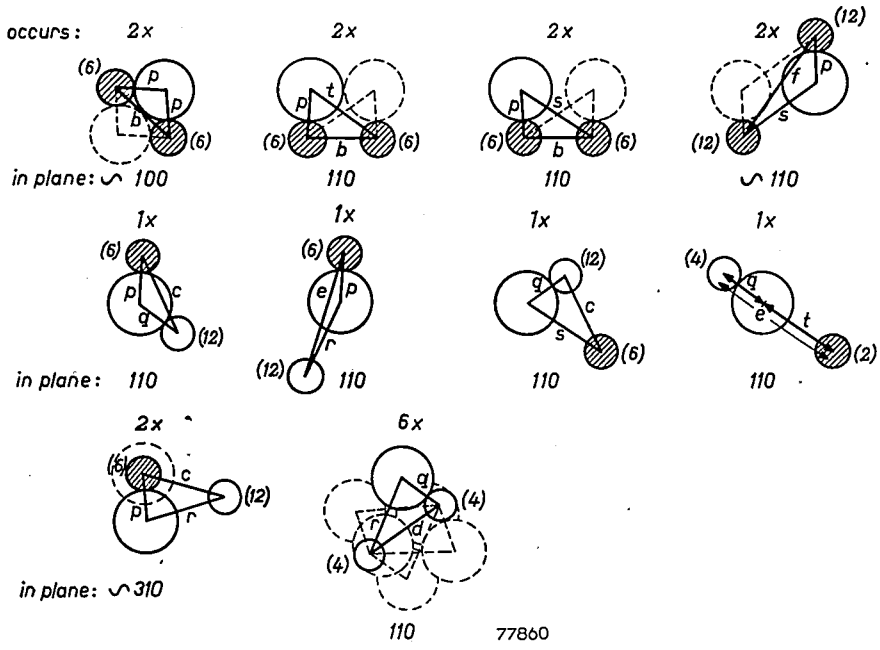

Fig. 6. The configurations Me-O-Me occurring in the spinel lattice with at least one short distance Me-O (p or q) and the other distance not larger than r, s and t.

In fig. 6 hatched circles again represent octahedral ions, open circles tetrahedral ions and large circles oxygen ions; the ratio of the radii and distances is roughly correct.

The figure above each triangle, or the total number of oxygen ions drawn near each triangle, indicates how many times this type of triangle occurs between two particular ions. The numbers in parentheses near each ion indicates the number of cation neighbours at this Me-Me distance with which it moreover forms this particular triangle (cf. *pre* and *tqe*). Thus the number of times a particular triangle occurs around a particular ion is the product of the number above each triangle and that near the ion concerned.

Finally the plane in or near which the triangle lies is given below each triangle.

1.2. Crystal chemistry of oxidic spinels

1.2.1. Metallic ions occurring in oxidic spinels

The metallic ions that have been found to occur on oxidic spinels are given below; their Goldschmidt radii are given between parentheses.
H^+(—); Li^+ (0·78); Cu^+ (1·01?)?; Ag^+ (1·13).
Mg^{2+} (0·78); Ca^{2+} (1·06) *); Mn^{2+} (0·91); Fe^{2+} (0·83);
Co^{2+} (0·82); Ni^{2+} (0·78); Cu^{2+} (0·85?); Zn^{2+} (0·82); Cd^{2+} (1·03).
Al^{3+} (0·57); Ti^{3+} (0·69)??; V^{3+} (0·65); Cr^{3+} (0·64); Mn^{3+} (0·70)?;
Fe^{3+} (0·67); Ga^{3+} (0·62); Rh^{3+} (0·68); In^{3+} (0·93).
Ti^{4+} (0·69); V^{4+} (0·65); Mn^{4+} (0·52); Ge^{4+} (0·44); Sn^{4+} (0·74).
Mo^{6+} (0·62?); W^{6+} (0·63?).

A question mark inside the parentheses indicates doubt about the ionic radius, a question mark outside the parentheses indicates doubt about the occurrence of this ion in oxidic spinels.

It is seen that the radii of all these ions lie between 0·44 and approximately 1·0 Å, with the exception of Ag^+.

Several ions having radii between these limits have not been found in oxidic spinels, amongst which all pentavalent ions. It may well be that several of these may prove to be able to occur in spinels, whereas for others the spinel would be unstable with respect to the constituting oxides, or generally to one or more compounds with different structure. Failure to obtain binary spinels has been reported for Zr^{4+}.

Binary spinels are known of the following types

$$Me^{I}_{1/2}\,Me^{III}_{5/2}O_4,\ Me^{I}_{4/3}\,Me^{IV}_{5/3}O_4\ **),\ Me^{I}_2\,Me^{VI}O_4;$$

$$Me^{II}\,Me^{III}_2O_4,\ Me^{II}_2\,Me^{IV}O_4.$$

*) Only up to 0·35 per formula unit Me_3O_4. **) See footnote on next page.

In addition to these types there are known two spinels that are reported to contain trivalent ions only and vacant lattice sites (γ-Fe_2O_3, γ-Al_2O_3), i.e. to have the formula $Me^{III}_{8/3}\square_{1/3}O_4$ ($\square$ = vacant lattice site). Mixed-crystal formation between all types containing mono-, di-, tri-, and tetravalent ions has been reported in a great number of cases. A few cases are known of mixed-crystal series with a miscibility gap, e.g. the system $CoFe_2O_4$-Co_3O_4 [5]), various systems reported by Romeijn [6]) and some systems investigated by Jonker [7]), e.g. $MgFe_2O_4$-$MgAl_2O_4$.

When metal ions are present that can occur in different states of valency, it is possible by chemical analysis to determine only the average state of valency. Thus the states of valency of the individual ions in e.g. Fe_3O_4, Co_3O_4, Mn_3O_4, $MnFe_2O_4$, Mn_2TiO_4 and Fe_2TiO_4 cannot be found by analysis.

Here the ionization potentials of the respective ions have to be considered in addition to the other factors determining the lattice energy of the spinels to be discussed in section 1.2.5.

The difference in ionization potentials for the different possibilities is usually not large, and it must be borne in mind that the possible error in the literature values of the 3rd and 4th ionization potentials is very large.

In many spinels, however, little doubt exists about the states of valency of the ions, either because of the known physical properties, or from analogy with similar compounds.

1.2.2. Cation distribution in binary oxide spinels

The distribution of the metallic ions in binary spinels $MeMe'_2O_4$ may be [8])

(1) "Normal", with 1 Me in the tetrahedral position and 2 Me′ in the octahedral position. Whenever we wish to indicate the ionic distribution in a formula, we shall in the following write the ions in octahedral sites between brackets, and here therefore $Me[Me'_2]O_4$.

(2) "Inverse", with the Me in the octahedral position, and one Me′ in the octahedral position and in the tetrahedral position each. This arrangement will be indicated by $Me'[MeMe']O_4$.

(3) "Intermediate", e.g. $Me'_{1-x}Me_x[Me_{1-x}Me'_{1+x}]O_4$.

In several cases, e.g. in spinels containing several metal ions of the first transition series, the ionic distribution cannot be determined by X-rays to any great accuracy, in view of the small difference in scattering power. This is true even when ions like Mg^{2+}, Al^{3+} are present as well, because the intensities depend on x as well as on the oxygen parameter u.

) Dr G. H. Jonker has obtained strong indications that a spinel $Li_{4/3}Ti_{5/3}O_4$ does exist, contrary to F. Bertaut and A. Durif (C.R. Acad. Sci., Paris **236, 212-214, 1953), who report a spinel $LiTi_{7/4}\square_{1/4}O_4$ (private communication Dr Jonker).

The method most often used is that of comparing the intensities of two reflexions with small difference in Σh^2, which intensities vary strongly and in a different sense with x and are least sensitive to differences in u. This method has been used for the determination of the cation distribution of several spinels. The factor limiting the accuracy of this method is the error in the scattering factors used [10]).

For the ferrites an indirect method has also been used. According to X-ray evidence the chromites $MeCr_2O_4$ have a "normal" distribution. The ferrites $ZnFe_2O_4$ and $CdFe_2O_4$ are normal, but $MgFe_2O_4$ and $CuFe_2O_4$ inverse *). The difference in lattice constant between the chromites and the corresponding ferrites is 0·12 Å for Zn^{2+} and Cd^{2+}, but about 0·05 Å for all other ions, amongst which are Mg^{2+} and Cu^{2+}. From these data it has been concluded [9]) that the ferrites $MeFe_2O_4$ for which Me = Mn^{2+}, Fe^{2+}, Co^{2+}, Ni^{2+}, Cu^{2+} or Mg^{2+} are inverse.

The aluminates are all normal [8]) [6]), except $NiAl_2O_4$ for which the approximate distribution $Al_{0\cdot75}Ni_{0\cdot25}[Ni_{0\cdot75}Al_{1\cdot25}]O_4$ has recently been found [6]).

MgV_2O_4, ZnV_2O_4, $MgRh_2O_4$ and $ZnRh_2O_4$ are normal [11]), $MgIn_2O_4$ and probably $MgGa_2O_4$ [8]) inverse.

$Li_{0\cdot5}Fe_{2\cdot5}O_4$ is inverse: $Fe[Li_{0\cdot5}Fe_{1\cdot5}]O_4$ [12]).

Several titanates $Me^{II}_2Ti^{IV}O_4$ [9]) as well as $Zn_2Sn^{IV}O_4$ [9]) and $Mg_2V^{IV}O_4$ [11]) have been found to be inverse: it is almost certain that all such titanates and stannates are inverse. Ni_2GeO_4 and Co_2GeO_4 are, however, normal [6]).

1.2.3. Long-range order in oxidic spinels

Originally it had been assumed that the distribution of different cations inside one sublattice is random [8]). In some spinels long-range order has since been found to occur in one of the sublattices. Three types have so far been found:

(1) 1 : 1 order in the octahedral position.

The ionic positions are approximately **) as follows

Me at $\frac{1}{8}\frac{5}{8}\frac{1}{8}$; $\frac{5}{8}\frac{1}{8}\frac{1}{8}$; $\frac{3}{8}\frac{7}{8}\frac{1}{8}$; $\frac{7}{8}\frac{3}{8}\frac{1}{8}$; $\frac{1}{8}\frac{1}{8}\frac{5}{8}$; $\frac{3}{8}\frac{3}{8}\frac{5}{8}$; $\frac{5}{8}\frac{5}{8}\frac{5}{8}$; $\frac{7}{8}\frac{7}{8}\frac{5}{8}$.

Me′ at $\frac{3}{8}\frac{5}{8}\frac{3}{8}$; $\frac{5}{8}\frac{3}{8}\frac{3}{8}$; $\frac{1}{8}\frac{7}{8}\frac{3}{8}$; $\frac{7}{8}\frac{1}{8}\frac{3}{8}$; $\frac{1}{8}\frac{3}{8}\frac{7}{8}$; $\frac{3}{8}\frac{1}{8}\frac{7}{8}$; $\frac{5}{8}\frac{7}{8}\frac{7}{8}$; $\frac{7}{8}\frac{5}{8}\frac{7}{8}$.

Successive (001) layers of octahedral sites are occupied alternately by Me and Me′.

Every Me ion has 4 Me′ and 2 Me ions as octahedral neighbours and vice versa.

This structure was proposed for $Fe[Fe^{II}Fe]O_4$ below 120 °K by Verwey and Haayman [13]), who deduced it from the resistivity jump at 120 °K.

*) Magnetic investigation has shown that these latter ferrites are only approximately inverse; see section 4.

**) It is clear that the long-range order is accompanied by a change of space group, so that ionic positions slightly different from these "ideal" ones may occur (see e.g. [12])).

The structure is essentially orthorhombic. It has recently been shown by various methods that Fe_3O_4 below 120 °K has indeed orthorhombic symmetry (see, however, [6]) for literature data).

(2) 1 : 3 order in the octahedral position.

The ionic positions are approximately *) as follows

Me at $\frac{5}{8}\frac{5}{8}\frac{5}{8}$; $\frac{1}{8}\frac{7}{8}\frac{3}{8}$; $\frac{7}{8}\frac{3}{8}\frac{1}{8}$; $\frac{3}{8}\frac{1}{8}\frac{7}{8}$.

Me′ at $\frac{1}{8}\frac{5}{8}\frac{1}{8}$; $\frac{5}{8}\frac{1}{8}\frac{1}{8}$; $\frac{3}{8}\frac{7}{8}\frac{1}{8}$; $\frac{7}{8}\frac{1}{8}\frac{3}{8}$; $\frac{3}{8}\frac{5}{8}\frac{3}{8}$; $\frac{5}{8}\frac{3}{8}\frac{3}{8}$; $\frac{1}{8}\frac{1}{8}\frac{5}{8}$; $\frac{3}{8}\frac{3}{8}\frac{5}{8}$; $\frac{7}{8}\frac{7}{8}\frac{5}{8}$; $\frac{1}{8}\frac{3}{8}\frac{7}{8}$; $\frac{5}{8}\frac{7}{8}\frac{7}{8}$; $\frac{7}{8}\frac{5}{8}\frac{7}{8}$.

The distribution of the ions is shown in fig. 3; see asterisks. Every row of octahedral ions in the [110] directions contains an ion Me in every fourth site. Every Me ion is surrounded by six ions Me′, every Me′ ion has 2 Me and 4 Me′ ions as neighbours.

This type of order has been found by Braun [12]) to occur in $Fe[Li_{0.5}Fe_{1.5}]O_4$, of which he determined the structure.

The structure is essentially cubic (space group very probably $P4_32$ (or $P4_12$) [12]). The same superstructure lines are found in $Al[Li_{0.5}Al_{1.5}]O_4$ and in γ-Fe_2O_3 (which probably is a mixed crystal $Fe[H_{1/2}Fe_{3/2}]O_4$-$Fe[\square_{1/3}Fe_{5/3}]O_4$ [12])), and it is probable that these compounds as well as γ-Al_2O_3 have the same superstructure.

For $Fe[Li_{0.5}Fe_{1.5}]O_4$ the transition temperature to the non-ordered spinel structure, which still contains all Li^+ in the octahedral position, is situated between 1008 and 1028 °K.

(3) 1 : 1 order in the tetrahedral position.

The ionic positions are

Me at 0 0 0; 0 $\frac{1}{2}\frac{1}{2}$; $\frac{1}{2}$ 0 $\frac{1}{2}$; $\frac{1}{2}\frac{1}{2}$ 0.

Me′ at $\frac{1}{4}\frac{1}{4}\frac{1}{4}$; $\frac{1}{4}\frac{3}{4}\frac{3}{4}$; $\frac{3}{4}\frac{1}{4}\frac{3}{4}$; $\frac{3}{4}\frac{3}{4}\frac{1}{4}$.

Every Me ion is surrounded by four Me′ ions and vice versa. This superstructure has recently been found to occur in our preparation $Li_{0.5}Fe^{III}_{0.5}[Cr_2]O_4$ [14]), to be discussed in section 7. The distribution of the ions is shown in fig. 2; see asterisks.

For all of these three superstructures it has been shown that the long-range order gradually disappears on departing from the 1 : 1, 1 : 3, or 1 : 1 ratios respectively.

(1) Verwey and Haayman showed that when the ratio Fe^{3+}/Fe^{2+} in magnetite is increased above 2·0, i.e. the ratio Fe^{3+}/Fe^{2+} in the octahedral position above 1·0 (a few cation vacancies are thereby introduced as well), the jump in the resistivity becomes smaller and moves to lower temperatures. It disappears for a ratio Fe^{3+}/Fe^{2+} in the octahedral position equal to 1·1.

(2) The superstructure lines of $Fe[Li_{0.5}Fe_{1.5}]O_4$ become weaker as the ratio Fe/Li in the octahedral position is increased above 3·0, e.g. by mixed-

*) See second footnote on preceding page.

crystal formation with $ZnFe_2O_4$. For $Zn_{0.15}Fe_{0.85}[Li_{0.42}Fe_{1.57}]O_4$ the superstructure lines have disappeared.
(3) The 1 : 1 order in the tetrahedral position, indicated by the (200) reflexion, is just perceptible in $Fe_{0.64}Li_{0.36}[Li_{0.14}Fe_{0.26}Cr_{1.60}]O_4$ [14]).

1.2.4. The hausmannite structure

Some compounds of the type Me_3O_4, viz. $CuFe_2O_4$ [16]), $CuCr_2O_4$ [17]), Mn_3O_4 [15]) and $ZnMn_2O_4$ [19]), have a tetragonal crystal structure, the hausmannite structure, after the mineral hausmannite, Mn_3O_4. This structure is most suitably described as a spinel structure elongated in the [001] direction; this description is different from that given in [15]). $CuFe_2O_4$ has an axial ratio = 1·06 when annealed at e.g. 300 °C: at higher temperatures the axial ratio decreases to become unity at 760 °C [16]).

Like Mn_3O_4, $CuFe_2O_4$ forms mixed crystals with cubic spinels: in the systems $Cu_{1-a}Me^{II}_aFe_2O_4$ in which Me^{II} represents Zn, Ni or Co, the axial ratio decreases with the Me^{II} content a [18]).

In the system $\left.\begin{matrix}Mn_3O_4\\ZnMn_2O_4\end{matrix}\right\} - \left\{\begin{matrix}MnFe_2O_4\\ZnFe_2O_4\end{matrix}\right.$ [19]), where the same decrease of axial ratio in the hausmannite phase occurs, a miscibility gap between hausmannite and spinel phases has been found: it is not known if this is a general phenomenon.

The cause of the occurrence of this elongated spinel structure is not known (see also [6])): the X-ray diffraction pattern of $CuFe_2O_4$ does not show any superstructure lines [16]).

1.2.5. Factors influencing the cation distribution and the stability of oxidic spinels

To a first approximation the chemical bond in oxidic spinels may be regarded as purely ionic, so that the main part of the lattice energy is formed by the Coulomb energy and the Born repulsive energy. Other effects that contribute terms to the lattice energy are polarization, an individual preference of certain ions for fourfold or sixfold coordination as a result of their electronic configuration, and other factors, amongst which the magnetic interaction will be considered.

The energy terms are all dependent on a, u and the ionic distribution. The equilibrium cation distribution could in principle be calculated by minimizing the total energy with respect to these variables, but as quantitative relationships between the various energy terms and these three variables are not known, this is at present not possible.

In the following a quantitative discussion of the Coulomb energy is given as a function of the unit-cell edge a, the oxygen parameter u and the charge distribution amongst the lattice sites of the cations. The contri-

bution of some other terms to the lattice energy is probably of a smaller order of magnitude.

1.2.5.1. *Coulomb energy and repulsive energy*

The Coulomb potential energy per "molecule",

$$V_C = -\frac{Me^2}{a},$$

is dependent on the charge distribution, on the oxygen parameter u and, of course, on the unit-cell edge a. Madelung constants (M) have been calculated by Verwey, De Boer and Van Santen [20]) as a function of u for an average ionic charge of 4, 3 or 2 in the tetrahedral position and 2, 2·5 and 3 respectivily in the octahedral position.

As we are interested in mixed crystals, often containing a broken number of charges per formula unit in both positions, the results are given here in a generalized form.

The M values for $u = 0{\cdot}375$ ($\delta = 0$) are given by the formula

$$M = 139{\cdot}8 - 10{\cdot}84\ q_a + 2{\cdot}61\ q_a^2 \quad [21]),$$

in which q_a represents the average ionic charge per formula unit in the tetrahedral position.

The curves giving the dependence of M on u for different values of q_a are very nearly straight lines [20]). We have assumed these to be straight, and further that the slope of these lines ($\Delta M/\Delta u$) varies linearly with q_a, which for $q_a = 4$, 3 and 2 is very nearly true.

The Madelung potentials expressed in units e^2/a as a function of q_a, for different values of u, are given by a set of parabolas represented in fig. 7. From this figure it is clear that a high Madelung potential is obtained:
(1) with low average charge in the tetrahedral position for large values of u;
(2) with high average charge in the tetrahedral position for small values of u.

Thus, as far as the Madelung constant is concerned, an ion that has a low charge and is large with respect to the other cations present will seek the tetrahedral position, if for other cation distributions the Madelung constant derived from fig. 7 is appreciably lower.

Perhaps this effect should account for the fact that in $CdFe_2O_4$ the large Cd^{2+} ions are found in fourfold coordination, whereas in CdO with NaCl structure they have sixfold coordination (see, however, also section 1.2.5.4). From the same point of view an ion with high charge will seek the tetrahedral position only if it is small with respect to the other cations present, and if for other cation distributions the Madelung constant derived

from fig. 7 is appreciably lower. In fact, amongst the Me^{4+} ions only Ge^{4+} is found to occupy solely the tetrahedral position.

It must be kept in mind that the unit-cell edge a is also dependent on the cation distribution, so that distribution a with high M may not give the largest Coulomb energy.

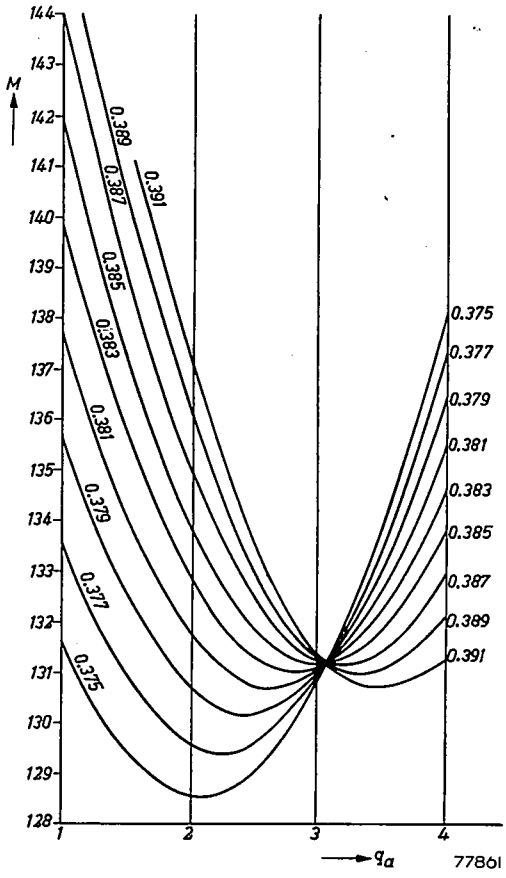

Fig. 7. Madelung constant (M) as a function of the ionic charge in the A position (q_a) for different values of the oxygen parameter (u).

The repulsive potential energy per molecule may be represented by

$$V_R = \frac{B}{a^n}.$$

For equilibrium between Coulomb and repulsive forces this expression gives a repulsive energy that is a constant fraction $1/n$ of the Coulomb energy (n is of the order of 10).

An exponential Born-Mayer expression might give a better approximation, but both expressions contain a constant (n and ϱ respectively) to be derived from compressibility data. For oxides of the transition metals no compressibility measurements are known, and the values of n and ϱ may be appreciably different from those of the alkali halides, which have so far been used [22]). Moreover the compressibilities should be measured for binary oxides having crystal structures without parameters, which for trivalent metal ions are not known.

For those few cases where not only a but also u is accurately known from experiment, the cation distribution may be derived from fig. 7 (e.g. for $GeCo_2O_4$ [6])) if the cations fit well in the interstices, the sizes of which are calculated from a and u. If the difference in Madelung constant for different distributions is small, geometrical considerations alone may be used to find the cation distribution: this method has been used for Fe_3O_4 [22a]). The parameter u may in principle also be calculated from the equilibrium condition for the Coulomb and repulsive forces.

On the other hand it is instructive to compare the experimental values of a and u with those calculated for a model consisting of a dense packing of rigid spheres. The cation radii of section 1.2.1 are used, and 4% is subtracted from the distance $r_{Me_A} + r_{O^{2-}}$ to obtain the distance Me_A-O.

For a number of spinels the cation radii are such that in this model there is contact between cations and anions only; for this case the unit-cell edges a thus calculated are not much different from the experimental ones.

For the inverse ferrites the calculated a value is 0·4-1·0% too large *); for the (inverse) titanates and stannates a_{calc} is too large by 0·9-2·8% and 0·7-1·9% respectively. In all these cases the higher discrepancies are found for the larger divalent ions.

When the cations on tetrahedral sites are large compared with those on octahedral sites, anion-anion contact occurs. The discrepancies between the calculated a values and the experimental ones are now often appreciably larger: i.e. for $Cd[Fe_2]O_4$ 4·5%, for $Zn[Fe_2]O_4$ 1·3%; for $Cd[Cr_2]O_4$ 4·5%, for (normal) Mn- *), Fe-, Zn-, Co-, Ni- and Mg-chromite 3, 2·2, 1·5, 1·5, 1·1 and 1·0% respectively; for (normal) Mn- *), Fe-, Zn-, Co- and Mg-aluminate 5·8, 5·0, 5·0, 5·0, and 4·0 % respectively.

From the above figures it appears that the Goldschmidt radii of the oxygen ion (1·32 Å) and of the *larger* divalent ions are too large to account satisfactorily for the unit-cell edges of the oxidic spinels, i.e. these ions may be "squeezed" in this structure with respect to the crystal structures with sixfold coordination, from which their radii were deduced.

*) For $MnFe_2O_4$, $MnCr_2O_4$ and $MnAl_2O_4$ the unit-cell edges have been redetermined for preparations made by the author with correct valency states, and were found to be 8·499 Å, 8·425 Å and 8·202 Å respectively.

It is comprehensible that such a squeezing effect, whatever may be its cause, tends to increase with ionic diameter and decrease with ionic charge, and the more so for fourfold coordination. This effect is not sufficiently accounted for by deducing 4% from the radius sums $r_{Me_A} + r_{O^{2-}}$ and nothing from the sums $r_{Me_B} + r_{O^{2-}}$.

From the above it follows that the room required for the smaller ions and those with a high charge (cf. [6])) in the first instance determine the cation distribution.

An effect of cation distribution on cell edge, as noted by Verwey and Heilmann, is found for the rigid-sphere model for $MnFe_2O_4$: a_{normal} is 1·5 % larger than $a_{inverse}$. For the $MgFe_2O_4$ model, however, where no anion-anion contact occurs, the two calculated cell edges are equal.

According to Verwey and Heilmann the experimental difference $a_{normal} - a_{inverse}$ is constant and about 0·07 Å, or about 0·8%. As the repulsion potential of course increases less steeply than for the rigid-sphere model, this may be an indication that the experimental difference $a_{normal} - a_{inverse}$ is due to anion-anion repulsion.

The upper and lower limits of u, calculated for the rigid-sphere model for anion-anion contact, are farther removed from the ideal value $u = 0{\cdot}375$ than has been found experimentally:

for $Zn[Fe_2]O_4$ $u_{calc} = 0{\cdot}390$, $u_{exp} = 0{\cdot}385 \pm 0{\cdot}002$;
for $Ge[Co_2]O_4$ $u_{calc} = 0{\cdot}369$, $u_{exp} = 0{\cdot}375 \pm 0{\cdot}003$.

This may also be explained by the "squeezing" of the larger ions with lower charge, i.e. the Zn^{2+} and Co^{2+} ions respectively.

1.2.5.2. *Short-range order*

The formation of the superstructures described in section 1.2.3. is accompanied by a gain in Coulomb energy with respect to the random distribution inside the octahedral position or inside the tetrahedral position respectively. These "ordering energies" for the first two superstructures mentioned have been given in [23]).

The position of the Me and Me′ ions in the 1 : 1 order in the tetrahedral position is equal to that of Zn and S in the zincblende structure, for which the Madelung potential is known from literature.

These ordering energies, like M expressed in e^2/a (a = cube edge of the unit cell) are given in table II.

A very rough computation indicates that polarization tends to increase these energies by something of the order of one quarter [23]). These ordering energies are large compared with the energy of thermal motion at the transition temperatures, so that one may conclude that above the transition temperatures a very pronounced short-range order must persist [23]).

TABLE II

Ordering energies in units e^2/a

charge difference ($q_{Me'} - q_{Me}$)	1 : 1 order in oct. position	1 : 3 order in oct. position	1 : 1 order in tetr. position
1	1·001	0·712	0·946
2	4·004	2·848	3·783

The values given in fig. 7 must therefore be corrected for a strong short-range order, the energy of which is approximately equal to the values for long-range order given above.

1.2.5.3. *Magnetic interaction energy*

We shall see that for ferrimagnetic spinels the magnetic (superexchange) interaction energy is strongly dependent on the distribution of the magnetic ions amongst the crystallographic positions. The question might be asked whether this energy will influence the ionic distribution. The Curie temperatures Θ, i.e. the temperatures at which the long-range order of the magnetic moments is destroyed, range up to 950 °K from which we might conclude that this energy is only of the order of $k\Theta \approx 2$ kcal/mole.

It must be borne in mind, however, that a short-range order of the moments may persist above the Curie temperature, i.e. up to temperatures at which ionic diffusion takes place.

An indication to this effect is the fact that very weak reflexions resulting from magnetic spin order in the neutron-diffraction pattern of antiferromagnetic MnO [24]) (see section 2) persist up to 3Θ (Θ = Néel temperature, at which the long-range order of the moments is destroyed).

As far as energy is concerned, however, it seems likely that the magnetic interaction energy above the Curie temperature is very small, like for nickel, for which the excess specific heat becomes negligible above the Curie temperature.

1.2.5.4. *Individual preference of cations for 4- or 6-fold coordination*

The influence of diameter and charge of a cation on its preference for the tetrahedral or octahedral sites in an oxidic spinel is not properly called an individual property, as the diameters and charges of the other ions present must be taken into account.

Apart from the influence of diameter and charge on the Coulomb energy and on other energy terms, individual differences between the cations exist as regards their tendency towards four- or six-fold coordination. This is shown by the fact that cations with equal diameter and equal charge, such as Zn^{2+} and Co^{2+}, or Ni^{2+} and Mg^{2+}, show quite different behaviour as regards ionic distribution in spinels with otherwise equal compositions.

One cause for such individual behaviour is the difference in electronic configuration between different cations: we shall differentiate between five groups with different electron configurations. Of course the resulting ionic distribution cannot be discussed without taking into account diameter and charge of the ions.

(1) The ions Zn^{2+} and Cd^{2+} with a filled 3d shell are known for their tendency to form covalent bonds with sp^3 orbitals. They therefore preferably occupy the tetrahedral sites in spinels. Zn^{2+} in ZnO has fourfold coordination, but Cd^{2+} in CdO, with NaCl structure, sixfold coordination. In the latter case the effect of size, in accordance with Pauling's rule, counteracts the individual preference for fourfold coordination.

The ions with filled d shells:

$$3d: Cu^{+},\ Zn^{2+},\ Ga^{3+},\ Ge^{4+},$$
$$4d: Ag^{+},\ Cd^{2+},\ In^{3+},\ Sn^{4+},$$

probably all have an individual preference for fourfold coordination in oxides, but this may be counteracted in spinels by the dependence of the lattice energy on q_a, u and a. We have seen that a large tetravalent ion in the tetrahedral position will give a low Madelung constant; as a consequence the stannates $Me_2^{II}SnO_4$ are inverse. Ag_2MoO_4 is probably normal because the inverse arrangement would have very large a.

(2) The ions with noble-gas shells have no individual preference for either coordination. Their distribution will be determined mainly by the dependence of the lattice energy on q_a, a and u. Thus amongst the ions of this kind that occur in spinels:

$$Li^{+},\ Mg^{2+},\ Al^{3+},\ Ti^{4+},$$

the tetravalent ion is too large to occupy solely the tetrahedral sites.

(3) The ions with half-filled 3d shell have spherical symmetry. Therefore Mn^{2+}, Fe^{3+} and Co^{4+} will not be expected to have an individual preference for either position (Co^{4+}, if it occurs at all in spinels, which nowadays seems unlikely, might choose the tetrahedral position for electrostatic reasons as discussed above).

The preference of the other transition metal ions is determined by the influence of the crystalline electric field orginating from the neighbouring

ions on the average energy level and on the spatial distribution of the 3d electrons; see [6]).

As a result these ions fall into two groups:

(4) Those with $3d^3$ and $3d^8$, which have a strong preference for sixfold coordination: Cr^{3+}, Ni^{2+} and possibly Mn^{4+}.

(5) All other transition-metal ions, which have no strong preference for either site.

The above scheme is an extension of the rules on the cation distribution in spinels given by Verwey and Heilmann [9]).

1.2.6. Spinels containing three or more different cations

Verwey and Heilmann [9]) found by X-ray diffraction that in mixed crystals between normal $Zn[Fe_2]O_4$ and inverse $Fe[CuFe]O_4$ the Zn^{2+} ions still occupied the tetrahedral position and the Cu^{2+} ions the octahedral position, giving a formula e.g. $Zn_{0.5}Fe_{0.5}[Cu_{0.5}\ Fe_{1.5}]O_4$.

As practically no other data were available in 1947 on the ionic distribution in ternary spinels, it was believed that the ions keep their preference for one crystallographic site with respect to other ions in all compounds. This means that a certain order of preference for e.g. the tetrahedral sites can be given, in which the authors placed Fe^{3+} directly after Zn^{2+}, Cd^{2+}, Ga^{3+} and In^{3+} and before the other divalent ions. Recently Romeijn [6]) has shown that in several ternary spinels the behaviour is quite different. Our magnetic measurements to be reported in sections 6-9 will yield further examples of cases where such simple behaviour is not found.

The total energy difference between the normal and inverse arrangements may be found experimentally for those spinels for which the distribution changes measurably with temperature.

For a spinel of the composition e.g. $Me'_{1-x}Me_x[Me_{1-x}Me'_{1+x}]O_4$ the equilibrium distribution is determined by a Boltzmann expression given by Néel [25]):

$$kT \ln \frac{(1-x)^2}{x(x+1)} = E, \tag{1.1}$$

in which E is the energy involved in the interchange of a Me ion in the octahedral position and a Me′ ion in the tetrahedral position. We have seen that an accurate determination of x from X-ray diffraction data is usually impossible, but Pauthenet and Bochirol [26]) have determined x, and thus E, from magnetic saturation data for $MgFe_2O_4$ and $CuFe_2O_4$ (see section 4): E was found to be fairly constant.

Knowledge of the interchange constants E of two binary spinels containing one cation in common would enable one to calculate the cation distribution in a mixed crystal between them, it if were permissible to

use one constant E for a specific pair of cations. This is certainly not the case, as E varies with the charge distribution (q_a), with the cell edge a and with the lattice parameter u: these quantities, as well as the short-range-order contribution will be different for different compositions.

REFERENCES

1) W. H. Bragg, Nature **95**, 561, 1915; Phil. Mag. **30**, 305-315, 1915.
2) S. Nishikawa, Proc. Tokyo math.-phys. Soc. **8**, 199-209, 1915.
3) International Tables for X-ray Crystallography, Kynoch Press, Birmingham, 1952, Vol. I, p.340.
4) P. P. Ewald and C. Hermann, Strukturberichte, Bd 1913-1926, p. 350 (type H 11).
5) J. Robin and J. Bénard, C. R. Acad. Sci., Paris **234**, 734-735, 1952.
6) F. C. Romeijn, Philips Res. Rep. **8**, 304-342, 1953.
7) G. H. Jonker, to be published.
8) T. F. W. Barth and E. Posnjak, Z. Kristallogr. **82**, 325-341, 1932.
9) E. J. W. Verwey and E. L. Heilmann, J. chem. Phys. **15**, 174-180, 1947.
10) F. Bertaut, J. Phys. Radium **12**, 252-255, 1951.
11) W. Rüdorff and B. Reuter, Z. anorg. Chem. **253**, 194-208, 1947.
12) P. B. Braun, Nature **170**, 1123, 1952.
13) E. J. W. Verwey and P. W. Haayman, Physica **8**, 979-987, 1941; E. J. W. Verwey, Nature **144**, 327, 1939.
14) P. B. Braun, Physica, forthcoming.
15) G. Aminoff, Z. Kristallogr. **64**, 475-490, 1926.
16) L. Weil, F. Bertaut and L. Bochirol. J. Phys. Radium **11**, 208-212, 1950.
17) T. R. McGuire, L. N. Howard and J. S. Smart, Ceramic Age **60** (1) 22-24, 1952.
18) Results not yet published by the author.
19) B. Mason, Amer. Min. **32**, 426-441, 1947.
20) E. J. W. Verwey, F. de Boer and J. H. van Santen, J. chem. Phys. **16**, 1091-1092, 1948.
21) J. H. van Santen, private communication.
22) E. J. W. Verwey, P. W. Haayman and F. C. Romeijn, J. chem. Phys. **15**, 181-187, 1947.
22a) E. J. W. Verwey and J. H. de Boer, Rec. Trav. chim. Pays-Bas **55**, 531-540, 1936.
23) F. de Boer, J. H. van Santen and E. J. W. Verwey, J. chem. Phys. **18**, 1032-1034, 1950.
24) C. G. Shull and J. S. Smart, Phys. Rev. **76**, 1256-1257, 1949.
25) L. Néel, C. R. Acad. Sci., Paris **230**, 190-192, 1950.
26) R. Pauthenet and L. Bochirol, J. Phys. Radium **12**, 249-251, 1951.

(To be continued)

VOL. 9 NR 5 OCTOBER 1954

Philips Research Reports

EDITED BY THE RESEARCH LABORATORY
OF N.V. PHILIPS' GLOEILAMPENFABRIEKEN, EINDHOVEN, NETHERLANDS

R 249 *Philips Res. Rep. 9, 321-365, 1954*

SATURATION MAGNETIZATION AND CRYSTAL CHEMISTRY OF FERRIMAGNETIC OXIDES *)

by E. W. GORTER

621.317.421:548.3:548.736.453.2

2. THEORY OF FERRIMAGNETISM

2.1. Introduction

In contradistinction to paramagnetics, ferromagnetic substances can be magnetized to saturation by a comparatively small magnetic field (usually 10^2-10^4 oersteds). This is because the magnetic moments of the atoms with partly filled 3d or 4f shells are parallel to their neighbours already in the unmagnetized state, as a result of an electron exchange interaction, which is very much stronger than the interaction forces between magnetic dipoles. The nature of this exchange mechanism does not concern us here. In the unmagnetized (virgin) state the overall magnetization is zero because in each crystal the parallelism of the atomic moments is maintained only within Weiss domains: the direction of magnetization of each Weiss domain is determined by the crystal, stress and shape anisotropies. The saturating field only has to turn the moments of all Weiss domains against these anisotropies.

Complete parallelism of the atomic moments within the Weiss domains exists only at 0 °K: the saturation magnetization decreases with temperature. At the Curie temperature the long-range order of the atomic moments is destroyed and at higher temperatures only paramagnetism remains. The saturation magnetization at 0 °K per magnetic atom or per "molecule", which we shall call the *saturation moment*, can be expressed in the spin moment of one electron, the so-called Bohr magneton μ_B ($= eh/4\pi mc$, where e, h, m and c have their usual meanings).

In the ferromagnetic metals with partly filled 3d shell the number of unpaired 3d electrons is not simply related to the total number of electrons present, so that the saturation moments cannot be simply predicted.

*) Continued from Philips Res. Rep. 9, 295-320, 1954.

On the other hand, for compounds that may be considered to be essentially ionic (like the oxides with which we shall concern ourselves) the situation would be expected to be much simpler. Here each magnetic ion contains a known number of unpaired electrons that do not take part in the formation of chemical bonds. For substances containing elements of the first transition series, the ferromagnetic and the paramagnetic behaviour are both almost entirely due to the spins of the unpaired 3d electrons. The ferromagnetic moment of each ion will thus be equal to $2S$ (S = total spin quantum number of the ion), if the orbital contribution is neglected, or gS, if this is taken into account. The g-factor g is $(2mc/e) \times$ (magnetic moment)/(angular momentum).

Table III gives the number of 3d electrons and the number of unpaired 3d electrons ($= 2S$) for these ions. Those ions occurring in the compounds to be discussed have been framed and printed in heavy type.

The exact calculation of the variation of the saturation magnetization with temperature in a crystal is not yet possible, and any such calculation, even with simplifying assumptions, is extremely difficult [27]). Therefore a simple approximation, due to Pierre Weiss [28]), is often used, in which each ion is considered to be situated in a fictitious magnetic field, the so-called molecular field, representing the resultant influence of the exchange forces with all surrounding atoms. The total alignment of the moments that exists at 0 °K, tends to be destroyed at higher temperatures, and the saturation magnetization decreases with temperature according to a Brillouin function in which a field $H + h$ acting on each moment figures: the external field H needed to reach saturation, i.e. to align the Weiss domains, at low temperatures usually can be neglected against the very large molecular field h.

At the Curie temperature the long-range order of the moments is destroyed, but the fact that ferromagnetics above the Curie temperature follow a Curie-Weiss law $\chi = C/(T-\vartheta)$, with $\vartheta > 0$ *), shows that here exchange interactions, and thus molecular fields, continue to play a role. Here h is not large compared to the external fields generally used, and $H + h$ enters into the Brillouin functions.

The exchange interactions may in other cases result in another state of minimum free energy, i.e. in antiparallel orientation of the spins of neighbouring atoms or ions, found in antiferromagnetics such as MnO, α-Fe_2O_3, CrSb. These may be considered to consist of two equal sublattices with equal, mutually antiparallel, spontaneous magnetizations, each decreasing with temperature according to the same Brillouin function in which only the molecular field h appears. The long-range order of the moments is destroyed at the so-called Néel temperature and above this temperature a Curie-Weiss law $\chi = C/(T-\vartheta)$ is usually obeyed with $\vartheta < 0$ *).

*) We have seen that small values of ϑ may occur even without exchange interaction.

TABLE III

ions										number of	
										3d electrons	unpaired 3d electrons (2S)
Sc^{3+}	**Ti^{4+}**	V^{5+}	Cr^{6+}	Mn^{7+}						0	0
	Ti^{3+}	V^{4+}	Cr^{5+}	Mn^{6+}						1	1
	Ti^{2+}	V^{3+}	Cr^{4+}	Mn^{5+}	Fe^{6+}					2	2
		V^{2+}	**Cr^{3+}**	Mn^{4+}						3	3
		V^{+}	Cr^{2+}	Mn^{3+}	Fe^{4+}					4	4
				Mn^{2+}	**Fe^{3+}**	Co^{4+}				5	5
					Fe^{2+}	Co^{3+}	Ni^{4+}			6	4
						Co^{2+}	Ni^{3+}			7	3
							Ni^{2+}			8	2
								Cu^{2+}		9	1
								Cu^{+}	**Zn^{2+}**	10	0

In paramagnetic substances containing magnetic ions with partly filled 3d shells, in which the magnetic ions are widely separated from each other, so that no exchange interaction is possible, a magnetic field tends to orient the ionic moments against the thermal motion.

Thus the magnetization per gram-ion, I, is

$$I = NgS\mu_B B_S\left(\frac{gS\mu_B H}{kT}\right) \quad \begin{matrix}(N = \text{Avogadro's number},\\ k = \text{Boltzmann's constant}),\end{matrix}$$

in which the Brillouin function B_S is given by

$$B_S\left(\frac{gS\mu_B H}{kT}\right) = \frac{S+\frac{1}{2}}{S}\coth\frac{(S+\frac{1}{2})g\mu_B H}{kT} - \frac{\frac{1}{2}}{S}\coth\frac{\frac{1}{2}g\mu_B H}{kT}.$$

For small values of $gS\mu_B H/kT$ one may write

$$B_S\left(\frac{gS\mu_B H}{kT}\right) = \frac{S+1}{3}\frac{g\mu_B H}{kT},$$

and thus $$I = \frac{Ng^2\mu_B{}^2 S\,(S+1)H}{3kT} \equiv \frac{CH}{T}.$$

Certain dilute paramagnetic substances e.g. those containing Fe^{3+} ions (e.g. $Fe^{III}NH_4(SO_4)_2.12\,H_2O$) indeed follow a Curie law $I/H = \chi = C/T$ (χ and C per gram-ion) in a wide range of temperatures, and the Curie constant C agrees closely with the theoretical value, thus proving that each magnetic ion contributes with its theoretical moment $gS\,\mu_B$. Other dilute paramagnetic substances in a limited temperature range follow a Curie-Weiss law $\chi = C/(T-\vartheta)$ with small positive or negative values of ϑ, caused by the coupling of the orbital moment with the crystalline electric field.

2.2. Outline of the theory of ferrimagnetism

2.2.1. Néel's theory

For a ferromagnetic, essentially ionic compound, the moment per formula unit should be expected to be the sum of the ionic moments; thus for magnetite $Fe^{II}Fe_2{}^{III}O_4$ assuming g to be 2 for both ions : $4 + 2 \times 5 = 14\ \mu_B$. Weiss and Forrer [29]) in 1929 had found $4{\cdot}08\ \mu_B$. From earlier work [30]) it was known that the (normal) ferrites $Zn[Fe_2]O_4$ and $Cd[Fe_2]O_4$ are paramagnetic and the (inverse) ferrites of Mn, Co, Ni, Cu and Mg ferromagnetic like $Fe[Fe^{II}Fe]O_4$.

Also it was known that above the Curie temperature several ferrites showed a curvature of the $1/\chi$ vs T curve concave towards the T axis.

Using these data, Néel, who had already contributed a great deal to the theory of antiferromagnetism, in 1948 made the basic hypothesis [31]) that a strong negative interaction, i.e. a tendency to antiparallel orientation, exists between ionic moments on tetrahedral sites on the one hand and octahedral sites on the other hand. Thus the moment of $Fe^{III}[Fe^{II}Fe^{III}]O_4$ should be $(5+4)-5=4$, in close agreement with experiment. This behaviour may be termed non-compensated antiferromagnetism. We shall use the word *ferrimagnetism,* coined by Néel.

At the same time [31]) Néel extended the Weiss molecular-field theory to a lattice with two different lattice sites on which different amounts of magnetic ions (atoms) are found. The theory was given for one kind of magnetic ion (e.g. Fe^{3+}) only.

We shall give the bare essentials of the theory, applying it to spinels only, and thus introducing from the start the fundamental assumption of negative tetrahedral-octahedral interaction.

Like Néel we shall use an index a for the tetrahedral position and b for the octahedral position. Using a notation slightly different from Néel's, we take a spinel

$$Fe^{III}_{x_a}Me_{1-x_a}[Fe^{III}_{x_b}Me_{2-x_b}]O_4, \qquad (2.1)$$

in which Me represents non-magnetic ions and x_a and x_b the number of ferric ions on A and B sites respectively.

2.2.1.1. *Paramagnetic behaviour*

Taking the *paramagnetic* behaviour above the Curie temperature, the total magnetization per mole $\vec{I}$ equals

$$\vec{I} = x_a\vec{I}_a + x_b\vec{I}_b, \qquad (2.2)$$

in which $\vec{I}_a$ is the magnetization per gram-ion on A, and $\vec{I}_b$ idem on B. The molecular field for an ion on A, h_a, originates from the resultant magnetization of its neighbours on B, and also from those on A, and is assumed to be proportional to $\vec{I}_b$ and $\vec{I}_a$ respectively. Thus

$$\vec{h}_a = n(-x_b\vec{I}_b + \alpha x_a\vec{I}_a), \qquad (2.3)$$

in which n is a positive constant related to the sum of the exchange integrals AB, and $-\alpha$ is the ratio of the interactions AA and AB. Likewise

$$\vec{h}_b = n(-x_a\vec{I}_a + \beta x_b\vec{I}_b), \qquad (2.4)$$

in which $-\beta$ is the ratio of the interactions BB and AB. The coefficients $n\alpha$, $-n$ and $n\beta$ are linearly related to the sums of the possible exchange integrals AA, AB and BB respectively. The partial magnetizations of the sublattices $\vec{I}_a$ and $\vec{I}_b$ can be written:

$$\vec{I}_a = \frac{C}{T}(\vec{H} + \vec{h}_a), \qquad (2.5)$$

$$\vec{I}_b = \frac{C}{T}(\vec{H} + \vec{h}_b). \qquad (2.6)$$

Eliminating $\vec{I}_a$, $\vec{I}_b$, $\vec{h}_a$ and $\vec{h}_b$ from (2.3-6) one obtains

$$\frac{H}{I_{\text{mole}}} = \frac{T}{C_{\text{mole}}} + \frac{n(2x_ax_b - \alpha x_a{}^2 - \beta x_b{}^2)}{(x_a + x_b)^2} - \\ - \frac{n^2C_{\text{mole}}x_ax_b[x_a(1+\alpha) - x_b(1+\beta)]^2/(x_a+x_b)^4}{T - nC_{\text{mole}}x_ax_b(2+\alpha+\beta)/(x_a+x_b)^2} \qquad (2.7)$$

or

$$\frac{1}{\chi_{\text{mole}}} = \frac{T}{C_{\text{mole}}} + \frac{1}{\chi_0} - \frac{s}{T-\vartheta}, \qquad (2.8)$$

in which the values of $1/\chi_0$, s and ϑ are read from eq. (2.7). It is seen that this expression represents a hyperbolic relation between $1/\chi_{\text{mole}}$ and T, as is found experimentally.

It has since been found that the slope of the experimental asymptote of the hyperbola is not equal to $1/C_{\text{mole}}$, and Néel has assumed that n (but for simplicity's sake not α and β) is linearly dependent on temperature:

$$n = n_0(1 + \gamma T),$$

giving

$$\frac{1}{C_{\text{mole}}} = \frac{1}{C'_{\text{mole}}} + \frac{\gamma}{\chi_0},$$

in which C'_{mole} is the theoretical Curie constant.

From the shape of the experimental curve χ_0, s and ϑ can be deduced. $x_a + x_b$ is known (2 for $MgFe_2O_4$, 2·5 for $Li_{0.5}Fe_{2.5}O_4$, etc.) and from χ_0, s, ϑ and from the ferromagnetic behaviour x_a, x_b, α, β and n can be found for those cases where only Fe^{3+} is present, when the molecular-field theory may be used (i.e. in the absence of a pronounced order of the ions in either position and for not too small x_a or x_b). We wish to stress again [32]) that if x_a/x_b changes with temperature, as has been found to be the case e.g. for $MgFe_2O_4$, the paramagnetic measurements do not correspond to one and the same chemical formula, so that calculations like this have no more than qualitative value.

All the same, Néel has been able to show in this way qualitatively for several ferrites that $|\alpha|$ and $|\beta| \ll 1$, which means that the AA and BB interactions are small with respect to the AB interaction. He also found that α and β, and thus the AA and BB interactions, are negative.

2.2.1.2. *Ferromagnetic behaviour*

We shall in the following concern ourselves only with the *ferromagnetic* behaviour. In the ferromagnetic case the molecular fields are

$$\vec{h_a} = n(-x_b\vec{I_{bs}} + \alpha x_a\vec{I_{as}}) \tag{2.9}$$

and

$$\vec{h_b} = n(-x_a\vec{I_{as}} + \beta x_b\vec{I_{bs}}), \tag{2.10}$$

in which $\vec{I_{as}}$ and $\vec{I_{bs}}$ are the spontaneous magnetizations per gram-ion of the A and B sublattices respectively. We have

$$I_{as} = NgS\mu_B B_S\left(\frac{gS\mu_B h_a}{kT}\right), \tag{2.11}$$

$$I_{bs} = NgS\mu_B B_S\left(\frac{gS\mu_B h_b}{kT}\right). \tag{2.12}$$

The resultant spontaneous magnetization per mole I_s is given by

$$I_s = x_b I_{bs} - x_a I_{as}. \tag{2.13}$$

We shall now consider the different behaviours of I_s when x_a/x_b is varied.

From equation (2.13) it is seen that the spontaneous magnetization at 0 °K (where $I_{as} = I_{bs}$) changes sign for $x_a/x_b = 1$. It can easily be seen from (2.11-12) that I_{as} and I_{bs} remain equal to each other for all temperatures only if h_a and h_b also remain equal, and this happens only if $\alpha = \beta$. Thus for $\alpha \neq \beta$, $I_{as} \neq I_{bs}$ for all temperatures except $T = 0$ °K, and the I_s vs T curve is as depicted in fig. 8 (d) (Néel's type (L)).

Near the absolute zero and Curie temperatures simplified expressions may be used for the Brillouin functions. Thus Néel calculates that near the Curie temperature, i.e. for small I_{as} and I_{bs}, the slope of the I_s vs T curve, $\mathrm{d}I_s/\mathrm{d}T$, changes sign for $x_a/x_b = (1+\beta)/(1+\alpha)$. I_s at 0 °K is then not equal to zero, so that I_s near the Curie temperature changes sign with respect to that at 0 °K. The I_s vs T curve is then as depicted in fig. 8 (f).

For x_a/x_b between 1 and $(1+\beta)/(1+\alpha)$ the I_s vs T curve becomes as given in fig. 8 (e).

The condition for which $\mathrm{d}I_s/\mathrm{d}T$ changes sign near 0 °K was found to be $x_a/x_b = (1-\beta)/(1-\alpha)$. Néel notes that for this condition the shape of the I_s vs T curve is equal to that of a normal ferromagnetic; see fig. 8 (b).

Thus for x_a/x_b between 1 and $(1-\beta)/(1-\alpha)$ the I_s vs T curve has the shape given in fig. 8 (c).

For x_a/x_b farther from 1 than $(1+\beta)/(1+\alpha)$ and $(1-\beta)/(1-\alpha)$ a I_s vs T curve is obtained with a more gradual variation in $\mathrm{d}I_s/\mathrm{d}T$ with temperature than for a normal ferromagnetic; see fig. 8 (a and g).

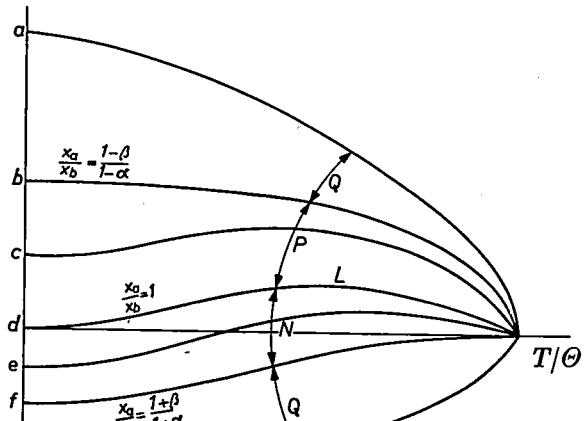

Fig. 8. Spontaneous-magnetization vs temperature curves for different relationships between the number of ferric ions in A and B sites (x_a and x_b respectively) and α and β. The capitals L, N, P and Q refer to Néel's nomenclature for these types of curves.

Fig. 8 shows that a continuous variation of x_a/x_b will necessarily result in a continuous variation of shape of the spontaneous-magnetization vs temperature curve from type a to type g as shown, except for the unlikely case that $\alpha = \beta$.

When x_a/x_b increases, thereby passing unity, the curves will change in the order g-a for negative α and β and for $|\beta| > |\alpha|$, whereas for $|\alpha| > |\beta|$ they would then change in the order a-g.

2.2.2. Non-parallel ionic moments inside each sublattice

Néel [31]) showed that the state of minimum energy due to the molecular field at 0 °K is not necessarily that in which all ionic moments inside each sublattice are parallel. Two more possibilities exist, in which on either sublattice A or B the ionic moments are not parallel, as a result of the negative interaction between the ionic moments inside the sublattice. Néel supposed the distribution of the non-aligned magnetic moments to be random. Yafet and Kittel [33]) showed that a lower energy is obtained if the ionic moments with non-parallel orientation form an ordered arrangement inside the A or B sublattices either in the two face-centred sublattices A' and A'' or in the four face-centred sublattices in the B position. In the latter case a simple, although formal, description is obtained when only two sublattices B' and B'' are considered. The ionic moments inside each of the sublattices A', A'', B' and B'' are mutually parallel but the ionic moments in the A' and A'', or in the B' and B'' sublattices form angles with each other as a result of the negative AA or BB interactions competing with the AB interactions.

In Yafet and Kittel's modification of Néel's theory Néel's σ-T curves of the types (V), (R), and (M) ([31]) p. 154), which have non-zero slope at 0 °K, cannot occur since the sublattices A', A'', $B'$and B'' are saturated at 0 °K*).

Whenever curves are found that down to low temperatures resemble curves (V), (R) and (M) they should be regarded as types (N), (Q) and (P) respectively. Thus e.g. even a σ-T curve that is convex towards the T-axis is considered as a curve of type (Q).

The possible arrangements of the sublattice magnetizations are shown in figs 9a and 9c respectively. The resultant magnetizations are

for 9a $$I_s = x_b I_{bs} - x_a I_{as} \sin \varphi \,, \tag{2.14}$$

for 9c $$I_s = x_b I_{bs} \sin \psi - x_a I_{as} \,, \tag{2.15}$$

in which $180° - 2\varphi$ and $180° - 2\psi$ are the angles between the directions of the magnetic moments in the A' and A'' sublattices and in the B' and B'' sublattices respectively.

*) There is no conflict here with the third law of thermodynamics.

For the case of fig. 9*a* the molecular fields in the A' sublattice due to the B sublattice and to the A'' sublattice have a resultant equal in magnitude to the latter:

$$n(x_b\vec{I}_{bs} + a_2x_a\vec{I}_{a''s}) = n\,a_2x_a\vec{I}_{a's}\,,$$

in which $-a_2$ is the ratio of the interactions $A'A''/AB$. Since the angle between $\vec{h}_{a'}$ and $\vec{h}_{a''}$ is $180° - 2\varphi$, this gives $\sin\varphi = -x_bI_{bs}/a_2x_aI_{as}$, and substitution in (2.14) gives

for 9*a*
$$I_s = x_bI_{bs}\left(1 + \frac{1}{a_2}\right). \tag{2.16}$$

Similarly one finds

for 9*c*
$$I_s = -x_aI_{as}\left(1 + \frac{1}{\gamma_2}\right), \tag{2.17}$$

in which $-\gamma_2$ is the ratio of the interactions $B'B''/AB$.

A fourth theoretically possible arrangement, viz. for predominant $A'A''$ and $B'B''$ interactions, is shown in fig. 9*d*. This case will not occur in practice when only one type of magnetic ion is present, because the geometry of the spinel lattice favours the AB interaction.

A series of mixed crystals between two materials that *at all temperatures* have the arrangements shown in figs 9*a* and 9*c* respectively will not give a series of magnetization vs temperature curves as depicted in fig. 8 *a-g*. Such anomalous curves occur only because they are the difference of two sublattice-magnetization vs temperature curves, each of which, however, is a Brillouin curve. In the present case, where I_s is determined by I_{as} *or* I_{bs} only, the theory predicts normal Brillouin curves for all materials, also for $a_2 \neq \gamma_2$.

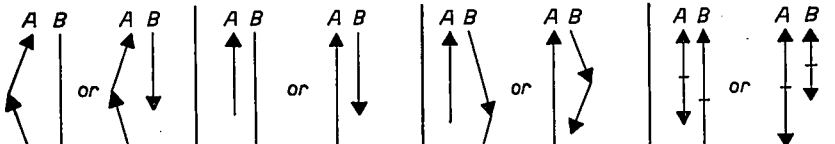

Fig. 9. Four different theoretically possible orientations of the ionic moments in A and B sublattices for different ratios between AA, AB and BB interactions. For each case *a-c* the figures are drawn for positive and negative I_s, and for *d* for $I_{a's} <$ or $> I_{b's}$.
(*a*) Interaction AA comparable to AB, and BB small with respect to AB.
(*b*) Interactions AA and BB both small with respect to AB.
(*c*) Interaction AA small with respect to AB, and BB comparable to AB.
(*d*) Interactions AA and BB large with respect to AB.

Yafet and Kittel have shown, however, that transitions between the arrangements 9*a-d* may occur for one and the same material, when the temperature is varied. The occurrence of angles between the ionic moments inside one sublattice at 0 °K does not mean, therefore, that the σ-T curves cannot become anomalous at higher temperatures.

It follows from equations (2.16) and (2.17) that for small negative values of α_2 and γ_2 ($|\alpha_2|$ or $|\gamma_2|<1$) the direction of the resultant magnetization is opposite to that of the sublattice magnetization determining its magnitude, i.e. as shown in fig. 9*a* (right) and in fig. 9*c* (left). Only for large negative values of α_2 or γ_2 ($|\alpha_2|$ or $\gamma_2|>1$) are these directions the same, i.e. as shown in fig. 9*a* (left) and in fig. 9*c* (right).

Large negative values of α_2 or γ_2 will not occur in a spinel containing only one type of magnetic ion, in view of the geometry of the spinel lattice, so that in this case the last-named two arrangements will not occur. The spinels containing two types of magnetic ions, Me_1 and Me_2, the interactions Me_1-Me_1, Me_1-Me_2 and Me_2-Me_2 may be widely different, and this may greatly increase α_2 or γ_2 when the simple theory is applied for this case (see however section 2.2.3.). It is quite possible that in this case, especially for γ_2, values $|\gamma_2|>1$ will occur.

We shall in the following sections use the symbols m_a and m_b for the sums of the ionic moments in the A or in the B position respectively, at 0 °K, irrespective of their orientation, expressed in Bohr magnetons per formula unit. We take both quantities positive.

The saturation moment $n_B = |m|$, where generally $m = m_b \sin\psi - m_a \sin\varphi$. Either $\sin\psi$ or $\sin\varphi$, or both, are equal to unity; m may be either positive or negative. The expressions (2.14) - (2.17) then become

$$m = m_b - m_a \sin\varphi = +m_b(1 + 1/\alpha_2), \tag{2.18}$$

$$m = m_b \sin\psi - m_a = -m_a(1 + 1/\gamma_2). \tag{2.19}$$

2.2.3. Spinels containing two or more magnetic ions

Many of the materials we have investigated (amongst which several ferrites that have industrial importance) contain in addition to Fe^{3+} ions one or more other magnetic ions. For this reason one should like to extend Néel's theory for this case. For the case of two magnetic ions Me_1 and Me_2 being located on both lattice sites there are 10 different interactions since the AA, AB and BB interactions depend on the type of interacting ions. It is clearly impossible to get any results with this large number of parameters, so that simplifying assumptions have to be made. Néel's assumption that the Me_1-Me_1(n), Me_1-Me_2(n') and Me_2-Me_2(n'') interaction constants are equal is certainly very crude. Niessen [34a-e]) has attempted a refinement of Néel's treatment by introducing three different interaction constants n, n' and n'' but still had to make a number of simplifying assumptions such as: α and β are constant for these three interactions, $nn'' = n'^2$, $g_1 = g_2$. Assumptions as regards ionic distribution may also be used, but only with care. Expressions may be derived for which the saturation-magnetization vs temperature curves shown in fig. 8*a-g* occur.

2.3. The nature of the exchange interactions

2.3.1. Indirect exchange interaction

The Heisenberg exchange integral depends on the extent to which the 3d-electron wave functions of adjacent metal atoms overlap. Slater and Néel have given curves showing the dependence of the magnitude of the exchange integral on D/d and $D-d$ respectively, in which D = the atomic separation and d = the diameter of the 3d orbit. For small values of D/d ($<$appr. 1·5) the exchange interaction is negative, above 1·5 it becomes positive, passes through a maximum at D/d = appr. 1·8 to become small but still positive at values of D/d = appr. 3. In ferromagnetic spinels for which $a \geqslant 8{\cdot}30$ Å the distances of adjacent ferric ions are $A\text{-}A \geqslant 3{\cdot}61$ Å, $A\text{-}B \geqslant 3{\cdot}44$ Å, $B\text{-}B \geqslant 2{\cdot}94$ Å whereas d is of the order of the ionic diameter, i.e. 1·34 Å, giving D/d = appr. 2·7, 2·6 and 2·2 respectively, i.e. values in the region of weak to strong *positive* interaction.

It is to be noted that in spinels the strongest, negative interaction is the AB interaction for which (considering only those configurations with the shortest Me-O distances) fig. 6, triangle *pqc*, shows that the oxygen ion obstructs the direct view between the metallic ions more than is the case for the AA and BB interactions (fig. 6, triangles *qrd* and *ppb* respectively). Néel has suggested that here an indirect exchange mechanism occurs, in which the anions play the role of an intermediary, as was first outlined by Kramers. This mechanism is usually called *superexchange*.

It has been proved by neutron diffraction [35]) that in antiferromagnetic MnO with NaCl structure the strongest negative interaction is between Mn^{2+} ions at a distance a, for which the angle Mn^{2+} - O^{2-} - Mn^{2+} is 180°, although there is a shorter distance Mn^{2+}-Mn^{2+} of $\frac{1}{2}a\sqrt{2}$, for which the angle Mn^{2+}-O^{2-}-Mn^{2+} is, however, 90° *).

Here a direct overlap of the 3d wave functions is clearly impossible, showing that the intervening oxygen ion must play a role in the exchange mechanism.

2.3.2. Dependence of superexchange interaction on the angle Me-O-Me

The collinearity of the Mn^{2+} - O^{2-} - Mn^{2+} configuration must be favourable to superexchange, as it must make up for the increased Mn^{2+}-Mn^{2+} distance with respect to the right-angle configuration

$$\begin{array}{l} \quad Mn^{2+} \\ \quad\ | \\ Mn^{2+}\!-\ O^{2-} \end{array}$$

*) Neutrons are scattered by the magnetic moments of the unpaired electrons as well as by the atomic nuclei, and the former magnetic contribution to the scattering power has opposite phase for ions with magnetic moments pointing in opposite directions. Thus the total scattering power has a different value for e.g. $Mn^{2+}\uparrow$ and $Mn^{2+}\downarrow$. The neutron-diffraction pattern of MnO below the Néel temperature showed superstructure lines yielding a cell edge twice as large as that found by X-ray diffraction.

Anderson [36]) has shown theoretically that this is indeed the case, i.e. that the exchange interaction has a maximum value for an angle Me-O-Me of 180° and a minimum for an angle of 90°.

Qualitatively this may be understood as follows [37]). The ground state of a pair of ions Mn^{2+}-O^{2-} is

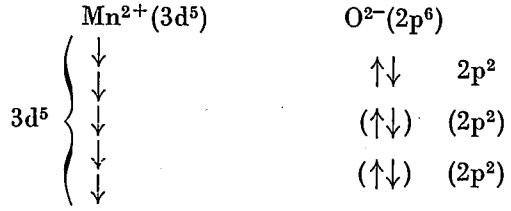

The six 2p electrons of the O^{2-} ions form three pairs, located in three different p orbits with dumb-bell shape: ∞

An excited state exists, in which one of a pair of 2p electrons having the axis of the dumb-bell in the direction of a Mn^{2+} ion goes over to this Mn^{2+} ion and, as the 3d orbit is half-filled, with spin presumably anti-parallel to that of the electrons present, giving a configuration

The remaining p electron, having the same dumb-bell axis as that of the electron that has gone to the Mn^{2+} ion, will now presumably be able to interact with the Mn^{2+} ion directly opposite to the one depicted. Provided the two assumptions are correct, Anderson's calculation shows that the disturbing influence of excited states yields a negative exchange coupling between the opposite Mn^{2+} ions of the right order of magnitude.

Because of the dumb-bell shape of the 2p orbits the superexchange interaction for the right-angle configuration must be very weak. A small interaction may in this case also result from hybridization of 2p and 2s wave functions, or from the presence of excited states in which an electron is raised from the 2p to a 3*l* orbit, which, however, takes a considerable energy.

2.3.3. Influence of the type of magnetic ion

If both ions have less than five 3d electrons, the p electron will be accommodated in the 3d orbit with parallel spin, and Anderson therefore expects positive interaction to result in all such cases, citing examples like CrTe (ferromagnetic) vs MnTe (antiferromagnetic). There are, however,

many oxides of metal ions with less than five 3d electrons that are antiferromagnetic, e.g. Cr_2O_3, whereas only a few really ferromagnetic oxides, i.e. with positive interactions, are known. Thus e.g. $CaMn^{IV}O_3$ with perovskite structure is antiferromagnetic, while mixed crystals $La_{1-x}Me_xMn^{III}_{1-x}Mn^{IV}_xO_4$, in which Me = Ca, Sr or Ba, are real ferromagnetics, i.e. with positive interactions [38]).

The interaction between ions with less than five 3d electrons and those with five 3d electrons according to this theory may be either positive or negative.

It may be noted that Zener [39]) proposes another exchange mechanism to account for the ferromagnetism of $La_{1-x}Sr_xMn^{III}_{1-x}Mn^{IV}_xO_4$. This involves the simultaneous transfer of an electron from one metal ion to an adjacent oxygen ion and of another electron from there to another metal ion ("double exchange"). This mechanism would thus occur in semiconductors for which De Boer and Verwey [40]) postulate the presence of two ions of one metal with different valencies in one crystallographic position.

It has been suggested [41]) that Zener's double-exchange mechanism plays a role in the *BB* interaction in magnetite. It will be seen in sections 4-9 that all saturation moments can be accounted for on the basis of negative exchange interaction.

The only transition-metal ion having less than five 3d electrons used in the preparations described in the present paper is the Cr^{3+} ion. It will appear that in the materials described in section 7 the Fe^{3+}_A-Cr^{3+}_B interaction is undoubtedly negative.

2.3.4. Influence of angles and distances on superexchange interaction in spinels

Although no theory is known regarding the influence of the distances Me-O on the strength of the superexchange interaction, it is assumed that generally exchange interactions fall off rapidly with increasing distance. We have seen in section 1.1 that the shortest distances Me-O in the spinel structure fall into two groups, that of nearest neighbours, formerly indicated by *p* and *q*, and a group of larger distances, indicated by *r*, *s* and *t* (see section 1.1). Configurations Me-O-Me with larger Me-O distances, as well as those with both distances of the group *r*, *s* and *t* will be assumed to give interactions that are negligible against those with one distance *p* or *q* and the other equal to *p*, *q*, *r*, *s* or *t*. From fig. 6 we see that only for triangle *pqc* are both distances Me-O and the angle Me-O-Me favourable. The arrangements *pre* and *tqe* have very favourable angles but one large distance. The *AB* interaction will therefore be strong. For *qrd* the angle is very unfavourable and one distance large: consequently the *AA* interaction will be very weak.

For *ppb* the angle is very unfavourable, but both distances Me-O are small; for *ptb*, *psb* and *psf* the angles are more favourable, but one of the distances is large. The *BB* interaction therefore will be expected to be intermediate between the *AB* and *AA* interactions.

In literature only those interactions have so far been taken into account for which the distances *AA*, *AB*, and *BB* are shortest (i.e. *d*, *c* and *b* respectively). As long as the relative influence of angles and distances are unknown, there is no reason why the other configurations should be neglected.

It is the merit of the molecular-field approximation that it does not concern itself with the number of configurations that are taken into account, as the molecular-field constants n, α, β, etc., comprise all interactions that play a role.

When it is attempted, however, to link the molecular-field constants to the exchange integrals, it seems appropriate to take into account all the configurations that contribute to the interactions.

R.S. Weisz [42]) has attempted to draw up an empirical quantitative relationship giving the dependence of the exchange interaction energy, $k\Theta$, as a function of the distance Me-O + O-Me′ (l), and the angle Me-O-Me′ (φ):

$$k\Theta = C\ S_1 S_2\ e^{-10l} \cos^6 \varphi\,,$$

in which C is a constant and S_1 and S_2 are the spin quantum numbers of the ions Me and Me′ respectively.

From the Néel temperatures of the antiferromagnetics MnO, FeO and CoO, for which $\cos \varphi = 1$, a constant value of C is found, but not for NiO.

For spinels the formula was applied to obtain the ratio of the exchange energies for the *AA*, *AB* and *BB* interactions: values for α and β were found of the order of 10^{-9} and 10^{-7} respectively. Weisz therefore assumed $E_{exch(AB)} = k\Theta$; the Curie temperatures thus calculated from the *AB* interaction agree with the experimental values to within 20 %; in a previous communication Weisz uses a factor e^{-7l}, giving agreement to within 15 %. It seems that many experiments described in the following sections cannot be understood with the small values of α and β Weisz derived. Theoretical background for his formula is so far lacking.

REFERENCES

27) For a general synopsis of the theoretical work in this field see
J. H. Van Vleck, Rev. mod. Phys. **17**, 27-47, 1945; Physica **15**, 197-206, 1949.
28) P. Weiss, J. Phys. (4) **6**, 661-690, 1907.
29) P. Weiss and R. Forrer, Ann. Phys., Paris (10) **12**, 279-374, 1929.
30) G. Hilpert, Ber. dtsch. chem. Ges. **42**, 2248, 1909;
H. Forestier, Thèse, Paris, 1925, or Ann. Chim. **10**, 9, 57, 1925;
J. L. Snoek, Philips tech. Rev. **8**, 353-360, 1946.
31) L. Néel, Ann. Phys., Paris **3**, 137-198, 1948.
32) J. Phys. Radium **12**, 160, 1951.
33) Y. Yafet and C. Kittel, Phys. Rev. **87**, 290-294, 1952.
34a) K. F. Niessen, Physica **17**, 1033-1047, 1951.
34b) K. F. Niessen, Physica **18**, 449-468, 1952.
34c) K. F. Niessen, Physica **19**, 445-450, 1953.
34d) K. F. Niessen, Physica **19**, 1127-1132, 1953.
34e) K. F. Niessen, Physica **19**, 1035-1045, 1953.
35) C. G. Shull and J. S. Smart, Phys. Rev. **76**, 1256-1257, 1949.
36) P. W. Anderson, Phys. Rev. **79**, 350-356, 705-710, 1950.
37) J. H. Van Vleck, J. Phys. Radium **12**, 262-274, 1951.
38) G. H. Jonker and J. H. van Santen, Physica **16**, 337-349, 1950.
39) C. Zener, Phys. Rev. **82**, 403-405, 1951.
40) J. H. de Boer and E. J. W. Verwey, Proc. phys. Soc. **49A**, 59-71, 1937.
41) A. Fairweather, F. F. Roberts and A. J. E. Welch, Ferrites, Rep. Progr. Phys **15**, 142-172, 1952;
C. Zener and R. R. Heikes, Rev. mod. Phys. **25**, 191-198, 1953.
42) R. S. Weisz, Ceramic Age **59**, 35-38, 1952.

3. EXPERIMENTAL PROCEDURES

3.1. Magnetic measuring methods used in sections 4-9

In the following sections we shall report and discuss measurements of the saturation magnetizations of various ferrimagnetic oxides.

The measurements were carried out by the ponderomotor method described by Rathenau and Snoek [43]) (see fig. 10), in which the material (p) is fixed to a horizontal pendulum (P) suspended from four wires (W), moving perpendicularly to an inhomogeneous field. The field varies very nearly as $H = H_0 - \frac{1}{2}\, ax^2$ in the direction x of the oscillations, which is brought about by the shape of the pole pieces which end in equal spherical segments (N and S). The constant of the restoring force on the magnetic material in this inhomogeneous field is $a\sigma m_p$, in which σ is the saturation magnetization in $\mathrm{cgs_{magn}.cm^3/gram}$, m_p the weight of the sample. The saturation magnetization σ is found from the formula

$$\sigma = \frac{4\pi^2 m_P}{a m_p}\left(\frac{1}{\tau^2} - \frac{1}{\tau_0^2}\right),$$

in which m_P is the weight of the pendulum, τ_0 the period of the oscillations

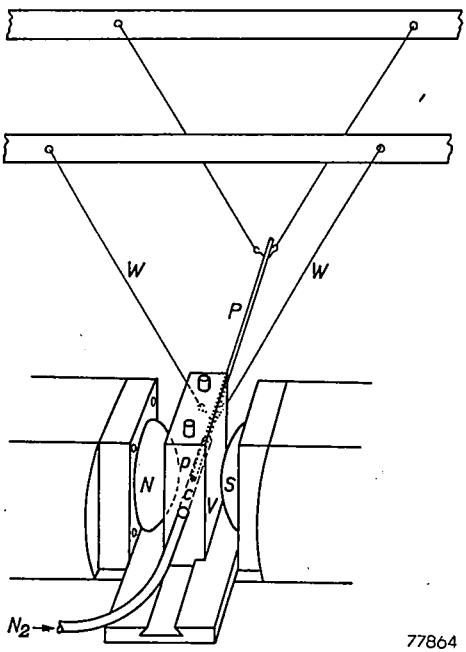

Fig. 10. Apparatus for measuring saturation magnetizations (for symbols see text).

in a magnetic field without the magnetic material fixed to the pendulum, and τ that with the magnetic material present. The constant $4\pi^2/a$ is determined by calibration with very pure iron and nickel.

The measurements reported in sections 4, 7 and 9 were carried out in fields up to 5900 oersteds, those in sections 5, 6 and 8 in fields up to 8000 or 9000 oersteds. For measurements at higher temperatures the end of the pendulum carrying the magnetic material moves in a small tubular furnace; for those at the lowest temperatures it moves in a channel (C) through a vessel (V) containing liquid nitrogen. For temperatures between about 80 °K and room temperature a stream of nitrogen is sucked from a Dewar flask through the vessel (V). By varying the suction rate any constant temperature can be obtained. At liquid-nitrogen temperatures a slow stream of dry nitrogen is passed through the channel in order to prevent condensation of oxygen on the pendulum. Temperatures were measured by means of a thermocouple fixed to the mV meter by very thin leads, so that the movement of the pendulum is not impeded.

Measurements of the saturation magnetization at liquid-hydrogen temperature were carried out by Dr J. Volger or by Mr P. Jongenburger *) by a ballistic method, using a watercooled solenoid for generating the field. These measurements were performed on rods of about $3 \times 3 \times 50$ mm^3 at field strengths up to 7000 oersteds.

Here the flux Φ through the rod is measured. The magnetization in $\mathrm{cgs}_{\mathrm{magn}}$ $I = \Phi/4\pi A$ (A = the area of the cross-section of the rod in cm^2), and σ is obtained from

$$\sigma = \frac{I}{d} = \frac{IAl}{m_{\mathrm{prep}}} = \frac{\Phi l}{4\pi m_{\mathrm{prep}}}.$$

(d = apparent density = (weight)/(external volume), l = length in cm).

The hydrogen liquefactor was not yet available when the measurements reported in section 4 were carried out. Therefore the values given in that section have not been extrapolated to 0 °K and are given to one decimal place less than the values reported in the later sections. The latter values were extrapolated with a T^2 law. Extrapolation with $T^{3/2}$, as postulated by the Bloch spin-wave theory, does not give appreciably different results.

The moment per formula unit Me_3O_4 (n_B) in Bohr magnetons is obtained from $\sigma_{\substack{T=0 \\ H\to\infty}}$ (σ_0) from the formula

$$n_B = \frac{\sigma_0 \times \text{molec. wt } (M)}{(\text{Avogadro's number}) \times (\text{Bohr magneton in ergs/gauss})} = \frac{\sigma_0 M}{5585}.$$

*) The author wishes to express his thanks to Dr J. Volger and Mr P. Jongenburger for performing these measurements.

3.2. Preparation of the materials

3.2.1. The final sintering operation

The final operation in the preparation of all materials investigated was a sintering process carried out on pressed bars, pellets, etc., placed in an alumina boat inside the gas-tight tube of a molybdenum-wire electric furnace. This operation is carried out at a temperature (900-1350 °C) and in an atmosphere that to a large extent determine the composition. For reducing atmospheres and high temperatures two concentric gas-tight tubes were used and the intervening space was rinsed with the same atmosphere as the preparation.

Practically all materials investigated are spinels, and contain ferric ions, and many also other ions of the transition metals, which can give ions of different states of valency, either higher or lower than that desired. All materials have an equilibrium oxygen pressure that increases with temperature, and which for every different composition will be different.

Because of the special feature of the oxidic spinels to form mixed crystals, containing ions varying from tetravalent to monovalent as well as vacant lattice positions, sintering in an atmosphere with an oxygen content appreciably different from the equilibrium pressure tends to yield a spinel with different composition, either alone, like e.g. in the case

$$MnFe_2O_4 + \tfrac{1}{2}x\ O_2 \rightarrow (1-3x)\ MnFe_2O_4 \,.\, x\ Mn_3O_4 \,.\, 3x\ Fe_2O_3\,,$$

which for $x \ll 1$ may form one phase, or with a second phase, like e.g. in the case

$$MnFe_2O_4 - \tfrac{1}{2}x\ O_2 \rightarrow (1-x)\ (Mn,Fe^{II})Fe_2O_4 + 3x\ (Mn,Fe^{II})O\,.$$

Divalent oxides are usually practically insoluble in the spinel phase.

For practically all materials, except e.g. Fe_3O_4, the equilibrium oxygen pressure exceeds one atmosphere below the melting point; the materials cannot, therefore, be melted in a stream of oxygen at 1 atm without serious decomposition.

The upper temperature limit for the sintering operation is thus primarily determined by the temperature at which the equilibrium oxygen pressure reaches 1 atm.

The possibility of a chemical reaction taking place with the receptacle affords another limiting factor. We have always used recrystallized alumina boats (fired above 1800 °C) or fused-alumina powder underneath the material to be sintered. This material proved to be very unreactive. Even so sintering temperatures have been kept below 1350 °C in order to avoid any reaction with the alumina: where this appeared advisable the surface that had been in contact with the alumina was ground away.

For a number of spinels, containing, apart from noble-gas-shell ions Li^+, Mg^{2+}, Al^{3+}, only Fe^{3+}, Ni^{2+}, Cr^{3+}, Cu^{2+}, the ions with valencies higher than those desired are very unstable, which appears from the fact that even in an oxygen atmosphere, at the minimum temperature required to obtain complete reaction, no ions with higher valencies are formed. These materials were fired in oxygen at a temperature low enough to give no perceptible reduction of Fe^{3+} to Fe^{2+}. The spinels containing Cu^{2+} were markedly reduced in oxygen above 900-1000 °C. Such materials may be kept porous so that any loss of oxygen occurring during firing may be corrected by oxygen take-up during cooling.

The preparation of spinels containing ions for which the valency states lower than those desired are difficult to obtain, e.g. $MnCr_2O_4$, is also fairly easy. Thus $MnCr_2O_4$ may be fired in a wide range of reducing atmospheres, without formation of metallic Mn (or Cr), and with imperceptible amounts of excess oxygen.

The problem of obtaining the correct composition is more difficult for spinels containing ions like Fe^{2+}, Mn^{2+}, and to a lesser extent Co^{2+}, for which higher valency states are stable up to high temperatures, as well as ions like Fe^{3+} for which lower valency states are formed at high temperatures.

In order to obtain the desired composition (i.e. oxygen content) one may choose from two methods:

(1) Using a constant atmosphere, the temperature is adjusted until chemical analysis of the material shows that the correct oxygen content is obtained.

(2) Using a constant temperature, the oxygen content of the atmosphere is adjusted until the material has the correct oxygen content.

It must be kept in mind, however, that an atmosphere in equilibrium with the material at the sintering temperature will reoxidize it at lower temperatures and mostly so at the outside surface, so that the composition becomes inhomogeneous during cooling down.

This might be largely avoided by quenching the material from the sintering temperature, but we shall see that the cation distribution amongst tetrahedral and octahedral sites is often strongly dependent on temperature, so that in this way a different material is obtained, quite apart from the effect of possible reoxidation.

We shall be interested in the properties of the material having the most stable ionic distribution, and therefore have to cool slowly.

The ideal method of obtaining a homogeneous material with the correct oxygen content and the most stable ionic distribution is that of cooling slowly in a continuously changing atmosphere at all temperatures in equilibrium with the oxygen pressure of the material. Smiltens has used

a stepwise-changing atmosphere in the preparation of Fe_3O_4 single crystals, using his own equilibrium-pressure data [44]).

The determination of the equilibrium oxygen pressure as a function of temperature is difficult and laborious, and has been carried out only for Fe_3O_4.

A method of diminishing reoxidation during cooling down, i.e. sintering to a high apparent density, so that the atmosphere cannot penetrate into the inside of the material through the pores, can sometimes be used with success [45]).

Another method is that of firing in a gas mixture the oxygen content of which changes with temperature (e.g. CO_2, $CO_2 + CO$, H_2O, $H_2O + H_2$). From Smiltens's work it is known that the decrease of oxygen content with decreasing temperature of a CO_2-CO mixture is not sufficient to keep it in equilibrium with Fe_3O_4, and this appears to be very general for the known gas mixtures.

As the firing temperature is decreased, the difference in oxygen pressure between the firing temperature and room temperature is decreased. The minimum sintering temperature is determined by the condition that complete reaction takes place. This temperature may be lowered by a suitable preparation of the powder to be sintered.

In practice we have in most cases left the preparations to cool in the same atmosphere after switching off the furnace. The cooling time was then 7-9 hours. In many cases we have annealed the sample at low temperatures, high enough for ionic diffusion to take place within convenient time intervals. Whenever this has been done, specific reference to this effect will be made.

For a fair comparison of the ionic distribution in a mixed-crystal series we have always fired the whole series at one temperature and therefore often had to use different atmospheres for different members of the series (e.g. the series $MnFe_2O_4$-$MnCr_2O_4$). One sintering temperature cannot be used if certain members of a series do not react completely at a temperature where for other members melting occurs (cf. the series $CaFe_2O_4$-$ZnFe_2O_4$).

In view of the volatility of ZnO and Li_2O care was taken that no free ZnO or Li_2O was present when the final sintering operation was started. As these oxides volatilize even from their compounds under the conditions used, these were sintered at temperatures not above 1300 °C for Zn compounds and not above 1150 °C for Li compounds.

3.2.2. Methods of preparation of the powder to be sintered

Several methods have been used:

(A) Pure oxides, or in certain cases carbonates, are ground together in a chromium-plated steel ball mill or in an agate Bloch-Rossetti mill under

ethanol. The mixture is dried under an electric (infrared) lamp, prefired, usually in air, at a temperature below the final sintering temperature and ball-milled again.

Zinc oxide was heated to 500 °C before being used in order to decompose any $ZnCO_3$ present. The other oxides were heated at 200 °C before chemical analysis and before being used.

(B) The pure metals (or, in some cases, oxides or carbonates) were dissolved in nitric acid, the solution evaporated to dryness under an infrared lamp, often on a sand bath, and the nitrates decomposed to oxides. When the powder was completely dry it was transferred from the porcelain dish to an alumina beaker and heated to about 800 °C. The powder was then ball-milled in an agate Bloch-Rossetti mill. The compounds containing titanium were prepared by adding TiO_2 (anatase, synthetic) to the nitrates solution before evaporation and heating to dryness.

(B′): like (B), but using sulphuric acid instead of nitric acid. The prefiring was interrupted at 600 °C for a milling operation, then continued up to 900 °C, after which the powder was milled again.

(B″): like (B), but ammonia is added to the nitrates solution. The hydroxides are filtered, washed, dried and decomposed at about 800 °C.

(C) To the nitrates or sulfates solution prepared like under (B) (B′) a sodium-carbonate solution is added at 100 °C, the precipitate boiled, filtered, washed well, dried and decomposed by prefiring at about 800 °C.

We shall describe in the following sections the preparation of the various materials by giving:

the raw materials with the main impurities if present in amounts above 0·01 %;

the method used;

the temperature and duration of prefiring, and the atmosphere, if different from air (e.g. pref. 2 h 800 °C in O_2);

the temperature and duration of the final sintering and the atmosphere (e.g. sint. 2 h 1200 °C in O_2).

3.3. X-ray analysis

X-ray diagrams for all materials mentioned have been obtained on a Norelco X-ray Diffractometer. All materials reported show a spinel diagram without additional lines, except for the cases where superstructure lines occur, or in a few other cases which will be mentioned. The lattice constants were determined with Co $K\alpha_1$, Fe $K\alpha_1$ or Mo $K\alpha_1$ radiation, using the wavelengths Co $K\alpha_1$: 1·78890 Å, Fe $K\alpha_1$: 1·93597 Å and Mo $K\alpha_1$: 0·70926 Å.

3.4. Chemical analysis

Analysis of the oxygen content of many of the materials has been carried

out. The method used has been worked out by Messrs G. W. van Oosterhout and A. Bol.

The weighed sample is brought in a glass tube of 7 mm inner diameter with a constriction. The tube is rinsed with carbon dioxide or with very pure nitrogen; a calibrated solution of Mohr's salt in 6 N hydrochloric acid is then introduced. After a rinse with the same gas the tube is sealed. The tube is heated to 120-200 °C till the material has dissolved, which usually takes 8-24 hours.

The tube is then opened, and the contents are transferred to a titration vessel that is rinsed continuously with carbon dioxide.

The ferrous iron is titrated potentiometrically, using a vacuum tube voltmeter as described by Claassen [46]), against 0·01 or 0·1 N ceric sulphate solution. In this way both an excess and a shortage of oxygen with respect to Fe^{3+}, Mn^{2+}, Co^{2+}, Ni^{2+} or Cu^{2+} can be determined. For the titration of an excess oxygen the amount of Mohr's salt in the hydrochloric-acid solution is adjusted so that there is a small excess in every case.

For the determination of a shortage of oxygen a small amount of Mohr's salt is added to the hydrochloric acid in order to reduce dissolved oxygen. The solution is calibrated at least a day after preparation.

It is convenient to store the solutions in flasks; an accurately measured quantity of the solution is passed from these flasks through a silver reductor [47]) to the reaction tube. Calibration of the solution is carried out exactly as described above, leaving out the material.

For the determination of the total iron content the solution of the sample is passed through a silver reductor before the titration.

The titrations were carried out by Mr T. Geraerts for the materials of section 4, for the materials of sections 5-9 at the Analytical Chemistry Department of our laboratories under the supervision of Dr A. Claassen and Mr J. Visser *). A determination of the proportion of the metal ions present was carried out in a few cases. This was found not to deviate from the proportion in the raw materials within the analytical error. Several of the spinels containing volatile oxides were weighed before and after the final sintering.

Provided the material had practically completely reacted at a temperature well below the firing temperature of 1150 °C, the loss in weight of the spinels containing lithium was small, in fact less than 1 % of the Li_2O present. For the spinels containing zinc but no manganous or ferrous ions no loss of zinc was observed; for those containing Zn^{2+} and Mn^{2+} ions no loss of zinc occurred when the presence of free ZnO was avoided at the final

*) The author is indebted to Dr Claassen and to Mr Visser for their help in these investigations.

sintering. For those containing Zn^{2+} and Fe^{2+} ions special measures were taken, to be described in section 4.

The order of magnitude of the amount of impurities present in the raw materials was determined by a semi-quantitative spectrochemical method by Dr N. W. H. Addink *).

*) The author is indebted to Dr Addink for carrying out these analyses.

REFERENCES

43) G. W. Rathenau and J. L. Snoek, Philips Res. Rep. **1**, 239, 1946.
44) J. Smiltens. J. chem. Phys. **20**, 990-994, 1952.
45) J. L. Snoek, New Developments in Ferromagnetic Materials, Elsevier Publ. Comp., New York-Amsterdam, 1947.
46) A. Claassen, Analyt. chim. Acta **2**, 602-605, 1948.
47) G. H. Walden, L. P. Hamett and S. M. Edmunds, J. Amer. chem. Soc. **56**, 350-353, 1934.

4. EXPERIMENTAL EVIDENCE FOR THE CORRECTNESS OF NEEL'S HYPOTHESIS: THE FERRITES

4.1. Introduction

In order to obtain experimental evidence supporting Néel's theory, we have prepared the single ferrites $MnFe_2^{III}O_4$, $Fe^{II}Fe_2^{III}O_4$, $CoFe_2^{III}O_4$, $NiFe_2^{III}O_4$, $Cu^{II}Fe_2^{III}O_4$, $MgFe_2^{III}O_4$, $Li_{0.5}Fe_{2.5}^{III}O_4$, $ZnFe_2^{III}O_4$ and $CdFe_2^{III}O_4$ and mixed crystals of the first seven ferrites (reported to have the inverse cation distribution) with zinc ferrite.

The saturation moments expressed in Bohr magnetons have been reported previously [48) 49) 53)]. More complete data on many of these materials have since been reported by other authors, giving the saturation-magnetization vs temperature curves and susceptibility vs temperature measurements above the Curie temperature.

In the present section we shall give no new magnetic data, and discuss the experimental data at present available.

As we shall see that the magnetic properties depend on the ionic distribution, and as this in turn depends on the method of preparation, we shall in section 4.2 give our methods of preparation of the ferrites investigated.

4.2. Preparation and analysis of the ferrites

(a) The manganese-zinc ferrites $Mn_{1-a}Zn_a\ Fe_2O_4$ were prepared from
$MnCO_3$ (Ca 0·1%, Mg 0·12%, Zn 0·05 %, Na < 0·04%),
ZnO (Mg < 0·01 %),
Fe_2O_3 (Si 0·04 %, Pb 0·03 %, Mn 0·1 %),
by method (A), pref. 2 h at 1000 °C in air, sint: heating up in O_2 up to 1100 °C, further up to 1250 °C and 2 h at 1250 °C in N_2, containing traces of O_2.
$MnFe_2O_4$ contained 0·05 % Fe^{2+}; those MnZn ferrites for which data have been given $\leqslant$ 0·1 % Fe^{2+}.
(b) The ferrous-zinc ferrites were prepared from
ZnO } as under (a),
Fe_2O_3 }
by method (A), pref. 2 h at 900 °C in N_2, sint. 2 h at 1250 °C in N_2 atmospheres containing varying amounts of oxygen.

The material was placed in an envelope of ZnO. For two of the materials analysis showed that the Fe^{2+} and Zn contents were correct to within 0·1 %.
The ferrous ferrite was fired for 2 h at 1350 °C in a CO_2-H_2 mixture and cooled down very slowly in a CO_2-H_2 mixture the composition of which was changed stepwise as Smiltens has indicated. The CO_2-H_2 ratios were the same as the CO_2-CO ratios given by Smiltens. Our Fe_3O_4, however, contained 1·04 Fe^{2+} on 2·00 Fe^{3+}.
(c) The cobalt-zinc ferrites $Co_{1-a}\ Zn_aFe_2O_4$ were prepared from
$CoCO_3$ (< 0·1 % impurities),
ZnO (as under (a)),
Fe_2O_3 (Ni 0·03%, Mn 0·02 %, Si 0·02 %),
by method (A), pref. 2 h at 800 °C in air, sint. 2 h in oxygen or air at 1250 °C.
The $CoFe_2O_4$ contained no Fe^{2+} or excess oxygen, the CoZn ferrites $\leqslant$ 0·1 % excess oxygen.

(d) The nickel-zinc ferrites $Ni_{1-a}\,Zn_a\,Fe_2O_4$ were prepared from
$NiSO_4$ solution (Na $<$ 0·07 %, Ca 0·03 %, Co 0·02 %, Si 0·02 %),
ZnO (as under (a)),
Fe ($<$ 0·01 % impurities),
by method (B'), sint. in oxygen for 2 h at 1200 °C or 4 h at 1250 °C.
The Fe^{2+} contents were negligible, the SO_3 contents small, i.e. $<$ 0·1 %.
(e) The copper-zinc ferrites proved difficult to prepare, as they easily lost oxygen at temperatures where complete reaction took place.
Raw materials were
CuO (Pb 0·03 %, Si 0·02 %),
ZnO (as under (a)),
Fe_2O_3 (as under (c)).
$CuFe_2O_4$: pref. 2 h at 700 °C, sint. 2 h at 900 °C in O_2, annealed 168 h at 360 °C in O_2. The sample showed the tetragonal hausmannite structure with $c = 8{\cdot}68$ Å, $a = 8{\cdot}24$ Å. It contained 0·1 % Fe^{2+} (or Cu^+).
$Cu_{0{\cdot}5}Zn_{0{\cdot}5}\,Fe_2O_4$: pref. 2 h at 800 °C, sint. 3½ h at 1050 °C. It contained 0·1 % Fe^{2+} (or Cu^+).
(f) The magnesium-zinc ferrites were prepared from
MgO (Ca 0·2 %, Fe 0·01 %),
ZnO (as under (a)),
Fe_2O_3 (as under (c)),
by method (A), pref. 2 h at 900 °C, sint. 4 h at 1200 °C in O_2. $MgFe_2O_4$ was annealed for 24 h at 700 °C in O_2 and cooled slowly. The materials contained $<$ 0·1 % Fe^{2+}.
(g) The "lithium-zinc ferrites" $Li_{0{\cdot}5-0{\cdot}5a}\,Zn_a\,Fe_{2{\cdot}5-0{\cdot}5a}O_4$ were prepared from
Li_2CO_3 (Mg 0·02 %, Na 0·1 %, Ca 0·02 %),
ZnO (as under (a)),
Fe_2O_3 (as under (a)).
1 Li_2CO_3 + 1 Fe_2O_3 were milled in an agate ball mill under absolute ethanol, and after drying heated to 700 °C in oxygen for 5 hours. The $LiFeO_2$ thus obtained was used in method (A), pref. 2 h at 750 °C, sint. 4 h at 1150 °C in O_2. Fe^{2+} content $\leqslant$ 0·1 %.
The following materials were quenched by dropping in saturated NaCl solution, which was subsequently rinsed out with boiling water, or in oil, which was rinsed out with benzene.
$NiFe_2O_4$ from 1250 °C;
$CuFe_2O_4$ from 900 °C;
$MgFe_2O_4$ from 1250 °C;
$Li_{0{\cdot}5}Fe_{2{\cdot}5}O_4$ from 1150 °C.
These samples all contained $<$ 0·1 % Fe^{2+}.

4.3. Saturation moments of the single ferrites ($Me^{II}Fe_2^{III}O_4$ and $Li_{0{\cdot}5}Fe_{2{\cdot}5}^{III}O_4$)

Our results given previously [53] [49]) will be given in table IV together with those obtained since by Pauthenet [51] [52] [53]) and Guillaud et al. [54a-d]) or [55]).

Guillaud states that his preparations, apart from being stoichiometric to within 0·2 %, contain $<$ 0·05 wt % of metal in lower or higher valency states. Pauthenet gives no data on preparation or purity, except that they were found to be pure spinels.

Contrary to our own results of the present section, which are calculated from the magnetization at 77 °K and 5900 Oe, these authors have measured also at 20 °K, and in fields up to 20000 Oe, and have extrapolated towards $H = \infty$ and $T = 0$ °K.

We have seen (section 1.2) that according to Verwey and Heilmann the six first-named ferrites are inverse: $Fe[Me^{II}Fe]O_4$.

Thus for these six ferrites antiparallelism of the ionic moments in the *A* and *B* positions respectively, as a result of a preponderant *AB*

TABLE IV

Saturation moments of single ferrites

	(1)	(2)	(3)	(4)	(5)
	Gorter [50] [49]	Guillaud [54] [55]	Pauthenet [51] [52] [53]	other authors	$2S_{Me^{2+}}$
$MnFe_2O_4$	5·0	4·60	4·40±0·04	—	5
$FeFe_2O_4$	4·2	4·03	4·08 (±0·01)*)	4·08 [20])*)	4
$CoFe_2O_4$	3·3	3·67; 3·70	3·94±0·002	—	3
$NiFe_2O_4$	2·3	2·40	2·224	—	2
$CuFe_2O_4$	1·3	—	1·37	⩾1·70 [56])	1
$MgFe_2O_4$	1·1	⩾1·0	0·86	1·1 [57])	0
$Li_{0·5}Fe_{2·5}O_4$	2·6	—	—	—	(2·5)
$ZnFe_2O_4$	0·0	0	—	—	0
$CdFe_2O_4$	0·0	—	—	—	0

*) Natural magnetite

interaction, leads to a saturation moment $(5 + m_{Me^{2+}}) - 5 = m_{Me^{2+}}$. Taking $g_{Me^{2+}} = 2$, then $m_{Me^{2+}} = 2S_{Me^{2+}}$. Comparison of columns (1) and (5) shows that our measurements to a first approximation confirmed Néel's hypothesis.

Braun [12]) has found that $Li_{0·5}Fe_{2·5}O_4$ is completely inverse. Thus for $Fe[Li_{0·5}Fe_{1·5}]O_4$ a saturation moment $7·5 - 5 = 2·5$ is calculated. The agreement with the experimental moment shows that $m_{Fe^{3+}} = 5$, as expected.

There are two different causes for the discrepancies between our values and the values of $2S$:

(1) the ferrites under discussion are not completely inverse;

(2) the g-factor of Me^{2+} is not equal to 2.

The first of these hypotheses was originally proposed by Néel [31]) in order to explain the increase of the saturation moments of $CuFe_2O_4$ on quenching [56]).

If a slowly cooled ferrite is not completely inverse or normal, it has not reached a state of lowest free energy. Thus the ionic distribution will be expected to vary with temperature. The highest entropy would be gained for a completely random arrangement i.e. $Fe_{2/3}Me^{II}_{1/3}[Me^{II}_{2/3}Fe_{4/3}]O_4$.

Thus the general formula of a ferrite $Me^{II}Fe_2O_4$ is

$$Fe_{1-x}Me^{II}_x[Me^{II}_{1-x}Fe_{1+x}]O_4. \qquad (4.1)$$

The theoretical limiting value of x, i.e. $x = \frac{1}{3}$, is in practice not reached at the highest temperature to which the ferrite may be raised without decomposition through reduction

of Fe^{3+} to Fe^{2+}. The value of x will further be determined by the cooling rate. When a ferrite is quenched from a high temperature the equilibrium distribution at the quenching temperature may be frozen in to a large extent.

When the ferrite is cooled slowly, the ionic distribution will adjust itself to maintain equilibrium till the temperature is reached where the ionic diffusion will be too slow to maintain equilibrium during cooling. Thus the distributions actually found are also frozen in, and x depends on the cooling rate.

The moment calculated for formula (4.1) is

$$n_B = 10x + m_{Me^{2+}}(1-2x). \qquad (4.2)$$

We had assumed that if $x \neq 0$ it must change with temperature. We therefore subjected several ferrites to a quenching treatment and found [50]) [49]) that for $MgFe_2O_4$ and $CuFe_2O_4$ the saturation moment is increased by quenching, but that for $NiFe_2O_4$ and $Li_{0.5}Fe_{2.5}O_4$ it remains the same. The results are given in table V.

TABLE V

	treatment	n_B	treatment	n_B
$MgFe_2O_4$	24 h 700 °C	1·1	quenched from 1250 °C	1·4
$CuFe_2O_4$	168 h 360 °C	1·3	quenched from 900 °C	2·3
$NiFe_2O_4$	cooled slowly	2·3	quenched from 1250 °C	2·3
$Li_{0.5}Fe_{2.5}O_4$	„ „	2·47 *)	quenched from 1150 °C	2·50 *)

*) material of section 7 (new data).

For $MgFe_2O_4$ we deduce from (4.2) $x = 0{\cdot}11$ and $x = 0{\cdot}14$ for annealed and quenched samples respectively.

Pauthenet and Bochirol [52]) have since reported measurements of the saturation moments of $MgFe_2O_4$ and $CuFe_2O_4$ quenched from various temperatures. The values of x calculated from (4.2) lie close to a curve representing a Boltzmann distribution formula

$$\frac{x(1+x)}{(1-x)^2} = e^{-E/kT},$$

in which E is the energy needed to bring an ion Me from the B to the A position and a ferric ion back from A to B. Bertaut [10]) had qualitatively confirmed the x values found by Pauthenet and Bochirol by X-ray intensity measurements but the accuracy of the X-ray method (appr. $\pm 0{\cdot}03$ in x according to Bertaut) is very much lower.

Also neutron-diffraction intensities for a sample of $MgFe_2O_4$ with $n_B = 1{\cdot}1$ [57]) show better agreement for $x = 0{\cdot}1_0$ than for $x = 0$ [58]).

For $NiFe_2O_4$ the equality of n_B for quenched and slowly cooled samples lead to the assumption $x = 0$; thus $m_{Ni^{2+}} = 2{\cdot}3$.

Thus we have been led to assume that for $NiFe_2O_4$ the discrepancy between columns (1) and (5) of table IV is due to $g_{Me^{2+}}$ being larger than 2. For $Fe^{II}Fe_2O_4$, $CoFe_2O_4$ and $CuFe_2O_4$ we have also assumed $g_{Me^{2+}} > 2$ in view of the known paramagnetic behaviour of salts containing Fe^{2+}, Co^{2+}, Ni^{2+} and Cu^{2+} ions. The n_B values of $CuFeO_4$ must be accounted for by $g_{Cu^{2+}}$ being larger than 2 as well as by the presence of some Cu^{2+} ions on A sites.

It may be noted that for $Mn^{II}Fe_2O_4$ and $Li_{0{\cdot}5}Fe_{2{\cdot}5}O_4$ the agreement between columns (1) and (5) is very good, in accordance with the fact that $g_{Mn^{2+}} = g_{Fe^{3+}} = 2$, since there is no contribution of the orbital moment.

The g-factors of the magnetic divalent ions may be obtained from measurements of the effective g-factors of the ferrites, when the cation distribution is known. These g-factors will be discussed in section 4.3.1 and such measurements as have been reported in literature will be given.

We shall first discuss the discrepancies between the n_B values found by different authors.

Our own values being obtained for 77 °K and 5900 Oe will generally be expected to be too low. This is especially so for $CoFe_2O_4$, which because of the large crystal and stress anisotropies is far from saturated under these conditions. Our value for Fe_3O_4 is, however, higher than that of other authors. Our preparation contained an excess of Fe^{2+} [50]) [49]). The FeO, originally present next to the spinel, presumably decomposes on cooling through 570 °C and gives Fe + Fe_3O_4. This may just account for the deviation of our value from that given by Pauthenet [51–53]) and Weiss and Forrer [29]). Our value of 2·3 for $NiFe_2O_4$ has been confirmed by measurements extended to liquid-hydrogen temperature and 9000 Oe (see section 8).

Pauthenet reports like ourselves that the saturation moment of $NiFe_2O_4$ does not change measurably on quenching, and finds the same behaviour for $CoFe_2O_4$. The discrepancies between the values for $NiFe_2O_4$ and $CoFe_2O_4$ in columns (2) and (3) might nevertheless be due to very slight differences in ionic distribution, as a very small amount of divalent metal may freeze in on tetrahedral sites during the formation of the spinel.

The only serious discrepancy in table IV is that between the values for $MnFe_2O_4$. Guillaud has prepared three mixed crystals $MnFe_2O_4$-$NiFe_2O_4$ and one MnNiCo ferrite, in all of which the saturation moments agree with that calculated with $m_{Mn^{2+}} = 4{\cdot}60$, $m_{Ni^{2+}} = 2{\cdot}40$, etc., to within 0·05. This according to Guillaud, adds weight to his assumed value $m_{Mn^{2+}} = 4{\cdot}60$.

Another value for $MnFe_2O_4$ since obtained by us is $n_B = 4{\cdot}85$ (section 9). We believe that the discrepancies in the n_B values are real, and that they are related to different cation distributions in the different preparations. The fact that Guillaud's sample was sintered at 1380 °C [54b]) and ours at 1250 °C lends some support to the latter assumption, which should, however, be checked by further experiments.

We cannot, however, account for the fact that for $MnFe_2O_4$ n_B is sometimes below 5. It might be suggested that $(m_{Mn^{2+}})_A > 5$, i.e. that $(g_{Mn^{2+}})_A > 2$ (see section 4.3.1), but a value $n_B = 4{\cdot}6$ would lead to impossibly high values of $(g_{Mn^{2+}})_A$, so that we assume that $(m_{Mn^{2+}})_A = (m_{Mn^{2+}})_B = m_{Fe^{3+}} = 5$.

Another possibility is that part of the Mn^{2+} and Fe^{2+} ions in the B sites change into Mn^{3+} and Fe^{2+} ions ($m_{Mn^{3+}} \approx m_{Fe^{2+}} \approx 4$), which state might be stabilized by the establishment of a higher degree of short-range order between the di- and tri-valent ions, but this seems rather unlikely to us.

Finally it may be that the ionic moments in the B position are not completely parallel. We shall discuss this possibility in section 4.4.

A direct confirmation of Néel's hypothesis of antiparallel moments in A and B positions has been provided by neutron-diffraction experiments on Fe_3O_4 [68]), $NiFe_2O_4$ [69]) and $MgFe_2O_4$ [58]) [70]). Moreover, Fe_3O_4 and $NiFe_2O_4$ were found to be qualitatively inverse, for $MgFe_2O_4$ the ionic distribution was even determined quantitatively [70]) ($x = 0{\cdot}12$).

A discussion of $Zn[Fe_2]O_4$ will be given in section 4.4.

4.3.1. Effective g-factors

Effective g-factors of the ferrites may be determined by microwave absorption measurements [60]). The method used in our laboratory will be described elsewhere [59]).

The specimen (here a sphere of 0·8-0·1 mm diameter) is placed in a cavity in a large external field H_z and a microwave field with angular frequency ω perpendicular to it.

The spins perform a precessional movement around H_z; by the h.f. field the magnetization M_z is decreased by ΔM and the angular momentum J_z by ΔJ. A resonance peak is observed for a fixed angular frequency ω when the field H_z is varied. The resonance condition for a sphere is $\omega = g(e/2mc)H_z$. For polycrystalline materials with random crystallite orientation the influence of crystalline anisotropy on the resonance condition may be neglected, when H_z is large and the crystalline anisotropy is fairly low. Let M be the magnetization and J the angular momentum per unit volume; then Kittel [61]) has shown that

$$g\frac{e}{2mc} = \frac{\Delta M}{\Delta J} = \frac{\Delta(M_{\text{spin}} + M_{\text{orb}})}{\Delta J_{\text{spin}}}. \tag{4.3}$$

As $M_{\text{spin}}/J_{\text{spin}} = e/mc$, and the changes ($\Delta$) in M and J are proportional to their absolute values, one obtains

$$g = \frac{2(M_{\text{spin}} + M_{\text{orb}})}{M_{\text{spin}}} = \frac{2(\text{total magnetic moment})}{\text{spin moment}}. \tag{4.4}$$

For the special case of a ferrimagnetic spinel with antiparallel ionic moments in A and B positions

$$g_{\text{eff}} = 2\,\frac{(M_{\text{total}})_A - (M_{\text{total}})_B}{(M_{\text{spin}})_A - (M_{\text{spin}})_B}. \tag{4.5}$$

Such a spinel containing different magnetic ions i (x ions per formula unit in either position) has at 0 °K

$$g_{\text{eff}} = \frac{\sum_i (x_i g_i S_i)_A - \sum_i (x_i g_i S_i)_B}{\sum_i (x_i S_i)_A - \sum_i (x_i S_i)_B} = \frac{\overrightarrow{\sum_i} x_i g_i S_i}{\overrightarrow{\sum_i} x_i S_i}. \tag{4.6}$$

In his first measurements [62]) Beljers found for $NiFe_2O_4$ $g = 2{\cdot}36$, but it has since been shown that the spheres he used were not small enough. In his later measurements spheres of 0·8 - 0·1 mm diameter, prepared by a method described by Bond [63]), have been used.

g-factor values, reported in literature for several ferrites, are given in table VI.

It is clear from this table that g_{eff}, which for a completely inverse ferrite is equal to $g_{Me^{2+}}$, as is seen from eq. (4.5), can qualitatively account for the discrepancies between the experimental saturation moments of columns (1)-(4) and the figures of column (5) in table IV.

4.4. Saturation moments of the mixed crystals of the ferromagnetic ferrites with zinc ferrite ($Me^{II}_{1-a}Zn_aFe_2O_4$ and $Li_{0\cdot5-0\cdot5a}Zn_aFe_{2\cdot5-0\cdot5a}O_4$)

Verwey and Heilmann have shown that in mixed crystals of $ZnFe_2O_4$ and $CuFe_2O_4$ the divalent ions occupy the same crystallographic positions as in the constituent single ferrites. Assuming the Zn^{2+} ions to occupy the tetrahedral sites only, the mixed crystals of $Zn[Fe_2]O_4$ with a completely inverse ferrite $Fe[Me^{II}Fe]O_4$ have the formula

$$Zn_a\,Fe^{III}_{1-a}[Me^{II}_{1-a}\,Fe^{III}_{1+a}]O_4,$$

which for complete antiparallelism of the ionic moments in the A and B positions respectively gives a saturation moment

$$n_B = m_b - m_a = 10a + (1-a)\,m_{Me^{2+}}, \tag{4.7}$$

TABLE VI

Experimental values of effective g-factors of various single ferrites *)

ferrite	g_{eff}	temperature (°C)	wavelength (cm)	author(s)	sample
$MnFe_2O_4$	2·05	room temp.	1·24	a)	polycryst.
$MnFe_2O_4$	2·16 ↓ 2·02	room temp.	3·14 ↓ 0·64	b)	polycryst.
$FeFe_2O_4$	2·06	—153	3·35	c)	synth.
	2·08; 2·09	—143	3·35; 1·25		single crystals
	2·17; 2·13	20	3·35; 1.25		
$CoFe_2O_4$	broad peak	room temp.	1·24	a)	polycryst.
$CoFe_2O_4$	2·22 ↓ 2·91 ↓ 2·08	100 ↓ 300 ↓ 480	3·2 3·2 3·2	d)	polycryst.
$NiFe_2O_4$	2·21	room temp.	1·24	a)	polycryst.
	2·19	room temp.	1·25	e)	single crystal
	$2{\cdot}25_5$(av.)	—195-588	3·33	f)	polycryst.
	2·43 ↓ 2·12	room temp. room temp.	3·14 ↓ 0·64	b)	polycryst.
$CuFe_2O_4$	2·20; 2·17 ↓ ↓ 2·05; 2·06	—195 ↓ 450	1·25 1·25	g)	single cryst.; polycryst.
$MgFe_2O_4$	2·03-2·06	room temp.	1·24	a)	
$Li_{0.5}Fe_{2.5}O_4$	2·08	room temp.	3·18	h)	

a) W. A. Yager, F. R. Merritt and C. Guillaud, Phys. Rev. **81**, 477-478, 1951.
b) T. Okamura, Y. Torizuka and Y. Kojima, Phys. Rev. **88**, 1425-1426, 1952.
c) L. R. Bickford, Phys. Rev. **76**, 137-138, 1949.
d) T. Okamura, Y. Torizuka and Y. Kojima, Phys. Rev. **84**, 372, 1951.
e) W. A. Yager, J. K. Galt, F. R. Merritt and E. A. Wood, Phys. Rev. **80**, 744-748, 1950.
f) D. W. Healy, Phys. Rev. **86**, 1009-1013, 1952.
g) T. Okamura and Y. Kojima, Phys. Rev. **86**, 1040-1041, 1951.
h) Unpublished value of Mr H. G. Beljers.

*) Results obtained on too large specimens have been disregarded.

in which m_a and m_b represent the resultant moments per formula unit in the A and B positions respectively. When the possibility of the presence of Zn ions in B sites and of Me^{II} ions in A sites is taken into account, the general formula is

$$Zn_{a-y}Fe_{1-a+y-x}Me^{II}_x[Me^{II}_{1-a-x}Zn_yFe_{1+a-y+x}]O_4,$$

with

$$n_B = m_b - m_a = 10a + (1-a)\, m_{Me^{2+}} + (10-2m_{Me^{2+}})x - 10y. \qquad (4.8)$$

Fig. 11 shows the results of our measurements of the saturation moments of the mixed-crystal series

$Mn_{1-a}Zn_a\ Fe_2O_4$,
$Fe_{1-a}\ Zn_a\ Fe_2O_4$,
$Co_{1-a}\ Zn_a\ Fe_2O_4$,
$Ni_{1-a}\ Zn_a\ Fe_2O_4$,
$Cu_{1-a}\ Zn_a\ Fe_2O_4$ (only for $a = 0$ and $a = 0{\cdot}5$),
$Mg_{1-a}\ Zn_a\ Fe_2O_4$,
$Li_{0{\cdot}5-0{\cdot}5a}\ Zn_a\ Fe_{2{\cdot}5-0{\cdot}5a}\ O_4$.

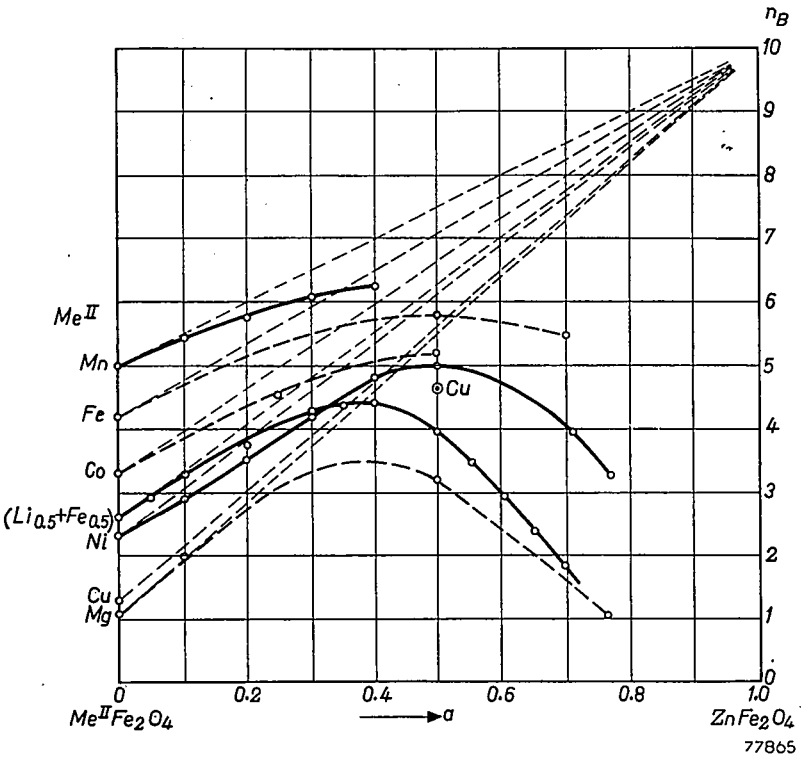

Fig. 11. Saturation moment in Bohr magnetons of various mixed-crystal series $Me^{II}Fe_2O_4$-$ZnFe_2O_4$ (measurements by the author).

The dashed lines represent the n_B values calculated from eq. (4.7), or from eq. (4.8) assuming x to be a constant fraction of $1-a$ and $y = 0$, i.e. assuming the relative distribution of Me^{2+} amongst the tetrahedral and octahedral sites to be unaffected by mixed-crystal formation with $Zn[Fe_2]O_4$.

It is seen that the saturation moments found for small values of the Zn content a indeed increase with a: the initial slopes of the curves in several cases are practically equal to those of the corresponding dashed lines.

The agreement of these slopes is considerably better for the curves obtained by Guillaud for several of these systems (fig. 12), which, as we have seen, were measured using higher fields and lower temperatures, and extrapolated towards $H = \infty$ and $T = 0$ °K.

The latter results prove (at least up to $a = 0{\cdot}4$) that the Zn^{2+} occupies practically exclusively the tetrahedral position and, incidentally, confirms that $m_{Fe^{3+}} = 5$. The distribution of the Zn ions is, however, dependent on temperature: Pauthenet [53]) has measured the saturation moments also of quenched samples of nickel-zinc ferrites up to $a = 0{\cdot}6$, and found that the

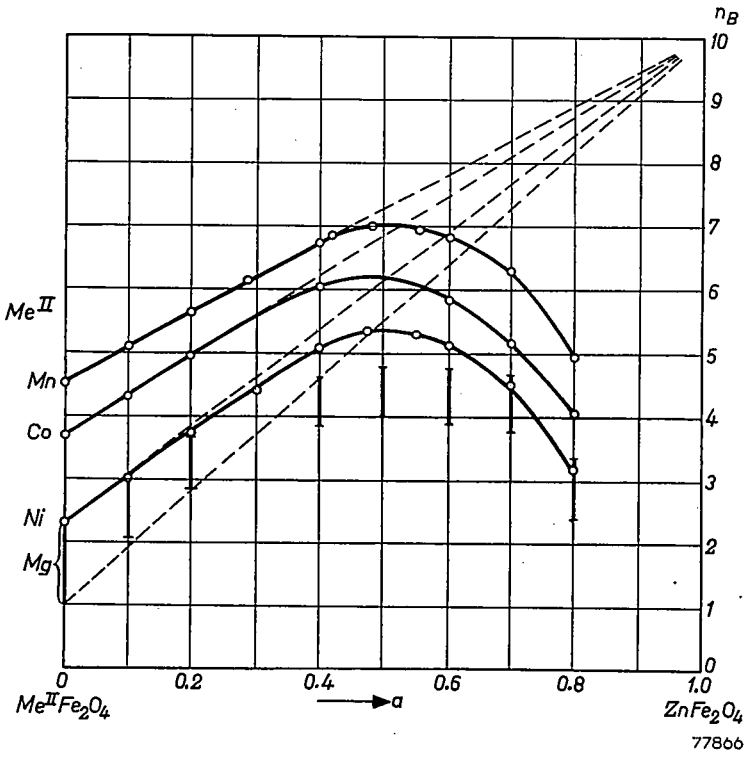

Fig. 12. Saturation moment in Bohr magnetons of various mixed-crystal series $Me^{II}Fe_2O_4$-$ZnFe_2O_4$ (measurements by Guillaud et al.).

slope of the curve then deviates more from the dashed line than for annealed samples. This proves that some Zn^{2+} now occupies the octahedral sites: the difference between the n_B values for annealed and quenched samples is equal to $10y$ (eq. (4.8)).

The decrease of n_B for higher zinc contents as shown in figs 11 and 12 must be explained as follows:

The number of ferric ions in the A position, and thus m_a, decreases with increasing a. Where the straight line $m = m_b - m_a$ intersects the straight line $m = -m_a\ (1 + 1/\gamma_2)$, angles between the ionic moments in the B position start to occur, according to the theory.

The curvature of the n_B vs a curve has been accounted for by Néel [64]) for NiZn ferrites by fluctuations in the ratio of the numbers of Zn^{2+} and Fe^{3+} ions in A sites surrounding different B sites, i.e. by local fluctuations in the AB interaction. In this calculation he used interaction constants derived from his own susceptibility data [65]). Considering the facts that these materials contain two different magnetic ions and that this theory should be modified along the lines of Yafet and Kittel's theory, the agreement is satisfactory. The interaction constant β, or γ_2, need not remain constant: it will depend on the cell edge and on the oxygen parameter and, when Me^{2+} has a magnetic moment, on the relative strengths of the interactions Fe^{3+}-Fe^{3+}, Fe^{3+}-Me^{2+} and Me^{2+}-Me^{2+}, and on the cation distribution.

If the interactions become weaker in the above order, $|\beta|$ or $|\gamma_2|$ will increase as the proportion of the Fe^{3+} ions in the B position increases.

If we would assume that in Guillaud's $MnFe_2O_4$ angles between the moments in the B position occur, eq. (2.19) would give $\gamma_2 = -0{\cdot}52$, whereas for $Zn_{0{\cdot}8}Mn_{0{\cdot}2}Fe_2O_4$ we obtain $\gamma_2 = -0{\cdot}17$. This is in itself an argument against this assumption, since the interactions here indeed become weaker in the order Fe^{3+}-Fe^{3+}, Fe^{3+}-Mn^{2+}, Mn^{2+}-Mn^{2+}.

A more serious objection against the assumption of angles in Guillaud's $MnFe_2O_4$ is the linear increase of n_B with the Zn content a he finds for the MnZn ferrites. Assuming angles to exist and γ_2 to be constant, m should decrease linearly with m_a, i.e. with $1-a$. In order to account for the linear *increase* of m we must assume that $|\gamma_2|$ decreases with a in such a way that the angle $180°-2\psi$ remains very small up to $a = 0{\cdot}5$, which seems very improbable.

If we assume that for $MnFe_2O_4$ $n_B < m_b - m_a$ only as a result of the above-mentioned local fluctuations in the AB interaction, it still remains difficult to explain why this effect should at first decrease with increasing Zn content a.

The decrease of the Curie temperature with $ZnFe_2O_4$ content [54a, c, d])

can also be accounted for by qualitative considerations. The Curie temperature is primarily determined by the strongest interaction(s), i.e. by the AB interaction as long as this is predominant. The Curie temperature will, therefore, decrease with the number of AB interactions, i.e. with increasing a.

It is clear that angles between the ionic moments in the B position will not occur for materials with very high Curie temperatures.

For normal $ZnFe_2O_4$, prepared by annealing, $n_B = 0{\cdot}0$. Here only BB interactions can occur, and an "antiferromagnetic" arrangement will result, probably with different spin directions in each of the four face-centred sublattices in the B position. A Néel temperature has not so far been found.

When $ZnFe_2O_4$ is quenched, it becomes ferromagnetic [67])[55]) with a high Curie temperature (60 °C). This is clearly caused by AB interaction, which occurs as a result of the presence of some Fe^{3+} in the A position, as has been suggested in both papers cited.

Guillaud has suggested that the presence of a certain amount of Zn^{2+} in the B sites as indicated by the intensities of the X-ray diagrams of his NiZn ferrites [55])[66]) may, apart from all other hypotheses, account for the decrease of the n_B vs a curve for large a values. It seems safe to assume that this effect only plays a secondary role. In fact, we shall give examples of materials for which the saturation moment cannot be accounted for at all without the presence of angles between the ionic moments inside the B sublattice (sections 6.4 and 7).

The presence of some Zn ions in the octahedral position must be assumed to account for the following results.

Néel and Brochet [65]) have calculated the ratios of the interactions AA/BB (α) and BB/AB (β) from their susceptibility data for the NiZn ferrites, assuming all Zn^{2+} ions to occupy A sites.

For this case they find extremely high α values for large Zn contents, which according to Anderson's theory are extremely unlikely from geometrical considerations. If it is assumed that a certain small percentage of Zn^{2+} occupies the B positions, α remains small throughout the series of mixed crystals.

REFERENCES

[48]) D. Polder, J. Instn elect. Engrs **97**, (II), 246-256, 1950.
[49]) E. W. Gorter, C. R. Acad. Sci., Paris **230**, 192-194, 1950.
[50]) E. W. Gorter, Nature **165**, 798-800, 1950.
[51]) R. Pauthenet, C. R. Acad. Sci., Paris **230**, 1842-1843, 1950;
L. Néel, C. R. Acad. Sci., Paris **230**, 190-192, 1950.
[52]) R. Pauthenet and L. Bochirol, J. Phys. Radium **12**, 249-251, 1951.
[53]) R. Pauthenet, Ann. Phys., Paris **7**, 710-747, 1952.
[54a]) C. Guillaud and M. Roux, C.R. Acad. Sci., Paris **229**, 1133-1135, 1949.
[54b]) C. Guillaud and H. Creveaux, C. R. Acad. Sci., Paris **230**, 1256-1258, 1950.
[54c]) C. Guillaud and H. Creveaux, C. R. Acad. Sci., Paris **230**, 1458-1460, 1950.
[54d]) C. Guillaud and M. Sage, C. R. Acad. Sci., Paris **232**, 944-946, 1951.
[55]) C. Guillaud, J. Phys. Radium **12**, 239-248, 1951 (or J. Rech. C.N.R.S. nr 12, 1950).
[56]) M. Fallot, unpublished, 1935, cited from L. Néel, [31]).

[57]) G. O. Jones and F. F. Roberts, Proc. phys. Soc. Lond. **B 65**, 390, 1952.
[58]) G. E. Bacon and F. F. Roberts, Acta cryst. **6**, 57-62, 1953.
[59]) H. G. Beljers and J. S. van Wieringen. Physica, forthcoming.
[60]) See e.g. H. G. Beljers and J. L. Snoek, Philips tech. Rev. **11**, 313-322, 1950.
[61]) C. Kittel, Phys. Rev. **76**, 743-748, 1949.
[62]) H. G. Beljers and D. Polder, Nature **165**, 800, 1950.
[63]) W. L. Bond, Rev. sci. Instrum. **22**, 344-345. 1951.
[64]) L. Néel, C. R. Acad. Sci., Paris **230**, 375-377, 1950.
[65]) L. Néel and P. Brochet, C.R. Acad. Sci., Paris **230**, 280-282, 1950.
[66]) M. Sage and C. Guillaud, C. R. Acad. Sci., Paris **230**, 1751-1753, 1950.
[67]) F. G. Brockman, Phys. Rev. **77**, 841-842, 1950.
[68]) C. G. Shull, E. O. Wollan and W. C. Koehler, Phys. Rev. **84**, 912-921, 1951.
[69]) J. M. Hastings and L. M. Corliss, Rev. mod. Phys. **25**, 114-121, 1953.
[70]) L. M. Corliss, J. M. Hastings and F. G. Brockmann, Phys. Rev. **90**, 1013-1018, 1953.

5. EXPERIMENTS ON THE ANGLE DEPENDENCE OF THE SUPER-EXCHANGE INTERACTION

5.1. The angle *A*-O-*B* in spinels

5.1.1. Introduction

The results obtained in many mixed-crystal series, discussed in the previous section, showed that the *BB* interaction was much weaker than the *AB* interaction. Theoretical background for this behaviour was at the time not available *).

Kramers's theory of the superexchange interaction [71]) gave no explicit indications about the order of magnitude of the superexchange interaction, nor about its dependence on the geometrical configuration. Néel, therefore, originally made a crude assumption, called by himself "*certainement inexacte*", that all superexchange interactions Me-O-Me are of equal strength for nearest neighbours Me-Me, and that the *BB* interaction is weak because a direct *positive* interaction Me-Me is active simultaneously with the negative superexchange interaction Me-O-Me.

We supposed that the angle *A*-O-*B* being larger than the angle *B*-O-*B* might play an important role.

The angle *A*-O-*B* varies with the parameter *u*, and *u* might be influenced by the size of the ions. Thus the angle *A*-O-*B* might be increased by incorporating a large ion in the *B* position.

We have therefore tried to incorporate Ca^{2+} ions in the spinel structure. $CaFe_2O_4$ is a well-defined compound but has no spinel structure: the crystal structure is up to now unknown [72]). We found, however, that at high temperatures over a third of the Zn^{2+} ions in $ZnFe_2O_4$ may be replaced by Ca^{2+} ions; these mixed crystals do not decompose when quenched.

It was believed that the Ca^{2+} ions would have a much greater preference for sixfold coordination than Mg^{2+} ions, as in many oxides Ca^{2+} occurs in sixfold or higher coordination.

We supposed that in these CaZn ferrites the large Ca^{2+} ions in the *B* position would cause the *BB* interaction to be less able to compete with the *AB* interaction than in other corresponding ferrites, i.e. that the CaZn ferrites would have higher saturation moments.

5.1.2. CaZn ferrite

5.1.2.1. *Experimental*

Materials with the composition $a\ CaO.(1-a)ZnO.1Fe_2O_3$ were prepared, with $a = 0{\cdot}20$, $0{\cdot}30$, $0{\cdot}35$, $0{\cdot}40$, $0{\cdot}50$, $0{\cdot}90$ and $1{\cdot}00$.

*) The magnetic measurements to be given in section 5.1.2.1. were performed after publication of the results described in section 4.4, but before Anderson's theory was known to the author.

The materials were prepared from
$CaCO_3$ (p.a. Merck),
ZnO (Pb 0·01 %, Mg < 0·01 %),
Fe (C 0·03 %),
by method (C), pref. 2 h 1000 °C, milling 4 h. The preparations were sintered at various temperatures and either slowly cooled or quenched.

The X-ray diagrams showed the following results (table VII).

TABLE VII

Phases found for preparations $a\,CaO.(1-a)ZnO.1Fe_2O_3$

$a =$	1·00	0·90	0·50	0·40	0·35	0·30	0·20
heat treatment	phase(s)						
1200 °C cooled slowly	$CaFe_2O_4$*)		spinel+$CaFe_2O_4$ and/or α-Fe_2O_3				
1250 °C cooled slowly	*melts* ($CaFe_2O_4$)		,,				
1300 °C cooled slowly	—	—	—	—	*melts* spinel (+α-Fe_2O_3)	spinel +α-Fe_2O_3	spinel
1250 °C quenched	—	—	$CaFe_2O_4$ + spinel		spinel	spinel+α-Fe_2O_3	
1280 °C quenched	—	—	*melts*	spinel +tr.$CaFe_2O_4$	spinel	spinel	
1300 °C quenched	—	—	—	—	*melts*	spinel	

*) An identical pattern is obtained after quenching from 1200 °C.

These results show:

(1) At 1280 °C and 1300 °C equilibrium is obtained for all compositions, but up to 1250 °C no complete reaction is obtained at least for $a = 0{\cdot}20$.

(2) The preparations with $a = 0{\cdot}30$ and $a = 0{\cdot}35$ are pure spinels at $\geqslant$ 1280 °C, but separate into two phases at lower temperatures: only the preparation with $a = 0{\cdot}20$ does not separate into two phases during cooling at the rate used by us.

(3) The temperature for which melting of at least part of the material occurs decreases with increasing a. Only the preparations quenched from 1280 °C are sintered pure spinels for $a = 0{\cdot}20$-$0{\cdot}35$.

The preparations for which partial melting occurs were not all investigated because the alumina support was slightly porous, so that the correct total composition was not maintained.

Amongst the pure spinels obtained by sintering, those with $a = 0{\cdot}35$, i.e. with the formula $Ca_{0{\cdot}35}Zn_{0{\cdot}65}Fe_2O_4$, obtained by quenching from 1250 °C and 1280 °C gave by far the highest saturation moment (5·30) [74])

and Curie temperature (appr. 300 °C). After heating to the Curie temperature the saturation moment had decreased by 3%, which is an indication of the instability of this composition at low temperatures.

The results for the other spinels are not given here; the saturation moments are below 1·0.

Recently Mr P. B. Braun has made an attempt to determine the cation distribution of $Ca_{0.35}Zn_{0.65}Fe_2O_4$. The intensities observed with a Norelco High-angle X-ray Diffractometer, using Mo $K\alpha$ radiation are given in table VIII.

TABLE VIII

Σh^2	3	8	11	12	16	19	24	27	32
observed	28	102	383	25	62	$\leqslant 1$	41	116	147
calculated	28	112	372	23	71	0	38	114	150

The amount of Ca^{2+} ions in the tetrahedral position per formula unit (t) could not be determined from the present data, because for Mo radiation the scattering power of Fe^{3+} is just intermediate between those of Zn^{2+} and Ca^{2+}.

We therefore write the general formula as follows:

$$Ca_t Zn_{s+t} Fe_{1-s-2t} [Ca_{0.35-t} Zn_{0.65-s-t} Fe_{1+s+2t}] O_4 , \qquad (5.1)$$

in which s could be determined. The best agreement with the observed intensities was found for $s = 0{\cdot}30 \pm 0{\cdot}05$; the intensities calculated for $s = 0{\cdot}30$ are given in table VIII.

The oxygen parameter $u = 0{\cdot}382 \pm 0{\cdot}005$, and slightly decreases with increasing t. The cell edge $a = 8{\cdot}49_5$ Å.

5.1.2.2. *Discussion*

The saturation moment of quenched $Ca_{0.35}Zn_{0.65}Fe_2O_4$ has been given previously. Originally we compared its value ($n_B = 5{\cdot}30$) with that of $Ni_{0.35}Zn_{0.65}Fe_2O_4$ ($n_B = 4{\cdot}8$) [73] [74]) and assumed that all Ca^{2+} ions occupy B sites. The latter assumption has now been proved to be wrong, but also the comparison with the Ni compound is not appropriate, because the replacement of non-magnetic Ca^{2+} by magnetic Ni^{2+} ions will increase the BB interaction more than the AB interaction, i.e. increase $|\beta|$ or $|\gamma_2|$ in the theory for one type of magnetic ion, quite apart from any effect of ionic size.

In the discussion that follows we shall show that the X-ray results since obtained neither prove nor disprove the picture previously proposed.

The general formula for the CaZn and MgZn ferrites is

$$Me^{II}_x Fe_{1-x} [Me^{II}_{1-x} Fe_{1+x}] O_4 , \qquad (5.2)$$

in which Me^{II} represents any mixture of two of the diamagnetic ions Mg^{2+}, Ca^{2+} or Zn^{2+}; x is not known.

The saturation moment is $n_B = 10x$ for antiparallel moments in A and B sites, or below $10x$ when the moments in the B sites are no longer mutually parallel.

It follows that for the CaZn ferrite with $n_B = 5{\cdot}3$, $x \geqslant 0{\cdot}53$ and for the MgZn ferrite with $n_B = 4{\cdot}7$, $x \geqslant 0{\cdot}47$.

For the MgZn ferrites it seems reasonable to assume that γ_2 is independent of an interchange of Mg^{2+} and Zn^{2+} ions between A and B sites, in view of the almost equal ionic radii, so that γ_2, and therefore n_B, will be practically only dependent on x.

A curve n_B vs x for MgZn ferrites has been schematically represented in fig. 13 (I), using a value of γ_2 deduced from $n_B = 3$ for $Zn_{0{\cdot}8}Mg_{0{\cdot}2}Fe_2O_4$, using eq. (2.19) and assuming arbitrarily that in the latter material $x = 0{\cdot}82$, i.e. that e.g. all Zn^{2+} ions and 10 % of the Mg^{2+} ions occur in A sites.

The radius of curvature of this curve is determined by the local fluctuations in the AB interactions, and since these radii are similar for different

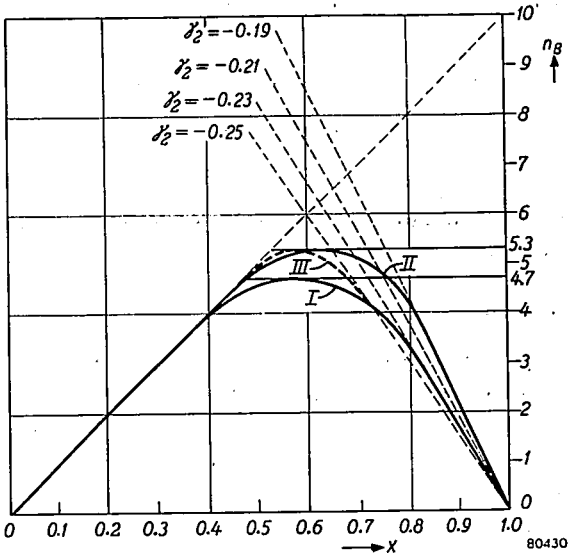

Fig. 13. Schematic representation of saturation moments for materials $Fe_{1-x}\,Me_x[Me_{1-x}\,Fe_{1+x}]O_4$, with Me = non-magnetic ion.
Curve I: Guillaud's experimental saturation moments for MgZn ferrites, schematically redrawn not against the Zn content, but against x.
Curve II: schematic curve drawn through a maximum $n_B = 5{\cdot}3$ with similar radius of curvature as curve I, in order to evaluate γ_2 for $Ca_{0{\cdot}35}Zn_{0{\cdot}65}Fe_2O_4$: γ_2 is then larger than for the MgZn ferrites.
Dashed curve III: schematic curve for $Ca_{0{\cdot}35}Zn_{0{\cdot}65}Fe_2O_4$ with smaller γ_2 than for the MgZn ferrites: the radius of curvature is then very small and therefore unlikely.

MeZn-ferrite series (fig. 12), we have drawn a schematic curve II through a maximum $n_B = 5{\cdot}3$ with a similar radius of curvature for our CaZn ferrite, in order to evaluate γ_2.

It is seen that a lower value of $|\gamma_2|$ is thus obtained than for the MgZn ferrites. Only if the radius of curvature is very much smaller (dashed curve III) would $|\gamma_2|$ be larger than for the MgZn ferrites.

We are tempted to conclude that for the CaZn ferrite $|\gamma_2|$ is indeed smaller than for the MgZn ferrites.

This is what we expected for the presence of the greater part of the large Ca^{2+} ions in the B position, i.e. for $t \leqslant 0{\cdot}17_5$. For $t \geqslant 0{\cdot}17_5$ we expected $|\gamma_2|'$ to be larger than for the MgZn ferrites.

The minimum value of t is obtained from the X-ray and magnetic measurements: $x = s + 2t \geqslant 0{\cdot}53$, in which $s = 0{\cdot}30 \pm 0{\cdot}05$, gives $t \geqslant 0{\cdot}11_5 \pm 0{\cdot}02_5$.

The values of x for which t is $<$ or $> 0{\cdot}17_5$ are deduced from $x = s + 2t$:
$t < 0{\cdot}17_5$ for $x < 0{\cdot}60$;
t either $<$ or $> 0{\cdot}17_5$ for $0{\cdot}60 < x < 0{\cdot}70$;
$t > 0{\cdot}17_5$ for $x > 0{\cdot}70$.

For $x < 0{\cdot}60$ the radius of curvature of the n_B vs x curve would be very small: this is very unlikely, so that we cannot prove that $t < 0{\cdot}17_5$. For $x > 0{\cdot}70$ the radius of curvature would probably be too large, so that a value $0{\cdot}60 < x < 0{\cdot}70$ is most likely. This means that we can only say that the possibility $t < 0{\cdot}17_5$ is not excluded.

The error in the oxygen parameter $u = 0{\cdot}382 \pm 0{\cdot}005$ does not exclude this possibility either.

The fact that the saturation moments of the CaZn ferrites with higher Zn contents are below 1 is no proof either against the picture of large ions influencing the angle A-O-B an thereby the ratio of the interaction BB/AB, because in these materials the values of x may be much larger.

5.2. Prediction of magnetic behaviour in other crystal structures from Anderson's theory

5.2.1. Introduction

Anderson's theory provides a useful rule of thumb for predicting the saturation moments of ferrimagnetics when the crystal structure is known: when one kind of magnetic ions is present, the strength of the interactions increases with the angle Me-O-Me from a minimum for 90° to a maximum for 180°; the strength of the interactions, moreover, decreases rapidly with the distances Me-O.

In crystal structures such as the spinel structure and the structures to be discussed in the present section the oxygen ions form an approximately close-packed arrangement with the cations fitting in the interstices. All shortest distances Me-O, therefore, will be of the same order of magnitude (like p and q in the spinel structure, see table I).

The relative directions of the ionic moments in ferrimagnetics, i.e. for the case that only negative interactions occur, may be found by allocating an arbitrary direction to an arbitrary ionic moment, and by

placing antiparallel to it the moments of those surrounding ions for which the angle Me-O-Me is largest and for which the distances Me-O are those of nearest neighbours, say 2·5 Å.

We have applied this rule to some compounds with hexagonal crystal structures, viz. $BaFe^{III}_{12}O_{19}$, $KFe^{III}_{11}O_{17}$ and $BaFe^{II}_{2}Fe^{III}_{16}O_{27}$ [78]).

5.2.2. Application to $BaFe^{III}_{12}O_{19}$ and $KFe^{III}_{11}O_{17}$

The hexagonal unit cells of $BaFe^{III}_{12}O_{19}$ (or $BaO.6Fe_2O_3$) and of $KFe^{III}_{11}O_{17}$ (or $K_2O.11Fe_2O_3$) are shown schematically in fig. 14. The "spinel blocks" consist of 4 horizontal planes containing 4 oxygen ions each, with the cations between these planes. The ionic positions in these "blocks" are not shown: apart from slight differences in parameters they

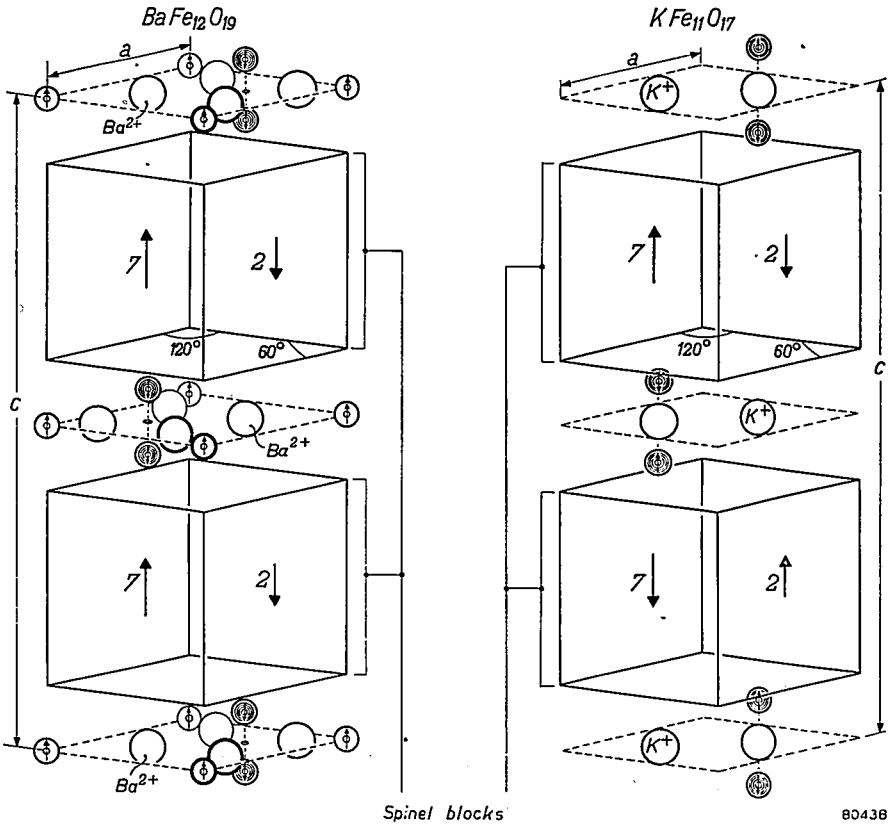

Fig. 14. Unit cells of $BaFe_{12}O_{19}$ and $KFe_{11}O_{17}$ (schematically). Large circles denote oxygen ions, or K^+ or Ba^{2+} ions where indicated; small circles represent ferric ions. The ionic positions inside the "spinel blocks" are not shown: each block contains 4 horizontal planes containing 4 oxygen ions each; between these planes 9 Fe^{3+} are situated, of which 7 have ionic moments pointing in one direction and 2 ionic moments in the opposite direction.

are identical with those in the spinel lattice, with vertical orientation of the [111] axis *).

$BaFe_{12}O_{19}$ *) is isomorphous [75]) with the mineral magnetoplumbite, which has the approximate composition $Pb(Fe_{7\cdot5}Mn_{3\cdot5}Al_{0\cdot5}Ti_{0\cdot5})O_{19}$ [76]). The crystal structure of this mineral was determined by Adelsköld [75]). $KFe_{11}O_{17}$ *) is isomorphous [75]) with "β-alumina", $NaAl_{11}O_{17}$, the structure of which was determined by Beevers and Ross [77]).

The average distances between the horizontal oxygen planes *), and the oxygen-oxygen distances inside the oxygen planes *) are compared with those for a spinel with $a = 8{\cdot}35$ Å (an average cell edge for a ferrite) in table IX.

TABLE IX

Comparison of dimensions in the structures of $BaFe_{12}O_{19}$ and $KFe_{11}O_{17}$ with those of a spinel with $a = 8{\cdot}35$ Å.

structure	c (Å)	a (Å)	average distance between O planes (Å)	distances O-O in O planes (Å)
$BaFe_{12}O_{19}$	$23{\cdot}21_5$**)	5.891**)	$\frac{1}{10}c = 2{\cdot}321_5$	$\frac{1}{2}a = 2{\cdot}945_5$
$KFe_{11}O_{17}$	$23{\cdot}73_9$**)	5·932**)	$\frac{1}{10}c = 2{\cdot}374$	$\frac{1}{2}a = 2{\cdot}966$
spinel	—	(8·35)	$\frac{1}{6}a\sqrt{3} = 2{\cdot}41_0$	$\frac{1}{4}a\sqrt{2} = 2{\cdot}95_2$

**) Values determined by Mr P. B. Braun. These values closely agree with those found by Adelsköld after conversion of the latter from kX into Ångström units.

The slight differences in dimensions shown, and the slight differences in parameter values, which undoubtedly occur but have not been accurately determined, are too small to have any influence on the application of the rule of thumb.

The difference between the two structures is apparent from fig. 14. In the unit cell of the Ba compound the planes containing the Ba^{2+} ion contain in addition three O^{2-} ions, thus giving a twelvefold coordination of the Ba^{2+} ion by oxygen ions, and one Fe^{3+} ion. In the unit cell of the K compound the corresponding planes contain in addition to the K^+ ion only one O^{2-} ion, thus giving a ninefold coordination for the K^+ ion, as has been found in other compounds.

*) For comparison of the complete unit cells see ref. [78]), part III, fig. 2.

Saturation-magnetization measurements have been made on oriented single crystals of $BaFe_{12}O_{19}$ [78]) *) and susceptibility measurements on these [78]) and on a polycrystalline specimen of $KFe_{11}O_{17}$. The results may be compared in fig. 15.

$KFe_{11}O_{17}$ was originally prepared by decomposing a solution of K and Fe^{III} nitrates in the stoichiometric proportion, obtained by dissolving in nitric acid

K_2CO_3 (p.a. Merck),
Fe (C 0·03 %).

After prefiring at 800 °C in O_2, milling and sintering for 2 h at 1200 °C in O_2, X-ray diagrams of the resulting preparations, obtained on a Norelco High-angle X-ray Diffractometer, showed strong α-Fe_2O_3 reflexions in addition to those of $KFe_{11}O_{17}$. The preparation became ferromagnetic in humid air, presumably through the presence of $KFeO_2$, which is known to react with water to give γ-Fe_2O_3.

The material was then treated with excess KNO_3 solution, dried, milled and sintered 2h at 1200 °C in O_2: the resulting material shows only $KFe_{11}O_{17}$ reflexions and is stable in humid air.

There is a striking difference in magnetic properties between the two materials: $BaFe_{12}O_{19}$ shows ferromagnetic behaviour with an extrapolated saturation moment of 40 *) (Bohr magnetons) per unit cell. $KFe_{11}O_{17}$ shows antiferromagnetic behaviour (fig. 15). This can be explained by the small difference between the two structures described above and shown in fig. 14. In the Ba compound the pairs of adjacent ferric ions on both sides of the Ba plane (indicated by ◎) have parallel ionic moments, because the (negative) interactions ◎-oxygen-○ outweigh the ◎-oxygen-◎ interaction, as the angle is nearer to 180° in the former case. In the K compound there is only a large negative interaction ◎-oxygen-◎ between these pairs, so that the ionic moments are antiparallel.

The resultant moments of the spinel blocks are antiparallel to the moments of the adjacent ions, so that in the Ba compound these resultant moments are parallel to those of adjacent blocks, but in the K compound antiparallel.

For the complete unit cells this gives an arrangement $\overrightarrow{16\ Fe^{3+}}\ \overleftarrow{8\ Fe^{3+}}$ with a saturation moment $n_B = 40$ for $BaFe_{12}O_{19}$, and an arrangement $\overrightarrow{11\ Fe^{3+}}\ \overleftarrow{11\ Fe^{3+}}$ with a saturation moment $n_B = 0$ for $KFe_{11}O_{17}$. The agreement between experimental and theoretical values shows that the saturation moment of $BaFe_{12}O_{19}$ may be accounted for without assuming angles to occur between the ionic moments inside one of the sublattices. The $1/\chi$ vs T curve (fig. 15, curve II) shows the hyperbolic shape characteristic of ferrimagnetics.

*) Recent measurements on polycrystalline $BaFe_{12}O_{19}$ at liquid-hydrogen temperature and in fields up to 26000 oersteds show that σ_0 is very near to 100 $cgs_{magn}\cdot cm^3/g$, i.e. that $n_B = 40$ (A. L. Stuyts and P. Jongenburger, to be published).

The $1/\chi$ curve of $KFe_{11}O_{17}$ (fig. 15, curve III) shows a break at about 530 °C: this is almost certainly the antiferromagnetic Néel temperature. In view of the above discussion it is not surprising that this is situated near, i.e. slightly above, the Curie temperature of $BaFe_{12}O_{19}$.

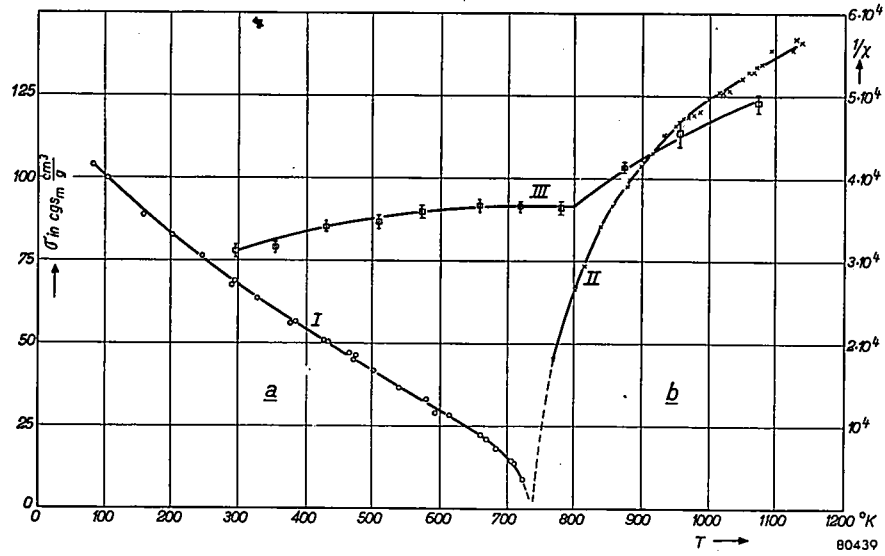

Fig. 15. Magnetic properties of $BaFe_{12}O_{19}$ and $KFe_{11}O_{17}$ as a function of temperature.
Curve I: saturation magnetization (σ) of $BaFe_{12}O_{19}$ (left-hand scale).
Curve II: the inverse of the susceptibility per gram ($1/\chi$) for $BaFe_{12}O_{19}$ above the Curie temperature (right-hand scale).
Curve III: the inverse of the susceptibility per gram ($1/\chi$) for $KFe_{11}O_{17}$ (right-hand scale).

The anomalous slope of the $1/\chi$ vs T curve of $KFe_{11}O_{17}$ below the Néel temperature cannot at present be accounted for. Above the Néel temperature the measurements have not been extended to high enough temperatures to show whether a hyperbola-like curvature, as found for ferrimagnetics, occurs here. From the fact that the tangent to the curve at high temperatures must intersect the T-axis below 0 °K, because all interactions are negative, it may be deduced that such a curvature indeed occurs.

It may be noted that $KFe_{11}O_{17}$ is not an ordinary antiferromagnetic, because inside fairly large regions (viz. the spinel layers) the antiferromagnetism is non-compensated, so that the magnetic behaviour may well be different from that of other antiferromagnetics.

We cannot at present account for the practically linear slope of the σ-T curve of $BaFe_{12}O_{19}$ (fig. 15, curve I).

A theoretical treatment like Néel has given for a lattice containing two sublattices, in order to evaluate the various interaction constants, is very difficult, as the $BaFe_{12}O_{19}$ lattice contains five crystallographically different sublattices [78]). Even if only those interactions involving shortest distances Me-O are taken into account, there are still six different interactions.

We wish to draw attention to a difference beween the $BaFe_{12}O_{19}$ and spinel structures that may have a bearing on this problem.

We have seen (section 2.3.4) that the geometry of the spinel lattice is such that the AB interaction is predominant with respect to the AA and BB interactions.

In $BaFe_{12}O_{19}$ one of the interactions that do not determine the orientation of the ionic moments is probably still fairly strong: the interaction between the sublattices ⊙ and ◍ ([78]), part II, fig. 2*a*), which have parallel ionic moments as a result of the predominant (negative) interactions ⊙ - ◉ and ◉ - ◍, must be fairly strong, since the angle ⊙ - oxygen - ◍ is approximately 125°.

Néel's simple theory for one type of magnetic ion distributed amongst two sublattices shows (see fig. 8) that anomalous σ-T curves (including practically linear ones, which occur between types f and g) occur in a wider range of x_a/x_b, as $|\beta|$ is larger and $|\alpha|$ smaller (or vice versa).

It may be suggested that the existence of one strong "competing" interaction in $BaFe_{12}O_{19}$ causes the linear curve to occur for full occupation by magnetic ions of all sublattices.

5.2.3. Application to $BaFe_2^{II}Fe_{16}^{III}O_{27}$

Another compound has been reported [78]) with an analogous crystal structure, viz. $BaFe_2^{II}Fe_{16}^{III}O_{27}$, or $BaO.2FeO.8Fe_2O_3$, or $BaFe_{12}O_{19}.2Fe_3O_4$. The crystal structure, which was determined by Braun [79]), differs from that of $BaFe_{12}O_{19}$ mainly in that the spinel layer is thicker: two formula units $Fe^{II}Fe_2^{III}O_4$ are inserted in each spinel "block" in the unit cell (see [78]) part III, fig. 2*c*).

The saturation magnetization of this compound has been measured on a single crystal, prepared by Wijn by a high-frequency melting technique described elsewhere [80]).

The saturation moment found is about $n_B = 48$ per unit cell *), whereas we calculated $n_B = 56$, assuming the Fe^{2+} ions to occupy octahedral sites inside the spinel blocks, i.e. for an arrangement $\overrightarrow{20\,Fe^{3+}}\ \overrightarrow{4Fe^{2+}}\ \overleftarrow{12Fe^{3+}}$.

Other antiparallel arrangements for which n_B is nearer to 48 (e.g. 44) are very unlikely.

*) Measurements at liquid-hydrogen temperature and in high fields are so far lacking.

REFERENCES.

[71]) H. A. Kramers, Physica **1**, 182-192, 1934.
[72]) A. Burdese, Ric. Sci. **22**, 259-264, 1952.
[73]) J. Phys. Radium **12**, 237-238, 1951.
[74]) E. J. W. Verwey, P. B. Braun, E. W. Gorter, F. C. Romeijn and J. H. van Santen, Z. phys. Chem. **198**, 6-22, 1951.
[75]) V. Adelsköld, Arkiv Kemi, Min. Geol. **12A**, No 29, 1-9, 1938.
[76]) L. G. Berry, Amer. Min. **36**, 512-514, 1951.
[77]) C. A. Beevers and M. A. S. Ross, Z. Kristallogr. **97**, 57-66, 1937.
[78]) J. J. Went, G. W. Rathenau, E. W. Gorter and G. W. van Oosterhout, Philips tech. Rev. **13**, 194-208, 1952.
[79]) P. B. Braun, Nature **170**, 708, 1952.
[80]) H. P. J. Wijn, Nature **170**, 707, 1952.

 Philips Res. Rep. 9, 366-376, 1954

A GENERAL ASYMPTOTIC SOLUTION OF REACTION EQUATIONS COMMON IN SOLID-STATE CHEMISTRY

by G. BROUWER 541.127-162(076.2)

Summary

A theory of the chemistry of semiconductors, given recently by Kröger, Vink and Van den Boomgaard, is based on a number of reaction equations and certain additional conditions, including electroneutrality. A simple way to find an analytical or graphical approximate solution of this set of equations is presented in this report. Two examples are given; the method, however, is not restricted to these systems. The accuracy of the method is quite sufficient to serve its purpose.

Résumé

Kröger, Vink et Van den Boomgaard ont proposé une nouvelle théorie sur la chimie des semi-conducteurs. Cette théorie se sert d'un nombre d'équations de réaction et de certaines conditions additionnelles, dont la condition de neutralité du réseau du semiconducteur. On donne une méthode d'approximation pour résoudre le système d'équations, qui peut être analytique ou bien graphique. La méthode est appliquée à deux systèmes et elle est tout à fait générale. Le degré d'approximation est bien suffissant pour réaliser le but.

Zusammenfassung

Eine kürzlich von Kröger, Vink und Van den Boomgaard gegebene Theorie der Chemie der Halbleiter gründet sich auf eine Anzahl Reaktionsgleichungen und gewisse Nebenbedingungen, wie zum Beispiel die der Elektroneutralität. Der Artikel bietet eine einfache Methode zur annäherungsweisen Lösung dieser Gleichungen auf analytischen oder graphischem Wege. Es werden zwei Beispiele gegeben; die Methode beschränkt sich jedoch nicht auf diese Systeme. Die Genauigkeit dieser Methode genügt völlig ihrem Zweck.

1. Introduction

Kröger, Vink and Van den Boomgaard [1]) have put forward a theory of the incorporation of vacancies in the lattice of a semiconductor as a result of heating in a certain atmosphere or adding foreign elements. First a brief summary of this theory will be given.

In a CdS crystal, for example, containing a known concentration of Ag^+ and Ga^{3+} ions, the following electronic levels are to be distinguished: Cd^+ or a free electron; S^- or a free hole; $Cd^+(Ga^{3+})$ being an electron bound to the Ga^{3+} centre and leaving an empty $Cd^{2+}(Ga^{3+})$ as it becomes ionized; $S^{2-}(Ag^+)$ being an occupied Ag centre, leaving $S^-(Ag^+)$ as the electron returns to the full band; a number of S vacancies with various

degrees of occupation: V_A, V_A^- and V_A^{2-}; the same for Cd vacancies: V_C^{2+}, V_C^+ and V_C. At the temperature at which the crystals are grown or tempered the levels V_C, V_A^{2-} and $Cd^+(Ga^{3+})$ are completely ionized. Thus these levels are not different from Cd^+ and are subsequently all denoted by the same symbol Cd^+. Next, the equations governing the concentrations of the remaining nine electronic states are to be formulated. The following nine reaction equations are valid for a crystal in high-temperature equilibrium with the atmosphere defined by the cadmium pressure P_{Cd}:

(a) $$\log K_R P_{Cd} = \log [V_A] + 2 \log [Cd^+],$$

describing the generation of S vacancies by incorporation of excess Cd drawn from the atmosphere and the reverse process; K_R is the reaction constant.

(b) $$\log K_S = \log [V_A^-] + \log [V_C^+],$$

which is a way to express the formation and annihilation of vacancies of opposite type.

(c) $$[Cd^+] + [S^{2-}(Ag^+)] + [V_C^+] = [S^-] + [V_A^-] + 2[V_A] + [Cd^{2+}(Ga^{3+})]$$

being the electro-neutrality condition; as all Ga^{3+} centres are assumed to be empty, we may substitute:

(d) $$[Cd^{2+}(Ga^{3+})] = [Ga^{3+}].$$

(e) $$[S^{2-}(Ag^+)] + [S^-(Ag^+)] = [Ag^+],$$

stating that the sum of the concentrations of both occupied and unoccupied Ag levels is equal to the Ag^+ concentration.

(f) $$\log K_i = \log [Cd^+] + \log [S^-],$$

the equation formulating the generation and annihilation of electron-hole pairs.

(g) $$\log K_5 + \log [V_A^-] = \log [Cd^+] + \log [V_A],$$

in which the transition of an electron from the V_A^- level to the conduction band is accounted for.

(h) $$\log K_3 + \log [V_C^+] = \log [Cd^+] + \log [V_C^{2+}],$$

a similar electron transition from a V_C^+ level.

(j) $$\log K_6 + \log [S^{2-}(Ag^+)] = \log [S^-(Ag^+)] + \log [Cd^+],$$

the same for a $S^{2-}(Ag^+)$ level.

From these expressions we readily derive eqs (1)-(6) and (41)-(48),

enabling us to compute the various concentrations of levels at high temperatures. The composition of the crystal after rapidly cooling may be determined by the redistribution process of electrons as proposed by Kröger, Vink and Van den Boomgaard [1]).

The calculation of the high-temperature equilibrium by approximation methods is to be the subject of this paper.

2. Asymptotic solution of the system CdS-Ga

The general equations describing the high-temperature equilibrium, as stated in the preceding section, may be simplified because of the absence of Ag in the case treated here.

Thus, after some minor algebraic operations, we arrive at the following conditions:

$$\log [V_A] = \log K_R P_{Cd} - 2 \log [Cd^+], \quad (1)$$

$$\log [S^-] = \log K_i - \log [Cd^+], \quad (2)$$

$$\log [V_A^-] = \log K_R P_{Cd} - \log [Cd^+] - \log K_5, \quad (3)$$

$$\log [V_C^+] = -\log K_R P_{Cd} + \log [Cd^+] + \log K_5 K_S, \quad (4)$$

$$\log [V_C^{2+}] = -\log K_R P_{Cd} + \log K_3 K_5 K_S, \quad (5)$$

$$[Cd^+] + [V_C^+] = [S^-] + 2[V_A] + [V_A^-] + [Ga^{3+}]. \quad (6)$$

The following constants are inserted:

$$\log K_i = 34{\cdot}0,$$
$$\log K_S = 32{\cdot}3,$$
$$\log K_5 = 17{\cdot}5,$$
$$\log K_3 = 15{\cdot}0.$$

Now we want to plot all logarithms of concentrations as a function of $\log K_R P_{Cd}$. If only the reaction equations (1)-(5), being of a logarithmic type, were to be considered, this could easily be done. Equation (6), representing the neutrality condition is, however, of a linear type and will therefore frustrate our aims. The main issue of this report is to show how this problem can be dealt with.

Suppose we were able to divide the $\log K_R P_{Cd}$ axis in such regions that only one concentration on opposite sides of the equality sign in the neutrality condition were to be considered, all other quantities being negligible. Then we could easily transform this equation into a similar type as the reaction equations by simply taking the logarithm of both main concentrations. In the region mentioned we would then get a linear approximation consisting of a pattern of straight lines, the equations of which might readily be derived. The task remains to show that actually such a division can be made generally.

Although the method may be regarded as a purely mathematical operation, chemical understanding of the system will guide us in our choice of the division.

We now return to the system CdS-Ga. From the chemical point of view we expect a tendency of cation vacancies and holes to decrease, and of anion vacancies and electrons to increase with $\log K_R P_{Cd}$. Thus for extremely low values of $\log K_R P_{Cd}$ all concentrations but $[V_C^+]$ and $[S^-]$ will lose their importance in the neutrality relation, as atmosphere-induced vacancies surpass those induced by incorporation of Ga. Holes effect charge compensation. As long as this situation persists the problem can be described by a linear system of logarithmic equations (1)-(5) together with the neutrality condition in the simplified form

$$\log [V_C^+] = \log [S^-], \tag{7}$$

leading to the result:

$$\log [Cd^+] = \tfrac{1}{2} \log (K_i K_R P_{Cd} / K_S K_S), \tag{8}$$

$$\log [S^-] = \tfrac{1}{2} \log (K_S K_S K_i / K_R P_{Cd}), \tag{9}$$

$$\log [V_C^+] = \tfrac{1}{2} \log (K_S K_S K_i / K_R P_{Cd}), \tag{10}$$

$$\log [V_C^{2+}] = \log (K_3 K_S K_S / K_R P_{Cd}), \tag{11}$$

$$\log [V_A^-] = \tfrac{1}{2} \log (K_S K_R P_{Cd} / K_S K_i), \tag{12}$$

$$\log [V_A] = \log (K_S K_S / K_i). \tag{13}$$

This result can be plotted, although we still have to determine the region of validity (fig. 1, region 1). Let us assume the Ga content to be 10^{19}

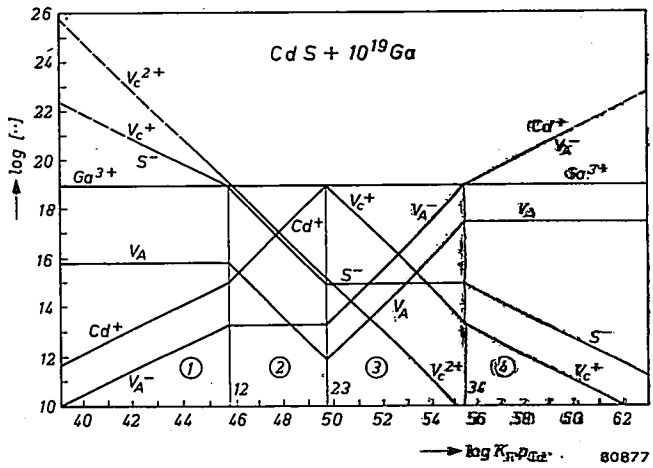

Fig. 1. Concentration lines of the system CdS + 10^{19} Ga obtained by linear approximations.

atoms/cm^3. This concentration line is also plotted. In this particular case we get an intersection between $[V_C^+]$, $[S^-]$ and $[Ga^{3+}]$. Beyond the boundary 1-2, marked by the intersection, the relations (7)-(13) certainly no longer hold. Throughout region 1, however, the expressions (7)-(13) are a first, but accurate approximation of the exact solution of the problem. The position of boundary 1-2 is derived from equations (1)-(5) and

$$\log [V_C^+] = \log [S^-] = \log [Ga^{3+}] \equiv \log X, \tag{14}$$

giving

$$\log K_R P_{Cd} = \log (K_i K_5 K_S / X^2). \tag{15}$$

Crossing this boundary, we have to reconsider the neutrality condition. This time only the vacancies, necessary to incorporate Ga^{3+} ions in the lattice remain; so in area 2 our system is governed by equations (1)-(5) and

$$\log [V_C^+] = \log [Ga^{3+}] = \log X, \tag{16}$$

resulting in:

$$\log [Cd^+] = \log (K_R P_{Cd} X / K_5 K_S), \tag{17}$$

$$\log [S^-] = \log (K_i K_5 K_S / K_R P_{Cd} X), \tag{18}$$

$$\log [V_C^+] = \log X, \tag{19}$$

$$\log [V_C^{2+}] = \log (K_3 K_5 K_S / K_R P_{Cd}), \tag{20}$$

$$\log [V_A^-] = \log (K_5 / X), \tag{21}$$

$$\log [V_A] = \log (K_5^2 K_S^2 / K_R P_{Cd} X^2). \tag{22}$$

These concentrations are also plotted, giving the approximation valid for region 2. The validity extends as far as the intersection of $[V_C^+]$, $[Ga^{3+}]$ and $[Cd^+]$:

$$\log [V_C^+] = \log [Ga^{3+}] = \log X = \log [Cd^+], \tag{23}$$

$$\log K_R P_{Cd} = \log K_5 K_S. \tag{24}$$

In the third region the incorporation of Ga^{3+} in the neutral lattice is effected merely by free electrons Cd^+; so besides the expressions (1)-(5) we have the condition

$$\log [Ga^{3+}] = \log X = \log [Cd^+], \tag{25}$$

leading to:

$$\log [Cd^+] = \log X, \tag{26}$$

$$\log [S^-] = \log (K_i / X), \tag{27}$$

$$\log [V_C^+] = \log (K_5 K_S X / K_R P_{Cd}), \tag{28}$$

$$\log [V_C^{2+}] = \log (K_3 K_5 K_S / K_R P_{Cd}), \tag{29}$$

$$\log [V_A^-] = \log (K_R P_{Cd} / K_5 X), \tag{30}$$

$$\log [V_A] = \log (K_R P_{Cd} / X^2). \tag{31}$$

The last boundary is given by

$$\log [Ga^{3+}] = \log X = \log [Cd^{+}] = \log [V_A^{-}], \tag{32}$$

$$\log K_R P_{Cd} = \log K_5 X^2. \tag{33}$$

Beyond the latter boundary only atmosphere-induced vacancies, balanced by free electrons, have to be considered:

$$\log [Cd^{+}] = \log [V_A^{-}], \tag{34}$$

leading to:

$$\log [Cd^{+}] = \tfrac{1}{2} \log (K_R P_{Cd}/K_5), \tag{35}$$

$$\log [S^{-}] = \tfrac{1}{2} \log (K_i^2 K_5/K_R P_{Cd}), \tag{36}$$

$$\log [V_C^{+}] = \tfrac{1}{2} \log (K_5 K_S^2/K_R P_{Cd}), \tag{37}$$

$$\log [V_C^{2+}] = \log (K_3 K_5 K_S/K_R P_{Cd}), \tag{38}$$

$$\log [V_A^{-}] = \tfrac{1}{2} \log (K_R P_{Cd}/K_5), \tag{39}$$

$$\log [V_A] = \log K_5. \tag{40}$$

In this way the complete approximation, as given in fig. 1, is obtained. If the result thus obtained is compared with the exact solution in fig. 2, it is seen that the approximation is satisfactory in wide ranges, only a slight smoothing of the sharp bends being required to get the exact answer to the problem. The shape of the smooth part of the curves depends only on the angle between the linear approximation on either side of the boundary. The error at the boundary may easily be computed.

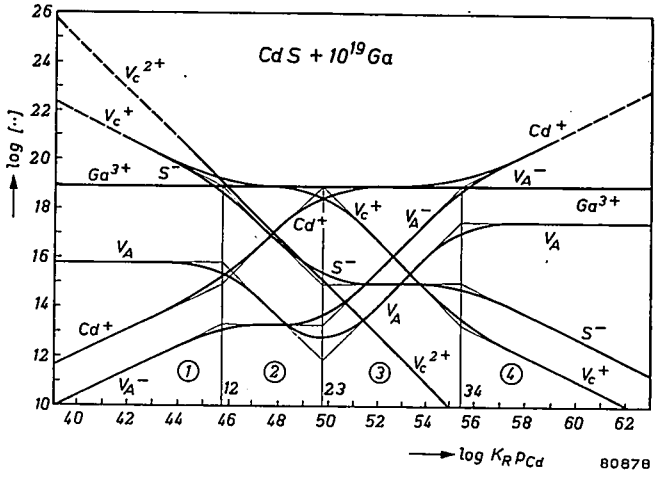

Fig. 2. Exact solution of the system CdS + 10^{19} Ga drawn in full, the approximate solution being indicated by minor lines. Note the close agreement.

Summarizing we have four areas to which a simplified neutrality condition may be applied in this particular case:

(1) $$\log [V_C^+] = \log [S^-],$$

where only atmosphere-induced vacancies and holes are present in appreciable quantities.

(2) $$\log [V_C^+] = \log [Ga^{3+}],$$

in which region the bulk of the vacancies is necessary to incorporate the Ga^{3+} ions in the CdS lattice.

(3) $$\log [Cd^+] = \log [Ga^{3+}],$$

the controlled-valency region in which no appreciable number of vacancies is necessary to introduce the Ga^{3+} ions into the crystal, every Ga^{3+} ion giving a free electron.

(4) $$\log [V_A^-] = \log [Cd^+],$$

where atmosphere-induced vacancies, compensated by free electrons, dominate.

In case other values are inserted for the reaction constants an entirely different pattern of concentration lines may result. In every particular case chemical understanding of the system has to be exploited to obtain the proper choice as to the division into the various regions.

The main feature of the method employed is that the solution is analytical, so that the influence on the result of changes in constants and inforced concentrations, e.g. of Ga, can easily be reviewed. This is all the more important as some of the constants can only be determined from experiments by an iterative process.

Once the high-temperature equilibrium of the lattice with the atmosphere is arrived at, the low-temperature concentrations can be determined by the redistribution process of electrons as proposed by Kröger, Vink and Van den Boomgaard [1]).

The slope of the linear approximation is independent of reaction constants or content of foreign elements as long as we stay in a certain region.

3. Graphical approximation of the system CdS-Ga

Instead of computing the analytical expression for each concentration line in every area, a more convenient method to approach the result can be applied. We have already seen that the linear approximation forms a continuous system. Moreover the slopes of the various lines within a particular region are only determined by the reaction coefficients. The value of the tangent can readily be determined by a simple differentiation

process. Thus in region 2 all slopes may be calculated from equations (1)-(5) and (16), so from the reaction equations and the modified neutrality condition for the region in question. Starting points of the graphical procedures are the known analytical solutions for extreme Cd pressures, boundaries being derived from intersections connected with conditions (15), (23) and (32).

As long as the coefficients in the reaction equations may be expressed by small integers, the slopes of the linear approximations can be represented by the ratio of two small integers.

4. Asymptotic solution of the system CdS-Ag

In the first section an example was given of a comparatively simple system. In order to show that even a more intricate system may be solved by the approximation method, the system CdS-Ag is to be considered. As only the mathematical procedure has to be explained, we will be unscrupulous as to the chemical possibility to realize a crystal containing 10^{21} Ag atoms per cm^3.

According to Kröger, Vink and Van den Boomgaard, the high-temperature equilibrium is given by:

$$\log [V_A^{\cdot}] = \log K_R P_{Cd} - 2 \log [Cd^+], \tag{41}$$

$$\log [S^-] = \log K_i - \log [Cd^+], \tag{42}$$

$$\log [V_A^-] = \log K_R P_{Cd} - \log [Cd^+] - \log K_5, \tag{43}$$

$$\log [V_C^+] = -\log K_R P_{Cd} + \log [Cd^+] + \log K_5 K_S, \tag{44}$$

$$\log [V_C^{2+}] = -\log K_R P_{Cd} + \log K_3 K_5 K_S, \tag{45}$$

$$\log [S^{2-}(Ag^+)] = \log [Cd^+] + \log [S^-(Ag^+)] - \log K_6, \tag{46}$$

$$[S^{2-}(Ag^+)] + [S^-(Ag^+)] = [Ag^+], \tag{47}$$

$$[Cd^+] + [V_C^+] + [S^{2-}(Ag^+)] = [S^-] + 2[V_A] + [V_A^-], \tag{48}$$

with the constants

$$\log K_i = 34{\cdot}0,$$

$$\log K_S = 32{\cdot}3,$$

$$\log K_5 = 17{\cdot}5,$$

$$\log K_3 = 15{\cdot}0,$$

$$\log K_6 = 15{\cdot}0.$$

Besides six logarithmic equations we have two linear relations. For the sake of expressions (46) and (47) a division into two regions is made:

(a) $$\log [Cd^+] \leqslant \log K_6, \tag{49}$$

where the Ag-induced level is almost empty and thus:

$$\log [S^{-}(Ag^{+})] = \log [Ag^{+}], \tag{50}$$

$$\log [S^{2-}(Ag^{+})] = \log [Ag^{+}] + \log [Cd^{+}] - \log K_6. \tag{51}$$

(b)
$$\log [Cd^{+}] \geqslant \log K_6, \tag{52}$$

where the Ag level is almost completely occupied:

$$\log [S^{2-}(Ag^{+})] = \log [Ag^{+}], \tag{53}$$

$$\log [S^{-}(Ag^{+})] = \log [Ag^{+}] - \log [Cd^{+}] + \log K_6. \tag{54}$$

Still another division has to be made for the neutrality relation. As the general procedure is the same as before, we merely state where the boundaries are to be found and which condition is valid in each region besides the expressions (40)-(44) and (49), (50) or (52), (53).

The boundaries are derived from:

1-2:

$$\log[V_C^{+}] = \log[S^{-}] = \log[S^{2-}(Ag^{+})], \quad \log K_R P_{Cd} = \log (K_5 K_S K_6/X); \tag{55}$$

2-3:

$$\log[S^{-}] = \log[S^{2-}(Ag^{+})] = \log[2V_A], \log K_R P_{Cd} = \tfrac{1}{2}\log (K_6 K_i^3/4X); \tag{56}$$

3-4:

$$\log[S^{2-}(Ag^{+})] = \log[2V_A] = \log[Ag^{+}], \log K_R P_{Cd} = \log (K_6^2 X/2); \tag{57}$$

4-5:

$$\log[2V_A] = \log[Ag^{+}] = \log[V_A^{-}], \quad \log K_R P_{Cd} = \log (2K_5^2 X); \tag{58}$$

5-6:

$$\log[Ag^{+}] = \log[V_A^{-}] = \log[Cd^{+}], \quad \log K_R P_{Cd} = \log (K_5 X^2). \tag{59}$$

The modified neutrality conditions in the various areas are:

(1)
$$\log [V_C^{+}] = \log [S^{-}]. \tag{60}$$

Here only atmosphere-induced vacancies and holes are present in appreciable quantities.

(2)
$$\log [S^{-}] = \log [S^{2-}(Ag^{+})]. \tag{61}$$

The bulk of Ag levels is empty and thus these centres are neutral; holes are required only to satisfy the neutrality condition for the remaining occupied levels.

(3)
$$\log [S^{2-}(Ag^{+})] = \log [2V_A]. \tag{62}$$

Here the incorporation of the occupied Ag levels is accomplished by empty vacancies. The majority of the Ag levels is still empty.

(4)
$$\log [2\,V_A] = \log [S^{2-}(Ag^{+})] = \log [Ag^{+}]. \tag{63}$$

Almost all Ag levels are occupied now, the charge being compensated by empty vacancies.

(5) $$\log [Ag^+] = \log [S^{2-}(Ag^+)] = \log [V_A^-] . \tag{64}$$

As the Fermi level is rising, vacancies are also occupied by electrons.

(6) $$\log [V_A^-] = \log [Cd^+] . \tag{65}$$

Atmosphere-induced vacancies containing one electron dominate, their effective charge being compensated by free electrons.

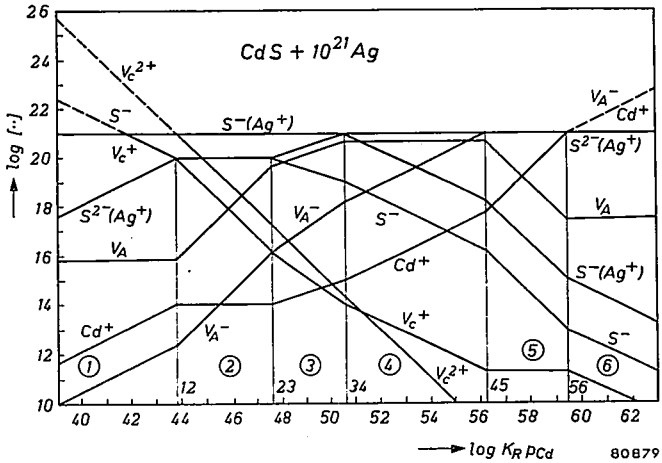

Fig. 3. Linear approximation of the system CdS + 10^{21} Ag. This system cannot be realized chemically, but has been chosen only to explain the mathematics in a clear way.

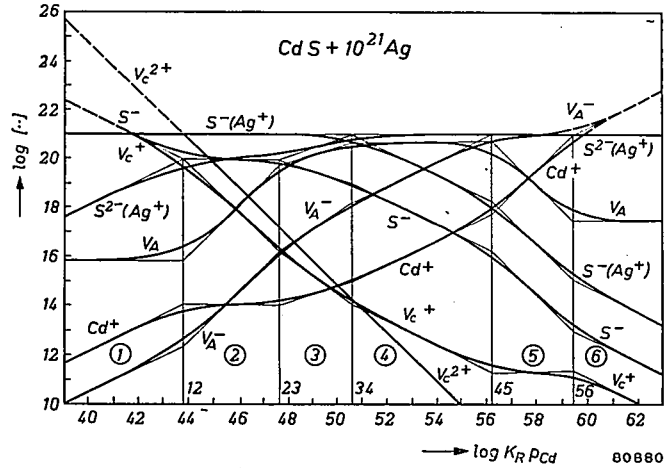

Fig. 4. Exact solution of the system CdS + 10^{21} Ag, indicated by major curves, the approximation by minor lines.

No we can proceed with the graphical method as depicted in fig. 3. The exact result is given in fig. 4.

The shape of a concentration curve for various amounts of foreign elements as a function of atmosphere is given in fig. 5 for V_A. In the upper part, Ag is the activator, in the lower part Ga.

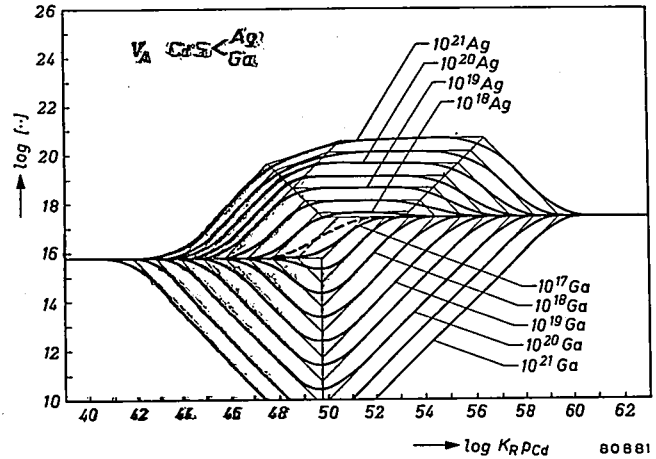

Fig. 5. Concentration lines of V_A obtained by graphical methods for various Ag and Ga contents.

5. Other applications

The approximation method can also be applied to a system of gases reacting under a constant pressure. The latter condition introduces a linear type of equation into a system of logarithmic equations, similar to the electrical examples treated in the preceding sections.

Eindhoven, June 1954

REFERENCE

1) F. A. Kröger, H. J. Vink and J. van den Boomgaard, Controlled conductivity in CdS single crystals, Z. phys. Chem. 203, 1-72, 1954.

Philips Res. Rep. 9, 377-390, 1954

TEMPERATURE DEPENDENCE OF THE LUMINESCENCE AND CHEMICAL STABILITY OF BASIC MAGNESIUM ARSENATE ACTIVATED WITH TETRAVALENT MANGANESE

by H. A. KLASENS

535.373.2:546.461.95

Summary

The effect of activator concentration and partial substitution of the lattice constituents by other ions on the temperature dependence of the luminescence of 6 $MgO \cdot As_2O_5$ — Mn is studied. The effect of the activator concentration is in agreement with the theory of Johnson and Williams. Incorporation of lithium improves the temperature dependence considerably. Measurements of the stability of various arsenates in reducing atmospheres show that phosphors containing lithium are less easily reduced. Incorporation of fluorine has the opposite effect. A theory for this induced variation of stability is given.

Résumé

On a étudié l'effet de la concentration du produit activant et de la substitution partielle des constituants du réseau par d'autres ions sur la dépendance de la température de 6 $MgO \cdot As_2O_5$ —Mn. L'effet de la concentration du produit activant est conforme à la théorie de Johnson et Williams. L'incorporation de lithium améliore considérablement la dépendance de la température. Les mesures de stabilité des divers arséniates dans des atmosphères réductrices montrèrent que les phosphores contenant du lithium sont réduits moins facilement. L'incorporation de la fluorine produit le résultat opposé. Une théorie de cette variation de stabilité est donnée.

Zusammenfassung

Es wird der Einfluß der Aktivatorkonzentration und einer teilweisen Ersetzung der Gitterbestandteile durch andere Ionen auf die Temperaturabhängigkeit der Lumineszenz von 6 $MgO \cdot As_2O_5$ — Mn untersucht. Die Wirkung der Aktivatorkonzentration stimmt mit der Theorie von Johnson und Williams überein. Einbau von Lithium erhöht die Temperaturabhängigkeit beträchtlich. Messungen der Stabilität verschiedener Arsenate in reduzierenden Atmosphären zeigen, daß lithiumhaltige Phosphore weniger leicht reduziert werden. Einbau von Fluor hat die entgegengesetzte Wirkung. Es wird eine Theorie für diese herbeigeführte Änderung der Stabilität gegeben.

1. Introduction

Several red fluorescent phosphors have been proposed for application in high-pressure mercury-discharge lamps. These lamps consist of the actual high-pressure discharge tube, made of quartz, which is mounted in a glas bulb. This bulb is usually filled with nitrogen. The light emitted by the mercury discharge has a bluish colour and its colour rendering

is poor mainly due to lack of red light. A much more pleasant light source is obtained if the glass bulb is coated on the inside with a red fluorescent phosphor. The requirements which this phosphor has to fulfil are rather severe. It must have a good absorption and a good quantum efficiency for the long- and short-wave U.V. radiation emitted by the mercury discharge. It must not have a strong absorption in the visible part of the spectrum. Its temperature dependence should be very good because this enables the lamp manufacturer to keep the dimensions of the outer bulb low. Finally its maintenance should be good. Since the outer bulb is filled with a gas of no or very low oxygen pressure, in order not to attack the molybdenum leads through the quartz discharge tube, this means that the phosphor should not easily be reduced at the temperature which the outer bulb reaches during running of the lamp.

The best red-emitting phosphors which are still being used in high-pressure mercury lamps are magnesium fluorogermanate [1]) and magnesium arsenate [2]), both activated with tetravalent manganese, and barium strontium lithium silicate activated with cerium and divalent manganese [3]), [4]). The temperature dependence of these three phosphors is given in fig. 1. The phosphors were excited with 3650-Å radiation while the emission was measured with a photo-multiplying cell through a red filter, Jena RG 1.

The silicate has the poorest temperature dependence. Its first slow drop in light output between 140 and 300 °C is mostly due to a broadening of the Mn-emission and a shifting of the whole emission curve to shorter wavelengths. The colour of the emission shifts from red to yellow in

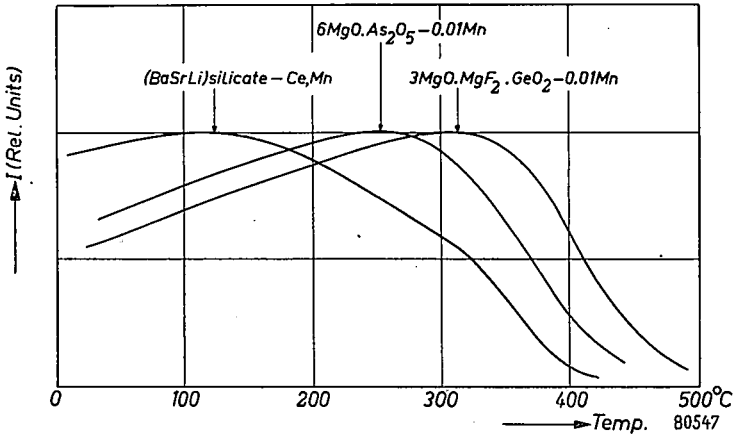

Fig. 1. Temperature dependence of the red emission of three phosphors used at present in colour-corrected high-pressure mercury-discharge lamps. Excitation with 3650 Å. Emission measured through Jena RG 1.

this temperature range. The emission of phosphors activated with tetravalent manganese is much less affected by high temperature, which makes these phosphors particularly suited for high-pressure mercury lamps.

The germanate has the best temperature dependence of the three. Its stability in nitrogen-filled lamps is moreover better than that of the arsenate. To prevent the arsenate from being reduced the usual nitrogen filling has to be replaced by carbon dioxide [5]).

The present paper describes the effects of various alterations in the composition of the arsenate on its temperature dependence and stability. It is shown that both are improved considerably by incorporation of lithium.

2. Preparation of samples

To prepare the arsenates the required amounts of MgO, As_2O_5 and $MnCO_3$ are mixed together with alcohol to a thick paste. The alcohol is evaporated and the residue prefired for about one hour in air and finally fired for about three hours in air at a temperature of 1100 to 1200 °C.

As_2O_3 may also be used as a raw material. It is mixed with water and the mixture is heated after addition of excess H_2O_2 to dissolve the oxide. The solution of As_2O_5 is cooled and filtered. The water is evaporated after adding the required amounts of MgO and $MnCO_3$. The residue is treated as above.

During the dry reaction between MgO and As_2O_5 the orthoarsenate is formed first. This compound then reacts with the excess MgO to form the basic arsenate. This reaction is promoted by the presence of small amounts of B_2O_3 or MgF_2. The effect of MgF_2 is especially noticeable at high Mn contents where it facilitates the incorporation of the activator. With increasing amounts of MgF_2 the body colour becomes more yellow. This is due to an increase in particle size of the phosphor. The phosphor has a weak absorption in the blue region of the spectrum [2]). When white light falls on the phosphor, part of the blue light is absorbed and part reflected. The finer the particle size, the larger the reflection and the whiter the appearance of the phosphor. When more than about 0·3 mole MgF_2 per mole As_2O_5 is added a new phase becomes noticeable in the X-ray diagram while the fired product is brownish discoloured. The presence of F is however not essential to get a good phosphor for long-wave U.V. excitation, contrary to the magnesium germanate. Addition of MgF_2 merely helps to reduce the temperature and duration of firing.

3. Apparatus

The apparatus used to measure the temperature dependence and the stability at high temperatures under exposure to U.V. radiation in various atmospheres is shown in fig. 2. The phosphor (a) is applied with a little

alcohol to a brass plate (b). The temperature of this plate is measured by means of a thermocouple (c). Two of these plates are fixed with silver solder to a Fernico cup (d). The cylindrical top half of this cup is sealed to a hard glass tube (e) with a ground flat part (f). The rest of the apparatus consists of a transparent quartz tube (h) with two side tubes for letting gas in and out. It also has a flat part closely fitting the flat portion of the central tube. A rubber gasket (g) is used to prevent leakage while the two parts are held together with a clamp, not shown in the drawing.

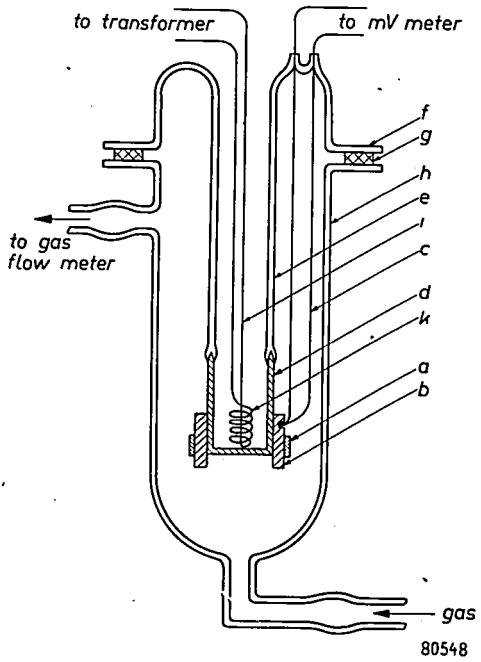

Fig. 2. Apparatus for measurements of temperature dependence and stability.

The phosphor can be heated to various temperatures by inserting a heater (k) in the Fernico cup. If desired the phosphor can also be cooled by pouring in liquid air.

For measuring the temperature dependence the phosphor is excited with long- or short-wave U.V. through the quartz envelope. The light emitted by the phosphor is thrown through a lens and a red Jena RG 1 filter on to the sensitive part of a photo-multiplying cell.

The stability of the phosphors can easily be measured with the same apparatus in various atmospheres under exposure to U.V. radiation.

A dismountable discharge lamp, used to measure the phosphors under

conditions closely resembling those in actual discharge lamps is shown in fig. 3. A 125-watt mercury-discharge tube (1) is faced by two holders (2) each containing a glass microscope slide coated with the phosphor to be measured. The holder is constructed in such a way that only half of the phosphor layer is exposed to the mercury radiation. The leads to the discharge tube and the wires on which the holders are mounted are fixed in a rubber stop (3).

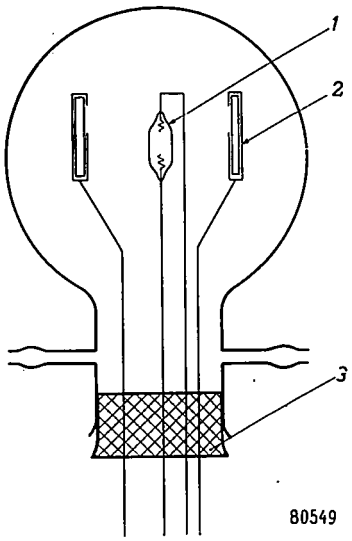

Fig. 3. Demountable discharge lamp for testing the stability of phosphors in various atmospheres under U.V. exposure.

4. Temperature dependence

The activator concentration has a marked effect on the temperature dependence as shown in fig. 4. The curves are shifted to lower temperatures with increasing Mn-content. At low temperatures the brightness increases when warming up until a broad maximum is reached. This is due to an increase of the absorption of the 3650-Å radiation because of a broadening of the absorption bands at 3000 and 4100 Å [2]).

The falling part of the curves at high temperatures can be represented fairly accurately by the well-known quenching formula

$$\frac{I}{I_0} = \frac{1}{1 + se^{-E/kT}}, \qquad (1)$$

with the exception of the curve for [Mn] = 0·1.

Values of log s and E are shown in table I.

TABLE I

[Mn]	Average Mn-Mn distance (Å)	E(eV)	log s
0·001	47	1·39	10·5
0·003	32	1·36	10·4
0·01	22	1·16	9·0
0·02	17·5	1·03	8·1
0·03	15	0·94	7·6
0·05	13	0·79	6·6

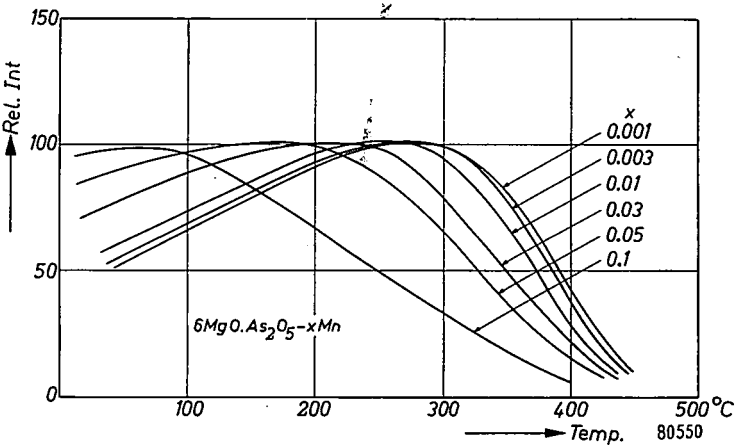

Fig. 4. Temperature dependence of 6 $MgO{\cdot}As_2O_5$ with various activator contents. Excitation with 3650 Å.

Johnson and Williams [6]) have given a theory for the concentration quenching based on the recognition that the activation energy for the radiationless processes in the activator is lowered by the presence of a second activator in the close vicinity. They assume this energy to be lowered by an amount approximately proportional to the overlap integral for the wave functions of the interacting activators. Since the overlap integral varies exponentially with the distance r, the activation energy of quenching should be given approximately by

$$E = E_0\,(1 - e^{-ar}). \tag{2}$$

Figure 5 shows that the results for Mn-activated Mg-arsenate are fairly well in agreement with this law for $E_0 = 1{\cdot}45$ eV and $a = 0{\cdot}075$ Å^{-1}.

A remarkable result is the linear relation between log s and E. This linear relation seems to hold quite generally for rate processes in the solid state. The law was first recognized to hold by Meyer and Neldel [7]) for the rate of release of electrons from donors in semiconductors.

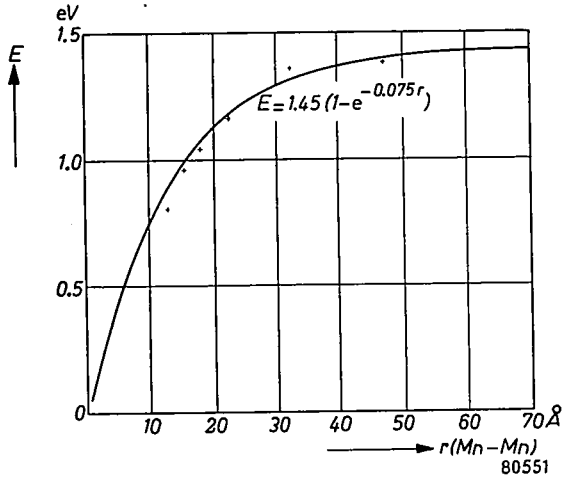

Fig. 5. Activation energy for the quenching of the Mn-emission as a function of the average Mn-Mn distance.

Busch [8]) has given an explanation of this law but only for defect semiconductors, while the law of Meyer and Neldel seems to be of much wider application. Smaller and Avery [9]) find the law also to hold for the release of electrons from traps of various depths in KJ-Tl. They conclude the entropy difference between two states to be linearly related to the energy difference because the factor s is proportional to $\exp(\Delta S/k)$ according to the absolute rate theory of Williams and Eyring [10]). No explanation has been given why ΔS and ΔE should be thus related.

Despite the large variations in activation energy for temperature quenching with varying Mn-content there is no change at all noticeable in the emission spectrum. The radiationless transition and emission apparently do not start from the same excited level or the Mn^{4+}-ion. One has to assume a third level or group of levels as shown schematically in fig. 6. The emission is represented by transition (a). Energy states I and II are little coupled with the lattice, a fact already apparent from the line structure of the emission spectrum. The transition I→II is forbidden. The corresponding absorption is therefore very weak and could not be found. The broad absorption band located near 4100 Å corresponds to a transition

to the higher energy state III. This state has a more extended wave function and is therefore more strongly coupled with the lattice. At low temperatures the system proceeds via A to B after excitation from where emission takes place. Because of the long life-time of the activator in state II (transition to I forbidden) a Boltzmann equilibrium between the various states can easily be established. At sufficiently high temperatures the system may reach C from where it returns radiationless to the ground state. Changes in the immediate neighbourhood such as the close vicinity of a second activator will affect III more strongly than II, resulting in a shifting of C where the curves cross and consequently an alteration in the energy difference between C and B, without affecting the emission spectrum. Too strong deviation in the surrounding lattice will however also affect the emission spectrum. Such deformations are caused by the incorporation of lithium as we shall see below.

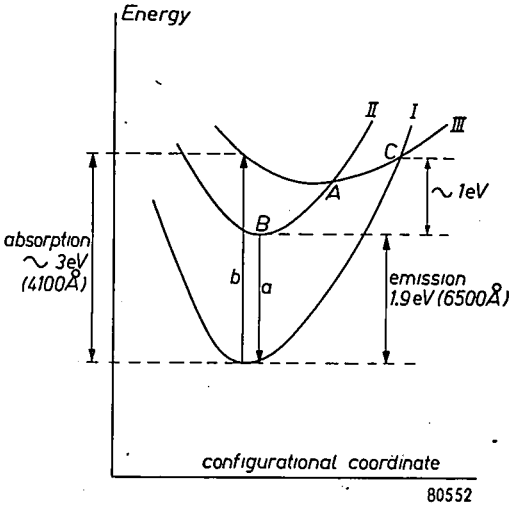

Fig. 6. Schematic diagram showing energy versus configurational coordinate for three electronic levels of the Mn^{4+}-centre.

Lithium can replace about 10% of the magnesium giving phosphors of the composition $(6-x)MgO \cdot \frac{1}{2}xLi_2O \cdot As_2O_5 - Mn$. With x greater than 0·8 a new phase appears in the X-ray diagram. It is of advantage to use small amounts of B_2O_3 or MgF_2 as flux to get a homogeneous product at not too high temperatures and too long firing times. The best results were obtained with 3 mole % B_2O_3 or 10 mole % MgF_2. Some temperature-dependence curves for various Li-contents are shown in fig. 7. With 0·3 mole Li_2O the temperature dependence has surpassed that of Mg-fluoro-

germanate. With more Li_2O the efficiency begins to drop. Values of log s and E are given in table II.

TABLE II

Values of log s and E for radiationless transitions in $(6-x)MgO\cdot\frac{1}{2}xLi_2O\cdot As_2O_5 - 0{\cdot}01$ Mn

x	log s	E
0·2	8·5	1·11
0·6	9·7	1·39
0·8	10·7	1·57

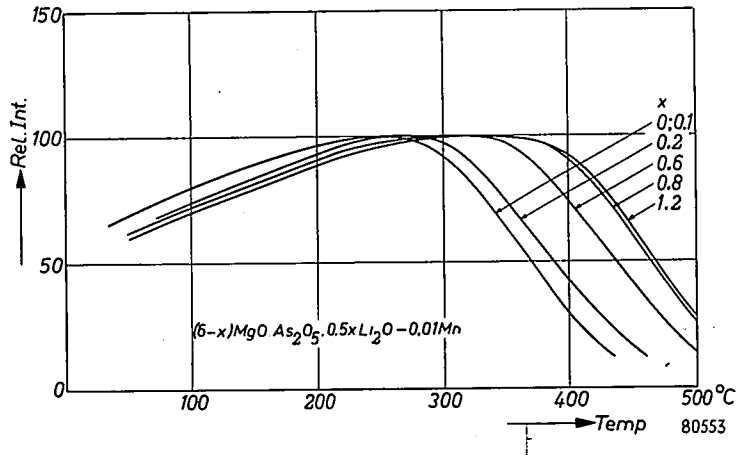

Fig. 7. Temperature-dependence curves for Li-containing Mg-arsenate phosphors.

Comparison with table I points to a slightly different relation between log s and E. With 0·3 Li_2O and 0·01 Mn the same value of E is obtained as with 0·001 Mn and no Li. Due to a lower s the temperature dependence of the Li-containing phosphor is much better. For practical application there is another reason why it is preferable to use Li instead of lowering the Mn-content to improve the temperature dependence because the latter will decrease the 3650-Å absorption, while Li has little effect on the absorption strength.

The presence of Li has a noticeable effect on the spectral distribution, as illustrated in fig. 8. At room temperature peaks are found at 6230,

6300, 6385, 6480, 6560 and 6660 Å. When Li is incorporated the peak at 6385 Å is lowered while that at 6480 Å is raised. This strong interaction may be due to pair formation between Li and Mn, which is quite likely to happen when both are occupying Mg-positions.

Accurate X-ray measurements indicate a contraction of the unit cell of approximately 0·15% when 10% of the Mg-ions is substituted by Li. A similar contraction was found by Prener [11]) in MgO containing Li_2O. With respect to possible term schemes for the Mn^{4+}-ion in the solid state it is of interest to note that at liquid-hydrogen temperatures not only the two bands at 6230 and 6300 Å have disappeared, as was noticed before, but that also the 6480-Å band has increased in strength much more than the 6550-Å band, while three bands can just be distinguished on the long-wave side of this 6550-Å band. This shows that the simple term scheme suggested by Travniçek et al. [2]) is not applicable.

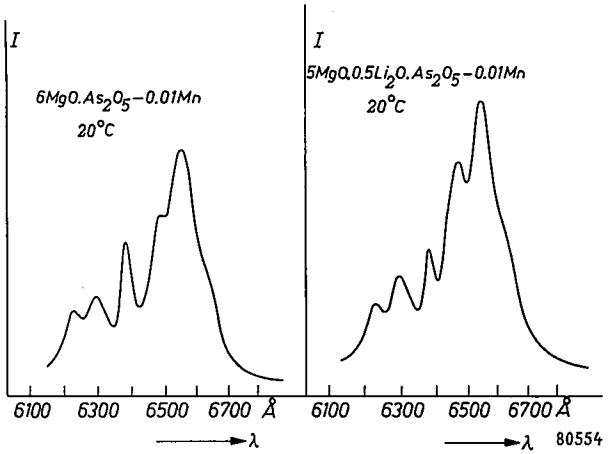

Fig. 8. Spectral distribution of the Mn-emissions in two arsenate phosphors at room temperature showing the effect of lithium.

Other substituents such as F, Al, B, S, Ge, Ca, Zn were also tried to see whether they have any effect on the temperature dependence. F does not alter the temperature dependence at low Mn-contents while at higher Mn-contents ($\approx$ 0·05 Mn) there is a slight shift to lower temperatures. This is probably due to an easier incorporation of Mn because of the fluxing action of MgF_2 resulting in a higher Mn-content in the lattice. Small amounts of LiF have the same effect but with more than 0·3 mole LiF per mole As_2O_5 the temperature-dependence curves are shifted to higher temperatures same as with Li_2O. Al and B have no appreciable effect. If $MgSO_4$ is added to the firing mixture most of the SO_3 is lost during

firing. Approximately 10% of Mg can be replaced by Zn causing a shift of the temperature-dependence curves to lower temperatures. The same effect was found with the germanate phosphor [1]). Only little Ca is taken up by the lattice. Addition of CaO however reduces the efficiency strongly. Addition of 15 mole % GeO_2 improves the temperature dependence slightly. With more germanium added the efficiency drops strongly.

5. Stability in reducing atmospheres

With the apparatus shown in fig. 2 the effect of the U.V. radiation on the stability of the Mg-arsenate in reducing atmospheres was studied. Two typical results are given in fig. 9. The phosphors were heated for a few hours at 400 °C in a mixture of 88% N_2 and 12% H_2. The efficiency of the phosphors drops slowly with time. Exposure to the radiation

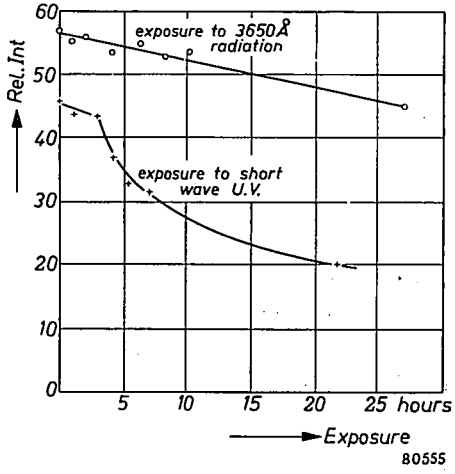

Fig. 9. Effect of U.V. radiation on the drop in light output of magnesium arsenate when heated at 400 °C in a mixture of 88% N_2 and 12% H_2.

from a high-pressure mercury arc speeds up this reduction in output considerably. Only the short U.V. part of the radiation below 3600 Å is photochemically active. Exposure to 3650 Å alone (filter Jena UG2) makes no difference to the rate of reduction. When the same experiments were repeated in a stream of CO_2 no noticeable drop in output was found, as was to be expected [5]). When a phosphor which had been partly reduced by exposure to U.V. in the nitrogen-hydrogen mixture was then heated in CO_2 at 400 °C without U.V. exposure the original output was not restored. For that an additional exposure to short-wave radiation is required. The oxygen pressure corresponding to the equilibrium:

$$2CO_2 \leftrightharpoons 2CO + O_2$$

is apparently not sufficient to oxidize the phosphor. It is known however [12]) that U.V. radiation increases the dissociation, which explains the observed results. Several arsenates were then compared as to their stability with the demountable lamp of fig. 3. While most substituents mentioned above had too small an effect to be easily detected in this way, the incorporation of lithium was found to increase the stability very remarkably. While the light output of a normal U.V.-exposed magnesium arsenate dropped 50 to 60% during 16 hrs in an atmosphere of pure oxygen-free nitrogen, the drop of an arsenate containing 30 mole% Li_2O (10% of Mg replaced by Li) amounted to only 12 to 14%. The stabilizing effect of lithium was also confirmed by heating a number of arsenates together in an oven at 550 °C in an atmosphere of 75% CO_2 and 25% H_2 during 3 hours. The arsenate without Li used normally for colour correction in high-pressure mercury lamps dropped 70% against 7% for the lithium-containing phosphor. Further confirmation of the stabilizing action of lithium was obtained from actual life tests with high-pressure mercury-discharge lamps. Table III gives a few results.

TABLE III

Drop in the amount of red light emitted by colour-corrected 125-watt high-pressure mercury-discharge lamps during life. Diameter of outer bulb 90 mm; N_2-filling.

With MgLi-arsenate		With Mg-arsenate	
time (hours)	% red	time (hours)	% red
0	7·2	0	6·2
100	6·7	40	3·2
600	6·7 *)		

*) This reduction in red percentage is to a large extent due to deterioration of the quartz envelope of the discharge tube.

Incorporation of fluorine has an adverse affect on the stability. This was not only found by heating arsenates with and without F in an oven in reducing atmospheres but had already been shown by life-test results with low-pressure fluorescent lamps [13]). To the halophosphate phosphor, used in these lamps, magnesium arsenate is sometimes added to improve the colour rendering [14]). The maintenance of these lamps was improved

considerably when the amount of MgF_2 used in preparing the phosphor was lowered.

The influence of Li and F on the stability can be understood as a special case of controlled valency [15]), [16]), [17]), [18]). When Mg^{2+} is replaced by Li^+ electroneutrality has to be preserved. This may be achieved in two ways, not accounting for a third possibility of interstitial Li^+. Starting from a lattice consisting only of Mg^{2+}, O^{2-} and As^{5+}-ions, one way to incorporate lithium is to replace two Mg^{2+}-ions by Li^+-ions while removing one O^{2-}-ion, thus producing an oxygen vacancy ($V_{O^{2-}}$). The other way, which does not produce vacancies, might be considered as the substitution of a Mg-atom by a Li-atom. Which of the two processes actually occurs depends on the firing conditions. At low oxygen pressures oxygen vacancies are more likely to be found (see also [16])). Both processes lower the Fermi level of the material. When an O^{2-}-ion is removed from the lattice a vacancy with an effective (2^+) charge is left constituting a low-lying unoccupied electronic level. The Fermi level is thereby lowered and electrons are removed from higher levels to fill the new vacancy levels.

When a magnesium atom is replaced by a lithium atom, leaving the charge distribution unaltered, the result may be described as a Li^{2+}-ion surrounded by O^{2-}-ions. This corresponds also to a low-lying empty electronic level because of the great electronic affinity of the Li^{2+}-ion, and electrons will again be withdrawn from higher occupied energy levels.

The opposite occurs when O^{2-} is replaced by F^-.

This process of raising or lowering the Fermi level by added impurities with valencies different from those of the host lattice is well known in semiconductors. The electronic conductivity of Fe_2O_3, for instance, is increased considerably by adding TiO_2 while addition of Li_2O to NiO gives rise to p-type conduction [15]).

The Fermi level in magnesium arsenate determines the ratio of Mn^{3+} to Mn^{4+} for the manganese incorporated in the lattice. When being heated in an atmosphere of low oxygen pressure, oxygen may be lost. The Fermi level and the Mn^{3+}-to-Mn^{4+} ratio are thereby raised until a new equilibrium has been established:

$$2\,(O^{2-})_{\text{lattice}} \rightleftarrows O_2 + 4\ominus + 2V_{O^{2-}}.$$

By incorporating lithium the Fermi level is lowered to such an extent that the phosphor can be heated in an atmosphere of much lower oxygen pressure before a large fraction of the Mn^{4+} is reduced. The stabilizing action of lithium on the fourfold valency of manganese in magnesium arsenate is thus explained.

The above principle of controlled valency can be an important tool in stabilizing the valency of activator ions. Another striking example

such a stabilization has been found with $Ca_3(PO_4)_2$-Ce. The fluorescent properties of this phosphor are due to Ce^{3+}. This ion can easily be oxidized by firing in air or reduced by firing in dry hydrogen [19]). Reduction may also occur in $Ca_3(PO_4)_2$-Ce, Mn when this phosphor is used for colour correction of high-pressure mercury-discharge lamps. The $Ca_3(PO_4)_2$— Ce phosphor can be made more stable against oxidation by the incorporation of Al_2O_3 [20]) while the stability against reduction can be improved by incorporation of alkaline oxides [21]), [22]). It is surprising that introduction of these monovalent ions also improves the temperature dependence of this phosphor while the excitation spectrum due to the Ce^{3+}-ion is extended to longer wavelengths. In this case there is apparently also an association between the activator and the monovalent ion.

6. Conclusion

By substituting about 10% of the Mg in $6\,MgO{\cdot}As_2O_5$—Mn by Li a phosphor is obtained which is much more stable against reduction and which has a considerably improved temperature dependence. Because of this improvement the arsenate phosphor has become more suited for use as a colour-correcting phosphor for high-pressure mercury-discharge lamps.

Eindhoven, March 1954

REFERENCES

1) L. Thorington, J. opt. Soc. Amer. **40**, 579, 1950.
2) M. Travniçek, F. A. Kröger, Th. P. J. Botden, and P. Zalm, Physica, 's-Grav. **18**, 33, 1952.
3) H. G. Jenkins and A. G. McKeag, Trans. illum. Eng. Soc. London **17**, 159, 1952.
4) A. H. McKeag and E. G. Steward, Paper No. 4 delivered at the Conference on Luminescence, Cambridge, 1954.
5) J. L. Ouweltjes, W. Elenbaas and K. R. Labberté, Philips tech. Rev. **13**, 109, 1951.
6) P. D. Johnson and F. E. Williams, J. chem. Phys. **18**, 1477, 1950.
7) W. Meyer and H. Neldel, Phys. Z. **38**, 1014, 1937.
8) G. Busch, Helv. phys. Acta **19**, 189, 1946.
9) B. Smaller and E. Avery, Phys. Rev. **92**, 232, 1953.
10) F. E. Williams and H. Eyring, J. chem. Phys. **15**, 289, 1947.
11) J. S. Prener, J. chem. Phys. **21**, 160, 1953.
12) S. Chadwick, J. E. Ramsbottom and D. L. Chapman, J. chem. Soc. **91**, 942, 1906.
13) J. L. Ouweltjes, private communication.
14) J. L. Ouweltjes, Philips tech. Rev. **13**, 346, 1951.
15) E. J. W. Verwey, P. W. Haaijman, F. C. Romeijn and G. W. van Oosterhout, Philips Res. Rep. **5**, 173, 1950.
16) F. A. Kröger, J. H. Vink and J. van den Boomgaard, Z. phys. Chem. **203**, 1, 1954.
17) G. Johnson and W. A. Weijl, J. Amer. ceram. Soc. **32**, 398, 1949.
18) G. H. Johnson, J. Amer. ceram. Soc. **36**, 97, 1953.
19) H. C. Froelich, Trans. electrochem. Soc. **91**, 241, 1947.
20) F. A. Kröger, private communication.
21) H. C. Froelich and J. M. Margolis, J. electrochem. Soc. **98**, 400, 1951.
22) Brit. Patent Spec. 695.175; U.S. Pat. Spec. 2.575.755

Philips Res. Rep. **9**, 391-402, 1954

THE SIMILARITY LAW OF SECONDARY EMISSION

by J. L. H. JONKER

537.533.8

Summary

In literature, the curves of the secondary-emission coefficient δ measured as a function of the energy εV_p of the primary electrons often show great deviations from the experimental universal curve, i.e. do not satisfy the similarity law. It is shown that some of these deviations may be caused by the fact that the target is partly or completely covered with foreign materials. Many materials were measured again with extra precautions for having a clean surface, and tables are given for a number of materials whose measured δ curve agreed with the experimental universal curve. In that case the indication of the values of δ and εV_p at the maximum of the $\delta = f(\varepsilon V_p)$ curve is sufficient; other values of δ can then be deduced from the experimental universal curve, for which a formula has been added.

Résumé

Dans la bibliographie, les courbes du coefficient d'émission secondaire δ mesurées en fonction de l'énergie εV_p des électrons primaires, accusent souvent de grands écarts par rapport à la courbe universelle découlant de l'expérience, c'est-à-dire ne satisfont pas à la loi d'équivalence. Il est démontré dans cet article que quelques-uns de ces écarts peuvent avoir pour cause le fait que l'anticathode est recouverte partiellement ou complètement de matériaux étrangers. De nombreux matériaux firent l'objet de nouvelles mesures et des précautions supplémentaires furent prises pour avoir une surface propre; nous donnons des tables pour un certain nombre de matériaux dont la courbe obtenue par la mesure a correspondu avec la courbe universelle expérimentale. Dans ce cas, l'indication des valeurs de δ et de εV_p dans la partie maximum de la courbe $\delta = f(\varepsilon V_p)$ est suffisante; les autres valeurs de δ peuvent alors être déduites de la courbe universelle expérimentale, et une formule a été ajoutée dans ce but.

Zusammenfassung

In der Literatur weisen die Kurven des als Funktion der Energie εV_p der Primärelektronen gemessenen Sekundäremissionskoeffizienten δ oft große Abweichungen von der experimentellen Normalkurve auf, d.h. sie genügen nicht dem Ähnlichkeitsgesetz. In dieser Abhandlung wird gezeigt, daß einige dieser Abweichungen dadurch verursacht sein können, daß die Fangscheibe teilweise oder vollständig mit Fremdmaterialien bedeckt ist. Eine Reihe von Materialien wurden aufs neue gemessen, wobei besondere Vorkehrungen zur Reinhaltung der Oberfläche getroffen wurden, und es werden Tabellen für eine Anzahl Materialien gegeben, deren gemessene δ-Kurve mit der experimentellen Normalkurve übereinstimmt. In diesem Fall genügt die Angabe der Werte von δ und εV_p im Maximum der $\delta = f(\varepsilon V_p)$-Kurve; andere Werte von δ können dann aus der experimentellen Normalkurve abgeleitet werden, für welche eine Formel hinzugefügt wird.

In a former publication [1]) we calculated, starting from theoretical considerations, the secondary-emission factor δ as a function of the energy εV_p of the primary electrons. Putting $\delta_0 = \delta . C_m \sqrt{\cos v}$ and $\xi = \varepsilon V_p . C'_m \sqrt{\cos v}$, where C_m and C'_m are material constants and v is the angle between the primary beam and the normal to the surface of the plane target, we found the relation

$$\delta_0 = f_0(\xi) ,$$

which is a universal relation for all values of v and for all materials and which we called the *similarity law* of secondary emission. For each of a few materials (lithium, nickel and nickel carbide) of which the curves $\delta = f(\varepsilon V_p)$ were available with v as a parameter [2]), and which curves had been measured under the best possible vacuum conditions, we were able to verify the existence of one curve $\delta_0 = f_0(\xi)$ for different values of v. This curve indeed appeared to be the same for all three materials. The experimental curve is in general agreement with the theoretical curve, but the latter has a maximum that is considerably more pronounced (see [1]), fig. 11). This is perhaps partly due to our simplifying supposition that all secondary electrons have the same velocity and consequently have the same absorption coefficient (see [1]), p. 3). In literature no further reliable measurements are available of the $\delta = f(\varepsilon V_p)$ curves taken with different angles v. On the other hand, the numerous curves of $\delta = f(\varepsilon V_p)$ taken with $v = 0$, which are of more practical importance, show a confusingly large spread [3]), and only a certain number of them can be considered as really similar [4]). In fig. 1 the experimental universal curve is given and compared with a few experimental curves [5]), [6]), [7]) showing great deviations.

How may these deviations be explained? It is not probable that they can be accounted for merely by the influence of the small difference in velocity distribution between the secondary electrons of the different materials investigated. It is possible that there are materials for which the suppositions on which our theory is based do not hold. On the other hand, different authors found different curves for one and the same material. In this paper we will indicate one of the circumstances that may have caused this discrepancy.

One of the difficulties in comparing the results of the measurements of different authors is that the measurements were made under quite different circumstances: (1) the apparatuses differ considerably, (2) the precautions for vacuum conditions and for cleaning the target are different and often not sufficient, if possible at all. We therefore decided to re-measure a number of materials and to make all measurements with tubes of the same design (central-field method) and with the best possible vacuum

technique (below 10^{-7} mm Hg). Testing our tube by using a nickel target, however, we found that even under the strict conditions mentioned it was impossible to get results reproducible within a few per cent unless we cleaned the target by heating it for some time at such a temperature that evaporation of the nickel was visible on the glass wall. Consequently, the surface of the target must be extremely clean and even a partial covering of the surface with foreign atoms, with a slight oxidation or with material evaporated from the cathode, may cause a change in the δ and in the shape of the $\delta = f(\varepsilon V_p)$ curve, e.g. by changing the work function of the target or by causing a shift of $\varepsilon V_{p\max}$, the value of εV_p where δ has a maximum.

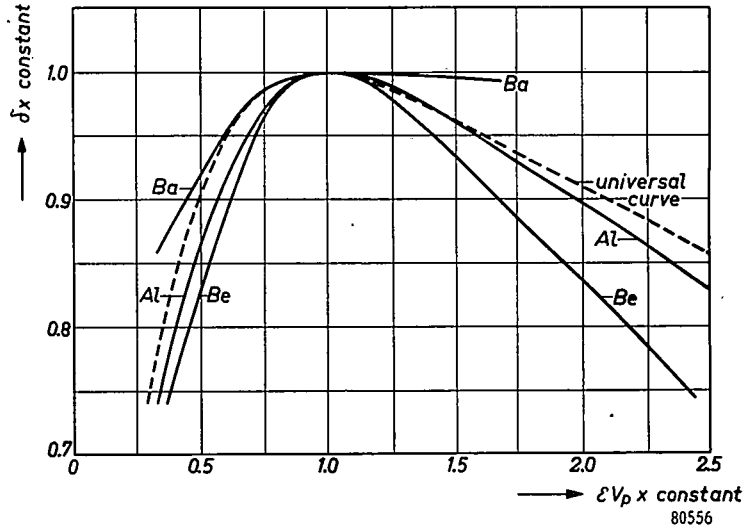

Fig. 1. Some experimental curves $\delta = f(\varepsilon V_p)$ published in literature [5],[6],[7]) compared with the experimental universal curve by making the maxima coincide. The curves diverge considerably.

The heat treatment is not always successful in case the oxide or other surface layer is much less volatile than the material of the target itself. The high temperature may also change the crystal structure and the smoothness of the surface of the target. Sometimes a clean surface can be better obtained by covering the target with a sufficiently thick layer of the desired material by means of evaporation in vacuo. But even then deviations from the universal curve may occur if the evaporated material oxidizes rapidly, as is the case with such materials as barium (see fig. 1). We will demonstrate how these deviations can arise by addition of the secondary emission of two surfaces having unequal values of $\delta_{\max}$ and of

$\varepsilon V_{p\max}$. We will restrict ourselves to the case $v = 0$, and we suppose that in the places where the target is covered the primary beam does not reach the target itself. If the total area of the covered parts amounts to a part P of the area of the target, and if δ_1 and δ_2 are the δ's of the covering material and of the pure target, respectively, we would get, using the result of the calculation of our former publication (ref. [1]), formulae (5) and (6) *)),

$$\delta = P\delta_1 + (1-P)\delta_2 =$$
$$= \tfrac{1}{2} PK_1 (a_1/\alpha_1)^{\frac{1}{2}} \int_0^1 \mathrm{d}z \exp\left(-\frac{\alpha_1}{a_1 z}\varepsilon^2 V_p^2\right) z^{\frac{1}{2}} \int_0^{\varepsilon V_p (\alpha_1/a_1 z)^{\frac{1}{2}}} e^{y^2}\,\mathrm{d}y +$$
$$+ \tfrac{1}{2}(1-P)K_2 (a_2/\alpha_2)^{\frac{1}{2}} \int_0^1 \mathrm{d}z \exp\left(-\frac{\alpha_2}{a_2 z}\varepsilon^2 V_p^2\right) z^{\frac{1}{2}} \int_0^{\varepsilon V_p (\alpha_2/a_2 z)^{\frac{1}{2}}} e^{y^2}\,\mathrm{d}y. \quad (1)$$

In this expression K is a material constant in the relation

$$\mathrm{d}I_{sx}/\mathrm{d}x = -KI_p \mathrm{d}[\varepsilon V(x)]/\mathrm{d}x$$

between the energy loss $\mathrm{d}[\varepsilon V(x)]$ in the primary beam over a distance $\mathrm{d}x$ in the material and the production $\mathrm{d}I_{sx}$ of secondary electrons in the range $\mathrm{d}x$ (I_p = primary-beam current); a is a material constant in Whiddington's law $\varepsilon^2 V^2(x) = \varepsilon^2 V_p^2 - ax$, governing the loss of energy of the primary beam in the material, and α is the absorption coefficient of the secondary electrons.

As mentioned before, the theoretical curves following from our calculation all have a sharper maximum than the universal curve deduced from experimental results. Consequently, an addition of two shifted theoretical curves will also give a deviation that is more pronounced, so that we can better turn to the experimental universal curve (e.u. curve). In fig. 2 this e.u. curve (I) is compared with a curve (II) found by adding two curves (a and b) **) with the same universal shape but with a shift of 1:6 in $\varepsilon V_{p\max}$ and with $(1-P)\delta_{a\max} : P\delta_{b\max} = 5:2$. The curves I and II are so reduced that $\delta_{\max}$ of the two curves is at the same point. Fig. 2 shows that in this way considerable deviations from the e.u. curve can arise.

Another possibility, which can give an even greater deviation, is that the target is fully instead of partly covered with a layer of, e.g., an oxide and that this layer is so thin that at a certain value of εV_p it will be pierced by the primary beam. When this beam reaches the base material a change of $\delta = f(\varepsilon V_p)$ can occur if the material constants of this material differ from those of the oxide layer, as mostly will be the case. If the thickness of the layer is d, then the energy εV_d with which the primary

*) See corrigenda at the end of the present paper.
**) The dashed part of curve a has been extrapolated.

electrons arrive at the base material is, according to Whiddington's law, given by

$$\varepsilon^2 V_d^2 = \varepsilon^2 V_p^2 - a_I d. \tag{2}$$

The maximum depth $x_{\max}$ to which they can penetrate into the base material is found from putting $\varepsilon V(x) = 0$ in $\varepsilon^2 V^2(x) = \varepsilon^2 V_d^2 - a_{II} x$, giving

$$x_{\max} = \varepsilon^2 V_d^2 / a_{II} = (\varepsilon^2 V_p^2 - a_I d)/a_{II}. \tag{3}$$

If we account for the absorption of the secondary electrons from the base material in the covering layer by a factor Q, our former calculation [1]) would now lead to

$$\delta = \delta_I + Q\delta_{II} = \tfrac{1}{4} K_I a_I \int_0^d \mathrm{d}x \int_0^{\pi/2} \mathrm{d}\varphi \left\{ \exp\left(-\frac{a_I x}{\cos\varphi}\right) \right\} (\varepsilon^2 V_p^2 - a_I x)^{-\frac{1}{2}} \sin\varphi +$$

$$+ \tfrac{1}{4} Q K_{II} a_{II} \int_d^{x_{\max}} \mathrm{d}x \int_0^{\pi/2} \mathrm{d}\varphi \left\{ \exp\left(-\frac{a_{II} x}{\cos\varphi}\right) \right\} (\varepsilon^2 V_d^2 - a_{II} x)^{-\frac{1}{2}} \sin\varphi, \tag{4}$$

where εV_d and $x_{\max}$ are to be substituted from (2) and (3).

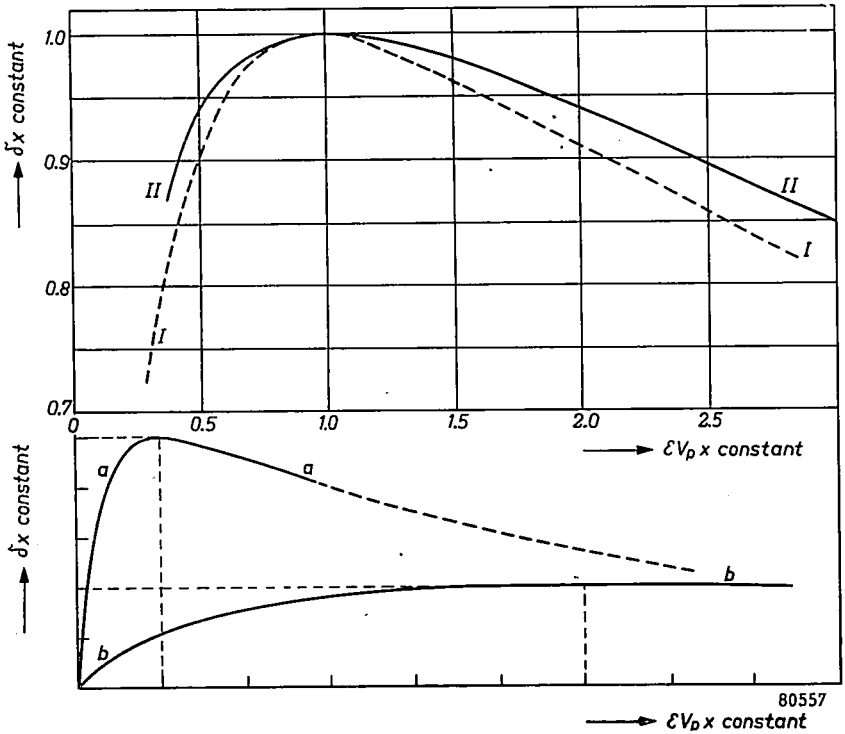

Fig. 2. When the surface of a target is not quite clean but partly covered with a foreign material, the δ curve will be the sum of two universal curves (a and b), provided that at the covered places the primary beam does not reach the base material. The sum curve (II) deviates from the universal curve (I).

To get an impression how in this case the curve $\delta = f(\varepsilon V_p)$ will deviate from the e.u. curve it is not necessary to plot the function (4) if we make the simplifying supposition that the covering layer is so thin that the absorption of the secondary electrons in it may be neglected. The production of secondary electrons in that layer will be in linear relation with the loss of energy of the primary beam:

$$\mathrm{d}I_{si} = -K_I I_p \mathrm{d}[\varepsilon V(x)]$$

(see second preceding page). When the maximum distance $x_{I\max}$ to which the primary beam can penetrate into the material of the covering layer is less than the thickness d of the layer, the whole energy εV_p will be consumed in the layer. $x_{I\max}$ is found by putting $\varepsilon V(x) = 0$ in Whiddington's law, giving $x_{I\max} = \varepsilon^2 V_p^2 / a_I$. For $x_{I\max} < d$, i.e. $\varepsilon V_p < \sqrt{a_I d}$, the secondary emission produced in the layer will thus be

$$I_{si} = \int_{\varepsilon V_p}^{0} -K_I I_p \mathrm{d}[\varepsilon V(x)] = K_I I_p \,.\, \varepsilon V_p ,$$

and, as we neglect absorption, a constant part R of it will be emitted. Thus

$$\delta_I = R I_{si}/I_p = R K_I \,.\, \varepsilon V_p \quad \text{for} \quad \varepsilon V_p < \sqrt{a_I d} ,$$

or, putting $\eta = \dfrac{\varepsilon V_p}{\sqrt{a_I d}}$,

$$\frac{\delta_I}{R K_I \sqrt{a_I d}} = \eta \quad \text{for} \quad \eta < 1 \tag{5}$$

(fig. 3, line a).

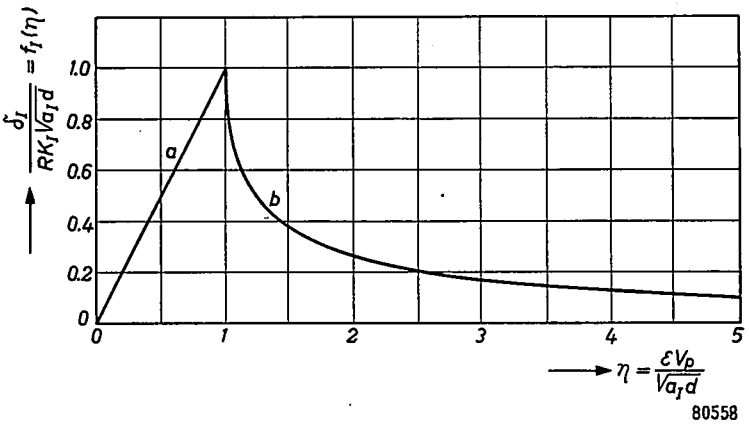

Fig. 3. Theoretical secondary-emission curve of a *layer* covering the whole target when absorption of the secondaries is neglected. For detailed description see the text.

For $\varepsilon^2 V_p^2/a_I > d$ the energy εV_p will be consumed partly in the layer and partly in the base material. As εV_d is the energy with which the primary electrons arrive at the base material, the secondary emission from the layer will in this case be given by

$$RI_{si} = R \int_{\varepsilon V_p}^{\varepsilon V_d} - K_I I_p \mathrm{d}[\varepsilon V(x)] = RK_I I_p(\varepsilon V_p - \varepsilon V_d),$$

so that, with the aid of eq. (2),

$$\delta_I = RK_I(\varepsilon V_p - \sqrt{\varepsilon^2 V_p^2 - a_I d}) \quad \text{for} \quad \varepsilon V_p > \sqrt{a_I d},$$

or

$$\frac{\delta_I}{RK_I\sqrt{a_I d}} = \eta - \sqrt{\eta^2 - 1} \quad \text{for} \quad \eta > 1 \tag{6}$$

(fig. 3, curve *b*).

We see, in fig. 3, that as soon as the primary beam is able to penetrate into the base material ($\varepsilon V_p > \sqrt{a_I d}$), the number of secondary electrons originating from the layer will fall off suddenly. Consequently, at rather low values of εV_p the presence of a layer can cause a peak in the $\delta = f(\varepsilon V_p)$ curve. This peak will be rounded off as a result of the non-homogeneity of the primary beam in the material and by the fact that, as we discussed on a former occasion (ref. [1]), p. 17), the a in Whiddington's law will not be a constant for $\varepsilon V_p < 150$ eV. The assumption on which this law is based, namely that the velocity of the primary electrons is much greater than that gained by a secondary electron, is no longer valid then.

When εV_p becomes larger than $\sqrt{a_I d}$, secondary electrons will also be produced in the base material. The secondary emission originating from there and reaching the partition plane of the target and the layer will answer a relation $\delta_{II} = f(\varepsilon V_d)$ similar to the e.u. curve $\delta_0 = f_0(\xi)$. A part Q of it will pass through the layer and enter the vacuum. For $\varepsilon V_p > \sqrt{a_I d}$ the secondary emission will thus consist of two parts, a part liberated in the layer and decreasing with increasing εV_p, and a part liberated in the target which at a certain value of εV_p will have a maximum. Thus it is possible to construct the curve $\delta_t = \delta_I + Q\delta_{II} = f(\varepsilon V_p)$ of the total secondary-emission coefficient of the target plus the layer, for different relations between the specific production of secondary electrons in the layer and in the target. This construction is done as follows.

In fig. 3 the secondary-emission part δ_I was plotted as $\dfrac{\delta_I}{RK_I\sqrt{a_I d}} = f_I(\eta)$,

$\eta = \dfrac{\varepsilon V_p}{\sqrt{a_I d}}$ being a measure for the primary energy εV_p. Likewise,

we shall plot the part $Q\delta_{II}$ as $\dfrac{Q\delta_{II}}{RK_I\sqrt{a_I d}} = f_{II}(\eta)$, and the sum curve $\delta_t' = f_I(\eta) + f_{II}(\eta)$ will then represent the δ of a target fully covered with a thin layer of a foreign material.

As was stated above, the curve $\delta_{II} = f(\varepsilon V_d)$ will be a transformation of the e.u. curve $\delta_0 = f_0(\xi)$ by means of the simple relations $\varepsilon V_d = C_1\xi$, $\delta_{II} = C_2 f_0(\xi)$, where C_1 and C_2 depend on the target material. Putting $C_1' = \dfrac{C_1}{\sqrt{a_I d}}$, $C_2' = \dfrac{QC_2}{RK_I\sqrt{a_I d}}$ and, cos ν being unity, $f_0(\xi) = g(\eta)$, we get the relations

$$\eta = \sqrt{(C_1'\xi)^2 + 1}, \qquad f_{II}(\eta) = C_2' g(\eta).$$

Fig. 4 shows the way of constructing curves $\delta_0 = g(\eta)$ from an e.u. curve $\delta_0 = f_0(\xi)$, with C_1' as a parameter. There are values of $g(\eta)$, and thus of $f_{II}(\eta)$, for $\eta > 1$ only.

In figs 5 and 6 we give some curves $\delta_t' = f_I(\eta) + C_2' g(\eta)$ for several values of the parameters C_1' and C_2', and these curves again show great deviations from the e.u. curve. As was discussed above, the peak in the part $f_I(\eta)$ (fig. 3) will be rounded off, and so will consequently the peak

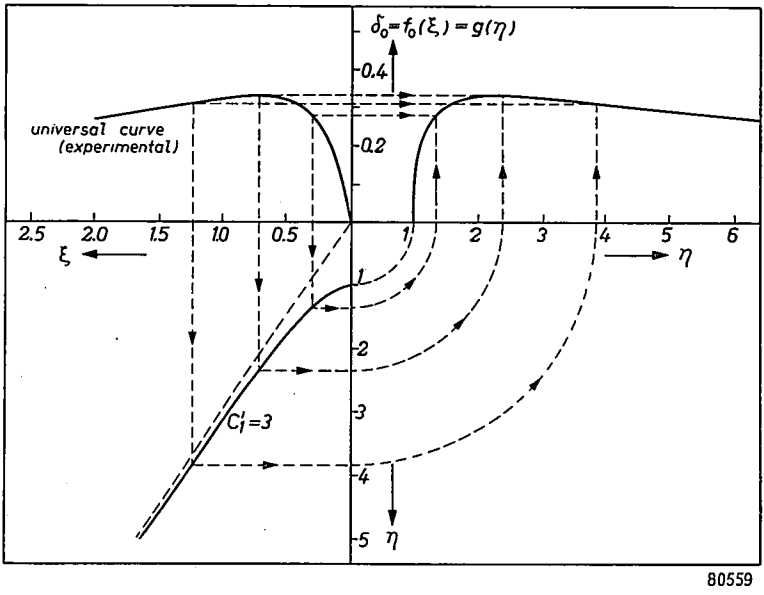

Fig. 4. Construction of the secondary-emission curve of the *base material* of a target fully covered with a foreign material, as a function of the *initial* primary energy. For detailed description see the text.

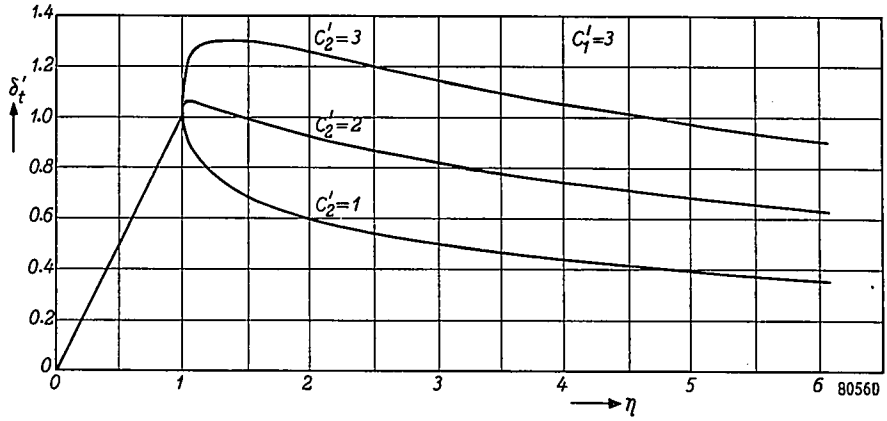

Fig. 5. Theoretical secondary-emission curves of a target fully covered with a foreign material. These curves are obtained by adding the curve of fig. 3 to curves constructed in the way shown in fig. 4 for different values of the parameter C'_2 with constant parameter C'_1 ($C'_1 = 3$).

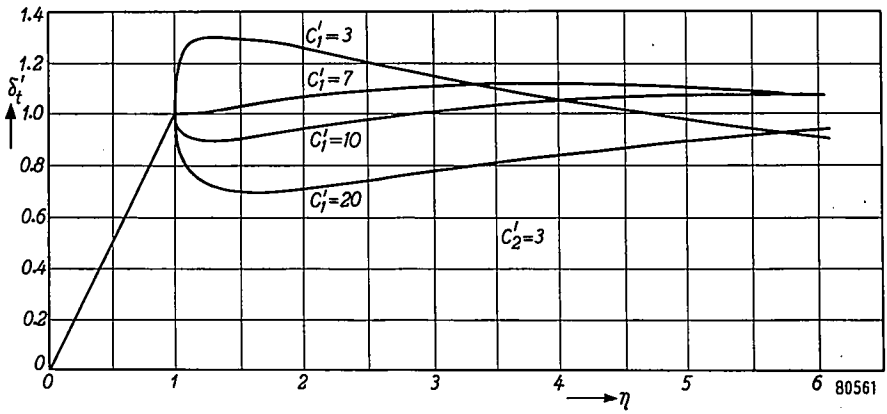

Fig. 6. The same as fig. 5 for different values of C'_1 with constant C'_2 ($C'_2 = 3$).

at $\eta = 1$ in the lower curves of figs 5 and 6 *). Of course it is possible that both effects, illustrated by the figs 2, 5 and 6, occur at the same time. *So we conclude that if a measured $\delta = f(\varepsilon V_p)$ curve can be reproduced and is similar to the experimental universal curve, there is a good chance that the surface was clean and the measurement correct.*

With the best possible precautions for having a clean surface we measured the δ curves of a number of materials important in the vacuum-

*) A specimen of a δ curve measured on a thin layer and having the shape of the lower curves in fig. 6, i.e. showing two maxima, is given in ref. [2]), fig. 19.

tube technique and we compared our results with the e.u. curve. Practically all curves measured under these strict conditions satisfied the similarity law. We also compared with the e.u. curve some curves measured by other authors. For each material whose measured δ curve agreed with the e.u. curve, we give in the tables I and II two numbers Δ and U_p indicating the maximum value of δ and the value of V_p for which this maximum occurs in the e.u. curve. *The δ for every other value of V_p can then, with an accuracy within a few per cent, be deduced from this curve*, a separate print of which has been added (fig. 7). The values of Δ and U_p given are such that the best possible similarity is obtained with the universal curve, and a consequence of this is that some of these values differ somewhat from the values of δ_{max} and $V_{p\,max}$ known from literature.

On some occasion it may be useful to express the e.u. curve in a formula. We found

$$\delta_0 = \left\{ e^{1-\xi-0{\cdot}152\ \xi^{-0{\cdot}152}} \right\}^{17{\cdot}36},$$

which curve has its maximum at $\xi = 1$, $\delta_0 = 1$ and which is correct within 2% in the range $0{\cdot}3 < \xi < 2{\cdot}6$.

The author wishes to express his thanks to Mr Cavens and to Mr Bos for their able assistance with the measurements and with preparing this paper.

Eindhoven, December 1953

REFERENCES

1) J. L. H. Jonker, Philips Res. Rep. **7**, 1-20, 1952.
2) H. Bruining, Thesis, Leyden, 1938, figs 21, 22 and 24. The figures of ref. 2) referred to in the present paper were also published in refs 8), 9) and 10), namely
fig. 11 in 9), fig. 3; fig. 21 in 8), fig. 67;
fig. 14 in 9), fig. 6; fig. 22 in 8), fig. 70 and in 10), fig. 3;
fig. 17 in 9), fig. 9; fig. 23 in 10), fig. 4;
fig. 18 in 9), fig. 10; fig. 24 in 10), fig. 5.
fig. 19 in 8), fig. 72;
3) R. Kollath, Phys. Z. **38**, 202-224, 1937.
4) E. M. Baroody, Phys. Rev. **78**, 780-787, 1950.
5) Ref. 2), fig. 23 (barium; $v = 72°$).
6) R. Warnecke, Onde élect. **16**, 509-540, 1937, fig. 3 (also published in ref. 11), fig. 14) (aluminium).
7) R. Kollath, Ann. Phys., Lpz. **33**, 285-299, 1938, fig. 3 (beryllium; curve *b*).
8) H. Bruining, Die Sekundär-Elektronen-Emission fester Körper, Springer, Berlin, 1942.
9) H. Bruining and J. H. de Boer, Physica, 's-Grav. **5**, 17-30, 1938.
10) H. Bruining, Physica, 's-Grav. **5**, 901-912, 1938.
11) R. Warnecke, J. Phys. Radium **7**, 270-280, 1936.

CORRIGENDA

Ref. 1), p. 8: In formula (6) and in the formula preceding formula (7), the lower limit of the second integral should read 0 instead of y.
Id., p. 19: In the legend of fig. 15 a sign of equality should be put after J_o/J_i.

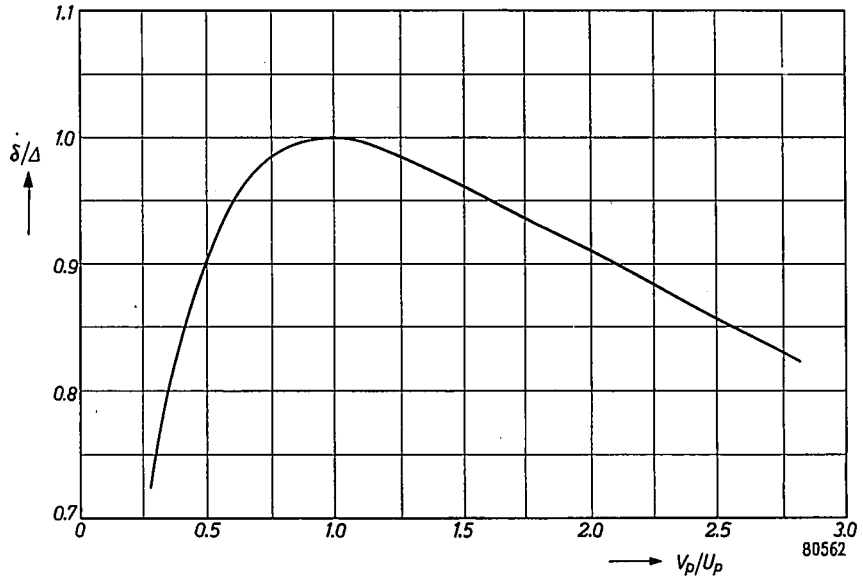

Fig. 7. The universal δ curve of secondary emission.

TABLE I

Values of Δ and U_p determined from our own measurements

Material	Δ	U_p, volts
Soot	0·406	300
Graphite (cube)	0·719	325
Graphite (layer) *)	1·913	335
Graphite (layer) **)	1·045	265
Ferro-titanium	1·695	315
"Ferralma" ***) (impure)	1·555	500
Nickel (≧99·5% Ni)	1·300	470
Nickel (≧97·5% Ni)	1·392	455
Copper	1·042	295
Germanium	1·400	300
Zirconium (woolly)	0·774	460
Molybdenum	1·330	350
Tungsten	1·260	720
Platinum (on molybdenum)	1·306	615
Platinum black	0·780	910
Gold (electrolytical)	1·420	765

*) Obtained by spreading a suspension produced by Acheson Colloids Limited, London & Plymouth, and brought out by them under the name (registered trade mark) "Dag" Dispersion No. 660 B.

**) Obtained by spreading a suspension consisting chiefly of 1 part by volume of the suspension mentioned in footnote *), 2 parts by volume of water and 1 part by volume of aethanol.

***) Aluminium-coated sheet-iron.

TABLE II

Values of Δ and U_p determined from measurements made by others

Material	Δ	U_p, volts	Determined from
Lithium	0·464	75	ref [2]), fig. 11 (curve II)
Beryllium	0·533	180	id., fig. 14
Aluminium	0·908	270	id., fig. 17 (curve I)
Nickel carbide	0·932	280	id., fig. 21 ($\nu = 0°$)
Silver	1·560	715	id., fig. 18 (curve ⊙)
Iron	1·30	350	ref. [3]), fig. 12
Platinum	1·53	1000	
Nickel	1·34	500	ref. [6]), fig. 3 (ref. [11]), fig. 14)
Copper	1·28	575	
Niobium	1·17	350	
Molybdenum	1·25	360	
Silver	1·475	800	
Tantalum	1·29	700	
Tungsten	1·33	650	
Gold	1·46	715	

Reprinted from
Philips Res. Rep. Vol. 9, Nr 5, pages 401-402, 1954

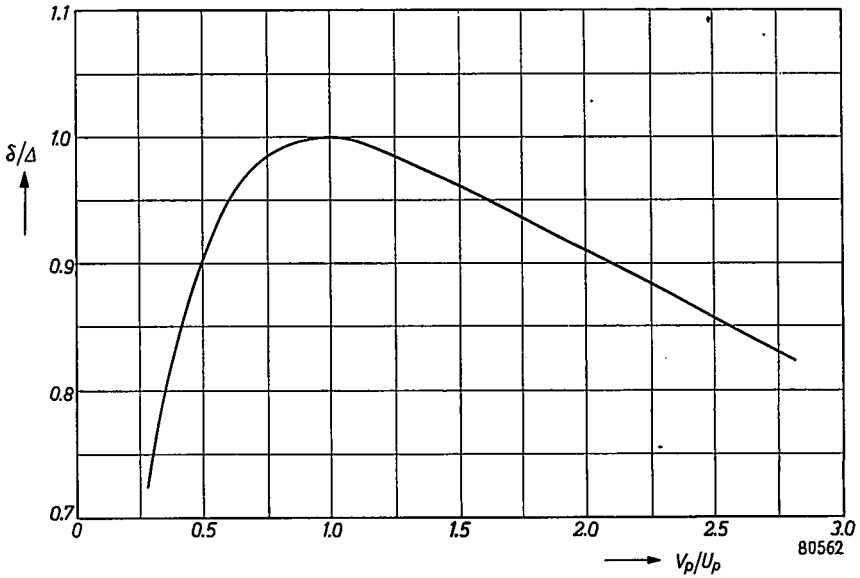

Fig. 7. The universal δ curve of secondary emission.

TABLE I

Values of Δ and U_p determined from our own measurements

Material	Δ	U_p, volts
Soot	0·406	300
Graphite (cube)	0·719	325
Graphite (layer) *)	1·913	335
Graphite (layer) **)	1·045	265
Ferro-titanium	1·695	315
"Ferralma" ***) (impure)	1·555	500
Nickel (≧99·5% Ni)	1·300	470
Nickel (≧97·5% Ni)	1·392	455
Copper	1·042	295
Germanium	1·400	300
Zirconium (woolly)	0·774	460
Molybdenum	1·330	350
Tungsten	1·260	720
Platinum (on molybdenum)	1·306	615
Platinum black	0·780	910
Gold (electrolytical)	1·420	765

*) Obtained by spreading a suspension produced by Acheson Colloids Limited, London & Plymouth, and brought out by them under the name (registered trade mark) "Dag" Dispersion No. 660 B.

**) Obtained by spreading a suspension consisting chiefly of 1 part by volume of the suspension mentioned in footnote *), 2 parts by volume of water and 1 part by volume of aethanol.

***) Aluminium-coated sheet-iron.

TABLE II

Values of Δ and U_p determined from measurements made by others

Material	Δ	U_p, volts	Determined from
Lithium	0·464	75	ref [2]), fig. 11 (curve II)
Beryllium	0·533	180	id., fig. 14
Aluminium	0·908	270	id., fig. 17 (curve I)
Nickel carbide	0·932	280	id., fig. 21 ($v = 0°$)
Silver	1·560	715	id., fig. 18 (curve ⊙)
Iron	1·30	350	ref. [3]), fig. 12
Platinum	1·53	1000	
Nickel	1·34	500	ref. [6]), fig. 3 (ref. [11]), fig. 14)
Copper	1·28	575	
Niobium	1·17	350	
Molybdenum	1·25	360	
Silver	1·475	800	
Tantalum	1·29	700	
Tungsten	1·33	650	
Gold	1·46	715	

VOL. 9 NR 6 DECEMBER 1954

Philips Research Reports

EDITED BY THE RESEARCH LABORATORY
OF N.V. PHILIPS' GLOEILAMPENFABRIEKEN, EINDHOVEN, NETHERLANDS

R 253 *Philips Res. Rep. 9, 403-443, 1954*

SATURATION MAGNETIZATION AND CRYSTAL CHEMISTRY OF FERRIMAGNETIC OXIDES *)

by E. W. GORTER

621.317.421:548.3:548.736.453.2

6. SATURATION MOMENT AND CRYSTAL CHEMISTRY OF FERRIMAGNETIC SPINELS CONTAINING TITANIUM

6.1. Introduction to the sections 6-8

The investigations to be reported in sections 6, 7 and 8 have been started in order to obtain a mixed-crystal series in which the difference of the sublattice saturation magnetizations at 0 °K, $m_b - m_a$, changes sign. Our discussion of Néel's theory (section 2.2.1) shows that for compositions near that for which $m_b - m_a = 0$ anomalous σ-T curves may be expected.

By replacing in an inverse ferrite $Fe^{3+}[Me^{2+}Fe^{3+}]O_4$ the ferric ion in the B position completely or partly by a non-magnetic ion, or by a magnetic ion with a smaller magnetic moment, the saturation moment is lowered, and a reversal in sign of $m_b - m_a$ might in principle be brought about in this way.

Supposing that the distribution of the other ions remains unaltered, and that all moments in the B position are antiparallel to all those in the A position, replacement of the ferric ion in the B position will give a change in saturation moment which can be simply calculated. The ferric ion in the B position might be replaced in the following ways:
(1) Substitution of 1 Al^{3+} for 1 Fe^{3+} would for the above supposition give $m_b - m_a = m_{Me^{2+}} - 5$, and thus give reversal if the moment of the divalent ion $m_{Me^{2+}} < 5$. Aluminium is known, however, not to have a great preference for sixfold with respect to fourfold coordination (cf. the silicates and $Al[Li_{0.5}Al_{1.5}]O_4$) **). Moreover it was known to us that a miscibility gap occurs in the system $MgFe_2O_4$-$MgAl_2O_4$ (section 1.2, ref. [7])). In view of the large difference in cell edge between the ferrites and the corresponding aluminates this might have been a very general phenomenon. For these reasons this substitution was not the first to be investigated.

The system $NiFe_2O_4$-$NiAl_2O_4$, as well as the systems $MgFe_2O_4$-$MgAl_2O_4$ and $Fe^{II}Fe_2O_4$-$Fe^{II}Al_2O_4$, investigated by other authors, are discussed in section 8.

*) Continued from Philips Res. Rep. 9, 295-320, 321-365, 1954.
**) Scandium has, but is very expensive.

(2) Substitution of 1 Cr^{3+}, which has a strong preference for sixfold coordination, for 1 Fe^{3+}, gives $m_b - m_a = m_{Me^{2+}} - 2$, assuming $m_{Cr^{3+}} = 3$, and would thus give reversal in sign of $m_b - m_a$ if $m_{Me^{2+}} < 2$. By substituting Cr^{3+} for Fe^{3+} in Mg ferrite or Cu ferrite, therefore, one might get such a reversal; these ferrites are, however, already partly normal. $Fe[Li_{0.5}Fe_{1.5}]O_4$ has a completely inverse arrangement, however, and thus, with the above suppositions, replacement of 1·25 Fe^{3+} by 1·25 Cr^{3+} gives $m_b - m_a = 0$, and replacement of $>1{\cdot}25$ Fe^{3+} by $>1{\cdot}25$ Cr^{3+} reversal of $m_b - m_a$. This system will be reported upon in section 7.

(3) Substitution of $0{\cdot}5\ Me^{2+} + 0{\cdot}5\ Ti^{4+}$ for Fe_B^{3+} would, with the above suppositions, give $m_b - m_a = 1{\cdot}5\ m_{Me^{2+}} - 5$ and thus reversal of $m_b - m_a$ for $m_{Me^{2+}} \leqslant 3{\cdot}33$, i.e. for $Me^{2+} = Ni^{2+}$ (or Cu^{2+} or Mg^{2+}). The system with $Me^{2+} = Ni^{2+}$ is one of the systems reported upon in section 6.

It will be seen, however, that neither Al^{3+} nor Ti^{4+} occupy octahedral sites only, and that substitution of Cr^{3+} for Fe^{3+} alters the distribution of the other cations.

In the first system to be described in the present section 6 we have replaced 1 Fe^{3+} in $Fe[NiFe]O_4$ by $(0{\cdot}5\ Ni^{2+} + 0{\cdot}5\ Ti^{4+})$. Nickel is known to have a strong preference for sixfold coordination: nickel titanate, Ni_2TiO_4, does not exist [81] [82] *). In another series, viz. $Zn_{2-a}Ni_aTiO_4$, investigated by Birnbaum and Scott [81], the spinel phase extends only up to $a = 1{\cdot}0$, which suggests that Ni^{2+} and Ti^{4+} will occupy octahedral sites only, corresponding to a formula $Zn[NiTi]O_4$ for $a = 1$. For this reason we have originally extended the series $Ni_{1+a}Fe_{2-2a}Ti_aO_4$, nickel ferrite-nickel titanate, only up to $a = 0{\cdot}5$, i.e. to the composition $Ni_{1.5}FeTi_{0.5}O_4$.

Materials with $a = 0{\cdot}60$, 0·70, 0·75 and 0·80 have since also been prepared: the X-ray diagrams of these preparations show reflexions of an ilmenite phase ($NiTiO_3$), with intensities increasing in the above order, next to the spinel pattern, and possibly NiO reflexions, which, however, coincide with strong spinel reflexions. This behaviour is the same as that found in the series $Zn_{2-a}Ni_aTiO_4$ for $a > 1$ [81] and shows up the instability of Ni_2TiO_4 even in mixed crystals.

Two more series of mixed crystals have been investigated in which with the above suppositions $m_b - m_a$ would change sign. These systems, $Ni_{1.5}FeTi_{0.5}O_4$-$NiZn_{0.5}FeTi_{0.5}O_4$ **) and $Ni_{1.5}FeTi_{0.5}O_4$-$Mn_{1.5}FeTi_{0.5}O_4$, are reported upon in sections 6.3 and 6.4 respectively.

6.2. The system $Ni^{II}_{1+a}Fe^{III}_{2-2a}Ti^{IV}_aO_4$ ($NiFe_2O_4$-$Ni_{1.5}FeTi_{0.5}O_4$)

6.2.1. Experimental

Materials with the above general formula were prepared with $a = 0$, 0·1, 0·2, 0·3, 0·4 and 0·5.

These materials were prepared from
Fe (C 0·03 %),
Ni (Si 0·02 %, Co 0·01$_0$ %, Pb 0·01 %),
TiO_2 (Si 0·13 %, Fe 0·02$_5$ %, Al 0·01 %, Mg 0·01 %),
by method (B), pref. 600 °C until complete decomposition of the nitrates is obtained, milling, pref. 4 h 1000 °C, remilling, sint. 4 h 1200 °C in O_2.

*) Unpublished observation by the author for various firing temperatures.

**) Here $m_b - m_a$ would change sign if an additional supposition is made, viz. that Zn^{2+} occupies tetrahedral sites only.

Two series of samples were prepared:
(1) cooled slowly from 1200 °C in O_2 and annealed in O_2 at low temperatures (3 h 800 °C, 7 h 700 °C, 30 h 600 °C);
(2) quenched from 1200 °C by dropping rapidly into a sodium-chloride solution, which is afterwards rinsed out with boiling distilled water.

Chemical analysis: no detectable amounts of Fe^{2+} were present in either series.

X-ray diffraction patterns obtained on a Norelco High-angle X-ray Diffractometer showed the preparations to be pure spinels, but yielded no data as regards ionic distribution, which fact is due to the small difference in scattering powers of the ions present. Saturation vs temperature curves were measured for all preparations *). The saturation moments in Bohr magnetons are given in fig. 16*a* and in table X. The Curie temperatures

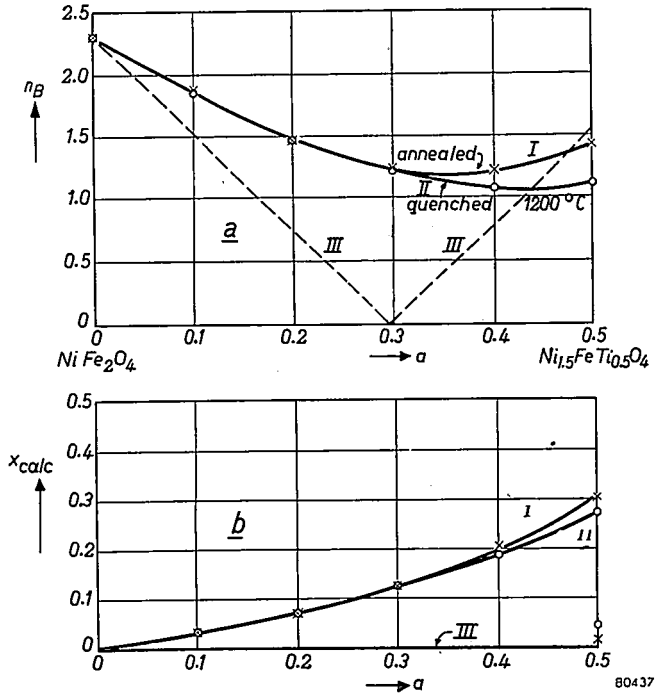

Fig. 16*a*. Saturation moments of the mixed-crystal series $Ni_{1+a}Fe_{2-2a}Ti_aO_4$, for $a = 0$-$0{\cdot}5$. Curve I: annealed samples; curve II: samples quenched from 1200 °C; line III: saturation moments calculated for all Ti^{4+} and Ni^{2+} ions in the octahedral position.
b. Amount of Ti^{4+} ions in the tetrahedral position per formula unit (x), calculated from the saturation moments shown in fig. 16*a*, assuming the Ni^{2+} ions to occupy octahedral sites throughout the series.
Curve I: annealed samples; curve II: samples quenched from 1200 °C; line III: the line $x = 0$, for which line III of fig. 16*a* was drawn.

*) Fields up to 5900 oersteds were used, also at 20 °K.

(Θ) for all samples, and the cell edges for the annealed preparations only, are also given in the table.

TABLE X

Saturation moments, Curie temperatures and cell edges for the series $Ni^{II}_{1+a}Fe^{III}_{2-2a}Ti^{IV}_{a}O_4$

Ti content a	formula	n_B annealed	n_B quenched	Θ annealed (°C)	Θ quenched (°C)	cell edge annealed (Å)
0	$NiFe_2O_4$	2·29	2·29	585	585	8·337
0·1	$Ni_{1·1}Fe_{1·8}Ti_{0·1}O_4$	1·88	1·85	550	550	$8·337_5$
0·2	$Ni_{1·2}Fe_{1·6}Ti_{0·2}O_4$	1·49	1·48	500	500	8·338
0·3	$Ni_{1·3}Fe_{1·4}Ti_{0·3}O_4$	1·25	1·23	440	440	$8·338_5$
0·4	$Ni_{1·4}Fe_{1·2}Ti_{0·4}O_4$	1·24	1·10	375	356	8·339
0·5	$Ni_{1·5}Fe_{1·0}Ti_{0·5}O_4$	1·45	1·12	293	265	—

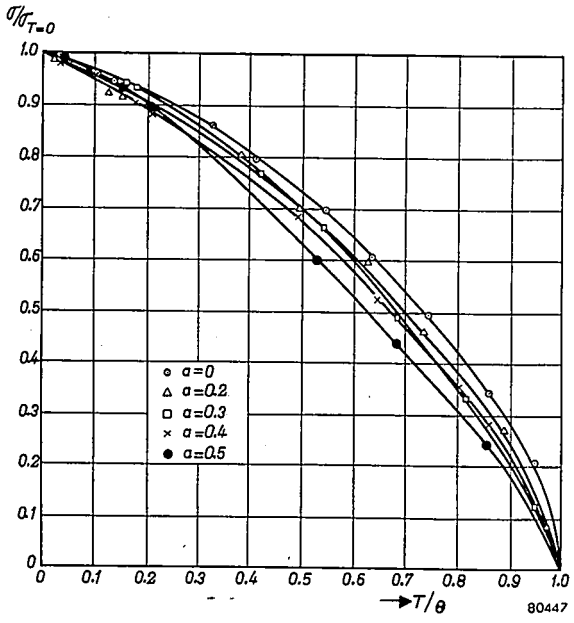

Fig. 17. Reduced saturation-magnetization vs temperature (σ/σ_0 vs T/Θ) curves for the mixed-crystal series $Ni_{1+a}Fe_{2-2a}Ti_aO_4$.

The reduced saturation-magnetization vs temperature (i.e. $\sigma_T/\sigma_{T=0}$ vs T/Θ) curves for the annealed preparations are given in fig. 17. Mr H. G. Beljers has kindly measured the effective g-factor (g_{eff}) of annealed $Ni_{1.5}FeTi_{0.5}O_4$ for us by the ferromagnetic resonance method at 3·18 and 1·24 cm wavelengths on spheres of about 0·5 mm diameter. The results are

$Ni_{1.5}FeTi_{0.5}O_4$ (annealed)

wavelength	temperature	g_{eff}
1·24 cm	300 °K	2·70-2·71
3·18 cm	293 °K	2·73
3·18 cm	83 °K	2·85
	(extrapolated towards 0°K)	2·90

6.2.2. Discussion of the results for the annealed samples and neutron-diffraction evidence

The saturation moments calculated on the assumption that all Ni^{2+} and Ti^{4+} ions occupy octahedral sites, and for mutually completely antiparallel orientation of the ionic moments on A and B sites, are indicated in fig. 16a by the dashed line III. It is seen that the experimental curves deviate widely from this line *). Moreover the σ-T curves of the compositions investigated show no anomalous behaviour. Obviously one of the assumptions made in the calculation of line II is incorrect.

Dr K. F. Niessen [83]), using experimental data from another mixed-crystal series ($NiFe_2O_4$-$ZnFe_2O_4$) in a Néel molecular-field theory, extended for the presence of two different kinds of magnetic ions, has shown that the occurrence of non-parallel ionic moments in B (or A) sites is unlikely in the present series ($NiFe_2O_4$-$Ni_{1.5}FeTi_{0.5}O_4$). We shall stick, therefore, to our assumption that in the present series the ionic moments inside each of the sublattices A and B are parallel.

The deviations of the experimental moments from line III must be explained, therefore, by a migration of some Ni^{2+} or Ti^{4+} ions, or both, to the tetrahedral position. The general formula is

$$Ni_y\, Ti_x\, Fe_{1-x-y}\, [Ni_{1+a-y}\, Fe_{1-2a+x+y}\, Ti_{a-x}]\, O_4\,, \qquad (6.1)$$

for which for antiparallel moments in A and B positions

$$n_B = |m_b - m_a|\,,$$

while

$$m_b - m_a = 2{\cdot}3 - 7{\cdot}7a + 10x + (7{\cdot}7 - p)y. \qquad (6.2)$$

*) Except for $a = 0{\cdot}5$, where, moreover, a cation distribution $Fe[Ni_{1.5}Ti_{0.5}]O_4$ apriori seemed likely because of the possibility of long-range order of the $Fe[Li_{0.5}Fe_{1.5}]O_4$ type.

In this equation $p = (g_{Ni^{2+}})_A$, the g-factor of Ni^{2+} in the A position *).

From the experimental n_B values of table X we obtain, using this formula

$$\text{for } a = 0{\cdot}1,\ 0{\cdot}2,\ 0{\cdot}3,\ 0{\cdot}4 \text{ and } 0{\cdot}5$$

$$10x + (7{\cdot}7 - p)y = 0{\cdot}35,\ 0{\cdot}73,\ 1{\cdot}26,\ 2{\cdot}02 \text{ and } 3{\cdot}00 \text{ or } 0{\cdot}10 \text{ respectively.}$$

For $a = 0{\cdot}5$ there are two solutions: the second figure indicates the solution for which $m_b - m_a < 0$.

There is ample evidence that it is mainly Ti^{4+} rather than Ni^{2+} ions which migrate to the tetrahedral position:

(1) Niessen [84]) has calculated, in a manner indicated above, that the Curie temperatures given in table X can be accounted for only by assuming an increasing migration of Ti^{4+} ions to the A sites with increasing a **).

(2) The value of g_{eff}, extrapolated towards $T = 0$ °K, may be used together with n_B to determine the cation distribution, using formula (4.6) for g_{eff}. Using the values for $Ni_{1{\cdot}5}FeTi_{0{\cdot}5}O_4$ ($a = 0{\cdot}5$) we have

$$n_B = |-1{\cdot}55 + 10x + (7{\cdot}7 - p)y| = 1{\cdot}45$$

and

$$g_{eff} = \left| \frac{n_B}{-1 + 5x + 3y} \right| = 2{\cdot}90,$$

which equations give only one physically possible solution:

$$x = 0{\cdot}30, \qquad y = 0.$$

This means that only (or, in view of the uncertainty of the extrapolation of g_{eff} towards 0 °K, practically only) Ti^{4+} ions migrate to the tetrahedral position and that $m_b - m_a > 0$.

We wish to draw attention to the fact that generally for ferrimagnetics containing two different kinds of magnetic ions, the cation distribution may be calculated from g_{eff} and n_B, provided the g-factors of the ions are known and sufficiently different, and provided the ionic moments inside each lattice position are parallel [85]) ***).

Although theory cannot yet account for details such as the frequency dependence of the effective g-factor, we feel justified in using g_{eff} in the above manner to determine the approximate cation distribution.

---

*) In view of the difference between the crystalline electric fields in the A and B positions $(g_{Ni^{2+}})_A$ will be different from (and presumably higher than) $(g_{Ni^{2+}})_B$. Dr J. S. Smart (private communication, to be published in Phys. Rev.) uses a value $(g_{Ni^{2+}})_A = 3{\cdot}5$, obtained from susceptibility measurements on $NiAl_2O_4$.

**) This result was obtained before the following experimental evidence, given sub (2) and (3), was available.

***) J. S. Smart has independently used this method for determining the cation distribution in the series $NiFe_2O_4$-$NiAl_2O_4$ (see section 8) (private communication from Dr Smart, to be published in Phys. Rev). For non-parallel ionic moments inside one lattice position see section 6.3.2.

(3) Neutron-diffraction patterns, kindly made for us by Dr C. G. Shull *) for the annealed preparations with $a = 0$, 0·3 and 0·5 show a regular decrease of the intensity of the 220 reflexion (structure factor $= 8f_{tetr}$), which points to an increasing amount of Ti^{4+} in the A sites in this order, in view of the very small neutron-scattering cross-section of the Ti nucleus.

A comparison of the experimental intensities of the neutron-diffraction pattern of $Ni_{1·5}FeTi_{0·5}O_4$, with those calculated for the distribution

$$Fe_{0·7}Ti_{0·3}[Ni_{1·5}Fe_{0·3}Ti_{0·2}]O_4\,, \qquad (6.3)$$

taking into account the magnetic contribution to these intensities, will be given elsewhere.

In view of the above evidence we feel justified in assuming $y \approx 0$ and calculating x from the saturation moments for the whole series of mixed crystals. The values obtained are given in fig. 16*b*. The distribution in the annealed samples is very near to one in which Ni^{2+} occupies the octahedral position and Fe^{3+} and Ti^{4+} are distributed at random amongst the remaining sites, i.e.

$$Fe_{0·667}Ti_{0·333}[Ni_{1·5}Fe_{0·333}Ti_{0·167}]O_4.$$

The presence of Ti^{4+} ions in tetrahedral coordination is rather unexpected. So far the only indication of the occurrence of Ti^{4+} ions in tetrahedral coordination, to our knowledge, is the incorporation of Ti^{4+} activator ions in SiO_2 and Zn_2SiO_4 phosphors [86]: in the structures of the latter compounds the cations occur in tetrahedral coordination only.

J. S. Smart **) has shown for another system of ternary spinels ($NiFe_2O_4$-$NiAl_2O_4$) that in the two Boltzmann-distribution formulae of the type of eq. (1.1.) of section 1.2.6 the values of the energies of interchange of two cations between the two crystallographic positions E can be chosen in such a way that the theoretical cation-distribution curves coincide with the experimental ones. These curves are of the same type as those found in the present system for the annealed and quenched samples (fig. 16*b*).

This suggests that our distribution curves can be qualitatively accounted for without taking into account the occurrence of short-range order. We shall see, however, that the decrease of n_B on quenching cannot be accounted for without the influence of short-range order.

6.2.3. Discussion of the results for the quenched samples

The saturation moments and the Curie temperatures for the quenched samples show a decrease with respect to those for the annealed samples near $a = 0·5$.

*) The author is indebted to Dr Shull for making these measurements for him.
**) See footnote on preceding page.

Quenching generally results in the preservation of a more random distribution of the cations amongst A and B sites. Equation (6.2) shows that an increase of y gives an increase of n_B, and even for an arrangement in which the Fe^{3+} and Ti^{4+} ions are kept distributed about at random amongst the sites not occupied by Ni^{2+}, i.e. for $x \approx (1-y)a/(2-a)$, the n_B values calculated are higher than the experimental values for the annealed samples. The saturation moment alone, therefore, leads to the conclusion that quenching primarily results in a decrease of x, and thus in a *less* statistical distribution of Ti^{4+} and Fe^{3+} ions amongst the available sites. This paradox is removed only by assuming that the Ti^{4+} ions have some preference for the B sites with respect to the Fe^{3+} ions, which is still noticeable in the quenched sample ($x = 0{\cdot}27$). During slow cooling entropy alone would cause more Ti^{4+} ions to migrate to the B sites, but in fact more Ti^{4+} then move to the A sites ($x = 0{\cdot}30$), presumably because the gain in short-range-order energy of Ti^{4+} and Fe^{3+} ions in the A sites outweighs the combined effect of entropy and any loss of short-range order in the B sites.

Our knowledge of the various energy terms involved is too small to account for this effect.

6.3. The system $Ni^{II}_{1\cdot5-a}Zn^{II}_{a}Fe^{III}Ti^{IV}_{0\cdot5}O_4$ ($Ni_{1\cdot5}FeTi_{0\cdot5}O_4$-$NiZn_{0\cdot5}FeTi_{0\cdot5}O_4$)

6.3.1. Experimental

Materials with the above general formula were prepared with $a = 0$ *), 0·1, 0·2, 0·3, 0·4 and 0·5.

The preparation was carried out in the same manner as for the materials described in the preceding system (6.2); ZnO (AnalaR) was used as an additional raw material.

Two series of samples were prepared, either annealed at low temperatures, or quenched from 1200 °C, like in section 6.2. Chemical analysis showed no detectable amounts of Fe^{2+} in either series.

The X-ray diffraction patterns obtained on a Norelco X-ray Diffractometer showed the preparations to be pure spinels; no data as regards ionic distribution could be obtained. The saturation moments **) in Bohr magnetons are given in fig. 18*a* and in table XI; the Curie temperatures for all samples, and the cell edges for the annealed preparations only, are also given in table XI.

The reduced saturation vs temperature ($\sigma_T/\sigma_{T=0}$ vs T/Θ) curves for the annealed preparations are given in fig. 19. For the annealed sample of $NiZn_{0\cdot5}FeTi_{0\cdot5}O_4$ the effective g-factor was measured by Mr H. G. Beljers.

*) This is the preparation of the preceding series with $a = 0{\cdot}5$.
**) Fields up to 5900 oersteds were used, also at 20 °K.

TABLE XI

Saturation moments, Curie temperatures and cell edges for the series $Ni^{II}_{1\cdot5-a}Zn^{II}_{a}Fe^{III}Ti^{IV}_{0\cdot5}O_4$

Zn content a	formula	n_B annealed	n_B quenched	Θ annealed (°C)	Θ quenched (°C)	cell edge annealed (Å)
0	$Ni_{1\cdot5}FeTi_{0\cdot5}O_4$	1·44	1·12	293	265	—
0·1	$Ni_{1\cdot4}Zn_{0\cdot1}FeTi_{0\cdot5}O_4$	1·02	1·04	267	250	8·348
0·2	$Ni_{1\cdot3}Zn_{0\cdot2}FeTi_{0\cdot5}O_4$	1·07	1·34	265	235	8·355
0·3	$Ni_{1\cdot2}Zn_{0\cdot3}FeTi_{0\cdot5}O_4$	1·32	$1\cdot52_5$	264	220	8·365
0·4	$Ni_{1\cdot1}Zn_{0\cdot4}FeTi_{0\cdot5}O_4$	1·73	1·82	240	195	8·372
0·5	$NiZn_{0\cdot5}FeTi_{0\cdot5}O_4$	2·1	2·1	225	172	8·382

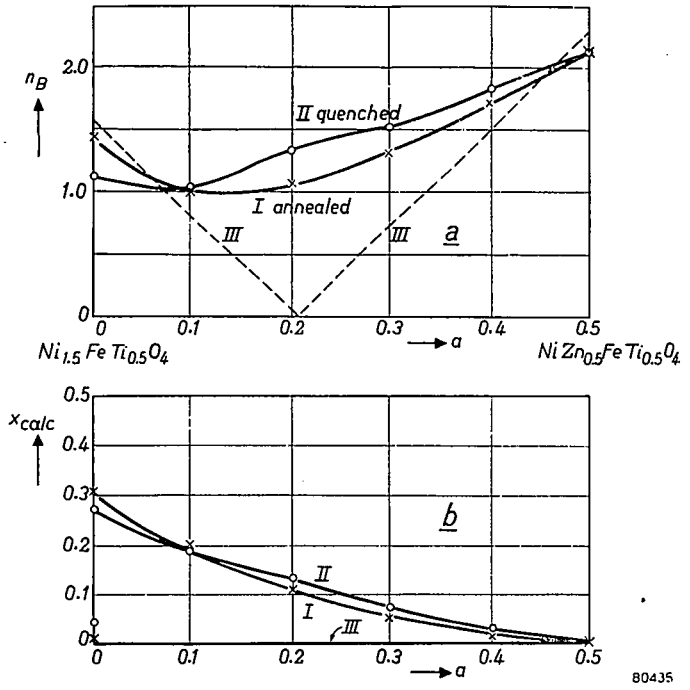

Fig. 18*a*. Saturation moments of the mixed-crystal series $Ni_{1\cdot5-a}Zn_aFeTi_{0\cdot5}O_4$, for $a = 0$ - 0·5. Curve I: annealed samples; curve II: samples quenched from 1200 °C; line III: saturation moments calculated for all Ti^{4+} and Ni^{2+} ions in the octahedral position and all Zn^{2+} ions in the tetrahedral position.

b. Amount of Ti^{4+} ions in the tetrahedral position per formula unit (x), calculated from the saturation moments shown in fig. 18*a*, assuming the Zn^{2+} ions to occupy tetrahedral sites and the Ni^{2+} ions octahedral sites throughout the series.

Curve I: annealed samples; curve II: samples quenched from 1200 °C; line III: the line $x = 0$ for which line III of fig. 18*a* was drawn.

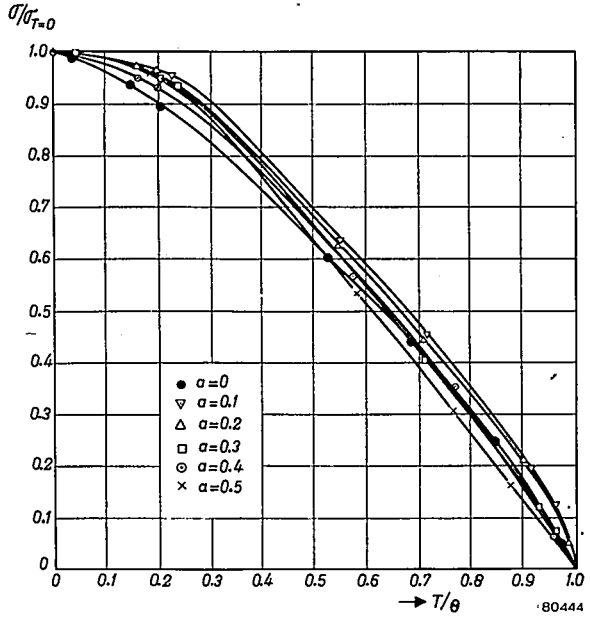

Fig. 19. Reduced saturation-magnetization vs temperature (σ/σ_0 vs T/Θ) curves for the mixed-crystal series $Ni_{1\cdot5-a}Zn_aFeTi_{0\cdot5}O_4$.

The results are

$NiZn_{0\cdot5}FeTi_{0\cdot5}O_4$ (annealed)

wavelength	temperature	g_{eff}
3·18 cm	301 °K	2·33
3·24 cm	90 °K	2·44
1·24 cm	298 °K	2·19
1·24 cm	143 °K	2·19
	(extrapolated towards 0 °K	≈2·19

6.3.2. Discussion of the results

The results obtained for the annealed samples in this system are very similar to those obtained in the previous section. The saturation moments do not pass through zero along the dashed line III, which is calculated for Zn^{2+} in tetrahedral sites and Ni^{2+} and Ti^{4+} in octahedral sites. None of the materials investigated show anomalous σ-T curves (fig. 19).

This result is understood from the fact that for $Ni_{1\cdot5}FeTi_{0\cdot5}O_4$, as we have seen, $m_b > m_a$. We shall now try to deduce the cation distributions from the experimental data. In view of the fact that the amount of Fe^{3+} ions in the A sites for $a = 0\cdot5$ is only about 0·5, we have to reckon with the possibility of non-parallel ionic moments inside the B position.

The general formula of $NiZn_{0.5}FeTi_{0.5}O_4$ ($a = 0.5$) is represented by

$$(Zn + Ti)_{x'}Ni_yFe_{1-x'-y}\,[Ni_{1-y}Fe_{x'+y}\,(Zn + Ti)_{1-x'}]\,O_4.$$

The usual equation for n_B and g_{eff} for parallel ionic moments in the B position yield one physically possible solution for the annealed sample, viz. $x' = 0.45$, $y = 0.07$ (for $(g_{Ni^{2+}})_A = 3.5$). As the simultaneous occurrence of appreciable amounts of Ni^{2+} ions in A sites and of Zn^{2+} ions in B sites in an annealed sample may be ruled out as being unlikely from every crystal-chemical point of view, another arrangement with not quite parallel moments in the B position, i.e. $x' \approx 0.5$ and $y = 0$, seems more likely *). It may be noted that, unlike the saturation moments, the Curie temperatures for the quenched and annealed samples are different, so that the cation distributions probably are not quite the same.

The amount of Ti^{4+} ions in the A position, which we shall denote by x, is $x = 0.30$ for Zn content $a = 0$, and probably $x \approx 0$ for $a = 0.5$, both with $y = 0$; it has been assumed that for intermediate compositions also $y \approx 0$. The x values calculated from n_B for $y = 0$ are given in fig. 18*b*.

The n_B values for the quenched samples with $a = 0.2$ - 0.4 may be explained by a more statistical cation distribution, whereas for the material with $a = 0.5$ the influence of short-range order may make itself felt again.

The system is too complicated to try to understand more about the crystal chemistry.

6.4. The system $Ni^{II}_{1.5-a}Mn^{II}_aFe^{III}Ti^{IV}_{0.5}O_4$ ($Ni_{1.5}FeTi_{0.5}O_4$-$Mn_{1.5}FeTi_{0.5}O_4$)

6.4.1. Experimental

Materials with the above general formula were prepared with $a = 0$ **), 0·2, 0·4, 0.57_5, 0.67_5, 0.77_5, 0·95, 1·1 and 1·5.

The preparation of the materials was carried out in the same way as for the materials described in the preceding section (6.2 and 6.3), using $MnCO_3$ (Na < approx. 0·1 %, Mg 0·01 %) as an additional raw material.

The samples were fired at 1200 °C in atmospheres containing N_2, H_2 and CO_2 in different proportions: X-ray diffraction patterns and chemical analysis showed that preparations with different a, i.e. different ratios Mn^{2+}/Ni^{2+}, required different atmospheres.

---

*) For the case that angles $180°-2\psi$ occur between the directions of the ionic moments inside the B sublattice, we read eq. (4.5) in such a way that $(M_{total})_B$ and $(M_{spin})_B$ are the *resultant* moments of the B sublattice, i.e. we use

$$n_B = \left| \sum_i (x_i g_i S_i)_A - \sum_i (x_i g_i S_i)_B \sin\psi \right|, \tag{6.3}$$

$$g_{eff} = \left| \frac{n_B}{\sum_i (x_i S_i)_A - \sum_i (x_i S_i)_B \sin\psi} \right|. \tag{6.4}$$

**) This is the preparation of section 6.2 with $a = 0.5$.

Adjustment of the oxygen content was carried out by heating for 3 h at 1100 °C fired rods with known oxygen deficit in sealed evacuated quartz tubes which also contained an amount of BaO_2 calculated to give off just the amount of O_2 necessary to oxidize the rods to the correct composition.

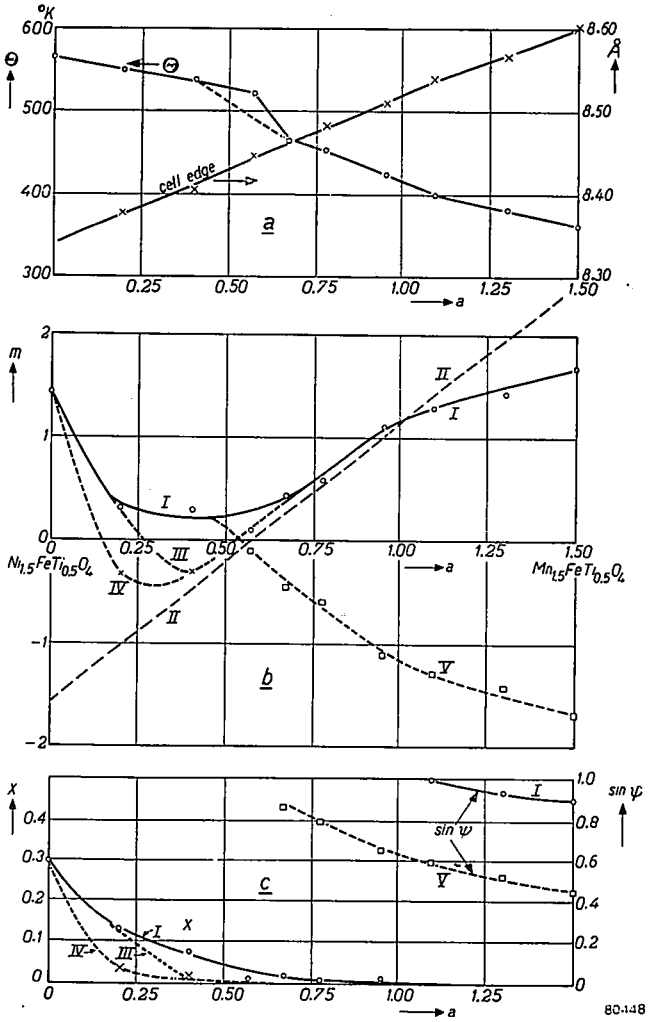

Fig. 20. Properties of the mixed-crystal series $Ni_{1\cdot5-a}Mn_aFeTi_{0\cdot5}O_4$.
a. Curie temperature Θ (°K, left-hand scale) and cell edges (Å, right-hand scale).
b. Saturation moments m; the sign of m is not known with certainty.
Curve I: most probable curve; line II: saturation moments calculated for all Ti^{4+} and Ni^{2+} ions in octahedral sites, without angles between the ionic moments inside one of the sublattices; curves III, IV, V: other possible curves.
c. Amount of Ti^{4+} ions in the tetrahedral position per formula unit (x) for the cases I, III and IV (left-hand scale).
$\sin\psi$, for angles $180° - 2\psi$ occurring between the directions of the ionic moments in *B* positions for the cases I and V (right-hand scale).

The preparations for which the measurements reported upon below were carried out contained the following amounts of excess *) oxygen:

a =	0·2	0·4	0·575	0·675	0·775	0·95	1·1	1·3	1·5
oxygen, wt %	0·04	0·11	0·04	−0·04	0·06	0·05	$-0{\cdot}01_5$	0·00	−0·1

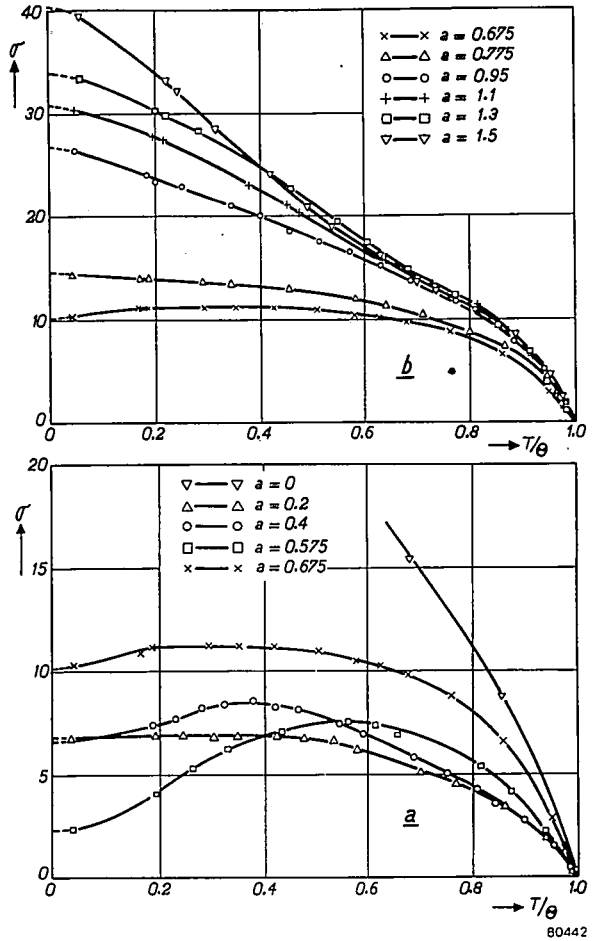

Fig. 21 *a* and *b*. Saturation-magnetization vs reduced-temperature curves for the system $Ni_{1\cdot5-a}Mn_aFeTi_{0\cdot5}O_4$.

X-ray diffraction patterns obtained with Fe $K\alpha$ radiation on a Norelco X-ray Diffractometer showed the preparations to be pure spinels. No data on the cation distribution could be obtained from these diffraction patterns.

Saturation-magnetization measurements were carried out using fields up to 6000 oersteds down to 77 °K; at 77 and 20 °K measurements were

*) An oxygen deficit is indicated by a minus sign.

made in fields up to 23000 oersteds by Mr P. Jongenburger by a method to be described elsewhere by him.

The saturation moments, the Curie temperatures and the cell edges are shown in figs 20*a* and *b* and in table XII.

The saturation-magnetization vs temperature measurements are given as σ vs T/Θ curves in fig. 21.

For the preparation with $a = 0{\cdot}77_5$ the effective g-factor was measured by Mr H. G. Beljers on a sphere of about 0·5 mm diameter. The results are

$Ni_{0{\cdot}72_5}Mn_{0{\cdot}77_5}FeTi_{0{\cdot}5}O_4$

wavelength	temperature	g_{eff}
$1{\cdot}25_5$ cm	293 °K	2·58
$1{\cdot}25_5$ cm	209 °K	2·68
$1{\cdot}25_5$ cm	143 °K	2·75
	(extrapolated towards 0 °K)	(2·80-)2·88

TABLE XII

Saturation moments, Curie temperatures and cell edges for the series $Ni_{1{\cdot}5-a}Mn_aFeTi_{0{\cdot}5}O_4$

Mn content a	formula	n_B	Θ (°C)	cell edge (Å)
0	$Ni_{1{\cdot}5}FeTi_{0{\cdot}5}O_4$	1·45	293	—
0·2	$Ni_{1{\cdot}3}Mn_{0{\cdot}2}FeTi_{0{\cdot}5}O_4$	0·32	277	8·3752 ± 10
0·4	$Ni_{1{\cdot}1}Mn_{0{\cdot}4}FeTi_{0{\cdot}5}O_4$	0·30	265	8·4033 ± 4
$0{\cdot}57_5$	$Ni_{0{\cdot}92_5}Mn_{0{\cdot}57_5}FeTi_{0{\cdot}5}O_4$	0·10	249	8·4456 ± 10
$0{\cdot}67_5$	$Ni_{0{\cdot}82_5}Mn_{0{\cdot}67_5}FeTi_{0{\cdot}5}O_4$	$0{\cdot}44_5$	192	8·4667 ± 10
$0{\cdot}77_5$	$Ni_{0{\cdot}72_5}Mn_{0{\cdot}77_5}FeTi_{0{\cdot}5}O_4$	0·60	181	8·4834 ± 4
0·95	$Ni_{0{\cdot}55}Mn_{0{\cdot}95}FeTi_{0{\cdot}5}O_4$	1·11	152	8·5096 ± 7
1·1	$Ni_{0{\cdot}4}Mn_{1{\cdot}1}FeTi_{0{\cdot}5}O_4$	1·28	126	8·5412 ± 7
1·3	$Ni_{0{\cdot}2}Mn_{1{\cdot}3}FeTi_{0{\cdot}5}O_4$	1·42	109	8·5691 ± 10
1·5	$Mn_{1{\cdot}5}FeTi_{0{\cdot}5}O_4$	1·68	89	8·6025 ± 10

6.4.2. Discussion of the results

The general formula of this mixed-crystal series is

$$Ti_xNi_y(Fe^{III} + Mn^{II})_{1-x-y}[Ni_{1{\cdot}5-a-y}(Fe^{III} + Mn^{II})_{a+x+y}Ti_{0{\cdot}5-x}]O_4\ ^*).$$

*) Since $m_{Mn^{2+}} = m_{Fe^{3+}} = 5$ an interchange of Mn^{2+} and Fe^{3+} between A and B sites does not influence n_B.

As long as the ionic moments in the A and B sublattices are antiparallel, the saturation moment will be

$$n_B = |m_b - m_a|;$$

in the present case

$$m_b - m_a = -1{\cdot}55 + 2{\cdot}7a + 10x + (7{\cdot}7 - p)y\,. \qquad (6.5)$$

For all values of a except $a = 0$ the sign of $m_b - m_a$ is unknown.

The values of $m_b - m_a$ for antiparallel ionic moments in A and B sites, for the case that all Ni^{2+} and Ti^{4+} ions occupy B sites, are represented by the dashed line II (fig. 20*b*).

For $a = 0{\cdot}77_5$ the above equation and that for the effective g-factor (using $g_{eff} = 2{\cdot}88$) yield one solution ($x = -0{\cdot}02$; $y = 0{\cdot}02$) that is near to a physically possible arrangement ($x \approx 0$; $y \approx 0$); in this case $m_b - m_a$ is positive *) and lies on line II.

If we assume that angles occur between the ionic moments inside the B position we find, using eqs (6.3) and (6.4), that solutions exist for which $m_b - m_a$ is negative (line V), but with larger values of y, e.g. $y \approx 0{\cdot}2$ for $x \approx 0$. We shall discard these solutions as very much less likely than the previous one ($x \approx 0$, $y \approx 0$, no angles) in view of the fact that $y = 0$ for $a = 0$, and that Ni^{2+} ions will certainly not be driven from the octahedral sites by Mn^{2+} ions, in view of their great individual preference for sixfold coordination.

From the fact that the materials with $a = 0{\cdot}4$, $0{\cdot}57_5$ and $0{\cdot}67_5$ show curves of fig. 8, type *c*, and those with $a = 0{\cdot}2$ and $0{\cdot}77_5$ curves practically of fig. 8, type *b*, we deduce that for all these preparations $m_b - m_a$ has the same sign, i.e. positive. Therefore m is positive for the complete system, and curves III and IV are also discarded.

The n_B values up to $a = 0{\cdot}95$ may be accounted for by a continuous decrease of the amount of Ti^{4+} ions in the tetrahedral position (x) (see fig. 20*c*). The curve for x as a function of the Ni^{2+} content has the same shape as in the previous sections 6.2 and 6.3.

The fact that the experimental n_B values for $a = 1{\cdot}1$-$1{\cdot}5$ fall below line II must in our view be explained by not completely antiparallel A and B moments.

The Curie temperatures show a break near $a = 0{\cdot}57_5$ but from the saturation moment we deduced that this preparation has less Ti^{4+} ions in the tetrahedral position than the value lying on the smooth line I drawn through the other points: this would explain a Curie temperature for this preparation higher than the value lying on the smooth dashed line I through the other points.

*) The fact that no physically possible solution is found is not surprising in view of the sensitivity of n_B to slight variations in e.g. x; the measurements of n_B and g_{eff} have been carried out on different parts of the same sample so that very slight inhomogeneities, i.e. differences in the average value of x of the order of $\pm 0{\cdot}01$, might cause such a small shift in values.

The cell edges vary practically linearly from $a = 0$ to $a = 1{\cdot}5$, although the amount of Ti^{4+} in the A sites does not vary linearly with a. The same behaviour can be observed in the two previous mixed-crystal systems (sections 6.2 and 6.3); it seems that the interchange of Ti^{4+} and Fe^{3+} between the A and B positions does not noticeably affect the cell edge.

The Mn^{2+}-Fe^{3+} distribution amongst the two sublattices cannot be deduced from the available data.

Though one type of anomalous σ-T curve occurs in the present system, no change of sign of $m_b - m_a$ has been found.

REFERENCES

[81]) H. Birnbaum and R. K. Scott, J. Amer. chem. Soc. **72**, 1398-1399, 1950.
[82]) N. W. Taylor, Z. phys. Chem. **9B**, 241-264, 1930.
[83]) K. F. Niessen, private communication.
[84]) K. F. Niessen, Physica **19**, 1127-1132, 1953.
[85]) E. W. Gorter, Nature **173**, 123-124, 1954.
[86]) F. A. Kröger, Some Aspects of the Luminescence of Solids, Elsevier Publishing Co., Inc., Amsterdam-New York, 1948, p. 158-160.

7. FERRIMAGNETIC OXIDES CONTAINING CHROMIUM: THE SYSTEM $Li_{0.5}Fe^{III}_{2.5-a}Cr^{III}_{a}O_4$ ($Li_{0.5}Fe_{2.5}O_4$-$Li_{0.5}Fe_{0.5}Cr_2O_4$)

7.1. Experimental

A series of materials with the general composition $Li_2O.(5-2a)Fe_2O_3.2aCr_2O_3$ was prepared with $a = 0$, 0·50, 0·75, 1·00, 1·25, 1·50, 1·60, 1·70, 2·00 and 2·50.

The materials were prepared from
Fe (Ni $0{\cdot}01_6$ %),
CrO_3 (Ca<appr. 0·2 %, Cu $0{\cdot}01_2$ %, Si 0·01 %),
Li_2CO_3 (Mg and Ca 0·02 %, Fe, Al and Si 0·01 %).
A Cr^{III} nitrate solution was prepared by dissolving the CrO_3 in water and reducing with ethanol at 40 °C; after leaving overnight the gelatinous mass was dissolved in concentrated HNO_3. To a mixed Fe^{III}-Cr^{III} nitrate solution excess ammonia was added; after boiling the precipitate was filtered, washed well to remove NH_4NO_3, dried in vacuo and slowly heated to 500 °C. The mixed-crystal oxides with the formula $Fe_{2-0{\cdot}8a}Cr_{0{\cdot}8a}O_3$ were milled in an agate Bloch-Rossetti mill with Li_2CO_3 under benzene. The mixture was dried and heated for 2 h at 700 °C in an atmosphere of equal volumes CO_2 and O_2. After remilling, bars and disks were pressed from the resulting powder and sintered for 2 h at 1150 °C in O_2 and cooled slowly. By this method of preparation undue loss of Li_2O by evaporation was avoided.

$Li_{0.5}Fe_2Cr_{0.5}O_4$ ($a = 0{\cdot}5$) was also prepared by an alternative method: 1 Li_2CO_3 and 1 Cr_2O_3 were milled in an agate ball mill under benzene, dried and heated for 2 h at 1100 °C in O_2. The resulting powder showed no X-ray diffraction lines of Li_2O, Li_2CO_3, Cr_2O_3 or spinel and is probably a compound $LiCrO_2$. This material was mixed with Fe_2O_3 in the required proportion, milled, dried and fired at 1150 °C in O_2.

A study of the X-ray diffraction patterns obtained on a Norelco High-angle X-ray Diffractometer [85]) showed that a spinel $Li_{0.5}Cr_{2.5}O_4$ is not formed: the preparation with $a = 2{\cdot}5$ showed practically only Cr_2O_3 lines *). Some additional weak reflexions were probably those of $LiCrO_2$.

The other preparations prepared as described above were pure spinels except that with $a = 2{\cdot}00$ which showed weak Cr_2O_3 reflexions.

A pressed disk of the unsintered material with $a = 2{\cdot}00$ was now embedded in slabs pressed from the same material in order to maintain a suitable Li_2O vapour pressure, and sintered in the same way as indicated above. The Cr_2O_3 lines had now become much weaker (for details see [85])).

The distribution of the Li^+ ions in the mixed-crystal series $Li_{0\,5}Fe_{2.5}O_4$-$Li_{0.5}Fe_{0.5}Cr_2O_4$ was determined by Braun [85]). His results are reproduced in fig. 22*b*.

Annealing the preparations for a long period at low temperatures (24 h at 500 °C, 96 h at 450 °C) did not change the diffraction patterns at all. The measurements of the magnetic properties were made on the samples that were only cooled slowly.

*) A report that "$Li_{0.5}Cr_{2.5}O_4$ is non-cubic" [86]) should be read: there is no cubic $Li_{0.5}Cr_{2.5}O_4$.

The preparation $Li_{0.5}Fe_2Cr_{0.5}O_4$ ($a = 0.5$) showed the same superstructure lines as $Fe[Li_{0.5}Fe_{1.5}]O_4$; the preparation $Li_{0.5}Fe_{0.5}Cr_2O_4$ ($a = 2$) showed a new superstructure (1 Li^+ : 1 Fe^{3+} in the tetrahedral position) already described in section 1.2.3 [85]). A beginning of this long-range order was detectable in the preparation with $a = 1.6$.

The relative distribution of the Fe^{3+} and Cr^{3+} ions cannot be determined by X-ray diffraction. The fact that a spinel $Li_{0.5}Cr_{2.5}O_4$ is not formed, and the migration of all Li^+ to the tetrahedral position as a is increased

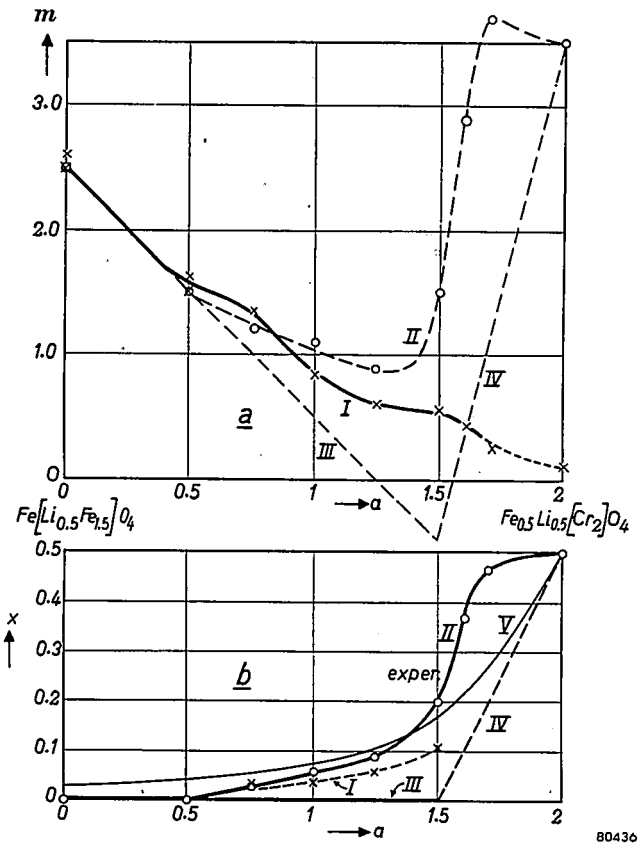

Fig. 22*a*. Saturation moments for the system $Li_{0.5}Fe_{2.5-a}Cr_aO_4$.
Curve I: experimental values; curve II: values calculated from the cation distribution determined by X-ray diffraction (fig. 22*b*, curve II); line III: values calculated for all Li^+ and Cr^{3+} ions in octahedral sites; line IV: values calculated for all Fe^{3+} ions in tetrahedral sites.
b. Amount of Li^+ ions in tetrahedral sites per formula unit (x) for the system $Li_{0.5}Fe_{2.5-a}Cr_aO_4$ $(Fe_{1-x}Li_x[Li_{0.5-x}Fe_{1.5+x-a}Cr_a]O_4)$.
Curve II: experimental values obtained by X-ray diffraction; curve I: values calculated from the saturation moments (fig. 22*a*, curve I); lines III and IV: values for which lines III and IV in fig. 22*a* were obtained, for all Cr^{3+} ions in octahedral sites.
Curve V: calculated distribution curve (see text).

to 2·0, however, clearly point to the presence of Cr^{3+} ions in the octahedral sites only.

Saturation vs temperature curves were measured for all preparations of the mixed-crystal series. Fig. 23 shows the reduced saturation magnetizations (σ/σ_0) against the reduced temperatures T/Θ. It is seen that here for several preparations anomalous σ-T curves occur of Néel's type (N) (see fig. 8, curve e) which have a compensation temperature T_{comp} for which $\sigma = 0$ [89]). In fig. 23 we have drawn the saturation magnetizations below and above the compensation temperature with different sign, although saturation measurements of course only give the absolute value of the spontaneous magnetization. In order to show that the spontaneous magnetization does change sign at T_{comp} we have measured the remanent induction (B_r) for $Li_{0.5}Fe_{1.25}Cr_{1.25}O_4$ in the absence of a magnetic field,

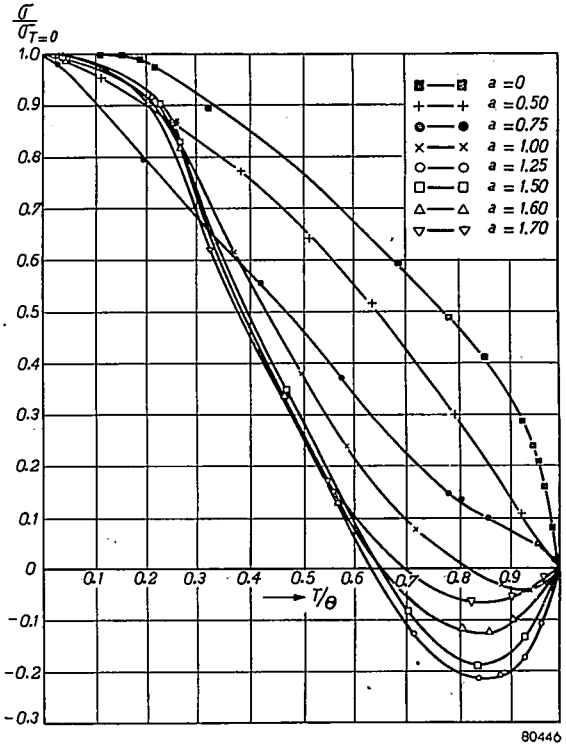

Fig. 23. Reduced saturation-magnetization vs temperature (σ/σ_0 vs T/Θ) curves for the system $Li_{0.5}Fe_{2.5-a}Cr_aO_4$. For clarity's sake the values of σ/σ_0 below and above the compensation temperature ($\sigma = 0$) have been drawn with different sign, although the measurements determine only the absolute values. More measuring points are shown in ref. [88b]).

perpendicularly to the earth's magnetic field. Fig. 25 shows that the remanent magnetization indeed changes sign at T_{comp}.

For $Li_{0.5}Fe_{0.5}Cr_2O_4$ ($a = 2.0$) σ was found to decrease almost linearly from $\sigma = 1$ $cgs_{magn} \cdot cm^3/g$ at appr. 100 °K to $\sigma \approx 0$ at the Curie temperature. Measurements of the remanent magnetization, however, clearly revealed a compensation temperature. The cause of this apparent paradox it discussed in section 8.2.4 for mixed crystals $NiFe_2O_4$-$NiAl_2O_4$.

The saturation moments (in Bohr magnetons) are given in fig. 22*a*, curve I, and in table XIII.

The Curie temperatures (Θ) and compensation temperatures (T_{comp}) are given in fig. 24 and in table XIII. Braun's values for the cell edges are also given in table XIII.

TABLE XIII

Cation distributions, cell edges, Curie temperatures, compensation temperatures and saturation moments for the system $Li_{0.5}Fe_{2.5-a}Cr_aO_4$.

Cr content a	ionic distribution	cell edge (Å)	Θ (°C)	T_{comp} (°C)	n_B
0	$Fe_{1.00}[Li_{0.50}Fe_{1.50}]O_4$	8.331	680		2.47; 2.60 *)
0.50	$Fe_{1.00}[Li_{0.50}Fe_{1.00}Cr_{0.50}]O_4$	8.306	500		1.62; 1.50 **)
0.75	$Fe_{0.98}Li_{0.02}[Li_{0.48}Fe_{0.77}Cr_{0.75}]O_4$	8.296	410		1.35
1.00	$Fe_{0.94}Li_{0.06}[Li_{0.44}Fe_{0.56}Cr_{1.00}]O_4$	8.292	315	205	0.84
1.25	$Fe_{0.91}Li_{0.09}[Li_{0.41}Fe_{0.34}Cr_{1.25}]O_4$	8.290	214	+38	0.61
1.50	$Fe_{0.80}Li_{0.20}[Li_{0.30}Fe_{0.20}Cr_{1.50}]O_4$	8.287	119	−16	0.55
1.60	$Fe_{0.64}Li_{0.36}[Li_{0.14}Fe_{0.26}Cr_{1.60}]O_4$	8.288	167	+11	0.42
1.70	$Fe_{0.54}Li_{0.46}[Li_{0.04}Fe_{0.26}Cr_{1.70}]O_4$	8.290	155	+20	0.22
2.00	$Fe_{0.50}Li_{0.50}[Cr_{2.00}]O_4$	8.288	80±16	+37±15 ***)	0.10

*) For material described in section 4.
**) Obtained for the material prepared from $LiCrO_2$ and Fe_2O_3.
***) Obtained from measurements of the remanent magnetization.

The effective g-factor of the materials that have a compensation temperature show an anomalous behaviour as a function of temperature. Fig. 25 shows the results of measurements by Van Wieringen [87]) [88a]) on $Li_{0.5}Fe_{1.25}Cr_{1.25}O_4$.

7.2. Discussion of the magnetic measurements

7.2.1. Saturation moments

The distribution of the Li^+ ions being known, and assuming the Cr^{3+} ions to occupy octahedral sites only, the saturation moments can be

calculated for complete antiparallelism between the ionic moments in A and B sites respectively. The moments thus calculated (with for Cr^{3+}: $g = 2$, $S = 3/2$) are represented by the dashed curve II in fig. 22a. For $0 \leqslant a \leqslant 1{\cdot}25$

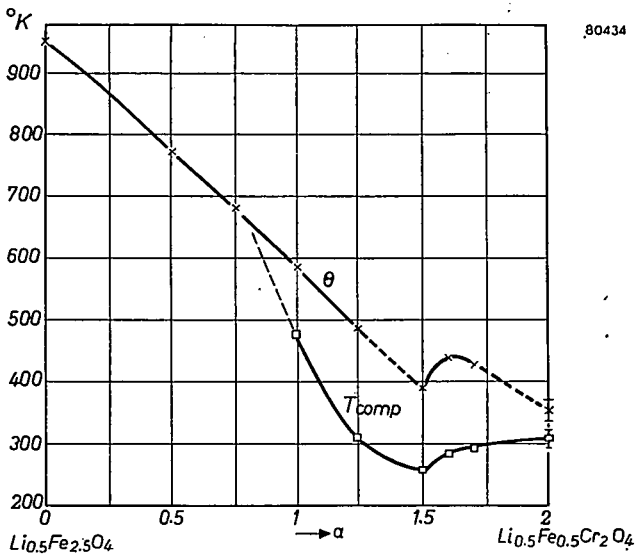

Fig. 24. Curie temperatures (Θ) and compensation temperatures (T_{comp}) for the system $Li_{0{\cdot}5}Fe_{2{\cdot}5-a}Cr_aO_4$.

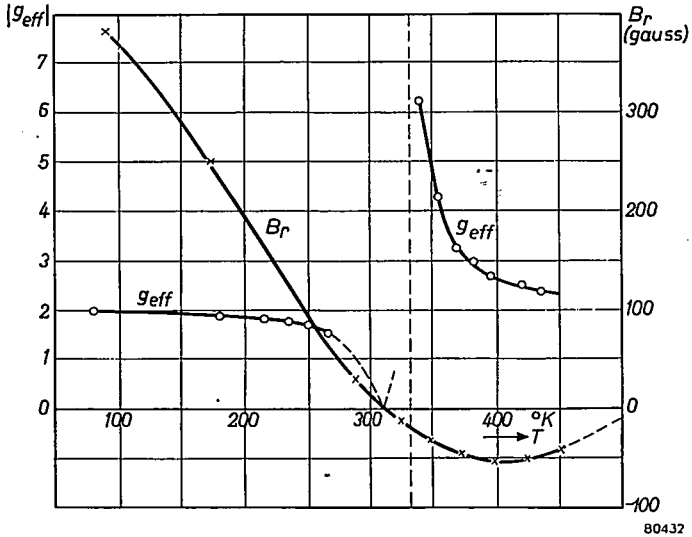

Fig. 25. Remanent induction ($B_r = 4\pi I_r$, right-hand scale) of $Li_{0{\cdot}5}Fe_{1{\cdot}25}Cr_{1{\cdot}25}O_4$ as a function of temperature: a change of sign is shown. Effective g-factor (g_{eff}, left-hand scale) of $Li_{0{\cdot}5}Fe_{1{\cdot}25}Cr_{1{\cdot}25}O_4$ measured by Van Wieringen [87]). A hyperbolic curve according to eq. (4.5) is shown.

the observed and calculated moments are practically equal. We have seen there is indirect X-ray evidence that the Cr^{3+} ions occupy octahedral sites only. The moment of $Li_{0.5}Fe_2Cr_{0.5}O_4$ ($a = 0.5$), for which the occurrence of angles between the ionic moments inside the B sublattice is very unlikely in view of the high Curie temperature (500 °C), which indicates a very large and therefore predominant AB interaction, shows that the Cr^{3+} ion indeed contributes 3 Bohr magnetons in ferrimagnetism. The fair agreement between observed and calculated saturation moments for $0 \leqslant a \leqslant 1.25$ shows that in this whole region the ionic moments in A and B sites are practically all antiparallel. The discrepancy between observed and calculated n_B values for the preparations with $a > 1.25$ must be explained by assuming that here the ionic moments inside one of the crystallographic positions are no longer parallel: the fact that m is lower than the calculated value shows that at 0 °K the angles occur in the B sublattice (see eqs (2.18) and (2.19)).

If this arrangement were maintained at higher temperatures, no anomalous σ-T curves could occur according to the simple theory (see section 2.2.2). The fact that for $a = 1.6$-2.0 anomalous curves do occur must be due either to the disappearance of the angles at higher temperatures, which is possible in Yafet and Kittel's theory, or to a temperature dependence of γ_2, whereby $\gamma_2 = -1$ at T_{comp}. A temperature dependence of the ratios of the interactions has so far been introduced into theory only by Smart [92]).

7.2.2. Curie temperatures

The Curie-temperature curve (fig. 24) shows a practically linear decrease between $a = 0$ and $a = 1.50$, then an increase, decreasing again after passing through a maximum at about $a = 1.6$. The unit-cell edges show a small decrease between $a = 0$ and $a = 1.50$, and increase again slightly near $a = 2.0$ (table XIII).

The anomaly in the variation of the Curie temperature with a cannot be attributed to this anomaly in the cell edges, as a decreasing cell edge would be expected to give an increase in Curie temperature and vice versa.

When the AB interaction is large compared with the BB interaction, i.e. as long as no angles occur between the moments in the B sites, the Curie temperature is mainly determined by the strengths of the interactions between ferric ions in the A sites and ferric or chromic ions in the B sites, and on the numbers of the respective neighbours. These numbers of neighbours are proportional to the products of the numbers of ions in each lattice site per formula unit. These products, taken from table XIII, column 2, are given in table XIV.

TABLE XIV

Cr content a / product	$Fe_A.Fe_B$ (1)	$Fe_A.Cr_B$ (2)	$Fe_A.(Fe_B + Cr_B)$ (3)
0	1·50	0·00	1·50
0·50	1·00	0·50	1·50
0·75	$0·75_5$	$0·73_5$	1·49
1·00	$0·52_5$	0·94	$1·46_5$
1·25	0·31	$1·13_5$	$1·44_5$
1·50	0·16	1·20	1·36
1·60	$0·16_5$	$1·02_5$	1·19
1·70	0·14	0·92	1·06
2·00	0·00	1·00	1·00

The material with $a = 0·5$ has an appreciably lower Curie temperature than that with $a = 0$, in spite of a slightly smaller cell edge. From the fact that the product $Fe_A.(Fe_B + Cr_B)$ is equal in the two cases, it follows that the interaction Fe_A-Fe_B is much stronger than the interaction Fe_A-Cr_B.

This can account only partly for the sudden rise of the Curie temperature for $a > 1·5$ (fig. 24), since the figures in table XIV, column 1, show an irregularity but not a rise for $a > 1·5$. Moreover the Curie temperature for $a = 2·00$ is still more than one third of that for $a = 0$, whereas neglect of all interactions except the Fe_A-Fe_B interaction would give $\Theta = 0$ °K.

The figures of table XIV, column 3, show a sharp decrease for $a > 1·5$, which shows that consideration of all AB interactions accounts even less for the rise in the Curie temperatures there. The BB interactions will, therefore, play an important role here: it was already apparent from the n_B values for $a > 1·25$ that these BB interactions could not be neglected there. Only a molecular-field theory, extended for the presence of two kinds of magnetic ions, like Niessen has developed for other cases, will be able to account for these anomalies more quantitatively.

The compensation temperatures also show a minimum near $a = 1·5$. A discussion of the behaviour of T_{comp}/Θ as a function of a will be given in section 7.2.3.

7.2.3. Anomalous temperature dependence of saturation magnetization and effective g-factor

We have seen in section 2.2 that for a ferrimagnetic spinel containing one kind of magnetic ion, a σ-T curve of Néel's type (N) (fig. 8, type e) occurs for x_a/x_b between 1 and $(1 + \beta)/(1 + \alpha)$.

Since in this case $|\alpha|$ and $|\beta|$ are small against 1 in view of the geometry of the spinel lattice, the occurrence of this type of curve, as well as of the other anomalous curves, is restricted to a narrow range of compositions. This means that T_{comp} will change from 0 °K to the Curie temperature for a small change in composition.

In the present system T_{comp} is not strongly dependent on composition above $a \approx 1{\cdot}25$, where it passes through a minimum. This is connected with (1) the anomaly in the Curie-temperature curve, which has been discussed in section 7.2.2;

(2) the minimum occurring in the ratio T_{comp}/Θ.

Fig. 8 showed that generally a curve of Néel's type (N) (fig. 8, curve e) will occur in a range of mixed crystals bounded by two materials, showing σ-T curves of the types d and f respectively, i.e. T_{comp}/Θ will then range from 0 to 1. Fig. 23 shows that in the present system the quotient $T_{comp}/\Theta = 1$ for a Cr content a slightly above 0·75 decreases up to the composition $a = 1{\cdot}25$, but then increases again.

This peculiar behaviour is primarily due to the sudden migration of Li^+ to the tetrahedral position, which prevents the saturation moment from passing through zero along the dashed line III in fig. 22a, calculated for the case that both Li^+ and Cr^{3+} would be situated in octahedral sites.

A theory for the occurrence of compensation temperatures extended for the presence of two kinds of magnetic ions has been given by K. F. Niessen [90]).

A magnetized rod of a material having a compensation temperature, suspended in a weak horizontal magnetic field (smaller than the coercive force), e.g. above a permanent magnet made from "Ferroxdure" *) will turn about on heating through the compensation temperature. This very simple experiment is the first visual demonstration of the existence of non-compensated antiferromagnetism, or ferrimagnetism.

A practical result of the fact that T_{comp} in the system does not vary strongly with composition, is to make the value of T_{comp} less sensitive to the exact composition and homogeneity of the preparation than would be the case if the phenomenon occurred only in a narrow range of compositions. Therefore it is easy to prepare a material for this experiment with T_{comp} conveniently situated, i.e. slightly above room temperature (viz. $Li_{0{\cdot}5}Fe_{1{\cdot}25}Cr_{1{\cdot}25}O_4$).

The effective g-factor for this type of material measured against temperature shows a hyperbolic behaviour, which is in accordance with the formula

$$g_{eff} = 2\,\frac{(M_{total})_A - (M_{total})_B}{(M_{spin})_A - (M_{spin})_B}. \qquad (4.5)$$

This formula gives $g_{eff} = 0$ for T_{comp}, but the denominator becomes zero at a slightly different temperature, giving $g_{eff} = \pm\infty$.

*) A permanent-magnet material with high coercive force with the approximate composition $BaFe_{12}O_{19}$ [91]).

7.3. Discussion of the cation distribution

The three mixed-crystal series of section 6 gave x vs a curves (figs 16*b*, 18*b* and 20*c*) of a type that must be considered to be normal in ternary or multiple spinels. This means that in the simple Boltzmann expressions as used by Néel and Smart the energies of interchange of two cations between the two lattice positions are usually not very large, and that we must keep in mind that the ionic distributions found in practice are frozen in and dependent on the cooling rate.

In the present system the presence of all Li^+ ions in the tetrahedral position in $Li_{0\cdot5}Fe_{0\cdot5}[Cr_2]O_4$ is easily understood from the very strong preference of the Cr^{3+} ions for sixfold coordination.

If we assume that for Li_A^+-Cr_B^{3+} the interchange energy is very large, but for Li_B^+-Fe_A^{3+} small, then the stability of the inverse arrangement in $Fe[Li_{0\cdot5}Fe_{1\cdot5}]O_4$ is due to the 1:3 order in the octahedral position. A replacement of Fe^{3+} by Cr^{3+} in this material is not expected to alter the factors determining the *most stable* Me^+-Me^{3+} distribution (a, u, order energy, etc.) to any great extent, so that the most stable distribution for $a = 1\cdot5$ is still $Fe[Li_{0\cdot5}Cr_{1\cdot5}]O_4$.

The fact that in this material 0·20 Li^+ is found in the tetrahedral sites is due to the strong preference of Cr^{3+} for the B sites, which alters the Li^+-Fe^{3+} distribution frozen in amongst the remaining sites.

When the interchange energy Li_A^+-Cr_B^{3+} is taken $E = \infty$, and the other interchange energy Li_A^+-Fe_B^{3+} adjusted to make the theoretical distribution curve coincide with Braun's experimental curve for $a = 1\text{-}1\cdot5$ (fig. 22*b*) a curve like the drawn curve (V) is obtained *). The fact that for $a = 0\text{-}0\cdot75$ and $a = 1\cdot6\text{-}1\cdot7$ the experimental values of x are nearer to 0 and 0·5 respectively than the theoretical values clearly points to the influence of short-range order in the A or B position respectively. It is clear that in the region $a = 1\text{-}1\cdot5$ short-range order cannot be neglected, but here the order energies gained in the two sublattices presumably compensate each other [85]).

*) The author is indebted to Dr J. S. Smart for a discussion on this subject and for performing this calculation.

REFERENCES

85) P. B. Braun, Physica, forthcoming.
86) E. Kordes and E. Röttig, Z. anorg. Chem. **264**, 34-47, 1951.
87) J. S. van Wieringen, Phys. Rev. **90**, 488, 1953.
88a) H. G. Beljers and J. S. van Wieringen, Physica, forthcoming.
88b) E. W. Gorter and H. A. Schulkes, Physica, forthcoming.
89) E. W. Gorter and J. A. Schulkes, Phys. Rev. **90**, 487-488, 1953.
90) K. F. Niessen, Physica **19**, 445-450, 1953.
91) J. J. Went, G. W. Rathenau, E. W. Gorter and G. W. van Oosterhout, Philips tech. Rev. **13**, 194-208, 1952.
92) J. S. Smart, Phys. Rev. **90**, 55-58, 1953.

8. FERRIMAGNETIC SPINELS CONTAINING ALUMINIUM

8.1. Discussion of data published on the systems $Fe^{II}Fe^{III}_{2-a}Al_aO_4$ and $MgFe^{III}_{2-a}Al_aO_4$

A small part of the system ferrous ferrite-ferrous aluminate, $Fe^{II}Fe^{III}_{2-a}Al_aO_4$, has been studied by Guillaud and Michel [93] [94] for $a = 0$-$0{\cdot}2$.

The saturation moments found for four preparations with increasing a decreased linearly, and very nearly had the values $n_B = 4-3a$.

Guillaud [94] assumes that either of the following two ionic distributions occurs:

(1) Al^{3+} gradually replaces Fe^{3+} in the octahedral position;

(2) Al^{3+} gradually replaces Fe^{2+} in the octahedral position, an equal amount of Fe^{3+} ions in the tetrahedral position becoming Fe^{2+} ions.

He states that the results, therefore, conform with Néel's theory, i.e. can be accounted for by these ionic distributions when the additional assumption is made that the ionic moments in A and B sites are completely antiparallel, which latter assumption is here undoubtedly justified.

The general formula is

$$Fe^{II}_yAl_xFe^{III}_{1-x-y}\,[Fe^{II}_{1-y}Fe^{III}_{1-a+x+y}Al_{a-x}]\,O_4, \tag{8.1}$$

for which, taking $g_{Fe^{2+}} = 2$, we find the saturation moment

$$n_B = |m_b - m_a| \quad \text{and} \quad m_b - m_a = 4-5a+10x+2y. \tag{8.2}$$

Guillaud's first assumption, i.e. $x = 0$, $y = 0$, would give $n_B = 4-5a$, and is therefore incorrect.

This does not mean, however, that his second assumption ($x = 0, y = a$) is the correct one, because there is yet another cation distribution that can account for the experimental data, viz. $x = 0{\cdot}2a$, $y = 0$. The latter distribution seems more likely for the following reasons:

(1) If all Al^{3+} ions occupy B sites and the interchange energy Fe^{3+}_A-Fe^{2+}_B is not exceptionally small, it may be expected that this interchange, which is only an electron transfer, is so easy that at low temperatures the most stable distribution is practically obtained, i.e. with the Fe^{2+} ions in B sites like in Fe_3O_4.

(2) For $Fe^{II}Fe^{III}AlO_4$ ($a = 1$), the large decrease of the conductivity on annealing [95], as well as the X-ray pattern [96], point to a formula

$$Fe^{III}_{1-x}Al_x\,[Fe^{II}Fe^{III}_xAl_{1-x}]\,O_4,$$

with $x \leqslant 0{\cdot}1$.

We therefore expect that also for $0{\cdot}04 < a < 0{\cdot}2$ a small part of the Al^{3+} ions is found in tetrahedral sites, rather than part of the Fe^{2+} ions.

The system $MgFe_{2-a}Al_aO_4$ has been investigated by Jones and Roberts [97]: contrary to Dr G. H. Jonker [98]) they do not find a miscibility gap. We can only account for this discrepancy by supposing that their preparations *) were cooled more rapidly after sintering. The saturation moments (values at 20 °K) are reproduced in fig. 26*a*.

The general formula for these materials is

$$Mg_xAl_yFe_{1-x-y}[Mg_{1-x}Al_{a-y}Fe_{1-a+x+y}]O_4. \qquad (8.3)$$

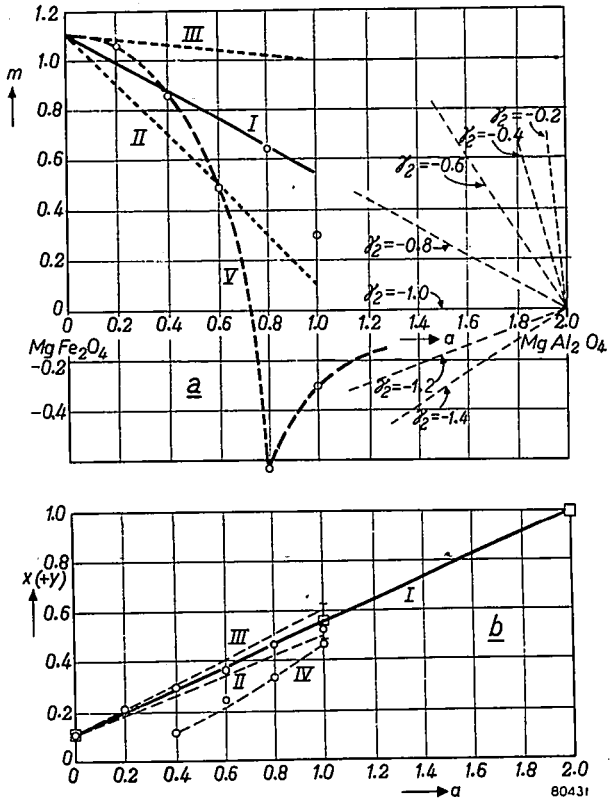

Fig. 26*a*. Saturation moments in the system $MgFe_{2-a}Al_aO_4$ (Jones and Roberts). The experimental points lie around line I and between lines II and III. Curve V: a hypothetical curve through the experimental points, for which m changes sign as a result of angles in the B sites.

The lines indicated by $\gamma_2 = -0{\cdot}2$ to $\gamma_2 = -1{\cdot}4$ are derived from (2.19) for the cation distribution of line I of fig. 26*b*.

b. The values of $x + y$, presumably of x, in the formula

$$Mg_xAl_yFe_{1-x-y}[Mg_{1-x}Al_{a-y}Fe_{1-a+x+y}]O_4,$$

derived from the saturation moments.

Lines I, II and III correspond to those of fig. 26*a*. Curve IV: alternative values for completely antiparallel moments in A and B positions.

□ — □: values determined by neutron diffraction (Bacon and Roberts).

*) Prepared by a method so far not published (see ref. in [97])).

Assuming with the authors complete antiparallelism of the ionic moments in the A and B positions, then

$$n_B = |m_b - m_a| \quad \text{and} \quad m_b - m_a = 10(x+y) - 5a. \tag{8.4}$$

The values of $x+y$ thus calculated from the experimental n_B values are given in fig. 26*b*. The points scatter around a straight line I through ($x+y=1$; $a=2$), for which $x+y = 0{\cdot}11 + 0{\cdot}44_5 a$, and lie between lines II and III, for which $x+y = 0{\cdot}11 + (0{\cdot}44_5 \pm 0{\cdot}04_5)\, a$.

The values of x for $a=0$ and $a=2$ were determined by Bacon and Roberts by neutron diffraction [99] [100a]), like the value of $x+y$ for $a=1$ *): the authors assume that in the latter case $y=0$, and that the Al^{3+} ions remain in the octahedral position throughout the series, i.e. that the migration of the Mg^{2+} ions to the tetrahedral position proceeds about linearly with the Al content a (fig. 26*b*, line I).

The scattering of the points around line I (figs 26*a* and *b*) is due, according to the authors [97]), to different heat treatments.

The possibility that for some of the materials m is negative will be briefly considered. This might occur in two ways:

(1) For completely antiparallel A and B moments, for $a = 0{\cdot}4$-$1{\cdot}0$ equation (8.4) yields a second solution for $x+y$ for which $m_b - m_a$ is negative: these values are represented by line IV in fig. 26*b*. In view of the unambiguity of the values of $x+y$ for $a = 0$, $0{\cdot}2$ and $2{\cdot}0$, this solution may, however, be ruled out.

(2) For the $x+y$ values of line I (fig. 26*b*) m might decrease along line V (fig. 26*a*), passing through zero near $a = 0{\cdot}7$, as a result of angles between the moments in the B position. When such angles occur, $m = -m_a(1+1/\gamma_2)$ (2.19), and this expression changes sign for $\gamma_2 = -1$. In the present case, where only one type of magnetic ion is present, we may expect $|\gamma_2|$ to remain well below unity (e.g. $\lesssim 0{\cdot}3$) in view of the geometry of the spinel lattice, so that m will not change sign in this manner either.

In fact, according to eq. (2.19) angles will not occur at all in the whole system $MgFe_2O_4$-$MgAl_2O_4$ as long as $|\gamma_2| < 0{\cdot}8$.

8.2 The system $Ni^{II}Fe^{III}_{2-a}Al_aO_4$ ($NiFe_2O_4$ - $NiFeAlO_4$)

8.2.1. Experimental

A series of mixed crystals $NiFe_{2-a}Al_aO_4$ were prepared with $a = 0$, $0{\cdot}25$, $0{\cdot}45$, $0{\cdot}50$, $0{\cdot}62_5$, $0{\cdot}66$, $0{\cdot}68$, $0{\cdot}68_6$, $0{\cdot}68_8$, $0{\cdot}70$, $0{\cdot}75$ and $1{\cdot}00$.

*) The latter data have recently been confirmed by X-ray diffraction [100b]).

These materials were prepared from
Ni (Si 0·02 %, Co $0{\cdot}01_8$ %, Pb 0·01 %),
Fe (C 0·03 %),
Al (Si $0{\cdot}01_3$ %, Cr $0{\cdot}01_5$ %, Pb appr. 0·01 %, Ti $0{\cdot}01_3$ %), by method (B), pref. 2 h 700 °C in O_2, sint. 2 h 1350 °C in O_2.

Three series of samples were prepared:
(1) cooled slowly from 1350 °C (only for $a = 0{\cdot}66$-$0{\cdot}75$);
(2) annealed 16 h 1250 °C, 16 h 1150 °C, 16 h 1000 °C, 45 h 600 °C, cooling rate between and below these temperatures about $^1/_4$ °C/min;
(3) quenched from 1350 °C (only for $a = 0$-$0{\cdot}62_5$ and $0{\cdot}75$-$1{\cdot}00$).
Analysis: Fe^{2+} content $<0{\cdot}1$ %.

X-ray diffraction patterns obtained on a Norelco X-ray Diffractometer showed all preparations to be pure spinels. No attempt was made to obtain information from the observed intensities about the cation distribution.

Saturation magnetizations were measured using fields up to 9000 oersteds down to 77 °K; at 77 and 20 °K measurements were made in fields up to 23000 oersteds by Mr P. Jongenburger. The saturation moments for the annealed and quenched samples are shown in fig. 27 and in table XV. The reduced σ-T curves ($\sigma/\sigma_{T=0}$ vs T/Θ) of the annealed samples for $a = 0$-$0{\cdot}62_5$ and $0{\cdot}75$-$1{\cdot}0$ are given in fig. 28 *). For $a = 0{\cdot}66$-$0{\cdot}75$ the σ-T curves are shown in fig. 29*a-e* **). The Curie temperatures and the cell edges of the annealed samples are also given in table XV.

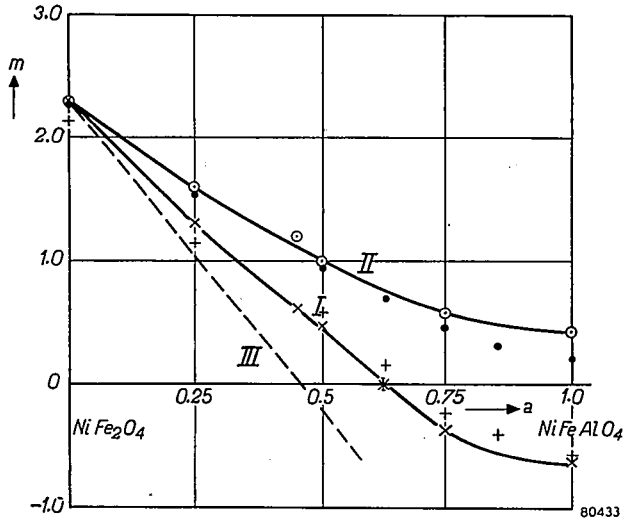

Fig. 27. Saturation moments (m) of the mixed-crystal series $NiFe_{2-a}Al_aO_4$ between $a = 0$ and $a = 1{\cdot}0$.
Curve I: Experimental values for annealed samples; ×—×: own measurements; +—+: measurements by Maxwell and Pickart. Curve II: Experimental values for quenched samples; o—o: own measurements on samples quenched from 1350 °C; •—•: measurements by Maxwell and Pickart on samples quenched from 1420 °C. Line III: values calculated for all Ni^{2+} and all Al^{3+} ions in the octahedral position.

*) These experiments were carried out by Mr F. Herbschleb.
**) These experiments were carried out by Mr J. A. Schulkes.

TABLE XV

Saturation moments, Curie temperatures and cell edges in the system $NiFe_{2-a}Al_aO_4$ ($NiFe_2O_4$-$NiFeAlO_4$)

Al content a	formula	cell edge annealed (Å)	Θ (°C)	n_B annealed	n_B quenched from 1350 °C
0	$NiFe_2O_4$	8·3370 ± 4	580	2·29	2·29
0·25	$NiFe_{1·75}Al_{0·25}O_4$	8·3062 ± 7	506	1·30	1·59
0·45	$NiFe_{1·55}Al_{0·45}O_4$	8·2769 ± 4	465	0·61	1·19
0·50	$NiFe_{1·50}Al_{0·50}O_4$	8·2705 ± 6	430	0·44	0·99
$0·62_5$	$NiFe_{1·37_5}Al_{0·62_5}O_4$	8·2521 ± 7	360	0-0·045	—
0·66	$NiFe_{1·34}Al_{0·66}O_4$	8·2420 ± 20	368	*)	—
0·68	$NiFe_{1·32}Al_{0·68}O_4$	8·2485 ± 1	356	*)	—
$0·68_6$	$NiFe_{1·31_4}Al_{0·68_6}O_4$	8·2388 ± 4	≈340	*)	—
$0·68_8$	$NiFe_{1·31_2}Al_{0·68_8}O_4$	8·2387 ± 2		*)	—
0·70	$NiFe_{1·30}Al_{0·70}O_4$	8·2385 ± 7		*)	—
0·75	$NiFe_{1·25}Al_{0·75}O_4$	8·2329 ± 7	294	0·38	0·58
1·0	NiFe Al O_4	8·1951 ± 7	198	0·64	0·42

*) extrapolation too uncertain, or not measured at liquid-hydrogen temperature.

The material with $a = 1$, $NiFeAlO_4$, has been quenched from various temperatures; the saturation moments are given in table XVI **).

TABLE XVI

Saturation moment of $NiFeAlO_4$ as a function of the quenching temperature

quenching temperature (°C)	saturation moment n_B
1350	0·42
1120	0·08
1020	0·05
1000	0·02
700	0·52
annealed	0·64

**) These experiments were carried out by Mr J. A. Schulkes.

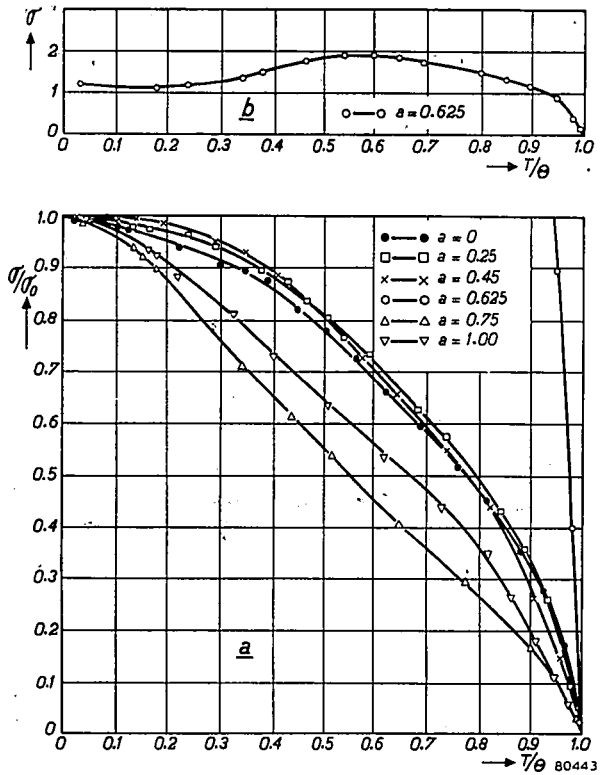

Fig. 28*a*. Reduced saturation-magnetization vs temperature (σ/σ_0 vs T/Θ) curves for the system $NiFe_{2-a}Al_aO_4$, for $a = 0\text{-}0{\cdot}62_5$ and $a = 0{\cdot}75\text{-}1{\cdot}00$.
b. Saturation-magnetization (σ) vs reduced-temperature (T/Θ) curve for $NiFe_{1{\cdot}375}Al_{0{\cdot}625}O_4$.

Maxwell, Pickart and Hall [101]) [102]) have investigated the same system up to $a = 2$. Their most recent results [102]) obtained for $a = 0$, 0·25, 0·50, 0·63, 0·75, 0·85 and 1·00 closely agree with ours (see fig. 27). McGuire [103a]) has measured the effective *g*-factors of their annealed samples and reports the following values *):

a	= 0	0·25	0·50	0·63	0·75
g_{eff} =	2·3	2·7	6·9	3·8	1·5 .

8.2.2. Discussion of the saturation moments

Our results for $a = 0{\cdot}25$, 0·45, 0·50, $0{\cdot}62_5$, 0·75 and 1·00 were first obtained. Table XV shows that values of the saturation moments of the annealed samples have a minimum near $a = 0{\cdot}62_5$. If it is assumed that for $a = 0{\cdot}75$ and 1·00 m is negative, a smooth curve for m vs a is obtained (fig. 27, curve I). Amongst the saturation-magnetization vs

*) For details see [103b]).

temperature curves of fig. 28 there is one having an anomalous shape, of the type *c* of fig. 8. It may be noted that the shape of the curves changes discontinuously between $a = 0{\cdot}62_5$ and $a = 0{\cdot}75$, which is an indication that m changes sign between these compositions. A further discussion of the σ-T curves is given in section 8.2.4.

The saturation moments of the quenched samples do not show a minimum and lie on a smooth curve (II), from which we deduce that for the quenched samples m remains positive throughout the series of mixed crystals. The σ-T curves of these materials, not reproduced here, are all of Néel's type (Q) and concave towards the T-axis.

In order to prove that for the annealed samples with $a \geqslant 0{\cdot}75$ m is negative, the preparation with $a = 1{\cdot}0$ was quenched from various intermediate temperatures. Table XVI shows that a minimum in the saturation moments occurs for quenching temperatures of approximately 1000 °C. Since discontinuous variations in the cation distribution as a function of *temperature* may be ruled out as being extremely unlikely, this proves that for the annealed sample m is negative, and thus also for $a = 0{\cdot}75$. A further proof that m changes sign near $a = 0{\cdot}62_5$ is provided by the measurements of g_{eff} by McGuire, which as a function of composition show a hyperbolic curve, like the measurements of g_{eff} as a function of temperature reported previously [87]).

8.2.3. Discussion of the cation distribution

The general formula of these mixed crystals is

$$\text{Ni}_y\text{Al}_x\text{Fe}_{1-x-y}[\text{Ni}_{1-y}\text{Fe}_{1-a+x+y}\text{Al}_{a-x}]\text{O}_4, \tag{8.5}$$

for which for antiparallel ionic moments in A and B positions, and assuming $(g_{\text{Ni}^{2+}})_B = 2{\cdot}3$, $(g_{\text{Ni}^{2+}})_A = p$ *), we have

$$n_B = |m_b - m_a| \quad \text{and} \quad m_b - m_a = 2{\cdot}3 - 5a + 10x + (7{\cdot}7 - p)y. \tag{8.6}$$

For $x = 0$, $y = 0$, therefore, the saturation moments would follow the dashed line III in fig. 27. For the annealed samples (curve I) and to a greater extent for the quenched samples (curve II) some Ni^{2+} or Al^{3+} ions, or both, must be present in the tetrahedral position.

Since the migration to the A sites of Ni^{2+} ions contributes much less to a rise of m than that of Al^{3+} ions, and in view of the ionic distribution recently found [105]) for $NiAl_2O_4$ by X-ray diffraction, viz. about $Al_{0{\cdot}76}Ni_{0{\cdot}24}Ni_{0{\cdot}76}Al_{1{\cdot}24}O_4$, it seems certain that it is mainly Al^{3+} rather than Ni^{2+} ions which are partly present in the tetrahedral sites.

*) See footnote in section 6.2.2.

The cation distributions may be calculated from n_B values and effective g-factors in the manner described in section 6.2.2. This has been done, independently from us, by Smart [104]) for the system $NiFe_2O_4$-$NiAl_2O_4$ from the data obtained at the U.S. Naval Ordnance Laboratory [102]) [103]); the results show that it is indeed mainly Al^{3+} rather than Ni^{2+} which is found in tetrahedral sites.

An investigation of the system $NiFe_{2-a}Ga_aO_4$ ($NiFe_2O_4$-$NiGa_2O_4$) has recently been reported by Maxwell and Pickart [102]).

The general formula is equal to formula (8.5), substituting Ga^{3+} for Al^{3+}, and, as long as no angles between the ionic moments in the B sites occur, the saturation moment n_B is given by (8.6). Gallium was expected to have a strong preference for the tetrahedral sites (i.e. $a \geqslant x \gg 0{\cdot}5a$), so that n_B is expected to increase with a, starting from $NiFe_2O_4$.

This behaviour has indeed been found: for $a = 0{\cdot}25$ it may be deduced from (8.6), assuming that all Ni^{2+} ions occupy B sites, that 32 % of the Ga^{3+} ions occupy B sites for the annealed samples and 38 % for the quenched samples, provided the above assumptions are correct.

8.2.4. Discussion of the shapes of the σ-T curves

In order to look for preparations showing anomalous σ-T curves of the types b-f of fig. 8, the preparations with $a = 0{\cdot}66$, $0{\cdot}68$, $0{\cdot}68_6$, 068_8, $0{\cdot}70$ were then prepared; the σ-T curves were measured both before annealing, i.e. after a slow cooling process (see section 3), and after annealing, as specified in section 8.2.1. The results for $a = 0{\cdot}75$ are also given. Figs 29a-e show that for $a = 0{\cdot}66$ before and after annealing a curve of type b is obtained. For $0{\cdot}68$ before annealing a curve of type c (Néel's type (P)) is shown; annealing changes this into a curve of an anomalous type not recognizable as one predicted by Néel. The latter type of curve is also shown by the preparations with $a = 0{\cdot}68_6$ and $a = 0{\cdot}68_8$ before annealing; after annealing curves closely resembling type f are obtained. The latter type of curve is again shown for $a = 0{\cdot}70$ before annealing, which is changed by annealing into a curve of Néel's type (Q), which is, however, still convex towards the T-axis. We recognize this latter type of curve for $a = 0{\cdot}75$ before annealing. Annealing changes this into a linear curve, also of type (Q). If we include the curves obtained for the other a values (fig. 28), it is seen that with increasing a there is a change from curves of the types a, b and c to curves of the types f and g *). Curves of type d (Néel's type (L)) and e (Néel's type (N)) are not found, but instead the curve of the type shown in figs 28b and c.

We shall show that this can be understood from the inhomogeneity of the preparations.

*) The fact that for the annealed sample with $a = 0{\cdot}62_5$ a curve of type c is obtained and for $a = 0{\cdot}66$ one of type b is probably due to the fact that the cooling rates during the annealing treatment for the preparations with $a = 0{\cdot}66$-$0{\cdot}75$ were slightly different from those used for the other preparations.

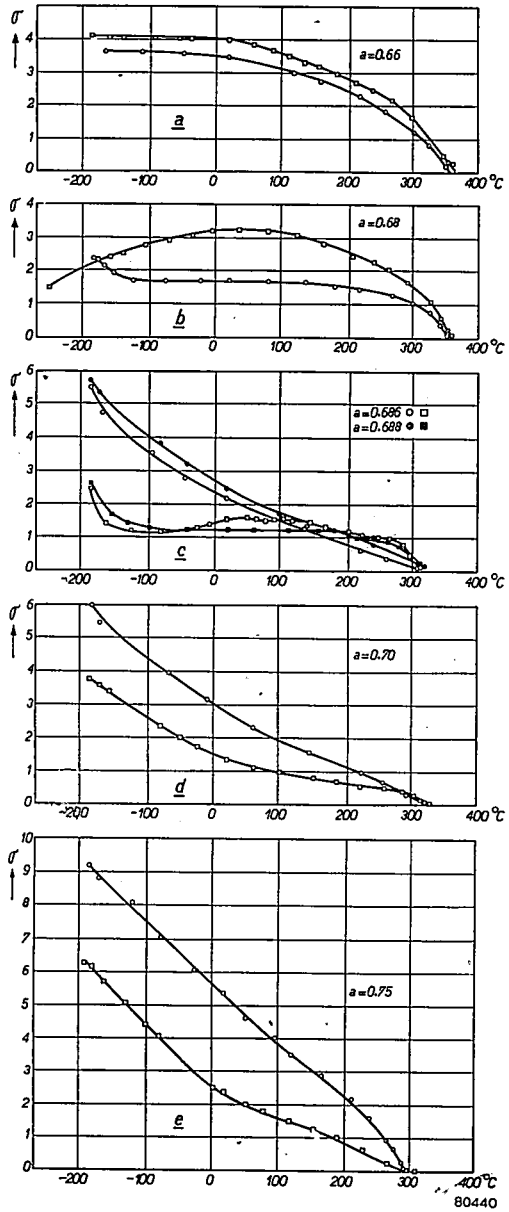

Fig. 29. Saturation-magnetization (σ) vs reduced-temperature (T/Θ) curves for the system $NiFe_{2-a}Al_aO_4$, for $a = 0{\cdot}66 - 0{\cdot}75$.
□ — □ before annealing (section 8.2.1, sub (1));
○ — ○ after annealing (section 8.2.1, sub (2)).

From eq. (8.2) it is deduced that a change in x of 0·01 results in a change in n_B of 0·1, i.e. a change in $\sigma_{T=0}$ of 2·6. From the fact that our annealing treatment results in a change of $\sigma_{T=0}$ of the order of 3 we may

deduce that this has produced a change — i.e. a decrease — of x of just over 0·01. Figs 29*a-e* show that this is sufficient to cause appreciable differences in type of σ-T curve. A change from type *d* (Néel's (type (*L*)) to type *f*, between which types curves of type *e* (Néel's type (*N*)) must occur with compensation temperatures ranging from 0 °K to the Curie temperature, will be brought about by a variation of x of a few hundredths at most.

An inhomogeneity of the material, caused by *local* variations of x of less than 0·01, therefore, will already result in a superposition of type-*d* curves with widely varying compensation temperatures. Since saturation measurements only yield the absolute value of the spontaneous magnetization, such a superposition results in just the type of "hybrid" curves as found for $a = 0{\cdot}68$ (annealed) and for $a = 0{\cdot}68_6$ and $0{\cdot}68_8$ (slowly cooled).

In order to show that this explanation is correct we have measured the remanent magnetization of these preparations for several temperatures. The remanence indeed changes sign with temperature.

The samples of $FeNiAlO_4$ quenched from 1020 °C and 1000 °C also show the above-mentioned type of "hybrid" σ-T curve; here also the remanent magnetization changes sign with temperature.

The slight rise of σ towards $T = 0$ °K for the annealed sample with $a = 0{\cdot}62_5$ (fig. 28*b*) indicates that this σ-T curve is also such a "hybrid" curve with average $m_b - m_a$ very near to zero.

The above-mentioned small local variations of x will of course be present in the whole series of mixed crystals and, in fact, in all ferrimagnetic spinels having cation distributions that change with temperature. The σ-T curve, therefore, is in all these cases an average curve, but only for materials for which $m_b - m_a$ changes sign with temperature is the inhomogeneity detectable from the saturation-magnetization vs temperature curves.

REFERENCES

93) C. Guillaud and A. Michel, J. Phys. Radium **12**, 65, 1951.
94) C. Guillaud, J. Phys. Radium **12**, 239-248, 1951 (or J. Rech. C.N.R.S. nr **12**, 1950).
95) E. J. W. Verwey, P. W. Haayman and F. C. Romeijn, J. chem. Phys. **15**, 181-187, 1947.
96) E. J. W. Verwey E. L. Heilmann, J. chem. Phys. **15**, 174-180, 1947.
97) G. O. Jones and F. F. Roberts, Proc. phys. Soc. Lond. **B 65**, 390-391, 1952.
98) G. H. Jonker, to be published.
99) G. E. Bacon, Acta cryst. **5**, 684-686, 1952.
100a) G. E. Bacon and F. F. Roberts, Acta cryst. **6**, 57-62, 1953.
100b) G. E. Bacon and A. J. E. Welch, Acta cryst. **7**, 361-363, 1954.
101) L. R. Maxwell, S. J. Pickart, and R. W. Hall, Phys. Rev. **91**, 206 (B7), 1953.
102) L. R. Maxwell and S. J. Pickart, Phys. Rev. **92**, 1120-1126, 1953.
103a) T. R. McGuire, Phys. Rev. **91**, 206 (B8), 1953.
103b) T. R. McGuire, Phys. Rev. **93**, 682-686, 1954.
104) J. S. Smart, private communication, to be published in Phys. Rev.
105) F. C. Romeijn, Philips Res. Rep. **8**, 304-342, 1953.

9. OTHER FERRIMAGNETIC OXIDES CONTAINING CHROMIUM: THE SYSTEM $Mn^{II}Fe^{III}_{2-a}Cr_aO_4$ ($MnFe_2O_4$-$MnCr_2O_4$)

9.1. Introduction

The general formula for the mixed-crystal series $MnFe_2O_4$-$MnCr_2O_4$ is

$$Cr_x(Fe^{III}+Mn^{II})_{1-x}\,[(Fe^{III}+Mn^{II})_{2-a+x}Cr_{a-x}]\,O_4, \qquad (9.1)$$

for which, for completely antiparallel ionic moments in A and B positions

$$n_B = |m| = |m_b - m_a| \quad \text{and} \quad m = m_b - m_a = 5 - 2a + 4x.$$

We have seen that Cr^{3+} has the strongest preference for sixfold coordination:
for $x = 0$, $m_b - m_a = 5 - 2a$ (fig. 30, line II).

For $MnCr_2O_4$ ($a = 2$) a value $n_B = 1{\cdot}5$, measured at liquid-helium temperature, has been reported [106]). We supposed that the discrepancy with the value $5-2a = 1{\cdot}0$ must be accounted for not by assuming $x = 0{\cdot}12_5$, but by the occurrence of angles between the ionic moments inside the B or A position. For angles in the A position eq. (2.18) gives $\alpha_2 = -1{\cdot}33$, and such a value is very unlikely from geometrical considerations. It was supposed that the strength of the Mn-O-Mn interaction is certainly not so much stronger than the Mn-O-Cr interaction as to counterbalance this geometrical argument.

When the angles between the moments occur in the B position, m will be <1, i.e. $-1{\cdot}5$. In this case in the system $MnFe_2O_4$-$MnCr_2O_4$ m will pass through zero as a result of these angles.

9.2. Experimental

A series of mixed crystals with the composition $MnFe_{2-a}Cr_aO_4$ was prepared with $a = 0$, $0{\cdot}12_5$, $0{\cdot}25$, $0{\cdot}50$, $1{\cdot}00$, $1{\cdot}08_5$, $1{\cdot}25$ and $1{\cdot}50$.

The following materials were used:
$MnCO_3$ (Na < appr. 0·1 %, Mg 0·01 %),
Fe (Ni $0{\cdot}01_6$ %),
CrO_3 (Ca < appr. 0·2 %, Cu $0{\cdot}01_2$ %, Si 0·01 %).

A chromic nitrate solution is prepared as described in section 7.1. The required weight of this solution is added to a solution of weighed quantities of Fe and $MnCO_3$ in dilute HNO_3. The materials were further prepared by method (C), pref. 2 h 700 °C, sint. 2 h 1250 °C.

The sintering was carried out in atmospheres containing N_2, H_2 and CO_2, of different compositions. X-ray diffraction patterns were obtained for all samples; the oxygen content was determined for those samples for which the diffraction patterns showed only spinel lines. The final adjustment of the oxygen content was carried out as described in section 6.4.

The magnetic investigations were carried out on samples that had the following excess oxygen contents:

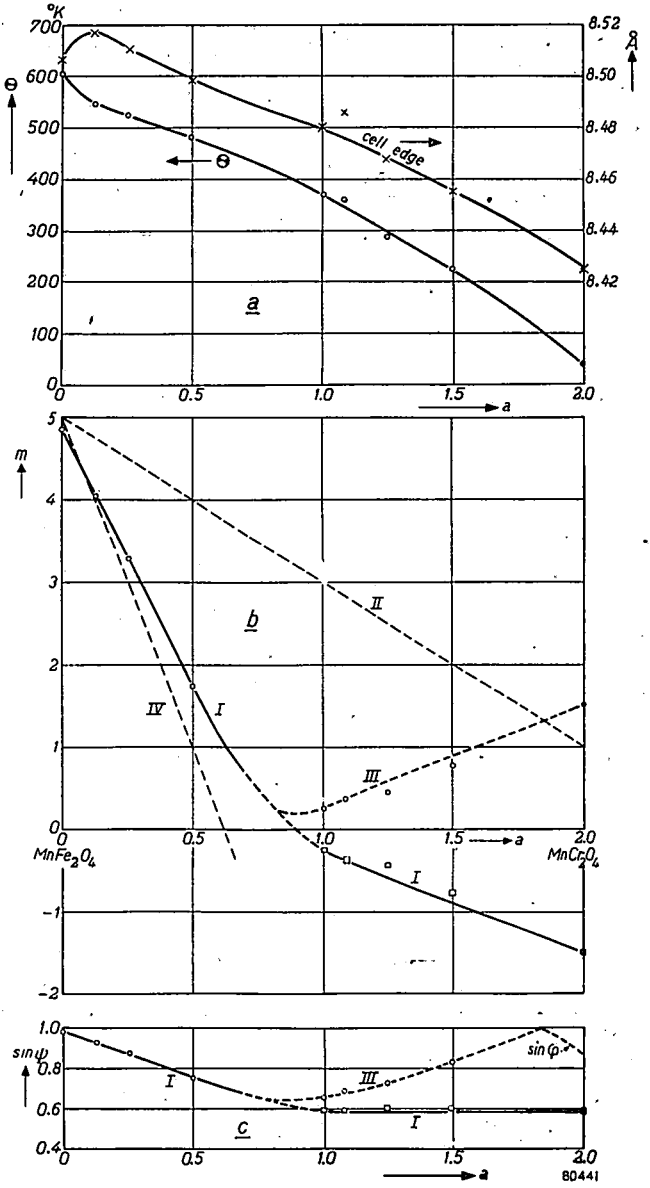

Fig. 30. Properties of the mixed-crystal series $MnFe_{2-a}Cr_aO_4$.
a. Curie temperatures (Θ in°K, left-hand scale) and cell edges (in Å, right-hand scale).
b. Saturation moments.
Curve I: saturation moments (most probable curve); curve I-III: saturation moments (other possible curve); line II: values calculated for all Cr^{3+} in the octahedral position and without angles between the ionic moments inside one sublattice; line IV: saturation moments calculated for the same assumptions as for line II, but with the moment of the Cr^{3+} ions (in the *B* position) *parallel* to those of the ions in the *A* sublattice.
c. sin ψ for angles $180° - 2\psi$ occurring between the directions of the ionic moments in the *B* position for the cases I and III of fig. 30*b*. On curve III above $a = 1{\cdot}8$, $\sin\psi = 1$, but $\sin\varphi < 1$.

a	0	$0{\cdot}12_5$	0·25	0·50	1·0	$1{\cdot}08_5$	1·25	1·50
wt % oxygen	+0·007	−0·075	−0·025	+0·05	−0·015	+0·05	+0·03	+0 01

An oxygen deficit is indicated by a minus sign.

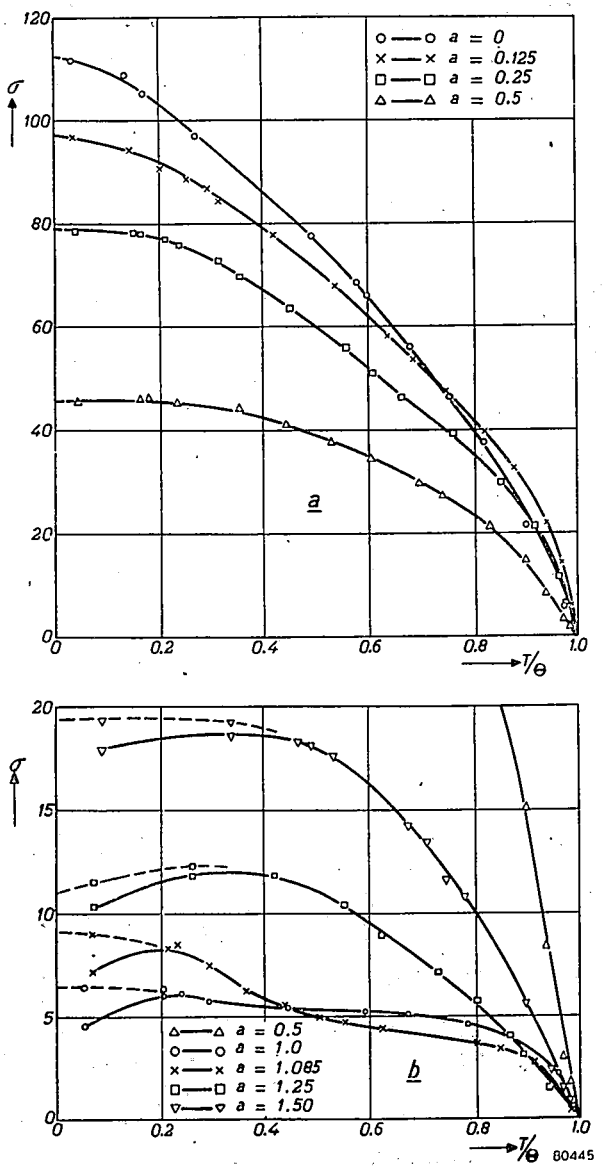

Fig. 31 *a* and *b*. Saturation-magnetization vs reduced-temperature curves for the system $MnFe_{2-a}Cr_aO_4$. The values down to 77 °K were measured in fields up to 6000 oersteds, those at 77 and 20 °K up to 23000 oersteds. For $a = 1 - 1{\cdot}5$ the drawn curves represent measurements at 6000 oersteds, the dashed curves those at 23000 oersteds.

The X-ray diffraction patterns, obtained on a Norelco High-angle Diffractometer using Mo $K\alpha$ radiation, showed only spinel reflexions for all compositions. No data on the cation distribution were obtained from these patterns.

The saturation magnetizations were measured against temperature: the σ vs T/Θ curves are shown in figs 31*a* and *b*.

The saturation moments are shown in fig. 30*b* and in table XVII, the Curie temperatures and the cell edges in fig. 30*a*.

TABLE XVII

Curie temperatures, cell edges and saturation moments in the system $MnFe_{2-a}Cr_aO_4$

Cr content a	formula	Curie temperature Θ (°C)	cell edge (Å)	saturation moment n_B
0	$MnFe_2O_4$	330	8·5074 ± 2	4·85
$0{\cdot}12_5$	$MnFe_{1{\cdot}87_5}Cr_{0{\cdot}12_5}O_4$	272	8·5185 ± 1	4.04
0·25	$MnFe_{1.75}Cr_{0.25}O_4$	247	8·5107 ± 3	3·28
0·50	$MnFe_{1{\cdot}50}Cr_{0{\cdot}50}O_4$	210	8·4977 ± 2	1·73
1·00	$MnFeCrO_4$	97	8·4809 ± 2	0·25
$1{\cdot}08_5$	$MnFe_{0{\cdot}91_5}Cr_{1{\cdot}08_5}O_4$	88	8·4869 ± 2	0·37
1·25	$MnFe_{0{\cdot}75}Cr_{1{\cdot}25}O_4$	15	8·4680 ± 2	(>)0·45
1·50	$MnFe_{0{\cdot}50}Cr_{1{\cdot}50}O_4$	—49	8·4567 ± 1	$0{\cdot}77_5$
2·00	$MnCr_2O_4$	—233 *)	8·426 **)	1·5 *)

*) [106])
**) see section 1.2.5.1.

9.3. Discussion

Table XVII shows that the saturation moments in the system $MnFe_2O_4$-$MnCr_2O_4$ m passes through a minimum, and probably through zero like drawn in fig. 30*b* (curve I): in any case all values except that for $a = 2$ lie below line II, so that an assumption $x \neq 0$ is not sufficient to account for them.

The maximum in the cell edges for $a = 0{\cdot}12_5$ is probably due to the migration of a fairly large amount of Mn^{2+} ions to the tetrahedral position as a result of the introduction of a small amount of Cr^{3+} in the B position. The linear decrease of the cell edge for $a > 0{\cdot}12_5$ shows that the migration of Mn^{2+} to the A sites there proceeds more gradually. It is possible that the steep decrease of m for $a < 0{\cdot}5$ must be ascribed to angles between the

moments in the B sites. It seems rather surprising, however, that even the introduction of only $0{\cdot}12_5$ Cr lowers the saturation moment by $0{\cdot}8\ n_B$. This may be explained, like the maximum in the cell edges, by the migration of a fair amount of Mn^{2+} to the A sites, thus further decreasing the number of Fe_A-Fe_B interactions, which make the strongest contribution to the total AB interaction.

If the saturation moment m changes sign (line I), it follows from (2.19) that $\gamma_2 = -1$ for $m = 0$ and $\gamma_2 = -1{\cdot}43$ for $m = -1{\cdot}5$ ($a = 2{\cdot}0$). This is quite possible if the Cr^{3+}-Cr^{3+} interaction is much stronger than the Mn^{2+}-Cr^{3+} interaction, so that the geometrical reasons for γ_2 being small are counterbalanced.

If m would not change sign (line I-III) this would mean that γ_2 at first decreases to almost -1, i.e. $\sin\psi$ to $0{\cdot}6$, that $\sin\psi$ then increases to 1 for $a \approx 1{\cdot}8$, after which angles $180° - 2\varphi$ in the A position would start to occur and $\sin\varphi$ would decrease to $0{\cdot}9$, i.e. α_2 to $-1{\cdot}33$: this behaviour is extremely unlikely.

Finally, it may be suggested that the possibility of the interaction Fe_A-Cr_B being positive in the present system cannot be ruled out.

In section 2.3.3 we saw that the superexchange interaction between an ion with less than five 3d electrons and one with five 3d electrons may be either positive or negative: in the system $Li_{0{\cdot}5}Fe_{2{\cdot}5}O_4$-$Li_{0{\cdot}5}Fe_{0{\cdot}5}Cr_2O_4$ (cell edges about 8·3 Å) the Fe_A-Cr_B interactions are negative, but it is possible that in the present system, where for $a < 0{\cdot}5$ the cell edges are of the order of 8·5 Å, this interaction is positive.

Line IV shows the saturation moments for the case that the Cr_B^{3+} ions would have moments parallel to those of the ions in the A position. We have seen that it is very probable that Mn^{2+} ions migrate to the A position as a increases, so that in this case the number of positive Fe_A-Cr_B interactions may decrease rapidly with increasing a, i.e. the saturation moments will be expected to deviate from line IV for increasing a.

The saturation vs temperature curves do not show one of the anomalous curves predicted by Néel: for $a = 1{\cdot}25$ σ does decrease with decreasing temperature, but probably only as a result of the saturating field of 23000 oersteds not being large enough.

A change of sign of m without the occurrence of anomalous curves of the types shown in fig. 8 was expected for a mixed-crystal series in which angles between the ionic moments in one of the sublattices (i.e. the B sites) occur at all temperatures (section 2.2.2).

It may be that the present series is an example of such a case.

REFERENCE

[106]) W. G. Schindler, T. R. McGuire, L. N. Howard and J. S. Smart, Phys. Rev. **86**, 599 (J14), 1952.

Acknowledgement

The author is indebted to Dr E. J. W. Verwey, director of Philips Research Laboratories, for his stimulating interest in the work.

The assistance of Messrs T. T. A. M. Geraerts, G. Menkveld and M. Vrolijks in the experiments described in section 4 is gratefully acknowledged.

The experimental assistance of Mr E. Hondema in sections 6.2-3, of Mr F. Herbschleb in section 8 and particularly of Mr J. A. Schulkes in sections 5.1, 6.4, 7, 8 and 9 has been invaluable.

The author should like to express his sincere thanks to Mr P. B. Braun, who obtained all X-ray data for him, to Mr J. Smit for instructive discussions on theoretical problems, and to Dr J. H. van Santen for his constructive criticism of the manuscript.

Eindhoven, June 1954

VORSCHLÄGE BETREFFEND DIE EINHEITEN DER FLÄCHE, DER DIELEKTRISCHEN VERSCHIEBUNG UND DER MAGNETISCHEN FELDSTÄRKE

by P. CORNELIUS

537.71:621.3.081

Summary

It is suggested that the units of dielectric displacement and magnetic fieldstrength be defined in a way similar to that of the unit of surface area. These suggestions are made to remove the difficulties which have manifested themselves in calculations with quantities in electrical science. These difficulties and various proposals for their removal are elucidated by means of a simple geometrical example. Doubt is cast upon the suitability of using the symbol for "corresponding to" between units.

Résumé

Il est proposé de définir les unités du déplacement diélectrique et de l'intensité de champ magnétique de même façon que l'unité de surface. Ces propositions sont faites en vue de supprimer les difficultés survenues dans le calcul des grandeurs électriques. Ces difficultés ainsi que plusieurs propositions à l'effet de les surmonter sont illustrées par un exemple géométrique simple. L'utilité du signe „correspond à" entre les unités est mise en doute.

Zusammenfassung

Es wird vorgeschlagen, die Einheiten der dielektrischen Verschiebung und der magnetischen Feldstärke in ähnlicher Weise zu definieren wie die Einheit der Fläche. Diese Vorschläge werden gemacht, um die Schwierigkeiten zu beseitigen, die sich beim Rechnen mit Größen in der Elektrizitätslehre gezeigt haben. Diese Schwierigkeiten und verschiedene Vorschläge zu ihrer Beseitigung werden an einem einfachen geometrischen Beispiel erläutert. Die Zweckmäßigkeit des „Entspricht"-Zeichens zwischen Einheiten wird bezweifelt.

1. Einleitung

Bei der Einführung des rationalisierten Giorgischen Maßsystems in die Elektrizitätslehre ist eine umfangreiche Diskussion über die Theorie der Größengleichungen und der Rationalisierung entstanden. Während über die zugrundeliegenden elektromagnetischen Phänomene Einmütigkeit herrscht, geht der Streit um die mathematische Beschreibung dieser Phänomene und um die Definition der gebrauchten Worte. Im Laufe dieser Diskussion sind verschiedene Vorschläge gemacht worden, um die *formellen* Schwierigkeiten zu beheben, die sich beim Gebrauch verschiedener Maßsysteme und bei der Anwendung der Größengleichungen in der Elektrizitätslehre ergeben.

Das Wesentliche dieser Schwierigkeiten und Vorschläge werden wir unter anderem in den Erläuterungen in vereinfachter Weise besprechen. Wir stellen diesen Vorschlägen unsere in Abschnitt 2 angegebenen Vorschläge gegenüber. *Unsere Vorschläge enthalten nichts neues, sondern rufen nur das Gebräuchliche,* das teilweise auch durch internationale Beschlüsse festgelegt ist, ins Bewußtsein zurück. Wir wollen damit verhindern, daß eine an die physikalischen Phänomene angepaßte Begriffsbildung unnötigerweise zugunsten mathematischer Formalitäten kompliziert oder in Verwirrung gebracht wird.

2. Vorschläge

Einheit der Fläche

I) 1 m^2 ist die Fläche eines Quadrates mit 1 m Seitenlänge.

Einheiten der dielektrischen Verschiebung

II) 1 C/m^2 ist die Verschiebung im Innenraum eines unendlich großen Plattenkondensators mit endlichem Plattenabstand (in Vakuum), wenn die Ladungsdichte auf seinen Platten 1 C/m^2 beträgt.

III) 1 E.S.E. der Verschiebung ist die Verschiebung (in Vakuum) in 1 cm Abstand von einer punktförmigen Ladung von 1 E.S.E.

Einheiten der magnetischen Feldstärke

IV) 1 A/m ist die magnetische Feldstärke in einer unendlich langen Zylinderspule (in Vakuum), wenn ihr Strombelag 1 Ampère je m Spulenlänge ist.

Va) 1 Oe ist die magnetische Feldstärke (in Vakuum) in 1 cm Entfernung von einem punktförmigen Magnetpol von 1 E.M.E.

Will man diese ursprüngliche Definition wegen des fiktiven Magnetpols vermeiden, so kann man sie durch die folgende gleichwertige ersetzen:

Vb) 1 Oe ist die magnetische Feldstärke (in Vakuum) im Mittelpunkt eines Kreises mit dem Radius 1 cm, wenn durch einen Teil seines Umfanges mit der Länge 1 cm ein Strom von 1 E.M.E. fließt.

Findet man diese Definition unbefriedigend, weil eine Realisierung schwierig oder unmöglich ist, so kann man sie durch eine der folgenden Definitionen ersetzen:

Vc) 1 Oe ist die magnetische Feldstärke (in Vakuum) im Mittelpunkt eines Kreises mit dem Radius 2π cm, wenn durch seinen Umfang ein Strom von 1 E.M.E. fließt;

Vd) 1 Oe ist die magnetische Feldstärke in einer unendlich langen Zylinderspule (in Vakuum), wenn ihr Strombelag $1000/4\pi$ Ampère je m Spulenlänge ist.

Der Nachteil der Definitionen Vc) und Vd) ist jedoch, daß der Zusammenhang mit dem magnetischen Coulombschen Gesetz bzw. dem Laplaceschen Gesetz in der einfachen Formulierung, die sie im elektromagnetischen CGS-System haben — $K = P_1 P_2 / r^2$ bzw. $dH = Idl \sin\alpha / r^2$— nicht mehr deutlich ersichtlich ist. Man kommt nämlich zum Oersted, indem man die Faktoren in diesen Gesetzen gleich der Einheit macht.

Der Nachteil der Definition Vb) ist, daß der ursprüngliche Gedankengang des elektromagnetischen CGS-Systems umgedreht wird. Ursprünglich definierte man nämlich in diesem System zunächst die Einheit der magnetischen Feldstärke mit Hilfe des magnetischen Coulombschen Gesetzes (vergl. Va), und danach mit Hilfe des Laplaceschen Gesetzes und der Einheit der magnetischen Feldstärke die Einheit der Stromstärke (vergl. Vb).

3. Erläuterungen

Um den Sinn und das Ziel unserer in Abschnitt 2 angegebenen Vorschläge deutlich zu machen und um die in der Einleitung erwähnten Schwierigkeiten und fremden Vorschläge zu erläutern, besprechen wir ein einfaches Beispiel aus der Geometrie, an dem das Wesentliche leicht zu erkennen ist. Die Übertragung der Gedanken und Begriffe des geometrischen Beispiels auf diejenigen der Elektrizitätslehre überlassen wir dem Leser.

Die Fläche eines Quadrates ist proportional der zweiten Potenz seiner Seitenlänge. Die Oberfläche einer Kugel ist proportional der zweiten Potenz seines Radius. Die Oberfläche einer Kugel mit einem bestimmten Radius verhält sich zu der Fläche eines Quadrates mit der Seitenlänge gleich diesem Radius wie 4π zu 1.

Auf Grund dieser Tatsachen kann man zunächst Flächen mit Hilfe von Längen messen und dimensionell mit der zweiten Potenz von Längen „identifizieren“ [1]). Weiterhin kann man zwei verschiedene Wege einschlagen:

a) Man kann den Zusammenhang zwischen der Fläche A_q eines Quadrates und seiner Seitenlänge l wiedergeben durch die Gleichung $A_q = l^2$ und muß dann den Zusammenhang zwischen der Oberfläche A_k einer Kugel und ihrem Radius l wiedergeben durch die Gleichung $A_k = 4\pi l^2$.

b) Man kann auch den Zusammenhang bei der Kugel wiedergeben durch $A_k = l^2$ und muß dann den Zusammenhang beim Quadrat wiedergeben durch $A_q = l^2 / 4\pi$.

Wählt man nun 1 m als Längeneinheit, so ergibt sich für das unter a) angegebene „rationale“ Gleichungssystem 1 m^2 im Sinne der unter I) gegebenen Definition als „kohärente“ Flächeneinheit. Für das unter b) angebene „nichtrationale“ Gleichungssystem ergibt sich als kohärent eine

Flächeneinheit, deren Fläche 4π mal so groß ist wie die Fläche der Einheit unter I). Formell ist man durchaus berechtigt, diese Einheit 1 m^2 zu nennen; da dieser Name jedoch durch die Definition I) schon für eine andere Einheit fortgegeben ist, muß man ihr einen anderen Namen geben, wenn man Verwechslungen vermeiden will. Wir nennen sie hier das Kugel-m^2.

Für die Umrechnung von Flächenangaben in Kugel-m^2 in solche in m^2 benutzt man die Tatsache, daß eine Fläche von 1 Kugel-m^2 4π-mal so groß ist wie eine Fläche von 1 m^2. Es ist gebräuchlich, diese Tatsache durch eine Gleichung

$$1 \text{ Kugel-m}^2 = 4\pi \text{ m}^2,$$

oder durch einen Umrechnungsfaktor

$$\frac{\text{Kugel-m}^2}{\text{m}^2} = 4\pi$$

wiederzugeben. Dieser Umrechnungsfaktor kann durch eine Messung innerhalb der Meßgenauigkeit kontrolliert werden.

Es sei bemerkt, daß sowohl die oben angegebenen rationalen wie auch die nichtrationalen Gleichungen unabhängig von den gewählten Längeneinheiten sind. Man kann denselben Gedankengang auch für cm, Zoll usw. benutzen. Als Flächeneinheiten ergeben sich einerseits cm^2, $Zoll^2$ usw., andrerseits Kugel-cm^2, Kugel-$Zoll^2$ usw. Man kann diese Gleichungen „Größengleichungen" nennen, weil sie von den benutzten Längeneinheiten unabhängig sind.

Beim Quadrat und bei der Kugel haben sich niemals formelle Schwierigkeiten ergeben, weill es gebräuchlich ist, bei der Identifikation der Fläche mit der zweiten Potenz einer Länge ausschließlich vom Quadrat auszugehen, d.h. nur ein einziges Gleichungssystem und zwar das rationale zu benutzen. In der Elektrizitätslehre wurden und werden dagegen hauptsächlich vier Gleichungssysteme benutzt: statisch, magnetisch, Gauss und Giorgi. Der wesentliche Unterschied dieser Systeme beruht darauf, daß man die Identifikation verschiedener Größen, wie z.B. Spannung oder Verschiebung, mit Produkten oder Quotienten anderer physikalischer Größen, wie z.B. Masse, Länge, Strom, längs verschiedener Wege laufen läßt.

Die Verschiedenheit kann im „nichtrationalen" gegenüber dem „rationalen" Gedankengang bestehen: Die Verschiebung und die magnetische Feldstärke werden z.B. bei den ersten drei Systemen in Kugelfeldern mit anderen Größen identifiziert, bei Giorgi dagegen in homogenen Feldern.

Die Verschiedenheit kann auch bestehen in der Wahl der zur Identifikation benutzten Naturgesetze: Bei dem statischen System wird z.B. die Spannung als Potentialdifferenz mit dem Quotienten Arbeit/Ladung mit Hilfe des elektrischen Coulombschen Gesetzes identifiziert, bei dem magne-

tischen System dagegen mit dem negativen Differentialquotient des magnetischen Flusses nach der Zeit mit Hilfe des Faradayschen Induktionsgesetzes.

Schließlich kann die Verschiedenheit auch noch darin bestehen, daß man mehr oder weniger Größen mit Kombinationen anderer Größen identifiziert (sogenannte Dreier-, Vierer-, Fünfersysteme) [2]). Im statischen System wird z.B. die Ladung und damit der Strom an Hand des Coulombschen Gesetzes und des Newtonschen Beschleunigungssatzes mit einem Potenzprodukt der Größen Masse, Länge und Zeit identifiziert, beim Giorgischen System dagegen kann man den Strom als selbstständige Größe auffassen.

Daß man beim statischen, magnetischen und Gaussschen System normalerweise die Einheiten cm und g, beim Giorgischen dagegen m und kg benutzt, hat leider lange Zeit den Blick von der Hauptsache abgelenkt, daß nämlich diese vier Systeme verschiedene Gleichungssysteme sind. Die formellen Schwierigkeiten, die sich beim gleichzeitigen Gebrauch verschiedener Gleichungssysteme zur Beschreibung derselben physikalischen Phänomene ergeben können und die fremden Vorschläge, die zu ihrer Behebung gemacht worden sind, wollen wir nun an unserem einfachen Beispiel des Quadrates und der Kugel besprechen.

Diese fremden Vorschläge beziehen sich in Wirklichkeit nicht auf diese geometrischen Begriffe, sondern auf Einheiten und Größen der Elektrizitätslehre, wie z.B. Verschiebung und magnetische Feldstärke. Jedoch ist bei unserm Beispiel das Wesentliche der formellen Schwierigkeiten und Vorschläge einfacher zu erkennen.

Wir geben zunächst an, wie man beim gleichzeitigen Gebrauch des rationalen und des nichtrationalen Gleichungssystems a) bzw. b) und der Flächeneinheiten m^2 bzw. Kugel-m^2 ohne formelle Schwierigkeiten rechnen kann. Eine einfache Methode ist die folgende: Man rechnet ausschließlich in einem einzigen Gleichungssystem und ausschließlich mit Angaben in für dieses System kohärenten Einheiten. Angaben in anderen Einheiten werden erst in diese Einheiten umgerechnet. Um das gegenseitige Begreifen der Anhänger dieser zwei verschiedenen Systeme zu ermöglichen, gibt man:

1) den Gedankengang der Systeme (siehe bei unserem Beispiel oben unter a) und b));
2) eine Vergleichstabelle der Gleichungen. Bei jeder Gleichung werden Einheiten angeben, die in dem entsprechenden Gleichungssystem kohärent sind.

In unserem Beispiel:

Fläche A_q eines Quadrates mit der Seitenlänge l:

Rational:

$$A_q = l^2 \tag{1}$$

$$A_q \ldots (\mathrm{m}^2); \; l \ldots (\mathrm{m}).$$

Nichtrational:

$$A_q = l^2/4\pi \qquad (2)$$

$A_q \ldots$ (Kugel-m^2); $l \ldots$ (m).

Fläche A_k einer Kugel mit dem Radius l:

Rational:

$$A_k = 4\pi l^2$$

$A_k \ldots$ (m^2); $l \ldots$ (m). (3)

Nichtrational:

$$A_k = l^2$$

$A_k \ldots$ (Kugel-m^2); $l \ldots$ (m). (4)

Es sei nachdrücklich erwähnt, daß man diese Gleichungen als Größengleichungen auffassen kann. Die dazugeschriebenen Einheiten sind dann als Beispiel zugehöriger kohärenter Einheiten zu betrachten *).

3) eine Umrechnungstabelle für die verschiedenen Einheiten eventuell mit einer Erklärung des Gleichzeichens.

In unserem Beispiel:

$$1 \text{ Kugel-m}^2 = 4\pi \text{ m}^2. \qquad (5)$$

Erklärung: Das Gleichzeichen in dieser Gleichung bedeutet, daß eine Fläche von 1 Kugel-m^2 4π-mal so groß ist wie eine Fläche von 1 m^2.

Diese Methode wird in der Elektrizitätslehre von Cornelius [3]) angewendet. *Sie enthält nichts neues* oder besonderes, sondern gibt einfach das an, was von jeher bei Personen, die mit dimensionsrichtigen Gleichungen und den zugehörigen kohärenten Einheiten rechnen, gebräuchlich ist. Bei dieser Methode ergeben sich keine Schwierigkeiten. Es ist mühelos zu erkennen, wie die Anhänger der verschiedenen Systeme zu ihren Gleichungen und Einheiten kommen; die für Umrechnungen erforderlichen Zahlenfaktoren ergeben sich ohne weiteres. Daß Cornelius den ausschließlichen Gebrauch

*) Wir finden es an sich ziemlich gleichgültig, ob man die Gleichungen (1) bis (4) als Größengleichungen auffassen darf, da ihr Sinn auch ohnedies deutlich sein wird. Es besteht jedoch die Gefahr, daß die hier besprochene Methode von dem ihr gebührenden Platz mit Hilfe der Behauptung gedrängt wird, daß sie keine Größengleichungen benutze.

Einige Methoden, die ausdrücklich Größengleichungen benutzen, werden hiernach besprochen. Ihre Anhänger nennen „Größengleichungen" Gleichungen zwischen „Größen", wobei Größe = Zahlenwert·Einheit. Ersetzt man nun die Symbole l, A_q bzw. A_k in den Gleichungen (1) bis (4) durch das Produkt der darunter stehenden Einheiten mit den zugehörigen an Quadraten oder Kugeln gemessenen Zahlenwerten, so erhält man richtige Ergebnisse. Weiter oben wurde schon erwähnt, daß die Gleichungen (1) bis (4) unabhängig von den benutzten Längeneinheiten sind, eine Eigenschaft, welche die Anhänger der ausdrücklich sogenannten Größengleichungen diesen zuschreiben.

des viel verwendeten rationalisierten Giorgischen Gleichungssystems (sogenanntes rationales Vierersystem) mit den zugehörigen kohärenten Einheiten des MKSA-Einheitensystems empfiehlt, sei nebenbei erwähnt.

Wir besprechen nun einige andere Gedankengänge, die bestimmte Vorteile erstreben *und dabei gewisse Schwierigkeiten erzeugen.*

Zum Beispiel weist Wallot [4]) darauf, daß man bei der Benutzung von Größengleichungen direkt mit Angaben in willkürlichen Einheiten rechnen kann, ohne diese Angaben erst auf bestimmte Einheiten umrechnen zu müssen, wie bei Cornelius. (1) Man setzt: Größe = Zahlenwert · Einheit. (2) Man gibt den Umrechnungsfaktor zwischen den verschiedenen Einheiten als reine Zahl an. (3) Man wählt die *rationale* Gleichungsform.
Beispiel: Gesucht die Fläche A_k in Kugel-m² einer Kugel, deren Radius $l = 5$ cm.

(1) $A_k = x$. (Kugel-m²);
$l = 5$ cm.

(2) $1\,\mathrm{cm}^2 = 10^{-4}\,\mathrm{m}^2$;
$$\frac{\mathrm{m}^2}{\text{Kugel-m}^2} = \frac{1}{4\pi}.$$

(3) $A_k = 4\pi l^2$.

Also:
$$x = 4\pi \,.\, 25 \,.\, \frac{\mathrm{cm}^2}{\text{Kugel-m}^2} = 4\pi \,.\, 25.10^{-4}\, \frac{\mathrm{m}^2}{\text{Kugel-m}^2} = 25.10^{-4}.$$

Diese Methode arbeitet soweit befriedigend. Eine Schwierigkeit ergibt sich jedoch, wenn man die Beschränkung (3) fallen läßt, also unter Anwendung desselben Umrechnungsfaktors die nichtrationale Gleichung für die Kugelfläche anwenden will: $A_k = l^2$. Zu dem Glauben, daß man dies tun darf, wird man durch die allgemein gehaltene Behauptung verführt, daß Größengleichungen unabhängig von der Wahl der Einheiten sind. Nun kann man $A_k = l^2$ als echte Größengleichung der Kugelfläche auffassen; sie enthält Größen und keinen überflüssigen Faktor. Setzt man jedoch die Angaben des eben erwähnten Zahlenbeispiels bei unveränderten Angaben (1) und (2) ein in:

(3) $A_k = l^2$,

also
$$x = 25\, \frac{\mathrm{cm}^2}{\text{Kugel-m}^2} = 25.10^{-4}\, \frac{\mathrm{m}^2}{\text{Kugel-m}^2} = 25.10^{-4}/4\pi,$$

so erhält man für x einen Wert, der nur der 4π-te Teil des richtigen ist. Man muß bei der nichtrationalen Gleichungsform einen anderen Umrechnungsfaktor, nämlich $(\text{Kugel-m}^2)/\mathrm{m}^2 = 1$, benutzen, der jedoch nicht in

Übereinstimmung mit dem Größenverhältnis der oben definierten Einheiten ist.

Eine andere Schwierigkeit ergibt sich, wenn man mit dem Umrechnungsfaktor (Kugel-m^2)/m^2 = 4π nicht zufrieden ist, da „Kugel" in einer Einheitengleichung keine Dimension hat und man daher den formellen Widersinn 1 m^2 = 4π m^2 erhält.

Landolt und De Boer [5]) erklären diese Schwierigkeit folgendermaßen. Man gebraucht unbewußt zwei verschiedene Flächengrößen unter demselben Namen und Symbol, die man jedoch unterscheiden muß. Die „rationale Fläche" zum Beispiel des Quadrates ist nicht dasselbe wie die „nichtrationale Fläche" dieses Vierecks. Die erste ist nämlich definiert durch $A_q = l^2$, die zweite durch $A'_q = l^2/4\pi$. Man muß keinen Unterschied zwischen den Einheiten m^2 und Kugel-m^2 machen, ihr Umrechnungsfaktor in der Einheitengleichung ist 1.

Dieser Auffassung nach hat ein Quadrat mit der Seitenlänge 1 m die „rationale Fläche" 1 m^2 und die „nichtrationale Fläche" $1/4\pi$ m^2. Eine Kugel mit dem Radius 1 m hat die „rationale Oberfläche" 4π m^2 und die „nichtrationale Oberfläche" 1 m^2. Formell verschwinden dadurch die erwähnten Schwierigkeiten. Wir bekommen jedoch dafür zwei neue. Erstens müssen wir uns daran gewöhnen, daß ein Quadrat formell zwei Flächen hat, während es nur eine einzige physikalisch meßbare gibt. Zweitens wird die Angabe „1 m^2" zweideutig, wenn man nicht hinzufügt, ob man eine „rationale Fläche" oder eine „nichtrationale Fläche" meint. Die von Landolt und De Boer benutzte „Einheit" m^2 liegt begrifflich zwischen dem Dimensionsfaktor [L^2] und der oben unter I) physikalisch eindeutig definierten Einheit m^2. Landolt und De Boer müssen also vorschlagen, daß man ihren Begriff „Einheit" in Zukunft Einheit nennen soll, und den bisherigen Begriff Einheit z.B. Normalmaß oder Etalon. *)

Vermeulen [6]) schlägt einen andern Weg ein, der die Nachteile des Weges von Landolt und De Boer vermeidet. Er weist darauf, daß in den zwei Größengleichungen für die Oberfläche einer Kugel $A_k = 4\pi l^2$ und $A_k = l^2$, die formell einander widersprechen, nicht die Oberflächen A_k, die un-

*) Landolt und De Boer errechnen, daß 1 Oe = 1 E.M.E. des Stromes/1 cm = 1000 A/m, was im Widerspruch mit dem meßbaren Verhältnis der oben definierten Einheiten Oe und A/m ist, bei denen sich der gebräuchliche Wert 1 Oe = $1000/4\pi$ A/m ergibt. Sie behaupten, daß der meßbare Wert falsch ist und daß man die rationale von der irrationalen magnetischen Feldstärke unterscheiden müsse, weil diese Größe durch zwei verschiedene Gleichungen $\int H_r ds = I$ bzw. $\int H_{irr} ds = 4\pi I$ definiert seien.
Die ursprüngliche Absicht bei der Einführung des Größenbegriffs war, die Eindeutigkeit einer physikalisch meßbaren Größe, wie z.B. die magnetischen Feldstärke, unabhängig vom Maßsystem auch symbolisch zum Ausdruck zu bringen. Landolt und De Boer sind durch ihren Gedankengang zu einem entgegengesetzten Ergebnis geführt worden. Dieses Ergebnis ist das Resultat einer formalistisch-mathematischen Definitionskunst, die sich weitgehend von den Meßergebnissen der Physik befreit hat.

zweifelhaft physikalisch sich selbst gleich sind und auch nicht die Längen l, die ebenfalls sich selbst gleich sind, die Verschiedenheit ausmachen, sondern das Produkt $l.l.$ Dieses Produkt bedeutet im ersten Fall die Fläche eines Rechteckes mit den Seitenlängen l und l, im zweiten Fall dagegen die Oberfläche einer Kugel mit dem Radius l. Will man also nicht die Methode von Cornelius anwenden, bei der das automatisch unterschieden ist, so muß man nicht A von A', sondern z.B. $(l.l)_r$ von $(l.l)_{irr}$ unterscheiden. Dabei verschwinden die oben bei der Methode Wallot erwähnten Schwierigkeiten weil $1(\text{m.m})_r = 1\ \text{m}^2$ und $1(\text{m.m})_{irr} = 1$ Kugel-$\text{m}^2 = 4\pi\ \text{m}^2$ ist. Bei dieser Methode braucht man weder die eine physikalische Fläche in zwei formelle Flächen aufzulösen, man braucht nicht „Einheit" von Einheit oder Normal (Etalon) zu unterscheiden, man kann seine Einheiten physikalisch eindeutig definieren und man kann den Umrechnungsfaktor zwischen verschieden definierten Einheiten derselben physikalischen Größe formell einwandfrei als reine Zahl in Übereinstimmung mit dem physikalisch meßbaren Größenverhältnis dieser Einheiten angeben. Es sei darauf gewiesen, daß die Methode von Cornelius und Vermeulens befriedigende Erklärung der „Rationalisation" noch nicht in das Bewußtsein der Fachkreise gedrungen ist. Man glaubt, daß nur die von Landolt und De Boer angegebene sogenannte „Größenrationalisation" formell in Ordnung ist.

Zum Schluß noch eine Bemerkung über das „Entspricht"-Zeichen. Um die formellen Schwierigkeiten des Gleichsetzens von zwei Einheiten aus verschiedenen Systemen zu vermeiden, hat man vorgeschlagen, die Beziehung zwischen diesen Einheiten mit Hilfe des „Entspricht"-Zeichens anzugeben, z.B.

$$1\ \text{Kugel-m}^2 \mathrel{\widehat{=}} 4\pi\ \text{m}^2, \text{ oder z.B.}$$

$$1\ \text{Oe} \mathrel{\widehat{=}} \frac{1000}{4\pi}\ \text{A/m}.$$

Das ist nicht empfehlenswert. Bei Anwendung der oben vorgeschlagenen physikalischen Definitionen, wie sie u.a. Cornelius und Vermeulen anwenden, muß ein Gleichzeichen benutzt werden, da das meßbare Größenverhältnis zweier gleicher physikalischer Phänomene, d.h. eine reine Zahl, gemeint ist. Auch bei der Methode nach Wallot muß man den Faktor Oe/(A/m) durch $1000/4\pi$ ersetzen können; dies wird durch das „Entspricht"-Zeichen formell unmöglich gemacht.

Landolt und De Boer vermeiden diese Schwierigkeit zum Teil, da bei ihnen der Systemunterschied „rational" - „nichtrational" nicht bei den „Einheiten", sondern nur bei den Größen zum Ausdruck gebracht wird. Weist man jedoch darauf, daß 1 Oe in einem Dreiersystem als $1\ \text{cm}^{-\frac{1}{2}}\text{g}^{\frac{1}{2}}\text{sec}^{-1}$

definiert ist, 1 A/m jedoch in einem Vierersystem, so müssen sie formell 1 Oe $\triangleq$ 1000 A/m setzen, wodurch auch für sie das Rechnen formell unmöglich gemacht wird. De Boer schlägt darum vor, die ursprüngliche „Dreier"-Definition des Oersted in eine „Vierer"-Definition (1 Oe = 1 Biot/cm) zu ändern. Der Nachteil dieses Vorschlages besteht darin, daß an einem historisch abgeschlossenen System vor seinem Tode noch Änderungen angebracht werden sollen.

4. Schlußfolgerung

In der Elektrizitätslehre können dieselben Phänomene mit Hilfe verschiedener Gleichungssysteme beschrieben werden. Die Verschiedenheit der Gleichungssysteme kann verschiedene Ursachen haben, z.B.: Rationaler gegenüber nichtrationaler Gedankengang; Identifikationen mit Hilfe verschiedener Naturgesetze (z.B. elektrostatischer oder elektromagnetischer Gedankengang); mehr oder weniger Identifikationen (sogenannte Dreier-, Vierer-, Fünfersysteme).

Eine einfache Methode, um sich in der auf diese Weise entstandenen Verwirrung rechnend und begreifend zurechtzufinden, wird von Cornelius benutzt. Diese Methode enthält nicht neues, sondern formuliert nur das Gebräuchliche; es treten keine formellen Schwierigkeiten auf. Sie scheint jedoch auf den ersten Blick unelegant und unnötig weitschweifig zu sein. Wallot zeigt, wie man mit Angaben in willkürlichen Einheiten rechnen kann, wenn man ein bestimmtes Gleichungssystem zugrunde legt. Diese Methode arbeitet einfach und elegant, wenn man sich auf ein einziges Größengleichungssystem beschränkt und wenn man die für das richtige Rechnen nötigen Umrechnungsfaktoren akzeptiert, ohne sich durch formelle Einwände abschrecken zu lassen. Landolt und De Boer ermöglichen den gleizeitigen Gebrauch von rationalen und nicht-rationalen Gleichungsformen und beseitigen formelle Schwierigkeiten bei der Umrechnung von Einheiten. Hierbei wenden sie jedoch Heilmittel an, die schlimmer sind als die zu heilende Krankheit. Vermeulen gibt eine Methode an, die die Vorzüge der von Cornelius benutzten Methode beibehält. Seine Methode ist an das ästhetische Gefühl von mathematisch geschulten Physikern angepaßt, ohne die Beschränkungen der Methode Wallot oder die revolutionären Vorschläge von Landolt und De Boer anwenden zu müssen.

Zum Schluß wird bemerkt, daß die Einführung des „Entspricht"-Zeichens nur scheinbar die formellen Schwierigkeiten des Umrechnens derjenigen Einheiten beseitigt, die an verschiedene Gleichungssysteme angepaßt sind. Die Methoden Cornelius und Vermeulen bedürfen dieses Zeichens nicht.

Einheitendefinitionen in der Art der am Anfang vorgeschlagenen ermögli-

chen die Angabe von Umrechnungsfaktoren als reine Zahlen. Sie beseitigen außerdem die Unklarheiten, die sich im Laufe der Diskussionen über Größengleichungen und Rationalisierung eingeschlichen haben.

Eindhoven, March 1954

LITERATUR

[1]) R. Fleischmann, Die Struktur des physikalischen Begriffssysteme, Z. Phys. **129**, 377-400, 1951. Insbesondere S. 393.

[2]) Siehe z.B. U. Stille, Größendefinition und Einheitenverknüpfung in der Elektrodynamik, Arch. Elektrotech. **40**, 249-256, 1952. Siehe auch [1]) S. 394.

[3]) P. Cornelius, Korte samenvatting der electriciteitsleer, Meulenhoff, Amsterdam 1948; Kurze Zusammenfassung der Elektrizitätslehre, Springer -Verlag, Wien 1951; L'électricité selon le système Giorgi rationalisé, Dunod, Paris 1953.

[4]) J. Wallot, Größengleichungen und Zahlenwertgleichungen, Elektrotech. Z. **64**, 13, 1943; Größengleichungen, Einheiten und Dimensionen, Barth, Leipzig 1953.

[5]) J. de Boer, Grootheden en eenheden, Ned. T. Natuurk. **16**, 293-316, 1950; Rationalisatie, Ned. T. Natuurk. **17**, 5-24, 1951; M. Landolt und J. de Boer, Quelle est la signification de la rationalisation totale?, Rev. gén. Élect. **60**, 499-507, 1951; M. Landolt, Ancienne et nouvelle définition de la notion champ magnétique, Bull. schweiz. elektrotech. Ver. **44**, 458-461, 1953.

[6]) R. Vermeulen, Dimensional analysis, units and rationalization, Philips Res. Rep. **7**, 432-441, 1952. Der Gedankengang von Vermeulen war im wesentlichen schon von A. Lodge, The multiplication and division of concrete quantities, Nature **38**, 281-283, 1888, angegeben.

[7]) Siehe [2]), U. Stille, S. 256.

APPENDIX

Für Leser, die sich aus Interesse oder in Verbindung mit Normungsarbeiten mit dieser Materie beschäftigen wollen oder müssen, möchten wir noch einige Einzelheiten, die zu langwierigen Diskussionen geführt haben, berühren.

Wie der Leser vielleicht bemerkt haben wird, ist unsere Antwort auf die Frage: „Was ist Rationalisation in der Elektrizitätslehre?" die folgende. In einigen Fällen, z.B. magnetische Feldstärke und dielektrische Verschiebung, geht man bei der Beschreibung derselben meßbaren physikalischen Größe, wie z.B. magnetische Feldstärke H, in derselben Konstellation, beispielweise der einmalige Umlauf um einen gleichstromdurchflossenen Draht, von der „irrationalen" Gleichungsform $\oint H_s \mathrm{d}s = 4\pi I$ zu einer anderen über, nämlich $\oint H_s \mathrm{d}s = I$; gleichzeitig geht man von der für die erstere Gleichungsform kohärenten Einheit für H — z.B. mOe, wenn man m als Einheit für die Länge s, und A als Einheit für den Strom I benutzt — zu der für die letztere Gleichungsform kohärenten Einheit für H — z.B. A/m, wenn man wieder m als Längeneinheit und A als Stromeinheit benutzt — über.

Da sich aus den Definitionen von Oe und A/m (siehe Vd) bzw. IV)) das meßbare Verhältnis 4π mOe $= 1$ A/m ergibt, sieht man, daß ein und dasselbe, mit sich selbst identische Phänomen auf beide Weisen numerisch richtig wiedergegebenen wird, sei es auch einfacher bei der rationalen Weise.

H_s, s und I sind physikalisch identisch und werden auch bei unserer Interpretation der Rationalisation numerisch und symbolisch als identisch wiedergegeben.

Bei unserem oben behandelten Beispiel vom Quadrat und der Kugel war der entsprechende Schritt z.B. für das Quadrat der Übergang von der Gleichungsform $A_q = l^2/4\pi$ zur Gleichungsform $A_q = l^2$, während wir gleichzeitig von der für die erstere Gleichungsform kohärenten Einheit Kugel-m^2 zu der für die letztere Gleichungsform kohärenten Einheit m^2 (im Sinne der Definition I)) übergingen.

Wenn man diesen Unterschied der Gleichungsform und der Einheit bei ein- und demselben physikalischen Zusammenhang, beispielsweise gegebener Strom, Abstand, magnetische Feldstärke und Konstellation, symbolisieren will, so sollte man nicht nach dem Vorschlag von Landolt und De Boer und anderen Anhängern der „Größenvariation" H_{irr} von H unterscheiden. Diese Unterscheidung kann vielleicht zu richtigen Rechenergebnissen führen, steht jedoch im Widerspruch zum Meßergebnis, bei dem ein Feldstärkemesser in derselben Konstellation bei demselben Strom im selben Abstand dieselbe Feldstärke mißt, unabhängig davon, ob der Zusammenhang dieser drei Messungen durch eine „rationale" oder eine „nichtrationale" Gleichungsform symbolisiert wird.

Will man nun durchaus beide Gleichungsformen durcheinander gebrauchen, richtig rechnen und mit seiner Symbolik nicht in Widerspruch mit den Meßergebnissen kommen, so kann man nach dem Vorschlage von Vermeulen $\oint (H_s\ \mathrm{d}s)_{\text{irr}} = 4\pi I$ von $\oint (H_s\ \mathrm{d}s)_{\text{r}} = I$ unterscheiden. Das irrationale Produkt bezieht sich auf ein Gleichungssystem, bei dem man die kohärente Einheit der Feldstärke in der Anordnung bestimmt, die in Definition Vb) angedeutet ist. Die für die irrationale Gleichungsform kohärente Einheit der magnetischen Feldstärke ergibt sich bei Benutzung der Einheiten Meter und Ampère, wenn man in dieser Anordnung den Radius und den stromdurchflossenen Umfangsteil 1m und den Strom 1A macht, zu: $1(\mathrm{A/m})_{\text{irr}} = 1$ mOe. Das rationale Produkt bezieht sich auf das Gleichungssystem, bei dem die kohärente Feldstärkeneinheit in der Anordnung der Definition IV) bestimmt wird. Die dafür kohärente Einheit ist bei Benutzung der Längeneinheit Meter und der Stromeinheit Ampère die unter IV) definierte A/m. Man sieht, daß $1\ (\mathrm{A/m})_{\text{r}} = 1\ \mathrm{A/m} = 4\pi(\mathrm{A/m})_{\text{irr}} = 4\pi$ mOe, ein Ergebnis, daß durch eine Messung der Feldstärken, der Ströme und der Längen in beiden Anordnungen kontrolliert werden kann.

Es wird deutlich sein, daß ein Einheitensymbol, wie z.B. A/m, ohne nähere Angaben weder den Meßwert festlegt, noch auch die Kohärenz in einem bestimmten Gleichungs- und Einheitensystem beweist. Daher unser Vorschlag, um den gebräuchlichen Sinn der Feldstärkeneinheit A/m entsprechenden Definition IV) ausdrücklich festzulegen. —

Wir wollen den Leser noch auf einige andere Punkte in der Physik bzw. Technik weisen, bei denen den Ansprüchen des mathematischen Formalismus nicht genügt wird und wo darum ebenfalls die Gefahr besteht, daß der physikalische Gehalt zugunsten der mathematischen Rechenregeln verwirrt wird.

Es ist bekannt, daß man sowohl die Energie wie auch das Drehmoment in N·m messen kann. Die Energieeinheit N·m wird auch Joule genannt. Wir raten ab, das Drehmoment wegen der Gleichheit des Symbols N·m in Joule zu messen.

Es ist bekannt, daß man sowohl den magnetischen Fluß wie auch das Zeitintegral einer Spannung in V·s messen kann. Die Flußeinheit V·s wird auch Weber genannt. Wir raten ab, das Zeitintegral einer Spannung wegen der Gleichheit des Symbols V·s in Weber zu messen.

Es ist bekannt, daß man sowohl die Frequenz wie auch die Kreisfrequenz von Wechselströmen in s^{-1} messen kann. Die Frequenzeinheit s^{-1} wird auch Hertz genannt. Wir raten ab, die Kreisfrequenz wegen der Gleichheit des Symbols s^{-1} in Hertz zu messen.

Man kann die Einheitengleichungen, daß J gleich N·m, daß Wb gleich V·s und daß Hz gleich s^{-1} ist, während das umgekehrte nicht stets der Fall zu sein braucht, in demselben Sinn begreifen wie die Tatsache, daß ein Hering immer ein Fisch ist, ein Fisch aber nicht immer ein Hering zu sein braucht. —

Es wird von Anhängern der Größenvariation vorgeschlagen, beispielsweise die Ladung Q^s von der Ladung Q^m zu unterscheiden [7]), d.h. die Ladung, die man entsprechend dem Gedankengang des statischen Systems findet von derjenigen des magnetischen Systems. Die gebräuchliche Auffassung ist dagegen, daß die Ladung z.B. des Elektrons unabhängig davon ist, mit welchem Gleichungssystem man rechnet und mit welcher Meßmethode man sie bestimmt; diese Auffassung ist auch die unsere.

Als Grund für den genannten Vorschlag wird angeführt, daß der Begriff Ladung in den verschiedenen Systemen der Elektrizitätslehre auf Grund verschiedener Grundmeßverfahren eingeführt wird; daß demzufolge dieser Begriff in den verschiedenen Systemen verschieden definiert wird, verschiedene Dimensionen erhält und sich darum auf verschiedene Größen bezieht. Diese Größen und ihre zugehörigen Einheiten lassen sich nur durch Proportionalitätsfaktoren, die dimensionsbehaftet sind, ineinander umrechnen.

Benutzt man nur ein einziges System mit einer bestimmten Anzahl und Art Grundmeßverfahren, z.B. ein sogenanntes Vierersystem, so wird z.B. die Ladung als eine einförmige Größe, Definition und Dimension eingeführt, sodaß man nun innerhalb dieses Begriffssystems ruhig verschiedene Einheiten der Ladung benutzen kann. Wird unter dieser Voraussetzung eine Ladung in verschiedenen Einheiten gemessen, so beziehen

sich die den Zahlenwerten nach verschiedenen Meßergebnisse auf dieselbe, gleich definierte Größe.

Anhänger dieses Gedankenganges glauben sich nun entscheiden zu müssen: a) Will man nur eine einzige Größe Ladung anerkennen, so muß man sich auf ein einziges Begriffssystem, z.B. ein „Vierersystem" wie das von Giorgi festlegen; die historischen „Dreiersysteme" (statisch, magnetisch, Gauss) sind unvollständig und müssen mit ihren Größen- und Einheitendefinitionen erst auf „Vierer"-Basis umgesetzt werden, wenn man ihre Größen und Einheiten mit denen des „Vierersystems" vergleichen will. b) Will man dagegen den verschiedenen „Dreier"- „Vierer"- oder auch „Fünfer"-Systemen ihre Auffassung und die Geschlossenheit ihres Systeme lassen, so muß man anerkennen, daß z.B. die Ladung in den verschiedenen Systemen eine andere Größe ist, sodaß z.B. dem Elektron nicht eine einzige Ladung zuzuschreiben ist, sondern eine statisch, eine magnetisch definierte, eine Giorgische usw.

Hierzu möchten wir bemerken, daß die Zwangslage, sich zwischen a) oder b) entscheiden zu müssen, nur durch die geschilderte abstrakte Auffassung des Begriffs Größe erzeugt wird. In Wirklichkeit verstehen die Anhänger der verschiedenen elektromagnetischen Begriffs-, Maß- und Einheitensysteme z.B. unter der Ladung eines Elektrons oder unter der Kapazität eines Kondensators dasselbe, so verschieden sie diese Größen und ihre Einheiten auch messen, definieren und symbolisieren. Es ist nämlich bei Anhängern aller Systeme gebräuchlich, die Maxwellsche Theorie im Gebiet der Elektrizitätslehre (ohne Quanten- und Atomtheorie) als gültig zu betrachten. Dann werden aber die verschiedenen Meßverfahren für Strom, Spannung usw. gleichwertig.

Wir können beispielsweise erst die Ladung auf Grund ihrer statischen Kraftwirkung bestimmen und finden dann das Laplacesche Gesetz betreffend die magnetische Wirkung der bewegenden Ladung. Wir können ebenso gut erst die bewegende Ladung auf Grund ihrer magnetischen Wirkung bestimmen und finden dann das Coulombsche Gesetz betreffend die Kraftwirkung der stillstehenden Ladung. Welchen Weg man einschlägt, ist für den physikalischen Begriff Ladung gleichgültig.

Der Formalismus der Gleichungen und Dimensionen, und die Größe der zugehörigen kohärenten Einheiten können dadurch jedoch stark beeinflußt werden. Man muß einsehen, daß unter Umständen dieselbe Größe auf verschiedene Weise gemessen werden kann. Man muß einsehen, daß unter Umständen dieselbe Größe verschieden definiert und symbolisiert erscheinen kann. Daß es sich um dieselbe Größe handelt, kann dann nicht aus der Definition und dem Symbolismus, sondern nur durch Nachdenken über den Zusammenhang der verschiedenen Phänomene und Messungen erkannt werden.

Res. Rep. 9, 458-459, 1954

A MAGNETLESS "MAGNETRON"

by A. VERSNEL and J. L. H. JONKER

621.396.615.141.2

Summary

A description is given of an oscillator tube that behaves like a magnetron. A feature of the new tube is that no magnetic field is needed. Measurements are discussed also.

Résumé

Cet article contient la description d'un tube oscillateur qui présente certaines analogies avec un magnétron. Le tube en cause comporte l'avantage qu'il ne nécessite pas de champ magnétique. Les mesures sont également traitées.

Zusammenfassung

Es wird eine Oszillatorröhre beschrieben, die Ähnlichkeit mit einem Magnetron aufweist. Eine charakteristische Eigenschaft dieser Röhre besteht darin, daß kein Magnetfeld erforderlich ist. Es werden auch Messungen diskutiert.

Between two coaxial cylindrical electrodes, the outer one having a potential lower than the inner one, electrons leaving an electron gun in a direction perpendicular to a plane through the common cylinder axis will follow paths that are concentric with these electrodes provided that the velocity of the electrons leaving the gun agrees with the natural potential between the cylinders [1) 2)] and that the current density does not exceed a certain value.

If we divide the inner cylinder into an even number of strips by means of equidistant slits in the axial direction and connect similar ends of the strips alternately into two groups with the common point of each group on the axis of the cylinder, and if we connect these points to the ends of two short-circuited Lecher wires, the combination strips-and-Lecher-wires will form a resonant system (fig. 1).

The electron velocity being chosen such that the electron transit time between equivalent points on two successive strips is about half the period of the resonant system, the electron beam will interact in the common way with that system. One half of the beam will then gain energy from the h.f. electric field between two successive strips, the other half will cede energy to it. The electrons gaining energy move away from the strips, are less influenced by the h.f. field and extract less energy from it than is ceded by the energy-losing electrons, whose orbits will gradually approach the strips. As a result of this, a tube constructed on the above-mentioned principle acts as an oscillator.

There is a great resemblance between such an oscillator and a magnetron. In both cases an electron beam moving between cylindrical electrodes interacts with a h.f. field in such a way that oscillations occur and that the electrons that disturb the action by gaining energy from the h.f. field are eliminated. In contrast to the common magnetron principle, however, no magnetic field is needed in this "magnetless magnetron".

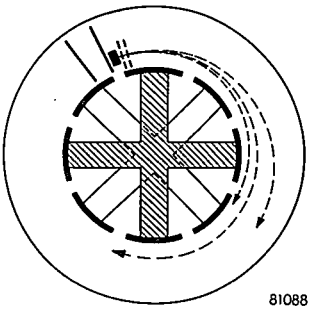

Fig. 1. Horizontal projection of the main electrodes and connections of the experimental magnetless "magnetron". The orbits of the electrons leaving the centre of the cathode at different moments during a cycle are indicated.

A simple relation exists between the free-space wavelength λ_0 of the oscillations in this tube and the initial velocity V_0 of the electron beam expressed in volts:

$$\lambda_0 \sqrt{V_0} = \frac{2pc}{\sqrt{\frac{2e}{m}}} = \text{constant},$$

in which p = distance on the beam orbit concurring with two equivalent points on two successive strips, c = velocity of light in free space, e = electron charge, m = electron mass.

This relation was tested on an experimental tube in which the inner cylinder (radius = 13·6 mm) was divided into 8 equal strips. A triode gun gave a ribbon-shaped beam (beam-orbit radius = 15·6 mm) ranging from 1·4 to 5·9 mA. When the beam velocity was varied from 100 to 260 V, the wavelength varied from 130 to 72 cm. The measured values did not deviate from the calculated ones by more than 6 per cent. The maximum h.f. output in this tube was of the order of some tens of milliwatts.

Eindhoven, August 1954

REFERENCES

1) H. C. Thompson, Proc. Inst. Radio Engrs **24**, 1295, 1936.
2) H. M. Wagner and W. R. Ferris, Proc. Inst. Radio Engrs **29**, 598-602, 1941.

 Philips Res. Rep. 9, 460-468, 1954

ELASTIC AFTER-EFFECT IN α-IRON IN RELATION TO THE ELASTIC CONSTANTS OF CUBIC METALS

by J. SMIT and H. G. van BUEREN

539.389.3:669.112.228.1

Summary

The elastic after-effect in α-iron, containing carbon or nitrogen in solid solution, can be interpreted as causing a change of the elastic moduli of the material. This interpretation renders it possible to estimate with a reasonable degree of accuracy the magnitude of the after-effect in polycrystalline materials. The estimate is based on a general relation which is shown to exist between the elastic constants of single crystals and of polycrystalline specimens of the cubic metals.

Résumé

La relaxation élastique du fer α contenant du carbone ou de l'azote en solution solide peut être interprétée comme une variation des modules d'élasticité du matériel. Cette interprétation permet de faire une estimation assez exacte de la magnitude de la relaxation élastique du matériel polycristallin. L'estimation se base sur une relation générale, demontrée dans cet article, existant entre les modules d'élasticité à l'état monocristallin et à l'état polycristallin des métaux cubiques.

Zusammenfassung

Die elastische Nachwirkung in kohlenstoff- oder stickstoffhaltigem α-Eisen kann als die Ursache einer Änderung der Elastizitätsmoduln des Materials aufgefaßt werden. Diese Auffassung ermöglicht eine ziemlich genaue Abschätzung der Größe der Nachwirkung im vielkristallinen Material. Hierbei wird Gebrauch gemacht von einer allgemeinen Beziehung zwischen den elastischen Konstanten von Einkristallen bzw. von vielkristallinen Proben von kubischen Metallen.

1. Introduction

The internal friction of α-iron, containing carbon or nitrogen in solid solution, shows in the temperature range between —100 °C and +300 °C a maximum at frequencies of the order of one cycle per second. This phenomenon has been explained by Snoek [1]) as being due to the migration of the solute atoms through the lattice under the influence of the varying internal strains. These atoms occupy interstitial sites between next nearest iron atoms in the b.c.c. lattice. The line joining these two iron atoms is directed along one of the cubic axes and therefore one distinguishes between three types of interstitial sites: x-, y- and z-sites. In the unstressed material the solute atoms are distributed equally over the three types of sites; on straining the material the solute atoms have tendency to diffuse to those sites in which there is most space for them. During this relaxation

process, if a constant load is applied at $t = 0$, the strain increases according to

$$\varepsilon(t) = \varepsilon(0) + \Delta\varepsilon(1 - e^{-t/\tau}), \tag{1}$$

where τ is the relaxation time. If the load varies sinusoidally in time (with angular frequency ω), damping of the vibrations occurs; this damping is greatest when $\omega\tau = 1$.

The relaxation time τ varies exponentially with the absolute temperature T according to

$$\tau(T) = \tau(\infty)\, e^{E/kT},$$

where E denotes the activation energy of the diffusion process. Due to this strong temperature dependence of τ the damping curve can be established at a fixed frequency by varying the temperature.

For a given material the relaxation time is independent of the orientation of the loading stress. Therefore we shall confine our attention to the differences between the relaxed and the unrelaxed state (i.e. to $\Delta\varepsilon$ in (1)).

2. Statistical mechanics of the after-effect

It will be assumed that the interaction between the dissolved atoms can be ignored. For the small concentrations encountered in practice ($< 0{\cdot}1$ weight %) this assumption is probably justified, as is borne out by the experiments (there exists a proportionality between the magnitude of the after-effect and the concentration).

The theory of Snoek [1]), elaborated by Polder [2]), may be put in the following form. If the material is stressed homogeneously (stress components σ_{ij}), the energy (or rather the enthalpy) due to the presence of one solute atom is changed by an amount

$$W = -\sum_{i,j} \sigma_{ij}\, v_{ij} \qquad (i, j = x, y, z), \tag{2}$$

where v_{ij} is the strain, integrated over the whole space, caused by one solute atom.

Since the after-effect gives no volume changes, the corresponding terms have to be omitted in (2): for an x-site holds

$$v_{xx} = 2v/3,\ v_{yy} = v_{zz} = -v/3, \tag{3}$$

whereas the mean shear strains are zero. Similar expressions hold for the y- and z-sites.

The energies of the solute atom on an x-, y- or z-site are then

$$\left.\begin{aligned} W_x &= -(v/3)\,(2\sigma_{xx} - \sigma_{yy} - \sigma_{zz}), \\ W_y &= -(v/3)\,(2\sigma_{yy} - \sigma_{zz} - \sigma_{xx}), \\ W_z &= -(v/3)\,(2\sigma_{zz} - \sigma_{xx} - \sigma_{yy}), \end{aligned}\right\} \tag{4}$$

respectively.

The presence of n solute atoms per unit volume gives rise to an extra factor in the partition function

$$Z = [\exp(-W_x/kT) + \exp(-W_y/kT) + \exp(-W_z/kT)]^n,$$

and to a corresponding change in the free enthalpy per unit volume

$$G = -nkT \ln[\exp(-W_x/kT) + \exp(-W_y/kT) + \exp(-W_z/kT)]. \quad (5)$$

If W_x, W_y and W_z (given by (4)) are much smaller than kT, which will be shown to be the case at room temperature, series expansion gives for G in second approximation:

$$G \approx n[-kT \ln 3 + (W_x + W_y + W_z)/3 - (W_x^2 + W_y^2 + W_z^2)/6\,kT]. \quad (6)$$

Since the zero point of the energy scale is such that $W_x + W_y + W_z = 0$ (compare (4)), we get by inserting (4) into (6):

$$G \approx n[-kT \ln 3 - (v^2/9kT)(\sigma_{xx}^2 + \sigma_{yy}^2 + \sigma_{zz}^2 - \sigma_{xx}\sigma_{yy} - \sigma_{yy}\sigma_{zz} - \sigma_{zz}\sigma_{xx})]. \quad (7)$$

Comparison of (7) with the contribution of the elastic energy to G, viz.

$$G_{el} = -\tfrac{1}{2}s_{11}(\sigma_{xx}^2 + \sigma_{yy}^2 + \sigma_{zz}^2) - s_{12}(\sigma_{xx}\sigma_{yy} + \sigma_{yy}\sigma_{zz} + \sigma_{zz}\sigma_{xx}) - \\ - \tfrac{1}{2}s_{44}(\sigma_{xy}^2 + \sigma_{yz}^2 + \sigma_{zx}^2),$$

shows that the result of the relaxation process can be interpreted as being equivalent to a change of the elastic moduli s_{ij} according to

$$\Delta s_{11} = 2b, \qquad \Delta s_{12} = -b, \qquad \Delta s_{44} = 0, \quad (8)$$

with

$$b = nv^2/9kT. \quad (9)$$

The transformation properties under space rotations are thus the same for Δs_{ij} and s_{ij}; so we get in particular for Δs_{11}, in an orientation with direction cosines α, β, γ:

$$\Delta s'_{11}(\alpha, \beta, \gamma) = 2b[1 - 3(\alpha^2\beta^2 + \beta^2\gamma^2 + \gamma^2\alpha^2)], \quad (10)$$

being zero in the [111] direction.

The interaction between the dissolved atoms, neglected in the above treatment, can be taken into account by addition to the energy (4) terms of the form pc_x, pc_y and pc_z respectively, where c_x, c_y and c_z stand for the deviations of the concentrations of dissolved atoms on the x-, y- and z-places respectively from the average concentration $n/3$ on those places, and p is a constant factor. The concentration c_x is given by

$$c_x = n\left[\frac{\exp(-W_x/kT)}{\exp(-W_x/kT) + \exp(-W_y/kT) + \exp(-W_z/kT)} - \frac{1}{3}\right],$$

and analogous expressions are valid for c_y and c_z. Series expansion yields

$$c_x \approx (nv/9kT)(2\sigma_{xx} - \sigma_{yy} - \sigma_{zz}), \quad (11)$$

and it is easily shown that (9) then goes over into

$$b' = (nv^2/9kT)\,(1 - np/3kT)\,. \tag{12}$$

The additional term in b' corresponds to a similar term, called χ, obtained by Polder [2]). That it is negligibly small can also be found from the temperature variation of the after-effect. Recently, Fast and Verrijp [3]) have shown the magnitude of the after-effect in nitrogen-containing iron to be within experimental error proportional to the reciprocal value of the absolute temperature, in accordance with (9).

The change in the elastic moduli also affects the elements of the reciprocal tensor, i.e. the elastic constants c_{ij}. The changes in these quantities are given by equations analogous to (8), viz.

$$\Delta c_{11} = -2a\,, \qquad \Delta c_{12} = a\,, \qquad \Delta c_{44} = 0\,, \tag{13}$$

where a is related to b according to

$$a = (c_{11} - c_{12})^2\, b\,. \tag{14}$$

It is assumed in (14) that a and b are relatively small quantities. The quantity a is the same as has been used by Polder [2]).

3. Value of the constant b

Snoek [1]) has emphasized that the magnitude of the after-effect is directly related to the tetragonal deformation ε_M of martensite. It is found by experiment that ε_M is proportional to the concentration of the solute atoms. Extrapolating to low concentrations, it is clear that in our case

$$v = \varepsilon_M / n_M\,, \tag{15}$$

with n_M the number of dissolved atoms per unit volume in the martensite. According to data recently published by Roberts [4]), $\varepsilon_M = 4{\cdot}5.10^{-4}$ for iron containing 0·01 carbon % by weight, from which it follows that v in the case of carbon is given by

$$v_C = 1{\cdot}13.10^{-23}\ \mathrm{cm}^3\,. \tag{16a}$$

For iron, containing nitrogen, v can only be estimated; from data obtained by Bose and Hawkes [5]) it follows that

$$v_N \approx 1{\cdot}1.10^{-23}\ \mathrm{cm}^3\,. \tag{16b}$$

Consequently the values of b can be calculated and are for iron containing c % solute atoms by weight

$$b_C = \frac{4{\cdot}29\, c_C}{T}\, 10^{-10}\ \mathrm{cm}^2/\mathrm{dyne}\,, \tag{17a}$$

$$b_N \approx \frac{3{\cdot}5\, c_N}{T}\, 10^{-10}\ \mathrm{cm}^2/\mathrm{dyne}\,, \tag{17b}$$

where T is expressed in °K.

The energy W_x of (4) is for $\sigma_{xx} = 10^8$ dyne/cm^2 about 10^{-15} erg, whereas the room-temperature value of kT is about 40.10^{-15} erg, so that the series expansions are indeed valid for not too high stress levels.

4. After-effect in polycrystalline specimens

The change in the elastic constants and moduli brought about by the relaxation in a polycrystalline specimen, in which the individual grains are assumed to be randomly oriented, can be described by equations analogous to (13) and (8):

$$\Delta\bar{c}_{11} = -2\bar{a}, \qquad \Delta\bar{c}_{12} = \bar{a}, \qquad \Delta\bar{c}_{44} = -\tfrac{3}{2}\bar{a}, \tag{18a}$$

$$\Delta\bar{s}_{11} = 2\bar{b}, \qquad \Delta\bar{s}_{12} = -\bar{b}, \qquad \Delta\bar{s}_{44} = 6\bar{b}. \tag{18b}$$

Barred quantities always refer to the polycrystalline material. In (18) $\Delta\bar{c}_{44}$ and $\Delta\bar{s}_{44}$ are finite, due tot the fact that with and without after-effect the material is elastically isotropic:

$$2\bar{c}_{44} = \bar{c}_{11} - \bar{c}_{12}, \tag{19a}$$

$$\bar{s}_{44} = 2(\bar{s}_{11} - \bar{s}_{12}). \tag{19b}$$

In the following we shall be concerned with the relation between $\bar{a}$ and a, and between $\bar{b}$ and b. For this it will prove useful to consider the elastic constants of cubic metals in general.

5. Connection between the elastic constants of polycrystalline specimens and those of single crystals of cubic metals

The differences between the elastic constants of a polycrystalline sample and those of a single crystal are closely connected with the elastic anisotropy of the material. For anisotropic materials the ratio

$$A = 2c_{44}/(c_{11} - c_{12}) = 2(s_{11} - s_{12})/s_{44} \tag{20}$$

differs from unity. It is a plausible assumption that the stiffness against volume-changes is the same for the polycrystalline material and the single crystal, and that only the stiffness against changes of shape is different in both cases. This assumption is justified by the approximate equality of the bulk constants $(c_{11} + 2c_{12})$ and $(\bar{c}_{11} + 2\bar{c}_{12})$ for a number of cubic metals, especially the noble metals, as is demonstrated in table I. It is therefore assumed that a universal functional relation does exist between the relative changes in the elastic constants referred to the shear constants and the anisotropy parameter A of (20). We express this presumed relation in the form

$$c_{44}/\bar{c}_{44} - \bar{c}_{44}/c_{44} = f(A - 1/A), \tag{21}$$

where f is a function independent of the bulk constants of the materials involved. A transformation from the elastic constants into the elastic moduli leaves the form of (21) unaltered, except for a change in sign of both the function and its argument.

The choice of $\bar{c}_{44}$ in (21) was made because one may expect that even if the bulk constants are not equal, $\bar{c}_{44}$ is not affected seriously. This is demonstrated in the case of tungsten (which is elastically isotropic), where the bulk constants differ by 11%, but the shear constants by 1·6% only.

TABLE I

Elastic properties at room temperature of some cubic metals, both for single crystals and for polycrystalline specimens; elastic constants in 10^{12} dynes/cm^2.

Metal	c_{11}	c_{12}	c_{44}	$c_{11}+2c_{12}$	$A-1/A$	$\bar{c}_{44}$	$\bar{c}_{11}+2\bar{c}_{12}$	$\frac{c_{44}}{\bar{c}_{44}}-\frac{\bar{c}_{44}}{c_{44}}$
Al	1·08	0·622	0·284	2·32	0·43	0·26	2·19	0·17
Fe	2·37	1·41	1·16	5·19	2·01	0·82	5·00	0·71
Ni	2·50	1·60	1·185	5·70	2·25	0·78	5·57	0·84
Cu	1·70	1·23	0·75	4·16	2·88	0·46	4·08	1·02
Ag	1·20	0·897	0·436	2·99	2·53	0·29	2·97	0·85
Au	1·86	1·57	0·420	5·00	2·55	$0·27_5$	5·08	0·88
Mo	4·6	1·79	1·09	8·18	$-0·51_5$	$1·23_5$	8·17	−0·25
W	5·01	1·98	1·514	8·97	0·00	1·49	10·03	0·03

In table I the elastic constants have been compiled for a number of cubic metals, both for single crystals and for polycrystalline materials. The single-crystal data have been taken from the review paper of Boas and Mackenzie [6]), the data referring to the polycrystalline state are those listed by Druyvesteyn [7]).

The representative points according to (21) have been plotted in fig. 1. It is seen that with reasonable accuracy a functional relationship can be established indeed. The only serious discrepancy occurs for nickel. This is probably due to the ferromagnetic ΔE-effect [8]). The values quoted apply to the unmagnetized state. Moreover, elastically highly anisotropic metals like sodium, potassium or lead do not presumably fit on the curve. It has to be borne in mind, however, that polycrystalline specimens nearly always show a certain degree of texture. The effect thereof has been neglected in our considerations.

It is of course also possible to relate the elastic constants of a polycrystalline material to those of the single crystal by means of some theoretical averaging procedure, as has been done frequently in the past.

Two extreme procedures are governed by the assumptions that any grain is in the same state of stress, or in the same state of strain. One then finds

$$c_{44}/\bar{c}_{44} = \tfrac{3}{5} + \tfrac{2}{5}\,A \text{ (uniform stress)}, \tag{22a}$$

$$\bar{c}_{44}/c_{44} = \tfrac{3}{5} + \tfrac{2}{5}\,A^{-1} \text{ (uniform strain)}. \tag{22b}$$

The functions (21) for these two cases have also been plotted in fig. 1 (dashed lines). The slopes at the origin are equal ($^2/_5$), and the position of the point referring to Al reinforces the conclusion that it is also the initial slope of the actual curve.

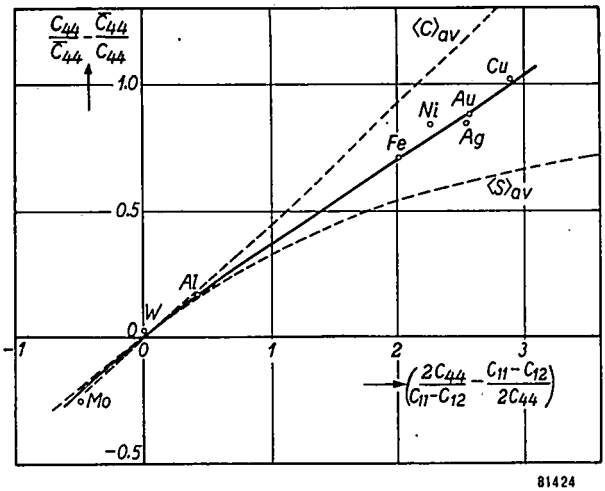

Fig. 1. Relation between elastic constants of single crystals and of polycrystalline cubic metals. The circles denote observed data referring to the various metals, the solid line drawn through these points represents presumably a general relationship. The dashed lines indicated by $<c>_{av}$ and $<s>_{av}$ show the theoretically derived relationships according to the hypotheses of uniform strain and uniform stress respectively.

6. Change of the elastic constants in polycrystalline specimens due to the after-effect

As has been discussed above, by the relaxation in α-iron the elastic constants will change, which means that the representative point for polycrystalline iron moves along the curve of fig. 1. For small changes the slope of this curve can be taken as constant, and it is found in this way, by differentiating (21) and using (13), (18a) and (20), that

$$\frac{\bar{a}}{a} = \frac{1 + (2c_{44})^2/(c_{11}-c_{12})^2}{1 + c_{44}^2/\bar{c}_{44}^2}\, f'(\text{Fe}). \tag{23}$$

The experimental slope $f'(\mathrm{Fe})$ at the point referring to iron is 0·33, hence

$$\bar{a}/a = 0{\cdot}75\,. \tag{24a}$$

For an elastically isotropic metal this ratio would be $^2/_5$. The same value is obtained by the theoretical averaging procedure according to (22b). In the case that (22a) should hold the ratio is 1·17.

The value of $\bar{b}/b$ corresponding to (24a) follows from (14):

$$\bar{b}/b = 0{\cdot}26\,. \tag{24b}$$

For an elastically isotropic metal this ratio is again $^2/_5$. The averaging procedures corresponding to (22a) and (22b) yield $^2/_5$ and 0·14 respectively.

7. Magnitude of the after-effect in polycrystalline materials

One of the purposes of internal-friction experiments in nitrogen- or carbon-containing α-iron is to determine the concentration of the foreign atoms in solid solution. These experiments are mostly carried out on polycrystalline strips or wires, which are subjected to free bending or torsional vibrations. The maximum value of the tangent of the loss-angle as a function of temperature is, using (1), equal to [9])

$$Q^{-1} = \Delta\varepsilon/2\,\varepsilon(0)\,. \tag{25}$$

If diffusion of the solute atoms over more than a few atom distances is neglected then in the case of bending (25) reduces to $\Delta\bar{s}_{11}/2\bar{s}_{11}$, which, according to (18b) and putting $\bar{s}_{11} = 1/\bar{E}$, where $\bar{E} = 2{\cdot}11.10^{12}$ dyne/cm^2 (derived from table I) is Young's modulus for the polycrystalline material, is equal to

$$\bar{Q}^{-1}_{\text{bending}} = \bar{b}\,\bar{E}\,. \tag{26}$$

For polycrystalline α-iron containing c % carbon or nitrogen by weight $\bar{Q}^{-1}_{\text{bending}}$ is, from (17) and (24b), calculated to be

$$(\bar{Q}^{-1}_{\text{bending}})_{\text{C}} = 2{\cdot}3.10^2 c_{\text{C}}/T\,, \quad (\bar{Q}^{-1}_{\text{bending}})_{\text{N}} \approx 1{\cdot}9.10^2\, c_{\text{N}}/T\,, \tag{27}$$

respectively, where T is expressed in °K.

In the case of torsion of a wire of circular cross-section (25) is equal to $\Delta\bar{s}_{44}/2\bar{s}_{44}$ which, according to (18b) and putting $\bar{s}_{44} = 1/\bar{G}$ where $\bar{G} = 0{\cdot}82.10^{12}$ dyne/cm^2 (see table I) is the modulus of rigidity of α-iron, is equal to

$$\bar{Q}^{-1}_{\text{torsion}} = 3\,\bar{b}\,\bar{G}\,. \tag{28}$$

For polycrystalline α-iron containing c % carbon or nitrogen by weight it is found that

$$(\bar{Q}^{-1}_{\text{torsion}})_C = 2{\cdot}7.10^2\, c_C/T, \quad (\bar{Q}^{-1}_{\text{torsion}})_N \approx 2{\cdot}2.10^2\, c_N/T, \tag{29}$$

respectively.

Recently Fast and Verrijp [10])*) have been able to measure very accurately the dependence of the after-effect on the concentration of solute N atoms in polycrystalline α-iron without texture, finding for torsional vibrations:

$$c_N = 1{\cdot}26\ (\bar{Q}^{-1}_{\text{torsion}})_N \quad \text{at } 22\ ^\circ\text{C}.$$

According to (29) this factor 1·26 should be $295/2{\cdot}2.10^2 \approx 1{\cdot}3$, so that the agreement is satisfactory.

---

*) We thank Prof. Fast for showing us his results prior to publication.

Eindhoven, August 1954

REFERENCES

1) J. L. Snoek, Physica **8**, 711-733, 1941; see also: New developments in ferromagnetic materials, Elsevier Publ. Comp., Inc., New York, Amsterdam, 1947, pp. 46-53; L. J. Dijkstra, Philips Res. Rep. **2**, 357-381, 1947.
2) D. Polder, Philips Res. Rep. **1**, 5-12, 1945.
3) J. D. Fast and M. B. Verrijp, J. Iron St. Inst. **176**, 24-27, 1954.
4) C. S. Roberts, J. Metals **5**, 203-204, 1953.
5) B. N. Bose and M. F. Hawkes, Trans. Amer. Inst. min. (metall.) Engrs **188**, 307-316, 1950.
6) W. Boas and J. K. Mackenzie, Progr. Metal Phys. **2**, 90-120, 1950.
7) M. J. Druyvesteyn, Philips Res. Rep. **1**, 77-80, 1945.
8) See for instance R. M. Bozorth, Ferromagnetism, D. van Nostrand Comp., Inc., New York, 1951, p. 684.
9) C. Zener, Elasticity and anelasticity of metals, University of Chicago Press, Chicago, 1948, p. 43.
10) J. D. Fast and M. B. Verrijp, to be published in J. Iron St. Inst.

LUMINESCENCE OF F-CENTRES IN ALKALI-HALIDE CRYSTALS

by Th. P. J. BOTDEN, C. Z. van DOORN and Y. HAVEN

535.37:546.13-162

Summary

Crystals of KCl, KBr, KI, NaCl and RbCl coloured additively have been irradiated in the F absorption band at liquid-hydrogen and liquid-nitrogen temperatures. In all crystals an infrared luminescence has been observed between about 1 and 1·5 μ. The luminescence is quenched at temperatures above 100-150 °K. The quantum efficiency is very low and the luminescence only appears when the crystals are kept at low temperatures after the formation of the F-centres and quenching in liquid nitrogen. Different results are obtained when the crystals are kept at room temperature in the dark or during irradiation. It is believed that the infrared emission is to be ascribed to F-centres.

Résumé

Les cristaux de KCl, KBr, KI, NaCl et RbCl colorés additivement ont été irradiés dans la bande d'absorption F aux températures de l'hydrogène et du nitrogène liquides. L'on a observé dans tous les cristaux une luminescence infra-rouge comprise entre 1 et 1,5 μ environ. La luminescence s'éteint aux températures comprises entre 100 et 150 °K. Le rendement quantique est très faible et la luminescence n'apparaît que lorsque les cristaux sont maintenus à des basses températures après la formation des centres F et la trempe dans le nitrogène liquide. Des résultats différents sont obtenus lorsque les cristaux sont maintenus à la température ambiante dans l'obscurité ou en cours d'irradiation. L'on pense que l'émission infra-rouge doit être attribuée aux centres F.

Zusammenfassung

Additiv verfärbte Kristalle von KCl, KBr, KJ, NaCl und RbCl wurden bei Temperaturen flüssigen Wasserstoffs und flüssigen Stickstoffs in der F-Absorptionsbande bestrahlt. Bei allen Kristallen wurde eine infrarote Lumineszenz zwischen etwa 1 und 1,5 μ festgestellt. Die Lumineszenz wird bei Temperaturen oberhalb von 100-150 °K gelöscht. Die Quantenausbeute ist sehr niedrig, und die Lumineszenz tritt lediglich dann auf, wenn die Kristalle nach Bildung der F-Zentren und Abschreckung in flüssigem Stickstoff bei niedrigen Temperaturen gehalten werden. Wenn die Kristalle im Dunkeln oder während der Bestrahlung Zimmertemperatur ausgesetzt werden, erzielt man abweichende Ergebnisse. Angenommen wird, daß die Infrarot-Emission den F-Zentren zugeschrieben werden muß.

1. Introduction

According to various theoretical investigations [1)2)3)] F-centres in alkali halides should show a luminescence at not too high temperatures with a quantum efficiency of practically 1.

Extensive experimental research to find this luminescence has been carried out by Klick [4)]. However, he could not find F-centre luminescence

above the limit of detection for his set-up, which corresponds to a quantum efficiency of 3 %, in LiF darkened at 4 °K by X-rays and in KCl coloured additively. Until now the only trace of an emission which might be due to F-centres has been found by Ghormley and Levy [5]) with KCl crystals coloured electrolytically*).

As more detailed information about the existence and the nature of any F-centre luminescence is of great interest from a theoretical point of view, we searched for F-centre luminescence in samples of NaCl, KCl, KBr, KI and RbCl. In this paper some experimental results will be given.

2. Preparation of the samples

Single crystals were grown from the melt, using analytical reagent chemicals (Merck) for NaCl, KCl, KBr and KI, and a material of unknown origin for RbCl.

The crystals were coloured by heating them at about 100 °C below the melting point in the metal vapour of Na and K respectively. Then the crystals were heated for 1 to 2 minutes in air, quenched in liquid nitrogen and kept at liquid-nitrogen temperature during the further operations.

Also, some samples were coloured electrolytically: the crystals were electrolysed at about 100 degrees below the melting point between a graphite plate cathode and a platinum point anode, with an electric field of about 200-500 V/cm. After the colouring had reached the cathode the crystals were quenched in liquid nitrogen. The RbCl crystals were coloured electrolytically only.

The concentration of F-centres was estimated from optical absorption data to be about 10^{16}-10^{18} cm^{-3}. The colour density of the electrolytically coloured crystals, however, was rather inhomogeneous.

3. Methods of measurements

The crystals were irradiated by a water-cooled super-high-pressure mercury lamp (d.c. 1000 watts; Philips S.P. 57302/2c), which was focussed on the crystals by a lens (focal length 8 cm, diameter 7 cm).

The infrared was filtered out with a 1-cm thick layer of a $CuSO_4$ solution or a glass filter (Chance ON20). Irradiation was carried out mainly in the F absorption bands of the crystals with the Schott filters BG12, VG9, RG1, RG5 and RG8. The emission spectra were taken with an automatically recording apparatus made in our laboratory. The apparatus is composed of a quartz double monochromator with wavelength-drive motor, light chopper intermitting 800 times per second, PbS cell with amplifier tuned

*) A luminescence that is not due to F-centres is described for LiF by Klick [4]), and for LiF and NaF by Feofilov [10]).

at 800 c/s, and recorder (Philips PR 4010 M/01). After the measurement the recorded curves were corrected for the change in sensitivity with wavelength of the PbS cell (in combination with the monochromator), with the aid of a calibrated tungsten lamp.

For measurements at low temperatures the crystals were placed in a quartz dewar vessel with liquid nitrogen or hydrogen; the bottom part of the vessel was left unsilvered. For the temperature dependence of the emission intensity the temperature was determined with a thermocouple pressed against the crystal. After evaporation of the liquid nitrogen or hydrogen the crystal warms up slowly, whilst the intensity of the peak of emission is measured at various temperatures during short exposures. The accuracy of the determination of the temperature is 5-10 degrees, since the crystal is heated by the exciting radiation. The quantum efficiency was calculated from the spectral distribution of the exciting radiation (measured via a MgO screen and integrated over the F absorption band) and the integrated emission spectrum. In this way the quantum efficiency will not be very accurate as, moreover, the geometrical distribution of the emitted radiation is not well known,

4. Experimental results

After quenching of the coloured crystals to liquid-nitrogen temperature, they were not warmed up until absorption and emission spectra had been measured.

The position and shape of the F-centre absorption bands, measured in KCl, KBr, KI, NaCl and RbCl, agree with the F-bands given by Mollwo [6]).

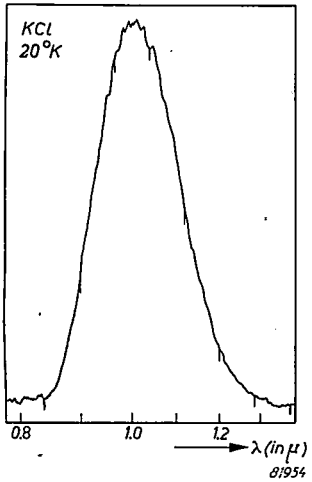

Fig. 1. Example of a recorded emission curve of coloured KCl at 20 °K. The vertical dashes on the curve are wavelength indications.

After it had been verified that the same emission bands were measured when holding in the exciting beam, in addition to the infrared-absorbing filter, a Schott filter that causes excitation mainly in the F-band, most measurements were carried out with the infrared-absorbing filter only. We also checked that no emission was found when the wavelength region corresponding to the F absorption band was filtered out from the exciting radiation.

In fig. 1 an example is given of the emission curve of a coloured KCl crystal at 20 °K, as it was shown on the recorder, uncorrected for the change in sensitivity with wavelength *).

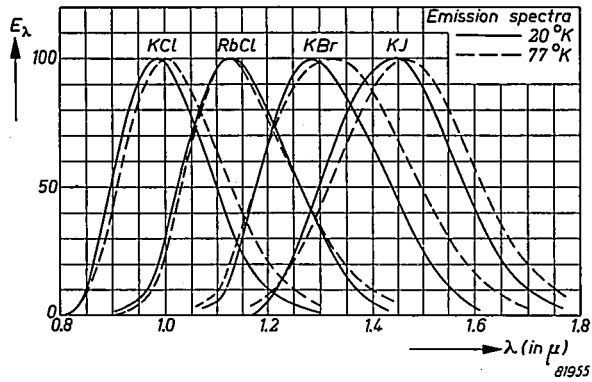

Fig. 2. Emission spectra of additively coloured KCl, KBr, KI and RbCl at 20 °K (full lines) and 77 °K (dashed lines).

Fig. 2 shows the (corrected) emission curves for the coloured crystals of KCl, KBr, KI and RbCl, at 20 °K and 77°K. Several crystals of each halide were measured, both coloured additively in the metal vapour phase and by electrolysis. For KCl and KBr the curves were found to be equal in all cases. For RbCl one crystal showed a curve that was somewhat broadened. The curves for KI varied slightly in band width and in position of the maxima (up to 0·02 μ to longer or shorter wavelengths); in fig. 2 the average curve is given.

For NaCl the results are quite complicated; some curves are given in fig. 3. The peaks of emission varied from 1·14 to 1·22 μ at 77 °K, whereas in one crystal two peaks were found at 1·12 and 1·24 μ. Further experiments will be carried out to provide more information about this complicated behaviour.

The values of the change of the half width of the emission bands from 20 to 77 °K were obtained by keeping the crystals at the same position

*) In this case the slit width was 0·15 mm, corresponding to a band width of about 0·015 μ. The slit width has been varied from 0·1 to 0·4 mm, depending on the emission intensity of the various crystals.

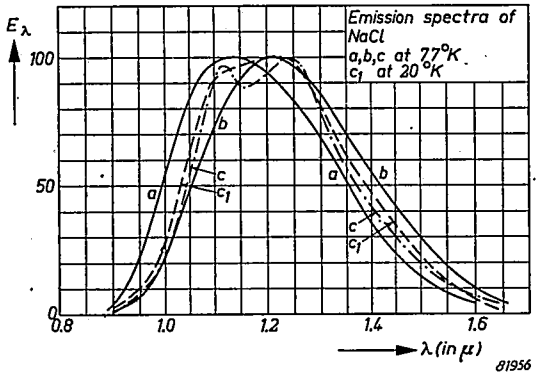

Fig. 3. Emission spectra at 77 °K of various crystals (*a*, *b* and *c*) of NaCl coloured additively; curve c_1 pertains to the same crystal as curve *c* and is taken at 20 °K.

during the measurements in order to eliminate the effect of inhomogeneities of the crystals. The results are given in table I, which also gives the maxima of the emission bands and the half widths of the F absorption bands according to Mollwo [6]).

TABLE I

Type of coloured crystals	Maximum of the F emission band		Half-value width		Broadening of the band from 20 to 77 °K	Half-value width of the F absorption band (Mollwo)
	at 20 °K	at 77 °K	at 20 °K	at 77 °K		
KCl	$0{\cdot}98_5$ μ	$1{\cdot}00_5$ μ	0·263 eV	0·269 eV	0·006 eV	0·23 eV at 87 °K
			0·256	0·264	0·008	
KBr	$1{\cdot}28_5$	$1{\cdot}32_5$	0·201	0·221	0·020	0·22 at 87 °K
			0·191	0·225	0·034	
KI	1·45	1·47	0·153	0·150	—0·003	$0{\cdot}19_5$ at 28 °K
			0·175	0·177	0·002	
RbCl	1·12	$1{\cdot}12_5$	0·224	0·230	0·006	0·22 at 113°K
NaCl		1·12-1·24	—	—	—	

The quantum efficiency was found to be very low, of the order of one per cent.

The temperature dependence of the intensity of emission for the various crystals is shown in fig. 4. The emission is quenched already at low temperatures. When the crystals are warmed up to the temperature at which the luminescence is practically quenched and are cooled again, then the emission comes up again and reaches the same intensity at low temperatures as before. Irradiation for half an hour at 77 °K did not give a change in intensity either, but remarkable effects occurred when the crystals were warmed up to room temperature.

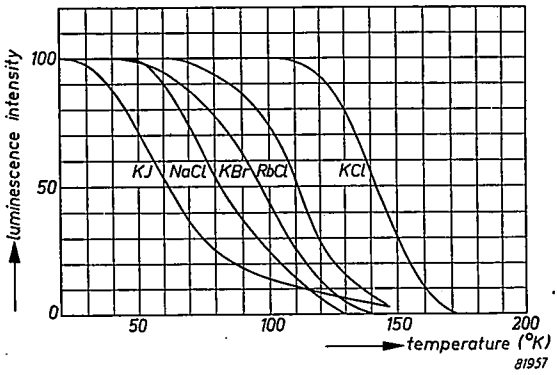

Fig. 4. Temperature dependence of the luminescence intensity in additively coloured alkali-halide crystals which have been kept at low temperatures.

When the crystals were irradiated for 15 minutes at about 350 °K, then no emission could be found again at 77 °K.

When the crystals were kept in the dark at room temperature for about 15 hours, the emission bands at 77 °K undergo considerable changes, as may be seen in figs 5, 6 and 7; only in KI could no emission be found. All the new bands are shifted to a longer wavelength, compared with the bands mentioned before, whereas in KCl and RbCl two bands appeared.

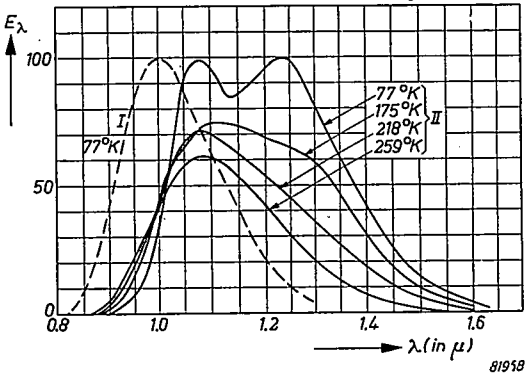

Fig. 5. Emission spectra of coloured KCl. Curve *I* and curves *II* apply to before, respectively after keeping the crystal at room temperature for 15 hours in the dark.

In KCl a new absorption band appeared at about 0·81 μ in addition to the F-band. Irradiation through the green VG9 filter favoured the short-wave band at 1·07 μ, while with the RG5 filter the long-wave band at 1·24 μ was relatively increased; but in both cases the two emission bands were present. The 1·24-μ band is quenched at lower temperatures than the

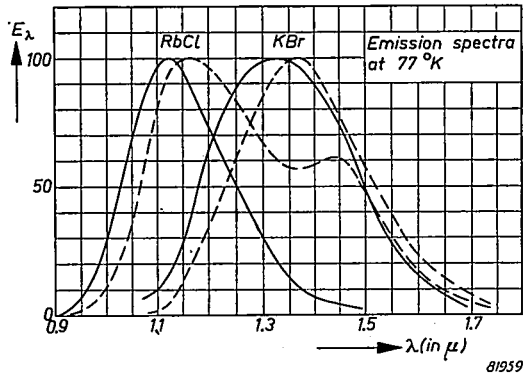

Fig. 6. Emission spectra of coloured RbCl and KBr at 77 °K. Full lines before and dashed lines after keeping the crystals at room temperature for 15 hours in the dark.

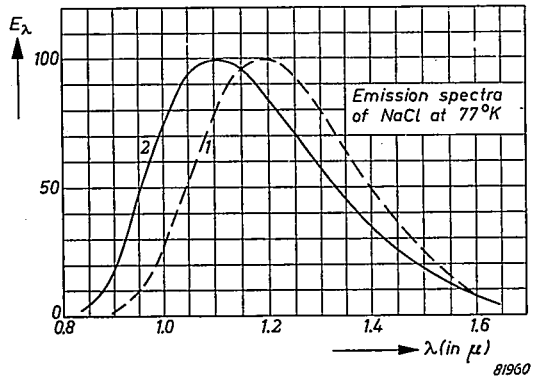

Fig. 7. Emission spectra of coloured NaCl at 77 °K. (1) before and (2) after keeping the crystal at room temperature for 15 hours in the dark.

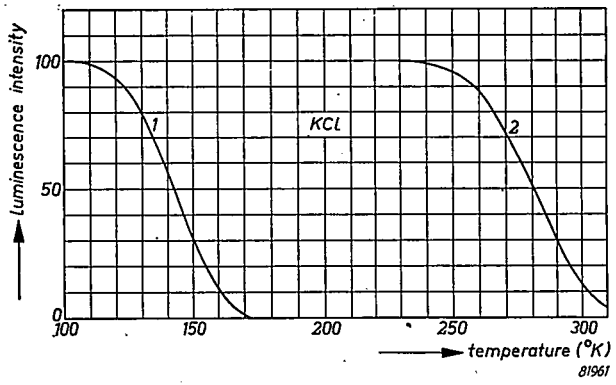

Fig. 8. Temperature dependence of the luminescence intensity in coloured KCl. Curve 1 before and curve 2 (for the 1·07-μ emission band) after keeping the crystal at room temperature for 15 hours in the dark.

1·07-μ band (fig. 5). The temperature dependence of the 1·07-μ band is given in fig. 8.

Irradiation for 15 minutes at room temperature now also caused the disappearance of the emission at low temperatures.

5. Discussion

It has been shown that excitation in the F-band of crystals of KCl, KBr, KI, NaCl and RbCl, coloured additively both in vapour phase and by electrolysis, does lead to emission in the infrared. In all crystals of the same type the situation and band width of the bands were almost independent of the F-centre concentration and the method of colouration; only the various samples of NaCl showed remarkable differences.

The emission bands in the various halides appeared only at excitation in the F absorption band. This fact and the position of the emission bands make it very probable that the observed emission is indeed due to F-centre fluorescence.

As regards the position of the emission bands theoretical predictions have been made by Pekar [2]), by Meyer *) and by Klick [4]). In table II the predicted values and the experimental results are given.

TABLE II. Positions of F-centre emission bands

	Theoretical values according to			Experimental values
	Pekar	Meyer (at 20 °K)	Klick	
KCl	1·31 μ	1·14 μ	—	$1{\cdot}00_5$ μ
KBr	1·35	1·40	1·2 μ	$1{\cdot}32_5$
KI	1·39	1·55	—	1·47
RbCl	—	1·01	—	$1{\cdot}12_5$
NaCl	1·25	1·98	—	1·12-1·24

The good agreement between theory and experiment, present in all cases except NaCl, is probably somewhat fortuitous *); but it supports our view that the observed emission is due to F-centres.

However, contrary to the theory, which predicts a quantum efficiency of 1, the quantum efficiency was found experimentally to be only of the order of 0·01. Although the efficiency measurements were not accurate until now, it is certain that the quantum efficiency is much lower than 1 **).

*) H. J. G. Meyer, private communication.

**) This may account for the fact that Klick did not find an emission (it may be remarked that from his paper it is not clear whether the crystals were kept at low temperatures or were irradiated at higher temperatures before cooling them).

The origin of this discrepancy is not known at present; we are inclined to believe that it has to be found in the interaction of the F-centre with some other impurity rather than in its interaction with the thermal vibrations of the "perfect" lattice alone.

As regards the temperature dependence of the intensity of the emitted radiation, it seems rather improbable that the rapid quenching of the emission between 100 and 150 °K is due to a *direct* radiationless transition of the excited F-centre to its ground state. It might be that the transformation $F \rightarrow F'$ is in some way connected with the observed quenching. According to Pick [7]) the F-centres are destroyed by irradiation in KCl, KBr and NaCl, and F'-centres are produced in the temperature ranges that correspond to those in which we observed quenching of luminescence. Rögener [8]) has shown that in the corresponding temperature ranges the photoconductivity in NaCl and KCl also changes remarkably.

The irreversible changes in the behaviour of the crystals with respect to emission, which are brought about by strong irradiation at room temperature or by keeping the crystals at this temperature in the dark for 15 hours, are possibly connected with the formation of other centres [9]) as e.g. M-centres.

In this connection it is doubtful whether the emission band found by Ghormley and Levy [5]) in KCl at wavelengths somewhat longer than 1 μ is characteristic of the F-band, since its behaviour is the same as that found by us in a KCl crystal kept at room temperature for 15 hours.

In conclusion it may be said that as yet the experimental situation is much too complicated to allow of any definite conclusions. Further work is now in progress from which it is hoped to obtain some insight into the mechanisms active in the observed phenomena.

Acknowledgement

The authors are indebted to their colleague H. J. G. Meyer for stimulating the work and for the many valuable discussions.

Eindhoven, September 1954

REFERENCES

[1]) K. Huang and A. Rhys, Proc. roy. Soc. A **204**, 406-423, 1950.
[2]) S. I. Pekar, J. exp. theor. Phys., Moscow **22**, 641-654, 1952.
[3]) H. J. G. Meyer, Physica **20**, 1954, in the press.
[4]) C. C. Klick, Phys. Rev. **79**, 894-896, 1950; **94**, 1541-1545, 1954.
[5]) J. A. Ghormley and H. A. Levy, J. phys. Chem. **56**, 548-554, 1952.
[6]) E. Mollwo, Z. Phys. **85**, 56-67, 1933.
[7]) H. Pick, Ann. Phys., Lpz. **5**, 365-376, 1938.
[8]) H. Rögener, Nachr. Ges. Wiss. Göttingen **3**, 219-225, 1941.
[9]) St. Petroff, Z. Phys. **127**, 443-454, 1950.
[10]) P. P. Feofilov, C. R. Acad. Sci. U.R.S.S. **92**, 743-746, 1953; J. exp. theor. Phys., Moscow **26**, 609-623, 1954.

AUTHOR INDEX

INDEX ACCORDING TO THE UNIVERSAL DECIMAL CLASSIFICATION SYSTEM